NBS SPECIAL PUBLICATION 387

Laser Induced Damage In Optical Materials: 1973

U.S.
ARTMENT
OF
MMERCE
National
Bureau
of
Standards

NATIONAL BUREAU OF STANDARDS

The National Bureau of Standards [1] was established by an act of Congress March 3, 1901. The Bureau's overall goal is to strengthen and advance the Nation's science and technology and facilitate their effective application for public benefit. To this end, the Bureau conducts research and provides: (1) a basis for the Nation's physical measurement system, (2) scientific and technological services for industry and government, (3) a technical basis for equity in trade, and (4) technical services to promote public safety. The Bureau consists of the Institute for Basic Standards, the Institute for Materials Research, the Institute for Applied Technology, the Institute for Computer Sciences and Technology, and the Office for Information Programs.

THE INSTITUTE FOR BASIC STANDARDS provides the central basis within the United States of a complete and consistent system of physical measurement; coordinates that system with measurement systems of other nations; and furnishes essential services leading to accurate and uniform physical measurements throughout the Nation's scientific community, industry, and commerce. The Institute consists of a Center for Radiation Research, an Office of Measurement Services and the following divisions:

Applied Mathematics — Electricity — Mechanics — Heat — Optical Physics — Nuclear Sciences [2] — Applied Radiation [2] — Quantum Electronics [3] — Electromagnetics [3] — Time and Frequency [3] — Laboratory Astrophysics [3] — Cryogenics [3].

THE INSTITUTE FOR MATERIALS RESEARCH conducts materials research leading to improved methods of measurement, standards, and data on the properties of well-characterized materials needed by industry, commerce, educational institutions, and Government; provides advisory and research services to other Government agencies; and develops, produces, and distributes standard reference materials. The Institute consists of the Office of Standard Reference Materials and the following divisions:

Analytical Chemistry — Polymers — Metallurgy — Inorganic Materials — Reactor Radiation — Physical Chemistry.

THE INSTITUTE FOR APPLIED TECHNOLOGY provides technical services to promote the use of available technology and to facilitate technological innovation in industry and Government; cooperates with public and private organizations leading to the development of technological standards (including mandatory safety standards), codes and methods of test; and provides technical advice and services to Government agencies upon request. The Institute consists of a Center for Building Technology and the following divisions and offices:

Engineering and Product Standards — Weights and Measures — Invention and Innovation — Product Evaluation Technology — Electronic Technology — Technical Analysis — Measurement Engineering — Structures, Materials, and Life Safety [4] — Building Environment [4] — Technical Evaluation and Application [4] — Fire Technology.

THE INSTITUTE FOR COMPUTER SCIENCES AND TECHNOLOGY conducts research and provides technical services designed to aid Government agencies in improving cost effectiveness in the conduct of their programs through the selection, acquisition, and effective utilization of automatic data processing equipment; and serves as the principal focus within the executive branch for the development of Federal standards for automatic data processing equipment, techniques, and computer languages. The Center consists of the following offices and divisions:

Information Processing Standards — Computer Information — Computer Services — Systems Development — Information Processing Technology.

THE OFFICE FOR INFORMATION PROGRAMS promotes optimum dissemination and accessibility of scientific information generated within NBS and other agencies of the Federal Government; promotes the development of the National Standard Reference Data System and a system of information analysis centers dealing with the broader aspects of the National Measurement System; provides appropriate services to ensure that the NBS staff has optimum accessibility to the scientific information of the world. The Office consists of the following organizational units:

Office of Standard Reference Data — Office of Technical Information and Publications — Library — Office of International Relations.

---

[1] Headquarters and Laboratories at Gaithersburg, Maryland, unless otherwise noted; mailing address Washington, D.C. 20234.
[2] Part of the Center for Radiation Research.
[3] Located at Boulder, Colorado 80302.
[4] Part of the Center for Building Technology.

Laser Induced Damage In Optical Materials: 1973

Proceedings of a Symposium Sponsored by
Office of Naval Research
The American Society for Testing and Materials
And by the National Bureau of Standards

May 15-16, 1973
NBS, Boulder, Colorado 80302

Edited by

Alexander J. Glass
Lawrence Livermore Laboratory
Livermore, California 94550

and

Arthur H. Guenther
Air Force Weapons Laboratory
Kirkland AFB, New Mexico 87117

U.S. DEPARTMENT OF COMMERCE, Frederick B. Dent, *Secretary*
NATIONAL BUREAU OF STANDARDS, Richard W. Roberts, *Director*

Issued December 1973

Library of Congress Catalog Number: 73-600331

National Bureau of Standards Special Publication 387

Nat. Bur. Stand. (U.S.), Spec. Publ. 387, 285 pages (Dec. 1973)

CODEN: XNBSAV

U.S. GOVERNMENT PRINTING OFFICE
WASHINGTON: 1973

For sale by the Superintendent of Documents, U.S. Government Printing Office, Washington, D.C. 20402
(Order by SD Catalog No. C13.10:387.) Price $2.65 cents.

Foreword

These proceedings report in detail the formal papers presented at the 5th Annual Symposium on Laser Damage in Optical Materials held at the National Bureau of Standards, Boulder, Colorado on May 15 and 16, 1973. This meeting was jointly sponsored by the Office of Naval Research, National Bureau of Standards, and the American Society of Testing and Materials. The major topics covered were damage at dielectric surfaces, damage due to self-focusing, damage to dielectric coatings, and damage to mirrors and windows in the infrared, as well as theoretical studies and the reporting of fundamental properties important in the damage process.

The co-chairmen, Dr. Alexander J. Glass of Lawrence Livermore Laboratory, Livermore, California, and Dr. A. H. Guenther of the Air Force Weapons Laboratory, Kirtland AFB, New Mexico, take full responsibility for the summary, conclusions, and recommendations contained in this report, as well as the summaries of the discussions at the conclusion of each presentation. It is suggested that individuals interested in the subject of this meeting obtain copies of those publications referenced in the bibliography contained in the summary and conclusions.

It is our intention to convene another symposium next year in Boulder during May to update and document the state of the art of Laser Damage in Optical Materials at that time. This meeting will cover the subject historically presented at these symposia with additional emphasis on thin film damage, the problem of the damage of materials and components at 10.6 μm, as well as address ourselves to the subject of optical reliability as influenced by laser applications. Hopefully, reports relating to very short pulses, short wavelengths, and multipulse damage effects will be heard. We wish to encourage the reader to contact us on matters pertinent to the intent of these conferences.

A. H. Guenther

Contents

OPTICAL COATING DAMAGE

DAMAGE TO INFRARED COMPONENTS

THEORY AND FUNDAMENTAL PROPERTIES

Laser Induced Damage in Optical Materials
5th ASTM Symposium
May 15-16, 1973

Abstract

The Fifth ASTM-ONR-NBS Symposium on Laser Induced Damage in Optical Materials was held at the National Bureau of Standards in Boulder, Colorado on May 15 and 16 of this year. These Symposia are held as part of the activities of Subcommittee II on Lasers and Laser Materials, of the ASTM. Subcommittee II is charged with the responsibilities of formulating standards and test procedures for laser materials, components, and devices. The chairman of Subcommittee II is Haynes Lee, of Owens-Illinois, Inc. Co-chairmen for the Damage Symposia are Dr. Arthur H. Guenther, Scientific Director, Technology Division of the Air Force Weapons Laboratory, and Dr. Alexander J. Glass, Head, Basic Studies, Y Division, Lawrence Livermore Laboratory.

Approximately 135 attendees at the Symposium heard 25 papers on topics relating to laser induced damage in crystalline and non-linear optical materials, at dielectric surfaces, and in thin film coatings as well as discussions of damage problems in the infrared region due both to cw and pulsed irradiation. In addition, several reports on the theoretical analysis of laser-materials interaction, relative to the damage process were given, along with tabulations of fundamental materials properties of importance in evaluation of optical material response to high power laser radiation. Several papers presented by title only are included within the proceedings for completeness.

The proceedings of these Symposia represent the major sources of information in the field of laser induced damage in optical materials. The Symposia themselves, along with the periodic meetings of Subcommittee II, provide a unique forum for the exchange of information regarding laser materials specifications among the manufacturers and users of laser devices, components, and systems. The Symposia also serve as a mechanism of information gathering to enable the Subcommittee to write informed and realistic specifications.

Key Words: IR windows and mirrors, laser damage, laser materials, self-focusing, thin films.

1. Principal Conclusions

During the 1973 Symposium on Damage in Laser Materials several specific topics received considerable attention. The papers presented to the approximately 135 specialists in attendance can logically be separated into categories on self-focusing damage, surface damage, coating damage, infrared component damage, and theory and fundamental properties. Highlighting the meeting were papers on small-scale self-focusing, the importance of surface or near-surface absorbing impurities as a major extrinsic influence in reducing the intrinsic damage level of coated and uncoated surfaces, development of new instrumental methods for evaluation of material properties important in the damage process, initial attempts at cataloguing these important properties, and finally, several reports on the spectral frequency and temportal aspects of laser-induced damage in a variety of materials, from the visible to the infrared, and from subnanosecond pulsed exposures to cw.

The past year has seen a remarkable increase in interest in detailed design considerations for subnanosecond, Nd glass lasers for fusion research. An almost universal conclusion has been reached, that the power density which can be transmitted in a subnanosecond pulse in glass is limited to a value of $<10^{10}$ W/cm^2. At this power density, the phase and amplitude distrubution of the beam is unstable against the formation of minute, intense filaments, with diameters of hundreds of microns, with consequent fine-scale damage and attendant increased scattering. These intensified regions can be initiated by the random inhomogeneities unavoidably present in the laser glass as well as defects or nonuniformities in coatings, surface finishes, etc. The effect of gain in the medium is to enhance the effect slightly,

but the major conclusions remain the same in pumped or unpumped systems, with or without weak focusing. In disk systems, the relative length of the disks and their separation may marginally influence the small-scale self-focusing. However, the range of spatial frequencies over which the instability can grow is sufficiently broad that geometrical factors have little influence on the instability. Clearly, geometrical considerations are important for the overall system design, and only detailed calculations can be relied upon to determine optimum operating levels.

The basic parameter for self-focusing is the index nonlinearity, n_2, or equivalently, the critical power, P_1. At present, there is an uncertainty in the best value of n_2 for common transparent dielectrics of a factor of two. Measurements by individual observers, however, show a much greater degree of internal consistency, and the relative values of n_2 can be inferred to something like 15%. There is a general trend for higher index materials to exhibit higher values of n_2, but the exact scaling of n_2 with material parameters remains unclear. There remains a considerable amount of work to be done on elucidating the relative contributions of various phenomena to the measured value of index nonlinearity.

While the ultimate or intrinsic strength of materials, within the bulk or on their surface, is related to an avalanche process, components encountered in practical situations exhibit lower damage levels, due mainly to various extrinsic influences. Two such major factors have been identified. They are field enhancement, caused by mechanical imperfections such as pits and scratches, and absorbing impurities. The influence of these types of defects has been carefully studied, and correlation with analytical models verified. Both failure modes are probabilistic in nature, and statistical models have been proposed and examined for both cases. From these observations it is obvious that only surfaces free of defects and impurities can achieve the same intrinsic damage level as the impurity-free bulk material. This has been well demonstrated over small areas. Of course, the production of large size, defect-free surfaces, while maintaining requisite geometrical tolerances, is a major engineering problem.

Some interesting empirical observations are worth mentioning. In general, for both thin films and bare surfaces, damage resistance seems to increase as materials of lower refractive index are employed. This trend is not solely attributable to the reduced effect of Fresnel reflections. Furthermore, in the investigation of surface damage in optical glasses, higher index materials exhibit a "pre-plasma" damage, unaccompanied by luminous plasma, with a threshold lower than that for plasma formation. This pre-plasma damage is not seen in lower refractive index glasses. Clearly, the observation of luminous plasma is not an adequate indication of surface damage when other mechanisms of damage can occur.

For many glasses, the choice of polishing compound does not seem to be important, with the exception of jewelers rouge (Fe_2O_3), which produces inordinately low damage threshold surfaces. However, with proper cleaning (e.g. slight acid etch or collodion cleaning), the damage threshold of the surface can be raised to the bulk value. Apparently surfaces can exhibit higher damage resistance levels when cleaned properly, whether by acid etch or ion planing (both of which also remove mechanical defects), collodion cleaning, or even low level laser irradiation.

For the specific case of thin films, there appears to be a definite relationship between the most damage sensitive absorbing particle size and the pulse length, just as in the case of bulk inclusions analyzed at a previous symposium. Longer (nanosecond) pulses interact more easily with larger defects than shorter (picosecond) pulses. Lower index materials can be expected to exhibit greater damage resistance, assuming that the films are produced suitably defect-free. One should not overlook the many, many other factors which can reduce damage resistance of thin dielectric films. While it is encouraging that on small area irradiation consistently higher damage levels are evidenced, there is still much work to be done on film variables. This will become evident later when we discuss infrared problems.

In the infrared component area, the assessment of damage in terms of a few basic and universal physical principles is much more difficult, because of the multitude of laser characteristics and component structures employed. Lasers operated cw, pulsed, and at various repetition rates produce different effects in amorphus, crystalline, or polycrystalline materials depending upon the presence or absence of coatings on the surfaces of different microscopic structures. An example is that for many cases plasmas can be produced at the surface of alkali halide crystals without concurrent structural modification. In fact, in experiments performed at a power level below that for catastrophic damage, a plasma is observed initially, which grows less intense on successive irradiations, and finally disappears entirely. These surfaces can then handle higher power densities without damage, due to this conditioning process. For defect and impurity-free surfaces, damage thresholds, in terms of the amplitude of the electron field, are identical to bulk values. This intrinsic strength (equal to the dc breakdown field) is achieved under pulsed conditions regardless of crystalline orientation. However, when these same materials (alkali halides) are subjected to high power cw loading, definite orientational effects are noted. Here the thermally induced stress components introduced in the crystalline material by residual absorption can be correlated quite adequately by invoking the critical resolved shear stress law.

For either pulsed or cw irradiation, alloys or mixtures of two materials tend to damage at a level intermediate to the levels for the two individual components. However, in essentially all cases coatings have led to a marked reduction in damage resistance over that exhibited by the bare surface.

In spite of these differences compared to the situation for glasses in the visible, the understanding of damage processes in the infrared is increasing. Since there are many variables, more investigation is necessary, particularly if synergistic effects occur. As more data becomes available, material properties important in the damage process are being identified, and instruments suitable for "in process" or quality control applications are becoming available. Thus, techniques for measuring absorption in thin films or in the bulk of materials have been developed, as has the scatterometer, to measure surface roughness or defect concentration.

With the growing interest in infrared laser systems at high power, much of the effort spent in previous years on the properties of laser glass, for example, is now being directed towards understanding the basic properties of infrared window materials. Alkali halides and semiconductors are the materials of choice for infrared window applications at present. There has been considerable advance in relating fundamental properties of these crystals to their basic optical parameters, especially those important at high flux levels, like photoelasticity and nonlinear absorption. These theoretical advances are of great value, especially in separating impurity effects from intrinsic properties. The latter are irrevocably given, of course, while the former can be reduced by material or processing improvements.

One of the most fruitful areas for research on damage in the infrared has been on coated and uncoated mirrors. Since electric fields are highest in the outer layers of coated reflecting optics, the effects of substrate surface quality can be minimized, thus attaining a more controlled analysis of the various interactions and damage mechanisms operative in different materials classes. Through this type of investigation, definite conclusions have been reached concerning electrical, thermal, and inclusion initiated processes in metal surfaces, as well as both narrow and wide band gap dielectric materials. Generally speaking, narrow band gap, II-VI semiconductors exhibit very low pulsed damage thresholds, while wide band gap dielectrics often exhibit a damage level considerably higher than even bare metal structures.

The nature of avalanche ionization is increasingly well understood, and this process is held responsible for both bulk and surface damage in glasses and alkali halides. There remains some uncertainty regarding the intrinsic damage processes in other materials, especially at longer wavelengths. As laser operations goes to longer pulse lengths, approaching cw, thermal limitations take over.

Various approaches to understanding the nature of surface damage and the role of surface states in the damage process are evolving. Of particular interest are those experimental techniques which relate the electrical or electronic properties of the surface or sub-surface layer to observed morphological changes on the surface under intense illumination. Methods such as exoelectron studies and surface conductivity measurements promise both enhanced understanding of surface changes and the possible development of nondestructive testing methods for estimating surface damage resistance.

Damage in nonlinear optical material is governed by the same considerations as in other transparent dielectrics. The effects of multiple frequencies remain uncertain, although this year, work was presented showing no significant difference in damage with and without second harmonic generation, a result in conflict with that reported in the past.

A rather significant conclusion which may be drawn is that by the use of so-called super-polishing techniques, and by careful attention to surface treatment, surface damage levels can be brought up to the intrinsic bulk value for transparent dielectrics, at least for small areas.

2. Summary of Papers

The papers included in the Proceedings of the 1973 Symposium can be logically divided into five categories. They are: Self-Focusing Damage, Surface Damage, Coating Damage, Infrared Component Damage, and Theory and Fundamental Properties. Several papers were presented in each category. In some cases it has been difficult to place a given paper into one particular category, so that the reader is encouraged to scan the discussion of each of the topical areas. The following summaries are intended to provide the reader with a brief but coherent review of the salient features of the included material and to draw his attention to papers of specific interest.

2.1 Self-Focusing

The intensity-dependent change in the index of refraction of a transparent dielectric leads to the concentration of light energy in regions of high intensity. This phenomenon, known as self-focusing, is the principal limiting factor in the design of high power, short pulse, solid state laser systems. The index nonlinearity is characterized by a single parameter of the material, n_2, on the order of 10^{-13} esu for most transparent solids. The nonlinearity can arise from several causes, depending on the pulse

duration. The Kerr contribution is essentially instantaneous, arising from nonlinearities in the electronic polarizability of the medium, and in the effect of redistribution of ions in regions of intense field ("molecular", or "nuclear" contribution). If the pulse duration is comparable to the acoustical transit time across the dimension of the intensified region, electrostrictive contributions can play a role as well. Finally, heating of the material gives rise to a "thermal" index nonlinearity, which is an integrated effect, dependent on pulse energy rather than on intensity.

Measurements on n_2 have been reported, especially for laser glass, for several years. This year, two independent techniques were reported. A. Owyoung of Sandia Laboratories has measureed the intensity dependent rotation of the polarization ellipse of elliptically polarized light in both isotropic materials (glass, fused silica) and cubic crystals (YAG), as a measure of the nonlinear susceptibility. In isotropic materials, the nonlinear susceptibility term has two independent components, and the ellipse rotation technique measures one of these, χ^{1221}; while in cubic materials, where there are three independent components, the technique yields values for χ_3^{1221} and the linear combination, $\chi_3^{1111} - 2\chi_3^{1122}$. On the assumption that the only factor contributing to the index nonlinearity is the electronic Kerr effect, it can be shown that $\chi_3^{1221} = \chi_3^{1122}$. Thus for either cubic or isotropic materials, for electronic Kerr effect only, the components of the nonlinear susceptibility can be completely determined. In this way, Owyoung obtains values for n_2 for several materials. For purposes of comparison, his values for n_2 are as follows, in units of 10^{-13} esu. Fused silica - 1.00, ED-4 laser glass - 1.73, YAG - 4.10 (along the 110 axis) and 4.27 (along the 100 axis). These data were obtained with a ruby laser emitting 38 mJ in 13 nsec (FWHM), focused to a radius of about 150 μm in the sample. No dependence on focal length was observed, indicating an absence of nonlinear intensification in the beam. Data were referenced to CS_2, in which $\chi_3^{1221} = 3.78 \times 10^{-13}$ esu ±2%. Although the assumption of electronic nonlinearity being the only operative factor was not inconsistent with the data obtained, it cannot be conclusively demonstrated without an independent measurement.

A. Feldman and co-workers from the National Bureau of Standards in Gaithersburg, Maryland have measured n_2 "directly", by measurements of self-focusing lengths in various transparent dielectrics. They used a Nd glass laser emitting a pulse of 25 nsec duration (FWHM). Various power densities were obtained by focusing the beam. Focal spots as small as 16.9 μm radius were used. The combined effects of electrostriction, Kerr effect, and thermal effects were considered in reducing the data. In general, the results obtained for n_2 were significantly lower than those reported by Owyoung. In addition, the estimated Kerr contributions were typically only 50 to 60% of those reported by Owyoung. The discrepancy between these two measurements may arise from several causes. One, it may be that the electronic Kerr effect does not account for the entire value of n_2 in pulses of this duration (13-25 nsec). Two, in the NBS experiment, a more nearly exact treatment of self-focusing might actually lead to lower power densities than those estimated in the paper, so that the actual n_2 value observed might have been higher. It is anticipated that independent measurements of n_2 now underway in several laboratories will help to resolve this discrepancy. However, it is encouraging to see the values agreeing within a factor of two at this time.

The consequences of index nonlinearity for high power laser design were discussed in four papers, each addressing itself to a different aspect of small-scale self-focusing. A. Glass of Lawrence Livermore Laboratory urged the adoption of the Talanov "critical power", P_1, as an alternate to n_2 for reporting index nonlinearity values. He showed that essentially all quantities of physical interest in either large-scale or small-scale self-focusing are succinctly expressed in terms of the ratio P/P_1. A simple derivation of the threshold condition and small-signal gain for small-scale self-focusing were also presented.

B. Suydam of the Los Alamos Scientific Laboratory also presented a derivation of the instability condition for the growth of small-scale self-focusing. In both this and the preceeding paper, it was stated that at intensities in excess of 10^{10} W/cm^2, large aperture light beams in glass are destructively unstable to the development of small-scale instabilities. Suydam also extended the theory to treat the case of well-developed instabilities, and found that catastrophic self-focusing would occur when the amplitude gain in the self-focused portion of the beam had reached a value of about 3. This result was corroborated by numerical calculation. Suydam further treated the case of an amplifying medium. He proposed that in such a medium that the critical length for self-focusing was the gain length, rather than the sample length, as in an unpumped medium. This leads to the surprising result that in an amplifying medium the maximum permissible power density is higher than in an unpumped medium. This point clearly warrants further investigation.

J. Marburger of the University of Southern California, and co-workers, treated the development of small-scale self-focusing initiated by random inhomogeneities in the medium. Employing a theoretical description similar to the well-known treatment by Tatarskii of propagation in a turbulent medium, they showed that at an rms phase front distortion of $\lambda/8$ due to index inhomogeneity, a profound instability will develop in a distance like twice the e-folding distance for the most unstable perturbation. The parameter of interest here is the e-folding distance, called ℓ_{min} by Margurger et al., given by the expression $\ell_{min} = 4n_0P_1/\lambda_0 I_0$, where n_0 is the refractive index, P_1 is the critical power for the medium, λ_0 is the vacuum wavelength of the light, and I_0 the local average intensity.

J. E. Howard and K. A. Brueckner, of KMS Fusion, treated another aspect of self-focusing. Using techniques of geometrical optics, they treated the growth of a macroscopic (approximately 1 cm) perturbation of the intensity distribution through a chain of disk amplifiers, represented for this discussion by a series of equidistant slabs placed at normal incidence to the beam. They conclude that for the KMSF system (consisting of 21 disks, 3 cm thick, placed 50 cm apart, with a small-signal gain of 1.13 per disk) that a one centimeter spike of 4 GW/cm^2 would self-focus in the system. They propose to reduce the effect by moving the disks closer together. Here the crucial difference between this calculation and the three preceeding reports is seen. Small-scale self-focusing occurs with a transverse dimension of the order of 100 μm, and the ensuing perturbation diffracts strongly. For such a case, moving the disks further apart will reduce the tendency to self-focus within the disk assembly. In the Howard paper, diffraction is neglected (geometrical optics), and only intermediate sized (one centimeter) disturbances are considered. Howard also states that in the absence of gain, the KMSF system, unpumped, would not self-focus a one centimeter, 4×10^9 W/cm^2 spike.

This latter set of four papers points out the interaction between material parameters, in this case n_2, and laser design. The sudden emphasis on small-scale self-focusing, which is limiting only for large-aperature, high-power, short-pulse systems, is clearly the result of the growth in the last year of the laser fusion program, and its present dependence on Nd-glass laser systems.

2.2 Surface Damage

A rapid appreciation of those factors influencing the characteristic of laser induced damage at dielectric surfaces is becoming evident. Our increased understanding relative to the intrinsic strength of optical surfaces exposed to high intensity laser radiation has called to our attention those major extrinsic factors which ultimately lead to a reduction in damage threshold. An increased degree of sophistication in the identification of important extrinsic variables and in the development of manufacturing and design procedures, is emerging, which increase the exposure levels at which material surfaces can be safely used without damage. We have heard of reports on improved surface polishing techniques for large optical elements, followed by an important paper on the effect of various polishing compounds and the identification of absorbing inclusions as a class of defects which lead to damage levels below the intrinsic value. Another paper described the implications of linear optics in evaluating the value of the electric field at which damage will occur as a function of optical geometry and incident laser light character (e.g. polarization).

Several classes of surface damage, characterized buy different morphologies, have been observed in proustite samples, arising under different illumination conditions. The surface damage in GaAs has been studied as a function of incident wavelength, and further information has been obtained of the thermal character of infrared damage, even in short pulses. Finally, the use of exoelectric techniques in studying surface damage has been developed and applied to new materials.

W. P. Barns of Itek Corporation reviewed his organization's work in the development of superpolishing techniques for large size optics (up to 27" diameter). Investigation of surface quality is normally accomplished through the use of electron microscopy to assess the reduced incidence of local and microscopic defects. Further tests employing scattering and FECO fringe measurements have shown good agreement with those performed by H. E. Bennett of the Naval Weapons Center. Itek has been able to determine the optimum polishing time when employing flooded surface techniques. As expected, they find when using de-ionized water, that after the oxide polishing compound has settled out, there is a further improvement in surface quality for a specific period of time, after which there is a steady decrease in the degree of surface finish. Best results using this techique have led to a surface finish of less than 20Å rms on large fused silica substrates.

At Owens-Illinois, N. Boling, G. Dube, and M. D. Crisp have been carefully and methodically studying the initial phases of laser induced damage in a variety of glasses ground and polished with various abrasive compounds. This was accomplished to determine which damage mechanism, be it laser absorption, isolated absorbing inclusions on the surface, or electron avalanche, was the dominant mechanism operative in normally employed optical components. Previous studies have established that electrostrictively driven acoustic waves and Stimulated Brillouin Scattering are not important mechanisms of surface damage. Damage was assessed both by surface microscopy and correlation with the presence or absence of a visible breakdown plasma.

While there were many morphologically interesting features arising from plasma formation at power levels far above threshold, such as fracture and melting at exit surfaces, due in part to reflection from the exit plasma, and thermally induced material surface rippling at the entrance, due to plasma shielding effects, the emphasis was on elucidating the characteristics of the damage process at threshold. Using a 30 nsec., 1.06 μm laser focused to an area of 1.8 mm at the $1/e^2$ points (large area), they determined the damage threshold for numerous glasses ranging in refractive index from 1.43 to 2.10, and the effect of seven different polishing compounds on the damage sensitivity of ED-2. Their major observations and conclusions were as follows.

Damage to the surfaces of normally polished optical materials is initially due to small absorbing inclusions, as deduced from microscropic examination, and the absence of a simultaneous plasma in a wide class of materials. In general, in low index materials damage occurs at relatively high power levels, accompanied by the production of visible plasma. For high index materials, the onset of microscopic damage occurs at much lower levels, without the production of a visible plasma. In these high index materials, damage accompanied by plasma formation also occurs, but at a still higher power level. The threshold for plasma formation is seen to decrease with increasing refractive index, over a broad range of index values. The low level pre-plasma damage is only seen in high index glasses. The effects of various polishing compounds on ED-2 surface damage were examined. With jewelers rouge (Fe_2O_3), pre-plasma damage was observed at 45 J/cm^2, and plasma formation at 70 J/cm^2, while with other polishing compounds, only plasma associated damage was seen at a threshold of 100 J/cm^2. However, when rouge and barnsite polished samples were subjected to a mild acid etch, both surfaces exhibited a pre-plasma threshold of 120 J/cm^2 without pre-plasma damage.

In another paper, M. D. Crisp of Owens-Illinois reviewed his previous work on quantitative predictions of surface damage thresholds from linear optics. He assumed that for a fixed pulse shape, damage will occur at oscillating fields greater than some threshold value for either damage due to absorption by inclusion or initiation of avalanche breakdown. This analysis was applied to entrance, exit, Brewster angle, and total internal reflection surfaces, as a function of refractive index and polarization. A strong recommendation was made to report damage not in terms of power density, but in terms of the electric field at threshold or an average energy density. Of course, the effective pulse width must be given as well.

In a short communication, C. Giuliano and D. Tseng of the Hughes Research Laboratories discussed surface damage in proustite (Ag_3AsS_3) at 1.06 and 0.69 μm. The ruby laser emitted single, 20 nsec. (FWHM) pulses, while both 18 nsec., single-shot, and 260-300 nsec., repetitively pulsed Nd:YAG lasers were employed for the 1.06 μm work. All lasers operated in the TEM_{00} mode. Specific sample areas were irradiated at low power, and power was then increased until damage was observed.

Three different forms of damage were observed under microscopic examination of the proustite entrance surface. Under high power cw illumination, or when an already damaged surface was irradiated at low cw power, a molten crater appeared, often accompanied by a plume of yellow smoke, presumably sulfur. Crater depth was about 25 μm. The formation of the crater is characterized by local melting and detectable chemical change. The second form of damage seen was micromelting of tiny regions, generally associated with imperfections in surface finish, such as scratches. The third damage form, termed "ghost sites", occured under cw illumination at 1.06 μm. It gave the surface a speckled appearance, and was seen at very low power, but faded away over a period of 30 seconds to 30 minutes after illumination. The decay time increased with increasing power level. Ghost sites were seen at all power levels above 300 W/cm^2, up to 2.3 kW/cm^2, where they persisted for long periods.

In general, damage thresholds were seen to decrease very slightly with increasing pulse repetition rate. Pulse duration dependence and damage morphology indicate that absorbing inclusions may be responsible for surface damage. This conclusion is tentative, since sample quality was widely variable.

Some increase in surface damage threshold was seen in proustite samples coated with sapphire films. Damage, when it occured, was seen at the interface between two materials, and exhibited the same morphology as in uncoated samples. Further development of this material for damage resistance is strongly dependent on the availability of material of good quality, with surfaces free from imperfections, and the bulk free from inclusions.

P. Braunlich of the Bendix Research Laboratories presented recent results obtained on the application of exoelectron imaging to the study of laser surface damage in glass, alkali halides, and pyroelectrics ($LiNbO_3$). Exoelectrons are emitted from surface layers from ten to one hundred Ångstroms below the surface of the material. They are released from traps near the surface upon heating of the material. These traps can be created in the material by bombardment with electrons or other ionizing radiation. In the present work, 3 kV electrons were used for bombardment.

ED-2 laser glass samples were irradiated at 1.06 μm with 25 nsec. pulses, at intensities from 10 to 110 J/cm^2. No conclusive results could be obtained correlating laser irradiation with exoelectron emission, as would be predicted from theory.

For $LiNbO_3$, being pyroelectric, a differe t phenomenon was observed, called "thermally stimulated field emission" (TSFE). This effect arises due to the presence of spontaneous polarization in pyroelectric crystals below the Curie temperature, which for $LiNbO_3$ is 1200°C. The resulting strong internal field serves to accelerate electrons out of the surface traps by field emission. Using a microchannel plate, the surface of the crystal could be imaged with a resolution of 300 μm. The use of TSFE for laser damage studies in pyroelectrics is now under study.

For non-pyroelectrics, like alkali halides, exoelectron imaging can be used to examine the state of surfaces exposed to laser radiation. The characteristic ring-like pattern seen in the exoelectron image of a laser irradiated surface can be understood on the basis of the rate equations for the population of traps and the conduction band in the insulating crystal. Near the periphery of the beam, photon energies are insufficient to excite valence electrons into traps, but are adequate to excite trapped electrons into the conductive band. At higher intensities, closer to the beam center, multiphoton processes start to excite valence electrons to the conductive band. The excess of conduction electrons refills the traps. At very high intensity, a nonlinear trap ionization process is proposed, or else local heating becomes sufficient to empty the refilled traps. This explains the alternate rings of filled and unfilled traps seen. Exoelectron imaging is proposed as a nondestructive test to measure the light flux required for trap ionization, at a power level below the actual damage threshold.

In a paper submitted for the proceedings, J. L. Smith of the U.S. Army Missile Command reported on the effects of pulsed 10.6 μm radiation on GaAs surfaces. A comparison was made among damage results at 0.69 μm in 20 nsec pulses, and 10.6 μm in 100 nsec pulses. Among the parameters varied were the doping of the crystal (p-type, n-type, or undoped) and the effect of "surface trash", or loose particulate matter, on the damage morphology. At 10.6 μm, p-type GaAs showed a somewhat lower damage threshold than other dopings. Aside from this one observation, no other correlation with doping was seen. Damage thresholds tended to be higher at longer wavelengths, ranging from 0.16 J/cm^2 in 20 nsec at 0.63 μm to 3 J/cm^2 in 100 nsec at 10.6 μm. Damage morphology was insensitive to the presence of loose material on the surface. Previously at 1.06 μm, 1 to 2 μm pits were seen, possibly attributable to localized imperfections on the surface. The acoustical pulse generated in the damage process at 1.06 μm was seen to correspond to an initial expansion of the sample attributed to a thermal pulse, rather than a compression, as would be produced by electrostriction. This is taken as evidence refuting the argument that Stimulated Brillouin Scattering is responsible for GaAs surface damage.

J. Giuliani of the U.S. Naval Research Laboratory has investigated the influence of pulsed 1.06 μm radiation on the surface recombination rates of charge carriers in bulk silicon. An n-p-n silicon photodiode was exposed to various levels of 1.06 μm radiation. Energy densities up to 1 J/cm^2 were incident on the surface, over a 1 mm diameter spot. The estimated penetration depth of the 1.06 μm light was approximately 0.5 mm. The response of the photodiode to subsequent 0.63 μm radiation was then investigated as a function of pulsed irradiation.

A He-Ne laser was focused to a diameter of 200 μm, and the focal spot was moved across the surface of the photodiode. By measuring the response of the device as the 0.63 μm focus was positioned relative to the junction location, the effective surface recombination lifetime could be measured for both types of carriers.

It was observed that weak irradiation (0.1 J/cm^2) caused an increase in the carrier diffusion length, or equivalently, in the surface recombination lifetime for both carrier types. Increasing the incident energy density further caused a monotonically decreasing value of carrier lifetime. Above 0.5 J/cm^2, an increase in dark current was observed. No data were reported regarding damage morphology or plasma formation. The author concludes that the decrease in carrier lifetime is associated with an increase in surface recombination centers, and that the increase in dark current arises from the creation of leakage paths across the junction.

2.3 Optical Coating Damage

As had been previously noted, thin film coatings generally have a great variation in sensitivity to laser-induced damage. More seriously, they are generally characterized by low values of damage threshold compared to the values for the base surface or within the bulk of many optical materials. This situation arises undoubtedly from the influence of many extrinsic variables characteristic of materials in thin film form and made manifest through specific coating processes. Last year the influence of the amplitude of the electric field on thin film damage was clearly shown, and consideration of this feature has been an important guideline for design of damage resistant film systems. This year a major extrinsic factor has been identified, namely defects. Effects related to their density, size, and composition have been studied and their influence in reducing the damage threshold below "semi-intrinsic" (i.e. defect-free) levels measured.

The role of coating defect density on damage initiation was determined through variation in irradiation areas in the first paper, while a closely related paper studied the effects of defect size on damage as a function of pulse width in the case of strongly absorbing defects. Last year, it was proposed to monitor the change in reflectivity as a sensitive indicator of damage in thin films. This year, correlation of reflectivity changes with damage observation, as indicated by plasma formation, attenuation of transmitted signal, and direct microscopic examination was reported. The reflectivity measurement was refined to include time resolution during and after the damaging pulse. Reflectivity changes were consistently seen in cases where microscopic examination revealed damage, even in cases where neither plasma formation nor pulse attenuation were observed.

L. G. DeShazer, B. E. Newnam, and K. M. Leung of the University of Southern California studied the damage threshold of coated surfaces as a function of the irradiated spot size. They found a general decrease in damage threshold as the spot size was increased, up to a diameter of 150 μm. Above 150 μm diameter, the damage threshold was invarient as the spot size was further enlarged. They explain this spot size dependence as an increasing probability of encountering a defect. The distribution was assumed to follow a Poissan function and be independent of whether the defect led to an absorption or electron avalanche initiated damage site. The diameter at which the damage level remains constant was correlated with a determination of the average defect separation from micrographic records. Good agreement was found. An appropriate scaling parameter is ω_0/d_0, where ω_0 = spot size and d_0 is the mean distance between defects. They further noticed that d_0 decreases as the deposition rate increases. Some general tendencies from this work included a general decrease in the intrinsic damage threshold with increasing refractive index, smaller values of d_0 for films than for surfaces of crystalline materials, and the reduction in damage threshold from the defect-free regions to those containing defects from 2 - 5x, depending on the specific enhancement factors produced by various classes of defects (Bloembergen). A specific example is ZrO_2 films where the defect damage level was 9.2 J/cm^2 with d_0 = 50 μm. In the defect-free region the damage threshold was three times greater when employing a TEM_{00} Q-switched ruby laser.

The role of absorbing inclusions in the damage initiation of thin films was treated by D. Milam and R. Bradbury of the USAF Cambridge Research Laboratories and M. Bass of Raytheon. This morphological centered investigation correlated the variation of damage sensitivity with pulse duration and the size of metallic or highly absorbing non-metallic inclusions. A series of experiments using double pulse techniques separated by a few to several nanoseconds verified absorption as the damage initiating mechanism in these films. Careful experiments on e-beam deposited TiO_2/SiO_2 and ZrO_2/SiO_2 films with reflectivity >90% gave the following results: at 20 psec., the damage level was 3.5 J/cm^2, damage site density 2-10 x 10^6 craters/cm^2 and the effective absorbing particle size was 0.2 to 0.5 μm; at 1.4 nsec., the damage level was 14 J/cm^2, site density 10^6/cm^2 and the particle size 1.5 μm; finally, at 20 nsec., the damage level was 16 J/cm^2, site density 10^4/cm^2 and particle size 4.5 μm. As can be noted, the longer the pulse the more damaging are the larger inclusions. Evidently the smaller the defects the greater density they have.

A final paper by N. Alyassini, J. H. Parks, and L. G. DeShazer described their continuing studies on utility of reflectance changes as a damage threshold indicator. With a time resolution of 2 nsec., they monitored the intensity of a HeNe laser beam, internally reflected from films at the critical angle (most sensitive to refractive index changes). Simultaneously, the presence or absence of a visible spark was monitored, as was the transmission of the incident damaging laser pulse. In cases of damage, increased scattering of the probe beam was seen, while effects due to index changes in the medium were absent. Neither the appearance of a spark nor attenuation of the damaging pulse were consistently correlated with the occurence of damage, although where increased scattering was observed, subsequent electron microscope examination of the surface revealed damage sites. Two transitory changes in reflection were identified, a fast component with a rise time of approximately 4 nsec., and a slow component with a rise time of approximately 10-20 nsec., followed by a 25-50 nsec. recovery phase for these 10-15 nsec. incident ruby TEM_{00} laser pulses.

2.4 Damage to Infrared Components

As expected, this year's Symposium contained many more reports on damage to infrared components than in previous years. This is not only indicative of the interest in this region of the spectrum but also of the growth of infrared laser technology, with many more different types of laser components and classes of high power laser systems. As a result of this diversity in component type and laser characteristics, there are as well numerous and sometimes quite different levels and definitions of damage. Reports were heard on damage to crystalline windows and mirrors, both coated and uncoated under illumination by pulsed and cw systems from 5 to 10 μm. In addition, a rapid and accurate new instrumental technique for the measurement of very low values of coating and surface absorption in infrared transmitting windows was presented. The absorption coefficient is a fundamental parameter of extreme impact in the damage process. This technique can be extended as well to the visible region and to coated reflecting surfaces.

Our first report on damage to optical components at 5 μm was given by S. Holms and P. Kraatz of Northrop. This initial study was concerned with the testing of coated metal mirrors and dielectric coated windows by a transverse excited e-beam CO laser operating multimode over several lines in the spectral range from 4.6 to 5.2 μm. The laser was capable of 40 J pulses in 100 μsec., and was focused to 2-3 mm diameter spot sizes. Considerable morphological analysis was performed on a wide variety of target configurations, resulting in rather broad, general conclusions. Extreme exposure produced primarily thermal effects, causing minor chemical alterations such as oxidation and tarnishing.

At higher powers, melting, blistering, and explosive vaporization were observed. Metal mirrors were initially polished to an rms finish of 30-40 Å, by a fresh feed technique employing alumina abrasive, and then coated by thermal evaporation or RF sputtering. Damage occured in the vicinity of 200 J/cm^2 for the target described above. There was an indication that aging of coated elements exposed to the atmosphere did not lead to a great variation or degradation in damage level over non-aged samples. In general Au-coated mirrors damaged at lower levels than Ag-coated ones, whether they were overcoated or bare. For tests on MgF_2/MgO and ThF_4/PbF_2 AR-coated, poorly finished CaF_2 windows, the latter coating gave consistantly better performance. Obviously, these initial observations need to be followed by more careful studies to determine exact damage processes and arrive at meaningful damage thresholds.

Moving on to pulsed damage measurements of coated and bare windows at 10.6 μm, A. F. Braunstein, V. Wang, M. Braunstein, J. E. Rudisill, and J. Wada of Hughes Research Laboratories reported detailed results on three prime candidate materials, namely KCl, ZnSe, and CdTe. Employing a UV-preionized, TEA laser, operating TEM_{00}, and emitting pulses of 600 nsec duration, they observed that damage occurred primarily at the surface for KCl and CdTe, but in the bulk of ZnSe. The failure within ZnSe was initiated at voids surrounded by Zn, or a Zn-rich ZnSe region. Although they concluded that failure was not initiated by the coating for As_2S_3 passivated KCl, ThF_4/As_2S_3 anti-reflective coated KCl, or BaF_2/ZnS-coated ZnSe samples, damage levels were generally lower for these coated elements than for the uncoated samples. Bulk absorption measurements indicated generally low values for KCl materials, ranging from 0.0007 cm^{-1} to 0.024 cm^{-1}, while coating absorption varied from 0.19 to 0.80 percent per surface. Damage threshold was >75 J/cm^2 in some cases for uncoated KCl, and as low as 6-10 J/cm^2 for coated elements. For the chemically vapor-deposited ZnSe samples, failure was primarily by explosion of included voids, surrounded by zinc-rich material, which grew in size with repeated exposures. Damage appeared to be most sensitive to void size. Thus in samples of ZnSe, under pulsed CO_2 laser irradiation, a damage threshold of 5.6 J/cm^2 was seen with a bulk absorption of 0.02 cm^{-1}, when opaque included voids up to 125 μm in diameter were present. In a sample with an absorption of 0.009 cm^{-1}, with included voids of intermediate size (approx. 100 μm), the damage threshold was 41 J/cm^2. For a sample with a bulk absorption of 0.0041 J/cm^2, with inclusions up to 50 μm in diameter, AR-caoted with BaF_2/ZnS, with a coating absorption of 0.02 percent per surface, the damage threshold was 27 J/cm^2. CdTe had the worst performance of any material, damaging from 1.2 to approximately 2.6 J/cm^2, the lower values being for coated elements. The bulk absorption coefficient was approximately 0.003 cm^{-1}.

A prolific contributor to laser induced damage studies of optical glasses in the past, J. Davit of the Compagnie Generale d'Electricite has moved his interest to laser damage at 10.6 μm. In a paper included in these proceedings he reports on damage to Ge, KCl, and NaCl from a TEM_{00}, 75 nsec pulsed CO_2 laser. He notes that in these materials, damage always occurs at the surface and may or may not be accompanied by a plasma. In addition, he has obtained plasma formation without damage. If this is the case, one may be able to clean surfaces by slowly raising the exposure levels and thus remove deletereous particles. Single shot damage on Ge surfaces occurred at 13 J/cm^2 while 100 irradiations at 7.5 J/cm^2 produced no visible damage. Similar results were obtained when employing good AR-coatings. For the alkali halides he notices a general dissipation of plasma breakdown over the first 50 exposures at 7.5 J/cm^2. For a subsequent 50 exposures at 7.5 J/cm^2 at the same location, there was no plasma formed, and in no case was damage observed. For these same materials he observed no difference in damage level between the <111> and <100> crystal orientations.

Continuing along these lines but at much shorter pulse lengths, W. H. Reichelt and E. E. Stark, Jr. of the Los Alamos Scientific Laboratory performed studies on the interaction of a nanosecond TEM_{00}, single line CO_2 laser with NaCl windows. The damage level determined under these conditions was approximately 3 J/cm^2. The observed damage site was characterized by right angle, linear cracking of the surface with "spall" evident along the failure lines. This structure is undoubtedly a manifestation of tensile stresses produced by subsequent local heating of the damage zone. Like Davit, they also noted plasma formation with and without microscopic damage and, on exposures where non-damaging plasma formation occurred, a general decrease in plasma luminosity with consecutive exposures.

In a very careful analysis H. Posen, J. Bruce, J. Comer, and A. Armington of the USAF Cambridge Research Laboratories studied the interaction of an intense cw 10.6 μm CO_2 laser with single crystals of KCl, KBr, and an alloy ALQLOY ($KCl_{0.33}$-$KBr_{.067}$) as a function of crystal orientation. For this last material under cw illumination, unlike the pulsed irradiations already discussed, they did find a definite effect of the crystal orientation on damage level. This difference is undoubtedly due to the relatively long term thermal interaction in the cw case as opposed to the transient processes in the case of pulsed damage. Furthermore, as in Fradin's work, the damage level of this alloy was found to be intermediate to those of the individual pure materials. Stresses arise primarily from thermal loading caused by measureable absorption within these alkali halide crystals. In the case of uncoated KCl at all crystal orientations, no failure was observed at power densities up to 38 kW/cm^2. This same level was achieved in KBr in the <100> orientation. For ALQLOY the <110> and <111> orientations again withstood >38 kW/cm^2 without damage, but failure occurred at approximately 28 kW/cm^2 in the <100> orientation. The observed failure is by cleavage propagation rather than by lattice yielding. In KCl, however, failure is predicted to be by slip rather than by rupture or cleavage. When dealing with coated windows, the probable controlling failure mechanism is the initiation of plastic deformation of the weaker element of the system be it either the coating or window. When KCl was coated with 12 μm of 99.999% Ge, the following damage levels

were obtained: ∿5.1 kW/cm^2 for <100>; ∿14.6 kW/cm^2 for <110>; and ∿14.6 kW/cm^2 for <111>. Interestingly, when ALQLOY was cleaned with HCl, there appeared cleavage in the <100> direction at levels of 6.5 kW/cm^2. The application of the critical sheer stress law to the orientational dependence observed was clearly shown.

The subject of pulsed CO_2 laser damage to metal and dielectric mirrors was also treated by the Hughes group in a report by V. Wang, A. Braunstein, M. Braunstein, J. E. Rudisill, and J. Wada. Employing a 600 nsec, single transverse mode CO_2 TEA laser, they investigated the damage susceptibility of bare metal mirrors, and CdTe/ThF_4, ZnTe/ZnS, and As_2S_3/KCl dielectric enhanced metal mirrors. From these experimental measurements, and morphological investigation, they conclude that under their experimental conditions, failure in narrow band gap II-VI semiconductors, such as CdTe or ZnTe, is characterized by avalanche impact ionization at very low levels. Although CdTe exhibited the lowest absorption coefficient of any sample tested, it also exhibited the lowest damage threshold for those pusled exposures. Microscopic examination revealed that threshold damage was characterized by microcraters, probably due to impurities or other defects. ZnTe was much the same story. In contrast to ThF_4, process control was found to be of great influence on the resultant absorption coefficient, failure levels and damage modes. Films characterized by high absorption values failed at low illumination levels through a cracking and separation of the film, while for low absorption coatings, damage sensitivity was greatly reduced, and the failure was characterized by an initial discoloration and subsequent appearance of interference patterns within the film. Fringes were separated by approximately 10 μm. In the other wide band gap materials, As_2S_3 and KCl, damage thresholds were also quite high, with the additional feature of surface conditioning being observed. As in other reports at this meeting on alkali halides, plasmas were seen without observable microscopic damage. In one series of tests, when the flux was suddenly increased to 5 J/cm^2, a plasma without damage was noted, but if there was a gradual increase in flux level, no plasma was noted until levels of approximately 65 J/cm^2 were reached. At these levels, a plasma and damage were seen simultaneously.

Generally speaking, bare metal mirrors of Cu and Mo damaged at 35 J/cm^2, while narrow band gaps II-VI semiconductors like CdTe and ZnTe exhibited damage thresholds of only 1-2 J/cm^2. Conversely, wide band gap dielectrics such as As_2S_3, KCl, and ThF_4 did not fail until 30-65 J/cm^2 exposure levels were reached. Unlike previously reported results in the visible portion of the spectrum, these single mode infrared exposures led to damage levels less than previous multimode measurements. However, no real conclusions should be drawn from this fact, because the pulse lengths were considerably different (600 nsec single mode vs. 2.2 μsec multimode). There was also difficulty in assessing the true exposure area for the multimode experiments.

As has been pointed out in the above summaries, the value of the absorption coefficient, particularly for coated elements, is of utmost importance in controlling the resultant damage levels. E. L. Kerr of Perkin-Elmer has devised a rapid, sensitive, and relatively inexpensive instrument suitable for quality control as well as research evaluation of the absorption present in coated elements. His device is called the Alphaphone. The sample to be tested forms one wall of a thin cell filled with air. The air is heated by a small fraction of the energy absorbed at the sample surface when it is illuminated by a laser beam. The resulting pressure rise is then detected by a capacitance microphone. The device is capable of being independently calibrated and employed at different wavelengths. The present sensitivity in absorption is approximately 10^{-5}, using a 10 watt cw CO_2 laser. The instrument, however is capable of a sensitivity of 1.5×10^{-7}, and is insensitive to scattering. The present sensitivity arises from an ability to detect a ΔT of 6×10^{-6}°C, corresponding to ΔP of 2×10^{-8} atmospheres, at T = 300°K. Measurements of the absorption of KRS-5 windows with anti-reflection coatings have been accomplished.

2.5 Theory and Fundamental Properties

In order to develop materials as nearly damage resistant as possible, and to be sure that, in the design of high power laser systems, the intrinsic capabilities of given materials are not exceeded, a full theoretical understanding of damage phenomena must be developed. This theoretical advance must be accompanied by a program of careful measurement, so that as the relevant material parameters are identified, their best values can be tabulated and reported for future reference.

This process of theoretical analysis, identification of parameters, and careful measurement has been carried out in previous years for Nd glass and some of the crystalline materials used in near-IR and visible lasers. With increasing emphasis on the infrared, there is expanded interest in phenomena and properties relevant to IR window materials, and in damage processes at IR wavelengths both within the bulk of materials and at their surfaces.

Three papers presented at this Symposium dealt with the theoretical aspects of damage phenomena in IR window materials. B. Bendow and P. Gianino of the USAF Cambridge Research Laboratories discussed the calculation of photoelastic constants of infrared window materials. The photoelastic tensor relates the change in the indicatrix (index ellipsoid) to the strain tensor, which in turn can be related to the stress tensor via the elastic constants of the medium. The photoelastic constants, P_{ij}, are calculated on the theory of Humphreys and Maradulin, which requires a knowledge of the interionic potential and dipole moment of the crystal, as a function of the interionic separation. For the insulating ionic materials such as alkali halides, a Born-Mayer potential was assumed, while for zinc blende semiconductors, such as GaAs and ZnS, a Morse potential was assumed. Once the potential and dipole moment model is established, the photoelastic constants can be computed as a function of optical frequency. Photoelastic dispersion results from the stress dependence of both the TO phonon frequency and the effective charge associated with the TO frequency, however, electronic dispersive effects are not significant at infrared frequencies. Computed values are tabulated for a large number of materials. In general, photoelastic disperion is significant for "rock salt"-type ionic crystals, less so for zinc blende semiconductors, and absent for diamond-type semiconductors. Photoelastic dispersion, in the first two classes of materials, is much more pronounced than refractive index dispersion. The authors relate the photoelastic constants to "thermal lensing" parameters, which measure the stress-induced birefringence resulting from thermal loading. These parameters are also tabulated for common IR window materials. Experimental confirmation of these computed values is eagerly awaited.

R. Hellwarth of the University of Southern California discussed a new technique for checking detailed theoretical computations of multi-phonon absorption processes in IR window materials. He shows that, in general, the optical absorption coefficient at a given IR frequency can be related to the ion-ion response function for the crystal, denoted by $S_{\alpha\beta}(\omega)$. He then derives a series of expressions for the successive frequency moments of the response function. These moment formulae are analogous to the sum rules of atomic spectroscopy. In fact, the first moment of $S_{\alpha\beta}(\omega)$ is just given by $(S_{\alpha\beta}/m_{\alpha})$ the Thomas-Kuhn-Reich sum rule. The fifth moment of the response function is then shown to contain the total effect of two-phonon absorption and emission processes. The result depends on a single anharmonicity parameter, which can be determined from measured values of TO frequency, ion mass, and bulk modulus data. For greatly unequal masses, such as in LiF, the two-phonon processes are shown to vanish, since only the light ion moves significantly, and it finds itself in a potential exhibiting inversion symmetry. For equal ion masses, the result for the two-phonon portion of the fifth moment of $S_{\alpha\beta}(\omega)$ can be expressed in terms of a universal function of temperature. This can be used as a check on detailed calculations of two-phonon processes. Extensions of the moments method are clearly possible to treat higher order processes.

C. Duthler and M. Sparks of Xonics, Inc., treated the effects of absorbing inclusions on laser damage in the IR. The analysis was quite similar to that employed by Hopper and Uhlman, and Bennett, in the 1970 Damage Symposium. The cross-section for absorption by a spherical particle is treated using Mie theory for particles small compared to the wavelengths, and geometrical optics for particles large compared to wavelength. Both metallic and dielectric inclusions are considered. The temperature rise of the inclusion and the surrounding material is calculated, as a function of particle size, incident intensity, and inclusion composition, and inferences drawn concerning the resultant damage thresholds.

In a paper contributed to these proceedings, R. A. Shatas, of the U.S. Army Missile Command, and co-workers, discussed the role of laser-induced collective electron oscillation in surface damage in the infrared. They propose that surface damage arises from the dampening of the surface plasmon instabilities by lattice ions. These plasmon oscillations are driven parametrically by the incident laser field. In order to create the conditions for plasma instabilities to occur, the electron plasma frequency must be comparable to the laser frequency. This requires a conduction electron density of $10^{19} cm^{-3}$ at 10.6 μm, increasing as the square of the light frequency. The authors propose that near the surface of a crystal, the presence of impruity levels and the bending of the crystal bands account for a reduction in the effective band gap to values at which field-assisted electron tunneling (Zener tunneling) can occur, creating the requisite electron density. The model is discussed, both in terms of GaAs and NaCl. The authors suggest that the observed surface damage in GaAs is due to this tunneling effect, rather than avalanche ionization. They refer to data discussed elsewhere in these proceedings, showing that the threshold for surface damage in GaAs decreases with increasing optical frequency, from 0.69 to 10.6 μm, contrary to the avalanche model predictions. The dc bulk value is much higher than the optical frequency surface values reported, so the discrepancy may be due to the fact that intrinsic surface damage is not being observed. The authors contend that because of the high mobility in GaAs, the avalanche process cannot be initiated, due to the effective absence of momentum reversing collisions during the optical cycle for electrons in the conduction band.

A rather different conclusion regarding both bulk and surface damage in alkali halides was presented by D. Fradin, of Harvard, and M. Bass, of Raytheon. They reported extension of previous work on intrinsic optical breakdown in alkali halides, which had demonstrated that bulk damage was due to electron avalanche ionization. The frequency dependence of the breakdown field has been extended to 0.69 μm by use of a ruby laser. A number of alkali halides have been tested. In NaCl, the rms breakdown field is essentially unchanged from 10.6 μm to 0.69 μm. In most other alkali halides, an increase was seen at the ruby frequency. This is taken as evidence that the ruby laser optical period is becoming comparable to the electron-phonon collision time in the materials. An obvious discrepancy was seen

in the case of NaF, which is expected to exhibit a longer collision time than NaCl. To explain the discrepancy, the authors suggest that deep-lying excitons may play a role in the avalanche process in NaF. They further investigated the dependence of the breakdown threshold on pulse duration, using pulses at 1.06 μm from 15 to 30 psec in NaCl. The breakdown field was seen to increase from 2.1 MV/cm at 10.3 nsec to 12.4 MV/cm at 15 psec. Self-focusing was not present. This difference was attributed to a field-dependent ionization rate, and qualitative agreement with dc experimental results was obtained.

Three disordered systems were investigated, polycrystalline KCl, a single crystal KCl-KBr alloy, and fused silica. The simple theory of electron avalanche breakdown predicts that as the electron mobility decreases, E^2 must increase proportionately. Thus, significant disorder should lead to an increased breakdown threshold, assuming that the disorder occurs on such a scale as to influence the mobility. In polycrystalline KCl, with a 20 μm grain size, the damage threshold was the same as in single crystal material. In the alloy, the damage field was intermediate between the values observed in the pure constituents, but in fused silica, however, the predicted result was obtained, with a damage threshold five times that in crystalline quartz.

Both the statistical aspects and the absolute values of damage thresholds in bulk and at the surface were seen to be similar. The statistics of the bulk breakdown starting times in fused silica were seen to be virtually identical to those observed in surface damage. The actual surface damage thresholds in fused silica, sapphire, and BSC-2 glass were seen to be essentially the same as bulk values, providing the surface was "super-polished", either by bowl-feed or ion-beam polishing. The reduction in threshold for conventionally polished surfaces was entirely consistent with Bloembergen's theory of field intensification in scratches and grooves. This implies that the intrinsic damage mechanism in the materials examined was the same in the bulk and at the surface. The authors conclude that laser breakdown studies in the bulk provide a valuable technique for the understanding of the electron avalanche breakdown process, and provide information which is not otherwise accessible experimentally. Data on the intrinsic breakdown provides the ultimate limit, both for bulk and surface damage.

C. Giuliano and D. Tseng of the Hughes Research Laboratories presented a short report of bulk damage in $LiIO_3$, at 1.06 μm and 0.69 μm, both with and without phase-matched, second harmonic generation. It had been reported, in the 1971 Damage Symposium, that damage thresholds were greatly decreased in the presence of the second harmonic. No difference in damage threshold was observed by Giuliano and Tseng with the harmonic present or absent. The variation in damage threshold from sample to sample was greater than either the variation with incident wavelength, pulse repetition rate, or second harmonic conversion. Observed damage thresholds for bulk damage at about 20 nsec (FWHM) pulse duration, ranged from 0.5 to 2.6 GW/cm^2.

Two papers were presented dealing with refinements of instrumentation. D. C. Stierwalt, of the Naval Electronics Laboratory Center, presented graphs of absorption coefficient versus wavelength for various crystalline IR window materials, including KBr, CdTe, $ZnSe_xTe_{1-x}$, ZnSe, and Pb-doped KCl. Data were presented over a wavelength range from 3 to 15 μm, at 273°K and 373°K. The data were obtained by a measurement of spectral emittance from the samples. By observing the emittance as a function of sample thickness, surface and bulk absorption could be differentiated.

G. Birnbaum, of Rockwell International, described the measurement of stress-induced birefringence using an optical interferometer arrangement. In the apparatus described, the samples were stressed mechanically. The sample and a Kerr cell are both located within a scanning Fabry-Perot interferometer. The Kerr cell voltage is varied to cancel the birefringence induced in the sample, as measured by the coupling of orthogonally polarized modes within the interferometer. Results are given for YAG, fused silica, and sapphire, as a function of temperature.

3. Recommendations

With the increased understanding and control of damage in visible and near-infrared lasers, the major emphasis in damage studies is now directed towards infrared materials. However, certain aspects of damage phenomena, which have been extensively investigated for pulsed, near-visible systems, remain to be elucidated. With regard to self-focusing, it is of crucial importance to assemble a body of reliable data recording the various contributions (electronic, Kerr, electrostrictive) to the index nonlinearity. The absolute values of index nonlinearity, or equivalent nonlinear susceptibilities, are still in question for the materials of principle interest. Unambiguous measurement techniques must be developed, which enable the various contributions to χ_3, n_2, or P_1 to be determined independently. The adoption of a standard reference material for measurement calibration is strongly urged. Fused silica of a specified refractive index, dispersion, absorption and homogeneity is proposed as a standard material for nonlinear susceptibility measurements.

It has been pointed out in this year's Symposium that the exact nature of self-focusing damage depends on the details of the system in which the material is used. This is the reason why fundamental, nonsystem related material parameters must be tabulated.

There is evidence that the index nonlinearity increases monotonically with refractive index, for a large class of materials. Clearly, this point must be verified, since it could point the way towards the development of new crystalline and amorphus laser hosts less susceptible to self-focusing. It should be kept in mind, however, that a reduced value of n_2 alone will probably not justify the expense associated with the development of a new solid state laser material.

The conclusions reached concerning avalanche ionization, in the bulk and at surfaces, are applicable over a broad range of operating frequencies, pulse durations, and materials. The only class of materials extensively studied to date has been the alkali halides. It is now apparent that, at least in these materials, and probably in glasses as well, the use of refined polishing techniques can raise the surface damage threshold to the bulk damage value, as limited by avalanche ionization. The hypothesis should be tested for a broader class of materials of interest, expecially semiconductors at infrared wavelengths, and manufacturing methods established to produce large size, defect-free surfaces while maintaining requisite geometrical tolerances. It would be useful to develop nondestructive tests to measure the susceptibility of a material to surface ionization. Some years ago, the detection of surface photocurrentas a precursor to plasma formation was proposed by J. Ernest. Unfortunately, unless the surface in question is clean and free of defects, this correlation may not be readily established. With the availability of super-polished surfaces, it would be of interest to examine the correlation between photocurrent and surface breakdown for a range of well-characterized materials, such as alkali halides or glasses of various refractive indices, surface finish, as well as coated optics.

In insulators and semiconductors, three independent material parameters seem to influence the damage level. These are the band gap width (which controls the carrier concentration), trap density (which affects carrier mobility), and the refractive index (which enters through the local field corrections and Fresnel relations). The influence of these factors should be investigated, both theoretically and experimentally. Pure crystalline materials like alkali halides, Si, Ge, and III-V and II-VI semiconductors, should provide a fertile area of study, since these materials are generally avaiable in high purity, and are well understood. Of course, other materials of practical interest must be investigated, but every effort should be made to characterize the material as well as possible. The influence of grain size and short range order may be of consequence in these studies, along with the effects of temperature, pressure, and impurity concentration.

In the past, the statement has been made that plasma formation was synonymous with surface damage. In this year's proceedings, several authors refer to damage without plasmas, and plasmas without damage. Clearly, as the conditions of investigation broaden, a new definition of damage is required.

For surfaces which are not free of structural defects and inclusions, a luminous plasma often appears on initial exposure diminishing on subsequent exposure (even at higher power density) until, after repeated exposures, it is not seen at all. Post-mortem examination of the surfaces may reveal no consequent damage to the surface, and surface scattering does not increase. Even when surface scattering does increase, it has been observed that it may be evanescent, disappearing in times from seconds to minutes. It is proposed that surface dmaage threshold refer only to the power density level at which irreversible change of the surface occurs. This change can be chemical or morphological, as evidenced by increased absorption or scattering.

Because a number of different processes can lead to damage in infrared components, it is crucial that experiments be carried out over a range of operating wavelengths, pulse durations, and pulse repetition times. The dependence of the damage observations on these variables is a guide to elucidating the specific mechanism responsible for the damage, be it purely avalanche breakdown, thermal failure, some quasi-thermal, or unknown synergistic effect.

Obviously, as pulse lengths become longer, heat conduction between adjacent layers in coated infrared components will become an important consideration. For example, one analysis has shown that for pulses less that 2 μsec long, the peak temperature rise is within 30% of the value obtained for instantaneous deposition of energy, while for 10 μsec long exposures, the peak temperature rise may be reduced by as much as 70%. Certainly, as pulse lengths vary, the particular damage mechanism and observable effects will change, although in many cases the initiating factor (e.g. absorption) may be the same.

It is a matter of almost religious conviction that meaningful damage studies can only be carried out with lasers operating in TEM_{00} mode, or at least with those with a well characterized, reproducible, temporal, and spatial output. It has been clearly demonstrated that multimode lasers yield damage thresholds orders of magnitude lower than single mode. It is equally true that the intrinsic damage level of optical materials is greater than that found in materials containing voids, defects, or inclusions. Reproducible damage results can only be obtained with well-characterized materials. The materials may not of necessity be pure. Thin film structures, alloys, and polycrystalline composites are not ideal pure materials but they must be well-characterized in terms of composition, structure, grain size, and absorption, as well as defect type and concentration in order for meaningful damage studies to be performed.

In actual practice, of course, deviation from the ideal must be carefully monitored. There is a real need for suitable inspection techniques and operational specifications for defect structure and surface finish, both in production for process control and for acceptance testing. Light scattering, reflectivity, and bulk and surface absorption are all techniques which may prove useful in this regard; but, the correlation between passive properties and damage thresholds, for a given damage mechanism, remains to be established. This is a most urgent and pressing need, and as such, is a very fruitful area for research and development.

In the infrared, damage processes tend to be thermal or thermostrictive in origin, especially in cw operation. In crystalline materials the damage threshold is seen to be sensitive to the relative orientation of the incident beam direction and the slip planes of the material. In thin films, the list of parameters which can influence the damage threshold is frighteningly long. Composition, defect concentration, structure, residual stress, scattering, absorption, angle of incidence, and substrate material are some of the factors which may influence the values obtained. In all infrared materials, because of the importance of phonon processes, sample temperature is a critical parameter as well. As the damage mechanisms become more clearly understood, the relative importance of these several parameters will become clearer, and fewer variables need to be considered. That state of understanding has not been reached at the present time, especially as regards thin films.

A great deal of work remains to be done regarding reflecting metal surfaces, both coated and uncoated. Particular attention must be paid to surface finish, absorption, and scattering of these materials as well.

Looking ahead, it is clear that ultraviolet lasers, operating in the nanosecond or subnanosecond pulse region, will be developed. Damage in the UV region will be dominated by multiphoton processes, as the photon energy approaches the band gap of the available materials. Scattering is expected to be enhanced in the UV, and the requirements on optical finishing will be correspondingly more severe. With lower diffraction, systems of smaller dimensions may be forthcoming, assuming that flux levels remain tolerable.

Finally, a catalogue of those optical properties of materials relevant to damage is beginning to be compiled. It is to be kept in mind that the goal of the ASTM Damage Symposium is not only to advance the state of understanding of damage phenomena, but also to increase the body of knowledge concerning optical materials available to the system designer, and to minimize laser damage occurence in practical systems. The accumulation of reliable data, and its dissemination, are essential to this purpose.

4. Acknowledgement

We would like to acknowledge the invaluable assistance of Dr. Harold S. Boyne, Mrs. Pauline W. Smith, Mrs. Marjorie L. Wilson, Mrs. Frances M. Starck, and Mr. Gunther W. Schulz of the National Bureau of Standards in Boulder, Colorado for their interest, support, and untiring efforts in the operation of this Symposium and in the preparation and publication of the proceedings. The continued success of the Damage Symposium would not have been possible without their support.

5. Bibliography

[1] "Damage in Laser Glass", A. J. Glass and A. H. Guenther, Editors, ASTM Special Technical Publication 469, ASTM, Philadelphia, PA (1969).

[2] "Damage in Laser Materials", A. J. Glass and A. H. Guenther, Editors, NBS Special Publication 341, U.S. Government Printing Office, Washington, D.C. (1970).

[3] "Fundamentals of Damage in Laser Glass", N. Bloembergen, National Materials Advisory Board Publication NMAB-271, National Academy of Sciences, Washington, D.C. (1970).

[4] "Damage in Laser Materials: 1971", A. J. Glass and A. H. Guenther, Editors, NBS Special Publication 356, U.S. Government Printing Office, Washington, D.C. (1971).

[5] "High Power Infrared Laser Windows", N. Bloembergen, National Materials Advisory Board Publication NMAB-292, National Academy of Sciences, Washington, D.C. (1972).

[6] Proceedings of the Conference on High Power Infrared Laser Window Materials, (October 1971). Edited by C. S. Sahagian and C. A. Pitha (Air Force Cambridge Research Laboratories, Special Report No. 127, December 1971).

[7] "Laser Induced Damage in Optical Materials: 1972", A. J. Glass and A. H. Guenther, Editors, NBS Special Publication 372, U. S. Government Printing Office, Washington, D.C. (1972).

[8] "Laser Induced Damage of Optical Elements, A Status Report", A. J. Glass and A. H. Guenther, Applied Optics 12, pp. 637-649 (1973).

A. J. Glass

A. H. Guenther

Opening Remarks

Arthur H. Guenther

Air Force Weapons Laboratory
Kirtland AFB, New Mexico 87117

Alex Glass and I would like to add our welcome to the 5th (now) Annual Symposium on Damage in Laser Materials. We would like to especially welcome our foreign visitors who have come so far to attend this meeting. The participation by visiting scientists from abroad, our increased attendance, and the lengthened meeting all attest to the growing interest and importance of the subject of this Symposium. The most tangible indicator is the financial support afforded us by the Office of Naval Research, for which we are most grateful. As such, this year's meeting is therefore jointly sponsored by the American Society for Testing and Materials, the National Bureau of Standards, and the Office of Naval Research, to whom we extend our most sincere appreciation.

This year we have been particularly successful in disseminating and bringing to the attention of others the results of our deliberations. This has been accomplished through our published proceedings, a special feature issue of Applied Optics, and articles in various trade publications both here in the United States as well as in Europe. A status report on the subject of Laser Induced Damage was presented at the Japan/US Joint Seminar on Laser Interaction and articles on specific aspects of this year's Symposium will reach others through additional publications and presentations at various conferences and workshops.

As Martin Stickley suggested last year, perhaps we should change our image to one more positive by renaming this meeting to one on Optical Reliability or The Avoidance of Laser Damage. However, regardless of the name, this meeting certainly has had its impact in acting to collate work in this general area and in acting as a forum for discussion and transfer of information. In this regard, I think it has been successful in bringing together research scientists, buyers, specifiers and fabricators who have found the return worth the price of the openness and frankness characteristic of this meeting.

In spite of this success, we shouldn't lose sight of the fact that our end goal is not purely to study laser induced damage or laser interaction, which may be an obvious prerequisite, but to arrive at design and engineering guides based upon those factors which affect laser induced damage and use them to direct future developments to avoid the onset of damage. From a practical standpoint, however, one must consider the environments in which the specific high power laser system will be operating. These environments will be somewhat hostile in many government and industrial applications. In many cases the cautious utilization possible in pristine laboratory situations is not transferable to the intended operational conditions.

This meeting has emanated from a responsibility of the ASTM to develop specifications and testing procedures suitable to the laser community. Obviously one of the most significant specifications is damage threshold. As in other situations when addressing new areas for ASTM consideration, we generally convene topical sessions, recruiting acknowledged experts on the subject under discussion, to aid us in our work. When the subject of damage susceptibility came up, we discovered most everyone was an expert and rarely did two people completely agree on definition, or understanding. In fact, however, many people did have something to contribute albeit on different aspects of the problem. When these meetings were initiated four years ago most problems dealt with high power solid state lasers such as ruby and glass systems, and these were the materials which initially received the greatest emphasis. As the years went on, our interest and emphasis changed to surfaces and coatings. We have also proceeded from empirical results to a more precise physical understanding of this subject.

I would like to say a few words about the general subject of the meeting. Optical surfaces are still the specific area where the most gain in damage resistance can be made whether by new surface preparation techniques or improved coating procedures as we endeavor to approach the generally adequate high level of intrinsic breakdown of most materials.

Considerable work still needs to be done on nonlinear optical materials. Perhaps the greatest advance could be made by following the lead of the glass manufacturers in developing chemically pure, defect and strain free crystalline materials. For until we realize the intrinsic strength of these materials, we may be led into working on extrinsic effects for which the payoff is marginal. Much the same argument can be made in the coatings area--although here there appears to be an unending list of possible extrinsic variables that one may never be able to unravel or sort through. However, the influence of specific physical consequences such as the magnitude of the electric field in different film designs certainly is a powerful design tool in developing damage resistance films.

Many of the features of laser induced damage particularly at short pulse lengths can be correlated in one way or another to the magnitude of the local electric field. One must strive to eliminate or reduce the influence of those factors or situations which tend to enhance this field. Two specific cases, besides the obvious ones of Fresnel reflection or interference in thin films, come to mind which should be addressed. The first is the case of small scale self-focussing, a result of intensity fluctuations on the wavefront of a high power laser. These intensity fluctuations can be produced by numerous causes, one of which is the presence of defects. Defects are as well most evident at surfaces or within thin films, and besides causing intensity variations are themselves the most obvious cause in reducing the damage threshold at these points by leading to an increase in the electric field. Therefore, a strong recommendation is to produce defect-free surfaces and coatings.

This year you will note a lengthening of the meeting and one whole day devoted primarily to the infrared region of the spectrum. In this area our previous work is laying the foundation for attacking this problem. We are seeing judicious application of physical principles early in this work; one just has to look at last year's proceedings for verification.

We should, however, draw our attention to some salient difference between the past and present situations. Previously, we emphasized temporal domains in the few to 10's of nsec. A most important infrared case of interest today is that relating to cw operation where "damage" is primarily due to fracture, or unacceptable amounts of distortion, a case never considered in previous damage situations. At the other extreme, we have the same breakdown dominated characteristics of short pulses albeit on a generally different class of materials.

Many recently developed IR lasers operate in the pulsed mode and over a wide range of repetition frequencies--these lasers may emit on a fractional μsec to 10 μsec time scale. A quasi-thermal region as it were where either distortion, fracture, plasma formation or all may be present under specific circumstances. Further, the rapid temperature cycling of components used in these systems may lead to new material dependent failure modes such as rapid dislocation growth, etc.

The future will certainly see a near term continued interest in the infrared, but in all probability a movement toward shorter wavelength perhaps to I_2 because of the better quality optical materials available, on to the metal vapor lasers in the visible, to Xe in the UV where a whole new realm of laser damage activities may develop (people are even using cavity mirror damage to "prove" laser action), on down to the vacuum UV and X-ray region with the probable use of crystalline optical elements.

The ARPA Program on Optical Surface and Coating Science

C. Martin Stickley

Advanced Research Projects Agency
1400 Wilson Boulevard
Arlington, Virginia 22209

1. Introduction

Over the past several years, ARPA has been supporting research in the problem of damage to the bulk of optical materials such as ruby and glass as well as to their surfaces. The results of these studies have been reported at this meeting and have generally formed the backbone of the material discussed here. I will not attempt to review all of this progress at this time but will only say that we have a rather good understanding of mechanisms that lead us to bulk damage, at least in typical Q-switched pulsed length regimes, and to surface damage. Over the past one to two years the results on the surface damage activities have been particularly rewarding since we have heard very encouraging reports of development of surface preparation techniques which would lead to higher surface damage thresholds. Today I am going to outline the recent chronology of the development of these fascinating results on surface damage and describe for you how they affected the development of a new program on surface damage in infrared window materials. I will describe for you the recommendations of a meeting which was held since the last laser damage conference as well as the program that was formulated on surface damage as a result of that meeting. Finally, I will mention some recent work confirming the influence of surface preparation on surface damage; this latter result gives us even more confidence that our decision to emphasize surface polishing processes as fundamental to retaining surface integrity in high power laser beams was a correct one.

2. Recent Measurement Results

The importance of the potential problem of surface breakdown of infrared laser windows led to the meeting held at ARPA's Materials Research Council on Cape Cod in July of 1972. The meeting was designed to bring together workers in the field of surface preparation and surface analysis of widely different backgrounds. The main purpose was to find out how their expertise could be brought to bear on the problem of absorption and damage to surfaces and coatings on windows transversed by high intensity IR laser beams. Such windows need anti-reflection coatings, and in many cases, protective coatings against atmospheric deterioration. The requirements are for 0.1% anti-reflection and protective coatings at 10.6 micrometers on alkali halides such as KCl and KBr with the absorption losses being less than 10^{-4} per surface. Anti-reflection coatings on zinc selenide and cadmium telluride are also needed with an absorption less than 10^{-4} per surface. For higher absorptions, phase distortion of the optical beam degrades the quality of the beam. Thus, coatings should be uniform to $\lambda/40$ with a coated window uniform to $\lambda/20$. With respect to mechanical properties coatings must be moisture resistant, cleanable, and make good thermal contact with the substrate. In addition, there is a requirement for damage threshold of the coatings and surfaces to approximate as closely as possible the damage threshold of the bulk materials.

In the process of this meeting a number of interesting topics were discussed but I will limit my comments today to two of them. The first part of the meeting was devoted to a summary of the state of knowledge about laser-induced breakdown in glass and ruby. One of the most interesting results discussed in this meeting were presented by Norman Boling representing Crisp, Boling, and

Dube of Owens-Illinois. He presented reasons for differences in the breakdown threshold of entrance and exit surfaces of glass cubes. The geometry and nomenclature of their experiments are shown on figure 1. Illustrated is a glass block in which various electric fields are defined. If reflections at these interfaces are taken into consideration and the phase shifts of the optical fields are properly considered, the Owens-Illinois group has shown that one can explain the higher breakdown threshold for the entrance surface as compared to the exit surface. This data is shown in table 1. In actuality, of course, the fields within the glass at breakdown are equal for each surface. The support for this argument is given in the results shown in table 2. The Owens-Illinois fabricated blocks of glass which could be irradiated with the blocks positioned at Brewster's angle to the entering laser beam. At Brewster's angle no reflection occurs and, thus, in this case one would expect the exit surface damage threshold to be the same as the entrance surface damage threshold. Their data shown on this table confirms this result. The significance of this work was that it made it clear that what one really has to consider in determining what causes breakdown is the internal optical electric field at the surface and not necessarily the incident field.

Table 1. Entrance and Exit Damage Thresholds For Normal Incidence Beam

Entrance Damage Threshold J/CM^2	Exit Damage Threshold J/CM^2	$\frac{\text{Entrance Threshold}}{\text{Exit Threshold}}$
195 - 230	111 - 120	1.9
125 - 130	90 - 105	1.3
160 - 209	120 - 146	1.5
150 - 179	100 - 110	1.6

Table 2. Entrance and Exit Damage Thresholds at Brewsters Angle

Entrance Damage Threshold J/CM^2	Exit Damage Threshold J/CM^2	$\frac{\text{Entrance Threshold}}{\text{Exit Threshold}}$
105 - 120	92 - 117	1.0
83 - 88	83 - 88	1.0
112 - 130	112 - 130	1.1
98 - 108	98 - 108	1.0

The second interesting result was presented by Connie Giuliano of Hughes. His findings are summarized on figure 2. They show that ion polishing of sapphire can raise the damage threshold by some 2-10 times, approaching to within a factor of 2 to 3 of the bulk breakdown threshold. The significance here is that the details of the state of the surface in fact do determine its damage threshold.

3. Bloembergen's Hypothesis

Professor Bloembergen of Harvard was a participant in this meeting at Cape Cod. Upon hearing the two previous results he suggested a mechanism which might explain the results reported by Giuliano; namely, that surface preparation will influence the surface damage level. Bloembergen proposed that the presence of submicroscopic cracks and pores in and near the surface will cause local increases in the electric field strengths and these enhancements can probably account for the apparent lowering of the surface breakdown threshold by some significant factor relative to that of the bulk. Figure 3 shows the model under consideration. The incident field is denoted by E_{inc} and the field in the material is E_o. What is illustrated here is a block of material with a crack, a cylindrical groove and a pore near the surface. Table 3 gives an indication of the degree of enhancement of the electric field within the optical material and in the vicinity of the defect. One can see from the table that the enhancement will be dependent upon the details of the defect. Approximate expressions are given for this enhancement factor for spherical defects, cylindrical defects, and cracks. Note that for the limiting case of a crack the field is enhanced by the factor E, the dielectric constant. In this case E is equal to n^2 where n is the refractive index. Recall that the intensity is proportional to the square of the electric field. Thus we have a mechanism in which the intensity in the defect can be enhanced by as much as the fourth power of the refractive index for the host material. For the range of refractive indices of materials we have to deal with for IR windows, this could give an intensity enhancement factor of from five up to 80 to 100, and could therefore, explain the lower surface breakdown threshold relative to the bulk. It should also be noted that the same enhancement factor will be operative if the damage mechanism is initiated by absorbing inclusions. This could very likely occur since the polishing material could be left at the bottom of the crack.

Table 3. Electric Field Enhancement

$$E_{ins} = \frac{1}{1 + \frac{1 - \epsilon}{\epsilon} L} E_o$$

L = depolarization factor

A. Sphere	B. Cylinder	C. Crack
$L = 1/3$	$L = 1/2$	$L = 1 - \frac{\pi}{2} \frac{c}{a}$
$E = \frac{3\epsilon}{2\epsilon+1} E_o$	$E_{ins} = \frac{2\epsilon}{\epsilon+1} E_o$	~ 1 for $c/a << 1/\epsilon < 1$
		$E_{ins} = \epsilon E_o$

4. Conclusions of the Cape Cod Meeting

The conclusions from this meeting can be broken down into ones pertaining to surface preparation and coatings. They are as follows:

A. Uncoated Surfaces

1. The ideal intrinsic surface, free from grooves, incipient cracks and impurities, should have abosrption and damage characteristics comparable to the bulk. It is true that specific surface states, surface vibrations and other excitations, as well as the breakdown of symmetry at the surface may cause variations in the absorption characteristics. If one stays sufficiently far away from bulk absorption edges, however, such intrinsic surface absorption mechanisms (surface states, surface vibrations) appear to be negligible.

2. Extrinsic surface characteristics such as scratches, inclusions from abrasive dust, chemical impurities, etc., play an important role in lowering the surface damage threshold (as discussed in more detail in a separate publication by N. Bloembergen). (Bloembergen, 1972).

3. The extrinsic properties of the surface are a sensitive function of the polishing techniques used. Much effort should be directed towards avoiding surface irregularities, such as pits and grooves on a scale larger than 0.01 μm. Polishing techniques which avoid the use of any solid materials which absorb at 10.6 μm and are liable to be deposited as damaging inclusions, should be developed for IR window materials; cleaning mechanisms to remove all absorbing materials and fluids should be included in the study of polishing techniques.

4. The surface of the window materials, before depositing coatings, should be characterized by:

a. optical scattering and flatness.

b. scanning electron microscopy to determine density and size of deviations from a smooth geometry.

c. surface absorption calorimetry.

d. damage threshold for high power density laser pulses.

It is believed that electron beam diffraction and other spectroscopic techniques are less useful in the development of acceptable IR window surfaces. In this connection it should be noted that a sizable coverage of the first surface layer by -O or -OH bonds is acceptable for operation at 10.6 μm.

B. Coatings

5. Film deposition techniques should be studied with the goal of minimizing the density and size of pores, absorbing inclusions, and achieving good film adherence with uniform thickness.

6. The films should be characterized by the same techniques as mentioned under (4) for surfaces with the addition of other techniques for determining surface contaminants which might affect coating adhesion.

7. In choosing film materials attention should be given to the following characteristics:

a. low intrinsic bulk absorption.

b. matched thermal expansion with that of the substrate.

c. adhesion and interfaces.

d. the possibility of epitaxial growth on single crystal substrates to avoid pores and cracks.

e. the influence of the structure of the film and substrate (i.e., single crystal, state of surface polish, absorbed surface layers, grain boundaries, amorphous or polycrystalline structure) should be investigated.

f. special attention should be given to the development of organic polymer coatings both for protective and anti-reflective purposes because of their promise to avoid cracks, pores and inclusions, their low optical index of refraction and mechanical strength.

8. The presence of pores and microcracks is detrimental to both the electrical and mechanical breakdown strength of the film. The problem becomes progressively more severe in thicker films. The anti-reflection coatings of the required properties will be much more difficult to produce than protective coatings. The presence of pores and microcracks is relatively more detrimental in materials with a high index.

5. Content of the Program on Optical Surface and Coating Sciences

Even though we had no direct experimental confirmation of Bloembergen's hypothesis it looked to be so well founded that it was decided to organize the optical surface and coating science program with surface preparation receiving major emphasis. The following then, is a list of the specific efforts in each contract.

1. Air Force Cambridge Research Labs (Dr. Harold Posen). A study of the structure of the coatings as it is influenced by orientation of the substrate (single crystal and polycrystal KCl, and alkali halide alloys), defect chemistry of the substrate as determined by scanning auger spectroscopy, electrical characterization of the coatings and evaluation of contractor-prepared coatings and IR window materials.

2. Pennsylvania State University (Professor Bruce Knox). Research on coating techniques, and surface and coating characterization. Substrates to be alkali halides and alkaline earth fluorides. Coatings to be B, Si, Ge, C, PbO, Bi_2O_3, and more complex oxides. Coating techniques to include sputtering, reactive chemical vapor deposition, plasma synthesis, and laser-generated thin films. Characterization to include infrared absorption, Raman spectroscopy, scanning electron microscopy, ellipsometry, x-ray emission, and determination of coating strain.

3. Raytheon Company (Dr. Perry Miles). Development of a new class of abrasive polishing compounds and the use of ion milling as a final polishing technique. To be used on KCl, ZnSe, and YVO_4 substrates. Some development of chemical-mechanical polishing. Subcontract to Itek for evaluation of their superpolishing technique.

4. Rockwell International - Autonetics (Dr. J. J. Licari). Development of organic materials as moisture protective coatings, and of chemical lapping techniques for polishing alkali halides.

5. Hughes Research Labs (Dr. Morris Braunstein). The major program contractor. To perform research and development on surface finishing, surface characterization, coating technology, laser induced damage to surfaces and coatings, optical evaluation techniques for coating and surface absorption, and chemical analysis of window surfaces, coating starting materials, and coatings. Responsible for quantitative comparison of competitive coating techniques and for deposition of glasses as coatings.

6. Honeywell, Inc. (Dr. Enrique Bernal). Explore novel techniques for preparing water resistant surfaces on alkali halides by chemically changing the fundamental composition of the window surface.

7. Lawrence Livermore Laboratory (Dr. Jhan Khan). Back-up study to determine the importance of and necessity for surface cleaning and coating deposition in ultrahigh vacuum. Surface monitoring tools to include high energy ion backscattering, reflection high energy electron diffraction, and transmission and scanning electron microscopy. Surface damage, reflectivity and surface absorption will be measured. Ion polishing, epitaxial regrowth, and ion plating will be explored, all in reasonably high vacuum, for their application to surface and coating preparation.

8. U.S. Naval Weapons Center (Dr. T. M. Donovan). Determination of the potential of covalent elemental and chalcogenide glasses as coatings for windows. Characterization of window surface properties and their influence on surface absorption.

6. Confirmation of Bloembergen's Hypothesis

During the development of the program I have just described I was in frequent touch with Mike Bass of Raytheon concerning results he was obtaining on a comparison of laser-induced surface and bulk damage, which he carried out with David Fraden of Harvard. Table 4 of this report summarizes their results. As you can see the materials they studied were fused quartz, sapphire, and boro-silicate crown glass. Note that for the fused quartz the conventional polish gave a ratio of the bulk electric field breakdown strength to the surface electric breakdown strength of about 1.3. This compares very well with the results for either spherical voids or cylindrical grooves, and detailed electron micrographs confirm that such were present at very high density such that these defects could, in fact, explain this lowered breakdown electric field. Note that both the bowl feed polish as well as the ion beam polish raises the surface breakdown field strength to a point where it is equal to that of the bulk. This result then confirms the hypothesis by Bloembergen, and puts the new program I have outlined on very firm ground, in that we are now convinced that the efforts on improved surface preparation for IR window materials to be carried out in this program will lead to the highest obtainable surface breakdown thresholds.

Table 4. Comparison of Bulk and Surface Damage Fields for Different Samples and Surface Finishes

Material	Finishing Procedure Finish Quality[a]	Predicted Ratio E_B/E_S Spherical Void	Cylindrical Groove	"Vee" Groove	Measured E_B/E_S	Surface Damage Morphology
Fused Quartz	Conventional #1 Standard 0-0 (See Fig. 1a)	1.21	1.35	2.1	1.3 ± 0.1	b
	Conventional #2 Standard 0-0	"	"	"	1.5 ± 0.1	b
	"Bowl" feed finish See Fig. 1b	"	"	"	1.0 ± 0.1	c
	Ion beam polish Standard 0-0 with final 1.25 μm by Ar ion beam	"	"	"	1.0 ± 0.1	c
Sapphire	Conventional Many scratches and digs with 50X mag and dark field	1.29	1.50	3.00	2.0 ± 0.2	b
BSC-2 Glass	Conventional Standard 0-0	1.23	1.39	2.25	1.3 ± 0.1	b
	"Bowl" feed finish See Fig. 1c	"	"	"	1.0 ± 0.1	b,c

a. All surfaces were cleaned with collodion

b. Very faint pit ~ 20 μm in dia. and ~ 0.25 μm deep

c. Extensive cracking out to ~ 150 μm with central hole ~ 20 μm dia. and ~ 3-10 μm deep

7. Conclusions

In conclusion I want to say that it has been immensely satisfying to me to be associated with these efforts over the last several years, to see that they have led to such significant results, and to realize that we are now building on them to solve a materials problem of major importance to the Defense Department. Many of you should feel equally proud that you have had an opportunity to contribute to this important topic.

Finally, I want to emphasize that none of these research results will very likely be widely used unless they are transferred to the general optical industry. I want to strongly encourage all of you who are participating in these programs to keep this in mind: that is, that I am strongly desirous of seeing the optical industry in this country being made aware of the kind of techniques that you are developing for improved surface and coating technology. I think one of the great strengths of having future results on this program reported at this meeting is that it is the meeting which is held in conjunction with the American Society for Testing and Materials. As some of you are aware ASTM is one of the principal ways of transferring measurement and processing results to users in this country, and I feel that the output of this program will be the kind of results which can be reduced to practice through ASTM.

I want to thank you for your attention here this morning and for inviting me here to talk, and I look forward to hearing results in the next several years to come from this program on optical surface and coating science.

8. Figures

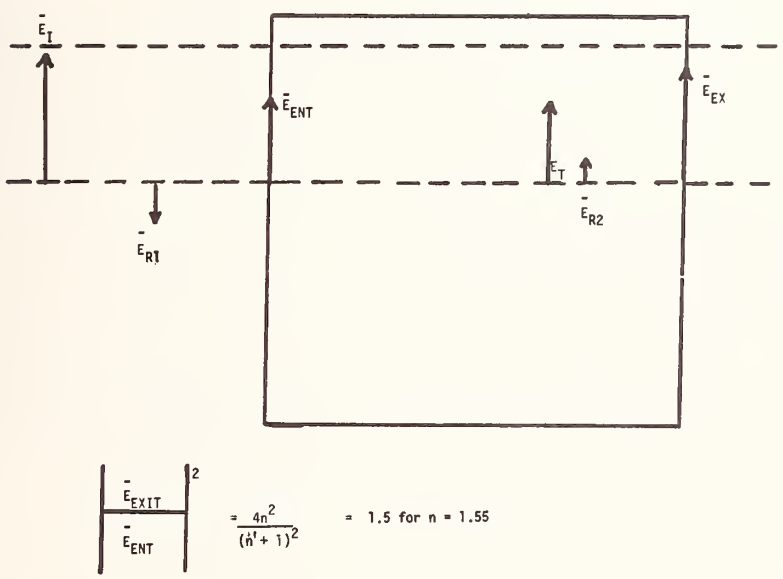

Figure 1. Definition of optical, electrical fields used by Boling, et al. in their damage experiments on glass cubes.

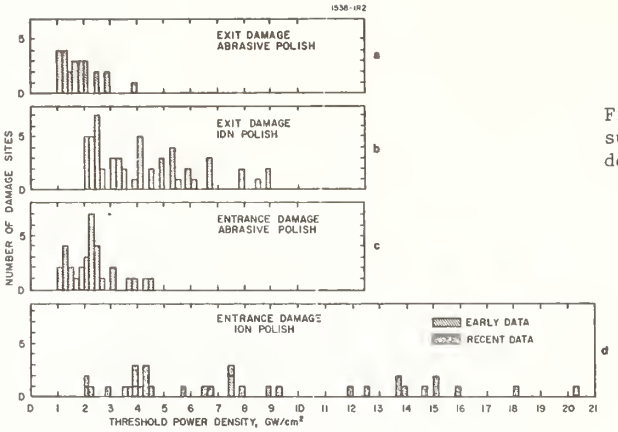

Figure 2. Number of damage sites on sapphire surface as a function of damage threshold power density for abrasive and ion beam surface polishing procedures.

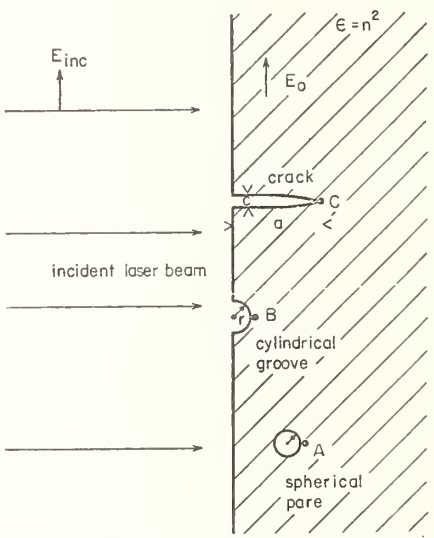

Representative geometries for electric field enhancement near pores, scratches and incipient cracks. Typical dimensions are: r = 0.1 μm, c = 0.1 μm and a = 1 μm.

Figure 3. Representative geometries for electric field enhancement near pores, scratches and incipient cracks. Typical dimensions are : r = 0.1 μm, c = 0.1 μm and a = 1 μm.

Nonlinear Refractive Index Measurements in Laser Media*

A. Owyoung

Sandia Laboratories
Albuquerque, New Mexico 87115

The ellipse rotation technique has been employed to measure nonlinear refractive index changes in YAG and several laser glasses using a Q-switched TEM_{00q} mode ruby oscillator-amplifier. By time resolving the 9 ns ellipse rotation signal, we obtain all of the information necessary to plot ellipse rotation vs. input power in a single shot, thereby also introducing the capability to detect transient contributions which would interfere with the measurement.

A small anisotropy is found in the third order nonlinear susceptibility of YAG and values for n_2 are inferred assuming electronic distortion to be the primary mechanism.

Key Words: Ellipse rotation, glass, nonlinear index, nonlinear susceptibility, self focusing, yttrium aluminum garnet.

1. Introduction

A knowledge of the nonlinear refractive index, n_2, of optical media used in high power laser systems is essential to the understanding of nonlinear propagation and damage in such systems. Yet an accurate direct determination of n_2 is extremely difficult because of the catastrophic nature of the self focusing process and its sensitivity to beam quality. [1,2][1] In this paper we report measurements using the ellipse rotation technique [3,4] whereby we obtain accurate (± 7%) nondestructive determinations of two of the three independent elements of the third order nonlinear susceptibility tensor $\chi_3^{ijkl}(-\omega,\omega,\omega,-\omega)$ [5] which are necessary to characterize self focusing phenomena for arbitrary input polarizations in cubic crystalline media. In isotropic media one of the two independent susceptibility elements is determined. Moreover, by assuming electronic distortion to be the primary mechanism responsible for the index nonlinearity we infer values of n_2 for several laser glasses and YAG ($Y_3Al_5O_{12}$).

This paper is divided into six sections. In section 2 the theoretical basis for ellipse rotation measurements using focused beams in cubic crystalline media is discussed. It is established that this technique can be used to obtain measurements of two independent elements of the nonlinear susceptibility $\chi_3^{ijkl}(-\omega,\omega,\omega,-\omega)$ and that the results obtained are unaffected by the degree of focusing. In section 3 the TEM_{00q} near Gaussian mode ruby laser system used in the experimental investigation is described in detail. Section 4 contains a description of the ellipse rotation apparatus and a discussion of the experimental procedure followed in making the measurements. Finally, the results of the measurements are discussed in section 5 and some comments concerning the interpretation of these results and the extension of this work are made in the concluding section 6.

2. Theory of the Ellipse Rotation Technique

2.1 Nonlinear Susceptibility Measurements

In media which exhibit inversion symmetry, the lowest order nonlinear polarization is cubic in the electric field strength and is expressed in terms of the fourth rank nonlinear susceptibility tensor $\chi_3^{ijkl}(-\omega,\omega_1,\omega_2,\omega_3)$ as defined by Maker and Terhune. [5] Here $\omega = \omega_1 + \omega_2 + \omega_3$.

---

*Work supported by the U. S. Atomic Energy Commission

[1]Figures in brackets indicate the literature references at the end of this paper.

More specifically "self induced" nonlinear index changes are specified at a frequency ω by the tensor $\chi_3^{ijk\ell}(-\omega,\omega,\omega,-\omega)$, which may be simplified considerably in specific cases by intrinsic permutation symmetry [6] and crystal symmetry. [7] For cubic media of point group symmetry 432 $\bar{4}3m$, or $m3m$, $\chi_3^{ijk\ell}(-\omega,\omega,\omega,-\omega)$ reduces to three independent tensor elements χ_3^{1111}, χ_3^{1221}, and χ_3^{1122} where the "1" and "2" denote x, y, or z and $1 \neq 2$. For the case of isotropic media one has the additional restriction $\chi_3^{1111} = \chi_3^{1221} + 2\chi_3^{1122}$ so that only two tensor elements need be determined.

The ellipse rotation technique was first used by Maker, Terhune, and Savage in 1964 to study nonlinear refractive index changes in liquids. [3] By observing the intensity dependent rotation of the polarization ellipse of an elliptically polarized beam as it propagates through a nonlinear medium, a direct measurement of the induced circular birefringence of the medium is made. This is illustrated schematically in figure 1 where ϕ is the relative phase shift induced in the two circularly polarized field components and $\phi/2$ is the resultant ellipse rotation angle.

For the case of isotropic or cubic crystalline media it is convenient to consider an input electric field of the form

$$\underset{\sim}{E}(t) = \mathrm{Re}\left\{\left(E_{o+}e^{i\phi}\hat{e}_+ + E_{o-}\hat{e}_-\right)\exp(i(kz - \omega t))\right\} \tag{1}$$

where z is chosen to be along a (100) crystal axis. Here $\hat{e}_\pm = (\hat{e}_x \pm i\hat{e}_y)/\sqrt{2}$ are the right and left circularly polarized unit vectors, $E_{o\pm}$ are the real amplitudes of the circularly polarized components of $\underset{\sim}{E}(t)$ and a phase angle ϕ is introduced to permit the orientation of the polarization ellipse with respect to the crystal axes. By writing the nonlinear polarization in terms of its two circularly polarized components and substituting directly into Maxwell's equations, it may be shown that the circular field components experience real refractive index changes, $\delta n_\pm$, for $\phi = 0$ and $\phi = \pi/2$. [8] For $\phi = 0$ (ellipse oriented along a (100) crystal axis) one finds,

$$\delta n_\pm = \frac{6\pi}{n}\left\{(\chi_3^{1111} + 2\chi_3^{1122} - \chi_3^{1221})\,|\underset{\sim}{E}|^2 + (\chi_3^{1111} - 2\chi_3^{1122} + \chi_3^{1221})E_{o\mp}^2\right\} \tag{2}$$

and for $\phi = \pi/2$ (ellipse oriented along a (110) crystal axis),

$$\delta n_\pm = \frac{6\pi}{n}\left\{(\chi_3^{1111} + 2\chi_3^{1122} - \chi_3^{1221})\,|\underset{\sim}{E}|^2 + 2\chi_3^{1221}E_{o\mp}^2\right\}. \tag{3}$$

Hence the input field given by eq (1) will experience no change in ellipticity for $\phi = 0$ or $\phi = \pi/2$ and the induced birefringence expressed by eqs (2-3) will result in a rotation of the polarization ellipse by an angle θ given by the relation [5]

$$\frac{d\theta}{dz} = \frac{\omega}{2c}(\delta n_+ - \delta n_-) = \frac{\pi\omega}{nc}B\left\{E_{o-}^2 - E_{o+}^2\right\} \tag{4}$$

for $\theta \ll \pi/2$. Clearly, from eqs (2-4), B is given by $B = 3(\chi_3^{1111} - 2\chi_3^{1122} + \chi_3^{1221})$ for $\phi = 0$ and $B = 6\chi_3^{1221}$ for $\phi = \pi/2$. For the isotropic case where $\chi_3^{1111} = \chi_3^{1221} + 2\chi_3^{1122}$, B is identically equal to $6\chi_3^{1221}$ independent of ϕ. Hence by measuring θ as a function of input intensity, a direct measurement of B is obtained.

2.2 Focusing

In the measurement of nonlinear refractive index changes in solids where typical values of n_2 are one to two orders of magnitude lower than those of liquids, care must be taken to avoid surface breakdown and to assure a well defined input polarization to the specimen. Several advantages result from focusing centrally into the sample and maintaining the intensity at the surface of the sample at a low level compared to the focal intensity: 1) the beam intensity in the polarizing optics is maintained at a low level, thus avoiding nonlinear interactions and beam distortion; 2) sample surface breakdown is avoided; 3) the requirements on sample quality are reduced since a smaller volume is being examined and regions containing inclusions and excessive birefringence may be avoided; and 4) the amount of ellipse rotation may be shown to be independent of all focusing parameters assuming that the focal region of the beam is completely encompassed by the specimen under study. [8]

The effects of focusing on the ellipse rotation experienced by a Gaussian beam may be calculated approximately by adopting a ray tracing analysis and integrating eq (4) along the ray paths. Since ellipse rotation studies are generally carried out under the conditions specified in eq (4) where $\theta \ll \pi/2$, beam distortion arising from self focusing may be neglected. Hence a constant shape Gaussian analysis may be used whereby the surfaces of constant energy flow are defined by the set of hyperboloids

$$K = \frac{r^2}{w^2(z)} = r^2\left[w_o^2 + \left(\frac{\lambda z}{\pi w_o n}\right)^2\right]^{-1} \tag{5}$$

where $w(z)$ is the 1/e radius of the electric field i.e., $E(r) = \exp(-r^2/w^2(z))$, n is the linear refractive index of the medium, and λ is the free space wavelength.

The intensity of each ray of the beam may be integrated along the ray path as suggested by eq (4) and illustrated in figure 2. The resultant set of ellipse rotation angles, θ_K, may then be used to calculate the fractional power in each ray which is rotated into a polarization orthogonal to that of the input polarization ellipse. This fractional rotation may be employed to take a weighted average over the cross sectional area of the entire beam thus giving the total fraction F of power emerging from the sample with a polarization orthogonal to the input wave. Assuming, as previously stated, that the intensity at the sample surface is low compared to the focal intensity intensity, it may be shown that [8]

$$F = \frac{16\pi^4\omega^4}{3c^6}\left\{\frac{1 - \exp(-6r_o^2/w^2)}{1 - \exp(-2r_o^2/w^2)}\right\}\left(\frac{B}{n} < P >_{av} \sin(4u)\right)^2 \tag{6}$$

Here $\omega = 2\pi c/\lambda$, $< P >_{av}$ is the total power in the Gaussian beam, r_o is the detection aperture, w is the 1/e beam radius at the detection plane, and $u \equiv \tan^{-1}(E_{o+}/E_{o-})$ is generally chosen to be $\pi/8$ to maximize the value of F. It is to be noted that eq (6) is entirely independent of the focal spot size. The exponential "aperturing factor" merely reflects the fact that most of the ellipse rotation signal arises from the center of the beam where the intensity is highest.

3. Single TEM_{ooq} Mode Ruby Laser System

In order to prevent premature beam distortion and damage due to spatial inhomogenities in the input beam and to assure a high degree of precision in obtaining ellipse rotation data we use a single TEM_{ooq} near Gaussian mode Q-switched ruby laser system in the experimental implementation of this study.

The relevant parameters of the ruby oscillator-amplifier system are summarized in table 1. Transverse mode selection in the oscillator is achieved with a 1.1 mm diameter carbide Mendenhall wedge [9] inserted into the optical cavity directly behind the output etalon which consists of two quartz flats optically contacted to a 3 mm thick quartz spacer. Q-switching is achieved with a solution of cryptocyanine in methanol in a 1 mm thick etalon dye cell which is formed by a 99.9% rear reflection and a quartz flat. In conjunction with the dye cell etalon, the anti-reflection coated ends of the rod and output etalon are all optically aligned to provide maximal longitudinal mode discrimination.

Table 1. Operational Parameters of Single Mode Ruby Laser System

Dimensions of Helically Pumped Ruby Rods	
Oscillator Rod	4 in. long x 3/8 in. diam. flat/flat
Amplifier Rod	5 in. long x 3/4 in. diam. 0.5°/0.5°
Temperature Control	
Oscillator	Nominal 10°C ± 0.05°C
Amplifier	Nominal 10°C ± 0.2°C
Output Wavelength, λ	6943 Å
Oscillator Fresnel Number	0.4
Pulse Length	Nominally 13 ns (FWHM)
Beam Radius $w/\sqrt{2}$ [(a)]	
At Amplifier Input	1.2 mm
At Input to Experiment	2.75 mm
Beam Divergence of [(a)]	
Oscillator	0.88 mrad
Amplifier	1.15 mrad
Total Energy Output	approximately 38 mJ

(a) Measured directly by a pinhole scan of the beam at various positions in the far field of the oscillator.

Thermal stability is a major consideration in the reproducibility of the oscillator output. We thus not only control the operating temperature of the ruby rod, but also cool the optical mounts on which the oscillator cavity rests and flow dye through the etalon dye cell after each laser shot to prevent heating. Since it has been well established that careful oscillator design, alignment, and diagnostics [10] are essential to true near Gaussian single mode operation, we employ a time resolved 150 μ pinhole scan of the oscillator output beam as a regular diagnostic tool in oscillator alignment. [10]

In figure 3 we show three oscilloscope traces which illustrate the usefullness of the pinhole scan and the importance of both temperature control and careful alignment in attaining a spatially and temporally smooth oscillator output. The first pulses are time resolved traces of the entire (spatially integrated) oscillator output whereas the second pulses are taken from a 150 μ pinhole centered approximately at a 1/e power point from the beam center. Clearly, slight misalignment arising either from thermal variations or lack of mechanical stability can cause severe beam distortions. It is to be noted that portions of the beam can be distorted or delayed in time without distorting either the energy distribution of the output beam or the spatially integrated time evolution of the output. In this investigation, the oscillator is considered to be aligned when a pinhole scan shows the beam to exhibit identical pulse shape and time evolution within 0.5 ns over its entire cross section. In figure 4 a graph is shown giving peak intensity in the oscillator output as a function of radius taken from a pinhole scan at 2.5 Rayleigh distances from the oscillator output. The smooth curve is a Gaussian fit to the data.

4. Ellipse Rotation Experiment

4.1 Experimental Apparatus

A schematic diagram of the ellipse rotation apparatus is shown in figure 5 along with a diagram of the laser system layout. A set of calibrated Schott ND-419 neutral density filters (F1) are used to determine the input power to the specimen. A Rochon prism polarizer (P1) is used to define the input linear polarization and is followed by a Fresnel rhomb (R1) which converts the beam to an elliptical polarization. Various Rayleigh limit lenses (L1) of focal lengths from 15 to 25 cm then focus the beam centrally through the sample and a matching lens (L2) recollimates the beam. A second Fresnel rhomb (R2) and Rochon polarizer (P2) are then oriented so as to separate the transmitted beam into two orthogonal components: a "transmitted" signal which corresponds to the elliptically polarized input to the sample and a "null" signal which gives the orthogonal polarization and is thus directly proportional to F as given by eq (6). Typical extinction ratios between these two channels in the absence of ellipse rotation are 8×10^{-5} for all except the crystalline YAG samples which averaged extinction values of approximately 2×10^{-4}.

Five specific aspects of the apparatus merit further comment:

a) Focusing is a major factor in the implementation of these measurements in solid media. In addition to the advantages already cited in section 2.2 we note that lenses L1 and L2 in figure 5 are kept at a fixed separation and the samples are cut to the length required to maintain a collimated beam at the output of lens L2. This permits the interchange of samples with minimum disturbance to the optical alignment of the apparatus.

b) The Schott ND-419 neutral density filters (F1) which determine the input power to the sample are individually calibrated on a Cary 17 spectrophotometer and exhibit a maximum absolute error of 0.002 density per filter. By transferring the filters from stack F1 to F2 to increase the input power, the total attenuation between the laser system and the "null" (D3) and "transmitted" (D4) detectors are maintained at a constant level. The diode D3 thus provides a direct measurement of F and the influence of detector nonlinearities on the interpretation of the data is kept at a minimum.

c) The apparatus as shown in figure 5 provides a direct determination of F and is consequently nulled at low input power levels for which ellipse rotation is virtually negligible. The null detector (D3) only sees a very small, ~ 20 mW, signal in the absence of ellipse rotation. This configuration provides maximum sensitivity and is also most natural in terms of the circular mode analysis outlined in section 2. Additionally, the use of Fresnel rhombs rather than $\lambda/8$ plates to produce the elliptical polarization renders the system to be essentially independent of wavelength. Hence, a cw HeNe laser may be used to align and null the system and any strain birefringence in the sample being examined is easily detected. As a rule the apparatus is nulled prior to sample insertion and the samples are positioned to maintain the null.

d) Absolute calibration of nonlinear index measurements have traditionally been a difficult problem. [2,11] This is particularly true in focussed beam experiments where beam truncation and aberration can add pronounced structure to the focal region of the beam. [12,13] Although approximate results are obtained by direct substitution into eq (6) and the data are found to be truly independent of focusing for the variety of lenses used, we choose to calibrate all of our results to a reference sample of carbon disulphide, CS_2, for which $\chi_3^{1221}(-\omega,\omega,\omega,-\omega)$ is known to be 3.78×10^{-13} esu with an absolute accuracy of ± 2%. [14,15]

Table 2. Results of Ellipse Rotation Measurements

Material	$B/6 \times 10^{15}$	Refractive Index n at 6943 Å	Length of Samples of L(cm)
Fused Quartz[a]	1.28	1.455	11.0
American Optical LSO Glass	1.92	1.505	10.3
Owens-Illinois ED-4 Glass	2.39	1.557	9.7
Owens-Illinois EY-1 Glass	2.93	1.61	9.1
$YAG_{\phi=0}$[b]	7.18	1.829	7.6
$YAG_{\phi=\pi/2}$[b]	6.34	1.829	7.6
CS_2 (reference)	378	1.623	9.0

[a] The results for fused quartz are approximately 15% lower than those quoted in Ref. 4. This discrepancy is presumably the result of a small error of 0.07 density in the attenuating filters employed in Ref. 4.

[b] The YAG samples are grown by Crystal Optics Research Inc. Dimensions are 9.5 x 9.5 x 76.2 mm cut with (100) faces and X-ray oriented to better than 0.5 degrees.

It is interesting to note that the values of B seem to scale in some manner with linear refractive index and that our previous results [4] when recalibrated to be approximately 15% lower† fit into this table quite well.

6. Discussion and Conclusions

6.1 The Use of Ellipse Rotation Measurements to Determine Values for n_2

Since two independent measurements are necessary to completely specify nonlinear refractive index changes in isotropic media (three in cubic crystalline media), it is impossible to conclusively determine values of n_2 for a linearly polarized beam from ellipse rotation data alone. A supplementary measurement giving accurate a.c. Kerr, self focusing, or spontaneous Raman scattering results would provide the additional information necessary to resolve this problem. [16]

Until sufficient supplementary information becomes available to ascertain the physical mechanisms responsible for nonlinear index changes, it is useful to calculate the nonlinear refractive index n_2 for a linearly polarized beam by using our ellipse rotation data and assuming the mechansim responsible for n_2 to be purely electronic. [17] This is not an unreasonable assumption since third harmonic [18] and three wave mixing studies [5,19] in glasses and a variety of crystalline solids all indicate that the electronic contribution should be of the order of magnitude which is observed in the present study. Yet the results of these studies are not extensive or accurate enough to conclude that the mechanism is purely electronic in origin. [16]

† A recalibration of our previous result is merited on the basis of the measurement of B in fused quartz and the assessment that a 15% error occurred due to a small < 2% error in the calibration of the attenuating filters. See table 2.

e) As a final point regarding the experimental apparatus we note that the biplanar photodiodes used in this investigation are all capable of subnanosecond resolution. The output signals from diodes D1, D2 and D4 are displayed on Tektronix Model 519 oscilloscopes whereas D3, which samples a much weaker signal, is monitored by a Tektronix 7904 oscilloscope. The ellipse rotation data are thus time resolved and we may plot F vs $< P >_{av}$ from information which is taken directly off of the leading and trailing edges of individual laser shots. Hence, the apparatus not only provides a practical means of obtaining results rapidly, but also provides the capability to detect transient contributions to the measurement by comparing data taken from leading and trailing edges of a single laser shot.

4.2 Data Reduction

Values for F as a function of input power $< P >_{av}$ are obtained from data as shown in figures 5-8. The center photograph in each figure displays the output from diode D3 on a 10 mv/div, 5 ns/div scale. Figure 6 shows data at low input levels to the sample (no ellipse rotation) when the signal into D3 is a factor of 10^4 down from that at D4. Figure 7 shows the effect of rotating the output polarizer (P2) by a two degree angle. This provides an accurate absolute calibration for F. Finally figure 8 shows a shot on which ellipse rotation resulted. Note in particular the pulse sharpening in figure 8b which occurs as a consequence of the $< P >^2_{av}$ dependence of F.

Graphs of F vs $< P >_{av}$ are obtained by reading the peak input power from diode D2 and using this to calibrate F vs $< P >_{av}$ as taken directly from diodes D3 and D4 respectively. Data taken from a typical shot on a sample of Owens Illinois ED-4 glass is shown in figure 9. The data are corrected for surface reflections and also for the small null signal level which was shown in figure 6. In accordance with eq (6) the graph exhibits a slope of 2 and the agreement of data taken from the leading and trailing edges of the pulse support the contention that electrostrictive mechanisms are not contributing to the measurement. This conclusion is found to be true for all of the samples examined. The independence of the data over the variety of focal length lenses used in this study lend further support to this assertion.

Although single shot data seem to give quite adequate results, it is found that significant shifts in the F vs $< P >_{av}$ curve occur as a consequence of detection aperture misalignment, slight beam steering arising either directly from small variations in the oscillator output or from the adjustment of attenuating filters, and inhomogenities in the sample being examined. The last problem is of particular importance in the crystalline YAG samples for which the extinction ratio is extremely sensitive to sample positioning. As a consequence of such fluctuations, the accuracy of single shot measurements are assessed to be approximately $\pm$ 15%, whereas the repeatability can be increased to approximately $\pm$ 5% variation by averaging over many shots. Figure 10 gives F vs $< P >_{av}$ data taken in YAG for $\phi = \pi/2$. The data points are taken from the peaks of each shot and the scatter in the data is indicative of a possible 15% error on any single shot.

5. Results

The resultant values of B which are obtained from this investigation are tabulated in table 2. All the results are obtained from multiple shot runs for increased accuracy and are thus expected to be reproducible with an error of less than $\pm$ 5% relative to the CS_2 standard. A total absolute accuracy of $\pm$ 7% is assigned to these values and includes the possible errors arising from filter calibration and the calibration of the CS_2 standard. A measurement of B was made in YAG relative to itself for $\phi = 0$ and $\phi = \pi/2$ which led to the conclusion that

$$2\chi_3^{1221} \Big/ \left(\chi_3^{1111} + \chi_3^{1221} - 2\chi_3^{1122} \right) = 0.88 \pm 0.04$$

for YAG.

In cubic crystalline media with the electric field linearly polarized along the (100) crystal axis, one finds the nonlinear refractive index to be given by [11]

$$n_2 = \frac{12\pi}{n} \chi_3^{1111}(-\omega,\omega,\omega,-\omega) \tag{7}$$

whereas for a field along the (110) axis

$$n_2' = \frac{6\pi}{n}\left\{\chi_3^{1111} + \chi_3^{1221} + 2\chi_3^{1122}\right\} \tag{8}$$

It is to be noted that eq (8) is also relevant to the propagation of a linearly polarized beam along the (111) axis which is the case common to the operation of YAG lasers.

By assuming electronic distortion to be the only mechanism relevant to the index nonlinearity one finds that $\chi_3^{1221}(-\omega,\omega,\omega,-\omega) = \chi_3^{1122}(-\omega,\omega,\omega,-\omega)$; thus sufficient information to calculate n_2 and n_2' is available from ellipse rotation alone. The estimates of n_2 obtained by making this assumption are tabulated in table 3.

To verify the conclusion derived from the assumption of electronic distortion that $n_2'/n_2 = 0.96 \pm 0.015$, we have performed preliminary damage studies in YAG using focusing lenses with focal lengths ranging from 24 to 38 cm. Any large anisotropy in the nonlinear index would presumably be manifested in an anisotropy in the critical power for self focusing. In all cases damage resulted in a short (< 5 mm) single filamentary track and no anisotropy was observed within the limits of accuracy of the measurement. This is clearly consistent with our prediction of $n_2'/n_2 = 0.96 \pm 0.015$ but inconclusive in establishing that the self focusing mechanism is electronic. If an additional molecular nonlinearity were to contribute to the nonlinear index, the estimates made for the materials listed in table 3 would be high or low depending upon whether the additional mechanism is of a type which gives rise to a depolarized or polarized light scattering process respectively. [16]

Table 3. Estimated Values of n_2
$\delta n = n_2 < E^2(t) >_{av}$

Material	$n_2 \times 10^{13}$	Refraction Index n at 6943 Å
Fused Quartz	1.00	1.455
American Optical LSO Glass	1.44	1.505
Owens-Illinois ED-4 Glass	1.73	1.557
Owens-Illinois EY-1 Glass	2.06	1.61
YAG$_{\phi=0}$	4.27	1.829
YAG$_{\phi=\pi/2}$	4.10	1.829

6.2 Extended Ellipse Rotation Studies

In the experimental investigation described in sections 4-5 the ellipse rotation data were purposely taken at input power levels which produced values of F approximately in the range of 5×10^{-4} to 2×10^{-2}. Thus the signal was large enough to avoid noise problems, yet small enough to assure the absence of beam distortion due to self focusing.

Recently, we have initiated further ellipse rotation studies under conditions where F is greater than 10^{-2} and processes other than ellipse rotation are no longer negligible. Figure 11 shows data taken on fused quartz with an input focusing lens (L1) 24.7 cm in focal length. Note in particular the backward Brillioun scattered pulse returning through the laser system and the depletion of the trailing edge of the transmitted pulse by this process. Nondamaging stimulated backward Brilloun scattering was observed in all of the glass specimens except the EY-1 glass for which none was observed even in shots where damage occurred. A plot of F vs $< P >_{av}$ taken from figure 11 is shown in figure 12. It should be noted that the leading edge of the pulse exhibits the functional $F \propto < P >_{av}^2$ dependence predicted by eq (6) but that the trailing edge has seemingly been pinned to some constant level by a transient contribution.

Figure 13 shows similar data for EY-1 glass on a shot which resulted in damage. In figure 14 the information obtained from this shot is plotted in a composite graph which also shows data from a number of shots where information was taken only from the peak of the pulse, and one shot where a transient trailing edge was observed but no Brilloun scattering was detected. Figure 14 is particularly interesting in that it shows a slight deviation from the slope 2 dependence of F for the higher input levels. This could result from an axis intensity enhancement caused by the onset of self focusing.

The significance of the ellipse rotation data taken at higher input power levels is possibly twofold. Firstly it establishes that ellipse rotation results may be obtained from the leading edge of a laser shot even in cases where the trailing edge is distorted or when damage occurs. This is particularly relevant to measurements in alkali halides in which electrostriction is quite strong. Secondly this type of data offers the possibility of obtaining information concerning self focusing mechanisms, not only in separating out the transient response, but also by using the fact that self focusing sets in at different values of F depending upon the origin of the mechanism responsible for the index nonlinearity. [16]

6.3 Summary

In this paper we have established that the ellipse rotation technique can be used to make accurate (± 7%) non-damaging determination of nonlinear susceptibility elements relevant to the self focusing process. Moreover, the feasibility of making such measurements on a one-shot time resolved basis with ± 15% accuracy greatly increases the practical value of the technique and introduces the possibility of time resolving transient effects and obtaining useful data even in situations where electrostrictive self focusing may result in damage.

Ellipse rotation susceptibilities have been determined in two laser host glasses and two other glasses of interest in high power laser systems. In addition, a small anisotropy is seen in the nonlinear susceptibility of YAG and values for the nonlinear refractive indices of all of these materials have been inferred from the measurements by assuming electronic distortion to be the primary contributing mechanism.

7. Acknowledgements

We are pleased to acknowledge the technical assistance of Richard W. Willey in the experimental phases of this work.

8. References

[1] C. R. Giuliano and J. H. Marburger, "Observations of Moving Self-Foci in Sapphire," Phys. Rev. Letters 27, 905 (1971).

[2] B. E. Newnam and L. G. DeShazer, "Direct Nondestructive Measurement of Self-Focusing in Laser Glass," Damage in Laser Materials, NBS Spec. Pub. 356, 113 (1971).

[3] P. D. Maker, R. W. Terhune, and C. M. Savage, "Intensity-Dependent Changes in the Refractive Index of Liquids," Phys. Rev. Letters 12, 507 (1964).

[4] A. Owyoung, R. W. Hellwarth, and N. George, "Intensity-Induced Changes in Optical Polarization in Glasses," Phys. Rev. B 5, 628 (1972).

[5] P. D. Maker and R. W. Terhune, "Study of Optical Effects Due to an Induced Polarization Third Order in the Electric Field Strength," Phys. Rev. 137, A801 (1965).

[6] J. A. Armstrong, N. Bloembergen, J. Ducuing, and P. S. Pershan, "Interactions Between Light Waves in a Nonlinear Dielectric," Phys. Rev. 127, 1918 (1962).

[7] P. N. Butcher, "Nonlinear Optical Phenomena," Bull. 200 Engineering Station, Ohio State University, Columbus (1965).

[8] A. Owyoung, "Ellipse Rotation Studies in Laser Host Materials," IEEE J. Quantum Electron (to be published).

[9] L. G. DeShazer and J. H. Parks, "Investigations Toward Understanding the Physics of Laser Damage to Thin Dielectric Films," Damage in Laser Materials, NBS Spec. Publ. 356, 124 (1971).

[10] G. L. McAllister, M. M. Mann, and L. G. DeShazer, "Transverse Mode Distortions in Giant-Pulse Laser Oscillators," IEEE J. Quantum Electron. QE-6, 44 (1970).

[11] C. C. Wang, "Nonlinear Susceptibility Constants and Self-Focusing of Optical Beams in Liquids," Phys. Rev. 152, 149 (1966).

[12] D. J. Innes and A. L. Bloom, "Design of Optical Systems for Use with Laser Beams," Spectra Physics Laser Technical Bulletin, No. 5, Spectra Physics, Inc., (1966).

[13] B. E. Newnam, "Laser-Induced Damage Phenomena in Dielectric Films, Solids and Inorganic Liquids," thesis, University of Southern California, 1972.

[14] Y. A. Volkova, V. A. Zamkoff, and L. V. Nalbandov, "Precision Measurements of the Absolute Value of Kerr Constants," Opt. Spectrosc. 30, 399 (1971).

[15] R. W. Hellwarth, A. Owyoung, and N. George, "Origin of the Nonlinear Refractive Index of $CC\ell_4$," Phys. Rev. A 4, 2342 (1971).

[16] A. Owyoung, "The Origins of the Nonlinear Refractive Indices of Liquids and Glasses," thesis, California Institute of Technology, Dec. 1971.

[17] W. Voight, Ann. der Physik 4, 197 (1901).

[18] C. C. Wang and E. L. Baardsen, "Study of Optical Third Harmonic Generation in Reflection," Phys. Rev. 185, 1079 (1069); Errata in Phys. Rev. B1, 2827 (1970).

[19] H. Hauchecorne, F. Kerherve, and G. Mayer, "Measures Des Interactions Entre Ondes Lumineuses Dans Diverses Substrates," Le Journal de Physique 32, 47 (1971).

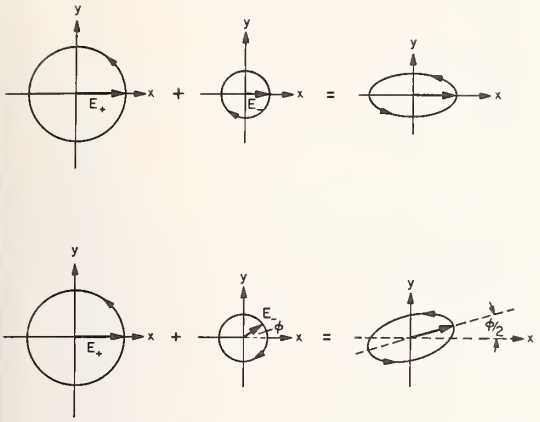

Figure 1. Diagramatic representation of ellipse rotation. Top: Elliptically polarized input with two circular components. Botton: Relative phase shift ϕ causes an ellipse rotation of $\phi/2$.

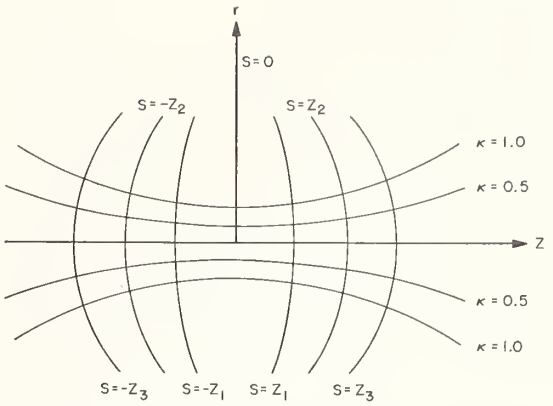

Figure 2. Representation of a Gaussian beam in prolate spheroidal coordinates. The surfaces of constant phase are parabolic and the rays form hyperbolic surfaces parameterized by $\chi = r^2/w^2$ (z) along which the intergration Eq.(4) proceeds.

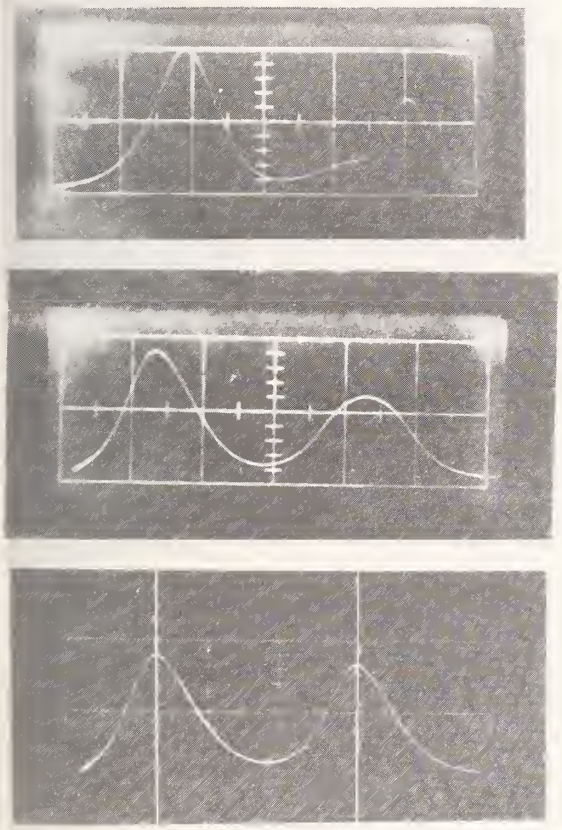

Figure 3. Photographs of oscillator output pulses (10 ns/div). The first pulse is a spatially integrated sampling of the entire beam whereas the second pulse shows the top 1/e power point of the beam as sampled by a 150 μ pinhole. Top, center, and bottom photographs show gradual alignment as the temperature of the optical bench is lowered from 80°F to 73°F to 70°F.

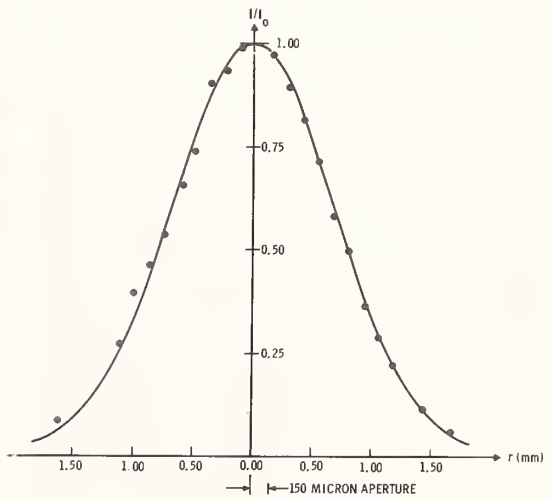

Figure 4. Pinhole scan of oscillator output at 2.5 Rayleigh lengths from the oscillator. Data points record peak intensity at each point normalized to the peak intensity at the beam center. Solid curve is a Gaussian fit to the data.

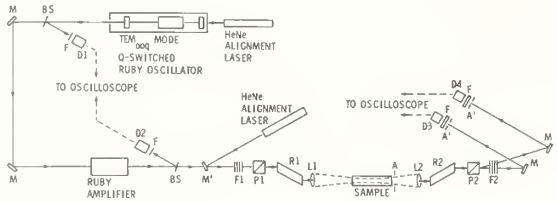

Figure 5. Schematic of ellipse rotation apparatus. P1 and P2: Rochon prism polarizers, R1 and R2: Fresnel rhombs, L1 and L2: Rayleigh limit focusing lenses, F1 and F2: calibrated neutral density filters, f: 100 Å BW spike filters, D1-D4: ITT FW114A S-20 biplanar photodiodes, M: 100% mirror, M': removable mirror, BS: beam splitter, A: aperture, A': 4mm aperture.

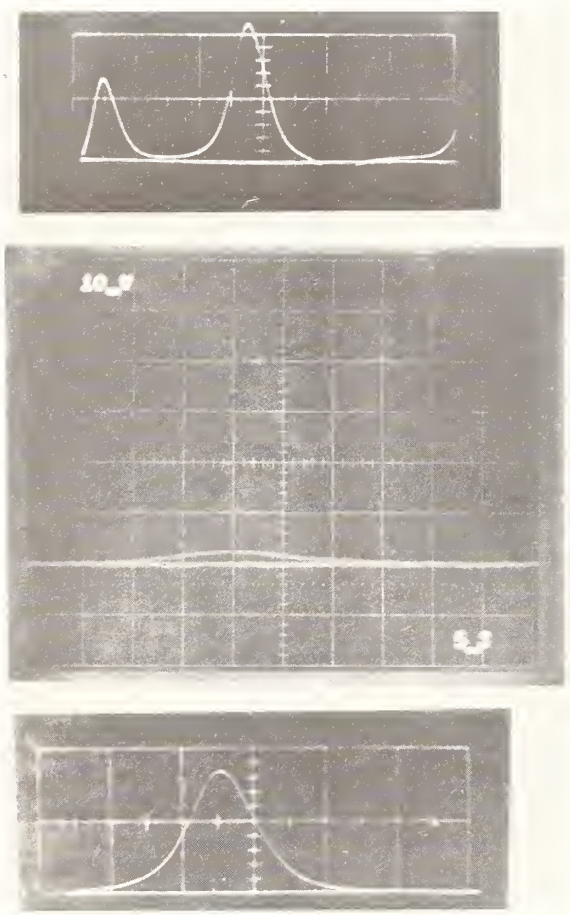

Figure 6. Data taken from diodes D1-D4 for low input power. Top: Oscillator (D1) and amplifier (D2) output 20 ns/div; Center: Null signal (D3) 5 ns/div; Transmitted signal (D4) 10 ns/div.

Figure 7. Data taken from diodes D1-D4 for calibration of F. Top: Oscillator (D1) and amplifier (D2) output 20 ns/div; Center: Null signal (D3) with polarizer (P2) turned 2^{o} off of the null position 5 ns/div; Transmitted signal (D4) 10 ns/div

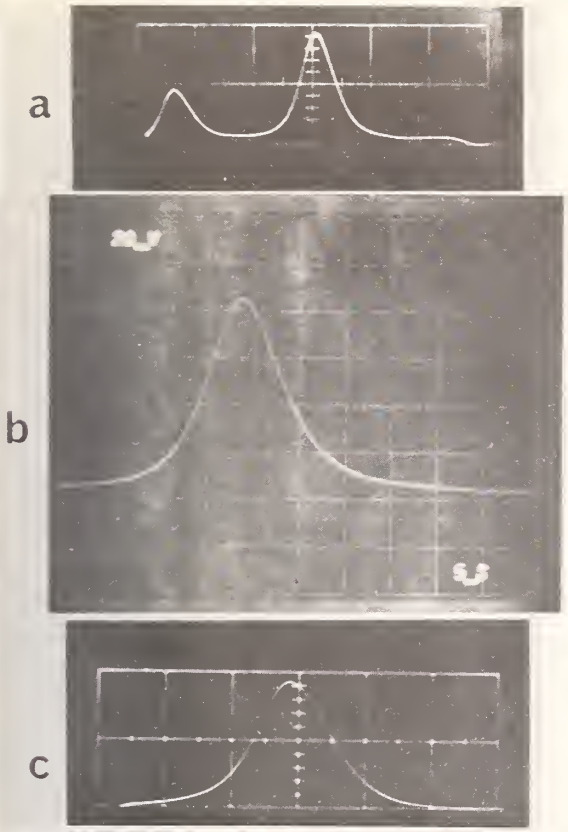

Figure 8. Data taken from diodes D1-D4 showing ellipse rotation. Top: Oscillator (D1) and amplifier (D2) output 20 ns/div; Center: Ellipse rotation signal (D3) 5 ns/div; Bottom: Transmitted signal (D4) 10 ns/div.

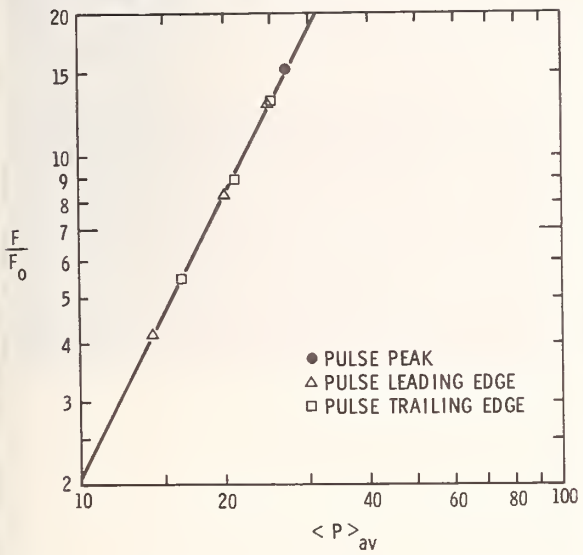

Figure 9. Graph of F vs $< P >_{av}$ for Owens-Illinois ED-4 glass obtained on a single time resolved laser shot. The data on the leading and trailing edges of the pulse are taken in 2 ns increments. The scaling factor $F_o \approx 8.7 \times 10^{-4}$ and $< P >_{av} = 1$ is approximately 14.5 kW.

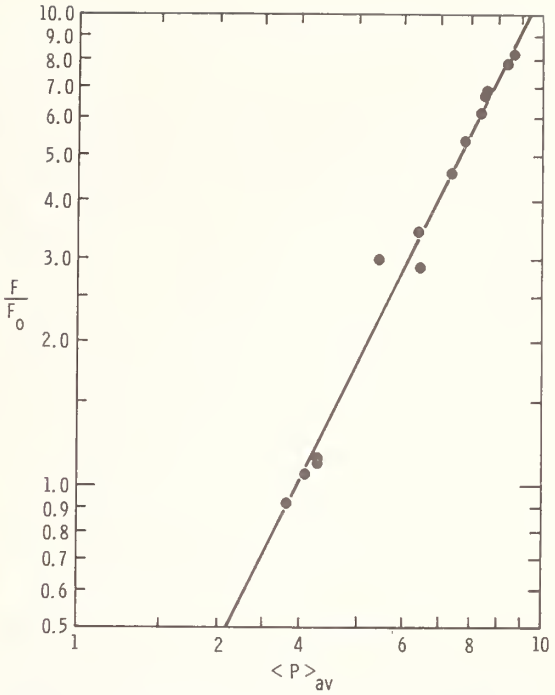

Figure 10. Graph of F vs $< P >_{av}$ for YAG with $\phi = \pi/2$ taking data only from the peaks of each laser shot. The scaling factor $F_o \approx 8.7 \times 10^{-4}$ and $< P >_{av} = 1$ is approximately 15 kW.

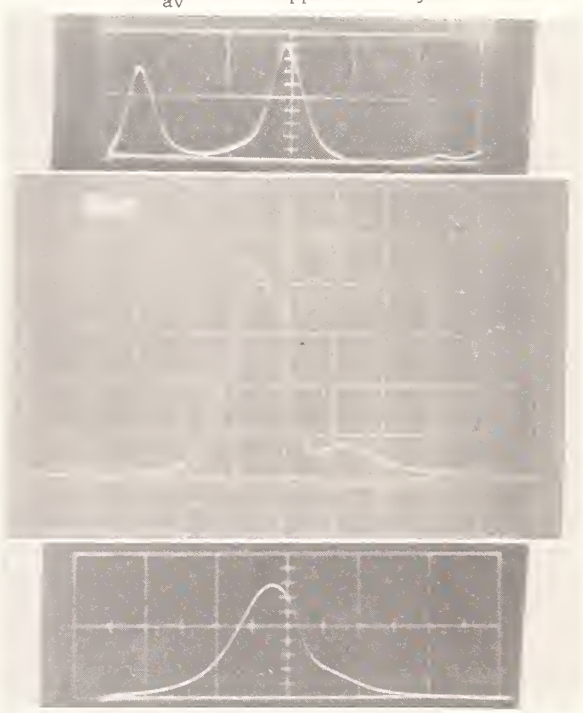

Figure 11. Data taken from diodes D1-D4 for a sample of fused quartz. Top: D1-D2; Center: D3; Bottom: D4. Note the depletion of the trailing edge of the transmitted pulse (D4) by the backward Brillioun pulse which is seen coming back through the laser system output detectors.

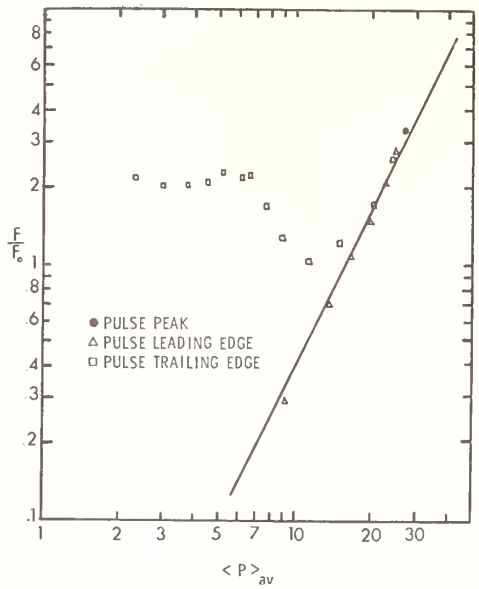

Figure 12. Graph of F vs $< P >_{av}$ for the data in Figure 11. The solid line is a slope 2 fit to the leading edge of the laser pulse. The dip in the trailing edge data corresponds roughly in time to the Brillioun pulse. The data points are taken in 1-2 ns increments.

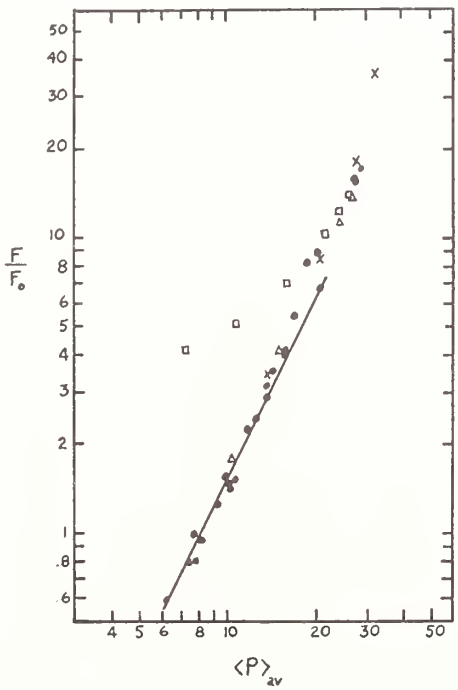

Figure 14. Composite graph of F vs $< P >_{av}$ for EY-1 glass. X - data taken from Figure 13; - data taken from peaks of many individual shots and Δ, - data taken from leading and trailing edges of a nondamaging shot slightly below the damage threshold.

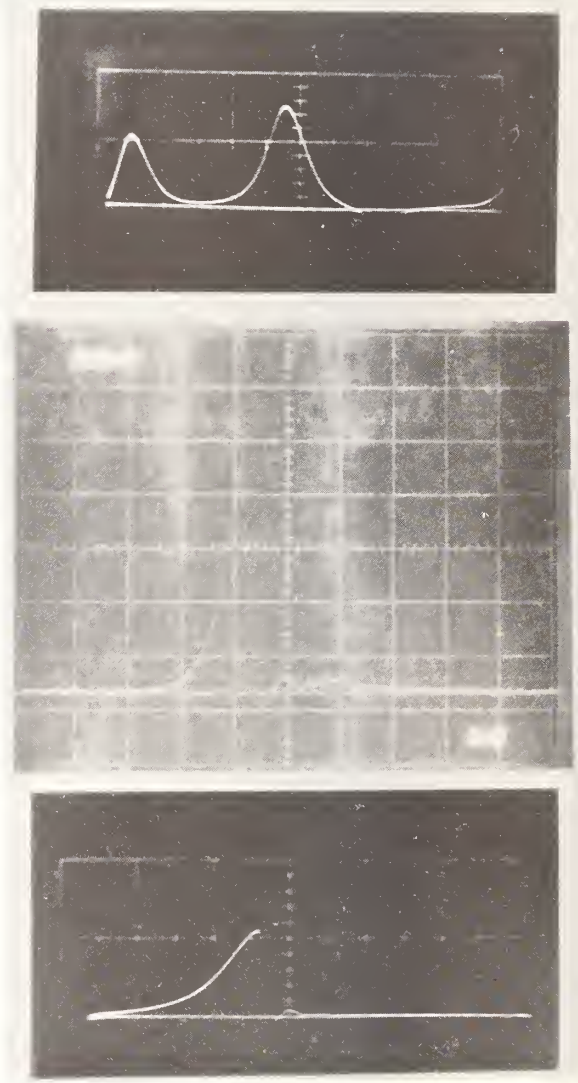

Figure 13. Data taken from diodes D1-D4 for a damaging shot on EY-1 glass.

Concern was expressed by a number of members of the audience concerning the validity of the assumption that only electronic contributions to the nonlinear susceptibility were operative. The speaker pointed out that the fact that the ellipse rotation signal followed the intensity profile of the pulse with good fidelity was evidence that electrostrictive effects were not present. However, he commented that it was possible that there could be contributions to the nonlinear susceptibility from Raman active modes in the medium and other non-electronic, but prompt, phenomena.

Self-Focusing in Yttrium Aluminum Garnet and Optical Glasses*

Albert Feldman, Deane Horowitz, and Roy M. Waxler

National Bureau of Standards, Washington, D. C. 20234

An analysis of damage threshold data in borosilicate crown glass, fused silica, and dense flint glass for linearly and circularly polarized radiation indicates that the Kerr effect is the dominant self-focusing measurement for 1.06 μm laser pulses with a 25 ns temporal width. The calculated thermal effect is found to be larger than the electrostrictive effect, which is small. Self-focusing length measurements in yttrium aluminum garnet (YAG) are found to agree with theory. In YAG, the Kerr effect also dominates.

Key Words: Absorption coefficient, electrostriction, Kerr effect, laser damage, nonlinear refractive index, optical glasses, self-focusing, thermal self-focusing, yttrium aluminum garnet.

1. Introduction

The question of which process is responsible for self-focusing [1][1] with pulses ∿ 25 ns has not yet been adequately answered. Three principal mechanisms have been proposed, the electrostrictive effect [2-6], the Kerr effect [2-4,7], and the thermal effect [8-11]. In general, each of the effects can contribute to the nonlinear index and which effect predominates would depend upon the particular material under study.

We have attempted to estimate the relative contributions of each of the effects to the nonlinear indices of yttrium aluminum garnet (YAG), borosilicate crown glass (BSC), fused silica and dense flint glass (SF 55) from an analysis of damage and self-focusing threshold data obtained with circularly and linearly polarized Nd:glass laser radiation. The analysis suggests that the Kerr effect is the predominant self-focusing mechanism in all the materials. Furthermore, it is shown that thermal effect can make an important contribution. The electrostrictive effect is found to be small. In addition, we find good agreement with the theory of self-focusing for measurements conducted on YAG. Similar measurements conducted on Nd:doped laser glass give poor agreement with theory.

2. Theory of the Nonlinear Index

Self-focusing of laser radiation occurs when the focusing effect due to the intensity-dependent refractive index exceeds the spreading of the beam by diffraction. The refractive index of the medium can be expressed in the form

$$n = n_o + n_2 E^2 \tag{1}$$

where E is the RMS electric field obtained from an average over several optical cycles. The nonlinear index n_2 is a linear sum of contributions from each of the proposed self-focusing mechanisms. If the mechanism instaneously follows the temporal shape of the laser pulse, its contribution to n_2 is a constant independent of time. For the experimental conditions in this paper, both the Kerr and electrostrictive effects are instantaneous and their respective contributions to n_2 are $n_2(K)$ and $n_2(ES)$.

---

*This research was supported in part by the Advanced Research Projects Agency of the Department of Defense.

[1]Figures in brackets indicate the literature references at the end of this paper.

The thermal effect, however, is not instantaneous. Its contribution to n_2 is a function of time, and hence, n_2 is a function of time. We define $n_2(T)$ as the contribution of the thermal effect to n_2 at the time corresponding to the peak of the laser pulse (t=o).

A critical power for self-focusing exists when n_2 is independent of time. At this power level, the self-focusing effect exactly cancels the spreading of the laser beam by diffraction. The presence of a thermal effect implies that a unique critical power does not exist. The concept of a critical power is still useful. Let us assume a sequence of laser pulses having the same temporal shape but with progressively increasing amplitude. Self-focusing will occur when the peak power of the pulse reaches a critical value, p_{cr}, and this value will be unique. For a given pulse shape, $E^2 = E_o^2 f(t)$, we can write eq (1) in the form

$$\delta n = n_2(t)\, E_o^2 , \tag{2}$$

where E_o^2 is the peak value of E^2, and the time dependence of E^2 is incorporated into $n_2(t)$. At a time $t \cong t_o$, δn will have a maximum value. At a critical value of E_o^2, self-focusing will take place and we can obtain an expression for p_{cr}. It must be emphasized that the maximum index change will not occur at the peak of the pulse. The expression for p_{cr} that we use has been derived for beams with a Gaussian profile [6,12,13]:

$$P_{cr} = \lambda^2\, c/(32\, \pi^2\, N_2) \tag{3a}$$

where λ is the wavelength of the laser radiation in air, c is the velocity of light, and N_2 is equal to $n_2(t_o)$. Equation (3a) is also equal to P_1 in the work of Dawes and Marburger [14]. P_{cr} can be derived from damage threshold data obtained by focusing the laser beam into the sample [15] with lenses of different focal lengths. For damage thresholds $P_t(1)$ and $P_t(2)$ obtained with lenses of focal lengths of f_1 and f_2 respectively, we find

$$P_{cr} = (f_2^2 - f_1^2)/[f_2^2/P_t(2) - f_1^2/P_t(1)]. \tag{3b}$$

We use f instead of the focal spot size a because for the lenses used in this work a is proportional to f. The validity of (3a) and (3b) for calculating N_2 has been discussed by Fradin [15] It is discussed further in Section 3.

2.1 The Kerr Effect

In this work we assume that the Kerr effect arises from nonlinearities in the electronic polarizabilities and that orientational effects can be ignored. Recent experimental work [16] suggests this may be the case. Thus the Kerr effect would be instantaneous up to optical frequencies.

For an isotropic material the nonlinear polarization is given by [17]

$$\vec{P}_{NL} = 3\, c_{1122} (\vec{E}\cdot\vec{E})\vec{E}; \tag{4}$$

c_{1122} is a constant. If we insert the field for a linearly polarized wave

$$\vec{E} = E_o \sqrt{2}[\cos(\omega t - kz),\ 0,\ 0] \tag{5}$$

and a circularly polarized wave of equal intensity

$$\vec{E} = E_o[\cos(\omega t - kz),\ \sin(\omega t - kz),\ 0] \tag{6}$$

into eq. (4) and calculate the Fourier component of $\vec{P}_{NL}$ at frequency ω, we obtain a ratio of 1.5 for $n_2(K)/n_2'(K)$. (Throughout this paper primed symbols refer to circular polarization, and unprimed symbols to linear polarization.) Third harmonic contributions can be ignored because the phase matching condition is not met.

2.2 Electrostrictive Self-Focusing

Electrostrictive self-focusing is due to refractive index changes caused by strains induced by the strong electric fields present in high-powered laser radiation. E. L. Kerr has treated the full dynamical problem of electrostrictive self-focusing [6]. He has shown that the electrostrictive response will depend on the parameter $X = a_o/v\tau$, where a_o is the 1/e intensity point radius of a Gaussian beam at the focus of a lens in the absence of self-focusing, v is the longitudinal sound velocity in the medium, and τ is the temporal pulse width of the laser beam at half the maximum

power. Kerr has shown that for $X < 1$, the electrostrictive strain has time to develop fully and hence $n_2(ES)$ can be calculated from the steady state. For our experimental conditions, $a_o \lesssim 16.9$ μm, $\tau = 25$ ns, and v varies from 3×10^3 m/s to 6×10^3 m/s, yielding $X \lesssim 0.2$. The electrostriction can follow the pulse shape and hence the instantaneous approximation is valid. Kerr, in treating the problem of electrostrictive self-focusing, has ignored the tensorial nature of the effect because of the complexity of solving vectorial differential equations. In view of the steady state nature of the problem as applied to our work, we treat the effect as a statics problem and therefore we can take into account the tensorial properties of electrostriction. We calculate $n_2(ES)$ and $n_2'(ES)$ for a material containing a uniform electric field in a cylindrical region and zero electric field outside this region. A rigorous calculation would be more complex due to the Gaussian spatial variation of the laser field. However, the solution we obtain is rigorously correct on the axis of the laser beam.

The strain induced in the cylindrical region due to the intense electric field is given by [18]

$$\varepsilon_{kl} = \gamma_{ijkl} \langle E_i E_j \rangle / 2 + S_{klmn} P_{mn} \quad , \tag{7}$$

where γ is the electrostriction tensor, S is the elastic compliance tensor, P is the stress tensor, and $\langle\ \rangle$ denotes a time average. The stress comes from the constraining effect of the field free region. From a set of thermodynamical Maxwell's equations, we can show that [19-21]

$$\gamma_{ijkl} = -\kappa_{im} \kappa_{jn} q_{mnkl} / 4\pi, \tag{8}$$

where κ is the dielectric tensor and q is the stress-optic tensor. The change in dielectric tensor with strain is given by

$$\Delta[\kappa^{-1}]_{ij} = p_{ijkl}\ \varepsilon_{kl}; \tag{9}$$

p is the elasto-optic tensor. In order to calculate $n_2(ES)$ and $n_2'(ES)$, we must first calculate the electrostrictive strains

$$\varepsilon^o_{kl} = \gamma_{ijkl} \langle E_i E_j \rangle / 2. \tag{10}$$

For an isotropic material the net strain becomes [22]

$$\varepsilon_{11} = [2(\varepsilon^o_{11} + \varepsilon^o_{22}) + (3 - 4\nu)(\varepsilon^o_{11} - \varepsilon^o_{22})]/[8(1 - \nu)]; \tag{11a}$$

$$\varepsilon_{22} = [2(\varepsilon^o_{11} + \varepsilon^o_{22}) - (3 - 4\nu)(\varepsilon^o_{11} - \varepsilon^o_{22})]/[8(1 - \nu)]; \tag{11b}$$

$$\varepsilon_{33} = 0, \tag{11c}$$

where ν is the Poisson ratio. These strain components are inserted into eq (9) and the final result is

$$n_2'(ES) = n_o^7 (q_{11} + q_{12} + 2\nu q_{12})(p_{11} + p_{12})/[64\pi(1 - \nu)]; \tag{12}$$

$$n_2(ES) = n_o^7 (q_{11} - q_{12})(p_{11} - p_{12})(3 - 4\nu)/[128\pi(1-\nu)] + n_2'(ES). \tag{13}$$

Equation (12) is identically equal to Kerr's [6] steady state limit.

2.3 Thermal Self-Focusing

Thermal self-focusing results from positive refractive index changes caused by absorptive heating of a sample exposed to high-energy laser radiation. For an isotropic material the change of index with temperature is

$$\frac{dn}{dT} = \left(\frac{\partial n}{\partial T}\right)_\rho - \frac{n_o^3 (1 + \nu)(p_{11} + p_{12})\beta}{12(1 - \nu)}\ ; \tag{14}$$

β is the volume coefficient of expansion. We assume that heat diffusion does not occur during the passage of the laser pulse. The thermal effect differs from the two previous effects in that it depends upon the integrated energy of the pulse.

The first term in eq (14), the change of index with temperature at constant density, follows the instantaneous temperature. The change in temperature is governed by electron-phonon relaxation times which are fast compared to 25 ns. The term is positive in most glasses.

The second term in eq (14) is the change in index with temperature due to thermcelastic strains. It is derived with the same boundary conditions used to compute the electrostrictive strain. These boundary conditions take into account the constraining effect of the material surrounding the irradiated portion of the sample. A similar term has been derived by Zverev et al. [23], who have pointed out that, due to the constraining stresses, thermal self-focusing can take place even though the conventional value of $dn/dT < 0$. The response time of the thermoelastic strain term is equal to the response time of electrostriction. Since $X < 1$ it will also respond to the temperature instantaneously. The change of index due to the thermal effect is [8]

$$\delta n(t) = \frac{\alpha c n_o}{4\pi C_p \rho} \frac{dn}{dT} E_o^2 \int_{-\infty}^{t} g(t_1/\tau) dt_1 \tag{15}$$

where $g(t/\tau) = f(t)$, α is the absorption coefficient, c is the velocity of light, C_p is the specific heat at constant pressure, and ρ is the density. We assume that the absorption coefficient is small so that the laser beam undergoes insignificant attenuation while passing through the sample. From eqs (3a) and (15) we see that the thermal self-focusing threshold will vary inversely with the pulse width. There will be no polarization effects for isotropic materials, i.e., $n_2(T)/n_2'(T) = 1$.

2.4 Combined Effect

The change of index will equal the sum of the contributions from each of the effects. At this point it becomes convenient to assume that f(t) has a Gaussian slope, i.e.,

$$f(t) = \exp[-4t^2/\tau_e^2] , \tag{16}$$

where $\tau_e \approx 1.2\ \tau$. The change of index is then

$$\delta n = [n_2(K) + n_2(ES)]\ E_o^2 \exp[-4t^2/\tau_e^2] + n_2(T)\ E_o^2\ [1 + \mathrm{erf}(2t/\tau_e)], \tag{17}$$

where

$$n_2(T) \approx \frac{.075}{\sqrt{\pi}} \frac{\alpha\ c\ n_o\ \tau}{C_p\ \rho} \frac{dn}{dT} \tag{18}$$

and erf(x) is the error function. The maximum value of δn occurs at times

$$t_o = \tau_e n_2(T)/2\sqrt{\pi}[n_2(ES) + n_2(K)]; \tag{19a}$$

$$t_o' = \tau_e n_2(T)/2\sqrt{\pi}[n_2'(ES) + 2n_2(K)/3]. \tag{19b}$$

The nonlinear index is then

$$N_2 = [n_2(K) + n_2(ES)]\exp[-(2t_o/\tau_e)^2] + n_2(T)\ [1 + \mathrm{erf}\ (2t_o/\tau_e)] \quad ; \tag{20a}$$

$$N_2' = [2n_2(K)/3 + n_2'(ES)]\exp[-(2t_o'/\tau_e)^2] + n_2(T)\ [1 + \mathrm{erf}\ (2t_o'/\tau_e)]. \tag{20b}$$

3. Results and Discussion

3.1 Optical Glass

At the previous symposium [24] we reported on damage threshold measurements in BSC glass, fused silica and SF 55 glass for linearly and circularly polarized radiation. The data were obtained by focusing into the sample the output of a Nd:glass laser operating in the TEM_{oo} mode (τ=25 ns). At that time we described in detail the experimental apparatus and the experimental procedure [24-26].

In this section we present a re-analysis of the earlier data on the basis of the theory presented in Section 2. In table 1 we summarize the damage threshold data, which were obtained using lenses with focal lengths of 76 mm and 181 mm. Corrections have been made for the recalibration of our thermopile

energy meter and for the reflection from the sample entrance face. The estimated errors in the data are ± 12%. The errors arise from several sources, including the scatter in the data, the calibration of the thermopile, the calibration of the oscilloscope time base, and the ability to integrate the temporal pulse in order to obtain the peak pulse power from the pulse energy.

We now proceed to calculate N_2, $n_2(ES)$, $n_2(K)$ and $n_2(T)$ making several assumptions. We assume that the damage results from the concentration of the laser energy due to self-focusing. The agreement of self-focusing length measurements with theory for the glasses discussed herein [24] suggests that the assumption is valid. We assume that stimulated Brillouin scattering can be ignored because experiments have shown that the effect is absent when broad band Nd:glass laser radiation is used [27].

Table 1. Contributions of Kerr, Electrostrictive, and Thermal Effects to Self-Focusing Thresholds.[a]

	BSC 517	Fused Silica	Dense Flint SF 55
$P_t(1)$[b] (MW)	0.47 ± .06	0.65 ± .07	0.124 ± .015
$P_t(2)$[c] (MW)	0.75 ± .09	1.01 ± .12	0.128 ± .015
$P_t'(1)$[b] (MW)	0.55 ± .07	0.71 ± .08	0.153 ± .018
$P_t'(2)$[c] (MW)	0.94 ± .13	1.25 ± .15	0.170 ± .018
P_{cr} (MW)	0.86 ± .14	1.15 ± .18	0.129 ± .018
P_{cr}' (MW)	1.10 ± .20	1.49 ± .25	0.174 ± .022
N_2 (10^{-13} esu)	1.24 ± .20	0.93 ± .15	8.3 ± 1.2
N_2' (10^{-13} esu)	0.97 ± .18	0.72 ± .12	6.1 ± 0.8
$n_2(ES)$ [10^{-13} esu]	0.13	0.16	0.68
$n_2'(ES)$ [10^{-13} esu]	0.11	0.13	0.68
$n_2(K)$ [10^{-13} esu]	0.80 ± .38	0.56 ± .27	6.4 ± 1.9
$n_2(T)$	0.29 ± .27	0.19 ± .19	1.1 ± 1.2
α (cm^{-1})	(3 ± 3) x 10^{-3}	(9 ± 9) x 10^{-4}	(7 ± 7) x 10^{-3}

[a] The errors occur from the scatter in the data and from the uncertainty in the power calibration.

[b] Obtained with 76 mm focal length lens [25]. The data have been corrected for thermopile calibration and for sample entrance face reflection.

[c] Obtained with 181 mm focal length lens.

We calculate P_{cr}, P_{cr}', N_2 and N_2' from $P_t(1)$, $P_t'(1)$, $P_t(2)$, and $P_t'(2)$ using (3a) and (3b). We justify the use of these equations as follows. For an unfocused laser beam of power P, in which the intensity does not exceed the damage threshold at the entrance to the sample, damage due to self-focusing will occur when $P_{cr} < P < P_2$, where $P_2 \approx 4\, P_{cr}$ [14]. For a tightly focused geometry, which corresponds to our experimental conditions, damage is expected to occur when $P < P_{cr}$, because when $P = P_{cr}$, the energy density at the geometrical focus is expected to exceed the damage threshold of all materials due to the cancellation of diffraction spreading by self-focusing. In this case, (3a) and (3b) are valid for calculating N_2. In the event that, contrary to our expectations, damage does not occur when $P = P_{cr}$, the value of n_2, obtained with (3a) and (3b) will form a lower bound to the true value. The fractional deviation of N_2' from its true value is expected to be smaller than the corresponding deviation for N_2 because $P_{cr}' > P_{cr}$ and it seems reasonable to assume that the damage threshold in the absence of slef-focusing is independent of polarization. The ratio of N_2/N_2' would be closer to unity than the true ratio and, hence, the calculated value of $n_2(T)$ would be enhanced at the expense of $n_2(K)$. We believe that the use of these equations is valid to a good approximation because the values of $n_2(K)$ we obtain are consistent with the work of others and the absorption coefficients obtained are reasonable for optical glasses.

The parameters necessary for all the calculations are given in table 2. We calculate $n_2(ES)$ and $n_2(ES)$ with eqs (12) and (13). The numbers for p_{11}, p_{12}, q_{11}, and q_{12} given in table 2 have been measured at visible wavelengths; however, we do not expect them to differ significantly at 1.06 μm. The values for $n_2(K)$ and $n_2(T)$ are calculated by numerically solving eqs (19) and (20) with the values for N_2, N_2, $n_2(ES)$ and $n_2(ES)$ as input parameters.

Table 2. Input Parameters Necessary for Calculating the Contributions to Self-Focusing.

	BSC 517	Fused Silica	Dense Flint (SF 55)
c_p (10^6 erg $g^{-1}K^{-1}$)	8.6[a]	7.5[b]	8.4[c]
ρ (g cm^{-3})	2.51[a]	2.2	4.72[c]
$(\partial n/\partial T)_\rho$ (10^{-6} K^{-1})	8.3[d]	9.7[e]	21.5[d]
β (10^{-6} K^{-1})	20.0[a]	1.5	24.6[c]
q_{11}($10^{-13}$$cm^2$/dyn)	0.315[f]	0.418[g]	1.7[h]
q_{12}($10^{-13}$$cm^2$/dyn)	1.92[f]	2.71[g]	2.2[h]
p_{11}	0.115[f]	0.120[g]	0.21[h]
p_{12}	0.221[f]	0.270[g]	0.23[h]
ν	0.204[a]	0.164	0.247[c]
n_o (1.06 μm)	1.507	1.450	1.733

[a] Taken to be the same as BK 7, see ref. c.

[b] A. B. Sosman, The Properties of Silica (Chemical Catalogue Company, New York, 1927), p. 314.

[c] Catalogue, Schott Optical Glass, Inc., Duryea, Pennsylvania.

[d] Calculated from dn/dT given in ref. c and from the elasto-optic coefficients.

[e] Calculated from dn/dT given in J. B. Austin, "A Vacuum Apparatus of Measuring Thermal Expansion at Elevated Temperatures, with Measurements on Platinum, Gold, Magnesium, and Zinc," Physics, vol. 3, pp. 240-267, (1932), p. 248, and from the elasto-optic coefficients.

[f] R. M. Waxler and C. E. Weir, J. Res. Natl. Bur. Std. 69A, 325 (1965); λ = 587.6 nm.

[g] W. Primak and D. Post, "Photoelastic Constants of Vitreous Silica and Its Elastic Coefficient of Refractive Index," J. Appl. Phys., vol. 30, pp. 779-788 (1959): λ = 546.1 nm.

[h] Ref. [25].

We summarize our results in table 1. An examination of the results indicates that the Kerr effect is the largest contributor to self-focusing for the beam parameters of this experiment. The data indicate that the electrostrictive effect is much smaller than the Kerr effect. This conclusion differs considerably from our earlier result [24,25] because in that work we had neglected two important effects: We had ignored the thermal effect and we had ignored the constraining effects of the medium surrounding the irradiated portion of the sample when calculating the electrostrictive effect.

Our results indicate that the thermal effect can be of considerable importance for self-focusing with 25 ns pulses. Because of the pulse width dependence of $n_2(T)$, the importance of the thermal effect for shorter pulses decreases. However, because of its integrating nature, thermal self-focusing can be very important in high repetition rate systems even though the individual pulses are quite short. It is of interest to deduce the absorption coefficient α necessary to account for $n_2(T)$. These values are presented at the bottom of table 1. The numbers obtained are consistent with parameters for optical glasses. Our value of α for BSC 517 is close to the value for a similar glass, BK 7 ($\alpha = 3 \times 10^{-3}$ cm^{-1}), as reported by McMahan [28]. The absorption coefficient for our fused silica is considerably larger than the largest value measured by Rich and Pinnow ($\alpha = 1.6 \times 10^{-4} cm^{-1}$) [29]. Because the sources of our material differ, the fused silica we used may actually have a higher absorption coefficient.

A comparison of our results with the data of other workers is shown in table 3. The data are grouped according to glass type. BK 7 and BSC 517 are borosilicate crown (BSC) glasses; SF 7, SF 55, and La SF 7 are flint glasses. We can only properly compare the values for BSC glass and fused silica since the flint glasses differ significantly. Owyoung et al. [16] have calculated $n_2(K)$ by measuring the rotation of the principal axes of elliptically polarized light from a single frequency ruby laser. Our values of N_2 agree quite well with their values of $n_2(K)$; however, our values of $n_2(K)$ are smaller than theirs. The fact that the ratio of their values to ours is approximately a constant (1.8) suggests that the numbers differ by a systematic constant and that the relative values we obtain are correct. The differences in the data might be explained by dispersion effects, by differences in the glasses, and by uncertainties introduced by our use of (3a) and (3b), which we discussed earlier in this section. On the other hand, our value of $n_2(K)$ for BSC glass falls between the value obtained by McMahon [28] from self-focusing measurements with picosecond pulses and the value of Duguay and Hansen [30]. Duguay and Hansen measure $n_2(K)$ from the intensity induced birefringence caused by picosecond pulses. Because of a difference in definition, the numbers given in table 3 for them are half the values in the reference [30]. While the values for the flint glasses are not directly comparable, they indicate that all these glasses will have low self-focusing thresholds.

From our calculations, we note that $n_2(K)$ increases with refractive index. This is in qualitative agreement with the work of Wang [31].

Table 3. Comparison of Nonlinear Index Coefficients in Units of 10^{-13} esu. Borosilicate Crown Glasses and Flint Glasses are Grouped Separately.

	N_2[a]	$n_2(K)$[a]	$n_2(K)$[b]	$n_2(K)$[c]	$n_2(K)$[d]
Fused Silica	0.93	0.56	1.00		
BK-7			1.47	0.6	1.0
BSC 517	1.24	0.80			
SF 7			5.9		
SF 55	8.3	6.4			
LaSF 7					3

[a] This work $-\lambda = 1.06$ μm

[b] Reference [16] $-\lambda = 0.69$ μm. Numbers are lowered by 15% [A. Owyoung, private communication].

[c] Reference [28] $-\lambda = 1.06$ μm

[d] Reference [30]. For comparison with our results the numbers given are half the values in the reference because of differences in definition.

3.2 Self-Focusing Lengths in YAG

Recent experiments [32-35] have shown that the filamentary damage observed when solids are exposed to high-intensity laser radiation is due to the movement of a self-focused spot which moves toward the laser source as the power rises on the leading edge of the pulse. Assuming that n_2 responds instantaneously to the laser pulse power, Dawes and Marburger [14] have made a detailed computer calculation that predicts the self-focusing length as a function of beam power. We have shown that self-focusing lengths calculated from damage tracks produced in several optical glasses agree well with the theory [24].

We have produced damage filaments in YAG by focusing the laser beam at different peak power levels P into the sample using a 181 mm focal length lens. Propagation was along the [111] axis. Both linearly and circularly polarized radiation were used. A length z_f was measured from the upstream end of the damage track to the sample entrance face. The self-focusing length z was calculated from the formula [36].

$$z^{-1} = z_f^{-1} - R^{-1},$$

where R is the radius of curvature of the laser wavefront at the sample entrance face. R is calculated from the measured focal point of the lens and the propagation characteristics of Gaussian beams.

The normalized inverse self-focusing length $(z^*)^{-1}$ is plotted as a function of $P^{1/2}$ in figure 1, together with the theoretically predicted curves [14], where $z^* = z/ka^2$ and $k = 2\pi n_o/\lambda$; n_o is the refractive index; λ is 1.06 μm; a is the 1/e intensity point radius at the sample entrance face. The square data points have been obtained with linearly polarized radiation; the circular points have been obtained with circularly polarized radiation. The theoretical curves have been fitted to the data empirically by varying the critical power P_2. Agreement between theory and experiment is quite good. The values for the critical power that we obtain are $P_2 = 0.40$ MW and $P_2 = 0.50$ MW.

A lower bound for the nonlinear index can be derived with eq (3a); we obtain $N_2 = 2.7 \times 10^{-13}$ esu and $N_2' = 2.1 \times 10^{-13}$ esu. The electrostrictive effect is considered to be negligible because YAG has exceedingly small stress-optic coefficients. For a beam propagating along the [111] axis, $n_2(K)/n_2'(K) = 1.5$ if we assume that the Kerr effect is of electronic origin [17]. Using eqs (20a) and (20b), we find that $n_2(K) = 1.7 \times 10^{-13}$ esu and $n_2(T) = 0.8 \times 10^{-13}$ esu. Thus we find that the Kerr effect is the dominant self-focusing mechanism. From the value of $n_2(T)$ we calculate an absorption coefficient $\alpha = 5 \times 10^{-3}$ cm^{-1} which is of the proper magnitude for YAG.

3.3 Nd:doped Laser Glass

In figure 2 we show a plot of $(z^*)^{-1}$ as a function of $P^{1/2}$ for a commercial Nd:doped laser glass. This curve is typical of five laser glasses that we have tested. The data are found to deviate strongly from self-focusing theory. We are not yet able to explain these data. The data indicate a large difference in damage properties for linear polarization (+) and circular polarization (O).

4. Conclusion

We find that the Kerr effect is the dominant self-focusing mechanism in three optical glasses and YAG for Nd:glass laser radiation with $\tau = 25$ ns. The electrostrictive effect is found to be small. We find that the thermal effect can be important for commercial optical glasses.

For laser systems with shorter pulses ($\tau < 1$ ns) the electrostrictive and thermal effects can be neglected; however, the thermal effect, because of its integrating nature, can be important for high repetition rate systems.

5. Acknowledgments

We thank Dale West and Alvin Rasmussen of the National Bureau of Standards for the calibration of our thermopile. We thank Roland De Wit of the National Bureau of Standards for his help in calculating the electrostrictive strains. We also thank Norman Boling of Owens-Illinois Glass Company, Erlan Bliss of the Lawrence Livermore Laboratories, Edwin Kerr of the Perkin-Elmer Corporation, A. Owyoung of Sandia Corporation, and David Fradin for valuable discussions concerning this work.

6. References

[1] S. P. Akhmanov, A. P. Sukhorukov, and R. V. Khokhlov, "Self-Focusing and Diffraction of Light in a Nonlinear Medium," Usp. Fiz. Nauk vol. 93, pp. 19-70 (1967)[Soviet Phys.--Usp., vol. 93, pp. 609-636 (1968)].

[2] R. Y. Chiao, E. Garmire, and C. H. Townes, "Self-Trapping of Optical Beams," Phys. Rev. Letters, vol. 13, pp. 479-482 (1964).

[3] Ya. B. Zel'dovich and Yu. P. Raizer, "Self-Focusing of Light. Role of Kerr Effect and Striction," Zh. Eksperim. i Teor. Fiz. Pis'ma v Redaktsiyu, vol. 3, pp. 137-141 (1966) [Soviet Phys. JETP Letters, vol. 3, pp. 86-89 (1966)].

[4] Y. R. Shen, "Electrostriction, Optical Kerr Effect and Self-Focusing of Laser Beams," Phys. Rev. Letters, vol. 20, pp. 378-380 (1966).

[5] A. A. Chaban, "Self-Focusing of Light in Solids Via the Electrostriction Mechanism," Zh. Eksperim. i Teor. Fiz. Pis'ma v Redaktsiyu, vol. 6, pp. 487-490 (1967) [Soviet Phys. JETP Letters, vol. 6, pp. 20-23 (1967)].

[6] E. L. Kerr, "Track Formation in Optical Glass Caused by Electrostrictive Laser Beam Self-Focusing," Phys. Rev. A, vol. 4, pp. 1195-1218 (1971).

[7] A. A. Chaban, "Self-Focusing of Light in the Kerr Effect," Zh. Eksperim. i Teor. Fiz. Pis'ma v Redaktsiyu, vol. 5, pp. 61-64 (1967) [Soviet Phys. -- JETP Letters, vol. 5, pp. 48-51 (1967)].

[8] A. G. Litvak, "Self-Focusing of Powerful Light Beams by Thermal Effects," Zh. Eksperim. i Teor. Fiz. Pis'ma v Redaktsiyu, vol. 4, pp. 341-345 (1966)[Soviet Phys. -- JETP Letters, vol. 4, pp. 230-233, (1966)].

[9] Yu. P. Raiser, "Self-Focusing of a Homogeneous Light Beam in a Transparent Medium Due to Weak Absorption," Zh. Eksperim. i Teor. Fiz. Pis'ma v Redaktsiyu, vol.4, p. 124-128 (1966)[Soviet Phys. -- JETP Letters, vol. 4, pp. 85-88 (1966)].

[10] Yu. P. Raiser, "Self-Focusing and Defocusing, Instability and Stabilization of Light Beams in Weakly Absorbing Media," Zh. Eksperim. i Teor. Fiz., vol. 52, pp. 470-482 (1967) [Soviet Phys. -- JETP, vol. 25, pp. 308-316 (1967)].

[11] F. W. Quelle, "Self-Focusing in Glass," in Damage in Laser Materials, ASTM STP 469, American Society for Testing and Materials, 1969, pp. 110-116.

[12] G. M. Zverev and V. A. Pashkov, "Self-Focusing of Laser Radiation in Solid Dielectrics," Zh. Eksperim. i Teor. Fiz., vol. 57, pp. 1128-1138 [Soviet Phys. -- JETP, vol. 30, pp. 616-621 (1970)].

[13] W. G. Wagner, H. A. Haus, and J. H. Marburger, "Large-Scale Self-Trapping of Optical Beams in the Paraxial Ray Approximation," Phys. Rev., vol. 175, pp. 256-266 (1968).

[14] E. L. Dawes and J. H. Marburger, "Computer Studies in Self-Focusing," Phys. Rev., vol. 179, pp. 862-868 (1969).

[15] D. W. Fradin, "The Measurement of Self-Focusing Parameters Using Intrinsic Optical Damage," IEEE J. Quantum Electronics, to be published.

[16] A. Owyoung, R. W. Hellwarth, and N. George, "Intensity-Induced Changes in Optical Polarizations in Glasses," Phys. Rev. B, vol. 5, pp. 628-633 (1972).

[17] P. D. Maker and R. W. Terhune, "Study of Optical Effects Due to an Induced Polarization Third Order in the Electric Field Strength," Phys. Rev., vol. 137, pp. A801-A818 (1965).

[18] J. F. Nye, in Physical Properties of Crystals, (Oxford University Press, London, 1957), p. 257. We have introduced an extra factor of one-half into our definition of electrostriction.

[19] H. Osterberg and J. W. Cookson, "The Piezodielectric Effect and Electrostriction in Anisotropic or Isotropic Media," Phys. Rev., vol. 51, pp. 1096-1101 (1937).

[20] P. W. Forsbergh, Jr., "Piezoelectricity, Electrostriction and Ferroelectricity," in Encyclopedia of Physics Vol. XVII, Dielectrics (Springer Verlag, Berlin, 1956), edited by S. Flugge, p. 360.

[21] A. A. Maradudin and E. Burstein, "Relation Between Photoelasticity, Electrostriction, and First Order Raman Effect in Crystals of the Diamond Structure," Phys. Rev., vol. 164, pp. 1081-1099 (1967).

[22] M. A. Jaswon and R. D. Bhargava, "Two-Dimensional Elastic Inclusion Problems," Proc. Camb. Phil. Soc., vol. 57, pp. 669-680 (1961).

[23] G. M. Zverev, E. A. Levchuk, E. K. Maldutis, and V. A. Pashkov, "Thermal Self-Focusing of Laser Radiation in Media with Negative dn/dT," Zh. Eksperim. i Teor. Fiz. Pis'ma Redaktsiyu, vol. 11, pp. 177-181 (1970) [Soviet Phys. -- JETP Letters, vol. 11, pp. 108-111 (1970).

[24] A. Feldman, D. Horowitz, and R. M. Waxler, "Relative Contribution of Kerr Effect and Electrostriction to Self-Focusing," in Laser Induced Damage in Optical Materials: 1972, NBS Special Publication 372 (U.S. Government Printing Office, Washington, D. C. 20402, 1972) pp. 92-99.

[25] A. Feldman, D. Horowitz, and R. M. Waxler, "Relative Importance of Electrostriction and the Kerr Effect to Self-Focusing in Optical Glasses," Appl. Phys. Letters, vol. 21, pp. 260-262 (1972).

[26] A. Feldman, R. Waxler, and D. Horowitz, "Laser Induced Damage Studies," in NBS Technical Note 703, ARPA-NBS Program of Research on High Temperature Materials and Laser Materials, edited by A. D. Franklin and H. S. Bennett, pp. 12-36.

[27] J. P. Budin, A. Donzel, J. Ernest and J. Raffy, "Stimulated Brillouin Scattering in Glasses," Electronics Letters, vol. 3, pp. 31-33 (1967).

[28] John M. McMahon, "Damage Measurements with Subnanosecond Pulses," in Laser Induced Damage in Optical Materials: 1972, NBS Special Publication 372 (U. S. Government Printing Office, Washington, D. C., (1972), pp. 100-103.

[29] T. C. Rich and D. A. Pinnow, "Total Optical Attenuation in Bulk Fused Silica," Appl. Phys. Letters, vol. 20, pp. 264-266 (1972).

[30] M. A. Duguay and J. W. Hansen, "Measurement of the Nonlinear Index n_2 of Glass Using Picosecond Pulses," in Damage in Laser Materials (NBS Special Publication 341), pp. 45-50.

[31] Charles C. Wang, "Empirical Relation Between the Linear and the Third-Order Nonlinear Optical Susceptibilities," Phys. Rev. B, vol. 2, pp. 2045-2048 (1970).

[32] G. M. Zverev, E. K. Maldutis, and V. A. Pashkov, "Development of Self-Focusing Filaments in Solid Dielectrics," Zh. Eksperim. i Teor. Fiz. Pis'ma v Redaktsiyu, vol. 9, p. 108 (1969) [Soviet Phys. -- JETP Letters, vol. 9, p. 61 (1969).

[33] C. R. Giuliano, "Time Evolution of Damage Tracks in Sapphire and Ruby," in Damage in Laser Materials: 1971, NBS Special Publication 356 (U. S. Government Printing Office, Washington, D. C. 20402, 1971) p. 44.

[34] C. R. Giuliano and J. H. Marburger, Phys. Rev. Letters 27, 905 (1971), "Observations of Moving Self-Foci in Sapphire."

[35] M. Bass and H. H. Barrett, "The Probability and Dynamics of Damaging Optical Material with Lasers," in Damage in Laser Materials: 1971, NBS Special Publication 356 (U.S. Government Printing Office, Washington, D. C., 1971), pp. 76-90.

[36] J. H. Marburger, "Theory of Self-Focusing for Fast Nonlinear Response," in Damage in Laser Materials: 1971, NBS Special Publication 356 (U. S. Government Printing Office, Washington, D. C. 20402, 1971) p. 51.

7. Figures

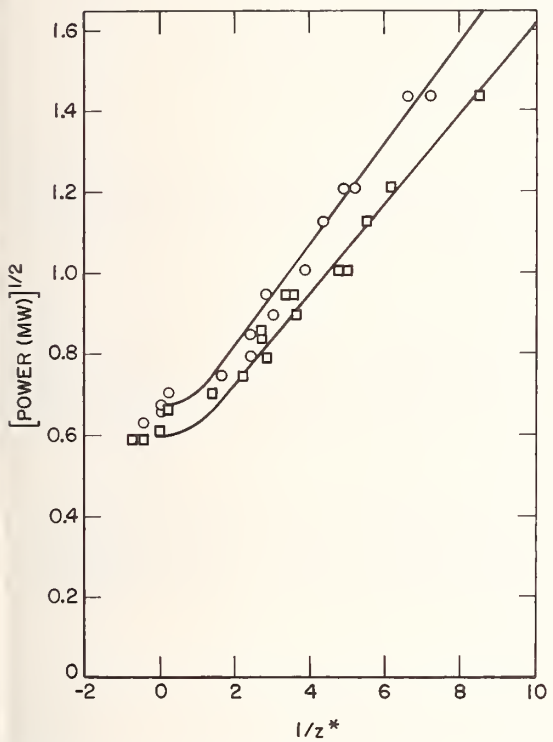

Figure 1. Self-focusing lengths as a function of the square root of peak beam power in yttrium aluminum garnet for linearly (□) and circularly (O) polarized radiation. A lens with a 181 mm focal length was used to obtain the data. The solid curves are from Dawes and Marburger [14].

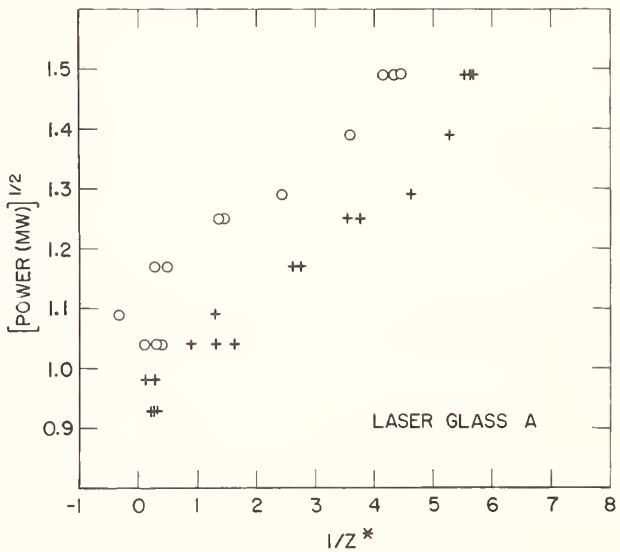

Figure 2. Self-focusing lengths as a function of the square root of peak beam power in a commercial Nd:doped laser glass for linearly (+) and circularly (O) polarized radiation. A lens with a 181 mm focal length was used to obtain the data.

COMMENTS ON PAPER BY FELDMAN

There was considerable discussion in the audience concerning the uncertainties involved in associating the threshold for observed damage in the case of a focused beam with the critical power given by the self-focusing theory. It was pointed out that the only reliable test of the influence of the prefocusing of the beam on the damage threshold is to observe damage at a variety of focal lengths. Clearly, if the focal length of the lens is sufficiently short, damage can occur without self-focusing at all.

A Rational Definition of Index Nonlinearity in Self Focusing Media*

Alexander J. Glass

Lawrence Livermore Laboratory, University of California
Livermore, California 94550

It is proposed that the index nonlinearity in self focusing media be reported in terms of a critical power for the medium, P_1, rather than in terms of n_2. The principal results of self focusing theory are expressed in terms of the ratio (P/P_1), where P is the total power in a Gaussian beam. Using P_1 not only simplifies the expressions for quantities of physical interest, but also will remove some of the confusion now existing in the literature of self focusing and laser damage.

Key Words: Critical power, laser damage, nonlinear index, self focusing.

At pulse durations shorter than a few nanoseconds, the principal cause of damage in solid state lasers is self focusing. This self focusing arises solely as a consequence of the nonlinearity of the refractive index of the medium. In the presence of an optical field of rms electric field strength E, the refractive index is written as [1][1].

$$n = n_0 + n_2 \langle E^2 \rangle, \tag{1}$$

where n_0 is the index at zero power, and n_2 is a parameter of the material, measured in esu. For most transparent solid dielectrics, n_2 is of the order of 10^{-13} esu.

There has been significant variation in the values of n_2 reported in the literature. [2-5] In part, this variation results from the use of different methods to obtain the index nonlinearity, and from the intrinsic difficulty of the measurement. There has not been consistency, however, in the interpretation of n_2, and some portion of the reported variation results from this lack of consistency. It is the purpose of this communication to propose a standard procedure for the reporting of index nonlinearity. It is proposed not to report values of n_2, but to report instead the equivalent parameter P_1, the "critical power" of Talanov, [6] defined as

$$P_1 = \frac{c\lambda_0^2}{32\,\pi^2 n_2}, \tag{2}$$

where c is the vacuum light velocity, and λ_0, the vacuum wavelength of the incident light. A simple numerical relation obtains for eq (2), on the substitution of appropriate values for c and π,

$$P_1(\text{Megawatts}) = 0.950\,\frac{[\lambda_0\ (\mu\text{m})]^2}{10^{13}\ n_2\ (\text{esu})}. \tag{3}$$

The local change in refractive index can be written as

---

*This work was performed under the auspices of the United States Atomic Energy Commission.

[1]Figures in brackets indicate the literature references at the end of this paper.

$$n - n_o = (P/P_1)/2\ n_o(k_oR)^2, \tag{4}$$

where n_o is the linear index of the material, $k_o = 2\pi/\lambda_o$, and R is the Gaussian parameter for the intensity distribution at the aperture. It is assumed that the intensity distribution is indeed Gaussian. We must bear in mind that the parameter P_1 is a characteristic of the material, not of an arbitrary intensity distribution. P_1 is the critical power, in the sense of Ref. 6, for a Gaussian beam of a given size, propagating in the specified material.

The physical interpretation of P_1 is straightforward. As a Gaussian beam propagates, starting from an initially plane phase front, the curvature of the phase front increases, due to diffraction. In a self focusing medium, the nonlinear index causes the opposite effect. P_1 represents that total power in the beam at which the two effects exactly cancel, so that initially, the beam propagates with a phase front of zero curvature.

The principal results of self focusing theory are readily expressed in terms of the ratio of the total power in the beam to the critical power, (P/P_1). Thus Marburger's numerical expression for the self focusing length [7] in a Gaussian beam takes the simple form,

$$\left(\frac{n_o k_o R^2}{Z_f}\right)^2 = 0.148 + [(2P/P_1)^{1/2} - 2.322]^2. \tag{5}$$

Asymptotically, this expression reduces to

$$Z_f = n_o k_o R^2/(2P/P_1)^{1/2}. \tag{6}$$

Kelley [8] has analyzed the development of small-scale instabilities in a large aperture beam, due to self focusing. His results can be conveniently rephrased in terms of P_1, as follows. If we consider the growth rate of a perturbation (either phase or amplitude) on an otherwise uniform beam of total power P, where the perturbation is characterized by a spatial dimension ℓ, then the value of ℓ for which the growth rate is a maximum is given by

$$(\ell/R) = (P/P_1)^{-1/2}. \tag{7}$$

The gain length for amplification of a perturbation of this dimension is given by

$$Z_\ell = 2n_o k_o R^2/(P/P_1). \tag{8}$$

A brief derivation of these results is given in the Appendix to this paper.
Two features of small-scale instability are immediately obvious from the formalism. One, essentially fortuitous, is that at $P = P_1$, the instability with the highest growth rate is just the self focusing of the entire beam. The other feature, more significant, is that while the self focusing length for self focusing the whole beam scales with the ratio $(P/P_1)^{-1/2}$, the gain length for the small-scale instability scales with the ratio $(P/P_1)^{-1}$. Thus for $(P/P_1) \gg 1$, a condition satisfied in most high-power, short-pulse, large-aperture laser systems, small-scale self focusing is the principal limiting factor.

The use of P_1 rather than n_2 provides a very convenient mnemonic device, for estimating the importance of self focusing effects. The relevant expressions turn out to be extremely simple, and contain quantities of immediate physical significance.

The advantage of reporting a power, P_1, rather than the nonlinear index coefficient, n_2, arises from the fact that power is indeed what one measures in the laboratory. Let us assume a self focusing measurement is used to obtain the nonlinear index. In terms of n_2, we would write

$$n_2 = \frac{n_o R^2}{2Z_f^2 \langle E^2 \rangle} \quad . \tag{9}$$

Clearly, we must use the mean squared electric field inside the medium in computing n_2 from a value of Z_f. In some cases in the literature, this apparently has not been done, although it does not make sense to refer the index nonlinearity of the medium to field conditions exterior to the medium.

If the critical power were to be obtained from the self focusing length, we would write

$$P_1 = \frac{2Z_f^2}{(n_o k_o R^2)^2} P, \tag{10}$$

where P is the total power in the beam, and R is the Gaussian parameter. Power is a quantity we measure directly, and the only correction needed is to compensate for Fresnel reflection at the dielectric surface.

The distinction between reporting P_1 and n_2 may appear trivial at first. However, under the auspices of the ASTM and NBS, it behooves us to adopt procedures of reporting material parameters which are based on measured quantities as much as possible. Inconsistency in obtaining n_2 values from measured quantities has resulted in considerable confusion in the literature, and has contributed to the existing uncertainty in the best accepted value of this parameter. Considering that the index nonlinearity is a parameter of great importance in high power laser design, the characterization of refractive index nonlinearity in terms of the critical power, P_1, is strongly advocated.

References

[1] Maker, P. and Terhune, R., Phys. Rev. 137, A, 801, (1965).

[2] Glass, A. J. And Guenther, A. H., Eds., Damage in Laser Glass, ASTM Special Technical Publication 469 (ASTM, Philadelphia, 1969).

[3] Glass, A. J. and Guenther, A. H., Eds., Damage in Laser Materials, NBS Special Publication 341 (U.S.Government Printing Office, Washington, D. C., 1970).

[4] Glass, A. J. and Guenther, A. H., Eds., Damage in Laser Materials, NBS Special Publication 356 (U.S.Government Printing Office, Washington, D. C., 1971).

[5] Glass, A. J. and Guenther, A. H., Eds., Laser Induced Damage in Optical Materials, NBS Special Publication 372 (U.S. Government Printing Office, Washington, D. C., 1972).

[6] Talanov, V. I., JETP Letters 2, 138 (1965).

[7] Marburger, J., "Theory of Self Focusing for Fast Nonlinear Response," in Ref. 4.

[8] Chiao, R., Kelley, P., and Garmire, E., Phys. Rev. Letters 17, 1158 (1966).

Appendix

The sagittal equation for light propagation in a nonlinear medium is written

$$2ik \frac{\partial \psi}{\partial z} + \nabla^2 \psi + 2k^2 \mu \psi = 0. \tag{A1}$$

Here the electric field has been written

$$E = \psi \exp i(kz - \omega t), \tag{A2}$$

and μ is the relative index nonlinearity

$$\mu = n_2 \langle E^2 \rangle / n_o. \tag{A3}$$

The Laplacian operator in eq (A1) operates only in the transverse plane.

If we define the complex amplitude in terms of a real amplitude and phase,

$$\psi = A \exp i\phi \tag{A4}$$

and introduce the intensity, $I = A^2$, and phase gradient, $\underline{u} = \nabla\phi/k$, we can write the equations of light flow,

$$\left[\frac{\partial}{\partial z} + \underline{u}\cdot\nabla\right] I + I(\nabla\cdot\underline{u}) = 0 \tag{A5}$$

$$\left[\frac{\partial}{\partial z} + \underline{u}\cdot\nabla\right] \underline{u} = \nabla[\mu + D(I)] \tag{A6}$$

where the diffraction term is given by

$$D(I) = \frac{1}{4k^2}\left[\nabla^2(\ln I) + \frac{1}{2}(\nabla \ln I)^2\right]. \tag{A7}$$

We want to examine the stability of small fluctuations in phase and amplitude in the presence of a strong light wave. Let us write

$$\underline{u} = \underline{u}_0 + \underline{u}_1 \tag{A8}$$

$$I = I_0 + I_1 \tag{A9}$$

$$\ln I = \ln I_0 + I_1/I_0 \tag{A10}$$

where the quantities subscripted "1" are small. We assume an intially plane wave, $\underline{u}_0 = 0$. To first order, eqs (A5-A7) yield the result,

$$\frac{\partial I_1}{\partial z} + (u_1\cdot\nabla)\, I_0 + I_0(\nabla\cdot u_1) = 0 \tag{A11}$$

$$\frac{\partial u_1}{\partial z} = \nabla\left[\mu_1 + \frac{\nabla^2 I_1}{4k^2 I_0}\right]. \tag{A12}$$

Assuming the perturbation structure is of much smaller scale than the main beam, we can drop the second term in eq (A11). Combining eqs (A11) and (A12), we obtain

$$\frac{\partial^2 I_1}{\partial z^2} + \nabla^2\left[\mu_0 I_1 + \frac{\nabla^2 I_1}{4k^2}\right] = 0. \tag{A13}$$

Here μ_0 is the index nonlinearity due to I_0 alone. If we examine a single Fourier component of I_1, with spatial frequency κ, we find

$$\left[\frac{\partial^2}{\partial z^2} - \kappa^2\left(\mu_0 - \frac{\kappa^2}{4k^2}\right)\right] I_1(\kappa) = 0. \tag{A14}$$

We see that $I_1(\kappa)$ will exhibit a growth rate given by

$$g(\kappa) = \kappa(\mu_o - \kappa^2/4k^2)^{1/2}, \tag{A15}$$

for $\mu_o > \kappa^2/4k^2$. The maximum growth rate occurs for

$$\kappa_{max} = (2k^2\mu_o)^{1/2}. \tag{A16}$$

At this value, the maximum growth rate is

$$g_{max} = k\mu_o. \tag{A17}$$

Large scale self focusing occurs when the maximum growth rate occurs for a value of κ corresponding to the inverse of the beam radius. If one sets $\kappa = 1/a$ in eq (A16), with a the Gaussian beam parameter, then the usual result for the onset of self focusing obtains. (The exact agreement between two approximate analyses of the problem can only be fortuitous, but it offers a guide to the interpretation of the stability analysis.) At the onset of self focusing, the gain length for whole beam focusing is twice the Fresnel length, $g_{max} = 2ka^2$, which is the rough equivalent of the original interpretation of the self focusing threshold, as being that power level at which self focusing and diffraction gave rise to canceling effects.

In large laser amplifiers, the total power may exceed the threshold value for self focusing by as much as 10^4. To avoid catastrophic damage, however, the path length in the medium is kept small. In analyzing this problem, let us express the index change μ_o in terms of the critical power for the medium, assuming a Gaussian intensity profile,

$$\mu_o = (2k^2a^2)^{-1} (P/P_{cr}) \tag{A18}$$

The maximum growth rate then becomes

$$g_{max} = \frac{(P/P_{cr})}{(2ka^2)} = \frac{\pi I_o}{2kP_{cr}}. \tag{A19}$$

If it is desired that $g_{max}\, \ell << 1$, in a path of length ℓ, then the intensity is limited to

$$I_o << (2kP_{cr}/\pi\ell). \tag{A20}$$

For Nd-Glass, with $P_{cr} \sim 10^6$ watts, in a one cm path, the peak intensity must be kept much less than 10^{10} watts/cm^2, scaling inversely with the length of the path. In a half-meter rod, the peak intensity must be much less than 10^8 watts/cm^2, which, in 100 psec, corresponds to only 0.01 J/cm^2.

To obtain the gain spectrum, let us write eq (A15) in terms of the values at maximum gain, with $x = \kappa/\kappa_{max}$, and $y = g(\kappa)/g(\kappa_{max})$.

$$y = x(2 - x^2)^{1/2}. \tag{A21}$$

This function is shown in figure 1. We see that gain exists for all vaules of $\kappa < \kappa_{max}$, but that a short wavelength cutoff exists, attributable to the greater diffraction of the high frequency disturbance. In reality, a lower limit exists on the value of κ at which instabilities can develop, since as κ approaches (1/a), the theoretical analysis no longer applies; and the result goes over to large scale self focusing of the entire beam.

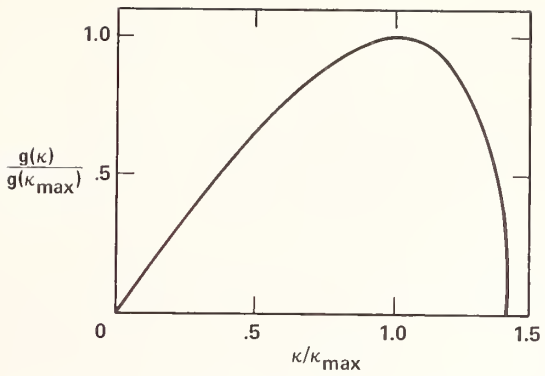

Figure 1. Gain coefficient, g/κ, for a disturbance of spatial frequency κ versus κ. κ_{max} is the spatial frequency at which the maximum growth rate occurs, as given in Eqs. (A16) and (A17).

COMMENTS ON PAPER BY GLASS

Under operating conditions in which small-scale self-focusing is observed, there is also a marked increase in small angle scattering. Although the spreading of the beam is not noticeable under these conditions, it is seen that the total energy impinging on a target some distance away from the laser is reduced by about a factor of 2 from the energy measured directly at the output of the laser.

Self Focusing of Very Powerful Laser Beams*

B. R. Suydam

University of California
Los Alamos Scientific Laboratory
Los Alamos, New Mexico 87544

Self focusing has heretofore been studied by assuming something equivalent to total collapse of the beam. Computer simulations at high power level show, however, that it is rather some small portion of the beam (e.g., a diffraction spike) which first collapses. We have therefore examined self-focusing as a problem in stability theory. The method can be applied to divergent beams and to any medium in which gain is a known function of field strength. The theory agrees well with computer experiments. We find an absolute limit to the intensity available from a glass laser of order 10^{10} watts/cm^2.

Key Words: Laser damage, non-linear, self focusing.

1. Introduction

Catastrophic self focusing is a very serious obstacle to the attainment of very high powers from glass amplifiers. Theories of self focusing exist [1,2,3][1] which give quite satisfactory predictions at levels of only a few critical powers, but when applied to beams of very high power, say 10^4 or more critical powers, the predictions are quite wrong. The reason is that all of the above quoted theories assume something more or less equivalent to the self-similar collapse of the beam as a whole to a single point focus. On the other hand, both experiment and numerical simulation agree that at very high power levels, the beam in fact breaks into many cells, each of which then proceeds to produce its own separate self focus. In other words, self focusing is essentially an instability phenomenon and the fastest growing mode has a structure which depends, among other things, on the power level.

If we have a beam profile free of any gross irregularities, for example a gaussian, there will be some small area near the center over which the deviation from a plane wave is negligible. At very high power level, this area may nevertheless contain many critical powers. Thus for beams of very high power, we are justified in drawing conclusions from the stability analysis of a plane wave. As this analysis assumes the initial perturbation to be small, such important questions as the effects of diffraction patterns and hot spots will be left unanswered. Thus the stability theory here presented will only set an upper bound to the power attainable provided all gross perturbations have been eliminated.

We shall base our analysis on the quasi-optical equation, which we write as

$$\frac{2i\omega}{v}\frac{\partial E}{\partial z} = \nabla^2 E + \gamma |E|^2 E \ . \qquad (1.1)$$

*This work was performed under the auspices of the United States Atomic Energy Commission.

[1]Figures in brackets indicate the literature references at the end of this paper.

In this and all that follows, ∇ operates in the plane perpendicular to the z-axis, and γ represents the nonlinear part of the dielectric function

$$\epsilon = \epsilon_o + \epsilon_2 |E|^2,$$
$$\gamma = \frac{3}{4}\frac{\omega^2}{c^2}\epsilon_2 , \tag{1.2}$$

and v represents light velocity in the medium. Units are Gaussian.

The linear stability theory of eq (1.1) has been given by Bespalov and Talanov. [4] What is new here is the extension of this theory to a medium with gain and the passage from the linear theory to a self-focusing length.

2. Perturbation of a Plane Wave

It is convenient for our analysis to rewrite eq (1.1) in terms of amplitude and phase, setting

$$E = Ae^{i\varphi} . \tag{2.1}$$

Our basic equations then become

$$\frac{2\omega}{v}\frac{\partial A}{\partial z} = A\nabla^2\varphi + 2(\nabla A)\cdot(\nabla\varphi) + \frac{2\omega}{v} A\, g(I) , \qquad I \equiv A^2 ,$$
$$-\frac{2\omega}{v} A \frac{\partial\varphi}{\partial z} = \nabla^2 A - A(\nabla\varphi)^2 + \gamma A^3 . \tag{2.2}$$

It will be noted that we have added to eq (1.1) a gain term, g (I), which we must assume to be a known function of the intensity I. Equations (2.2) possess the plane wave solution

$$A = A_o(z) ,$$
$$\varphi = \varphi_o = \text{const} - \frac{\gamma v}{2\omega}\int_o^z [A_o(z')]^2\, dz , \tag{2.3}$$

where, A_o satisfies the equation

$$\frac{dA_o}{dz} = A_o\, g\,(A_o^2) . \tag{2.4}$$

We now perturb eqs (2.2) by writing

$$A = A_o[1 + u(z)\,\psi_k(x_\perp)] ,$$
$$\varphi = \varphi_o + \tilde{\varphi}(z)\,\psi_k(x_\perp) . \tag{2.5}$$

where A_o, φ_o are given by eqs (2.3) and ψ_k is any solution to the equation

$$\nabla^2\psi_k = -k^2\psi_k . \tag{2.6}$$

If we suppose u, $\tilde{\varphi}$ to be sufficiently small, it is legitimate to neglect their products and squares. Substituting eqs (2.5) into eqs (2.2) and making this neglection, we obtain the linearized perturbation equations

$$\frac{2\omega}{v}\frac{du}{dz} = \frac{4\omega}{v} A_o^2\, g'\, u - k^2\tilde{\varphi},$$
$$\frac{2\omega}{v}\frac{\partial\tilde{\varphi}}{\partial z} = (k^2 - 2\gamma A_o^2)u. \tag{2.7}$$

We can eliminate $\tilde{\varphi}$ obtaining

$$\frac{d^2u}{dz^2} - 2A_o\, g'\frac{du}{dz} - \left\{\frac{v^2k^2}{4\omega^2}(2\gamma A_o^2 - k^2) + 4A_oA_o'(g' + A_o^2 g'')\right\} u = 0. \tag{2.8}$$

In this equation A_o' means dA_o/dz and g' means dg/dI. Equation (2.8) can be put into a rather simpler form if we transform both the dependent and the independent variables, writing

$$y = [A_o(z)]^2 \equiv I_o(z) \ ,$$
$$u = y^{-\frac{1}{2}} w \ . \tag{2.9}$$

In these new variables, eq (2.8) becomes

$$\frac{d^2w}{dy^2} - \frac{1}{4y^2g^2}\left\{\frac{v^2k^2}{4\omega^2}(2\gamma y - k^2) - g^2 + 4yg(g' + yg'')\right\}w = 0. \tag{2.10}$$

In this form, given g as a function of y, we can solve by the well known JWKB method. Stability hinges upon whether or not the small perturbation u grows out of hand.

To date we have studied stability only in three cases. Equation (2.10) is trivially soluble when g = 0 and readily so for g = a constant, and these two cases will be reported here. For a spherically divergent wave in a passive medium, one again finds an equation of the type of eq (2.10). We have also solved this case, but it will not be reported on here.

3. Passive Medium: g = 0.

When g = 0, the transformation of eqs (2.9) is singular and we use eq (2.8), which is obviously solved by

$$u = \delta e^{\alpha z} \ , \quad \tilde{\varphi} = -\frac{v}{2\omega}(2\gamma A_o^2 - k^2)\delta e^{\alpha z} \ ,$$
$$\alpha^2 = \frac{v^2k^2}{4\omega^2}(2\gamma A_o^2 - k^2) \ , \tag{3.1}$$

where δ is a constant, as also is A_o. It is clear that for $0 < k^2 < 2\gamma A_o^2$ one of the roots for α is positive and we have an exponentially growing mode. Fastest growth rate is clearly for

$$k^2 = k_M^2 \equiv \gamma A_o^2 \ , \tag{3.2}$$

and the maximum growth rate is

$$\alpha_M = \frac{vk_M^2}{2\omega} = \frac{v\gamma}{2\omega} A_o^2 \ . \tag{3.3}$$

When a spectrum of normal modes is present in the initial perturbation, those with fastest growth rate will soon outstrip the others and ultimately will be the only modes seen. One possible form of such a mode is

$$\tilde{A}_1 \equiv A_o u\psi_k = A_o(\delta e^{\alpha z}) \cos k_x x \cos k_y y \ ,$$
$$\tilde{\varphi}_1 = \tilde{\varphi}\psi_k = -(\delta e^{\alpha z}) \cos k_x x \cos k_y y \ , \tag{3.4}$$
$$k^2 = k_x^2 + k_y^2 \ ,$$

with k^2, α given by eqs (3.2) and (3.3). We see that there is an infinite set of modes, depending on how we break k^2 into k_x^2 and k_y^2, all with the same growth rate. A normal mode of square cells contains a power per cell given by

$$P_{cell} = \frac{10^{-7}\pi c\sqrt{\epsilon_o}}{\gamma} \text{ watts} \tag{3.5}$$

whereas a rectangular cell of aspect ratio R ($k_x/k_y \equiv R$) contains $(1 + R^2)/2R$ times this power. This is exactly the same factor Marburger [2] found connecting critical power for an elliptical as compared with a circular beam.

It is our purpose to obtain a self focusing distance from the above results. Accordingly, we must somehow answer the question of the nonlinear effects of the perturbation upon itself once it has grown to finite amplitude. The beginnings of nonlinear behavior can readily be calculated by estimating the nonlinear terms of the perturbation equation with the aid of eqs (3.4), rather than dropping these terms, and then solving for the lowest order nonlinear corrections $\tilde{A}_2$, $\tilde{\varphi}_2$. For the case $k_x = k_y = \ell$ the result is

$$\tilde{A}_2 = \frac{1}{8}(\delta e^{\alpha z})^2\{3\cos 2\ell x \cos 2\ell y + 3(\cos 2\ell x + \cos 2\ell y) - 1\} ,$$

$$\tilde{\varphi}_2 = -\frac{1}{4}(\delta e^{\alpha z})^2\{\cos 2\ell x + \cos 2\ell y\} , \qquad (3.6)$$

$$\ell = k_M/\sqrt{2} .$$

At x = 0 = y (and all harmonically related points), the perturbation is a maximum and the field has the values

$$A(o,o) = A_o\{1 + \delta e^{\alpha z} + (\delta e^{\alpha z})^2 + \cdots\} ,$$

$$\varphi(o,o) = \varphi_o - (\delta e^{\alpha z}) - \frac{1}{2}(\delta e^{\alpha z})^2 \cdots . \qquad (3.7)$$

We have also worked out the case $k_x \neq k_y$ and find that the nonlinear correction is largest for square cells.

Clearly, once the perturbation becomes finite, it starts growing faster than an exponential and in fact reaches infinity, the self-focus, at finite z. [3] Formulas for collapse of single filaments [2,3] as well as numerical simulations, all agree that once the perturbation becomes three or four times the background, the collapse is extremely fast. This suggests that we can say that when $\delta e^{\alpha z}$ reaches some critical value ρ, the perturbation has really collapsed to a point focus. Thus we set, for the self focal distance

$$z_f = \frac{1}{\alpha_M} \log (\rho/\delta) . \qquad (3.8)$$

Equation (3.7) suggests that ρ somewhere in the range 1 to 5 would probably be about right. We shall see that $\rho = 3$ represents a good choice. We can express α_M in terms of the background intensity, γ in terms of ϵ_2 and then solve eq (3.8) for the intensity. We thus obtain the alternative expression

$$I = \frac{10^{-7} c \epsilon_o}{3\pi\epsilon_2} \frac{c/\omega}{z_f} \log (\tfrac{3}{\delta}) . \qquad (3.9)$$

If c is in cm/sec, z_f in cm., ϵ_o and ϵ_2 in e.s.u., then I is in watts/cm^2.

For an inert glass rod one obtains an upper limit to the permissable intensity by equating z_f to the length of the rod. For an amplifier one might expect eq (3.9) to be about right if z_f is set equal to the power e-folding distance. This is, in fact, a somewhat pessimistic estimate.

As a numerical example we consider the 1.06μm Nd. line in glass with

$$\epsilon_o = 2.415 ,$$

$$\epsilon_2 = 6.4 \times 10^{-13}/(\text{esu})^2 .$$

Taking z_f = 20 cm. and $\delta = 10^{-5}$ we obtain

$$I = 1.3 \times 10^{10} \text{ watts/cm}^2 .$$

as the limiting power.

4. Medium with Linear Gain: g = const.

With constant gain, g', g" vanish and eq (2.10) becomes a recognizable form of Bessel's equation with the solutions

$$u = J_{\pm ip}\left(ipe^{gz}\sqrt{2\gamma A_{oo}^2/k^2}\right), \qquad p \equiv \frac{vk^2}{2\omega g}\ ; \quad A_{oo} = A_o\big|_{z=o}\ . \tag{4.1}$$

At very high power levels, and for the modest values of g likely to be found in high power amplifiers, $p \gg 1$ and the asymptotic expression

$$J_{ip}(ip\sec\mu) \sim \frac{1}{\sqrt{3\pi p\tan\mu}}\exp\{p(\tan\mu - \mu)\}, \qquad \cos\mu = \frac{ke^{-gz}}{k_o\sqrt{2}} \equiv xe^{-gz}; \quad k_o^2 \equiv \gamma A_{oo}^2\ , \tag{4.2}$$

is a very good approximation so long as $p\tan\mu \gg 0$. If now we ask for the growth over the interval $z = -z_1$ to $z = 0$, we find

$$\frac{u(o)}{u(-z_1)} \sim \sqrt{\frac{\tan\mu_1}{\tan\mu_o}}\exp\left\{\frac{vk_o^2}{\omega g}\,\Phi\right\},$$

$$\Phi \equiv x\left\{\sqrt{1-x^2} - x\cos^{-1}x - \frac{1}{\beta}\sqrt{1-\beta^2x^2} + x\cos^{-1}(\beta x)\right\}, \qquad \beta \equiv e^{gz_1}\ , \tag{4.3}$$

and x is as defined in eq (4.2). This is precisely what JWKB would have given.

So long as the turning point lies well outside the interval, the exponential of (4.3) varies much more rapidly than the square root and maximum growth is achieved for that value of x (i.e. of k) which maximizes Φ, say x_M, given by

$$2x_M\cos^{-1}x_M - \sqrt{1-x_M^2} = 2x_M\cos^{-1}(\beta x_M) - \frac{1}{\beta}\sqrt{1-\beta^2x_M^2}\ . \tag{4.4}$$

For this value of x, the (maximum) value of Φ is

$$\Phi_M = \frac{x_M}{2\beta}\left[\beta\sqrt{1-x_M^2} - \sqrt{1-\beta^2x_M^2}\right]. \tag{4.5}$$

Our prescription for self-focusing, eq (3.8), thus becomes

$$\frac{vk_o^2}{\omega g}\,\Phi_M = \log\left(\frac{\rho}{\delta}\right) + \log\left[\frac{\beta\sqrt{1-x_M^2}}{\sqrt{1-\beta^2x_M^2}}\right]. \tag{4.6}$$

Still remaining well clear of the turning point, the second logarithm is small compared with the first provided only δ is small. Dropping this term and writing everything out in terms of ϵ_2 and the intensity at z = 0, we obtain

$$I_o = \frac{10^{-7}c\epsilon_o}{3\pi\epsilon_2}\left(\frac{c/\omega}{4\Phi_M\ell_e}\right)\log\left(\frac{3}{\delta}\right)\ , \tag{4.7}$$

where $\ell_e = 1/2g$ is the power e-folding distance in the amplifier.

Equation (4.4) has been solved numerically for x_M as a function of β over the range $0 < \beta < \beta_c = 2.5366$ and the resultant values of x_M and Φ_M are tabulated versus

β in table 1. At $\beta = \beta_c$, $x_m = 1/\beta$ and the turning point has been reached. At the turning point, our formula is not expected to be too good. Bessel function expansions valid at the turning point are available. Their use gives a corrected value of Φ_M at the turning point which differs by less than one percent from the tabulated value above. Thus eq (4.7) is in fact good right up to the turning point; dropping the second term on the right hand side of eq (4.6) has lead to compensation of errors. If the overall gain of an amplifier is greater than β_c, then the perturbation which will ultimately become largest is oscillatory rather than growing until the turning point is reached. Thus we have the following rule:

a.) For low gain amplifiers, $0 < \beta < \beta_c$, the β for the whole amplifier is used. Corresponding values of x_M, Φ_M may be obtained from Table 1 and entered into eq (4.7) to obtain limiting output intensity.

b.) For high gain amplifiers, $\beta > \beta_c$, we use β_c and the corresponding values of $x_M = 1/\beta_c$ and $4\Phi_M = 0.7246$. Again eq (4.7) gives limiting output power.

If we take the same constants as for our numerical example at the end of the last section, $\ell_e = 20$ cm. and $\beta > \beta_c$, we obtain

$$I_{Max} = 1.8 \times 10^{10} \text{ watts/cm}^2$$

Table 1. The Quantities $4\Phi_M$ and x_M vs. Amplitude Gain β

For Small Gain $x_M \approx 1/\sqrt{2}$, $\Phi_M \approx \frac{\beta - 1}{2}\left(1 - \frac{\beta - 1}{2}\right)$

$\beta = e^{gz}$	$x_M = k_M/k_o\sqrt{2}$	$4\Phi_M$
1.000	0.7071	0
1.5	0.5690	0.5404
1.6	0.5479	0.5872
1.7	0.5282	0.6237
1.9	0.4924	0.6742
2.1	0.4600	0.7036
2.3	0.4297	0.7190
2.536	0.3942	0.7246

5. Check of Self-Focusing Formulas

The only experimental checks of our theory to date are that maximum levels predicted by our formulas have not in fact been exceeded. For a more convincing check, we are forced to rely on numerical simulation. A code has been developed to solve numerically the quasi-optical equation, including self-focusing terms and gain computed from rate equations. By starting with perturbations of known size and computing up to the first self-focus, we can check our formulas. Briefly we find:

a.) The wavelength of the perturbation which ultimately focuses matches theory as well as this wavelength can be measured on our output plots.

b.) The self focal distance given by our formulas checks that of the numerical simulations within about ten percent. For this close a check at the larger values of δ, we need to take $\rho \approx 3$.

c.) As we make the input $\delta \to 0$, the self focal length levels off, clearly indicating an internal noise level of our calculational scheme.

In figure 1, we show the results of one set of such calculations. The individual points are machine computed focal distances whereas the solid line was computed from eq (3.8), with ρ adjusted to the value 2.7, and with δ computed as a superposition of the input perturbation and machine noise. Similar calculations have been made for other input intensity levels. We have moreover made similar checks of eq (4.7) for various input levels and various values of gain. The agreement between the formulas here presented and numerical simulation has in no case been worse than that illustrated in figure 1.

6. Conclusion

We have found simple analytic expressions for self focusing distance for high powered beams. At a certain point, we had to rely on an heuristic argument, but the resulting formula agrees with numerical simulation experiments by well under ten percent. The formulas do not necessarily represent what might be observed but rather the best that can be achieved in beam and glass systems without optical fault.

7. Acknowledgements

The author is indebted to D. O. Dickman, Los Alamos Scientific Laboratory, for invaluable assistance in setting up the code for the numerical simulations.

8. References

[1] Kelley, P. L., Phys. Rev. Lett., 15, 26, 1005 (1965).

[2] Marburger, J., Laser Induced Damage in Optical Materials: 1972, A. J. Glass, A. H. Guenther eds. NBS Special Publication 372, 84 (1972).

[3] Vlasov, S. N., Petrishchev, V. A., and Talanov, V. N., Radiofizika 14, 9, 1353, (1971), (English translation not known to exist.)

[4] Bespalov, V. I. and Talanov, V. I., ZhETP Pis'ma 3, 11, 471 (1966). English translation ... 3, 12, 307 (1966).

9. Figures

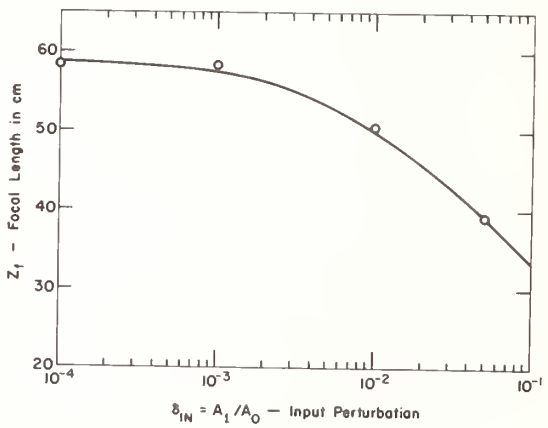

Figure 1. Comparison of eq. (3.8) with Numerical Simulation. The points o are numerical simulation results and the solid line is the equation $z_f = 1/\alpha_M \log 2.807/\delta_n + \frac{1}{2}\delta_{IN}$. In this equation $\delta_n = 0.00576$ and is machine calculational noise; δ_{IN} is the input perturbation and the factor $\frac{1}{2}$ is used because only amplitude was perturbed whereas eq. (3.8) assumes both amplitude and phase perturbation.

COMMENTS ON PAPER BY SUYDAM

It was stated in discussion that the power density at which small-scale self-focusing occured (10^{10} W/cm^2) is also the power density at which two-photon absorption has been reported in laser glass by Penzkofer and Kaiser. A comment from the floor was made that in an attempt to reproduce that result in ED-2 laser glass, no two-photon absorption was observed at power levels up to and greater than 10^{10} W/cm. It was felt that the spectral character of the two glasses was sufficiently different that the absence of two-photon absorption at 1.06 microns in ED-2 glass was entirely consistent with the Penzkofer and Kaiser result.

Homogeneity Requirements for Minimizing Self Focusing Damage

J. Marburger

University of Southern California
Los Angeles, California 90007

R. Jokipii

California Institute of Technology
Pasadena, California 91109

A. Glass and J. Trenholme

Lawrence Livermore Laboratory
Livermore, California 94550

The theory of wave propagation in random media is generalized in a straightforward way to include the effects of self focusing. Simple solutions are obtained which show how the intensity fluctuations which are induced by random inhomogeneities grow catastrophically. These solutions can be used to obtain conditions on the homogeneity of the medium, and on the fluctuations in the incident beam, for elimination or reduction of catastrophic self focusing in the medium.

Key Words: Laser damage, non-linear index, random index variation, self focusing.

1. Introduction

Bulk optical damage in solid dielectrics is known to occur at incident intensity levels much less than the intrinsic dielectric breakdown value. Under controlled conditions at low powers, such premature breakdown has been shown to arise from the catastrophic intensity enhancement near a self focus of the incident optical beam (we are assuming that extrinsic damage mechanisms such as inclusions are inoperative).[1,2][1] Under less controlled conditions, and at higher powers, the damage pattern is very complex. Much experimental and theoretical evidence suggests that, in this case too, self focusing is responsible, but that the observed damage arises from self focusing fluctuations on the incident intensity profile, and not from the self focusing of the beam as a whole. Since the self focal length of small scale fluctuations is generally much shorter than that of large scale intensity variations, the self focusing of fluctuations determines the effective damage threshold of beams propagating in nonlinear dielectrics.

Theoretical studies of self focusing fluctuations are available in which the fluctuations are already present in the incident beam, and are simply enhanced by self focusing, or diminished by diffraction.[3] We wish to point out that even when the incident beam is "clean," intensity fluctuations can accumulate during propagation through an inhomogeneous medium. Since all media are inhomogeneous to some extent, it is imperative to determine the magnitude of the influence of weak random inhomogeneities on the self focusing process. Fortunately, there are simple approximate theories of random propagation which are easily modified to include the initial stages of self focusing. In this paper, we exploit one of these theories to provide information on the influence of random inhomogeneities on bulk damage thresholds.[4]

[1] Figures in brackets indicate the literature references at the end of this paper.

2. Theory of Incipient Self Focusing in Random Media

Our starting point is the slowly varying envelope equation for the optical field amplitude E' (see ref. 2 for more information on this equation)

$$2ik\frac{\partial E'}{\partial z} + \nabla_T^2 E' + \frac{k^2}{\epsilon_o}\left(\epsilon_1 + \tfrac{1}{2}\epsilon_2|E'|^2\right)E' = 0 \tag{1}$$

Here ϵ_1 is the random component of the dielectric constant at frequency ω, and ϵ_2 is the nonlinear part of the dielectric constant:

$$\epsilon = \epsilon_o + \epsilon_1 + \tfrac{1}{2}\epsilon_2|E'|^2 . \tag{2}$$

ϵ_o is the mean linear dielectric constant, and E' is related to the total electric field strength $\mathcal{E}$ by

$$\mathcal{E} = \tfrac{1}{2}E' \exp i(kz - \omega t) + c.c. \tag{3}$$

Only linearly polarized beams are considered, and the vector properties of $\mathcal{E}$ are suppressed. k is the mean wave number in the medium: $k^2 = \epsilon_o \omega^2/c^2$; and $\langle\epsilon_1\rangle = 0$, where the brackets denote an average over an ensemble of propagation volumes.

If $\epsilon_1 = 0$, and if E' has no transverse variation at $z = 0$, then a solution of eq (1) is

$$E' = E_o \exp i\frac{k\epsilon_2}{4\epsilon_o}|E_o|^2 z . \tag{4}$$

To simplify the analysis for the general case, we introduce a new envelope function f defined through

$$E' = E_o f(x,y,z) \exp i\frac{k\epsilon_2}{4\epsilon_o}|E_o|^2 z \tag{5}$$

so that f is of order unity for small transverse intensity variations. Insertion of eq (5) into eq (1) yields

$$2ik\frac{\partial f}{\partial z} + \nabla_T^2 f + \frac{k^2}{\epsilon_o}\left[\epsilon_1 - \tfrac{1}{2}\epsilon_2|E_o|^2\right] +$$

$$+ \tfrac{1}{2}\frac{k^2\epsilon_2}{\epsilon_o}|E_o|^2|f|^2 f = 0 . \tag{6}$$

Now we introduce the logarithm of f, which is small because f is near unity in the incipient self focusing regime. Taking

$$f = \exp(\chi + i\sigma) \tag{7}$$

and ignoring all terms nonlinear in χ and σ, we find from the real and imaginary parts of eq (6) the coupled equations

$$2k\frac{\partial\sigma}{\partial z} - \nabla_T^2\chi - \frac{\epsilon_2}{\epsilon_o}k^2|E_o|^2\chi = \frac{k^2\epsilon_1}{\epsilon_o} \tag{8}$$

$$2k\frac{\partial\chi}{\partial z} + \nabla_T^2\sigma = 0 . \tag{9}$$

It is easy to solve these equations for the transverse Fourier transforms $\hat{\chi}$, $\hat{\sigma}$, where

$$\hat{\chi}\left(q_x, q_y, z\right) = \iint dx dy \chi(x, y, z) \exp i\left(x q_x + y q_y\right) . \tag{10}$$

The reader may verify the solutions

$$\hat{\chi}(q, z) = \hat{\chi}(q, 0) \cosh(z/\ell) + \hat{\sigma}(q, 0) \frac{q^2 \ell}{2k} \sinh(z/\ell)$$

$$+ \frac{\ell q^2}{4\varepsilon_o} \int_o^z \hat{\varepsilon}_1(q, z') \sinh\left[(z - z')/\ell\right] dz' \tag{11}$$

$$\hat{\sigma}(q, z) = \hat{\sigma}(q, 0) \cosh(z/\ell) + \hat{\chi}(q, 0) \frac{2k}{q^2 \ell} \sinh(z/\ell)$$

$$+ \frac{k}{2\varepsilon_o} \int_o^z \hat{\varepsilon}_1(q, z') \cosh\left[(z - z')/\ell\right] dz' . \tag{12}$$

Here ℓ is a function of q:

$$\ell = \frac{2k/q^2}{\sqrt{\left(I_o/I_q\right) - 1}} \tag{13}$$

where I_o is the mean incident intensity and I_q is a "critical intensity" for self focusing a fluctuation of transverse wavenumber q:

$$I_q = \frac{n^3 c q^2}{8\pi \varepsilon_2 k^2} = P_1 q^2 / 2\pi . \tag{14}$$

P_1 is the lower critical power for self focusing of a smooth gaussian beam of any radius, and $n^2 = \varepsilon_o$.

From these solutions for $\hat{\chi}$ and $\hat{S}$, we may compute a variety of important properties of the propagating field.

3. Ripple Gain through a Self Focusing Slab

Before examining the effects arising from intrinsic index fluctuations, we shall compute the influence of the medium on the initial fluctuations $\hat{\chi}(q, 0)$ and $\hat{\sigma}(q, 0)$. In the region $z < 0$ prior to the nonlinear medium, the fluctuation characterized by $\hat{\chi}(q, 0)$ and $\hat{\sigma}(q, 0)$ has maximum amplitude R_{in}, where

$$R_{in}^2 = \hat{\chi}^2(q, 0) + \hat{\sigma}^2(q, 0) . \tag{15}$$

After propagating through length z of the medium, and then into a linear medium of the same index, the maximum fluctuation amplitude is R_{out}, where

$$R_{out}^2 = \hat{\chi}^2(q, z) + \hat{\sigma}^2(q, z) . \tag{16}$$

This may be evaluated using eqs (11) and (12) (with $\varepsilon_1 = 0$). We define the ripple gain as

$$G = R_{out}/R_{in} . \tag{17}$$

This gain clearly depends upon the incident phase angle $\varphi = \tan^{-1}(\hat{\sigma}_o/\hat{\chi}_o)$. The maximum ripple gain G_{max} is the maximum value of G with respect to variations in φ. Since this maximization problem requires the solution of a cubic equation for $\tan\varphi$, we can obtain a tractable form for G_{max} only in certain limiting cases. Thus for very long wavelength incident fluctuations, (very small q), the reader may verify that

$$G_{max}^2 = \frac{5Q^2 + 3Q\sqrt{Q^2 + 1} + 1}{Q^2 - Q\sqrt{Q^2 + 1} + 1} \tag{18}$$

where

$$\begin{aligned} Q &= \pi I_o z/4kP_1 \\ &= z/2\ell_{min} . \end{aligned} \tag{19}$$

For short propagation lengths, G_{max} approaches

$$\begin{aligned} G_{max} &\approx 1 + 2Q \\ &\approx 1 + z/\ell_{min} \end{aligned} \tag{20}$$

so for this case ℓ_{min} is the minimum gain length for fractional growth of incident fluctuations.

This minimum gain length is also the minimum value of ℓ obtained by varying the fluctuation wave number q. Notice that if q becomes too large, ℓ becomes an imaginary number, and the fluctuation does not grow exponentially. Figure 1 shows the maximum ripple gain G_{max} for several interesting cases. The circled points indicate the approximate values $1 + 2Q$ at the ripple frequencies for which ℓ is a minimum. The point is that the actual ripple gain is not simply related to the scaling length ℓ. Not only does G_{max} exceed the approximation (eq (20)), but it peaks at a ripple frequency greater than that for which ℓ is minimal.

4. Intensity Fluctuations Induced by Index Inhomogeneities

We can gain insight into the influence of index inhomogeneities by considering a localized fluctuation $\hat{\epsilon}_1(q, z)$ in the vicinity of z_o which vanishes outside the small interval Δz. The last terms in eqs (11) and (12) then give

$$\hat{\chi}(q, z) \approx \frac{\ell q^2 \Delta z \hat{\epsilon}_1}{4\epsilon_o} \sinh\left[(z - z_o)/\ell\right] \tag{21}$$

$$\hat{\sigma}(q, z) \approx \frac{k\Delta z \hat{\epsilon}_1}{2\epsilon_o} \cosh\left[(z - z_o)/\ell\right] . \tag{22}$$

This is exactly the solution we would have found if a phase fluctuation of magnitude

$$\hat{\sigma}(q, z_o) = k\Delta z \frac{\hat{\epsilon}_1}{2\epsilon_o} \tag{23}$$

had been introduced at z_o in a homogeneous medium. Since the effect of an index inhomogeneity is to retard the phase by precisely this amount, the result satisfies our intuition.

For an index fluctuation of order 1% confined to $\Delta z \approx 100\mu m$, eq (23) predicts a phase fluctuation of order π for $\lambda = 1\mu m$, radiation. If the transverse scale of the fluctuation is such that $\ell = \ell_{min}$, then the output ripple amplitude R_{out} satisfies

$$R_{out}^2 = \left(\frac{k\Delta z \epsilon_1}{2\epsilon_o}\right)^2 \left[\cosh\, 2(z - z_o)/\ell_{min}\right] , \tag{24}$$

which grows exponentially with characteristic length ℓ_{min}.

5. Statistical Treatment of Fluctuations

Because the mechanisms which give rise to intensity, phase, and index fluctuations often possess an element of randomness, it is useful to develop a formalism which describes the evolution of the mean intensity distribution. While damage is caused by fluctuations of greater than average magnitude, at least we can formulate homogeneity criteria which assure that the average fluctuations do no harm. In the following, angular brackets refer to averages over an ensemble of systems. The random variables χ and σ at $z = 0$ and ϵ_1 everywhere are assumed to be uncorrelated and to possess zero mean.

The mean intensity at any point is

$$\langle I \rangle \approx I_o\left(1 + 2\langle \chi^2 \rangle\right) , \tag{25}$$

ignoring higher powers of χ. To avoid a cumbersome exposition we shall proceed here as if the small fluctuation approximation were exact. An analysis of the range of validity of our results will be reported elsewhere.

The mean square fluctuation of χ is related to the initial fluctuation at $z = 0$ and the inhomogeneity of the medium through eq (11) and

$$\langle \chi^2(x, y, z) \rangle = \iint d_q^2 d_{q'}^2 \langle \hat{\chi}(\underset{\sim}{q}, z)\hat{\chi}(\underset{\sim}{q}', z) \rangle \exp i(\underset{\sim}{q} + \underset{\sim}{q}') \cdot \underset{\sim}{r} . \tag{26}$$

Here $\underset{\sim}{q}$ and $\underset{\sim}{r}$ are vectors in the transverse (x, y) plane. To proceed, we make the simple assumptions that all the random variables appearing in eq (11) are independent, and that fluctuations in the same variable for different values of q are independent.

The first assumption implies, for example, that

$$\langle \hat{\chi}(\underset{\sim}{q}, 0)\hat{\epsilon}_1(\underset{\sim}{q}', z) \rangle = 0$$

and the second allows us to write

$$\langle \hat{\chi}(\underset{\sim}{q}, z)\hat{\chi}(\underset{\sim}{q}', z) \rangle = X(\underset{\sim}{q}, z)\delta(\underset{\sim}{q} + \underset{\sim}{q}') \tag{27}$$

$$\langle \hat{\sigma}(\underset{\sim}{q}, z)\hat{\sigma}(\underset{\sim}{q}', z) \rangle = \Sigma(\underset{\sim}{q}, z)\delta(\underset{\sim}{q} + \underset{\sim}{q}') \tag{28}$$

$$\langle \hat{\epsilon}_1(\underset{\sim}{q}, z)\hat{\epsilon}_1(\underset{\sim}{q}', z) \rangle = E(\underset{\sim}{q}, z)\delta(\underset{\sim}{q} + \underset{\sim}{q}') \tag{29}$$

where X, Σ and E are the power spectra of the corresponding transverse fluctuations. With these assumptions, we may write

$$\delta(\underset{\sim}{q}+\underset{\sim}{q}')X(\underset{\sim}{q},z) = \left[X(\underset{\sim}{q},0)\cosh^2(z/\ell) + \Sigma(\underset{\sim}{q},0)\frac{q^4\ell^2}{4k^2}\sinh^2(z/\ell)\right]\delta(\underset{\sim}{q}+\underset{\sim}{q}') + \frac{q^4\ell^2}{4\varepsilon_o}\int_o^z\int_o^z dz'dz''\langle\hat{\varepsilon}_1(\underset{\sim}{q},z')\hat{\varepsilon}_1(\underset{\sim}{q}',z'')\rangle \times \sinh\left[(z-z')/\ell\right]\sinh\left[(z-z'')/\ell\right] \quad (30)$$

The last term can be simplified if the correlation length of $\hat{\varepsilon}_1$ in the z direction is much less than ℓ, which will be seen to be reasonable for our applications. This allows the replacement $z' \approx z''$ in the sinh functions in eq (20), and allows the integral

$$\int_o^z dz''\,\langle\hat{\varepsilon}_1(\underset{\sim}{q},z')\hat{\varepsilon}_1(\underset{\sim}{q}',z'')\rangle \quad (31)$$

to be evaluated separately. If the correlation length of $\hat{\varepsilon}_1$ is indeed short, the integrand falls rapidly to zero unless $z'' \approx z'$, and the limits can be replaced by $\pm\infty$. Defining the Fourier transform on z of E as

$$\delta(\underset{\sim}{q}+\underset{\sim}{q}')\hat{E}(\underset{\sim}{q},\eta) \equiv \int_{-\infty}^{\infty} dz\,\langle\hat{\varepsilon}_1(q,z')\hat{\varepsilon}_1(q',z'+z)\rangle\exp i\eta z\,,$$

we find that eq (31) is simply

$$\hat{E}(\underset{\sim}{q},0)\delta(\underset{\sim}{q}+\underset{\sim}{q}')\,.$$

Putting all this together, we finally obtain

$$X(\underset{\sim}{q},z) \approx X(\underset{\sim}{q},0)\cosh^2(z/\ell) + \Sigma(\underset{\sim}{q},0)\frac{q^4\ell^2}{4k^2}\sinh^2(z/\ell) + \frac{q^4\ell^2}{8\varepsilon_o}\hat{E}(\underset{\sim}{q},0)\left[\ell\sinh(z/\ell) - z\right]. \quad (32)$$

The intensity fluctuation is of course proportional to

$$\langle\chi^2(x,y,z)\rangle = \int d^2q X(\underset{\sim}{q},z)\,. \quad (33)$$

6. Growth Rates for Fluctuations

Eq (32) shows that each fluctuation component grows in a characteristic length ℓ, but each different kind of fluctuation grows according to a different function of z/ℓ. A fluctuation will not grow appreciably unless ℓ is real, which requires the background intensity to exceed I_q in eq (13). Thus only fluctuations with values of q^2 less than

$$q^2_{lim} = 2\pi I_o/P_1 \quad (34)$$

will grow catastrophically. The most dangerous q is that for which ℓ is least, which occurs for

$$q_{max}^2 = \tfrac{1}{2} q_{lim}^2 \quad . \tag{35}$$

For $q > q_{max}$, diffraction diminishes the influence of the induced nonlinear lens. For $q < q_{max}$, the strength of the induced lens is relatively weak because the intensity fluctuation is "smooth." The minimum characteristic length is ~

$$\ell_{min} = 2k/q_{max}^2 = (2/\pi) P_l k / I_o \quad . \tag{36}$$

We have seen in section 3 how the actual "ripple gain" is related to ℓ_{min}. Since the present statistical discussion is cruder than that treatment, we shall focus our attention here on the intensity fluctuations which have their origin in index inhomogeneities. These lead to fluctuations in the optical path length to the z plane, and it is convenient to relate them to this observable quantity.

The fluctuation in optical path in distance z caused by ϵ_1 is

$$\Lambda = \frac{1}{2n} \int_o^z \epsilon_1 dz \tag{37}$$

and therefore

$$\langle \Lambda^2 \rangle = \frac{1}{4\epsilon_o} \int_o^z \int_o^z dz' dz'' \langle \epsilon_1(z') \epsilon_1(z'') \rangle$$

$$\approx \frac{z}{4\epsilon_o} \int \hat{E}(q, 0) dq^2 \quad . \tag{38}$$

This should be compared with the net intensity fluctuation at z arising from the index inhomogeneities:

$$\langle \chi^2 \rangle = \int dq^2 \hat{E}(q, 0) \frac{q^4 \ell^2}{8\epsilon_o} \left[\ell \sinh(z/\ell) - z \right] \tag{39}$$

If the index fluctuation spectrum is peaked at wave number q_o and has width much less than q_{lim}, then this can be written approximately as

$$\langle \chi^2 \rangle \approx \langle \Lambda^2 \rangle \frac{q_o^4 \ell_o^2}{2} \left[\frac{\sinh(z/\ell_o)}{(z/\ell_o)} - 1 \right] \tag{40}$$

The rms path length distortion is conveniently measured as a fraction of the wavelength $2\pi/k$ in the medium:

$$\langle \Lambda^2 \rangle^{\frac{1}{2}} = \nu 2\pi/k \quad . \tag{41}$$

Thus in the worst case, where $q_o = q_{max} = \frac{1}{2} q_{lim}$, we find

$$\langle \chi^2 \rangle_{max} \approx 8\pi^2 \nu^2 \left[\frac{\sinh\left(z/\ell_{min}\right)}{\left(z/\ell_{min}\right)} - 1 \right] . \tag{42}$$

For an rms distortion of 1/8 λ, eq (42) implies a fluctuation in $\langle \chi^2 \rangle$ of order unity at distance

$$z \simeq 2\ell_{min} . \tag{43}$$

Thus an eigth wave rms optical inhomogeneity over the operating path length is potenially as troublesome as an incident phase fluctuation of unity.

7. References

[1] Giuliano, C. and Marburger, J., Phys. Rev. Lett. 27, 905 (1971).

[2] Giuliano, C., "Time Evolution of Damage Tracks in Sapphire and Ruby," in Damage in Laser Materials, 1971 (NBS Special Publication 356); also Marburger, J., "Theory of Self-Focusing for Fast Nonlinear Response," Ibid.

[3] Bespalov, V. I. and Talanov, V. I., JETP Lett. 3, 307 (1966).

[4] Tatarski, V. I., Wave Propagation in Random Media (McGraw-Hill Book Co., New York, 1961).

8. Figures

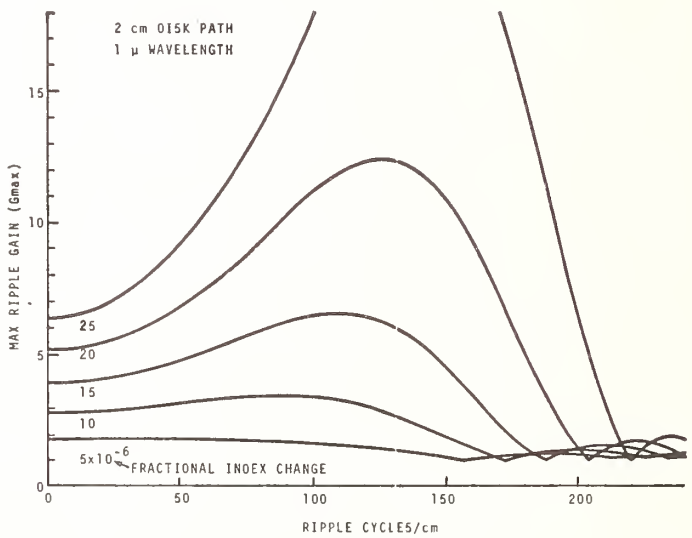

Figure 1. The maximum gain of small transverse ripples on a uniform beam in a 2 cm slab of material. Gains are shown as a function of crest-to-crest ripple spacing for various fractional refractive index changes $\delta = (n - n_o)/n_o$ due to the incident beam. The gain depends on the phase with which the ripple strikes the slab; the quantity plotted is the maximum value. The gains first increase as the ripples become more closely spaced (because the spatial index gradients which amplify the ripples are larger), and then drop off as diffraction becomes stronger than self-focusing. Note the large gains available for small index variations, and the broad range of ripple sizes which can be amplified.

COMMENTS ON PAPER BY MARBURGER

It was pointed out that, not only the small-scale structure which arises from random inhomogeneities in the optical medium can lead to self-focusing, but also that larger scale structure such that arises from the introduction of apertures into the system can lead to self-focusing. The small-scale self-focusing will be a limiting factor in systems in which the aperture size is very large compared to the dimensions of the amplified structure. Or put another way, this is the condition in which the power in the beam is greatly in excess of P_1, the critical power.

Self-Focusing and Saturation in Disk Amplifiers

K. A. Brueckner and J. E. Howard

KMS Fusion, Inc.
Ann Arbor, Michigan

The methods of geometrical optics are used to investigate self-focusing in arbitrarily spaced Nd glass disk amplifiers. Difference equations describing the growth of a localized ring or spot beam inhomogeneity are derived and solved numerically. The corresponding differential equations are solved in closed form for the case of equally spaced disks, yielding explicit constraints on the allowable amplitude and width of spikes in terms of the thickness and spacing of the disks. In a more refined calculation, the decrease in gain at large flux densities is taken into account. The analytic and numerical results are applied to a typical laser system, wherein a chain of slab amplifiers is used to produce a high energy pulse for CTR experiments.

Key Words: Damage threshold, disk amplifiers, eikonal, saturation, self-focusing.

1. Introduction

Self-focusing [1][1] is more likely to occur in disk amplifiers than in glass-rod systems, due to the larger spacing between disks. Further, the large beam profiles typical of high power systems exhibit myriad small-scale inhomogeneities, caused by diffraction and interference as the beam interacts with the various optical components in the system. These spots and rings may well self-focus before the beam as a whole [2], and we shall speak of "localized self-focusing" to distinguish the former from the latter. This effect is to be further contrasted with "small-scale self-focusing", which describes the growth of microscopic filaments in very high power beams [3]. We shall deal here with inhomogeneities large enough that negligible diffraction occurs between slabs, so that geometrical optics may be employed.

2. Localized Self-Focusing in Equally Spaced Disks

Although disk amplifiers are usually arranged in a zig-zag fashion in clusters, we shall for simplicity treat the idealized case of equally spaced slabs normal to the longitudinal axis. Consider a spike localized at some definite radius and azimuth on the beam profile as it enters the first slab. Figure 1 depicts a flux tube of initial radius b_o cm and flux density Φ_o W/cm^2 passing through a slab of thickness Δz. The ray paths in the slabs are determined by the eikonal equation [4,5]

$$\frac{d\hat{s}}{ds} = \nabla_\perp \ell n \, n \tag{1}$$

and assumed to be straight lines elsewhere. Here $\hat{s}$ is a unit vector along the ray path and $\nabla_\perp$ denotes the gradient perpendicular to $\hat{s}$. Continuity of flux along the tube, ignoring gain, requires

$$\nabla \cdot (\Phi \hat{s}) = 0 \ . \tag{2}$$

[1] Figures in brackets indicate the literature references at the end of this paper.

Combining eqs (1) and (2) for small angles of deflection, we obtain

$$\frac{\partial}{\partial z}\left(\frac{1}{\Phi}\frac{\partial \Phi}{\partial z}\right) \approx -\frac{1}{r}\frac{\partial}{\partial r}\left(r\frac{\partial}{\partial r}\ell n\, n\right) \quad , \tag{3}$$

where r and z are cylindrical coordinates. The index of refraction varies with flux as

$$\begin{aligned} n &= n_o + n_2 E^2 \\ &= n_o + \frac{8\pi n_2}{c\, n_o}\Phi \quad . \end{aligned} \tag{4}$$

Equation (3) therefore becomes, for $n_2 E^2 \ll n_o$,

$$\frac{\partial}{\partial z}\left(\frac{1}{\Phi}\frac{\partial \Phi}{\partial z}\right) = -\frac{8\pi n_2}{c\, n_o^2}\frac{1}{r}\frac{\partial}{\partial r}\left(r\frac{\partial \Phi}{\partial r}\right) \quad . \tag{5}$$

This equation may be solved by standard methods for an arbitrary initial beam profile $\Phi_o(r)$, and arbitrarily spaced disks.

To estimate the conditions for localized self-focusing, consider a local gaussian profile $\exp(-r^2/b^2)$. Translating the origin to the center of the spike and evaluating the radial derivatives there we obtain

$$\frac{1}{r}\frac{\partial}{\partial r}\left(r\frac{\partial \Phi}{\partial r}\right) = -\frac{4\Phi}{b^2} \quad . \tag{6}$$

Equation (6) can be applied to a more general distribution with a suitably defined width b. The beam is assumed to retain its configuration, apart from a change in width, in going through the optical system. Integrating eq (5) once through the m^{th} disk and ignoring the flux change yields

$$\frac{1}{\Phi}\left(\frac{\partial \Phi}{\partial z}\right)_{m+} - \frac{1}{\Phi}\left(\frac{\partial \Phi}{\partial z}\right)_{m-} = \frac{32\pi n_2}{c\, n_o^2}\frac{\Phi_m}{b_m^2}\Delta z \quad . \tag{7}$$

The focal length for the flux emerging from the m^{th} slab is given by

$$\frac{2}{f_{m+1}} = \frac{1}{\Phi}\left(\frac{\partial \Phi}{\partial z}\right)_{m+} \quad , \tag{8}$$

and the change in beam radius from the m^{th} to the (m+1)th disk by

$$b_{m+1} = b_m(1 - L/f_{m+1}) \quad , \tag{9}$$

where L is the disk spacing, assumed uniform. The flux changes with b and m as

$$\Phi_m b_m^2 = G^m(\Phi_o b_o^2) \quad , \tag{10}$$

with G the gain per slab, assumed constant.

The above procedure yields the difference equations,

$$\frac{1}{f_{m+1}} - \frac{1}{f_m} = \frac{16\pi n_2}{c\, n_o^2}\, \Phi_o b_o^2\, \Delta z\, \frac{G^m}{b_m^4}$$

$$b_{m+1} - b_m = - L\, \frac{b_m}{f_{m+1}} \quad . \tag{11}$$

If the changes in f_m and b_m are slow, eqs (11) can be approximated by differential equations,

$$\frac{d}{dm}\left(\frac{1}{f}\right) = \frac{16\pi n_2}{c\, n_o^2}\, (\Phi_o b_o^2)\, \Delta z\, \frac{G^m}{b^4}$$

$$\frac{db}{dm} = - \frac{Lb}{f} \quad . \tag{12}$$

These equations have the closed form solution,

$$f/f_1 = 2\alpha\, \cot(2\, m\, \alpha) - \tfrac{1}{2} \ell n\, G$$

$$(b/b_o)^2 = G^{m/2}\left[\cos(2\, m\, \alpha) - \frac{1}{4\alpha} \ell n\, G \sin(2\, m\, \alpha)\right] \quad , \tag{13}$$

where

$$\alpha^2 \equiv \frac{L}{2 f_1} - \left(\frac{\ell n\, G}{4}\right)^2 \tag{14}$$

$$\frac{1}{f_1} \equiv \frac{16\pi n_2}{c\, n_o^2}\, \Delta z\, \frac{\Phi_o}{b_o^2} \quad . \tag{15}$$

The parameter f_1 is the self-focusing length as the spike emerges from the first disk. The focal length goes to zero, i.e. self-focusing occurs, when

$$\frac{\tan 2\, m\, \alpha}{2\, m\, \alpha} = \frac{2}{m\, \ell n G} \quad , \tag{16}$$

valid for real or imaginary α. The flux is given by

$$\Phi/\Phi_o = \frac{G^{m/2}}{\cos 2m\alpha - \frac{\ell n\, G}{4\alpha} \sin 2m\alpha} \quad . \tag{17}$$

Equations (11), (13) or (17) may be used to estimate the value of m at which localized self-focusing of spots occurs. In the case of rings, eq (10) should be replaced by

$$\Phi_m b_m = G^m \Phi_o b_o \quad , \tag{10a}$$

the effect of which is to change b^4 to b^3 in eqs (11) and (12). Closed form solutions similar to (13) also exist in this case.

To apply the above results to practical cases, the following procedure is recommended. Given the system parameters Δz, L, G and n_2/n_o, one plots the flux (17) vs. m for various values of the ratio Φ_o/b_o^2. In this way one may determine the value of Φ_o/b_o^2 for which $\Phi(m)$ exceeds some allowable limit, with $m < m_{max}$. For the KMSF system[6], Δz = 3 cm, L = 50 cm, m_{max} = 21 disks, G = 1.13 per slab and $n_2 \approx 10^{-13}$ esu (electrostriction) . Figure 2 shows Φ/Φ_o vs. m for various values of L/f_1. Self-focusing is seen to occur at about $L/f_1 = 10^{-3}$, which leads to the constraint

$$\Phi_o/b_o^2 < \frac{c\, n_o^2}{16\pi\, n_2\, L\, \Delta z} \left(\frac{L}{f_1}\right) = 4 \times 10^9 \quad \text{watts/cm}^4 \quad . \tag{18}$$

Thus, a 1 cm spike with an amplitude greater than about 4×10^9 W/cm^2 would be expected to self-focus. Possible remedies in this case would be to move the amplifiers closer together, or to introduce a spatial filter into the system.

In the case of a passive medium, G = 1 and eq (16) reduces to

$$2m\alpha = \pi/2 \quad . \tag{19}$$

With the help of eqs (14) and (15), we obtain an explicit formula for the slab at which self-focusing occurs:

$$m^2 = \frac{\pi\, c\, n_o^2}{64\, n_2\, L\, \Delta z} \left(\frac{b_o^2}{\Phi_o}\right) \quad . \tag{20}$$

For the numerical values used in eq (18), we find $m \approx 50 > 21$, so that a 1 cm spike of height 4×10^9 W/cm^2 would not be expected to self-focus within the KMSF system operated as a passive medium.

When the gain per slab is small, we may write $G = 1 + \epsilon$, $\epsilon \ll 1$, so that $\ell n\, G \approx \epsilon$ and eq (16) becomes

$$\cot 2m\alpha \approx \epsilon/4\alpha \quad . \tag{21}$$

The critical slab number is thus reduced to

$$m \approx m_o - \epsilon/8\alpha^2 \quad , \tag{22}$$

with m_o given by eq (20).

3. Saturation Effects

In the above calculations the gain was taken to be constant. When operating near saturation, however, the decrease in gain with increasing flux must be taken into account. The effect of a chain of amplifiers on an initial pulse form $\Phi_o(t)$ is described by the following equations:

$$\frac{\partial \Phi}{\partial z} = G\Phi$$

$$\frac{\partial G}{\partial t} = -\alpha G\Phi \quad , \tag{23}$$

where α is the depletion factor. These equations may be solved approximately, one disk at a time, by computing the gain from the input flux:

$$G_n(t + \Delta t) = G_n(t) - \alpha\, G_n(t)\, \Phi_{n-1}(t)\, \Delta t$$

$$\Phi_n(t) = \Phi_{n-1}(t) + G_n(t)\, \Phi_n(t)\, \Delta z \quad . \tag{24}$$

These results may be incorporated into the self-focusing calculation as follows. First, eq (5) is generalized to allow for nonconstant gain:

$$\frac{\partial}{\partial z}\left(\frac{1}{\Phi}\frac{\partial \Phi}{\partial z}\right) = -\lambda \frac{1}{r}\frac{\partial}{\partial r}\left(r\frac{\partial \Phi}{\partial r}\right) + \frac{dG}{dz} \quad , \tag{25}$$

where λ is a scale factor. Using eq (23) we write

$$\Phi = \Phi_o \exp(X + Gz) \quad , \tag{26}$$

with X a slowly changing function of z. Equation (25) then gives

$$\frac{\partial^2 X}{\partial z^2} = \lambda \frac{1}{r}\frac{\partial}{\partial r} r \frac{\partial}{\partial r}\left(\Phi_o e^{X+Gz}\right) \quad . \tag{27}$$

This equation is readily solved by an explicit difference scheme. Initial conditions can be taken from experimental measurements of the beam intensity. We have also solved eq (27), using as initial conditions the Fresnel diffraction patterns from the aperture in the laser used to drive the disk amplifiers. These calculations will be reported in a separate publication.

4. References

[1] J Marburger, ASTM Special Technical Publication 373 (ASTM Philadelphia, 1971) p. 51.

[2] J. A. Fleck and C. Layne, Appl. Phys. Lett. 22, 467 (1973).

[3] B. R. Suydam, these proceedings.

[4] Born and Wolf, Principles of Optics (Pergamon Press, Ltd., Oxford, 1965).

[5] C. Wang, Phys. Rev. 173, 908 (1968).

[6] J. Tillotson, reference abstract in these proceedings.

5. Figures

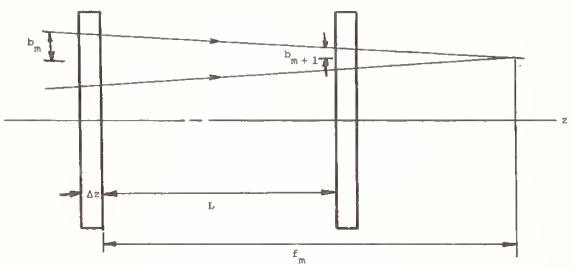

Figure 1. Arrangement of slabs, showing the evolution of a spike of radius b.

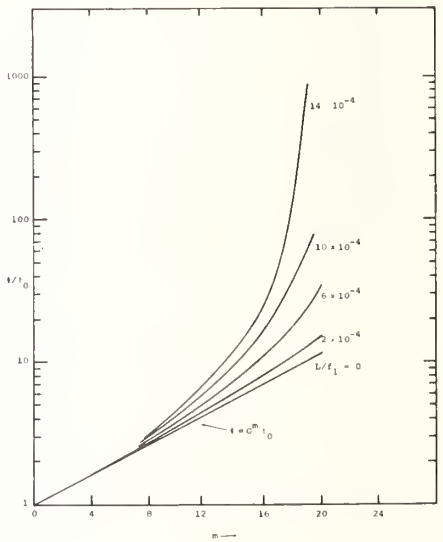

Figure 2. Normalized flux vs. slab number for various values of L/f_1. Self-focusing occurs at about $L/f_1 = 10^{-3}$.

NO COMMENTS ON PAPER BY HOWARD

Damage Control in a 100 GW High Power Laser System*

J. Tillotson, B. Guscott, and K. Moncur

KMS Fusion, Inc.
Ann Arbor, Michigan 48106

With the development of high power Nd^{+++} lasers for CTR research, severe damage in laser glass and optical components can be expected from both the output energy and from reflected plasma energy. At KMS, laser operating procedures, system diagnostics, and several isolation devices have been developed in an effort to reduce damage effects and to maximize laser lifetime. Since December, 1972, the KMS laser system has operated in the 50 - 100 GW power range (up to 300 J at 3 nsec pulse width) for a total of 310 shots[1] on target. An additional 2,379 laser shots[1] have been fired for purposes of laser beam diagnostics. Plasma experiments with f/1 and f/1.5 focusing lenses have been performed with plane targets of CD_2, CH_2 and aluminum. This paper will discuss the KMS laser system, with particular emphasis on damage control procedures and equipment necessary for conducting high energy plasma experiments.

Key Words: Disc laser, laser damage, laser fusion, Nd-Glass lasers.

---

*Unavailable at time of publication.

[1]As laser experiments are continuing, these numbers can be expected to increase by the starting date of the Symposium.

NO COMMENTS ON PAPER PRESENTED BY TILLOTSON.

Low Scatter Finishing of Optical Elements

by

William P. Barnes

Itek Corporation
Optical Systems Division
Lexington, Massachusetts 02173

The adaptation of bowl-feed polishing techniques to the low-scatter finishing of large optical elements is described. Electron micrographs of the surface of a 27 inch diameter fused silica spherical mirror indicate promise for the successful superpolishing of large, high-precision, optical elements.

Key Words: Low scatter, mirror, optical surfacing.

1. Introduction

The Optical Systems Division of Itek Corporation has a principal interest in large aperture, high performance optical lenses and camera systems. We are finding that systems requirements are emphasizing more and more not only geometrical perfection of the optical elements but also a further reduction in local and microscopic defects of the surfaces. These applications include some which are coronagraphlike in that one wishes to observe a small source in the close neighborhood of a relatively intense source; some in the ultra-violet where a given defect will scatter more energy; and some which must handle very high energy densities. The latter include high powered lasers for which small surface defects in the optics used can markedly increase the probability of catastrophic failure at a given energy flux.

2. Scattering Effects

It is not within our scope here to review prior theoretical and experimental studies of scattering in any detail. An extensive literature exists. Our present knowledge of the relationship between materials and polishing methods, surface rms roughness, and the normally incident visible light which is scattered (as a percentage of total reflectance) is summarized in table I. Several approaches to scattering theory yield the result that the scattered fraction R_{sc} from a surface whose height is a normally distributed random function, is given by

$$R_{sc} = 1 - e^{-\left(\frac{4\pi\sigma}{\lambda}\right)^2}$$

for light at normal incidence. Here σ is the rms surface height, and λ is the wavelength of the light. The experimental correlation between surface roughness, substrate material, and finishing method is drawn from the work of Bennett et al.[1,2][1] and Dietz and Bennett.[3] Directional reflectance, relative to a magnesium carbonate standard, and FECO (fringes of equal chromatic order) interference observations at Itek are in agreement with Bennett's work. An example of our directional reflectance results is shown in figure 1, for Kanigen surfaces finished with a) Linde alumina powders and a beeswax lap, and b) a chemical/mechanical polishing process proprietary to Itek.

---

[1] Figures in brackets indicate the literature references at the end of this paper.

2.1 Laser Damage Effects

To illustrate the problems encountered in high energy laser applications the theoretical exposition of Bloembergen [4] may be cited. This theoretical development indicates that for surface and volume defects with characteristic dimensions between 20 and 500 Å the electric field may be enhanced by the following factors:

1) For a shperical void, $3n^2/(2n^2 + 1)$, where n is the index of refraction

2) For a cylindrical groove, $2n^2/(n^2 + 1)$, and

3) For a "V" groove, the factor is simply n^2.

Experimental testing of these theoretical predictions has been done by Fradin and Bass.[5] They compare the electric field required to produce dielectric breakdown within a defect free volume of glass to the electric field required to produce breakdown at conventionally finished or low scatter surfaces of the same material. Photomicrographs of typical damage sites are shown in figure 2. It may be noted that the total damage produced at a surface defect failure is less than for failure in the bulk or at a smooth surface, since the defect induced failure occurs at a much lower flux density. The results compare well with theory, if one assumes that the conventionally finished surfaces contained cylindrical grooves and that the bowlfeed low scatter surfaces produced at Itek Corporation had no defects larger than 20 Å.

3. Large Element Finishing

Recent efforts at Itek have included the application of flooded surface polishing techniques to larger optical elements using a system shown schematically in figure 3. After conventional pitch lap and Barnesite polishing is completed, the system is charged with a cerium oxide polishing mixture which is recirculated through the baffled settling tank for several hours of operation. When most of the oxide has settled out, the system is flushed and filled with deionized water alone, and lapping continued for several more hours. We have found that this final pure water operation improves the surface up to some optimum operational time, after which more defects are introduced than are removed, and the superpolished finish is lost. This modification was applied to our computer assisted optical surfacing machine [6] (CAOS) shown in figure 4, and the results of working a 27" diameter fused silica spherical surface are presented in the series of electron micrographs of figures 5 and 6.

It is likely that the reproduction process will further obscure the rather subtle differences among the micrographs shown, and it is, of course, difficult to extract reliable quantitative data from the shadowed replica process used. A comparison of the original photographs, however, leads us to believe that the surface has been improved from a beginning rms roughness of 30 to 50Å, to something probably better than 20 Å rms.

Noting that not only surface finish, but also overall geometry, must be kept under close dontrol for high performance optics, we followed the changes in surface geometry. The spherical surface, which had an rms geometrical error of 0.09 wavelengths (at 633 nm) before low scatter finishing, was found to have an rms error of 0.12 wavelengths on completion of the low scatter operation. Before and after interferograms are shown in figure 7.

The CAOS machine operations used a lap about 1/3 the diameter of the workpiece. In order to cover a broader range of finishing operations, we are presently conducting trials of similar settled slurry to pure water operations using a full-sized lap. The first two trails to date have not yielded a noticeable improvement in the surface, and further studies of the potential effects of lap surface aging or other factors appear necessary.

We plan to continue the development of low scatter techniques for real and sizeable optical elements for both glass and metal mirrors and for transmitting elements, and have been encouraged by the success achieved in these first trails. Our most pressing need now is for a reliable, economical, quantitative method for in-process and final evaluation of the microscopic perfection of the surface of these larger optical elements.

4. References

[1] Bennett, H. E. and Bennett, J. M. "Precision Measurements in Thin Film Optics," Physics of Thin Films, Ed. by G. Hass and R. E. Thun, Academic Press, 1967.

[2] Bennett, H. E., "Very Smooth Surfaces," presented at the Tenth Midcourse Measurements Meeting, 3 February 1971.

[3] Dietz, R. W. and Bennett, J. M., Appl. Opt. 5, 881 (1966).

[4] Bloembergen, N., Appl. Opt. 12, 661-664 (1973).

[5] Fradin, D. W. and Bass, M., Appl. Phys. Lett. 22, 157 (1973).

[6] Aspden, R., McDonough, R. and Nitchie, F. R., Jr., Appl. Opt. 11, 2739 (1972).

5. Figures

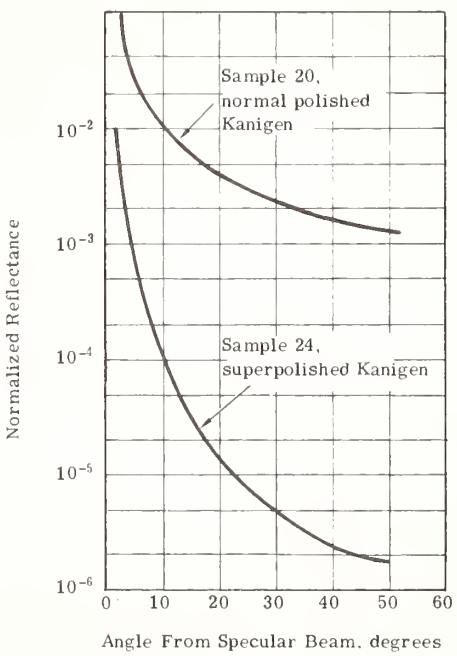

Figure 1. Relative directional reflectance for Kanigen surfaces, near normal incidence, 633 nm.

Figure 2. Photo micrographs of 1.06 μm laser damage sites in fused silica.

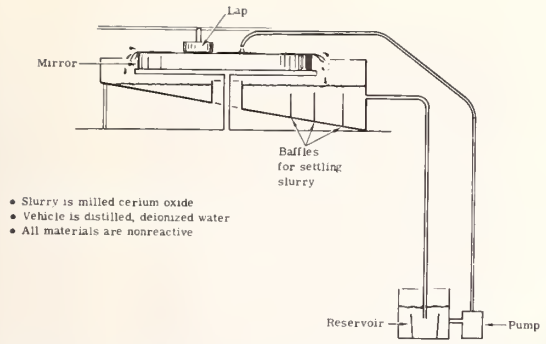

Figure 3. Schematic diagram of slurry settling tank and recirculator for the CAOS polishing machine.

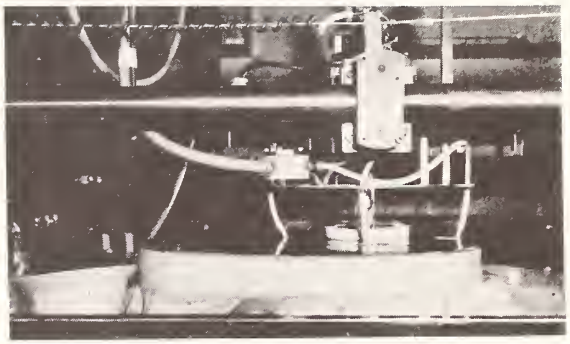

Figure 4. Photograph of the CAOS polishing machine with slurry recirculation modification.

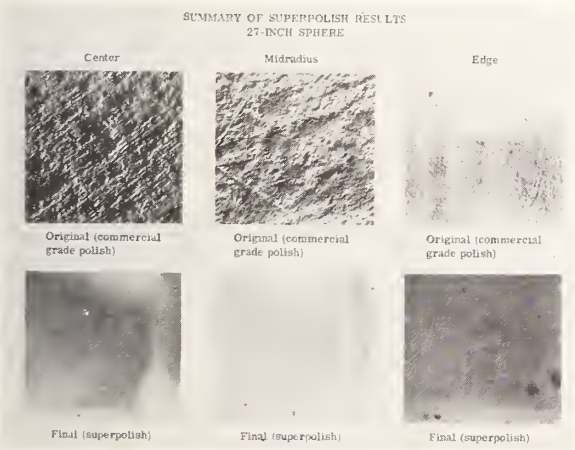

Figure 5. Replica electron micrographs of a large fused silica mirror surface before and after low scatter finishing.

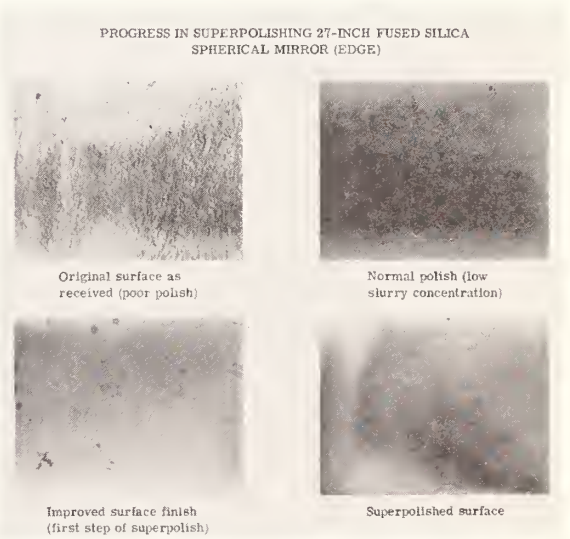

Figure 6. Replica electron micrographs of a large silica mirror surface showing progress of low scatter finishing.

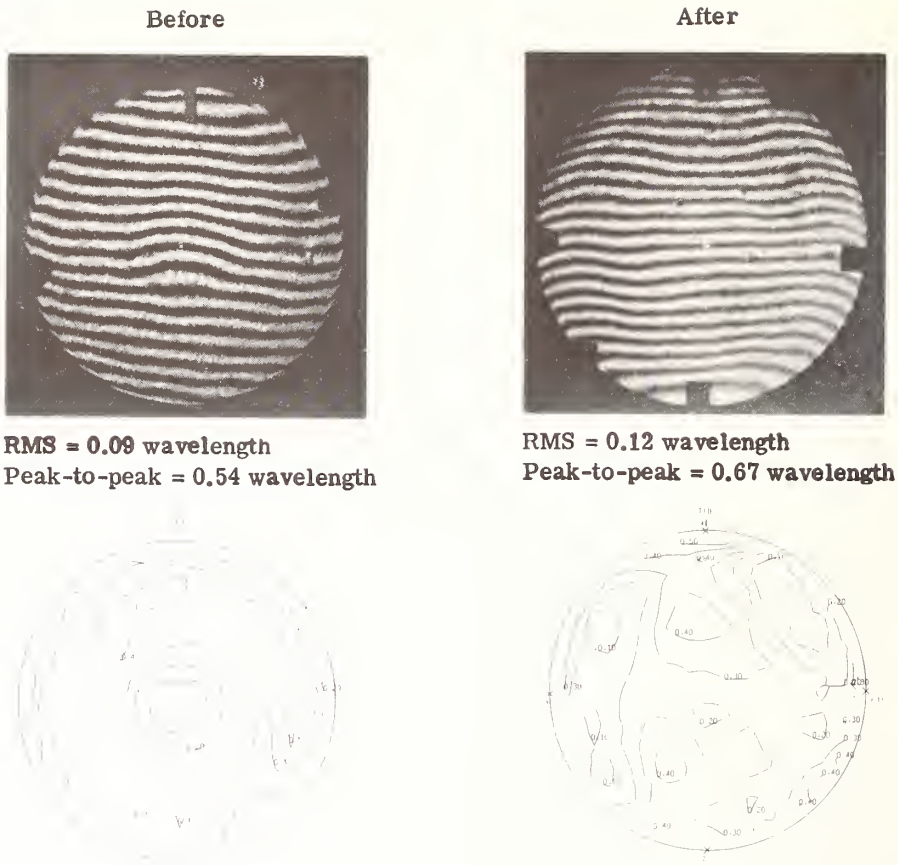

Figure 7. Interferograms of a large fused silica mirror surface before and after low scatter finishing.

NO COMMENTS ON PAPER BY BARNES.

Laser Surface Damage Studies on Several Glasses*

N. L. Boling, G. Dube', M. D. Crisp

Owens-Illinois, Inc.
1700 N. Westwood
Toledo, Ohio 43666

Q-switched laser induced surface damage studies on several glasses and sapphire are reported. By measuring thresholds on these various glasses, investigating the effect of various polishing compounds on damage of laser glass, studying damage morphologies, and taking care to detect damage in its initial stages, several conclusions are reached. Initial damage in practical situations is probably due to absorption by isolated submicron inclusions, and not electron avalanche. Inclusion type damage is found to occur without formation of the bright plasma associated with electron avalanche. The damage threshold is found to depend strongly on polishing compound in some cases. It is found that increased smoothness of a surface does not necessarily lead to an increased threshold.

Key Words: Absorption, electron avalanche, laser damage, plasma formation, polishing compound.

1. Introduction

During the past several years there have been many investigations of laser induced damage to dielectric surfaces. Reports on these investigations have often seemed to conflict. This conflict has sometimes been due to misinterpretation of experimental results; but at least as often it has, we believe, stemmed from varying definitions of damage, difficulty in detecting damage, or the results of a study on a particular dielectric prepared in a particular manner being extrapolated to include dielectrics in general.

In an attempt to avoid some of these pitfalls and to better understand our own studies of Q-switched laser damage to the surface of laser glass, we have broadened our studies to include several kinds of glasses with widely varying properties. By measuring thresholds on these various glasses, investigating the effect of various polishing compounds on damage of laser glass, studying damage morphologies, and taking care to detect damage in its initial stages, we have expanded some of the conclusions we had reached earlier by studying only laser glass polished with one compound. We find, for example, that damage can definitely occur without an accompanying visible plasma. This, in conjunction with morphology studies, allows us to conclude that electron avalanche is not the cause of initial damage in many, perhaps most, practical situations. Instead, damage is often initiated by absorption by submicron inclusions near the surface.

In addition to speculating on the basic physical processes responsible for damage, we note some pragmatic aspects of damage prevention.

2. Experimental Arrangement

Only the salient features of the experimental procedure will be mentioned here. A more detailed description can be found in reference 1. A glass oscillator-amplifier system operating in the TEM_{oo} mode was used to damage 1.3 cm cubes. The pulse was 30 ns FWHM, and the beam on the sample cubes was approximately 1.8 mm in diameter at the $1/e^2$ points. Damage thresholds reported herein refer to the average energy density passing through a 1 mm aperture placed at the position normally occupied by the sample to be tested. Peak energy densities are estimated to be 25% higher than this average, so the thresholds reported are conservative.

Neutral density filters with transmission varied in steps of 10% were used to control the energy density on the sample. The output of the laser was repeatable to within ±10%. These things taken together lead us to judge that there was a relative uncertainty of approximately ±20% in any one measurement of average energy density on the sample.

---

*This work was supported by Advanced Research Projects Agency of the Department of Defense under Contract DAHC 15-72-C-0170.

All samples were cleaned for two minutes in an ultrasonic cleaner with a mild soap solution. Following this they were rinsed in distilled water and then placed in the vapors of boiling isopropyl alcohol. Final inspection was made with a microscope light. The samples had to be cleaned very carefully to pass this inspection. However, the damage testing of a particular sample often lasted several hours during which the sample was not cleaned again. The conditions under which the samples were tested were therefore comparable to what might be obtained in a very well cleaned laser system.

3. Damage Mechanisms and Detection of Plasma Formation

Of the many mechanisms that have been proposed to be responsible for laser damage to surfaces of uncoated transparent dielectrics, there are three that we believe merit consideration. These are as follows:

1. Absorption in a uniform surface layer.
2. Absorption by isolated inclusions near the surface.
3. Electron avalanche.

The reader will note that such mechanisms as electrostrictively driven acoustic waves and Stimulated Brillouin Scattering have not been included here. These and some other mechanisms have been ruled out by experiment during the past year. For example, explanation of the assymetry between entrance and exit damage [2][1] has indicated that there is no need to postulate internally created shock waves as a damage mechanism.

We will argue in this paper that in many practical situations the mechanism initiating surface damage is absorption by isolated submicron inclusions. This is contrary to the conclusion by some that electron avalanche is solely responsible for surface damage on glass. This conclusion is intimately related to the co-conclusion that a plasma invariably accompanies surface damage. This has led to the sometimes explicit and sometimes implicit definition of damage as the formation of a visible plasma, and inferences regarding the basic mechanisms of surface breakdown are drawn accordingly. [3,4] Reports by various experimenters of observations of damage without plasma [5,6,7,8] are often answered by the argument that the plasma is always present, but is sometimes too tenuous to be detected. In view of these considerations, we will describe at some length our efforts to ascertain whether a plasma of any consequence invariably accompanies surface breakdown under the influence of a Q-switched laser pulse.

We have used two techniques to detect the formation of a plasma on a given shot. First, the surface tested was photographed as the damaging laser pulse passed through it. Second, the damage morphology was studied.

Both an overhead camera and a camera in conjunction with a microscope were used to photograph the surface. Figure 1 shows the experimental arrangement with both the microscope and the camera in position. The overhead camera yielded a 4X magnification of the 1.3 cm glass sample. The microscope magnified by 20X the region exposed to the 1.8 mm diameter laser beam.

Detection of a visible plasma by this technique depends on, among other things, the brightness and duration of the plasma. Less light is given off for detection by the camera if the plasma is small. Consequently, initially smaller plasmas are more difficult to detect photographically. Recognizing this caveat, we present the results obtained.

Figure 2 shows the "smallest" plasma we have detected with the microscope. This plasma has an apparent diameter of 200 microns, about one-fifth the diameter of the laser beam. The same plasma was also readily detected by the overhead camera. (This allowed us to use only the overhead camera in routine damage tests.)

The plasma of figure 2 was produced at 30 J/cm^2 on a sample of high index glass that clearly showed damage visible to the unaided eye at 7 J/cm^2. No indication of a visible plasma appeared between 7 J/cm^2 and 30 J/cm^2, although the damage grew much worse. This preplasma damage, which will be described in detail below, consisted of smooth pits of 1-5 microns diameter and approximately 0.5 microns depth. To indicate the density of these pits and the degree of damage, figure 3 shows a 20X photo of the damaged region after the damage was formed; that is, the sample was illuminated by white light and photographed through the microscope used to detect the plasma. This damage site had been exposed to energy densities up to 25 J/cm^2 and no visible plasma had been detected. Note the high density of small sites and the resolution of the microscope. If an initially visible microplasma had formed at each of the small sites, it seems very likely that the combined effect from all the sites would have been detectable.

[1] Figures in brackets indicate literature references at the end of this paper.

We emphasize that when a visible plasma was detected its presence was never ambiguous. There was never just a dim glow or suspicion that a plasma might have been present. The onset of a visible plasma was clearly evident. We note, incidentally, that the plasma could often be seen with the unaided eye; however, it was also often missed this way.

Although use of the photographic plasma detection technique described above strongly suggests to us that surface damage is not always accompanied by a visible plasma, further arguments can be presented to support this view. These arguments involve damage morphology. Certain morphological characteristics are associated with plasma formation as judged by photographic detection. These characteristics are never seen without a bright plasma. We will discuss each of these in turn:

1. Differences between entrance and exit morphology have often been pointed out in the literature (see reference 11 for example). The specific form of the damage is material dependent and varies widely, so no comprehensive description can be given. However, exit damage accompanied by a plasma is generally much more severe than entrance damage. Plasma accompanied exit damage in many materials often takes the form of a pit in which the material appears to have been molten and/or fractured (figure 4). Plasma accompanied entrance damage, on the other hand, is often very difficult to detect at all, sometimes consisting of only a slight rippling of the surface. In more advanced stages, entrance damage is sometimes described as a "crazing" or "cracking" of the surface with little removal of material. Figure 5 shows such damage in sapphire. These entrance and exit morphologies are to be compared with damage seen without a plasma. This damage takes the form of small, isolated pits and invariably appears the same on entrance and exit faces. Figure 6 is a scanning electron micrograph (SEM) of such entrance damage on sapphire.

That difference between entrance and exit morphology is connected with a dense plasma is also evinced by theoretical considerations. [9] Reflection of the laser beam from the exit plasma creates a standing wave inside the material. Fields in this standing wave can be great enough to cause intrinsic breakdown of the material, leading to the severe pitting often seen at the exit. At the entrance surface, reflections from the plasma cause a standing wave in air, not in the material. Damage results primarily from thermal shock by the hot plasma spreading over the surface rather than intrinsic breakdown of the material.

2. The second characteristic often seen with a plasma is a ring of material around the damage site. Figure 7 shows an example of such a ring. The ring diameter is dependent on the amount of plasma formed and is often several times as large as the laser beam. The clarity of the ring is material dependent. Such rings are not seen with preplasma damage, either around the overall damage site or as individual rings around each small pit. However, a microplasma does sometimes occur at a pit. Figure 8 shows a pit of 5 microns diameter and an associated plasma ring. Note that although the original plasma must have been less than 5 microns in diameter, it has still left very clear footprints. These rings are described more fully in reference 9.

3. Thermal cracking of both entrance and exit surfaces is often associated with a plasma. [10] This cracking at the exit is often seen around the pit described above. The region of the cracking is related to the size of the plasma and, as in the case of the rings described above, is often much larger than the laser beam. The cracking arises from thermal stresses created by the hot plasma spreading over the surface. The plasma temperature can still be several thousand degrees K after it has spread to several times the size of the laser beam. [10] Figures 5 and 9 show thermal cracking on the entrance surfaces of glass and sapphire respectively. Note the ordered arrangement on sapphire as opposed to the random cracks on glass.

4. On the exit surface one often observes a roughly circular set of ripples. These can be seen in the overall damage shown in figure 10 which was taken with a Nomarski lens. Davit [13] has suggested that these ripples arise from an interference pattern resulting from reflections between the surface and the expanding plasma.

We emphasize that none of the four effects listed above are ever manifested without a bright visible plasma appearing on the photograph used to detect the plasma. Taken together, the observations seem strong evidence for the view that no plasma of consequence appears before the very bright unambiguous plasma seen on the photographs.

We have argued now at some length that a plasma does not always accompany surface damage. This is obviously wrong.

That irradiation of a dielectric surface with power densities far below the damage threshold always produces a plasma, in the strictest sense of the word, at that surface has been experimentally demonstrated. Henderson, et al [14] have shown that at power densities well below the damage threshold, electrons and ions are emitted from dielectric surfaces under the action of normal or Q-switch mode laser pulses. Other studies have shown that there exists a critical photocurrent density at laser irradiated dielectric surfaces. At laser power densities above that which produces this critical photocurrent, damage results. However, in these studies the number of charged particles emitted per unit surface area was extremely small compared to the number emitted when a visible plasma is formed. For example, data given in reference 14 indicate that the number of charged particles emitted was never more, and usually much less, than $10^{10}/cm^2$, while electron emission greater than $10^{19}/cm^2$ is found for a laser glass subjected to power densities above the plasma formation threshold. [15]

Thus, one is forced to acknowledge that a laser pulse incident on a dielectric surface produces a plasma. In fact, considering the nature of surfaces, the surprise would lie in the absence of such a plasma. The question, however, is whether the existence of this relatively ethereal plasma is relevant to surface breakdown. An analogy between plasma formation under the action of a laser pulse and dc breakdown of transparent dielectrics can be drawn to help answer this question. This analogy is perhaps particularly appropriate in light of recent studies showing the relation between optical and dc breakdown of transparent dielectrics.

When a thin glass sheet is sandwiched between two electrodes and a dc field of a few thousand volts/cm is applied, a small current per unit area, typically in the region of 10^{-8} - 10^{-14} amps/cm^2, flows between the electrodes. The current remains in this region until a critical field is reached, at which point the current increases catastrophically -- an arc is struck between the two electrodes. The current density in this arc is of the order of 10^3 - 10^4 amps/cm^2. Since a new and highly apparent set of physical phenomena became operative at the onset of arcing, the occurrence of the arc is unambiguous. The arc is manifested by a loud crack; a bright, highly visible, plasma; and gross damage to the glass sheet. Damage is never seen in the glass before the arc occurs. If damage were observed without an accompanying arc, one would search for mechanisms other than the avalanche which leads to, or at least invariably accompanies, the arc.

The major point here is that one cannot argue that the small pre-arc current is associated with damage in the same sense as are the large current and bright plasma accompanying damage. Different phenomena are operative in the two current regions as manifested by the ten to fifteen orders of magnitude difference in current densities. However, analogous arguments are often made with respect to laser induced surface damage where the same kind of large jump in charged particle emission from the surface is observed. The tenuous plasmas detected at subthreshold levels are not relevant to damage.

We have gone on now almost "ad nauseam" about whether a visible always accompanies surface damage. We have done this because the implications bear heavily on the mechanisms responsible for surface damage. If one defines damage as the occurrence of a visible plasma, as is often done, it seems quite likely that damage is due to avalanche breakdown, in analogy with the dc case. However, if one defines damage as an irreversible disruption of the surface, which seems more practical, then damage without a visible plasma is probably due to another mechanism. More evidence for this will be offered in the following section.

4. Morphology of Preplasma Damage and Dependence of Damage on Polishing Compound

The tendency to exhibit damage before plasma formation varies with glass type, polishing compound, and geometry. Although preplasma damage has been reported on fused quartz, [6] we have not been able to detect such damage on materials of relatively low refractive index such as laser glass or fused quartz. Clear exceptions to this occur when jewelers rouge (Fe_2O_3) is used to polish the laser glass or when damage at points of total internal reflection in a Porro prism made of laser glass is examined. Damage to prisms will be discussed in a future publication. The relation between refractive index and damage will be discussed in the next section. Here the morphology of preplasma damage and its dependence on polishing compound will be described.

For a normally incident laser beam with energy density near the damage threshold, preplasma damage invariably takes the form of small pits of circular cross section. Figures 6 and 11 are scanning electron micrographs (SEM) of such damage on the entrance surface of sapphire. The pits range in diameter from slightly less than 1 micron to approximately 5 microns. They are about 0.5 microns deep and are usually very smooth. The average distance between pits on materials we have tested is approximately 5-15 microns. This distance decreases as the energy density increases above threshold.

This type of damage has been reported previously as being small hillocks, [6] and indeed it is difficult to tell whether the sites in figures 6 and 11 are pits or mounds. However, the shadows in the photos, resulting from the angle at which the SEMs were taken, indicate pits. To verify this, we have used an interference microscope to examine the sites. By noting the direction of motion of the fringes as the microscope is focused, one can easily and unambiguously differentiate between a mound and a pit as well as measure the depth or height thereof.

The small, circular pits described above are not unique to damage on uncoated transparent dielectrics. Although others have often not observed the relation between plasma formation and pit formation, micrographs and descriptions of damage in the literature indicate that these pits occur on a wide range of materials. For example, in reference 12, in which damage to thin films is discussed, the pits described and shown seem quite similar in shape and size to those described above. Complementing this, another study [16] of thin dielectric films indicates that damage occurs on some films without the occurrence of plasma.

Damage of metallic surfaces also often bears a striking resemblance to the microcraters we see on transparent dielectrics. [17]

We have found that preplasma damage is often very difficult to detect. Unless lighting is done very carefully, the damage sites do not show up under an optical microscope. Because of the low contrast between the undamaged surface and the smooth pits, the pits are also difficult to find with a scanning electron microscope. Use of a large beam, so that a large number of pits are created in a small area, was a great help to us in detecting this damage. The damage could usually be seen by examination under a bright microscope light. Because of the difficulty of detection, it appears that preplasma damage might often be missed when a small beam is used to create the damage.

The morphology of preplasma damage in suggestive of absorption by small isolated particles near the surface. Further evidence for this is furnished by the dependence of damage on polishing compound that we will discuss next.

We have investigated the effect of different polishing compounds on the surface damage threshold of ED-2 laser glass. The polishing compounds used are listed in table 1. No significant variation of damage threshold was found except for the samples polished with jewelers rouge (Fe_2O_3). (One chrome oxide polished sample exhibited preplasma type damage, but this was not repeatable.) Since jewelers rouge yields a very good polish, the surfaces of the rouge polished samples were in general more free of scratches than samples polished with other compounds. Nevertheless, the rouge polished samples began to exhibit the characteristic preplasma type damage described above at 45 J/cm^2. Plasma formation occurred at 70 J/cm^2. This is to be compared to the absence of preplasma damage and a plasma formation threshold of 100 J/cm^2 for ED-2 samples polished with other compounds.

Table 1. Various polishing compounds used on ED-2 laser glass

Barnesite	Aluminum Oxide
Diamond	Chromium Oxide
Cerium Oxide	Tin Oxide
Rouge	

In order to ascertain that the rouge polishing compound was indeed the cause of the low threshold, a sample of ED-2 polished with rouge and one polished with barnesite were subjected to a mild acid etch and then damage tested. Both of these samples exhibited exit thresholds of 120 J/cm^2 with no preplasma damage. (There has been, for some time, conflicting reports in the literature on the efficacy of acid etching on increasing the damage threshold. We see here how this might come about. The threshold on ED-2 glass is in one instance almost unaffected by acid etching, while in another instance the same glass exhibits a much increased threshold after etching.)

In an attempt to better describe the particles responsible for damage, a microprobe analysis of the surface of a rouge polished sample was made. The microprobe could detect particles $\geq$1 micron in size. Although a few particles were found, none of these contained iron. They were primarily carbon particles resulting from preanalysis treatment of the sample. The fact that no iron containing particles larger than 1 micron were found is not surprising when one considers that such particles can be detected with an optical microscope. Also, the preplasma damage sites are often less than 1 micron, and these sites are surely larger than the particle or imperfection causing them.

Theory also indicates that submicron particles can cause damage. [18] However, we believe that care should be taken in applying the theory of reference 18 to particles so close to the surface. Phase changes can occur and material is definitely removed.

To investigate the possibility that a thin layer of polishing compound was left in the surface and that damage was due to absorption in this thin layer, Auger spectrometry was used. This technique is sensitive to surface layers of one atom thickness. Again no trace of iron was found on the rouge polished samples, indicating that any iron present was in the form of isolated particles.

We have strong indications that in rouge polished ED-2 damage arises from the presence of submicron particles near the surface. Furthermore, the composition of the particles indicates that they absorb strongly at 1.06 microns. Further yet, initial damage occurs without a visible plasma and the morphology is the same as seen on all materials exhibiting preplasma damage. This suggests that the mechanism underlying such damage is absorption by isolated particles and not electron avalanche or absorption in a uniform surface layer. However, once such absorbing particles are removed, electron avalanche, signaled by a bright plasma, is probably the limiting factor on the surface damage threshold.

5. Plasma and Damage Threshold of Several Glasses and Sapphire

We have measured both the surface damage and plasma formation threshold for several glasses and one crystal, sapphire. The results of the measurements are shown in table 2. Only exit thresholds are given. Entrance thresholds for both damage and plasma formation at normal incidence can be calculated, as shown by Crisp, et al [19], from the relation

$$S_{ent} = \frac{4\,n^2}{(n+1)^2}\,S_{ex},$$

where S_{ent} and S_{ex} are the entrance and exit damage thresholds as determined by measuring the energy per unit are incident on the entrance face, and n is the index of refraction.

Table 2. Exit damage and plasma formation thresholds at 30 ns

Material	n	Preplasma damage threshold J/cm^2	Plasma threshold J/cm^2#
FK-6	1.43	N.D. (No damage)	123
Fused Quartz	1.46	N.D.	210
AO Laser Glass	1.51	N.D.	105
Schott Laser Glass	1.51	N.D.	110
ED-2 Laser Glass	1.55	N.D.	100
EY-1	1.61	N.D.	60
Sapphire	1.75	14	30
SF-6	1.78	25	34
E-2	2.10	7	36
E-11	2.10	8	37

The materials listed in table 2 were all polished with barnesite and pitch, except for the sapphire which was polished with diamond. The quality of the finish varied, the materials of higher indices generally having more scratches due to their softness.

All thresholds were determined by moving the sample after each shot; that is, new areas were exposed to shots of progressively higher energy densities until damage and/or a plasma was detected. Unless this procedure was followed, plasma formation thresholds for the materials which exhibited preplasma damage were lower than given in table 2. This was due to accumulation of preplasma damage.

The relative and absolute accuracies of the thresholds in table 2 are as discussed in section 2. We emphasize that the uncertainty in threshold is not due to the probabalistic phenomenon presented by Bass and Barrett. [4] In practical situations, one must consider the probability of damage per unit area. The beam used in our experiments was much larger than would be required to mask any probability effects. Threshold uncertainties reflect the measuring technique. Therefore, the quantity given in table 2 can be regarded as a number useful in a real system.

There are two salient features in the data of table 2. First, the damage and plasma threshold generally decrease as the index of refraction increases, with the exceptions of fused quartz and preplasma damage on SF-6. Secondly, only the higher index materials exhibit preplasma damage, at least as detected by the methods described above.

It is of interest to note that similar correlations between the refractive index and damage threshold have been observed in widely varied damage studies. In Q-switched laser damage to thin films, both features mentioned above have been observed. [16] Data given in reference 19 indicate that long pulse surface damage thresholds of many glasses generally decrease with increasing refractive index. The same thing has been reported for internal breakdown under Q-switched pulses. [20]

We do not understand the increasing tendency of materials to exhibit preplasma damage as the index of refraction increases. It can be argued that the higher index materials are softer and therefore might retain remnants of polishing compound. The sapphire was polished with diamond while the other samples were polished with barnesite, but ED-2 polished with diamond shows no preplasma damage.

The data of table 2 indicate the dangers involved in extrapolating the results of measurements on one dielectric to dielectrics in general. There has, in the past, been some controversy over whether damage can occur without a plasma, with one investigator declaring he observed such preplasma damage; another declares his studies showed the opposite and the first investigator simply hadn't looked hard enough for the plasma. If one studies only ED-2 laser glass for example, he might find himself in the position of the second investigator, while a study of sapphire only might put him in the opposite position.

The case of sapphire, which is widely studied, also shows how a rather large error could be made in measuring the damage threshold if the formation of a plasma is used as a criterion for damage. Furthermore, our measurements of inclusion density on diamond polished sapphire indicate that it would be virtually impossible to miss inclusions on any one shot even with a beam as small as 20 microns.

6. Damage Threshold as a Function of Surface Smoothness

Bloembergen [21], extending the work of Crisp, et al [2], has suggested that the increased electric field at surface scratches and digs leads to a damage threshold lower than one would expect on an ideal surface. Guenther [22] suggested and Giuliano [23] showed experimentally that an ion polished surface did indeed exhibit a higher threshold than a conventionally polished surface (sapphire was used in the study). Recently, Fradin and Bass [24] reported that bowl feed polishing, which yields a very good surface, resulted in the probability of damage at the surface, for a given electric field, being equal to the probability of damage in the bulk material.

In an attempt to extend these results to large test beams, we damage tested ED-2 polished with a bowl feed process. The surfaces on the samples were very good, generally much better than we had achieved for any previous testing. The damage threshold, however, was strikingly low. Preplasma type damage, as described above, was detected at 30 J/cm^2 on the exit face. A plasma appeared at 90 J/cm^2 on this face. This is to be compared with exit damage thresholds of 100 J/cm^2 with no preplasma damage for ED-2 conventionally polished with barnesite.

In searching for the cause of such low thresholds, we found that jewelers rouge had been used in the polishing compound. This explained the low threshold, but it also illustrated that a decreased surface roughness does not necessarily lead to increased thresholds. Other factors must be taken into account. It also illustrated that users of laser components that must withstand high powers should be aware that vendors sometimes use detrimental polishing compounds. We have found that jewelers rouge is fairly widely used in polishing laser components.

The reader will have noted that the threshold given for the rouge super-polished samples was lower than that for the conventionally rouge polished samples listed in table 2, 30 J/cm^2 vs. 45 J/cm^2. This discrepancy apparently arises from details of the polishing process. The two opposite faces of the bowl feed polished samples we tested exhibited quite different thresholds. The one face, when used as an exit, damaged at 30 J/cm^2 with a plasma at 90 J/cm^2, as reported above. The other face used as an exit did not damage until 60 J/cm^2, with a plasma appearing at 130 J/cm^2. The two faces were of similar quality as regards scratches and digs. Although no detailed records were kept of the polishing process, one face was polished for a much longer time than the other. This probably left more polishing compound in the surface. It therefore appears that not only can the type of polishing compound used cause a marked difference in threshold, the manner in which it is applied can lead to large differences, even when the resulting finishes are the same as regards roughness.

7. Conclusions

Laser induced surface damage can occur in uncoated dielectrics without an accompanying visible plasma. The ethereal nonvisible plasma detected at subthreshold energy densities is not relevant to damage. The preplasma damage seen in this study appears to be due to absorption by isolated, submicron particles near the surface and not to absorption by a surface layer or electron avalanche. Electron avalanche, which is associated with a bright plasma, may be the limiting mechanism on the surface damage threshold. The limit can only be reached after the surface is free of absorbing particles.

Higher index materials tend to show preplasma damage more readily. The reason for this is not completely understood.

Damage threshold can depend strongly on polishing compound and the details of the polishing technique. Jewelers rouge is particularly deleterious at 1.06 microns, and other compounds might be similarly undesirable at other wavelengths.

Acid etching can raise the damage threshold of laser glass by a factor of at least four when the surface has been polished with jewelers rouge.

A super-polished surface does not necessarily lead to an increased damage threshold.

8. References

[1] Boling, N. L., Spanoudis, L., and Wengert, P. R., Semiannual Technical Report, ARPA Order 1441 (December 1971).

[2] Crisp, M. D., Boling, N. L., and Dube', G., Appl. Phys. Lett., 21, 364 (October 15, 1972).

[3] Glass, A. J., Guenther, A. H., Applied Optics, 12, 637 (April 1973).

[4] Bass, M. and Barrett, H. H., IEEE J. Quantum Electron., 8, 338 (1972).

[5] Newman, B. E. and DeShazer, L. G., Laser Induced Damage in Optical Materials, NBS Spec. Pub. 372, 123 (October 1972).

[6] Fersman, I. A., Khazov, L. D., and Tikhomirov, G. P., Sov. J. of Quantum Electron., 1, 248 (November 1971).

[7] Kuznetsov, A. Ya, Varnasheva, I. S., Poplavskiy, A. A., and Tikhomirov, G. P., Sov. J. of Optics Technology, 39, 158 (March 1972).

[8] Giuliano, C. R., NBS Spec. Pub. 372, Ed. by Glass, A. J. and Guenther, A. H., (October 1972).

[9] Boling, N. L., Crisp, M. D., and Dube', G., Applied Optics 12, 650 (April 1973).

[10] Boling, N. L. and Dube', G., NBS Spec. Pub. 372, Ed. by Glass, A. J. and Guenther, A. H., (October 1972).

[11] Giuliano, C. R., NBS Spec. Pub. 372, Ed. by Glass, A. J. and Guenther, A. H., (October 1972).

[12] Bliss, E. S., Milam, D., and Bradbury, R. A., Applied Optics 12, 677 (April 1973).

[13] Davit, J., Decoux, J., Gautier, J., and Soulie, M., C. R. Acad. Sc. Paris, t. 266, 1236-1238 (April 29, 1968).

[14] Henderson, B. E., Getty, R. R., and Leroi, G. E., NBS Spec. Pub. 356, Ed. by Glass, A. J. and Guenther, A. H., (November 1971).

[15] Boling, N. L. and Beck, R. W., NBS Spec. Pub. 356, Ed. by Glass, A. J. and Guenther, A. H., (November 1971).

[16] Newman, B. E. and DeShazer, L. G., Laser Induced Damage in Optical Materials, NBS Spec. Pub. 372, 123 (October 1972).

[17] Vogel, K. and Backlund, P., J. of Appl. Phys., 36, 3697 (December 1965).

[18] Hopper, R. W. and Uhlman, D. R., J. Appl. Phys., 41, 4023 (1970).

[19] Neuroth, N., Hasse, R., and Knecht, A., NBS Spec. Pub. 356, Ed. by Glass, A. J. and Guenther, A. H., (November 1971).

[20] Hasse, Von R., Knecht, A., Neuroth, N., and Mainz, Schott Optical Comp. Information, No. 2 (1972).

[21] Bloembergen, N., Applied Optics 12, 661 (April 1973).

[22] Guenther, A. H., Air Force Weapons Laboratory Commander's Report (AFWL, Kirtland AFB, New Mexico, 1971), p. 8.

[23] Guiliano, C. R., Appl. Phys. Lett., 21, 39 (1972).

[24] Fradin, D. W., and Bass, M., Appl. Phys. Lett. (February 1973).

9. Figures

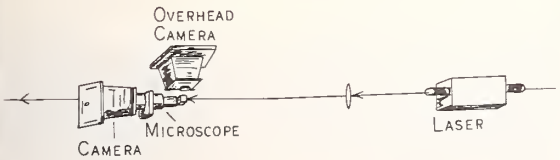

Figure 1. Camera and microscope arrangement for detecting visible plasma.

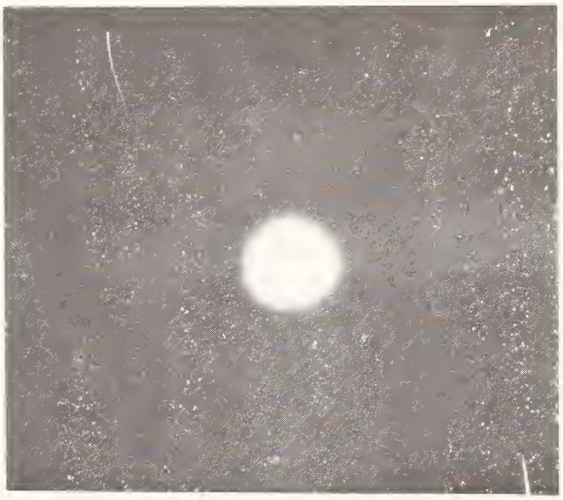

Figure 2. 200 micron plasma detected by microscope. Note the unambiguity of the presence of the plasma. The specks on photo result from dirt on the original photo.

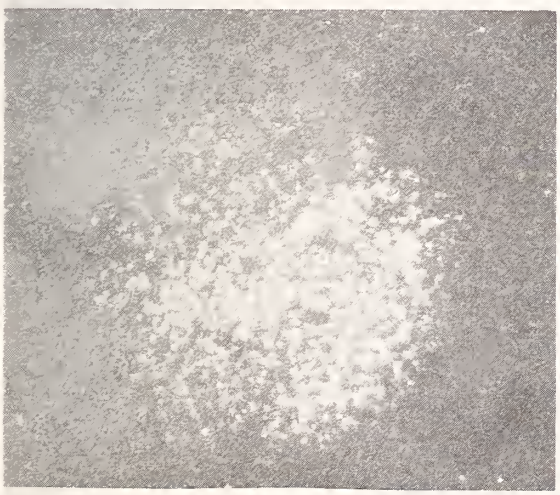

Figure 3. Preplasma damage on high index material. Photo is of area 2 mm wide.

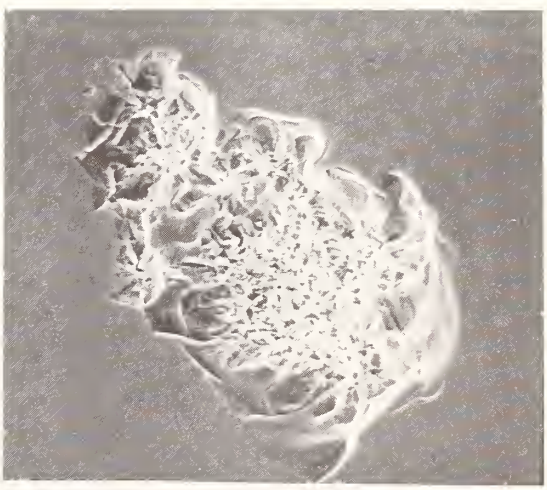

Figure 4. SEM of exit damage. This site is approximately 0.5 mm in diameter.

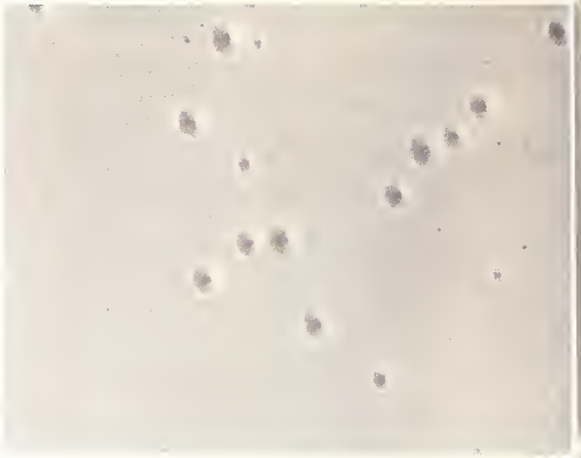

Figure 5. SEM of 150 micron wide area showing thermal cracking on sapphire.

Figure 6. SEM of preplasma damage on sapphire. Photo is of area 100 microns wide.

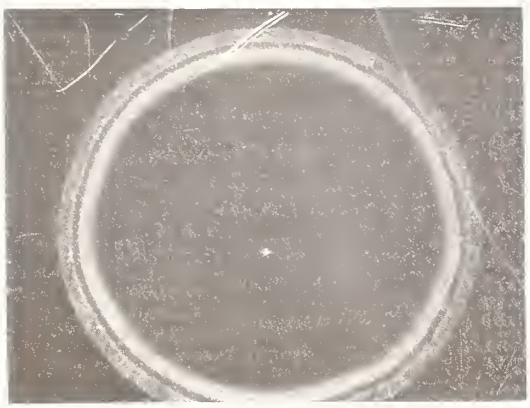

Figure 7. Plasma deposited rings around damage site. These rings are 4 mm in diameter.

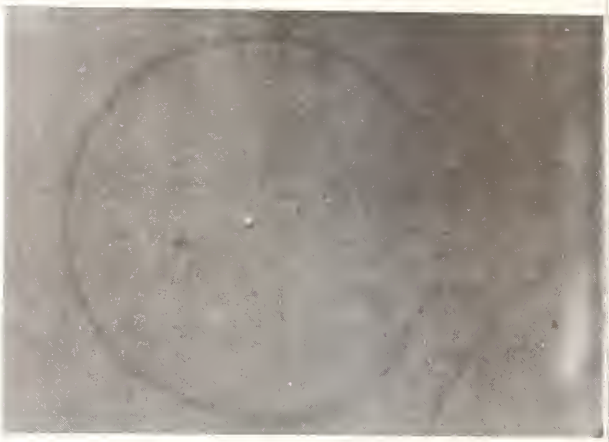

Figure 8. Optical micrograph of ring deposited by microplasma. Photo is of 0.5 mm wide area.

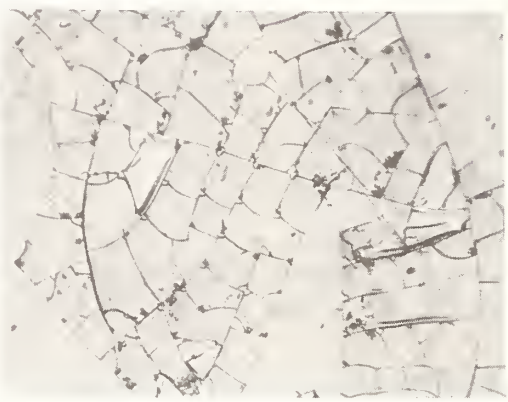

Figure 9. Plasma induced thermal cracking on glass. Area in photo is 0.6 mm wide.

Figure 10. Optical micrograph taken using Nomarski lens. Note interference rings within the damage. Photo shows 1.1 mm width.

Figure 11. SEM of preplasma damage on sapphire. This pit is 4 microns in diameter. The black specks are probably from the coating used in the SEM process.

COMMENTS ON PAPER BY NORMAN BOLING

It was pointed out that the fogging mentioned in Dr. Boling's talk has also been used both as a locator and an indicator of damage due to inclusions in thin film structures irradiated at 0.69 micrometers. It was indicated that damage due to inclusions of less than a micrometer in diameter separated by a few micrometers can be located by observing the pattern of fogging on a film under low power illumination in a microscope. The identification of the damage sites as due to particulate inclusions was later substaniated by electron microscope examination.

In the discussion, it was commented that there was no evidence of iron oxide particles of greater than a micrometer diameter despite the use of both Auger spectrometry and electronmicroprobe analysis. In response to a question regarding why this is so, the speaker indicated that it is probably true that the particles are just simply too small to be observed by either of these techniques. A comment was made that one should be able to estimate the particle size from the size of the crater, by analogy to the well-known scaling relation for surface craters generated by explosive charges. It is known that the radius of the crater is proportional to the 1/3 power of the energy deposited in the absorbing medium. Therefore, if the constituents of the absorbent particle where known, or at least if the absorption constant could be estimated, then from the statistics of crater dimension one could estimate the statistics of particle size. It was also indicated that even for the pre-plasma damage observed in the denser flint glasses the field asymmetry determined by the Fresnel relations and by the field intensification due to cracks and crevices, would still be expected to apply.

The speaker then further elaborated on the particularly damaging nature of polishing with jewelers rouge on high power laser components, and indicated that although it is well known that iron oxide is a damaging material when left on the optical surface, it is still widely used in the optical industry for finishing. He further commented that similar results to those obtained with iron oxide residue have been seen on surfaces polished with barnsite or with diamond.

Some Aspects of Surface Damage That Can Be Explained With Linear Optics

M. D. Crisp

Corporate Technology
Owens-Illinois Technical Center
Toledo, Ohio 43666

Quantitative predictions of the relative values of surface damage thresholds for various geometries are found to follow from linear optics and simple assumptions concerning the damage mechanism. It is assumed that, for a fixed pulse shape, a surface will damage when it experiences an oscillating field of amplitude greater than a threshold value. This assumption is consistent with both absorption by inclusions and avalanche breakdown as a damage mechanism. The ratios of damage thresholds for entrance and exit surfaces at normal incidence, surfaces at Brewsters angle and a total internal reflection surface are found to depend only on the index of refraction of the material. It follows from the analysis that the different threshold values obtained from measurements made with various geometries are simply related and contain information about only one intrinsic surface parameter.

Key Words: Laser damage, surface damage.

1. Introduction

Over the past nine years surface damage experiments have indicated that the exit damage threshold is significantly lower than the entrance threshold. [1,2][1] The existence of this asymmetry has caused researchers to postulate some complex mechanisms for surface damage. [1,3,4] It turns out that, instead of being a clue to some exotic damage mechanism, the asymmetry is merely a consequence of linear optics. A quantitative explanation of the observed asymmetry requires only that the damage mechanism depends upon the amplitude of the oscillating electric field at the surface. It follows from the analysis of this paper that the asymmetry which is due to reflection can be removed by performing surface damage experiments at Brewsters angle.

2. Importance of Reflections in a Damage Experiment

When a damage experiment is performed at near normal incidence there are reflections at the entrance and exit surfaces of a sample. A naive analysis of the role of reflections in such an experiment leads to the conclusion that the entrance surface would damage at a slightly lower incident power density than the exit face because there is roughly 4 per cent more power incident on the entrance face than the exit face. A correct analysis [5] of the role of reflections in a near normal incidence experiment is illustrated in figures 1 and 2. It is assumed that the sample is wedged or misaligned so that light reflected from the entrance face does not overlap the beam passing through the entrance face. For a dielectric of index of refraction n = 1.5 the interference between incident and reflected light at the entrance face reduces the electric field at the entrance face to approximately 80 per cent of the electric field that is incident from the laser. Referring to figure 2 it is seen that interference at the exit face results in an electric field amplitude that is roughly 96 per cent the amplitude of the field that is incident on the sample for n = 1.5. Thus it follows from linear optics that interference between incident and reflected light waves results in a significantly larger electric field strength at the exit surface than at the entrance surface.

3. Assumption About Damage Mechanism

In order to translate this fact about the field strengths that occur at the surfaces of a sample into a prediction about damage thresholds, it is necessary to make an assumption about the damage mechanism. It will be assumed here that whether a surface will damage or not depends only on the amplitude of the electric field that occurs at the surface. This assumption differs from earlier assumptions that considered the electric fields in the bulk material [1,4] and outside the sample [3] to be important. The most general dependence of the damage threshold on this local electric field would include information about its time dependence from the start of the light pulse up to the occurrence of damage.

[1] Figures in brackets indicate the literature references at the end of this paper.

For example, if conduction losses are negligible, an inclusion of dimensions small compared with a wavelength, located near the entrance face would cause damage when the electric field amplitude at the entrance face $\mathcal{E}_{ent.}$ satisfied a threshold condition such as

$$\int_{-\infty}^{t} \mathcal{E}^2_{ent.}(t')dt' \geq Q^D \quad . \tag{1}$$

A pulse longer than a nanosecond will cause avalanche breakdown at an entrance face if it gives rise to an electric field whose time average (over an optical period) satisfies a condition similar to

$$\overline{E^2_{ent.}(t)} = \mathcal{E}^2_{ent.}(t)\overline{\cos^2(\omega t)} \geq \tfrac{1}{2}(\mathcal{E}^D)^2 \quad . \tag{2}$$

When comparing threshold measurements made with pulses that have the same time dependence, both the threshold condition for inclusion damage and the condition for avalanche breakdown can be reduced to simpler conditions. For an experiment performed at normal incidence, it is sufficient to assume that a surface will damage when it experiences a pulse of amplitude $\mathcal{E}$ greater than or equal to a threshold amplitude $\mathcal{E}^D$. The threshold amplitude $\mathcal{E}^D$ is characteristic of the composition and polish [6] of the surface. According to this assumption an incident pulse of amplitude $\mathcal{E}_I$ would have to satisfy

$$\mathcal{E}_I \geq \frac{(n+1)}{2}\mathcal{E}^D \tag{3}$$

in order to damage the entrance surface of a sample and the incident pulse amplitude would have to satisfy

$$\mathcal{E}_I \geq \frac{(n+1)^2}{4n}\mathcal{E}^D \tag{4}$$

to damage the exit surface. Damage thresholds are usually reported in terms of incident power or energy densities. In either case, it follows from eqs (3) and (4) that the ratio of entrance to exit damage thresholds is only a function of index of refraction of a sample

$$\frac{\text{Entrance damage threshold}}{\text{Exit damage threshold}} = \frac{4n^2}{(n+1)^2} \quad . \tag{5}$$

An experimental test of this prediction appears in reference 5.

4. Damage Thresholds Measured at Brewsters Angle

If reflections were the sole source of asymmetry, then an experiment performed with light polarized in the plane of incidence, on a sample which has surfaces oriented at Brewsters should exhibit no asymmetry in damage thresholds. This experiment was carried out and it was found that the entrance and exit surfaces exhibited the same damage threshold. [5] In terms of the threshold amplitude $\mathcal{E}^D$ used earlier, a surface placed at Brewsters angle requires an incident amplitude that satisfies

$$\mathcal{E}_I \geq n\,\mathcal{E}^D \tag{6}$$

to cause damage.

A comparison of eqs (3), (4) and (6) shows that the different damage thresholds which are obtained for different geometries are simply related to the surface parameter $\mathcal{E}^D$. Knowledge of $\mathcal{E}^D$ and the index of refraction of the material would enable one to predict when a surface would exhibit damage for any geometry. This result suggests that it would be useful to express the results of a surface damage experiment in terms of $\mathcal{E}^D$ or a simple function derived from $\mathcal{E}^D$. It is suggested that the average energy density that results in damage

$$U^D = \frac{(\mathcal{E}^D)^2}{8\pi} \tag{7}$$

would be a convenient number to compare the resistance to damage of various surfaces. A more convenient parameter may be found when the theory of damage mechanisms matures.

5. Damage Measurements Performed on a TIR Surface

Lyubimov, Fersman and Khazov [7] have investigated the damage thresholds of a total internal reflection (TIR) surface. The analysis of the TIR experiment which appears in reference 7 erroneously

neglected the phase shift which occurs when light is reflected at a TIR. A correct analysis of the experiment appears in reference 8. The threshold for damage of the TIR surface depends on the polarization of the damaging light pulse. It is predicted that the relative damage thresholds for the entrance surface and the TIR surface for light polarized perpendicular to (s-polarization) and in (p-polarization) the plane of incidence is

$$1 : \frac{(n^2-1)}{4n^2\cos^2\theta} : \frac{(n^2-1)\tan^2\theta}{4(n^2\sin^2\theta-\cos^2\theta)} \qquad (8)$$

for different angles of incidence θ with respect to the normal. Comparison with the experiment of reference 7 is obtained by setting $\theta = 45°$.

6. Summary

It has been proposed that it is the amplitude of the light wave in the vicinity of the surface which determines if the surface will damage. When this assumption is combined with a calculation of interference effects between incident and reflected light waves at surfaces, it is possible to calculate the relative values of surface damage thresholds for arbitrary angles of incidence and polarizations. It is suggested that the different values of surface damage thresholds that can be obtained from different experimental geometries can be reduced to a single parameter which is related to the maximum amplitude of electric field which a surface can sustain without damage.

7. References

[1] Giuliano, C. R., Appl. Phys. Letters 5, 137 (1964).

[2] Giuliano, C. R., Appl. Phys. Letters 21, 39 (1972).

[3] Fersman, I. A. and Khazov, L. D., Sov. Phys.—Tech. Phys. 15, 834 (1970).

[4] Kerr, E. L., IEEE J. Quantum Electron. QE-8, 723 (1972).

[5] Crisp, M. D., Boling, N. L. and Dubé, G., Appl. Phys. Letters 21, 364 (1972).

[6] Bloembergen, N., Applied Optics 12, 661 (1973).

[7] Lyubimov, V. V., Fersman, I. A, and Khazov, L. D., Sov. J. Quantum Electron. 1, 201 (1971).

[8] Crisp, M. D., Opt. Commun. 6, 213 (1972).

8. Figures

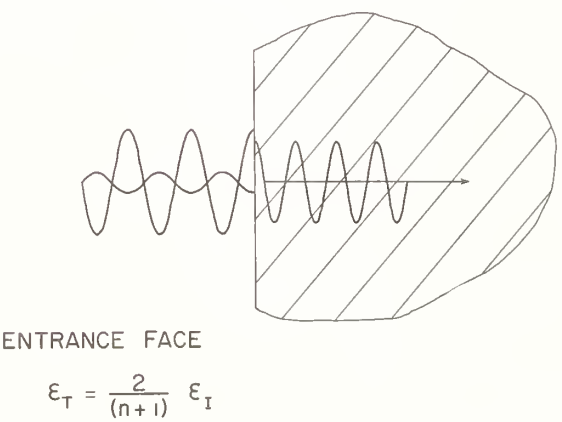

Figure 1. This figure illustrates interference between incident and reflected light waves at the entrance face of a sample. The relative scale of the electric field amplitudes is correct for a sample of index of refraction n = 1.5.

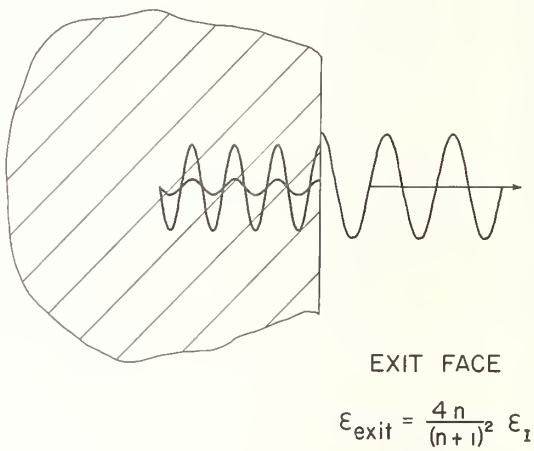

Figure 2. Interference at the exit face of a sample.

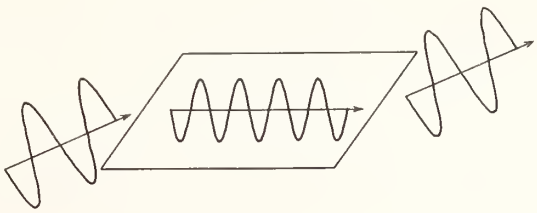

$$\varepsilon_{ent.} = \varepsilon_{exit} = \frac{\varepsilon_I}{n}$$

Figure 3. Electric field amplitudes that appear at the surfaces of a sample with Bresters angle faces.

COMMENTS ON PAPER BY CRISP

The question was asked regarding the time dependence expected in surface damage as pulse durations are shortened to below 100 picoseconds. It was commented that experimental observations, although not very accurate, indicate that surface damage, as the pulse goes below 100 picoseconds, does not scale purely with incident power density. In the discussion it was pointed out first of all, that a time dependence is expected in the avalanche breakdown mechanism and, that as the pulse duration is shortened, the intensity required for significant surface damage due to avalanche breakdown is expected to increase. Also, that damage due to inclusion heating is expected to exhibit similar temporal dependence. In any case the effects due to linear optics, that is effects due to the Fresnel relations, are expected to apply, independent of the particular mechanism operative in creating the damage.

Damage in Lithium Iodate With and Without Second Harmonic Generation*

C. R. Giuliano and D. Y. Tseng

Hughes Research Laboratories
3011 Malibu Canyon Road
Malibu, California 90265

The purpose of this study has been to determine whether a significant difference exists between bulk damage thresholds under conditions of phase matching (PM) for second harmonic generation (SHG) compared with the condition where phase matching is absent. Bulk damage in lithium iodate was studied both at 1.06 μm and 0.694 μm using single mode Q-switched lasers. Under the conditions of the experiment no significant difference was observed in damage thresholds between PM and non-PM conditions for single shot damage at 0.694 μm and for both single pulse and 10 pps at 1.06 μm.

Key Words: Bulk damage, lithium iodate, phase matching, second harmonic generation.

1. Introduction

Second harmonic generation has been of interest in the laser field for many years and the problem of damage in the nonlinear medium is ever present. Over the years a number of unpublished reports have arisen concerning the likelihood of damage during second harmonic generation. It has been suggested that for a number of nonlinear materials damage occurs more easily under phase matched (PM) conditions than under non-PM conditions. [1,2][1] In most of these reports the damage was not the main phenomenon of interest but was observed incidental to other observations. The main purpose of our experiments has been to explore this phenomenon in bulk lithium iodate ($LiIO_3$) both at 1.06 μm and 0.694 μm. At these two wavelengths the doubling was accomplished external to the laser cavity, and the experiments were carried out under both single pulse and repetitively pulsed conditions. For all the experiments performed we observed no significant difference in the thresholds between PM and non-PM conditions.

2. Damage Morphology in $LiIO_3$

The internal damage formed close to threshold in $LiIO_3$ consists of one or two small cracks about 20 μm across. If the damage is formed well above threshold or if one of the small threshold sites is exposed repeatedly to additional pulses (as often happens in the 10 pps experiments), the damaged area is appreciably larger, and the center of the fractured region is brownish in color suggesting the presence of free iodine. In fact it is possible to smell iodine when a sample has been very extensively damaged. In the better quality samples studied, the damage was found in the focal region.

If a damaged region is repeatedly exposed to additional damaging pulses, the damaged region grows in an upstream direction giving the appearance of a track. This track, however, grows relatively slowly (approximately one second at 10 pps) and although reminiscent of a self-focusing track does not arise from self-focusing. It is merely the result of a continued deposition of energy at the upstream end of a damaged region. Self-focusing damage has been observed occasionally when samples were subjected to single shots well above threshold.

---

* Work supported by the Air Force Avionics Laboratory on Contract No. F33615-71-C-1715 monitored by Air Force Cambridge Research Laboratories.

[1]Figures in brackets indicate the literature references at the end of this paper.

3. Experimental Setup

The setup for the experiments at 1.06 μm is illustrated schematically in figure 1. The Nd:YAG laser is pulse excited by a Kr-arc lamp and electro-optically Q-switched. It has the capability of being triggered externally from single shot operation to maximum repetition rate of 10 pps or internally triggered at 10 pps. The Nd:YAG rod is 0.25 in. diameter by 2 in. long, pumped by the 2 in. arc length Kr lamp in a close coupling configuration. The output coupler is a flat 47% transmission mirror, and the high reflectivity mirror has a 53 cm radius-of-curvature. To achieve single transverse mode control, the resonator cavity is internally apertured by a 2mm diameter hole placed 14 cm from the HR mirror. The laser resonator is 52 cm in length.

At full output (i.e., no transverse mode control), the output energy is approximately 100 mJ/pulse with about a 20 nsec pulse width. However, when apertured to produce the desirable transverse mode profile, the output energy is reduced to about 7 mJ/pulse with an 18.5 nsec pulse width. For single shot operation, there exists a ±3% amplitude fluctuation in the pulse height from shot to shot. When operated at 10 pps, the amplitude fluctuation disappears and the output level is even more stable.

The ruby laser that was used to study damage at 6943Å has been described elsewhere [3] and will not be described here. The characteristics of the two lasers are summarized in table 1.

Table 1. Characteristics of Lasers Used for Damage Studies

Properties	Nd:YAG	Ruby Laser
Wavelength	1.06 μm	0.694 μm
Operating Characteristics	Single shot to 10 pps	Single shot
Mode Properties	TEM_{00}	TEM_{00}
Peak Power (Pulsed Mode)	300 kW	1MW
Energy per Pulse	6 mJ	15 mJ
Pulse Width (FWHM)	18.5 nsec	20 nsec
Measured Beam Radius[a] at Lens Focus for Damage Experiments	25 μm	56 μm
Focal Length of Lenses Used in Damage Experiments	3.5 cm	19 cm

[a] The beam radius is defined here as the 1/e radius for the electric field.

4. Beam Diagnostics and Power Calibrations

4.1 Beam Diagnostics at 1.06 μm

Details of the beam spot sizes were determined by measuring the diameter of burn spots on unexposed developed Polaroid film for known incident powers ranging from the burn threshold to the maximum power available from the laser. The spot size for the Nd:YAG laser was measured at the waist beyond the 3.5 cm lens used for focusing the output inside the $LiIO_3$ samples that were studied.

About 40 shots were taken for which burn spots were measured. The diameter of the burn spots were measured using an optical microscope with a calibrated reticle at 200X magnification. The technique was found to be surprisingly well suited to this

sort of measurement. It was found that the burn spots are extremely well defined, in that the boundary between the burned and unburned regions of the film is very sharp. Examples of burn spots are shown in figure 2. The validity of this technique is based on the assumption that the film possesses a sharp burn threshold and that the diameter of a given burn spot is equal to the beam diameter at which the intensity (or energy density) equals the burn threshold.

The following expression would then apply for gaussian beam:

$$I_t = I_o \exp(-d_t^2/4a^2) \quad (1)$$

where I_o is the peak intensity, I_t is the intensity at burn threshold, d_t is the diameter of the burn spot, and a is the characteristic 1/e radius for the intensity.

Taking logarithms we have:

$$\ell n I_o = d_t^2/4a^2 + \ell n I_t \quad (2)$$

From eq (2) we see that a semilog plot of peak power versus the square of the burn spot diameter should give a straight line with slope equal to $1/4a^2$ and intercept equal to $\ell n\ I_t$ for a gaussian beam profile. Deviations from gaussian behavior will be evidenced as curvature in these plots. Data for the Nd:YAG laser focused spot are plotted in figure 3. Deviations from linearity are evident at the high power end of this plot (corresponding to the wings of the distribution), and the curvature is such that the actual beam profile contains more energy in the wings than an ideal gaussian distribution. That is, the burn spots formed at high powers are larger than those expected for gaussian beams.

From the slope in figure 3, we obtain a value for a, the 1/e radius for the intensity of 18.0 ± 1.5 μm. The corresponding value for $a = \sqrt{2}a$, the 1/e radius for the field (also the $1/e^2$ radius for the intensity) is 25 μm.

4.2 Beam Diagnostics at 6943Å

A detailed series of beam profile and spot size measurements on the single pulse ruby laser have been described elsewhere. [4] The beam was photographed using a multiple exposure camera incorporating nine lenses, each one having a different amount of optical attenuation. Hence, each photograph contains nine different exposures of the same spot. By taking densitometer scans of the different spots, detailed information can be obtained about the spatial beam profile without requiring knowledge of the film response characteristics. [5] The results of a series of beam profile measurements are included in Reference 4. The far field spatial profile was found to be gaussian down to 8% of the peak. The spot size at the beam waist under the focusing conditions (19 cm lens) for the experiments carried out using the pulsed ruby laser is 56 μm radius at the 1/e points for the electric field.

4.3 Power Calibration Measurements

For the pulsed ruby and high power pulsed Nd:YAG lasers, the output energy was measured using a calibrated Hadron thermopile and by simultaneously comparing the measured energy with the output of the monitoring photodetectors. From that point, the photodiodes were used as secondary standards. The energy of a single pulse was measured with the ruby laser while the total energy in a series of ten pulses was typically measured for the Nd:YAG laser operating at 10 pps. The energy per pulse was then obtained by dividing the total energy by the number of pulses. Temporal peak powers quoted in this paper are obtained by dividing the total energy per pulse by the pulse width (FWHM).

5. Experimental Procedure for Measuring Damage Thresholds

We will briefly describe the procedure used in obtaining damage thresholds reported in this paper. The light was focused inside the samples (typically 1 cm cubes) using a 3.5 cm focal length lens. Incident power was monitored using a silicon photodiode and in the phase matching experiments, the second harmonic was also monitored with a photomultiplier tube placed beyond the sample. In the single pulse experiments, the power was monitored for each shot; in the experiments carried out at 10 pps, several shots (~10) were superimposed and photographed on the oscilloscope screen. To change from PM to non-PM conditions on samples that were appropriately oriented the

sample was rotated slightly (~0.5°), such that the second-harmonic intensity was seen to drop about two orders of magnitude from that at the optimum orientation. In this way, damage thresholds were measured for both conditions in the same sample.

A typical set of experiments would consist of the following procedure. The sample would be irradiated at a level generally below threshold and examined between irradiations for the presence of damage. If no damage was seen to have occurred, the incident power level would be increased (10 to 20%) and the sample again subjected to another exposure. Examination for internal damage was done by looking visually for light from the He-Ne alignment laser scattered from the damage sites and by viewing the sample through a microscope that could be moved in and out without disturbing the sample. For single pulse experiments, the sample was examined after each shot. For 10 pps experiments, a typical exposure would consist of about 30 sec (300 shots) and the sample subsequently examined. In virtually all cases at 10 pps, it is possible to see easily with the unaided eye the incandescence of the internal sites at the time they are formed. In such cases, the beam was quickly interrupted and the exposure time noted. By the time the self-incandescence is seen and the beam interrupted, it is found that the damage is fairly extensive, i.e., the brownish color of iodine in the center of the internal fracture is apparent, indicating that the damage site has been hit more than once after it was formed.

Many experiments were carried out at 10 pps for two different samples under both PM and non-PM conditions. The peak power at which damage was seen to occur from one site to another was fairly variable (see figure 4), but for a given damage site the threshold is well defined. To emphasize this point, the following findings summarize our documentation of 50 damage sites on two different crystals.

- In every case, the site in question was subjected to at least 300 shots whose peak powers were between 85 and 90% of the level at which damage finally was seen to occur.
- In 16 cases, the damage site in question was subjected to up to 1200 shots (in one case, 1800 shots) whose peak powers ranged from 65 to 90% of the power at which damage finally occurred.
- When damage level was reached, damage was seen to occur (by observation of incandescence) within 3 sec (30 shots) of exposure to the pulse train.

These results indicate that a given site has a well-defined threshold power; whereas the threshold can vary considerably from site to site within the material.

6. Results of $LiIO_3$ Damage Experiments

The results of measurements of bulk damage thresholds in $LiIO_3$ are tabulated in table 2. Samples were obtained from various sources. Many of the samples studies in the early stages were grown at HRL. Others were obtained from Stanford University,* Isomet, Clevite, and Gsanger. The quality of the material from the different sources did not vary widely; most of the damage threshold values are of about the same order.

The damage threshold measurements at 6943Å were taken early in the study on an HRL grown sample (sample E), the optical quality of which was not as high as samples studied later. The low threshold for sample E compared with sample A at 6943Å is probably a reflection of the difference in crystal quality.

A comparison of single shot and 10 pps thresholds for sample B in table 2 suggests an appreciable difference between the two. However, it should be noted that the single shot data were taken at an earlier time in the program than the 10 pps data, and a different calibration pertained to that situation. The same is true for the lower thresholds listed for samples C and D (phase matched). Hence, the apparent difference between the group of thresholds around 2 GW/cm^2 and those around 1.4 GW/cm^2 may be a reflection of the reliability of different calibration procedures, although the precision of a given calibration procedure is greater than the above difference.

---

* We are grateful to Dr. Robert Byer of the Materials Research Laboratories of Stanford University for providing a sample of $LiIO_3$.

Table 2 Damage Thresholds for Various Samples of $LiIO_3$

Sample	λ, μm	Second-Harmonic Conversion %	Pulse Rep. Rate	Damage Threshold Power Density[a], GW/cm^2		
				Av Value	Av Deviation	Range[b]
A	1.06	19 to 28	10 pps	1.92	0.23	1.39 to 2.36
A	1.06	0	10 pps	2.14	0.20	1.80 to 2.77
A	1.06	0	single shot	2.01	0.47	1.54 to 2.80
A	0.694	0	single shot	2.63	0.52	1.9 to 3.6
B	1.06	0	10 pps	2.16	0.25	1.68 to 2.80
B	1.06	0	single shot	1.50	0.40	0.95 to 2.90
C	1.06	0	single shot	1.30	0.18	0.98 to 1.85
D	1.06	20	single shot	1.34	0.28	1.0 to 2.5
D	1.06	0	single shot	1.83	0.28	1.32 to 2.40
E	0.694	0	single shot	0.55	0.07	0.36 to 0.70
E	0.694	10	single shot	0.60	0.08	0.40 to 0.85

[a]These values are given as total power (or energy) divided by the beam area defined as πa^2, where a is the 1/e radius for the electric field. The on-axis intensities (energy densities) are twice as large as the values quoted in the table.

[b]These are the maximum and minimum values observed for a series of 10-25 measurements on a given sample.

7. Conclusions

We conclude that the threshold for laser induced bulk damage in $LiIO_3$ is independent of whether the crystal is phase matched for second-harmonic generation under the conditions of our experiments. The experimental conditions upon which this conclusion is based are:

- Single pulse operation at 0.694 μm and 1.06 μm
- 10 pps operation at 1.06 μm, with ~20% second-harmonic conversion for both conditions.

Without further research, proof that this conclusion would be valid or different under high average power conditions such as exist in cw or high repetition rate intracavity systems cannot be offered.

We also conclude that although a wide spread of values was observed for a given sample, there appeared to be a well defined threshold for a given site in the sample as illustrated by the discussion in Section 5. Because of the high value for damage threshold and the fact that the damage is found in the focal region inside the sample it is reasonable to expect that the damage is not caused by absorption due to inclusions although this possibility cannot be definitely discounted. We are not able to interpret the spread in our results in the manner used by Bass and Barrett [6] but the conditions of the experiments were not the same. The focal spot diameter in our experiment was 50 μm compared to 30 μm in the aforementioned workers' experiment and although the difference is not a large one it may be sufficient that the statistical behavior they have observed would not be expected [7,8] for our conditions.

8. Acknowledgment

The authors wish to acknowledge the many helpful suggestions of V. Evtuhov, E. S. Bliss and D. Milam as well as the technical assistance of R. Morrison and G. R. Rickel.

9. References

[1] Webb, R., Damage in Laser Materials: 1971, edited by Glass, A. J. and Guenther, A. H., NBS Special Publication 356, 1971 (U. S. GPO, Washington, D. C.) p. 98.

[2] Nath, G., communicated at the Sixth International Quantum Electronics Conference, Kyoto, Japan, 1970.

[3] Giuliano, C. R., Damage in Laser Materials: 1971, edited by Glass, A. J. and Guenther, A. H., NBS Special Publication 356, 1971 (U.S. GPO, Washington, D. C.) p. 44.

[4] Giuliano, C. R., DuBois, D. F., Hellwarth, R. W., and Rickel, G. R., Damage Threshold Studies in Laser Crystals, HRL Semiannual Report 3 (Jan. 1971) AFCRL-71-0064.

[5] Winer, I. M., Appl. Optics 5, 1437 (1966).

[6] Bass, M., and Barrett, H. H., IEEE-JQE 8, 338 (1972).

[7] Bass, M., and Barrett, H. H., Laser Induced Damage in Optical Materials: 1972, Edited by Glass, A. J. and Guenther, A. H., NBS Special Publication 372, 1972 (U.S. GPO, Washington, D. C.) p. 58.

[8] Milam, D., private communication.

10. Figures

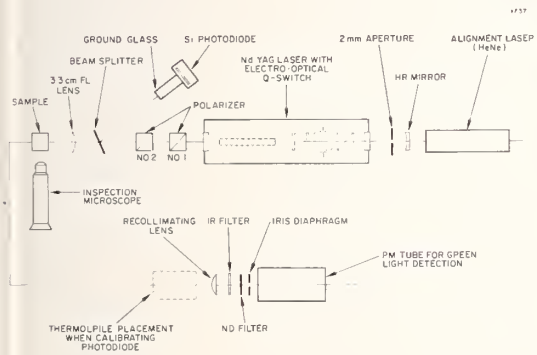

Figure 1. Experimental setup for damage experiments using pulsed Nd:YAG laser.

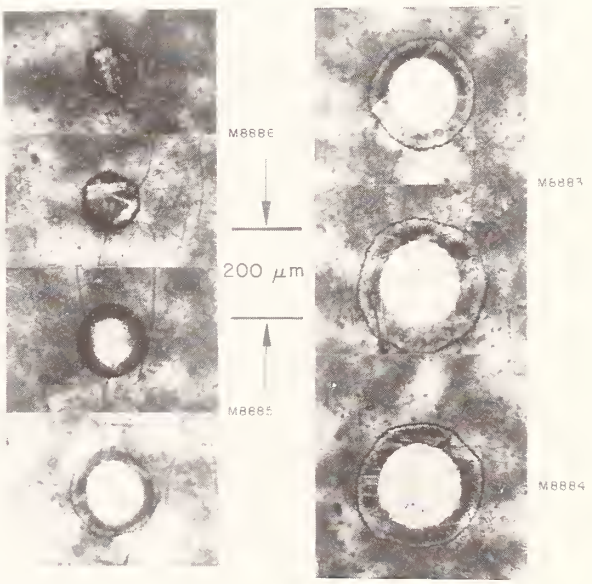

Figure 2. Examples of burn spots at lens focus on unexposed developed Polaroid film (Type 47).

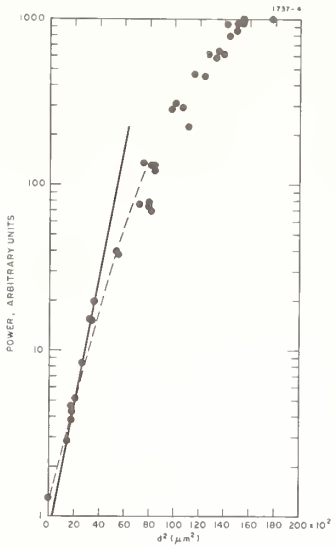

Figure 3. Log P versus d^2 for burn spots taken at lens focus.

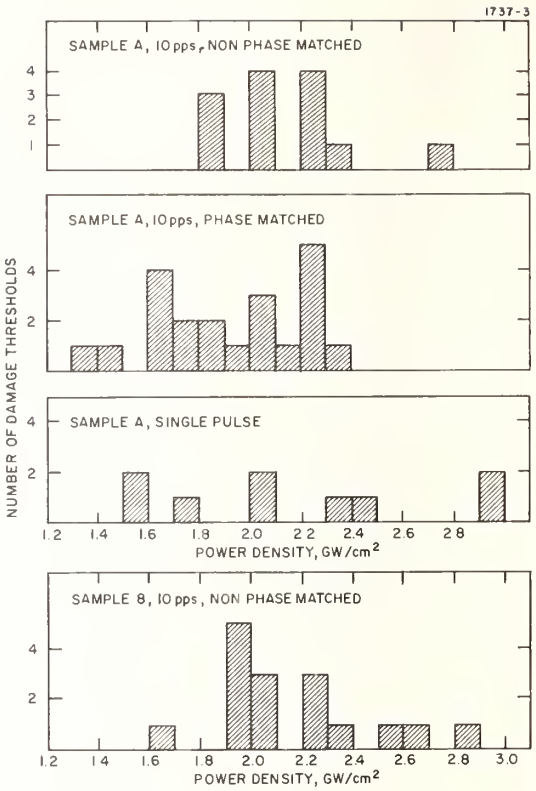

Figure 4. Number of damage thresholds versus power density for $LiIO_3$ showing distribution of values obtained.

NO COMMENTS ON PAPER BY GIULIANO.

Laser Surface Damage Studies at Bendix*

P. Bräunlich, J. Carrico, B. Rosenblum, and A. Schmid

Bendix Research Laboratories
Bendix Center
Southfield, Michigan 48076

A status report will be presented which describes the application of the exoelectron imaging technique as a nondestructive test method for laser surface damage. The mechanism of exoelectron emission from dielectrics will be discussed and an outline of a theory of laser induced exoelectron emission will be given. It will be shown that thermally or optically stimulated electron emission images represent a record of physical phenomena that are precursors of laser surface damage. Experimental techniques used to obtain exoelectron images after laser exposure of the sample will be described and recent results presented.

Key Words: Exoelectron emission, laser surface damage.

1. Introduction

At the 1970 Laser Damage Symposium we speculated that a connection existed between exoelectron emission (EE) from the surface of an optical material and its susceptibility to laser surface damage. [1] A research program, designed to study this problem, was initiated in August 1972. In this paper, we report the progress achieved during the first half-year of the program.

Our approach to the study of laser surface damage is based on a series of preliminary experiments suggesting that the two-dimensional intensity distribution of the exoelectron emission from a surface represents an accurate record of the physical processes which took place during and sometime after the exposure to an intense pulse of laser light. Since little or no work on this subject is available in the literature, our investigations are concerned with (a) the study of exoelectron properties of various optical materials of interest, especially after exposure to laser radiation, (b) the development of new experimental techniques to obtain and evaluate exoelectron images on surfaces of optical materials after exposure to intense laser light, and (c) the theoretical interpretation of the experimental results.

Exoelectrons are emitted from surface layers (10-100 Å thick) of a variety of optical materials usually after exposure to ionizing radiation, including intense laser radiation. [2,3] This emission of electrons may occur spontaneously, or it may be stimulated thermally or optically. Thermally stimulated exoelectron emission (TSEE) from insulators is occasionally called "low-temperature thermionic emission." The prevailing interpretation of this particular type of exoelectron emission is the following. [4] Because of the interaction of the ionizing radiation with the solid, electrons from levels below the thermal-equilibrium Fermi level are lifted into higher metastable levels (traps). Upon subsequent heating of the sample, the trapped electrons are released and a fraction of them leave the surface.

The initial rise of the emission current with temperature can be described by an equation similar to the Richardson equation. However, the work function is now replaced by an effective work function, which is smaller than the former. This effective work function is the energy difference between the trap level and the vacuum level. It explains the occurrence of thermionic emission at considerably lower temperatures. Since the supply of trapped electrons is limited, the emission current decreases again after reaching a characteristic peak. A typical exoelectron curve is shown in figure 1.

Even though EE properties of insulating solids have been, and continue to be, the subject of intensive investigations, [2] little is known about materials of laser interest. Except for the work by Bendix on LiF, [3] nothing has been reported on EE from such materials after laser exposure.

Figures in brackets indicate the literature references at the end of this paper.

*This work is sponsored by the Advanced Research Projects Agency under Contract No. F19628-73-C-0032 through Air Force Cambridge Research Laboratories.

The materials of interest include: alkali halides (mostly for IR windows and other optical components); laser glass; certain sulfides, tellurides and selenides; alkaline earth halides; IR transparent mixed crystals (alkali halide mixtures); and nonlinear optical materials such as $LiNbO_3$, $Ba_2NaNb_5O_{15}$, KDP, $LiIO_3$, α-HIO_3, Ag_3AsS_3 and $LiHCO{:}H_2O$. This list continues to grow as new laser optical materials are developed. No work has been reported in the literature on EE from any of the nonlinear materials or laser glass. Fairly extensive work has been reported on EE after excitation with ionizing radiation of alkali halides, some sulfides, and earth alkaline halides. Laser glass, ferroelectric materials, and most notably pyroelectric materials are of particular interest with respect to their extensive use in high power laser applications. We therefore selected $LiNbO_3$ (representative of the pyroelectric-ferroelectric group) and ED-2 laser glass as the first materials for our initial experimental studies.

2. Test Facility for Measurement of General Exoelectron Emission Properties of Laser Materials

A schematic of the test apparatus is given in figure 2. This system was developed to facilitate the collection of data on laser materials. It consists of a sample holder, an electron gun, and a channel electron multiplier, all mounted in an oil diffusion pump high vacuum station. Typical operating pressures are in the low 10^{-7} Torr range. A high intensity monochromator permits photostimulation of the sample.

Samples are easily fastened to the holder with good thermal contact. Both heating and cooling capability are provided. A thermocouple is used to monitor sample temperature. The electron gun is a pentode configuration with two-dimensional deflection capability. Its spot size, intensity, and energy are adjustable. This gun permits us to outgas samples and fill traps under vacuum. Thus, we are able to study general exoelectron phenomena on the samples without opening the system to air for X-ray treatment. This procedure is both cost- and time-saving. Of course, when necessary, samples irradiated by either X-rays or the laser can also be studied. The photostimulation system consists of a high intensity Bausch and Lomb monochromator, a window into the vacuum, and appropriate optical collimation and focusing. This capability permits us to investigate nonlinear optical materials without interference from high energy electrons produced by thermally induced field emission.

The channel electron multiplier and detection electronics provide wide dynamic range capability for obtaining data on samples ranging from very weak emitters such as glass to strong emitters such as BeO. In the scheme shown in figure 2, the electron multiplier is used in a pulse counting mode. Each detected exoelectron gives rise to a high gain pulse which is integrated and displayed.

Figure 3 shows exoelectron emission intensity as a function of temperature for NaCl. The traps were filled by bombardment with 3 keV electrons. The integrator output and sample temperatures as measured by a thermocouple are displayed on a two-channel strip chart recorder. Similar data have been collected for ED-2 Nd-doped glass (figure 1). In the situation where the emission intensity is very weak, the electron multiplier output pulses can be counted and stored in a 400-channel analyzer. The log amplifier and divider shown in figure 2 enable us to record directly the log of the emission intensity as a function of 1/T on an x-y recorder so that activation energies can be readily determined. We felt that the study of Nd-doped glass was important because of its use in laser systems. Also, nothing is known about exoelectron emission from glassy compounds except for some work by Becker [5] and Gourgé [6,7]. Becker observed that radiation-induced thermally stimulated exoelectron emission was much stronger from crystalline than from glassy lithium borate. Thermally stimulated emission from quartz glass and from silver-activated phosphate glass was measured by Gourgé.

Because of Becker's work, little or no emission from glass was expected. Accordingly, the detection system was designed to measure weak emission. The system shown in figure 4 was used in early work. It consisted of a microchannel electron multiplier and a phosphor screen which could be read out visually or by means of a photomultiplier. More recently, the channel electron multiplier scheme shown in figure 2 was used.

ED-2 Nd-doped glass samples (1.25 mm x 1.25 mm x 1 mm) were obtained from Owens-Illinois. These samples were of optical quality and prepared (polished and cleaned) by Owens-Illinois. Six of these samples were then exposed to the Owens-Illinois, high intensity, Nd-glass laser operated in the TEM_{00} mode. Each sample was exposed to a different laser intensity. The intensities ranged from slightly above the threshold for damage [110 J/cm^2 for 25 ns (FWHM) pulse] to about 10 percent of damage threshold. These irradiated samples were then packaged in dry ice in order to minimize depopulation of traps (if any) and brought to the Research Laboratories for measurement. Care was exercised in the handling of the samples to prevent possible bleaching by ambient light. The system shown in figure 4 was used to obtain the data. The detector was operated at very high gain. The exoelectron emission from these samples above room temperature was very weak. Furthermore, the emission could not be correlated with previous exposure of the sample to high peak powers of laser light.

A second batch of samples was obtained and exposed to laser light by Owens-Illinois. Again the results were inconclusive. More recently, some samples from this second batch were inserted into the system shown in figure 2. Reproducible but very weak exoelectron emission was detected after electron

bombardment (figure 1). However, at this point, we have to conclude that exoelectron emission from laser glass appears to be too weak to be of any practical interest for laser surface damage studies.

3. Exoelectron Emission From Pyroelectric Materials*

Pyroelectric materials constitute a special class of materials with respect to their exoelectron emission properties. Any work that aims at an understanding of the mechanism of exoelectron emission from insulators must pay special attention to these materials.

All experiments reported so far in the literature on ferroelectric and pyroelectric crystals were done in air, and they are therefore not reproducible. [8] For this reason, we have performed a series of experiments in vacuum ($<10^{-6}$ Torr). We selected $LiNbO_3$ single crystals which were poled in an electric field and therefore consisted of a single domain or revealed, after etching in HF, a well defined domain structure. All surfaces examined were perpendicular to the c-axis, the axis of polarization. The crystals were nominally pure. As a result of this investigation, we now understand exoelectron emission from pyroelectric materials. By slowly heating the crystals from room temperature to about 100°C, we measured electron emission current densities of 10^{-10} to 10^{-9} A/cm^2 (averaged over the sample surface). Depending on the direction of the c-axis (either c^+ or c^-), a similar effect was observed upon cooling. Multidomain samples (nearly circular domain boundaries in the crystal surface perpendicular to the c-axis) emitted upon cooling, as well as upon heating. This type of exoelectron emission, observed for the first time, may be called thermally stimulated field emission of electrons (TSFE).

TSFE turned out to be a useful means for imaging the surface of the crystal. We have obtained simple proximity images with the aid of a closely packed bundle of electron multipliers, each 50 μm in diameter. The emitted electrons are multiplied in this device and projected onto a phosphor screen. The spatial variations in emission current density could be easily displayed in this manner with a resolution of about 300 μm. The image obtained when the front of the multiplier bundle was only 2 mm above the crystal surface showed quite clearly the structure of the ferroelectric domain. Typical TSFE images of a multidomain $LiNbO_3$ crystal are shown in figures 5 and 6. Figure 7 is a photograph of the same crystal after etching in HF.

As indicated above, the mechanism of TSFE from $LiNbO_3$ is field emission of electrons. The theory of this effect has to explain the existence of electric fields that are strong enough ($\geq 10^7$ V/cm) to cause such emission.

Pyroelectric crystals have a spontaneous polarization P_S below the Curie temperature T_c. In the case of $LiNbO_3$, $P_S = 0.7$ C/m^2 at room temperature and $T_c \approx 1200$°C. Due to this polarization, the c-faces of the crystal are charged with a surface charge of density η_i, and we have the relation $P_S = \eta_i$. The resulting internal field is $|E_i| = 4\pi\,|\eta_i| = 4\pi\,|P_S|$ [figure 8(a)].

When the crystal is placed between the grounded heating block [figure 8(b)] and the microchannel plate, an external field E_0 develops:

$$E_0 = 4\pi \frac{\varepsilon}{\varepsilon - 1} P_S \approx 4\pi P_S. \qquad (1)$$

where ε is the dielectric constant ($\varepsilon = 50$ for $LiNbO_3$ along the c-axis).

The internal field E_i eventually causes compensation of the surface charges η_i in any real crystal because of its finite conductivity σ. In air, additional compensation occurs by ions that move from the surrounding atmosphere onto the crystal surface. In vacuum, the decay of η_i is given by $\eta_i = \eta_i\,(t = o)\,\exp(-\varepsilon t/\sigma)$. As a result, the surface charge of a pyroelectric crystal is compensated completely after $t > \sigma/\varepsilon$.

Experimentally, one can observe pyroelectric properties only by changing the crystal temperature at a rate that is characterized by a time constant smaller than σ/ε. In our experiments, σ/ε was typically 30 minutes or more. We started with a compensated crystal and, by changing its temperature, generated a change in spontaneous polarization ΔP_S. This results in a field $E_0 \approx 4\pi\,\Delta P_S$. Assuming that we changed P_S by only 1 percent, we obtain a field perpendicular to the surface of the crystal $E_0 = 7.9 \times 10^6$ V/cm, which is sufficient to cause the observed field emission of electrons. Fields of this strength will also exist between different domains (regions of opposite orientation of the c-axis at the surface). The microchannel plate intercepts part of the emitted electrons, and the typical images of figures 5 and 6 are formed.

* The work reported in this section was initiated under a contract sponsored by the Air Force Office of Scientific Research.

The observation of TSEE after laser exposure of pyroelectric materials is not possible. TSFE will, in general, be a much stronger effect than TSEE when c-faces are investigated, and we expect that the strong fields generated will make the observation of TSEE from other crystal faces difficult if not impossible. For the release of trapped carriers, photons have to be used. A uniform light beam of low power density is employed in the work on pyroelectric materials. To obtain the curve shown in figure 9, the c-face of a single domain $LiNbO_3$ crystal was bombarded with 3 keV electrons to fill the surface traps. Afterwards, the face was illuminated with an unfiltered beam from a tungsten filament lamp. The trapped electrons are released with a characteristic decay time that depends on the power density of the stimulating photon. Care was taken that the temperature of the sample did not change during this experiment.

The implications of TSFE and the associated electric field, which is sufficiently strong to modify the surface by emission of charged particles, are of particular interest. We will focus on this aspect of laser surface damage in future investigations. We expect the generation of strong electric fields to be due not only to free carriers (photo-excitation), but also to a rise in temperature upon exposure of the crystal to high peak power laser pulses. This is especially true for "imperfect" surfaces. Small increases in temperature will cause sufficient changes in polarization to generate strong electric fields. In initial experiments, we have observed electron emission from the spot of the crystal that was exposed to one pulse from a ruby laser having a power density sufficient for surface damage. The c-face of a single domain $LiNbO_3$ crystal was viewed through the imaging device (microchannel plate plus phosphor screen) a few seconds after exposure. The emission was clearly visible for about 30 s.

4. The Laser Surface Damage Test Facility

The experimental techniques which are employed in the study of the precursors of laser surface damage were described in references 3 and 9. The so-called exoelectron imaging technique permits the investigation of the spatial distribution of electrons that are emitted from the irradiated surface upon heating or upon optical stimulation. These electrons are released from electron traps in a thin surface layer. The exoelectron emitting surface is imaged directly with the aid of a multichannel electron multiplier of high spatial resolution, or an electron immersion lens (exoelectron microscope) can be used in order to obtain magnified images. [9] Direct imaging is employed whenever the laser power density is sufficiently high over a spot size of several millimeters in diameter. Since the ruby and Nd-glass lasers available in our laboratory permit spot sizes of sufficient power density up to about 100 μm in the TEM_{00} transverse mode, the exoelectron microscope is required in most of our studies.

The optical table-laser system and the pump-experimental chamber system are independent. Therefore, an alignment system had to be developed in order to provide a precise location of the high power laser beam with respect to the sample (figure 10). The chamber is fixed on a three-stage table which permits linear movement in two directions normal to the incident beam and rotation around a vertical axis also normal to the beam. We use a Korad K-1 laser, Q-switched with the aid of either a bleachable dye or a Pockel's cell. The laser is operated with a Nd-glass rod or a ruby rod emitting in excess of 100 MW power (multi-mode). For the experiments we tuned the plane-mirror cavity in order to achieve a TEM_{00} mode operation of about 5 MW power output. A fast photodiode (ITT 4000) with a rise time of 0.65 ns and a fast oscilloscope (Tektronix 519) are used to measure the time distribution of our Q-switched pulses. The spatial distribution is measured in a photometric manner. The beam is divided by a beam splitter, and the split beams are focused by identical lenses. One beam is focused onto the sample and the other onto an optical microscope lens operating as a projector lens. The microscope lens produces an enlarged image of the focal spot on a photographic plate. Curves of equal intensity will be traced by a microdensitometer.

The electrostatic exoelectron microscope (figure 11) is presently used as a one-stage system, and consists only of an objective lens (immersion lens). However, the mechanical parts are constructed so that a projector lens can be added with little effort if the requirement arises. The magnification of the instrument using the objective lens alone is on the order of 100 X, which is sufficient for most of the work planned for this instrument.

5. Outline of A Theory of Exoelectron Emission From Nonpyroelectric Materials

Exoelectron emission measurements constitute an excellent means for probing traps at or near the surfaces of solids. The basis for probing traps is the expectation that the one or more links exist between laser-generated free carriers and the traps. The carriers, produced by multiphoton processes, are free to absorb laser energy and accelerate to energies capable of avalanche ionization. Evidence for this free carrier generation comes from photoemission and photoconductivity measurements. The link between the traps and the laser-generated free carriers is that the traps act to "freeze out" a portion of the free carriers. [4] This portion is then measured by thermal or optical stimulation of the traps. Exoelectron images obtained in LiF at laser power densities above and somewhat below the surface damage threshold feature a characteristic ring shape [3] (figure 12).

In addition to a "freezing out" of free carriers, the traps may act as intermediate levels for multiphoton generation of the carriers and, in the case of resonance, increase the cross sections for the processes. Another possibility for trap involvement is that populated traps may act as electron donors for ensuing avalanche processes.

The theory of exoelectron emission from an insulating solid exposed to intense laser radiation has to describe the features of the exoelectron images obtained in such experiments. Each experiment consists of two distinctly different phases:

(1) The exposure of the sample to the laser pulse: The solid interacts with the photon field. Electrons are redistributed over available electron levels by such processes as multiphoton ionization, recombination, trapping, photoemission, avalanche ionization, and thermal transitions. In this phase, a small number of electrons are trapped in metastable levels. Only those traps that are in a thin surface layer have to be considered for exoelectron studies. The spatial distribution of the trapped electrons is a map of the spatial distribution of the conduction electrons which were generated during the laser pulse.

(2) The subsequent heating of the exposed sample (thermally stimulated exoelectron emission): The probability for thermal release of the trapped electrons increases with increasing temperature. A small portion of the electrons released from the traps overcomes the work function barrier and is emitted as exoelectrons into the vacuum and used to record the exoelectron image (figure 12).

The theory to be developed has to provide the link between the processes occurring during the time of the laser exposure and the intensity distribution of the exoelectron emission image.

At high laser power densities, the physical processes involved are identical to the processes occurring during laser surface damage. The investigation of exoelectron emission after exposure of the sample to intense laser light below the surface damage threshold is of importance because it deals with processes that apparently are precursors of laser surface damage and therefore are likely to shed light on laser breakdown of transparent material.

The seemingly impossible task to analyze these various processes has been simplified considerably by recently published quantitative work on multiphoton excitation of conduction electrons [10] and on the nature of laser breakdown in alkali halides, [11] one of the more important classes of materials to be considered in this research project.

Multiphoton absorption must be considered the most important source of conduction electrons during the duration of the laser pulse, [10] and avalanche ionization has now been identified as the prevailing mechanism of laser breakdown in alkali halides [11] at laser power densities above the damage threshold. Aside from this, it is now established that the theory of dc dielectric breakdown [12] of these materials is applicable without major modification to ac electric fields of optical frequency.

In the following, we will use an electron kinetics approach to describe the spatio-temporal behavior of the density of conduction electrons in both experimental phases described above. The parameters, which enter the set of electron rate equations that are to be developed, will be measured during the course of the experimental work or obtained from the literature. Rate equations of the type to be discussed here can be found in an article by Franz. [13]

The energy levels of an insulating solid are, in the simplest case, described by a band model. In thermal equilibrium and in the absence of radiation, the electrons occupy the completely filled valence band. All trap levels and the conduction band can be assumed empty. Denoting the concentration of conduction electrons as n_c, the concentration of trapped electrons in N_t traps as n_t, and the concentration of electrons in the valence band as n_v, and neglecting for the time being diffusion of electrons and any dc electric fields, we can write (figure 13):

$$\frac{dn_c}{dt} = n_c\,\omega_i + n_v\,\omega_{vc} + n_t\,\omega_{tc} - n_c\,(n_c + n_t)\,\omega_{cv} - n_c\,(N_t - n_t)\,\omega_{ct} \tag{2}$$

$$\frac{dn_t}{dt} = n_v\,(N_t - n_t)\,\omega_{vt} + n_c\,(N - n_t)\,\omega_{ct} - n_t\,(n_c + n_t)\,\omega_{tv} - n_t\,\omega_{tc} \tag{3}$$

where the ω_{ik}'s are the transition probabilities in appropriate units. The subscripts designate the transitions (e.g., ω_{cv} is the transition probability for an electron in the conduction band to reach the valence band, etc.); ω_i is the avalanche ionization probability.

Charge neutrality is required; therefore, the number of holes in the valence band is equal to $n_c + n_t$. A correction for emitted electrons from a thin surface layer is neglected at this point. It is important to point out that all electron concentrations and transition probabilities are functions of the coordinates z (along the axis of the laser beam and perpendicular to the entry surface of the sample) and r (the radial distance from the beam axis), as well as the time t.

The avalanche ionization rate ω_i pertains only to the ionization of valence electrons and does not include ionization of filled traps. Franz does not consider this process. [12,13]

Only traps that are in a surface layer of thickness δ (escape depth of the exoelectrons) participate in the formation of the exoelectron image in the phase 2 experiment. The goal of the theory is therefore to calculate n_t (t_p, r, $0 \leq z \leq \delta$), where t_p is the time duration of the laser pulse. In order to do this, we must know the transition probabilities ω_{ik}, all of which depend on the spatio-temporal characteristics of the laser beam, that is, the dependence of the laser photon flux on t, r, and z. Furthermore, the temperature T of the sample enters as an important parameter and it also will be a function of these variables.

Transitions of electrons between the bands and the impurity levels (traps) are due to different processes. The avalanche ionization rate ω_i has been the subject of several theoretical calculations [13] and Yablonovitch and Bloembergen [11] have recently shown that the theory of dc-avalanche ionization is applicable also to laser photon fields by straightforwardly converting the photon flux density to the equivalent rms field strength E. The authors report the field dependence of ω_i in the case of NaCl for laser frequencies from the infrared to the frequency of the ruby laser. Their calculations can be extended to other alkali halides as well. All other remaining transitions are either of thermal origin or are caused by recombination and single or multiphoton absorption.

Field emission of electrons from the valence band or the traps, an important process in dc-dielectric breakdown, is of course absent for electric fields of optical frequencies.

The transition probabilities ω_{ik} in eqs (2) and (3) contain contributions from optical transitions and thermal transitions. Using the superscripts "o" and "th" to distinguish between these two processes, we have

$$\omega_{tc} = \omega_{tc}^{th} + \omega_{tc}^{o} \tag{4}$$

$$\omega_{vc} = \omega_{vc}^{th} + \omega_{vc}^{o} \approx \omega_{vc}^{o} \tag{5}$$

$$\omega_{vt} = \omega_{vt}^{th} + \omega_{vt}^{o} \approx \omega_{vt}^{o} \tag{6}$$

Since, in our case, the traps are expected to be at most 2 eV below the lower edge of the conduction band, the energy difference between the upper edge of the valence band and the traps is large in wide band-gap materials such as alkali halides. We may therefore safely neglect ω_{vt}^{th} and ω_{vc}^{th} at laser photon fluxes below the onset of catastrophic avalanche ionization. The thermal transition probabilities may be expressed in terms of the spontaneous recombination probabilities. Of importance is the relation

$$\omega_{tc}^{th} = 2\,\omega_{ct}\left(\frac{m^* k T}{2\pi h}\right)^{3/2} \exp(-E/k T) \tag{7}$$

where E is the trap depth and m* the effective electron mass at the bottom of the conduction band. The transition rate ω_{cv} is known from the lifetime of free carriers.

In wide band-gap insulators, ω_{vc}^{o} is a multiphoton transition and requires special consideration. The most recent description of multiphoton absorption in various alkali halides was given by Catalano et al. [10] They summarize theoretical and experimental results which we will use in the course of this research project. The transition probability per unit time for N-photon absorption is given by

$$\omega_{vc}^{o} = \sigma_N f(z)^N \tag{8}$$

where σ_N is the cross section for N-photon absorption, measured in $cm^{2N}\ sec^{N-1}$, and f(z) is a function which describes the z-dependence of the laser photon flux.

Assuming that single photon absorption from impurity levels is a process that is much weaker than multiphoton absorption, the z-dependence of the laser flux is calculated from the equation

$$df(z) = -\alpha_N\, f(z)^N\, dz \tag{9}$$

The absorption coefficient α_N is given by

$$\alpha_N = \sigma_N / n_v \tag{10}$$

The concentration of valence electrons n_v is equal to the density of active atoms in the solid. The solution of eq (9) is

$$f(z) = F_o \left[1 + (N-1)\, F_o^{N-1}\, \alpha_N z\right]^{1/(1-N)},\quad N > 1 \tag{11}$$

Equation (11) is correct only for a laser flux that is not sufficient to initiate avalanche ionization. The absorption coefficient changes as soon as avalanche ionization is initiated. The absorption coefficient α_i due to free carrier absorption was given by Yablonovitch and Bloembergen: [11]

$$\alpha_i = 4\pi\, e^2\, \tau_i\, n_c \left[c n_r\, m^* \left(1 + \omega^2\, \tau_i^2\right)\right]^{-1} \tag{12}$$

where

e = electron charge

τ_i = collision time

ω = frequency of the laser light

n_r = linear refractive index of the sample

c = velocity of light

Even though the role of free carrier absorption (α_i) is generally acknowledged to be a dominant one in laser-induced breakdown of transparent dielectrics, it is at the moment still uncertain whether an avalanche ionization is required or not. Hellwarth [14] argues that enough energy can be absorbed before electrons gain the kinetic energy required for ionization. Assuming the ionization avalanche is launched, the free carrier concentration n_c grows exponentially with time and we have

$$n_c = n_c(o)\, \exp\left[\int_o^t \omega_i\, dt\right] \tag{13}$$

as one can see from eq (2).

Due to the absorption of laser photons, the temperature of the sample will change, thus influencing all thermal transition probabilities, especially ω_{tc}^{th}, which determines the concentration of electrons remaining in the traps after the laser pulse has hit the sample. Also, since trap ionization by electrons appears to be present, knowledge of this process will be necessary in order to evaluate the characteristic exoelectron images that are obtained after the sample is subjected to a high power laser pulse. However, up to this point, we have not been able to find relevant information on trap ionization by electrons.

Since NaCl is one material which has been studied most extensively, we will attempt to apply the outlined kinetic theory to this material first. For the moment, we will make use of eqs (2) and (3) to explain the main features of figure 12.

In figure 14 a schematic representation of the laser intensity profile and the EE current density distribution is shown. We can clearly distinguish three different regions of EE intensity: (I) bleaching of originally filled traps at low laser power densities, (II) trap filling at medium power densities, and (III) trap ionization at the peak power density.

5.1 Trap Bleaching

At a low light flux F and at constant temperature, eq (3) reduces to $\frac{dn_t}{dt} = -\omega_{tc}\, n_t + \omega_{ct}\,(N_t - n_t)\, n_c$. We neglected, as is usually done, [4] ω_{tv} and assumed that the photon energy is insufficient to lift valence electrons into the trap ($\omega_{vt} = 0$). Since $\omega_{tc} = \sigma F$, where σ is the absorption cross section for photons in filled traps, n_t decreases with time. In case the recombination of free electrons exceeds retrapping ($\omega_{cv} >> \omega_{ct}$), we have:

$$n_t(t) = n_t\ (t = o)\ \exp(-\sigma F t). \tag{14}$$

5.2 Trap Filling

As the intensity of the laser pulse increases, multiphoton photocarrier generation sets in. The concentration n_c increases sharply, and retrapping can no longer be neglected. Since $\omega_{vc} \propto F^N$, the term $n_v\, \omega_{vc}$ becomes dominant in eq (2). Bleaching, being proportional to F, will be exceeded by retrapping, which increases approximately proportional to $n_c \propto F^N$. Eq (2) reduces to

$$\frac{dn_t}{dt} \approx \omega_{ct}\, n_c\, (N - n_t) \propto F^N\, \omega_{ct}\, (N - n_t). \tag{15}$$

5.3 Trap Ionization

Ionization of traps (release of trapped electron) again takes over at very high photon fluxes F. The exact mechanism for this occurrence is not known at this time; however, two processes may be involved

- Electrons in the conduction band absorb enough photon energy to ionize filled traps by a collision process.
- The kinetic energy of the free carriers never reaches a level sufficient to ionize traps by the first process but instead is dumped to the lattice by a Hellwarth mechanism [14] whereby the trapped electrons are released.

Both processes require a threshold density n_c or, in other words, a threshold laser flux F, in order for free carrier absorption to be the dominating absorption process.

This threshold flux will in most cases be lower than the laser surface damage threshold. The onset of trap ionization is therefore a measure for a certain critical density of free carriers at a known critical laser flux. For a material with a given surface layer, this critical flux is expected to be a certain fixed fraction of the laser surface damage threshold. Once this relation has been experimentally determined, it will suffice to measure the flux at the onset of trap ionization in order to predict the laser surface damage threshold. Then a NDT method would be available for laser surface damage.

6. Acknowledgement

We are indebted to Dr. N. Boling for providing the ED-2 glass samples and for the use of the Owens-Illinois ND-glass laser.

7. References

[1] Bräunlich, P., NBS Special Publication 341, 102 (1970).

[2] Becker, K., Critical Reviews in Solid State Science (Chemical Rubber Company, Cleveland, Ohio, 1972), Vol. 3.

[3] Bräunlich, P., Appl. Phys. Lett., 20, 4 (1972).

[4] Kelly, P., Phys. Rev. B 5, 749 (1972).

[5] Becker, K., CONF-680920, 200 (1968).

[6] Gourgé, G. and Hanle, W., Acta Phys. Aust. 10, 427 (1957).

[7] Gourgé, G., Z. Physik 153, 186 (1958).

[8] Sujak, B. and Kusz, J., Acta Physica Polonica 28, 491 (1965).

[9] Bräunlich, P., Rosenblum, B., Carrico, J. P., Himmel, L., and Rol. P., Appl. Phys. Lett. 22, 61 (1973).

[10] Catalano, I. M., Cingolani, A., and Minafra, A., Phys. Rev. B. 5, 1629 (1972).

[11] Yablonovitch, E. and Bloembergen, N., Phys. Rev. Lett. 29, 907 (1972).

[12] Franz, W., Z. Physik 132, 285 (1942).

[13] Franz, W., Handbuch der Physik XVII, 153 (1956), S. Flügge, ed., Springer, Berlin.

[14] Hellwarth, R. W., NBS Spec. Publication 341, 67 (1970).

8. Figures

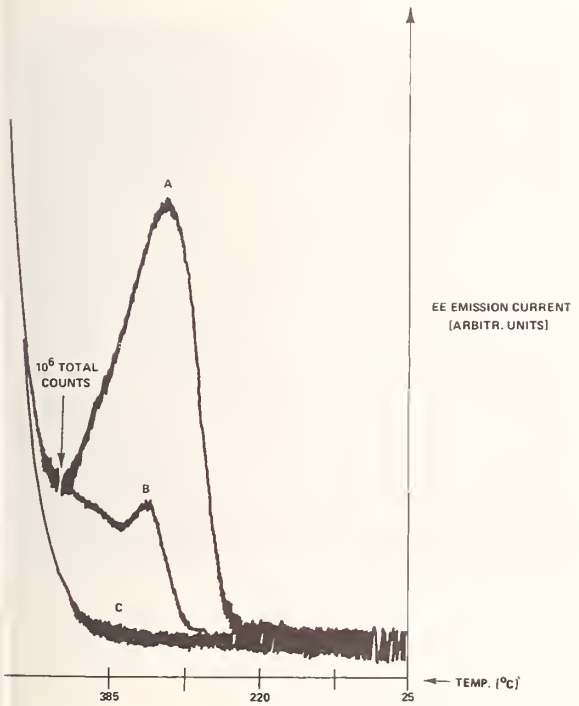

Figure 2. Schematic of test system comprising electron gun, sample holder, channeltron, and photostimulation capability.

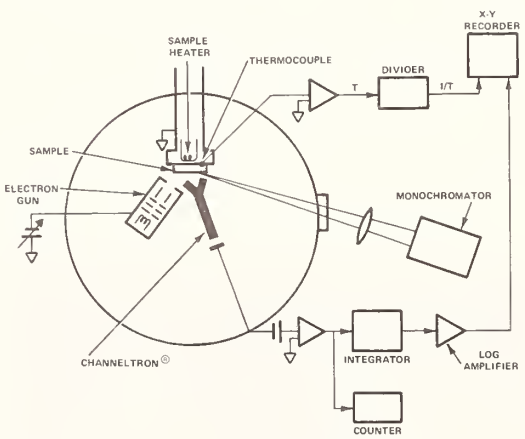

Figure 1. Thermally stimulated exoelectron emission from ED-2 laser glass after bombardment with 3 keV electrons at 6 x 10^{-7} amp/cm^2 for (a) 10 minutes (b) 150 seconds (c) 0 seconds.

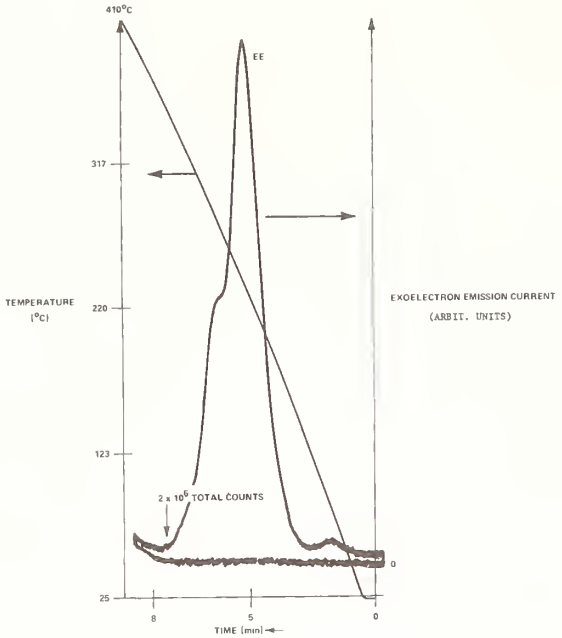

Figure 3. Thermally stimulated exoelectron emission from a NaCl single crystal after bombardment with 3 keV electrons at 6 x 10^{-7} amp/cm^2 for 7 seconds.

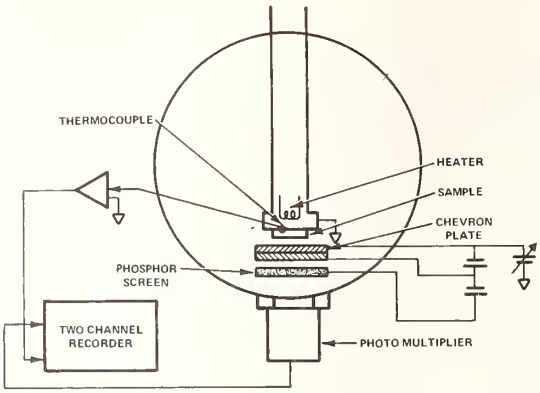

Figure 4. Schematic of test system for proximity exoelectron imaging with a Chevron plate and/or detection of weak exoelectron emission by monitoring the Chevron plate signal with a photomultiplier.

Figure 5. Thermally stimulated field emission from a multidomain $LiNbO_3$ crystal.

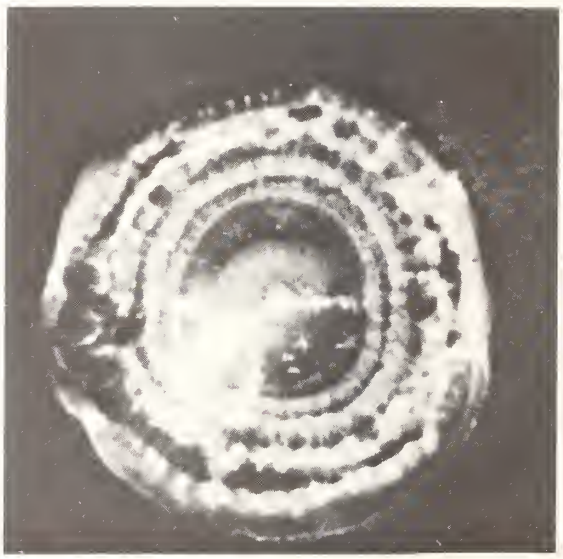

Figure 6. Emission image of the same crystal as in Figure 5 photographed at increasing temperatures.

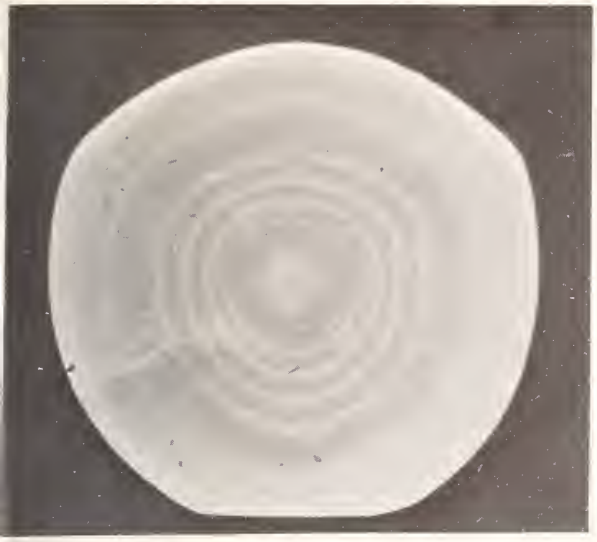

Figure 7. $LiNbO_3$ crystal used in Figures 5 and 6, photographed after etching in HF. Crystal diameter: 5/8".

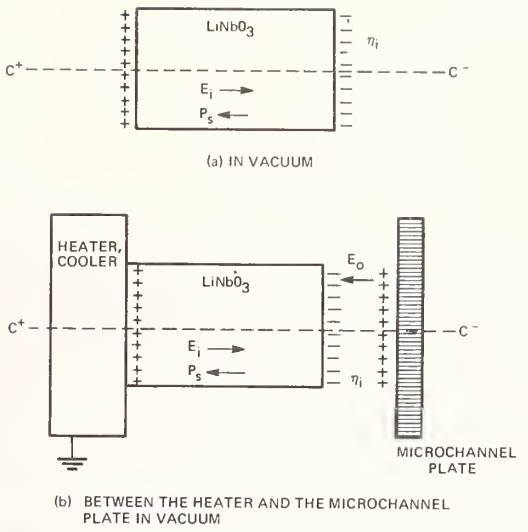

Figure 8. Polarization P_s, surface charge η_i and internal electric field E_i of an uncompensated $LiNbO_3$ crystal (a) in vacuum and (b) between the heater and the microchannel plate in vacuum.

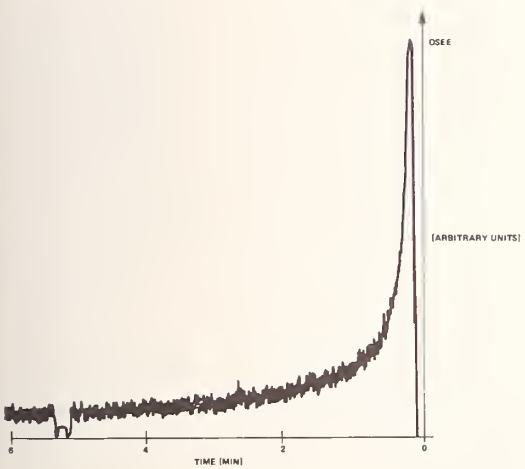

Figure 9. Optically stimulated exoelectron emission from the c-face of a single domain $LiNbO_3$ crystal after bombardment with 3 keV electrons of 6×10^{-7} amp/cm^2 for 3 minutes. The stimulating light is turned on at t=0 s.

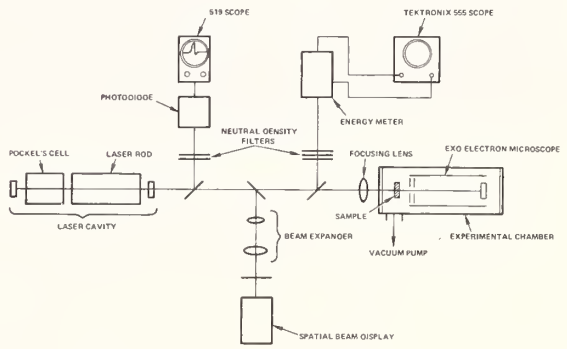

Figure 10. Schematic of exoelectron - laser damage test facility.

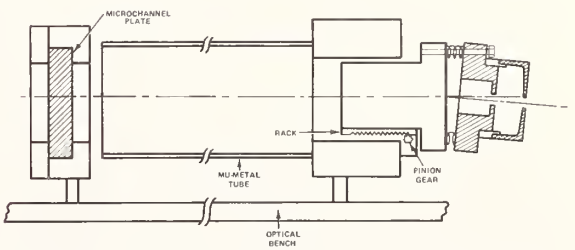

Figure 11. Schematic of the exoelectron microscope used in the laser damage test facility.

Figure 12. Thermally stimulated exoelectron image of a polished LiF single crystal after exposure to 45 min of 50 kV, 15 mA X-rays and subsequently to a single 2.3 J 50-nsec pulse from a Nd glass laser. There was no observable surface damage.

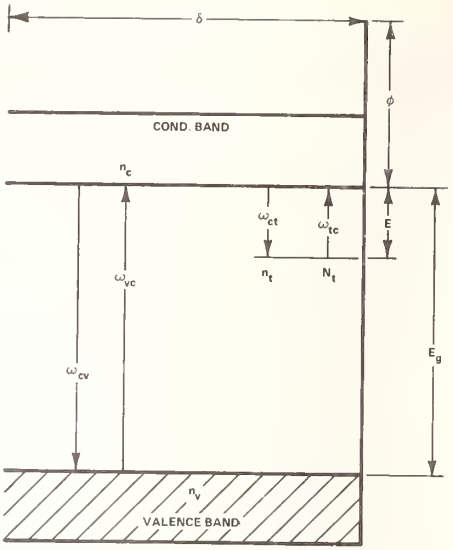

Figure 13. Simple energy band model for an insulator for the transition probabilities w_{ik} and electron densities n_c and n_v are explained in the test. The thickness of the surface layer involved is δ (escape depth of the exoelectrons).

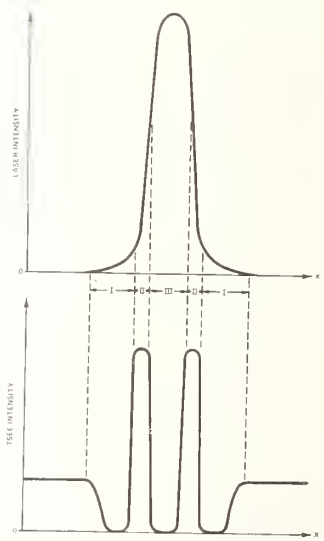

Figure 14. Schematic representation of the laser intensity profile (upper curve) and the corresponding exoelectron current density (lower curve).

COMMENTS ON PAPER BY BRAUNLICH

It was pointed out that the emission of exoelectrons should be a sensitive indicator of the presence of embedded particles even down to submicron diameters, at which size other detection techniques do not seem to reveal the particles. Even with laser irradiation below the level which would lead to visible damage of the surface, it was felt that the presence of microplastic deformation in the vicinity of the heated inclusion would increase the exoelectron yield. It was further felt that with the imaging technique described by the speaker, these regions of microplastic deformation could be identified.

Effects of Laser Flux on GaAs

J. Lynn Smith

Quantum Physics, Physical Sciences Directorate
U. S. Army Missile Command
Redstone Arsenal, Al 35809

Pulsed laser damage thresholds for surface damage of GaAs have previously been measured for 0.694 and 1.06 μm laser beams. Measurements have recently been made for a 10.6 μm laser beam. These wavelengths were obtained with ruby, Nd^{3+}-glass, and TEA CO_2 lasers with pulse halfwidths of 20 nsec, 60 nsec, and 100 nsec, respectively. The first two lasers utilized dye Q-switched cells. Later work with the Nd^{3+}-glass laser incorporated a Pockels cell for Q-switching. Surface damage thresholds ranged from about 8 MW cm^{-2} for 0.694 μm radiation to 30 MW cm^{-2} for 10.6 μm radiation, and except for 10.6 μm radiation did not depend significantly on whether the GaAs was p-type, n-type, or undoped. For 10.6 μm radiation, the p-type GaAs was damaged at one third the value for the n-type GaAs and mostly exhibited bulk cracking rather than surface damage. The damage threshold of GaAs shows some dependence on the 1.06 μm laser pulse time, becoming lower as the pulse duration increases. Highly localized damage sites occurring at 1.06 μm cannot be accounted for by laser beam inhomogeneities. A study of the effects of surface trash on this localization revealed that, although visible trash does play a role, it need not be present for surface pits of approximately 2 μ size to occur. An arrangement utilizing a Pockels-switched Nd^{3+}-glass laser and quartz transducer was devised to determine whether the leading acoustical pulse induced in undoped GaAs bulk by the laser beam was rarefaction or compression. Rarefaction could result if the material were strongly electrostrictive, and this would bring out the question of the possibility of stimulated Brillouin scattering which depends on the effect. On the other hand, compression would result, for example, from thermal expansion. The study confirmed that the main effect of the 1.06 μm laser beam is to produce a compression in the leading pulse. The compression pulse amplitude was found to be proportional to the laser power up to the damage threshold.

Key Words: GaAs, laser-induced acoustical pulse, laser-induced damage, stimulated Brillouin scattering, threshold dependence on wavelength and doping.

1. Introduction

One of the programs of the quantum physics group at the Physical Sciences Dir. has been the investigation of laser damage on GaAs. Published work in this area has included a study of the surface damage of GaAs from 0.694 and 1.06 μm laser beams [1][1]. The work has recently been extended to include damage at 10.6 μm, and an experiment has been devised to determine whether the leading acoustical pulse excited in GaAs by a 1.06 μm, Q-switched laser is a rarefaction or compression.

Liquid dye cells were used to Q-switch the ruby (0.694 μm) and Nd^{3+} (1.06 μm) lasers which were used for most of the damage threshold data. A TEA CO_2 pulsed laser beam was used for the 10.6 μm work. The focused CO_2 laser beam was made visible for alignment purposes by using a thermal image plate.

2. Results

Table 1 displays the damage threshold data. In most cases the first damage was to the surface, and did not depend on whether the GaAs was undoped or p-type or n-type. The exception was for 10.6 μm where p-type material degraded at a lower threshold than n-type and displayed bulk (rather than surface) damage. The striking feature of this table is that for wavelengths representing an energy range from 1.79 to 0.117 eV (above and below the bandgap), the surface damage threshold changes only from about 8 MW cm^{-2} to 30 MW cm^{-2}.

[1] Figures in brackets indicate the literature references at the end of this paper.

Table 1. Damage threshold of GaAs

Doping level of GaAs (cm^{-3})	Threshold intensity (MW/cm^2)		
	$h\nu$ (eV) = 1.79[a]	1.17[b]	0.117[c]
p-Zn 2.5×10^{19}	8 ± 2	13 ± 5	10 ± 5
n-Te 2×10^{18}	8 ± 2	13 ± 5	30 ± 10
purest $n_e \lesssim 10^{13}$	[d]	13 ± 5	30 ± 10
pure $n_e \lesssim 5 \times 10^{16}$	[d]	13 ± 5	30 ± 10

[a]Ruby 0.694 μ Q-S, 20 nsec

[b]Nd^{3+}-glass 1.06 μ Q-S, 60 nsec

[c]TEA CO_2 10.6 μ pulse, 100 nsec

[d]At the time of experiments with the ruby laser arrangement, undoped GaAs was not available. Due to the across-the-bandgap electron transitions induced by ruby laser light, the undoped GaAs damage threshold is not expected to be different from that of p- and n-type GaAs.

Figure 1 compares surface damage on undoped GaAs (slightly n-type due to impurities) for (a) 1.06 μm and (b) 10.6 μm laser irradiation. The highly localized pits (1 to 2 μm) seen in (a) do not occur in (b). The large, discontinuous patches in (b) are no doubt due to beam inhomogeneity, but the pits in (a) are too small to be accounted for by beam inhomogeneity. Figure 1(c) shows the bulk damage which occurred to p-type GaAs for 10.6 μm.

The question of localization of surface damage to small sites for 1.06 μ was investigated further. The possibility that surface trash caused the localization was considered. Cleaved samples (110) were prepared with and without rinsing with acetone and petroleum ether. Under the microscope, unrinsed surfaces showed trash (largely GaAs dust resulting from cleaving). The surface was photographed, exposed to the laser beam and again photographed. Comparison of "before" and "after" photographs showed damage pits did coincide with surface trash. Darkfield photographs of rinsed surfaces before and after laser exposure showed that pits occur even where trash particles were not seen. Figure 2 shows two regions (250 μm) of a sample exposed to the laser beam; 2(a) depicts the density of trash particles (circled for ease in location) on a region masked-off from the laser beam; 2(b) shows the larger density of damage sites in an unmasked region.

A rough check on the effect of beam aperturing on GaAs surface damage was made. Internal aperturing of a 64 cm, Pockels switched, horizontally polarized, Nd^{3+}-glass laser cavity from 1.27 cm to 0.32 cm diameter should reduce the complexity of the multimode structure of the laser beam. Upon such aperturing, no difference was seen in the time or shape properties of the 35 nsec laser pulse output within 0.3 nsec resolution. (A Tecktronics 519 oscilloscope was used for this observation.) Also no difference in the appearance of the microscopic damage sites was seen on the GaAs due to such aperturing. This indicates that the fundamental surface damage mechanisms are not connected with the spacial mode structure of the laser beam.

Figure 3 depicts the experiment to ascertain whether the first response of undoped GaAs ($n \lesssim 10^{13}$ cm^{-3}) to the 1.06 μm laser beam is to produce a compression or rarefaction. This response propagates through the bulk as an acoustical pulse. A sample was placed behind a mask arranged in such a way as to produce a "line" wave in the GaAs which propagates through an X-cut quartz transducer sandwiched between the GaAs and a copper block. The sign of the transducer output signal indicated a compressional wave, the amplitude of which, within 10%, was proportional to the laser pulse power over a factor of 8 (up to the damage threshold).

The damage threshold of GaAs was seen to be somewhat dependent on pulse duration for 1.06 μm. Whereas the dye-switched Nd^{3+}-glass laser pulse was 60 nsec, the Pockels-switched laser pulse was 35 nsec. As shown in table 1, undoped GaAs was damaged at about 13 MW cm^{-2} for 60 nsec pulses, but the threshold was found to be about 30 MW cm^{-2} for the 35 nsec pulses. This result lends support to the values 35-50 MW cm^{-2} reported in the literature [2] for 20 nsec 1.06 μm laser pulses.

3. Summary

In conclusion, the extension of surface damage threshold data (to include that from the longer wavelength 10.6 μ laser light) shows some increase in value. The fact that visible trash (≳ 0.3 μm) is unnecessary for the occurrence of highly localized damage sites turns the question inward toward material flaws or intrinsic processes which are highly localized in nature. Further work in this area is needed. Theories involving free or "quasi-free" electron production and subsequent plasmon formation are under study in our group. The compressional nature of the laser-induced acoustical pulse implies the predominant material response is thermal expansion and not electrostriction which would produce rarefaction. Electrostriction is a mechanism involved in stimulated Brillouin scattering [3], which Kressel [4,5] has argued to be the cause of surface damage in GaAs. Because of the above reported observation and others previously cited [1], we believe this is not the case.

4. Acknowledgments

The author thanks Dr. G. J. Dezenberg for help in getting data at 10.6 μm and R. A. Shatas for comments on this paper.

5. References

[1] Smith, J. Lynn, J. Appl. Phys. 43, 3399 (1972).

[2] Sam, C. L., Appl. Optics 12, 878 (1973).

[3] Chiao, R. Y. and Townes, C. H., Phys. Rev. Lett. 12, 592 (1964).

[4] Kressel, H. and Mierop, H., J. Appl. Phys. 38, 5419 (1967).

[5] Ettenberg, M., Sommers, Jr., H. S., Kressel, H., and Lockwood, H. F., Appl. Phys. Lett. 18, 571 (1971).

6. Figures

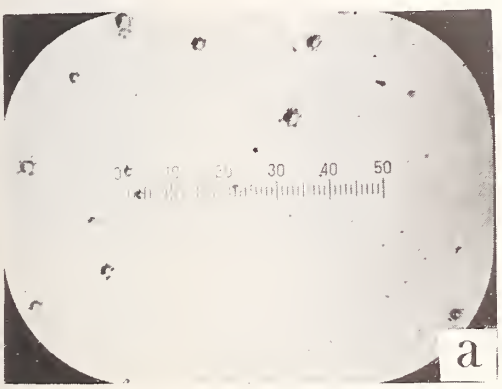

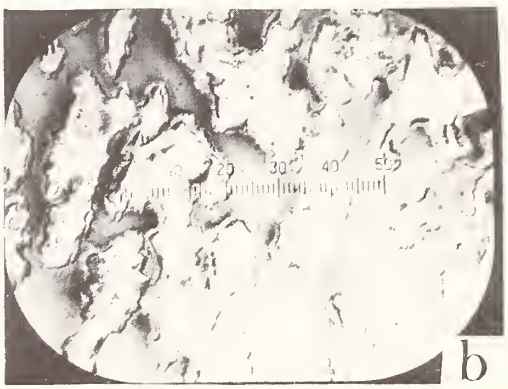

Figure 1. Damage to GaAs from 1.06 μm and 10.6 μm laser beams. (a) Surface damage to an undoped n-type sample due to 1.06 μm Q-switched laser light. (b) Surface damage to the same type sample due to a 10.6 μm, TEA CO_2 laser pulse. (c) Bulk damage to p-type GaAs from the 10.6 μm laser beam. Surfaces shown here were all either cleaved or chemically polished. The scale is 2.5 μm/division.

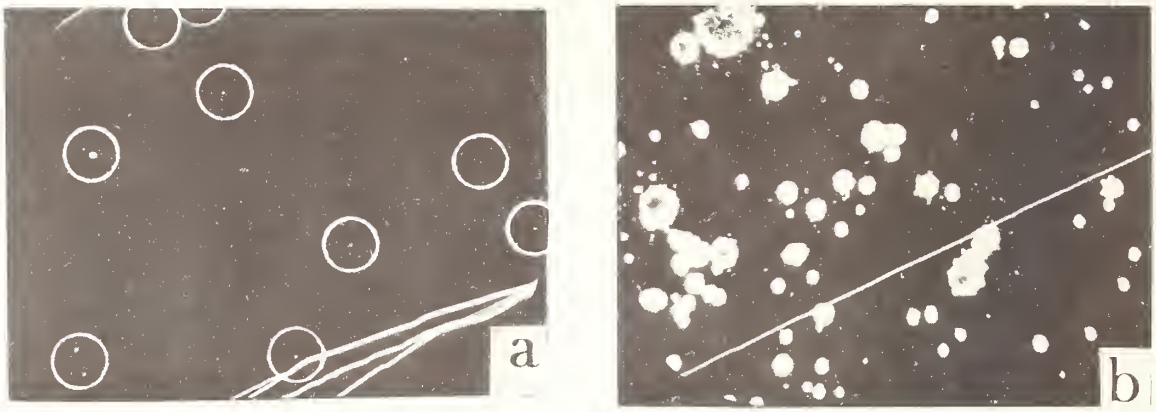

Figure 2. Darkfield comparison of surface trash density (a) to damage site density (b) after 10.6 μm, Q-switched laser beam exposure. The material is cleaved, undoped, n-type GaAs which was rinsed in acetone and then petroleum ether. Circles are drawn around the visible trash paricles shown in (a) for a region masked off from the laser beam. The more numerous damage sites are shown in (b) for a nearby unmasked region. Lines are steps in the cleavage planes. The width of both photomicrographs represents about 250 μm.

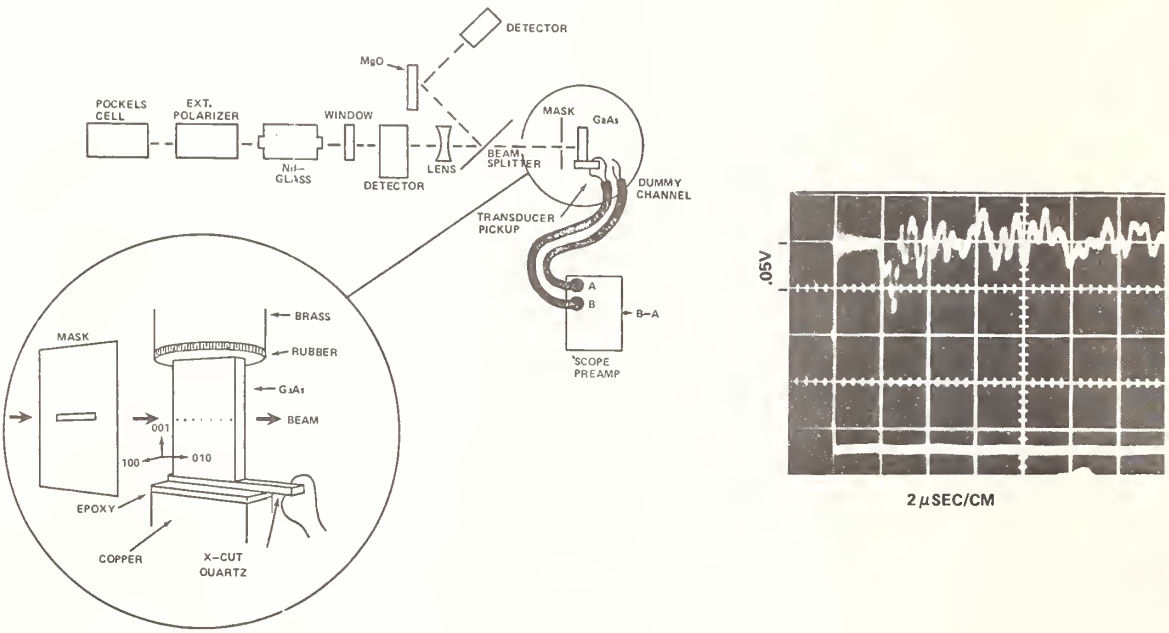

Figrue 3. Laser induced acoustical pulse experiment. A Q-switched, 1.06 μm laser beam is masked in such a way as to induce a "line wave" in an undoped GaAs sample cut to act as a waveguide to a doped GaAs sample cut to act as a waveguide to a quartz transducer pickup. The sample dimensions are 19 mm by 9 mm by 1.5 mm. The leading pulse-form induced (upper trace in oscillogram) was seen to be compressional. The lower trace is for the integrated laser energy output which displays an abrupt step downward at the beginning where the laser discharge occurs. Electrical noise was reduced by subtracting noise pickup on a dummy channel from the signal.

NO COMMENTS ON PAPER BY J. L. SMITH.

Carrier Effects Observed In Laser-Induced Damage In A Silicon Junction Photodetector

John F. Giuliani

Naval Research Laboratory
Washington, D.C. 20375

Damage induced by a pulsed 1.06 μm laser was studied in a n-p-n silicon photodiode on the basis of measured surface changes using a technique of He-Ne beam probing of the photoconductive gain and excess minority carrier diffusion lengths as functions of increasing cumulative pulsed-laser energy.

These preliminary studies suggest that the pulsed laser produces significant changes in the surface recombination rates for the charge carriers and this in turn can be related to the measured changes in detector gain and dark current also as functions of increasing laser energy.

Key Words: Laser damage, silicon photodetector, surface damage, surface recombination lifetimes.

1. Introduction

A great deal of laser-induced surface and bulk damage information has been obtained on elemental semiconductors such as silicon [1,2][1], and germanium [3] and on several III-V compounds [4,5]. Most of these studies have involved microphotographic, X-ray, and electron-microprobe analysis of laser damage. However, very little experimental data has been published up to the present time concerning the effects of laser damage on the behavior of charge carriers in these materials.

Carrier effects should be most easily studied in materials in which junction barriers are present. It is to be expected therefore that charge carrier behavior across these junction regions may be useful as a sensitive indicator for assessing laser damage. This paper summarizes what is believed to be a new approach in characterizing laser-induced damage from optical-probe measurements on the diffusion lengths of minority carriers, photo-excited in this experiment across a silicon n-p-n junction device.

2. Theoretical Considerations

The gain G of a photoconductor may be expressed as the ratio of the lifetime of a free photoexcited carrier τ to its transit time τ_r, the time required for that carrier to move between the electrodes of the detector [6,7]. This gain may also be expressed in terms of generated photocurrent by

$$G = \frac{I}{eF} = \frac{\tau}{T_r} \tag{1}$$

where

I is the measured photocurrent in amperes,

e is the electronic charge in coulombs, and

F is the total number of carrier-pairs created per second by light absorption.

For the case of an n-p-n barrier detector the photoconductive gain is determined by the ratio of the trapping time for a hole in the p-region to the diffusion time of an electron across this region. For a phototransistor this ratio is about 100. The photodetector* under present study can be considered as a hybrid between a true p-n

*Texas Instruments, Type IN2175 Photo-Duo-Diode

[1] Figures in brackets indicate the literature references at the end of this paper.

photodiode and a low gain phototransistor. The reason for this will become evident from an inspection of figure 1. In this figure is shown a simplified schematic of the geometrical structure of the device in the upper part, and the corresponding energy band scheme pertinent to the usual operation of the device in the lower part. The overall dimensions of the detector chip are 0.5 mm long X 0.5 mm wide X 0.3 mm thick. The latter dimension is in the direction of the incident light. The thickness of the base region transverse to the junction is denoted by W_p (see figure 1), and for this detector is about 0.46 mm; the two n-type emitter and collector regions are about 0.02 mm thick. For a typical phototransistor, however, the p-region is generally much narrower. For a narrower base region the electron transit time is shorter than it would be for a broader p-region, and hence from eq (1) the gain G is correspondingly greater. From this it is expected that the gain of this device would be lower than that of the usual phototransistor and indeed a value of about 18 was measured for this detector.

In the lower part of figure 1 is a schematic illustration of the theory [6,7] for the operation of the device when a reverse bias is applied across junction J_2. As in the phototransistor configuration, illumination of the p-region generates some trapped holes which produce a positive space charge pulling more electrons across from the region-n_1 to collector region-n_2. This results in some secondary current emission across the detector and accounts for the gain of this device in excess of unity.

3. Experimental

3.1 Measurement of Diffusion Length

A method [8,9,10] which allows the measurement of the diffusion lengths for photoexcited excess minority carriers across a reverse biased p-n junction region is shown in figure 2. A milliwatt-powered helium-neon laser provides a non-damaging light probe beam which is focused to a spot size of less than 0.02 mm in the plane of the detector. The depth of light penetration at this wavelength in silicon is about 3 μ and thus significant changes in the surface photoconductivity of this device may be effectively probed. It was convenient to mount the detector on a movable translation stage, such that the detector itself was moved transversely across the fixed light spot. The maximum photoconductive output is thus observed at x = 0 where the light spot crosses the reverse biased p-n junction of the detector [9]. The slopes of the experimental "fall-off" in photo-output on either side of x = 0 allows an indirect measurement to be made of the diffusion lengths L_n and L_p for electrons generated on the p-side of the junction, and for holes produced on the n-side of the p-n region. The measurements of L_n and L_p are related to the effective surface recombination lifetimes of both carrier types, τ_n and τ_p by

$$L_{n,p} = \sqrt{D_{n,p}\tau_{n,p}} \tag{2}$$

where $D_{n,p}$ are the diffusion coefficients for electrons and holes in the semiconductor material. In the lower half of the figure is shown a standard op/amp circuit for measuring the photo-response output.

Figure 3 shows a typical spatial photo-response or "spot-profile" curve from which the diffusion lengths and lifetime data for this particular detector were obtained, before exposure to the neodymium pulsed laser. The nominal diffusion coefficients D_n and D_p were obtained prior to laser damage from the known resistivity and concentration of dopants in this detector provided by the manufacturer and the application of Einstein's relation at room temperature given by [11]

$$D_{n,p} = \frac{kT}{q}\,\mu_{n,p} \tag{3}$$

$D_{n,p}$ were calculated from eq (3) to be 35 cm^2/sec and 12 cm^2/sec respectively. The diffusion lengths and effective lifetimes for the electrons in this device are somewhat larger than for the holes, and this is readily evident from the above parameters and the asymmetric shape of the response curve in figure 3. Moreover, for efficient transfer of n-type carriers from the emitter side to the collector side, the diffusion length L_n must be larger than the width of the base or p-region, W_p. The measured

L_n-value of 0.49 mm displayed in figure 3, verifies this design parameter, i.e., $L_n \geq W_p$, as well as serving as check for reliability of the scanning technique used in these measurements. Thus, the external photocurrent produced in this device is controlled primarily by the effective distance for n-type carriers which are able to survive surface recombination in traversing the p-region. It is to be expected therefore, that changes in L_n will affect the measured photoconductor gain. The measured values of L_p are probably not as accurate as those of L_n due to the fact that the He-Ne spot size is on the order of the dimensions of the n-region.

3.2 Pulsed-Laser Damage Experiments

Once the carrier diffusion lengths are measured for the undamaged detector, it is then centered in the focused beam of a neodymium glass laser. The glass laser employed is capable of generating a single dye q-switched pulse of about 22 nsec duration, and a maximum of about 12 mJ in a focal spot of about 1.0 mm at the detector. The depth of penetration of the 1.06 μm radiation is on the order of 500 μm. Therefore radiation at this wavelength should cause extensive bulk damage in the device. The detector was positioned such that the p-region which constitutes a greater part of the detector area received most of the neodymium laser irradiation. Unfortunately, the output of the neodymium laser beam contained a number of "hot spots" which introduces some uncertainty into the energy density. For the systematic investigation of laser damage, the glass laser beam initially is attenuated to a low energy of about one millijoule and increased in subsequent irradiations of the same detector to its maximum output. "Spot profile" curves are taken after each pulsed-shot.

3.3 General Results

In order to avoid non-thermal equilibrium effects, the spot-profile scans were made several minutes after irradiation by the Nd: glass laser. In this way it was hoped to obtain data which are characteristic of the nearly-steady state thermal conditions of the device. Figure 4 displays a series of spot profile curves as a function of increasing cumulative pulse laser energy. The photoresponse is the measured photo-voltage minus the dark voltage. The diffusion lengths $L_{n,p}$ for both carrier types may be computed from the slopes depicted in figure 4 by comparison with

$$V = V_{peak} \exp\left(-\frac{X}{L_{n,p}}\right) \tag{4}$$

Here, V_{peak} is the measured photoresponse minus the dark level response in volts at X = 0; V is the measured output minus dark level at some distance X from the p-n junction. The curve marked ⓪ is the same as that plotted in figure 3 except that the dark level has been subtracted out, and more points are presented. Curves ① thru ④ correspond to measurements taken several minutes after exposure to the laser energies indicated in the figure. There are a number of salient features which can be obtained by inspection. Firstly, the changes in the slopes and the peak photo output as functions of pulsed irradiation reflect significant changes in the minority carrier diffusion lengths and hence reflect changes in the surface recombination rates. Secondly, these curves appear to show that the behavior of these minority carriers is associated with certain levels of cumulative pulsed laser energy. For example, curve ① indicates that 1 mJ of pulsed laser energy increases the diffusion length for both type carriers and at the same time enhances the photo-conductive output from that of curve ⓪ measured prior to irradiation. This curve therefore indicates that a reduction in surface recombination takes place, thus enhancing the carrier lifetimes. Curve ② shows that after about 6 mJ of cumulative energy the diffusion lengths for both carrier types decrease from those of curve ① . A very sharp increase in slope is evident particularly for the p-type carriers but not for the n-type carriers. Also the peak photo-response is lowered from that of curves ⓪ and ① . This may reflect laser-induced creation of surface recombination or defect centers, which would tend to decrease the diffusion lengths of the carriers. No change in the dark level was observed up to 6 mJ of laser energy. This indicates that the junction regions of this device have not been significantly damaged. However, from about 9 mJ onward, as indicated by curves ③ and ④ , the slopes, particularly for the n-type carriers, significantly steepen. The dark level was also observed to rise as a function of laser energy over the region for which curves ③ and ④ are plotted. This appears to indicate the onset of a new level of laser damage. Although curve ③ indicates that the effective diffusion length for the electrons decreases and thus would predict a further reduc-

tion in the photoresponse, the slope for the holes on the n-side of detector shows an anomalous behavior which has not as yet been adequately explained. Curve (4) indicates a further decrease in the diffusion lengths for both electrons and holes as would be expected for greater laser damage.

The mechanism responsible for the pulsed laser-dependent rise in dark level is not known with certainty but again may be associated with surface recombination effects in which the intense heating of the detector by the laser partially destroys the surface of the p-n junction region such that the electrical conductivity increases across this junction. In effect a leakage path is formed between the emitter and collector regions of the device. More will be said about this effect in a separate paper.

A correlation can be made at this point between the measured detector gain and the diffusion length for the n-type carriers measured from the slope data of figure 4. The initially measured gain is the spatial peak value of the photo-current measured before irradiation by the Nd: glass laser divided by the rate at which carrier pairs are produced by the He-Ne laser flux times the electronic charge. After each exposure of the detector to the glass laser, the peak photocurrent is again measured and compared with the photo-output prior to irradiation after the dark current is subtracted from the total measured photocurrent.

Figure 5 shows the resulting curves obtained as a function of increasing cumulative pulsed laser energy at 1.06 μm. It is immediately obvious from this figure that the diffusion lengths for the n-type carriers vary directly as the photoconductive detector gain and this appears to indicate that laser-induced damage is principally associated in this device with an increase in the number of surface recombination or defect centers which tend to shorten the diffusion length for the n-type carriers. It is hoped to perform similar experiments in the future using a pulsed-probe laser light source to directly measure the lifetime for electron-hole pairs in the p-region as a function of cumulative laser energy. These experiments would complement the steady state studies.

To graphically display the dark current behavior as a function of laser damage, figure 6 is shown. The photo current is also plotted for comparison. These two parameters taken together appear to allow for a natural division of observed changes in detector output as a function of laser pulsed energy into three main regions. These energy regions had been inferred from the above analysis of the diffusion data.

4. Summary

It has been shown that the study of pulsed-laser-induced damage in junction photodevices, through measured changes in carrier diffusion lengths by this probe technique, affords a useful approach in assessing optical damage. The establishment of correlations among the measured diffusion lengths, the photoconductivity gain and the dark current of the device makes possible the identification of various levels of laser damage as well as demonstrating the extreme sensitivity of detector surfaces to thermal degradation from pulsed-lasers of relatively low power. Finally, this technique may be useful in evaluating laser thermal damage in other types of junction detectors.

5. Acknowledgements

The author wishes to thank E. Brooks and D. Frazer of the Metallurgy Division at the Naval Research Laboratory for their undertaking of the electron probe micro-analysis of the detector, and D.L. Weinberg and H. Shenker for many helpful suggestions in certain phases of this work.

Special thanks go to C.L. Marquardt of the Naval Research Laboratory Solid State Division for fruitful discussions concerning impurity effects aspects of the work.

6. References

[1] Grinberg, A.A., Mekhtiev, R.F., Ryvkin, S.M., Salmonov, V.M., and Yaroshetskii, I.D., Soviet Physics-Solid State, 9 1085 (1967)

[2] Ryvkin,. S.M., Salmonov, V.M., and Yaroshetskii, I.D., Soviet Physics-Solid State, 10 807 (1968)

[3] Bertolotti, M., Sette, D., Stagni, D., and Vitali, G., J. Appl. Phys., 41 818 (1970)

[4] Bertolotti, M., Sette, D., Stagni, L., and Vitali, G., Radiation Effects, 16 197 (1972)

[5] Smith, J. Lynn, "Damage to GaAs Surfaces from Ruby and Nd-Glass Laser Illumination", Damage in Laser Materials (NBS Spec. Pub. 372, June 1972), pp. 70-74

[6] Rose, A., "Performance of Photoconductors", Photoconductivity Conference, spon. by Univ. of Penn., RCA, ONR (Wiley & Sons, Inc., N.Y., Chapman and Hall, LTD, London 1954), pp. 3-48

[7] Bube, R.H., Trans. of Mettalurgical Soc. of AME, 239 291 (1967)

[8] Goucher, F.S., Phys. Rev., 31 475 (1951)

[9] Goucher, F.S., Pearson, G.L., Sparks, M., Teal, G.K., Shockley, W., Phys. Rev., 81 637 (1951)

[10] Shive, J.N., JOSA, 43 239 (1953)

[11] Runyan, W.R., Silicon Semiconductor Technology, McGraw-Hill (1963), pp. 177, 179

7. Figures

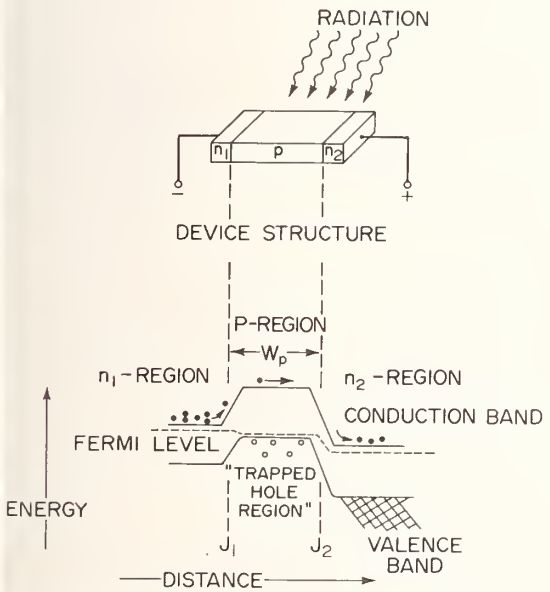

Figure 1. Simplified schematic of detector geometry and energy level diagram illustrating the mechanisms for producing photocurrent gain.

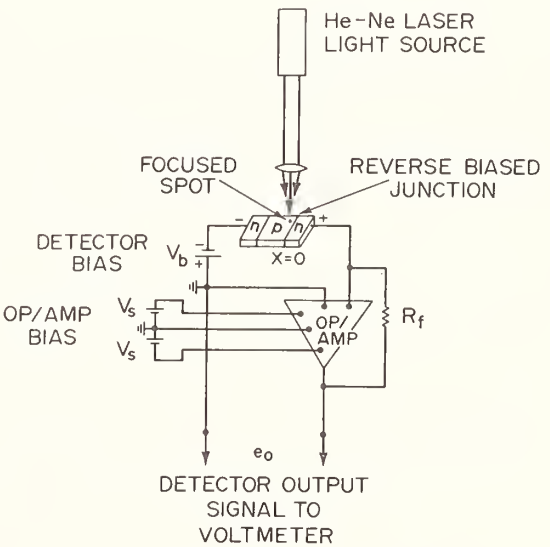

Figure 2. Minority carrier diffusion length measuring setup.

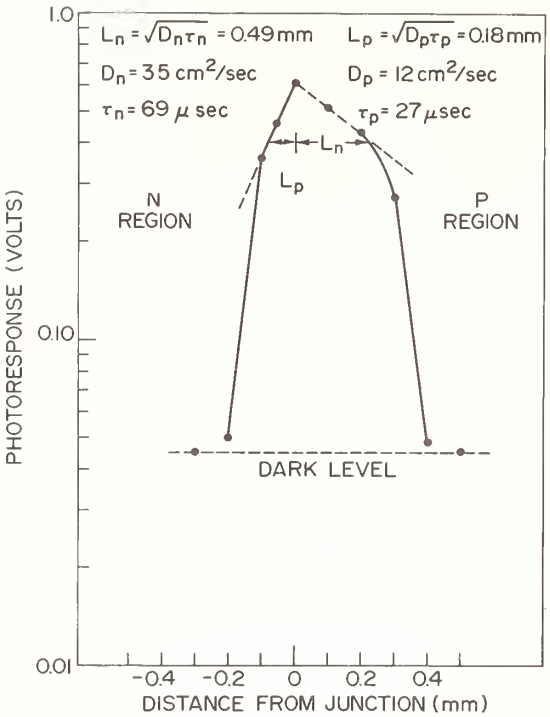

Figure 3. Typical He-Ne laser "spot profile" across the undamaged n-p-n Photo-Duo-Diode detector. The dotted slope lines extending from either side of the peak of the photoresponse determine the diffusion lengths for excess minority carriers across the reverse biased p-n region of the device. The measured dark level is shown for comparison at the bottom of the figure.

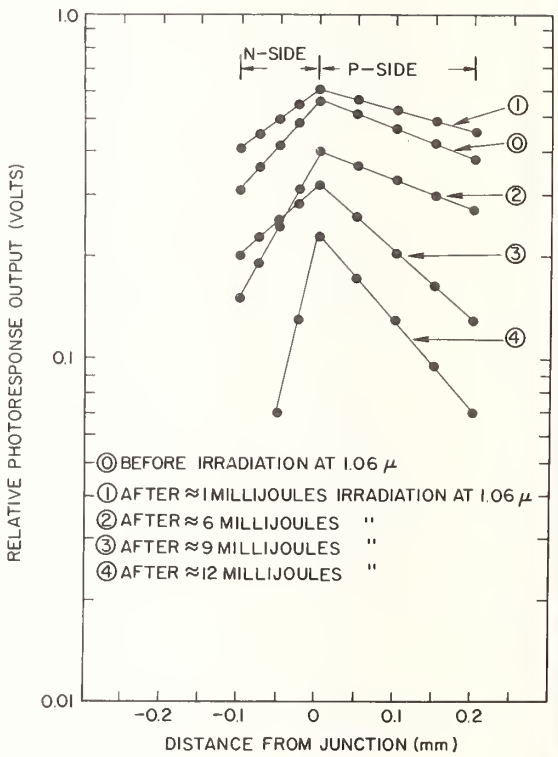

Figure 4. A series of He-Ne laser "spot profiles" across the reversed biased p-n junction of the n-p-n Photo-Duo-Diode taken before and after exposure to the indicated pulsed-laser energies at the 1.06 μm wavelength. A steep slope indicates a small diffusion length whereas a shallow slope indicates a large diffusion length.

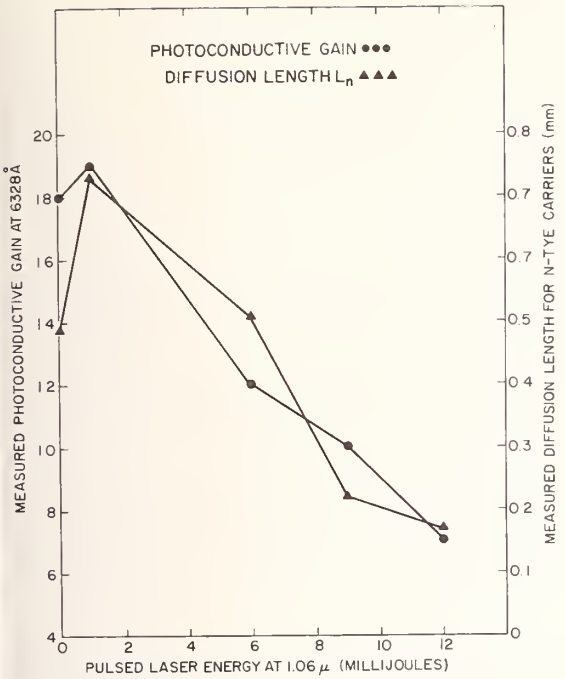

Figure 5. Comparison between the measured detector gain and the diffusion length for n-type carriers at 6328Å as a function of cumulative laser irradiation energy at 1.06 μm.

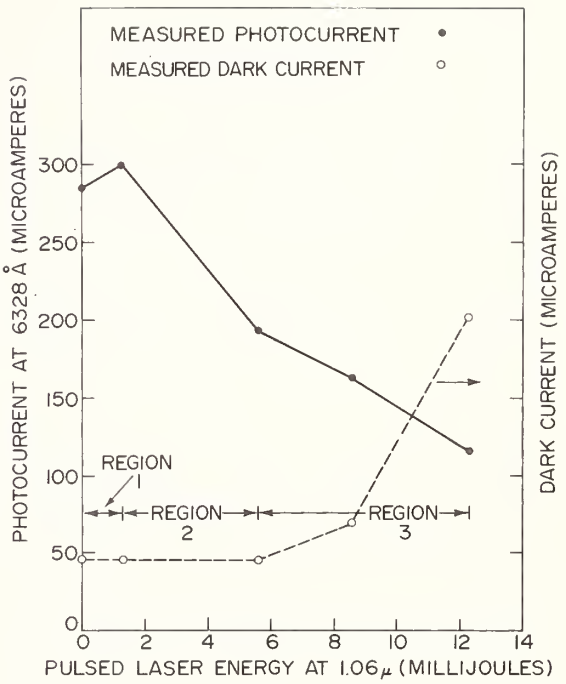

Figure 6. Comparison between the measured photocurrent, and measured dark current at 6328Å as a function of cumulative laser irradiation energy at 1.06 μm.

NO COMMENTS ON PAPER BY GIULIANI.

The Role of Coating Defects in Laser-induced Damage to Thin Films

L. G. DeShazer, B. E. Newnam* and K. M. Leung

Departments of Electrical Engineering and Physics
University of Southern California
Los Angeles, California 90007

Laser damage to dielectric thin-film coatings was investigated using a TEM_{00} Q-switched ruby laser. The laser-induced damage thresholds of several thin-film coatings increased with decreasing laser beam spot-size and were invariant for spot-sizes greater than 150 μm. A simple model has been suggested that the distribution and nature of coating defects have played an important role in this spot-size dependence, e.g., the probability of the laser beam striking a defect site will be greater for larger spot-sizes and that damage in materials can be distinguished as defect damage and intrinsic damage. This model can be also applied to surface damage.

Key Words: Coating defects, damage morphology, damage thresholds, laser-induced scatter, mean distance between defects, rutile crystal damage, thin-film damage.

1. Introduction

During the last two years we have been investigating laser-induced damage to dielectric thin-film coatings using a TEM_{00} Q-switched ruby laser with a variety of thin-film coatings on a variety of substrates. A series of general survey experiments studied almost every possible variable associated with the materials and laser. However, variables such as properties of coating and substrate materials preparation of film coatings, pulse duration of the laser, laser beam spot-size and mode-structure of the laser beam as well as incidence direction, all appear to be significant in the damage process. As a result, no single mechanism can be formulated to explain the damage phenomena in dielectric thin film coatings. For example, one of the experimental results is shown in figure 1, which may support a trend that was pointed out by Turner [1][1]: the damage threshold increases as the index of refraction of the thin film decreases. However, the result is inconclusive. There are other notable experimental results [2]. Among those results, a particularly interesting one is displayed in figure 2. The laser beam spot-size decreases as the damage threshold of the thin-film increases. An 80% variation of damage threshold for the same film could be observed by just varying the spot-size. It is noted that in the literature the spot-size of the laser beam was seldom reported along with its corresponding laser induced damage thresholds.

In this report, we would like to suggest a simple model to correlate the distribution and nature of coating defects to this spot-size dependence, e.g., the probability of the laser beam striking a defect site will be greater for larger spot-sizes and that damage in materials can be distinguished as defect damage and intrinsic damage. Experimental evidence will be presented for both thin-film damage and surface damage.

---

*Present address: Los Alamos Scientific Laboratory/L-2, P. O. Box 1663, Los Alamos, N. M. 87544

[1]Figures in brackets indicate the literature references at the end of this paper.

2. The Role of Coating Defects (a Simple Model)

For a random distribution of points on a plane, the probability that a randomly chosen unit area (e.g., a circle of radius r) will contain exactly n points can be described by the Poisson function [3]

$$P(n) = \{(\rho\pi r^2)^n/n!\} \exp(-\rho\pi r^2) \tag{1}$$

where ρ is the main surface density of the defects. The probability that no points will be contained in this area is

$$P(0) = \exp(-\rho\pi r^2) \tag{2}$$

which is the probability that the area will contain no point within a distance r. Hence, the proportion of distances of nearest neighbors less than or equal to the distance r is

$$P(r) = 1 - \exp(-\rho\pi r^2). \tag{3}$$

Now, if r is allowed to vary, the probability distribution of r is then expressed as

$$dP(r) = 2\,\rho\pi r \exp(-\rho\pi r^2)\, dr. \tag{4}$$

Thus, if we consider the case of a square pulse with width w less than or equal to r, the probability of such a pulse hitting one or more defects will be easily derived as

$$P(w) = 1 - \exp\left[-\frac{\pi}{4}(w/d_o)^2\right] \tag{5}$$

where d_o is the expectation value of r, or the mean distance of two defects, and is related to the mean density ρ. In the actual case, a TEM_{00} ruby laser pulse was used so that the square pulse should be modified to the form of a Gaussian beam with spot-size w_o. Then, eq (5) becomes

$$P(w_o) = 1 - \exp\left[-\frac{\pi^2}{32}(w_o/d_o)^2\right] \tag{6}$$

Now, by assuming that the coating defects on a dielectric film surface have a damage threshold I_d (in joules/cm^2) much less than the intrinsic damage threshold I_i of the film, the total damage threshold I can be expressed in terms of the probability given in eq (6).

$$I = I_d\, P(w_o) + I_i \{1 - P(w_o)\} \tag{7}$$

To analyze our experimental data, it is convenient to normalize the total damage threshold I with respect to the defect damage threshold such that

$$\mathcal{I} = 1 + (\eta - 1) \exp\left[-\frac{\pi^2}{32}(w_o/d_o)^2\right] \tag{8}$$

If the distribution of defects on the coating is random, only one parameter, namely d_o, is needed to completely describe the distribution. I_d and η will be parameters which can be related to the type of defect, whether defect damage is associated to absorption or electron avalanche.

For a digression, let us take a closer look at the parameter η which can be viewed as a function of the defect damage mechanism. A recent calculation by Bloembergen [4] concerning the role of pores in laser-induced damage to surfaces can be extended to structural defects in films. If a defect was a cylindrical groove on the surface, then

$$\eta = 4n^4/(n^2 + 1)^2 \tag{9}$$

which has a maximum value of 4 when the refractive index is infinite. If a defect was a needle cavity or the so-called 'crack' defect which is an oblate ellipsoidal void in the surface, the enhancement factor η will have a much larger value. Table 1 gives some estimates of the enhancement factor η for three different films of high indices. Other types of defects will have different values of the enhancement factor. Hence, the parameter η is very sensitive to the type of defect on the coatings or the surface of the bulk materials.

To illustrate the results of such a probability model, figure 3 displays a theoretical plot of the total damage threshold I versus spot-sizes w_o. For very large spot-sizes, the measured threshold

Table 1. Some estimates of enhancement factor η due to structural defects

Sample	n	$\eta = 4n^4/(n^2+1)^2$	$\eta \sim n^4$
ZnS	2.32	2.84	29
TiO_2	2.28	2.81	27
ZrO_2	1.98	2.54	15

will be the defect damage threshold I_d. For decreasing spot-sizes, the damage threshold will follow a variety of curves depending on the distribution of defects, e.g., the mean distance d_o. In the case of thin-film coatings, the damage thresholds are very low because d_o is a small fraction of the spot-sizes used in the usual laser damage tests. Hence, the curve is similar to the one for $d_o = 0.5\ w_o$, and the threshold value is close to the defect damage I_d and not to the intrinsic damage, I_i. However in the case of single crystal damage studies, e.g., for NaCl [5], the spot-size is very small with respect to the defect distance d_o. Then the curve is similar to the one for $d_o = 4\ w_o$, and in fact, the measured threshold would be very close to the intrinsic damage I_i. Therefore, using this model both thin film and surface damage can be related for a single material.

3. Experimental Arrangements and Detection Methods

The experimental setup and procedure used in measuring the damage threshold of dielectric thin-film coatings was described by Newnam and DeShazer [6]. Three methods were used to monitor the onset of the damage: spark detection, optical microscopy and laser-induced scatter (LIS). However here we emphasize that the LIS technique was our primary tool for diagnosis. A probe beam of low intensity He-Ne laser beam that follows the path of the Q-switched ruby laser beam onto the sample was used to indicate the scatter from the thin-film coating before and after we irradiated the area with the ruby laser.

The spot-size is the $1/e^2$ radius of the intensity profile of the TEM_{00} ruby laser beam, and is measured by a pinhole scan. The axial intensity after a focusing lens was directly determined by using measurements of the damage threshold of Polaroid film which was independent of the laser beam spot size. Spot-sizes ranging from 52 microns to 280 microns were used and areas of a test sample were irradiated by one shot only. The mean distance d_o between defects of each sample were measured by using a scanning electron microscope with magnification of 1000.

4. Thin-film Damage and Coating Defects

A half-wave film of ZrO_2 and a quarter -wave film of ZnS with glass substrate were used in studying the spot-size dependence on damage thresholds. By varying the spot-size of the laser beam, damage thresholds were determined by the onset of LIS. The laser pulsewidth was 8 nsec. Figures 4 and 5 display the experimental data as well as the theoretical curves using the forementioned model. For ZrO_2 film, the defect damage threshold I_d was found to be 9.2 joules/cm^2 and the data was fitted to a curve with η of 3 and d_o of 50 microns. The dotted curve is plotted with the measured value of 30 microns for d_o. Similarly, for ZnS film, I_d was 10.3 joules/cm^2 and the fitted d_o was 30 microns as compared with the measured d_o of 20.4 microns.

A closer look at the morphology of the coating defects or impurities on the films using the electron microscope has indicated that defects are irregular both in sizes and shapes and the density may strongly depend on several film parameters and preparation methods. In general, six types of defects were observed. Figures 6 to 12 show that such local defects can be found in different films. For the ZnS film used in the experiment, five types of defects were found (see figure 13). It is recalled that the measured d_o was 20.4 microns and the fitted d_o was 30 microns, which indicates that the damage may be primarily caused by those defects having irregular forms (or "mountain chains") and "shadows with strips." One can also easily observe in this case that a small mean distance between defects occurs for the most prevalent defect, namely "shadows with a dot."

By examining coating procedures, one may be able to change the mean distance between coating defects. At USC, we have attempted to vary the coating defects on one type of film by varying the deposition rate in the preparation of the coatings. It was found that by doing so, d_o decreases as the deposition rate increases. Figure 14 simply illustrates this result for MgF_2 films. The idea was

then to damage all three of these films of the same material and find out how it relates to the parameter d_o.

5. Surface Damage

If the model of spot-size dependence is good for thin-film damage, it should also be true for surface damage. A single crystal of rutile (TiO_2) with a conventional polished surface was used to test the spot-size dependence on surface damage threshold. Rutile was chosen simply because TiO_2 is an important coating material. Figure 15 shows this is indeed the case. Here, η is chosen to be 3 and 4, and the fit is very good for d_o equal to 75 microns. In fact, we did not use large enough spot-sizes to accurately determine the defect damage I_d, so that the curves were plotted slightly different from the thin-film data.

6. Damage Morphology

It was found that damage occurs without always producing a spark. The sensitivity of our spark detection system was such that it could detect a spark with a temperature comparable to the melting point of the film material [2]. The following scanning electron micrographs (figures 16 to 26) illustrate such findings for two typical tested samples, ZnS and rutile crystal. The presence of a spark during damage gives a very characteristic and unmistakable damage morphology which was also pointed out by N. Boling [7] for glass surface damage. Damage with a spark shows a very round hole of rather large size. Figure 20 displays a typical example for damage with a spark in TiO_2 film.

7. Summary

We have suggested a simple probability model to analyze our experimental data of the spot-size dependence on laser-induced damage to transparent dielectrics. We feel that the distribution of coating defects have played an important role in the spot-size dependence. Damage due to local defects or impurities are different from the intrinsic damage of the material. It is important to note that in testing laser materials, the scaling parameter w_o/d_o should not be omitted. It is pointed out that some of our earlier results (for example, see figure 1) were inconclusive. However, if we do take into account the scaling parameter in our data, the interpretation may have been different and explanable.

Both experimental results on thin-film damage and surface damage agree very well with the model. It was also demonstrated that the distribution of the local defects can be varied on one type of material such that production of laser-resistant films and surfaces would be reduced to a problem of quality control. Finally, this spot-size dependence can be used to uncover what type of defects cause damage.

8. Acknowledgements

The authors wish to thank H. R. Owen of the University of Southern California and L. P. Mott of Optical Coating Laboratory Inc. who supplied the thin-film test specimens for this study. The SEM work of J. Worrall at USC is gratefully acknowledged. We are also indebted to Prof. J. H. Marburger for his valuable comments. The thin-film investigations were supported by the Advanced Research Projects Agency of the Department of Defense and was monitored by the Air Force Cambridge Research Laboratories under Contract No. 19628-71-C-0220. The rutile damage study was supported by Crystal Products Department, Union Carbide Corporation, San Diego, California.

9. References

[1] Turner, A. F., in Damage in Laser Materials: 1971, edited by A. J. Glass and A. H. Guenther (NBS Special Publication 356, November 1971), pp. 119-123.

[2] Newnam, B. E., "Laser-induced Damage Phenomena in Dielectric Films, Solids and Inorganic Liquids," dissertation, Univ. of Southern California (1973). Available from University Microfilms, Ann Arbor, Mich.

[3] See for example, Feller, W., An Introduction to Probability Theory and Its Applications, Vol. I, 3rd ed. (John Wiley, New York, 1957).

[4] Bloembergen, N., Appl. Opt. 12, 661 (1973).

[5] Fradin, D. W., Yablonovitch, E., and Bass, M., Appl. Opt. 12, 700 (1973).

[6] Newnam, B. E., and DeShazer, L. G., in Laser Induced Damage in Optical Materials: 1972, edited by A. J. Glass and A. H. Guenther (NBS Special Publication 372, October 1972), pp. 123-134.

[7] Boling, N. L. and Dubé, G., elsewhere in these proceedings (1973).

10. Figures

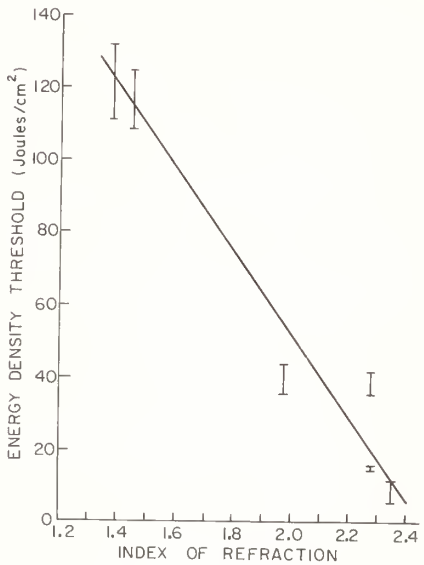

Figure 1. Experimental setup.

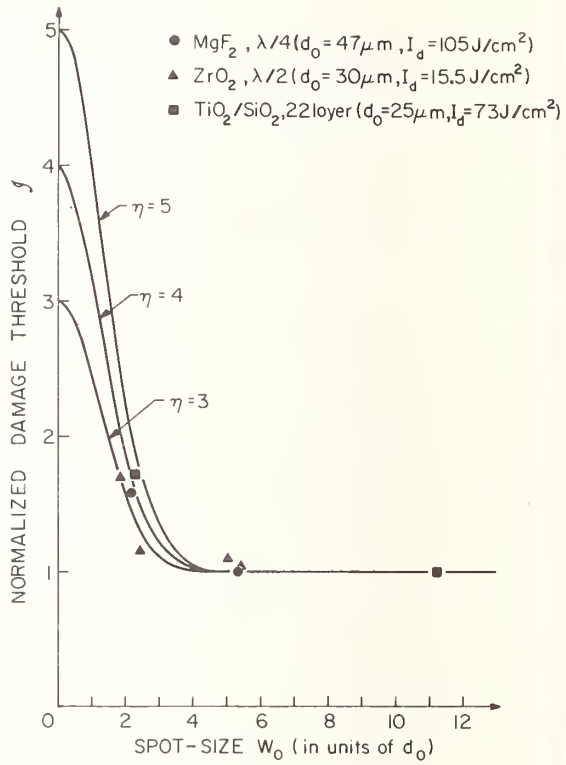

Figure 2. Entrance surface damage to λ/4 ZnS. (a) Probe trace (upper trace) and the damaging ruby pulse (lower trace). The maximum decrease in the probe intensity is 35% of peak intensity (peak intensity is 38 mV). (b) The output damaging pulse is shown followed by the input delayed reference pulse. (c) SEM photograph taken at 10 degrees tilt.

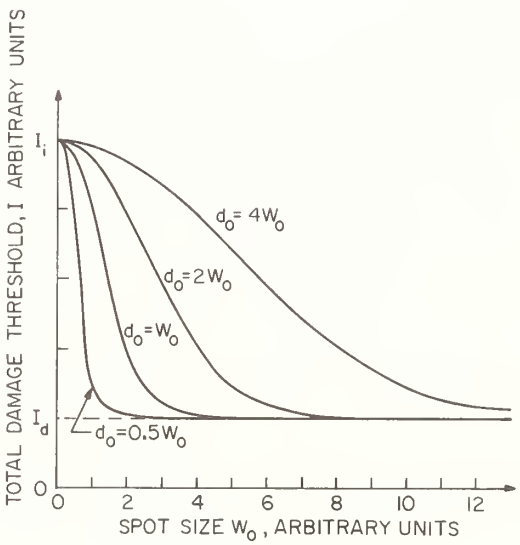

Figure 3. Entrance surface damage to λ/4 ZnS. (a) Probe trace and the damaging ruby pulse. (b) Output and input pulses. (c) SEM photograph taken at 10 degrees tilt.

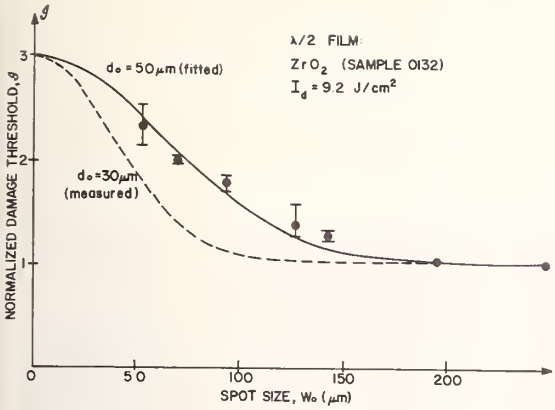

Figure 4. Entrance surface damage to λ/4 ZnS.
(a) Probe response and the damaging ruby pulse.
(b) SEM photograph taken at 10 degrees tilt.
(c) SEM photograph taken at 79.6 degrees tilt.

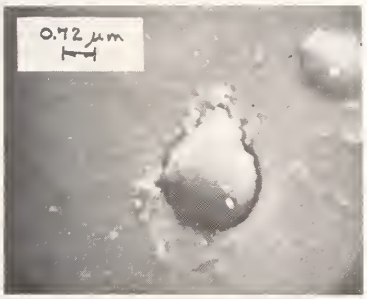

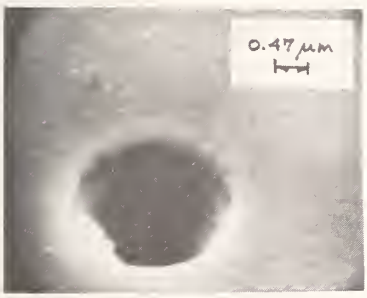

Figure 6. SEM photograph of defects of the two extreme forms, a hill (upper) and a hole (lower), on an eleven layer CeO_2/SiO_2 reflector (sample number SSI01).

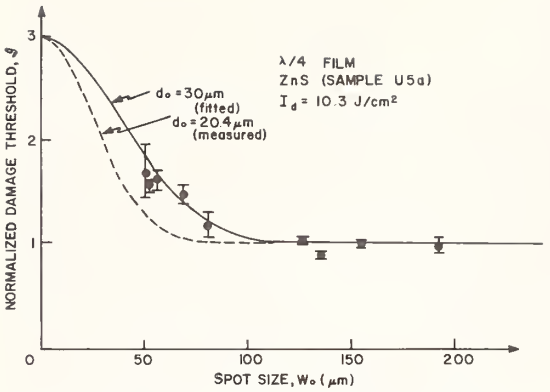

Figure 5. Spot-size dependence for single quarter-wave thick film on ZnS on glass substrate.

Figure 7. SEM photograph of defects of a group of holes on a single quarter-wave MgF_2 film.

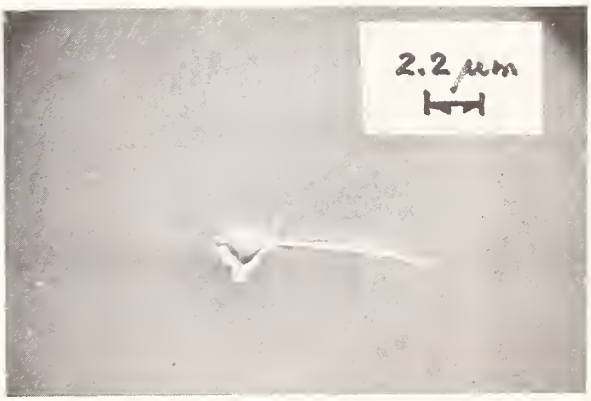

Figure 8. SEM photograph of defects in the form of a crack on a single quarter-wave MgF_2 film.

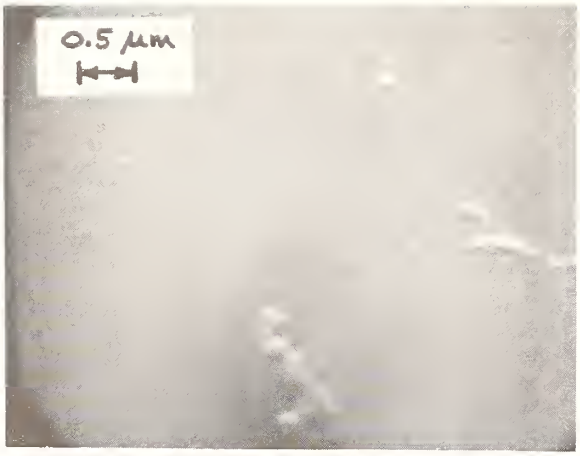

Figure 9. SEM photograph of defects in the form of irregular shaped hills, or "mountain chain," single quarter-wave MgF_2 film.

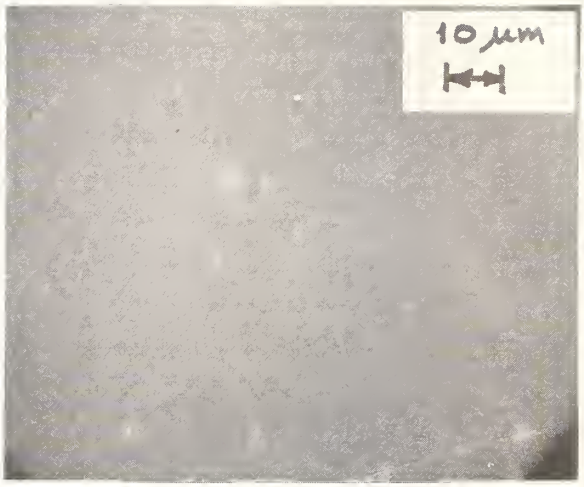

Figure 10. SEM photograph of defects in the forms of shadow with dot, crack and hill on a single quarter-wave ZnS film.

Figure 11. SEM photograph of defects in the form of "shadow with strips" on a single quarter-wave ZnS film.

Figure 12. SEM photograph of clean area (no defect observed) on a single quarter-wave MgF_2 film.

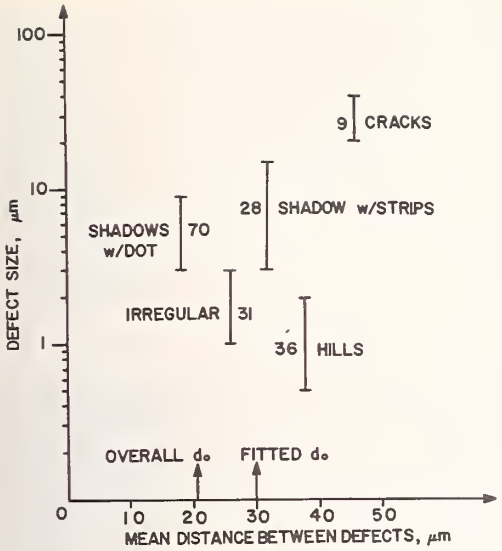

Figure 13. A schematic plot of size versus distribution and nature of coating defects, for a single quarter-wave film of ZnS (sample number U5a).

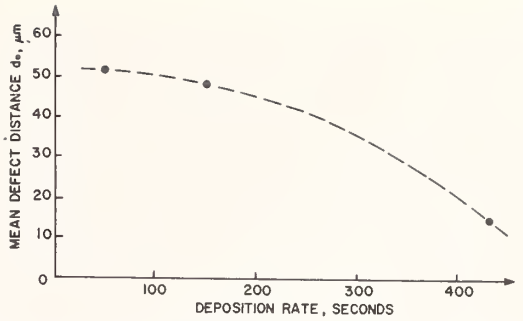

Figure 14. Mean defect distance d_o versus deposition rate for single quarter-wave films of MgF_2.

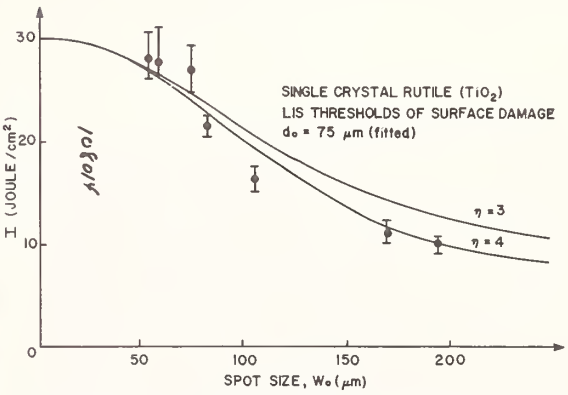

Figure 15. Spot-size dependence for surface damage on a single crystal of rutile (TiO_2).

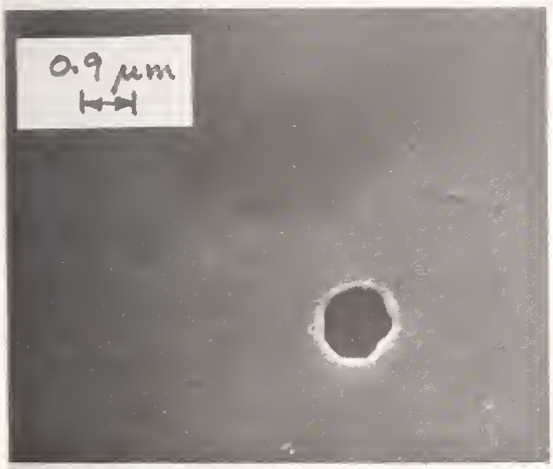

Figure 16. SEM photograph of a damage site on a single quarter-wave film of ZnS (U5a) using LIS diagnosis.

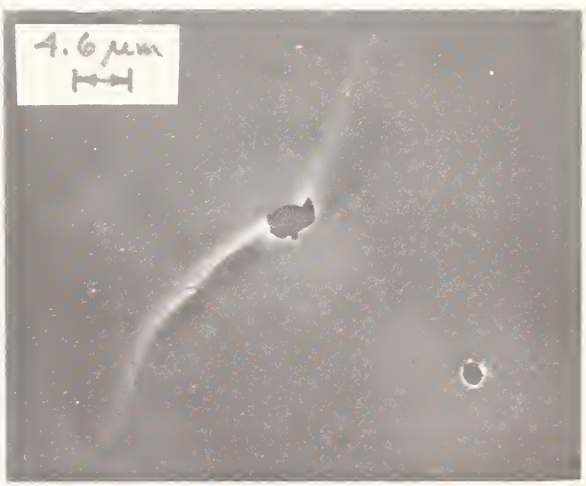

Figure 17. Different damage site on the same film as shown in figure 16.

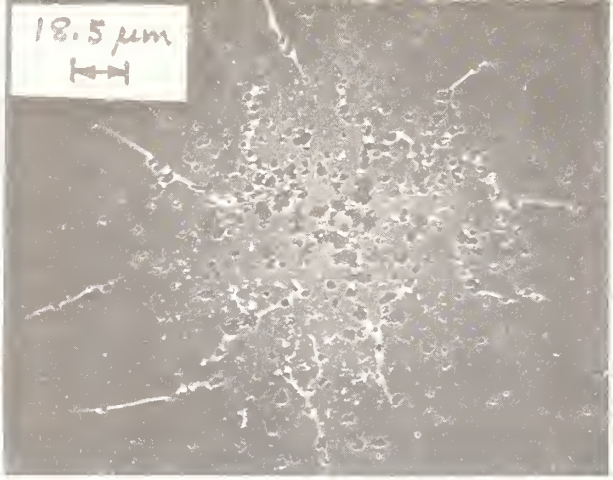

Figure 18. Still another damage site on the same film as shown in figure 16.

Figure 20. SEM photograph of a damage site on a single quarter-wave thick film of TiO_2 (sample 0121) where a spark was detected. The site dimension is 110 microns, from left to right.

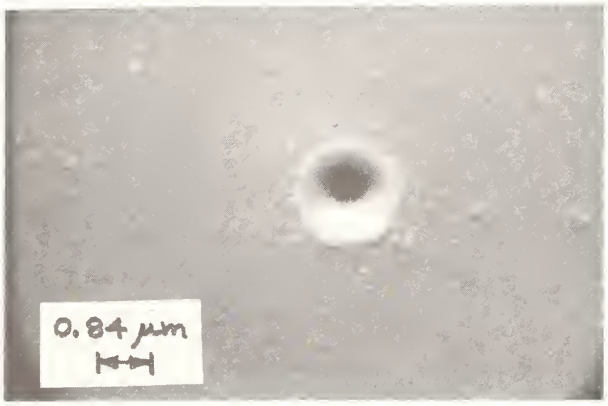

Figure 22. SEM photograph of a small damage site on rutile surface; no spark was observed.

Figure 19. A large damage site on a single quarter-wave film of ZnS (U5a) with laser beam spot-size of 166 microns.

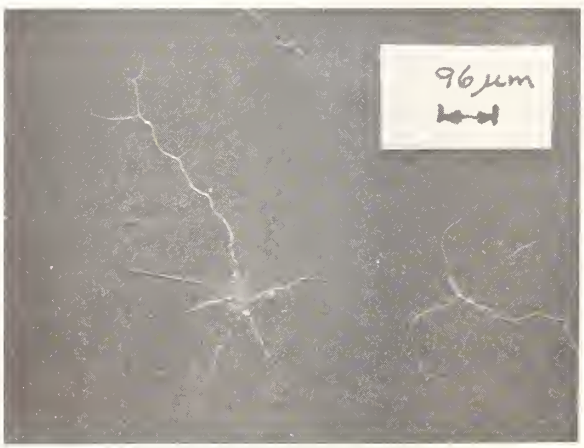

Figure 21. SEM photograph of a damage site on MgF_2, $\lambda/4$ film (sample 0133). The site dimension is 100 microns from left to right (80° sideview of the site).

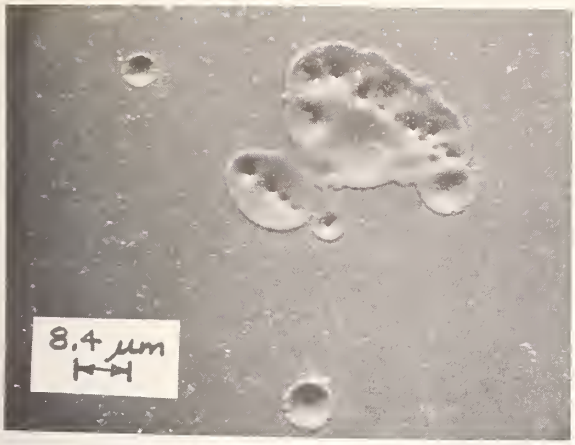

Figure 23. A larger damage site on rutile surface; no spark observed.

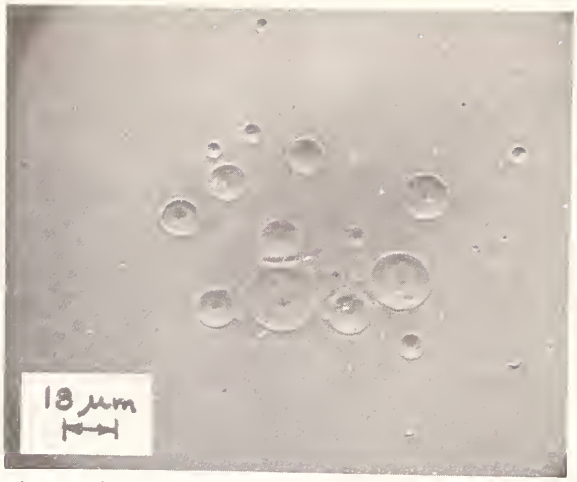

Figure 24. Another damage site on rutile surface; no spark observed. This is a single shot damage site using a laser beam spot-size of about 160 μm. Note that the small damage craters are irregularly distributed.

Figure 25. A close-up view of the craters shown in figure 24. The cracks were neatly formed according to some crystallographic orientation.

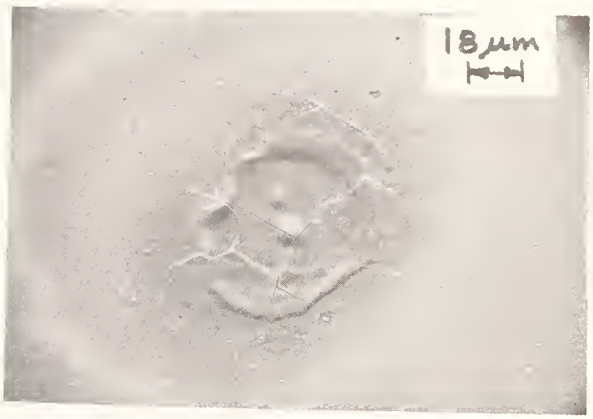

Figure 26. A large damage site with a surrounding white ring on the rutile surface. A spark was observed in this case.

COMMENTS ON PAPER BY deSHAZER

It was pointed out that in all the materials reported in this paper the value of the parameter η was equal to 3. The speaker responded that work was in progress on quartz and magnesium fluoride, which should show a rather different value of the η factor. This would provide further test of the theory. He also commented that in the case of zinc sulfide, that it was a very nonreproducible material in vacuum deposition. Both in his own work and in the literature the values of absorption measured in zinc sulfide films were widely varying, from values of 10 per centimeter to 4,000 per centimeter. The incidence of imperfections in zinc sulfide films seemed to be extremely sensitive to the technique of deposition and to the temperature of the substrate and other factors in the deposition process. It was noted that the morphology of damage observed in the results presented in this paper was very similar to that observed both on the surfaces of germanium single crystals and on the surfaces of glass, in the work of Boling.

The Role of Inclusions and Linear Absorption in Laser Damage to Dielectric Mirrors

David Milam and R. A. Bradbury †
Air Force Cambridge Research Laboratories
Laser Physics Branch
L. G. Hanscom Field
Bedford, Massachusetts 01730

and

Michael Bass *
Raytheon Research Division
Waltham, Massachusetts 02154

By studying the morphology of threshold damage and observing the predicted "pulse duration-inclusion size" relationship we have found that laser damage to dielectric coatings is primarily determined by the presence of metallic or highly absorbing nonmetallic inclusions. It is also shown that linear absorption does not determine the damage resistance of coatings when they are properly prepared from materials which do not show bulk absorption.

Key Words: Dielectric mirror, inclusions, laser-induced damage, linear absorption.

1. Introduction

By studying the morphology of damage produced at threshold and observing the predicted [1, 2][1] "pulse duration-inclusion size" relationship we have found that laser damage to dielectric coatings is primarily determined by the presence of metallic or highly absorbing non-metallic inclusions. Specifically, inclusions less than $\sim 0.4\,\mu m$ in diameter are most easily damaged by single 20 psec duration ruby laser pulses while inclusions with diameters greater than $\sim 3.5\,\mu m$ determine damage resistance due to 20 nsec pulses. This suggests that coating damage resistance to Q-switched pulses can be improved by eliminating the larger inclusions.

To study linear absorption in films, experiments were performed in which the mirror sample was irradiated by a pair of pulses separated by an interval of several nanoseconds. Significant linear absorption would be indicated if neither pulse alone could produce damage, but damage occurred when both pulses were used. These experiments showed that linear absorption in films does not determine the damage resistance of coatings when they are properly prepared from materials which do not show bulk absorption.

---

† This research was supported jointly by the Air Force and the Advanced Research Projects Agency of the Department of Defense.

* Supported in part by the Advanced Research Projects Agency of the Department of Defense and monitored by the Air Force Cambridge Research Laboratories under Contract No. F19628-73-C-0127.

[1] Figures in brackets indicate the literature references at the end of this paper.

2. Experimental Conditions

2.1 Damage Apparatus

Experiments have been performed at a wavelength of 0.69 μm using Gaussian-mode pulses with durations between 20 psec and 20 nsec. The picosecond pulses were selected from a mode-locked pulse train, while the longer pulses were generated in a dye-Q-switched oscillator. For both systems, the temporal profile, pulse energy, and a magnified image of the laser spot incident on the damage specimen are recorded for each firing. Details of the two systems are reported elsewhere. [3,4]

The Q-switched system has recently been modified by the installation of an electro-optic pulse shaper between the oscillator and the amplifier. This has allowed generation of strictly bandwidth-limited pulses 1.4 nsec in duration [5], and pairs of pulses separated by a predetermined and reproducible interval. All damage experiments with shutter-shaped pulses were monitored in the same fashion as has been described elsewhere. [3,4]

2.2 Damage Specimens

With a single exception noted in the next paragraph, all damage specimens were electron-gun deposited, quarter-wave stacks of either TiO_2/SiO_2 or ZrO_2/SiO_2 on fused silica substrates. The reflectivity of each of the mirrors exceeded 90% at 0.69 μm. A large number of samples from several manufacturers were examined; the data presented is generally true for all specimens.

A single set of experiments was performed on a ThF_4/ZnS reflector. This exception will be noted in the text.

3. Inclusion Damage in Coatings

3.1 Damage at 20 psec

Characteristic "near-threshold" damage induced by a 20 psec pulse [3,6] focussed to a spot 190 μm in diameter (FWHM of the intensity distribution) is exhibited in the scanning electron micrograph (SEM) of figure 1. [7] The large ridges in the photo on the left are imperfections in the gold coating applied to permit scanning electron microscopy, and are not properties of the dielectric coatings or the laser damage. The laser damage is the array of small craters in the center of this photograph, which corresponds to the central part of the irradiated region. The fact that damage is not produced in the weakly irradiated outer regions is consistent with the assignment of damage threshold to this level of irradiation (3.5 J/cm^2 in 20 psec, or 1.7×10^{11} watts/cm^2).

A magnified view of several of the small craters is shown in the photo on the right. Craters are randomly located in the plane of the coating, but restricted primarily to the top two layers of the stack. There are between 2 and 10×10^6 such craters per cm^2.

Since the size at the top of the craters may be characteristic of explosive rupture of the material, a more meaningful measure of the size of the damage site can be obtained at the bottom of the crater. The mean site diameter obtained using this criterion is 0.2 μm. In no case with a single 20 psec pulse has a site with diameter greater than 0.5 μm been observed.

It should be emphasized that the damage described in this section is caused by a single 20 psec pulse and is not necessarily characteristic of damage produced by a train of several such pulses. The distinction between these two cases will be discussed in Section 4.

3.2 Damage at 1.4 nsec

The SEM in figure 2 illustrates threshold damage caused by a laser pulse 1.4 nsec in duration focussed to a diameter of 130 μm at the mirror sample surface. The energy density was 14 J/cm^2. Again we see that the damage is an array of randomly located small craters, only now the mean crater diameter is 1.5 μm. The density of these craters, 10^6 per cm^2, is less than the density of damage sites produced by picosecond pulses. These craters often extend further into the coating than the first one or two layers.

Smaller craters, such as those resulting from irradiation with picosecond pulses, were never produced by these longer laser pulses.

3.3 Damage at 20 nsec

The SEM in figure 3 illustrates threshold damage caused by a laser pulse 23 nsec in duration focused to a diameter of 400 μm at the sample surface. The energy density was 16 J/cm^2. The mean site diameter was 4.5 μm and the site density was 10^4 per cm^2. In order to measure so low a site density, it was necessary to irradiate a larger area of the sample. Craters produced by 20 nsec pulses frequently extend into several layers of the coating.

3.4 Interpretation of Threshold Damage

It has been shown that small impurity inclusions, opaque at the laser frequency and in good thermal contact with the surrounding medium can be heated by a laser pulse to temperatures in excess of the melting point of the medium. [1] The material near such inclusions can undergo a phase change and so laser damage results. When damage due to the presence of inclusions occurs, the residual morphology is characterized by an array of many damage sites randomly located within the irradiated volume. [8, 9, 10, 13] A similar morphology would be expected if the damage were due to any other type of localized material or physical defect.

A morphology characterized by using randomly located sites is precisely that of the threshold coating damages shown in figures 1, 2, and 3. We conclude therefore that localized defects are the pincipal cause of laser damage to these optical coatings.

A hint that the defects are impurity inclusions is obtained from the size of the sites damaged by laser pulses of different durations. By considering both the heating and cooling of spherical, metallic inclusions in laser glasses, Hopper and Uhlmann [1] and Bliss [2] have shown that for a particular laser pulse duration a particular size of inclusions will be most easily heated to damaging termperatures. [11] These studies show that short pulses can more easily damage small inclusions than long pulses and vice versa. From eq 4 in Ref. 1 for the inclusion termperature as a function of the radius, R_i, one can easily show that to a first approximation the inclusion which is most readily heated by a laser pulse of duration τ_p, has radius proportional to $(\tau_p)^{1/2}$. Thus, for the three pulse durations used in this work we would expect the damaged inclusions to have radii in the ratios

$$R_i(23 \text{ nsec}):\ R_i(1.4 \text{ nsec}):\ R_i(20 \text{ psec}) = 34:8.3:1$$

Note that for a particular pulse duration a range of sizes of "easily damaged inclusions" can be expected because the relationship between the temperature reached and the inclusion size is not a very sharply peaked function. [1] In addition, if the level of irradiation is even slightly above the absolute minimum required for damage then several different sizes of inclusions can be heated to damaging temperatures.

Because there is this range of site sizes in each case, the ratios of the mean site diameters,

$$\overline{R}_i(23 \text{ nsec}):\ \overline{R}_i(1.4 \text{ nsec}):\ \overline{R}_i(20 \text{ psec}) = 22:7.5:1$$

are to be compared with the expected ratios. These sets of ratios are in acceptable agreement in view of the difficulty in finding the exact size of the inclusions which produced the damage sites.

Hopper and Uhlmann have also shown that for non-metallic inclusions having moderate absorptivity there is no "pulse duration-inclusion size" relationship as above. [1] However, if the absorptivity of the inclusion is very high (i.e. $\frac{1}{\alpha} < R_i$ where α is the absorption coefficient in cm^{-1} at the laser wavelength) the same model as used for metallic inclusions can be applied. Thus, the observed damage morphology and "pulse duration-inclusion size" relationship suggest that the damaging defects are either metallic or very highly absorbing non-metallic included impurities.

Inclusions of either type may arise from impurities in the starting material, incomplete oxidation of the high index material (particularly in the case of TiO_2), introduction of material from the electrongun [12], dust, or general deposition of dirt from the chamber. All of these indicate the possibility of improving the damage resistance of optical coatings by improving the coating process control. Note that long pulse damage resistance can be increased simply by eliminating the large inclusions.

Non-metallic absorbing inclusions are likely to be more strongly absorptive at shorter wavelengths and in the infrared than they might be near 1 μm. Thus, their importance in damage problems will grow as the need for high peak power devices in these spectral regions increases.

3.5 Above-Threshold Damage

The morphology of damage sites produced by irradiation at levels significantly above threshold is consistent with the conclusion that damage is caused by metallic or highly absorbing inclusions. In figure 4 there are four SEM's of damage produced by single 20 psec pulses of successively higher energy. These photographs are highly suggestive that damage for above-threshold irradiation is the result of the compounding of damage at many independent sites. Above-threshold damage with single 1.4 nsec pulses appears to follow the same pattern.

A possible exception to the observation that massive damage is a compounding of damage at many small inclusions occurs with the 20 nsec duration pulses. Above-threshold damage sites at this pulse duration frequently consist of a smooth area, one or two layers deep which is similar in size and shape to the incident laser beam (see figure 5). A number of inclusion damage craters may occur either within or outside the edges of the large site. Since the inclusion craters are seldom centered on the larger area, it is not clear that the larger area results from massive inclusion damage. In addition, the material surrounding these sites is not strewn with small inclusion damages as in figure 4.

The appearance of these large damage sites suggest that other damage interactions might take place with 20 nsec pulses. Numerous mechanisms involving combinations of inclusion damage and/or intrinsic processes can be involved to account for the correlation between the shape of the laser beam and that of the larger sites. One possibility is that the outer layers are simply heated to a damaging temperature due to irradiation of the great number of small absorbing inclusions present. Linear absorption by the coating materials will also contribute to a damage morphology similar to the laser beam cross-section. This is explored in detail in the double-pulse experiments described below.

It is to be emphasized that observations concerning the potential importance of other mechanisms for 20 nsec irradiation in excess of threshold in no way effects the conclusion that threshold at this pulse duration is determined by large inclusions.

4. Double-Pulse Damage Experiments

If a damaging quantity of energy H is absorbed from a single 1.4 nsec pulse of energy E, the same energy H can be supplied by two pulses each of energy E_p ($E/2 < E_p < E$) provided that the interpulse interval is shorter than the cooling time of the absorbing volume. Addition of the two pulses to produce damage can occur in a uniformly absorbing film or at inclusions too large to be effectively heated by single 1.4 nsec pulses. This would not occur at small inclusions which could

cool during the interpulse interval, or if damage is due to a fast response mechanism such as an electron avalanche breakdown.

As noted in Section 2.1, pairs of optical pulses are readily generated by the pulse-shaping shutter. The Pockels cell in this shutter is constructed as an electrical transmission line element. The driving voltage pulse propagates through the Pockels cell into a cable terminated by an impedance-matched load. Removing the load results in a reflection of the voltage pulse, which in turn opens the shutter a second time. Single-and double-pulse operation of the shutter are both illustrated in figure 6.

During the experiment, a mirror was probed by single 1.4 nsec pulses at a number of sites to determine the energy E_t, required to produce damage with single pulses. A given site was irradiated only once during this sequence. Additional sites were irradiated with a series of several single subthreshold pulses at intervals greater than one minute. As a general rule, even several pulses with intensities less than that required for single pulse damage produced none. This implies that permanent damage, undetectable by optical microscopy, did not occur with single subthreshold pulses. Subsequent observations of damage due to the addition of two closely spaced pulses could therefore be of thermal origin.

A record of an experiment performed in this fashion is shown in figure 7. An approximate threshold for damage by single pulses is indicated by the horizontal dashed line, and a lack of cumulative undetected damage by sequences of near-threshold shots which were fired on a given site without causing damage.

A record of some of the double-pulses experiments performed on the same mirror is shown in figure 8. The total energy ($2E_p$) of each pair of pulses satisfies the requirement $2E_t > 2E_p > E_t$, so that damage was possible only if summation occurred. In several cases, damage did indeed occur. Damage sites produced by addition on this morror were characteristic of damage due to large inclusions. Such inclusions would not be expected to damage upon irradiation by single 1.4 nsec pulses. This observation, coupled with the failure of addition at many sites is taken as evidence that there is no severe linear absorption present in this mirror beyond that presented by the localized inclusions.

The observation that large inclusions can be damaged due to cumulative heating by successive pulses can be generalized to explain damage by a train of mode-locked pulses. If the intensity of each of the pulses is such that singly they cannot produce damage, damage to large inclusions can still be the pincipal failure mechanism. This may explain the difference between the damage threshold found for single 20 psec pulses, $\sim 10^{11}$ watts/cm^2, and the intensity limits of mode-locked oscillators set by coating damage, $\sim 1 - 4 \times 10^9$ watts/cm^2.

It was a general observation that there was no consistent pattern of pulse-pair addition indicative of material absorption in the mirrors used in this study.

In order to ascertain that the double-pulse experiment does indeed detect absorption, we have used the technique to study a ThF_4/ZnS reflector which is known to be linearly absorptive at $\lambda = 0.69\,\mu m$. Typical double-pulse data for this mirror is shown in figure 9, where the single-pulse damage threshold is again represented by the dashed line. For this reflector, the expected consistent addition of pulses is seen to occur.

These results indicate that if the coating materials are non-absorbing then a combination of linear absorption and/or absorption by small inclusions can not be invoked to explain results such as those shown in figure 5. It is possible therefore that this type of damage was caused by an intrinsic process. To study this possibility, experiments in which a spot size sufficiently small such that the irradiated area of the coating is not likely to contain inclusions which are easily damaged by the pulses used are in progress.

5. Conclusions

The principal conclusions of this work are:

1. The practical damage threshold for optical coatings at 0.69 μm is determined by the presence of absorbing impurity inclusions.

2. The predicted "pulse duration-inclusion size" relationship for metallic or highly absorbing non-metallic inclusions was observed.

3. Very small ($<0.3\,\mu$m) inclusions are the limiting factor in coating damage resistance to single 20 psec ruby laser pulses.

4. Larger inclusions ($>4\,\mu$m) are responsible for threshold coating damage when long duration pulses ($\approx$20 nsec) or trains of mode-locked pulses are used. Damage resistance to such irradiation would be improved if only this class of larger inclusions could be eliminated. Inclusions of these sizes are appropriate to laser radiation in the visible or near infrared. For other wavelengths the limiting inclusion sizes must be scaled according to the wavelength.

5. Linear absorption in films does not determine the damage resistance of coatings when they are properly prepared from materials which do not show bulk absorption.

6. Acknowledgments

The authors wish to acknowledge the use of data collected by E. S. Bliss (currently with Lawrence Livermore Laboratories) while he was employed at Air Force Cambridge Research Laboratories. They also acknowledge the assistance of C. C. Gallagher in design and construction of the laser-triggered spark gaps and fast pulse circuitry, and the assistance of E. E. Hoell and H. Miller in collecting some of the data presented here. The latter three individuals are employed at Air Force Cambridge Research Laboratories.

7. References

[1] Hopper, R. W. and Uhlmann, D. R., "Mechanism of Inclusion Damage in Laser Glass", J. of Appl. Physics 41, 4023 (Sept. 1970).

[2] Bliss, E. S., "Pulse Duration Dependence of Laser Damage Mechanisms", Opto-Electronics, 3, 99 - 108, 1971.

[3] Bliss, E. S. and Milam, D., "Laser Induced Damage to Mirrors at Two Pulse Durations", Proc. 4th ASTM Symp. Damage in Laser Materials, NBS Spec. Pub. No. 372 (1972).

[4] Bliss, E. S. and Milam, D., "Laser Damage Study with Subnanosecond Pulses", AFCRL Report No. 72-0233 (1972). Available from Defense Documentation Center, the National Technical Information Center, or the authors.

[5] Milam, D., Bradbury, R. A., and Gallagher, C. C., "Evaluation of Three Techniques for Producing Laser Pulses of Nanosecond Duration", AFCRL Report No. 73-0007. Available from Defense Documentation Center, the National Technical Information Center, or the authors.

[6] Bliss, E. S., Milam, D., and Bradbury, R. A., "Dielectric Mirror Damage by Laser Radiation over a Range of Pulse Durations and Beam Radii", Applied Optics 12, 602, (1973).

[7] Damage sites shown in SEM's used as illustrations in this report are distorted since the specimen is viewed at an angle of 45°. True dimensions are obtained by measurements on a diagonal aligned on the long axis of the ellipse.

[8] Bass, Michael, "Nd:YAG Laser-Irradiation-Induced Damage to $LiNbO_3$ and KDP", IEEE J. of Quantum Electronics QE-7, 350 (July 1971).

[9] Yablonovitch, E., "Optical Dielectric Strength of Alkali-Halide Crystals Obtained by Laser Induced Breakdown", Appl. Phys. Letters 19, 495 (Dec. 1971).

[10] Fradin, D. W., Yablonovitch, E., and Bass, M., "Confirmation of an Electron Avalanche Causing Laser-Induced Bulk Damage at 1.06 Microns", Appl. Optics 12, 700 (April 1973).

[11] The treatments in references 1 and 2 require that the inclusion be completely embedded in the surrounding material. The morphology of the damage indicates that this condition is satisfied for almost all of the inclusions which contribute to coating damages.

[12] Schwartz, H., "Thin Films of Metals and Inorganic Compounds Vacuum Deposited by High Energy Laser" in "Laser Interactions and Related Plasma Phenomena", Vol. I, Ed. by Helmit J. Schwarz and Heinrich Hora (Plenum Press, New York, N. Y. 1972) p 71.

[13] DeShazer, L. G., "Role of Coating Defects in Laser Induced Damage to Thin Films", Proc. 5th ASTM/NBS Boulder Damage Symposium, to be published.

8. Figures

Figure 1. Laser damage in a dielectric mirror produced by a single 20 psec duration pulse focused to a spot size of 190 μm (FWHM in intensity profile.) Left side: near-threshold damage consisting of many small craters in the center of the most intensely irradiated area. The large dark features are defects in the gold coating applied to allow electron microscopy. Right side: magnified view of a portion of the irradiated area.

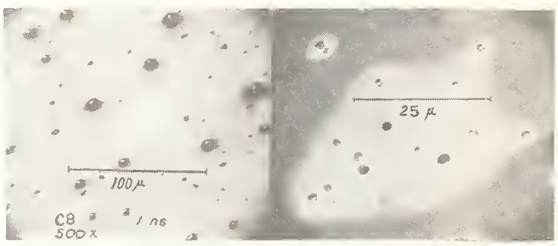

Figure 2. Laser damage in a dielectric mirror produced by a single 1.4 nsec duration pulse focused to a spot size of 130 μm (FWHM in the intensity profile. Left side: near-threshold damage consisting of approximately 20 small craters near the center of the most intensely irradiated area. Dark spots are defects in the gold coating applied to allow scanning electron microscopy. Right side: magnified view of the damaged region.

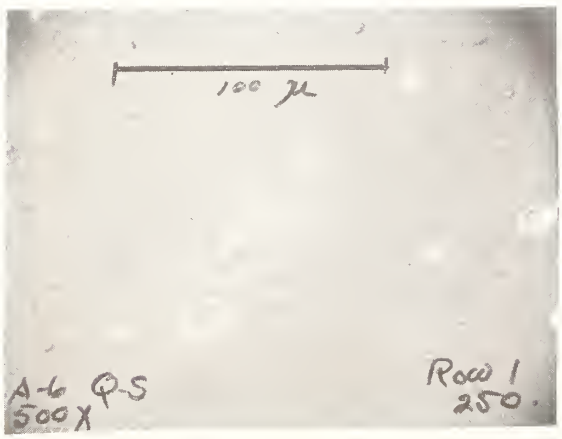

Figure 3. Near-threshold damage in a dielectric mirror produced by 23 nsec duration pulse focused to a spot size of 400 μm (FWHM in the intensity profile).

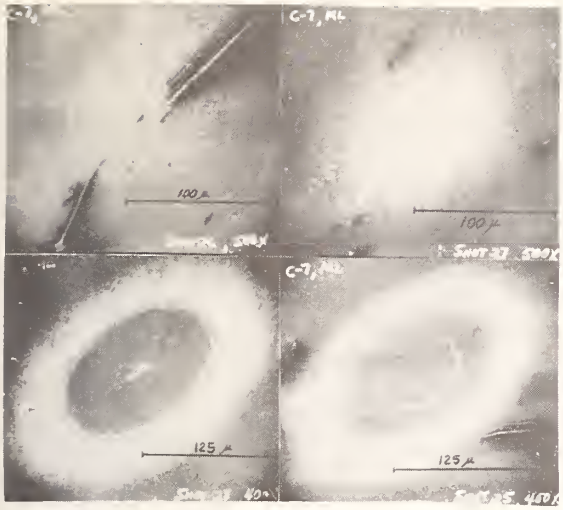

Figure 4. Damage in a dielectric mirror produced by single 20 psec pulses of successively higher energy.

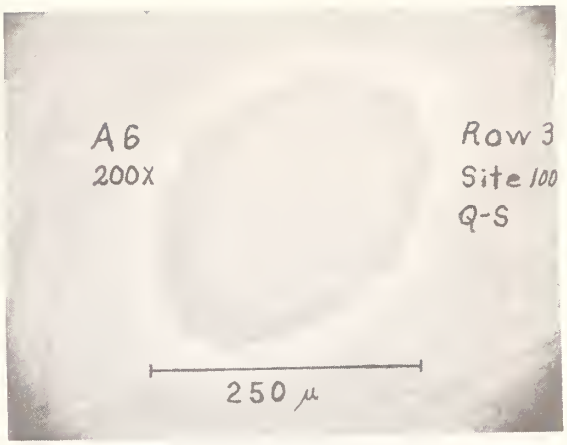

Figure 5. Above-threshold damage in a dielectric mirror produced by a 23 nsec duration pulse focused to a spot size of 400 μm. Five small inclusion craters are located within the damaged area which is itself two layers deep. The area has a shape like that of the incident laser beam, and is not centered on the obvious inclusion damage.

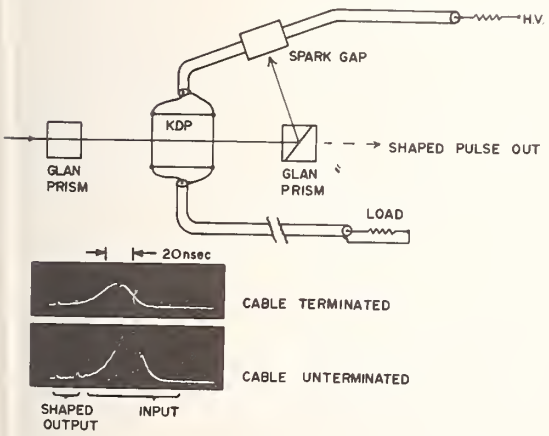

Figure 6. Shutter for generating single pulses of 1.4 nsec duration, or pairs of 1.4 nsec pulses spaced by a reproducible interval. Removing the load from the cable causes a voltage reflection which gates the Pockels cell a second time.

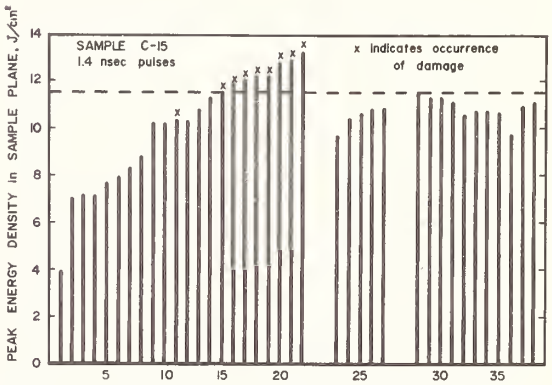

Figure 7. Histogram of a damage experiment on a ZrO_2/SiO_2 mirror. Shots 1-22 were single shots each fired on a different site to determine single-pulse threshold (indicated by a horizontal dashed line). The set of shots 23-27 were fired onto a single site at one minute intervals to verify that detectable damage did not occur as a result of accumulation of undetected permanent damage. No damage could be detected after the five firings. Shots 28-38 were fired onto a second site at one minute intervals without causing damage.

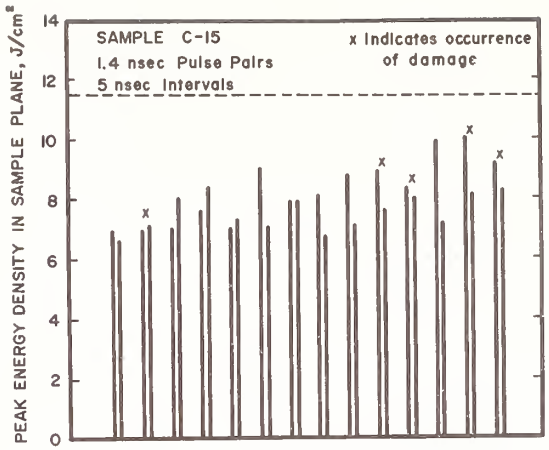

Figure 8. Record of some double-pulse experiments on the sample for which single-pulse data is shown in Figure 7. The failure to observe a consistent pattern of damage due to pulse-pair summation indicates that linear absorption in the film itself is not a limiting problem. A study of the morphology of the sites at which damage did occur by summation shows that damage was due to a class of larger inclusions than would have been damaged by single 1.4 nsec duration pulses.

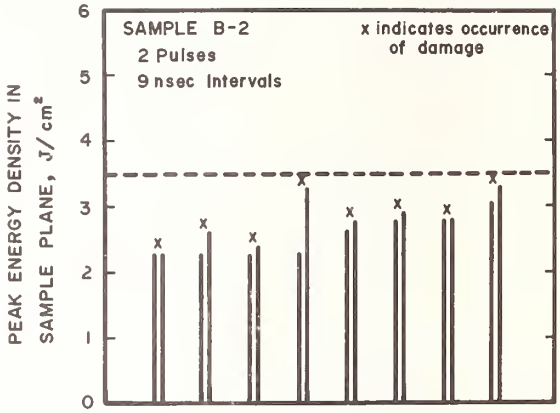

Figure 9. Double-pulse damage experiments on a ThF_4/ZnS mirror. Single-pulse threshold is indicated by the dashed horizontal line. A consistent pattern of damage due to addition of two subthreshold pulses indicates linear absorption in the coating.

COMMENTS ON PAPER BY MILAM

The question was asked concerning the applicability of the Hopper-Uhlman theory to surface damage since the theoretical work of Hopper and Uhlman did not take into account changes of state of the included material, and only applied to inclusions embedded deep within the material. The speaker responded that the theory was only applied to this case as a guide in the absence of other techniques. However in the discussion it was pointed out that many of the inclusions that lead to damage are not actually on the surface but are in reality embedded fairly far below the surface, so that the Hopper-Uhlman theory would apply. The speaker further commented on the ease with which confirmation was achieved of the statistical nature of the damage process in this experiment.

Time Resolution of Laser-Induced Damage to Thin Films*

N. Alyassini, J. H. Parks and L. G. DeShazer

Departments of Physics and Electrical Engineering
University of Southern California
Los Angeles, California 90007

The time evolution of laser-induced damage to ZnS films was measured by monitoring the intensity of a He-Ne probe beam internally reflected from the films at the critical angle. The time behavior of the damage was measured with a resolution of 2 nsec, and was correlated to the ruby laser pulse and the spark emission, when present. This technique was used to compare the damage time evolution with the related damage site morphology observed in SEM photographs.

Key Words: Laser induced film damage, optical probe, surface plasma, time resolved laser damage.

1. Introduction

This paper reports the measurement of nanosecond time resolved damage to thin films using optical probe techniques described previously [1][1]. The damage time evolution can indicate the presence of damage processes having different formation rates as shown below in the case of ZnS films. Scanning electron microscope photographs of the damage sites have been taken to compare the temporal and spatial data. In addition, the damaged film was monitored for the ocurrance of spark emission and the transmitted ruby pulse shape was recorded. Experimental observations indicate that spark emission and pulse shape distortion cannot be relied upon to infer near-threshold damage in thin films.

2. Optical Probe Technique

The technique we have developed, figure 1, consists of illuminating the surface site to be damaged with a He-Ne laser and then detecting the reflected beam with a fast electro-optical system. Any change at the surface of the sample is recorded as a change in the intensity of the reflected probe beam, and the temporal behavior of the reflected probe beam is directly related to the temporal change at the sample surface. The damage is caused by a TEM_{oo} Q-switched ruby pulse of pulsewidth 10-15 nsec. The temporal shape of the ruby pulse is recorded as a delayed reference pulse by a fast photodiode/Tek 519 scope and will be referred to as the input pulse. The transmitted portion of the pulse after passing through the sample is also recorded on the same oscillograph trace and is referred to as the output pulse.

An RCA 6199 photomultiplier covered with a notch filter at 4000 Å is used to detect any visible spark that might be created at the surface of the sample.[2] A 40× telescope is also employed to examine the film surface site before and after each shot to obtain an optical measure of the damage size and to observe the probe location with respect to the damaged region. The sample is later examined under a 1000× microscope and photographs of the damaged site are taken with the aid of a scanning electron microscope. Each damage site is indexed to allow comparison of the SEM photograph and the corresponding time resolved damage trace.

---

*This research was supported partially by the Advanced Research Projects Agency of the Department of Defense and was monitored by the Air Force Cambridge Research Laboratories under Contract No. 19628-71-C-0220.

[1] Figures in brackets indicate the literature references at the end of this paper.

As shown in figure 1, the probe beam enters the substrate and is internally incident on the film-air surface at the critical angle. The critical angle was chosen to maximize the reflected probe sensitivity to changes at the film-glass interface. Also by internally probing the site to be damaged, any perturbation on the probe due to the spark is eliminated. The calculated radius of the probe beam at the film-air interface is 5μ while that of the ruby was adjusted from 15 to 25μ.

The probe detection system is DC coupled to a Tek 7904 scope thus permitting a direct measure of the change in the intensity of the reflected probe. The detection system/scope combination has a rise and fall time of less than 2 nsec. In this experiment it was necessary to record the leading edge and subsequent time dependence of the reflected probe beam and simultaneously correlate the damage initiation with the ruby laser pulse. A reliable technique to synchronize the probe change signal and the ruby pulse to within a few nanoseconds was developed.

3. Optical Probe Intensity Variation - Examples

The He-Ne probe beam which optically samples the thin film damage can exhibit reflected intensity changes as the result of several possible mechanisms. We will briefly discuss two clear examples and avoid speculating on the details of more complex processes. Whereas the index of refraction change has not been indicated by our damage studies, the scattering process explains several details of the damage time evolution as will be shown in the discussion of results.

3.1 Refractive Index Change

Consider the possibility that the index of refraction of the ZnS film might be altered during the ruby pulse without the ocurrance of structural damage. It follows from the Fresnel equations that the maximum change in the reflected probe intensity occurs for critical angle incidence. A decrease in the reflected probe intensity associated with a decrease in the index of refraction from n_o to $n_o - \Delta n$ is given by:

$$R_{\parallel} = 1 - \left[\frac{(n_o^2 - 1)^{\frac{1}{2}} - \Delta n^2 \left(\frac{n_o}{\Delta n} - 1 \right) \left(\frac{2n_o}{\Delta n} - 1 \right)^{\frac{1}{2}}}{(n_o^2 - 1)^{\frac{1}{2}} + \Delta n^2 \left(\frac{n_o}{\Delta n} - 1 \right) \left(\frac{2n_o}{\Delta n} - 1 \right)^{\frac{1}{2}}} \right]^2$$

$$R_{\perp} = 1 - \left[\frac{\left(\frac{n_o}{\Delta n} - 1 \right) (n_o^2 - 1)^{\frac{1}{2}} - \left(\frac{2n_o}{\Delta n} - 1 \right)^{\frac{1}{2}}}{\left(\frac{n_o}{\Delta n} - 1 \right) (n_o^2 - 1)^{\frac{1}{2}} + \left(\frac{2n_o}{\Delta n} - 1 \right)^{\frac{1}{2}}} \right]^2$$

for a beam polarized parallel or perpendicular to the plane of incidence respectively.

3.2 Scattering After Structural Damage

The structural damage to the film will result in scattering of the optical probe beam depending on the degree of overlap of the probe focal spot and the damage region. When the probe beam is incident at the critical angle for the ZnS-air interface, it will also be incident at the critical angle for the glass-air interface after the film is removed. Thus if the probe beam is totally within the damage area, the reflected probe intensity will recover to its initial value after the film is removed. However if the damage site cross section is smaller than the probe cross section, or if the probe is only partially obscured at the edge of a damage, then the reflected probe intensity will not totally recover to its initial value before damage, because diffuse scattering by the edges of the damage is appreciable.

4. Experimental Results and Discussion

Results presented here are representative of entrance surface damage to $\lambda/4$ ZnS films on BSC2 glass. Each site of the sample was irradiated only once. The following results summarize these thin film damage studies.

(a) Time resolved damage has been measured with a resolution of 2 nsec.

(b) The damage time evolution falls into two classes: a fast damage initiation process starting near the peak of the ruby pulse and having a rise time of ~ 4 nsec, and a slow process initiating at the trailing edge or after the ruby pulse and having a rise time ~ 10-20 nsec. When the probe intensity recovers under conditions described in 3.2, the recovery time is ~25-50 nsec.

(c) Thin film damage areas on the order of ~4μ diameter have been observed without spark emission.

(d) Film damages similiar to (c) have been observed without distortion occurring in the transmitted ruby pulse.

(e) No effects directly related to a change in refractive index have been observed.

In figure 2a the probe response indicates a fast damage initiation process starting near the peak of the ruby pulse results in a fast decrease of the reflected probe intensity to a minimum value typically in less than 4 nsec. The probe was located within the central region of the damage and as the film is removed the detected probe intensity recovers to its initial value in about 20 nsec. The damage of the film is also indicated by the distortion in the output pulse which occurs at about the peak of the pulse and lasts for about the same time as the fast falling edge of the probe beam response. A spark was detected with this damage.

A ruby pulse of 20% less energy, 15% smaller in peak power, than the damaging pulse of figure 2, results in the damage of figure 3. In this case the damaged region is within the probe diameter. This probe response is an example of the class of slow damage processes. The probe intensity starts to decrease in the trailing edge of the ruby pulse. The highly scattering edges of the damage and within the probe beam result in a decrease in the reflected probe intensity to a minimum in about 15 nsec. No spark or distortion to the output pulse could be detected with this damage. Small sub-regions of damage can also be seen in the SEM photo. These may result from defect sites having a lower damage threshold since they occur in the lower intensity wing of the ruby pulse cross-section.

One of the smallest damage sites detected by the probe technique is shown in figure 4. Figure 4 represents a fast damage initiation process starting at the peak of the ruby pulse. Film structure remains in the damaged area as can be seen in the SEM photo. No spark or distortion in the output pulse could be detected with this damage.

5. Acknowledgments

Valuable discussions were held with Prof. J. Marburger and Prof. R. W. Hellwarth. The film depositions were prepared by Mr. H. R. Owen and the SEM photos taken by Mr. Jack Worrall, both of USC.

6. Reference

[1] Parks, J. H., and Alyassini, N., in Laser induced Damage in Optical Materials: 1972, edited by A. J. Glass and A. H. Guenther (NBS Special Publication 372, October 1972), pp. 104-107.

[2] For the analysis of the sensitivity of the spark detector see: Newnam, B.E., dissertation, University of Southern Calif. (1973).

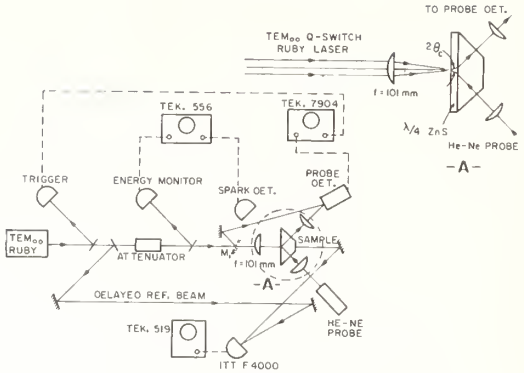

Figure 1. Experimental setup.

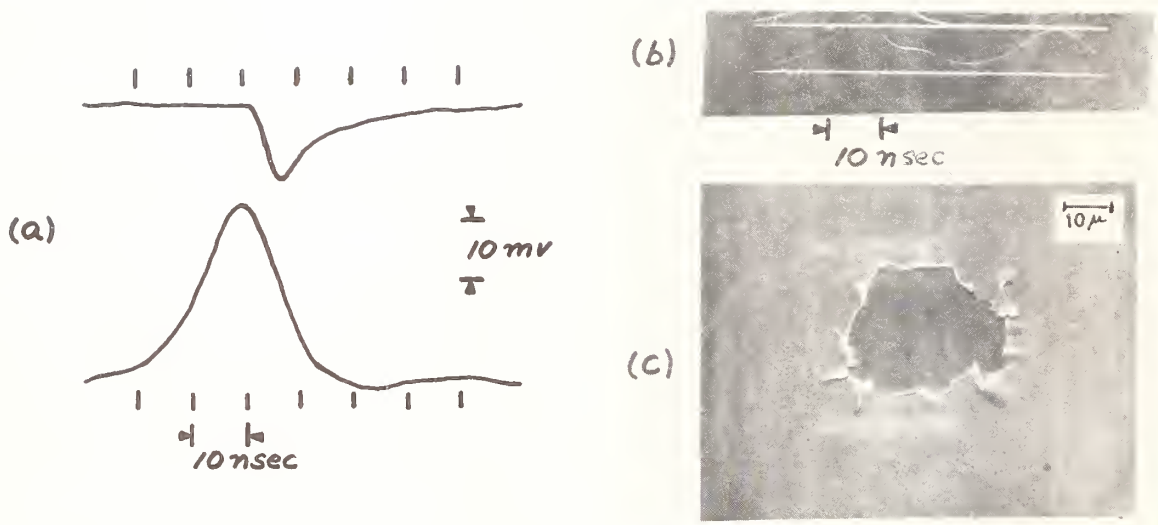

Figure 2. Entrance surface damage to λ/4 ZnS.

a: Probe trace (upper trace) and the damaging ruby pulse (lower trace). The maximum decrease in the probe intensity is 35% of peak intensity (peak intensity is 38 mV).

b: The output damaging pulse is shown followed by the input delayed reference pulse.

c: SEM photograph taken at 10 degrees tilt.

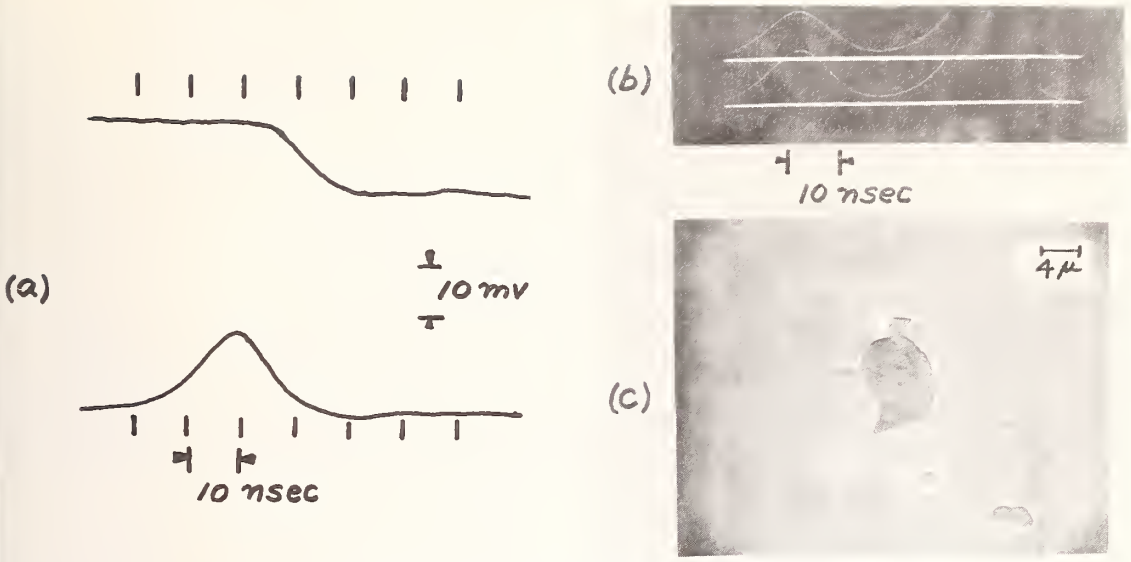

Figure 3. Entrance surface damage to λ/4 ZnS.
a: Probe trace and the damaging ruby pulse.
b: Output and input pulses.
c: SEM photograph taken at 10 degrees tilt.

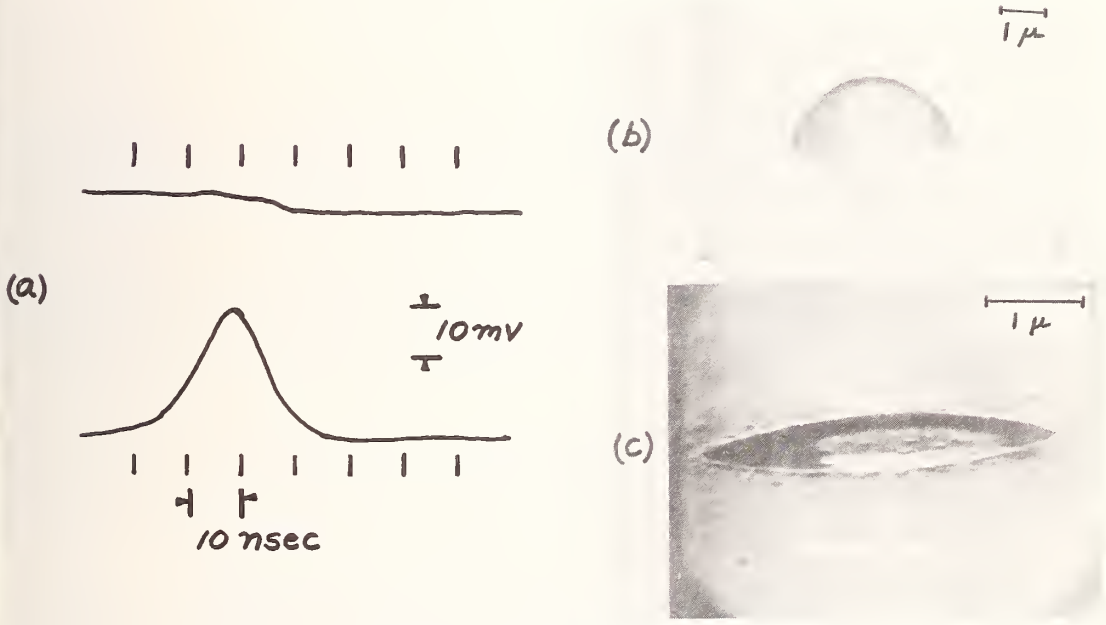

Figure 4. Entrance surface damage to λ/4 ZnS.
a: Probe response and the damaging ruby pulse.
b: SEM photograph taken at 10 degrees tilt.
c: SEM photograph taken at 79.6 degrees tilt.

NO COMMENTS ON PAPER BY ALVASSINI.

Investigation of Pulsed CO Laser Damage in Coated Metal Mirrors and Dielectric-Coated Windows

S. Holmes and P. Kraatz

Northrop Research and Technology Center
Laser Technology Laboratories
Hawthorne, California 90250

Results of some pulsed high power CO laser damage tests of metal-coated metal mirrors and AR-coated CaF_2 windows are reported. The laser employed in these tests is an E-beam pumped, CO gas laser which produces a multimode output pulse of ~100 μsec duration at a wavelength of 5 μm. It was focused to a spot size of ~2-3mm, yielding maximum energy densities in excess of 700J/cm^2. The mirrors tested were polished beryllium copper substrates coated with either silver or gold; the windows were polished CaF_2 having multilayer AR-coatings comprising combinations of ThF_4, PbF_2, MgF_2, and MgO. Damage threshold measurements and effects of fabrication parameters on performance are discussed.

Key Words: CaF_2 windows, CO laser damage, damage threshold, dielectric antireflection coatings, metal coatings, metal mirrors, protective overcoatings.

1. Introduction

For the past two years, the Northrop Research and Technology Center, Laser Technology Laboratories, has been involved in the fabrication of mirrors and windows for use in high power CO lasers. Recent progress in the field has necessitated the initiation of a damage testing program to evaluate materials, surface finishes, and coating designs for these components, under conditions approximating actual use. The results of some preliminary tests of optical components at the 5 μm wavelength are reported here.

The laser characteristics, testing configuration, and calibrations of energy and spot size are detailed in section 2. Test materials, including substrate and coating preparation, are described in section 3, and illustrations of damage to various materials are given in section 4. The test results are summarized and discussed in section 5.

2. Experimental Setup

2.1 Laser Characteristics

Some of the more important characteristics of the laser device employed in damage testing are summarized in table 1. The experiments were performed using a transverse E-beam discharge pulsed CO gas laser operating at several wavelengths between 4.6 μm and 5.2 μm. A typical output consisted of a 25 joules pulse of 100 μsec duration. The spatial structure of the output was multimode, both transverse and longitudinal. The temporal profile of the output beam is shown in figure 1.

Table 1. Laser Characteristics

Type of laser	Carbon monoxide
Method of pumping	E-beam discharge
Operating wavelengths	Several between 4.6 μm and 5.2 μm
Energy output	Up to 40 joules
Pulse width	100 μsec full width
Output structure	Multimode

2.2 Optical Layout

Figure 2 shows schematically the optical layout of the experimental setup. A stable resonator was used with a partially transmitting output mirror and the output was focused onto the target test plane with a 37 cm focal length spherical mirror. The test samples were mounted on an x-y-z translator and placed at varying distances near or in front of the focal plane. A calibrated calcium fluoride beam splitter directed a small fraction of the output to a calorimetric laser-thermopile, and the energy was registered on a digital voltmeter.

2.3 Spot Size and Energy Density

Beam patterns burned into Plexiglas samples placed in the same plane as the test samples were used to determine the area of the laser beam and thus obtain the incident energy density. The focal spot was elliptical in shape and the area was calculated from the measured lengths of the major and minor axes. The focused spot was typically ~2mm x 3mm, with an area of 0.05 to 0.06 cm^2.

3. Test Materials

3.1 Mirrors

The mirror samples tested were polished beryllium copper substrates coated with either silver or gold and an uncoated polished OFHC copper substrate.

All of the mirror substrates were polished on a pitch lap prepared by standard optical shop techniques. The polishing was achieved by the fresh feed technique utilizing Linde A 0.3 μm alumina abrasive. Finished substrates had a flatness within one-quarter wavelength of visible light and a rms surface roughness which typically fell in the range between 30 and 40Å.

Conventional thermal evaporation in a vacuum and rf bias sputtering were used for the deposition of the metallic coatings.

For the vacuum evaporation method, silver or gold of 99.999% purity was evaporated from molybdenum boats onto unheated mirror substrates to a thickness of about 1000Å. The vacuum was at a pressure of 10^{-7} torr and the deposition rates were greater than 100Å/sec. An overcoating of thorium fluoride was deposited onto some of the silver coatings for protection and prevention of tarnishing.

In the rf bias sputtering method, the system was pumped down to a predeposition pressure of 10^{-6} torr and then backfilled with carrier grade argon to a pressure of 20 microns. All of the mirror substrates were lightly sputter etched to remove residual surface contaminants or oxides and then the silver or gold coating was deposited with a 10-20% bias applied to the substrates. Thicknesses of the sputtered films were between 800 and 1000Å.

3.2 Windows

Three calcium fluoride windows were tested. Two of the windows were polished and coated in-house. The third window was coated in-house as received from the vendor. The coatings are multilayer antireflection coatings having quarter-wave optical thicknesses at 5.0 μm.

The two calcium fluoride windows that were polished in-house, were polished on a pitch lap. The surfaces were first polished using Linde C 1.0 μm alumina abrasive and water. The final polishing was achieved by using Linde A 0.3 μm abrasive and water. The fresh feed technique was utilized throughout the polishing process. Finished surfaces have a flatness within one-quarter wavelength of visible light and a surface finish of better than 20-10 (scratch/dig).

All of the antireflection coatings were deposited by electron beam deposition. The windows were heated to 250°C and glow discharge cleaned prior to the deposition of the coatings. The vacuum was at a pressure of 5×10^{-6} torr. All of the windows were coated on both surfaces with multilayer antireflection coatings comprising combinations of ThF_4 and PbF_2, and MgF_2 and MgO.

4. Results

The damage inflicted upon the sample mirrors and windows tested is documented in this section. All photographs are scanning electron micrographs taken in the secondary electrom emission mode with an accelerating voltage of 25 kV on the electron beam. Mirror surfaces were examined as tested; windows were coated with ~100Å of gold after testing to minimize charging problems and enhance resolution.

4.1 Damage to Metal Mirrors

Several types of laser damage induced in metal mirror surfaces which were protected by a ThF_4 overcoating are illustrated in figures 3 through 14. Damage to metal-coated metal mirrors without an overcoating is shown in figures 15 through 22. Although the damage is primarily thermal in origin, effects vary from minor chemical alteration of the film (i.e., oxidation and tarnishing) to melting, blistering, and explosive vaporization of both coatings and substrates.

For purposes of description only, it is sometimes convenient to subdivide a given damage site into zones, on the basis of severity of the observed effects. The most severe zone, which may or may not be centrally located, includes gross melting and partial vaporization of coatings and substrate. An intermediate zone comprises partial melting and blistering of coatings, with minor substrate damage (chemical alteration, pitting, etc.). The lease severe zone includes chemical alteration and minor melting, distortion, or blistering of films with little or no damage to the substrate. It must be emphasized that the zone concept is purely descriptive and does not necessarily reflect the spatial uniformity of the incident laser beam, the coatings, or the substrate.

This concept of damage zones is well illustrated in figures 3-5, showing a test site on a sample of beryllium copper, coated with vacuum evaporated silver and a protective overcoat of ThF_4. In figure 3, an area of gross melting of coatings and substrate can be distinguished inside a zone of blistering and chemical alteration, shown in detail in figure 4. Figure 5 shows evidence of slight chemical alteration and possible incipient blistering of the coating, following polishing sleeks (or scratches) and other relatively minor defects in the substrate surface. The latter phenomenon is common in samples which have been exposed to the ambient atmosphere for substantial periods of time (e.g., 2-3 weeks); the sample in question was exposed for 4 months.

Somewhat different damage mechanisms in a similar zonal sequence are illustrated in figures 6-8, although the coating and substrate materials and their age are essentially identical to those in figures 3-5. Figure 6 shows a zone of heavy damage at the lower left and a zone of intermediate level damage in the center, with light alteration surrounding the latter. Figure 7 shows that the intermediate zone comprises burst blisters in the coatings with little obvious substrate damage, while figure 8 illustrates complete removal of the coatings in the zone of heavy damage. Surficial thermal alteration and the differing response of matrix and grain boundary phases in the substrate are also well defined in this figure.

Figures 9 and 10. showing another damage site on the same sample as figures 6-8, again illustrate the applicability of the zone concept. However, the severity and areal extent of damage at this site is significantly lower than at the previous site, in contrast to the incident energy density of 416J/cm^2 at the latter site (as compared to 233J/cm^2 at the previous site). On the other hand, the total energy incident on the site of figures 9 and 10 was 26.4J, as compared to 33.6J in the area of figures 6-8. This discrepancy will be discussed in a later section.

Figures 11 and 12, showing damage induced in a silver film deposited by rf bias sputtering and overcoated with ThF_4, do not illustrate the zone concept. Figure 12 shows that the primary damage mechanisms are blistering and surficial alteration of the coatings occurring intermixed in the same area. This type of damage was unique to this sample and test site (227J/cm^2).

At a higher energy density (395J/cm^2), figure 13 shows that the zone concept is again applicable to this sample. Figure 14, of the intermediate zone, shows blistering, melting, and partial removal of the coatings, with relatively minor substrate damage. This may indicate failure or inefficiency in the transfer of absorbed energy from the coatings to the substrate, i.e., poor bonding or adhesion of the coatings. This is unexpected in a sputtered film and will be discussed in a later section.

Figures 15-17 illustrate damage inflicted upon a mirror comprising a vacuum evaporated silver coating on a polished beryllium copper substrate. This sample was also exposed to the ambient atmosphere (while protected from dust by a plastic petri dish) for 4 months, without benefit of a ThF_4 protective overcoat. Figure 15 shows that the overall damage was slight and concentrated in two spots. The detail of the central portion of the larger spot shown in figure 16 illustrates an unfamiliar damage effect, apparent general tarnishing and roughening of the surface, with relatively minor damage to the substrate. The detail of the smaller spot shown in figure 17 illustrates a phenomenon which was unique to this sample and damage site, the apparent growth of a mass of crystalline material in the most heavily damaged region. The mechanism of growth appears to involve redeposition of molten material removed from the surface during the pulse.

Comparison of the damaged area on the bare silver film with the undamaged area shown in figure 18 illustrates that at least some of the observed effects are associated with the pattern of tarnishing developed during exposure to the atmosphere.

Figures 19 and 20 show damage induced in a bare gold film on beryllium copper, aged 4 months in the ambient atmosphere prior to testing. The incident energy density is low (134J/cm^2) and the damage is at a threshold level, i.e., minor alteration and blistering of the coating, again following scratches and minor defects in the substrate.

Figures 21 and 22 illustrate severe damage to this same sample at a different test site, where the energy density was approximately 347J/cm^2. The typical zone sequence is again evident. The detail in figure 22 illustrates melting, blistering, and bead formation at the edge of the damaged film with relatively minor substrate involvement. This again may indicate inefficient transfer of absorbed energy from the gold film to the substrate.

5. Discussion and Conclusions

The damage test results obtained to date are tabulated, summarized, and discussed in this section. It should be emphasized at the outset that these results represent only a first attempt at interpretation of damage induced by pulsed CO laser testing. Hence they are preliminary in nature and conclusions from the data should be viewed as tentative. On the other hand, several interesting questions are raised by these results; some of them are discussed here.

5.1 Mirrors

Initial test results on mirrors are summarized in tables 2 and 3. Results for mirrors protected by a ThF_4 overcoating are presented in table 2, while table 3 shows the results of tests conducted on coated or uncoated metal mirrors with no protective overcoating.

Table 2. Damage test results for coated metal mirrors with protective overcoating.

Material	Pretest Reflectance ($\lambda = 5\ \mu m$)	Age at Test	Incident Energy Density (J/cm^2)	Damage
Evap. ThF_4/evap. Ag/BeCu	0.992	4 mo.	278	Moderate
Evap. ThF_4/evap. Ag/BeCu	0.991	4 mo.	233	Moderate
			394	Slight
			416	Slight
Evap. ThF_4/evap. Ag/BeCu	0.989	2 wks.	181	No visible damage
			406	Extensive
Evap. ThF_4/bias sp. Ag/BeCu	0.989	4 mo.	227	Moderate
			395	Extensive

Table 3. Damage test results for coated and uncoated metal mirrors without protective overcoatings.

Material	Pretest Reflectance ($\lambda = 5\ \mu m$)	Age at Test	Incident Energy Density (J/cm^2)	Damage
Evap. Ag/BeCu	0.993	4 mo.	229	Light-moderate
Evap. Au/BeCu	0.990	4 mo.	134	Slight
			347	Extensive
Polished OFHC Cu	0.985	3 mo.	305	No visible damage

In an attempt to define a damage threshold for metal mirrors with a protective overcoating, we note that one sample showed no visible damage when subjected to a pulse of approximately $180 J/cm^2$ (table 2) but that two samples showed moderate damage at approximately $230 J/cm^2$. Hence, we might conclude that the threshold level of damage lies in the vicinity of $200 J/cm^2$.

However, some confusion arises from the observation that only slight damage was incurred by a similar sample tested at two separate locations at an incident energy density of about $400 J/cm^2$. As pointed out in section 4.1, the total energy incident upon the sample for the latter two shots was 23 to 26J, as compared to 33.6J for the shot which produced moderate damage at an apparent energy density of $233 J/cm^2$. This may indicate errors in the energy density calibration, inhomogeneity of the sample or laser beam, or inadequacy of the energy density criterion for defining damage thresholds. The general consistency of the other results suggests that the energy density calibration is reasonable as a gross average. However, the beam is almost certainly not uniform and the sample only approximates homogeneity. Hence, the questions of adequacy of the energy density criterion and uniformity of the sample and laser beam remain unresolved.

Some questions concerning the relative importance of reflectance, composition and adherence of the reflecting metal film, and effects of exposure to the atmosphere arise from the data in tables 2 and 3. Taking the last question first, we observe that an incident pulse having an energy density of $406 J/cm^2$ (total incident energy 21.9J), produced extensive damage in a sample aged only 2 weeks in the atmosphere. Comparing this with the slight damage produced by a pulse of $416 J/cm^2$ (figure 9) on a sample 4 months old, we note that aging in itself may not lead to substantial deterioration in damage resistance.

Examination of the results in table 3 shows that evaporated gold has a much lower apparent damage threshold than any silver sample tested, whether or not it had been overcoated with ThF_4. On the other hand, the reflectance of the gold and silver are comparable at 5 μm. However, the adherence of evaporated gold is notoriously poor and may contribute to the low damage threshold observed. Further study of the performance of both gold and silver deposited by rf sputtering techniques is required to further elucidate the adherence problem, since the single bias sputtered silver coating tested apparently fared no better than the evaporated coatings and exhibited some evidence of poor adherence (figure 14).

Finally, some questions concerning the importance of both reflectance and integrity of surface material and substrate arise from the single result on polished OFHC copper listed in table 3. An incident pulse of 305J/cm^2 produced no visible laser damage in this polished surface, although its reflectance value of 0.985 is well below that of any coated mirror sample tested. Since the sample is opaque, it should absorb ~50% more energy than the coated samples and could be expected to damage at this energy density, based on the other data. The lack of observed damage may indicate the importance of integrity between surface material and substrate in efficiently dissipating whatever energy is absorbed. Again, further data are required to elucidate this area.

5.2 Windows

Test results for the three AR coated CaF_2 windows are presented in table 4. The data are more or less self-explanatory, but some comments are in order.

Table 4. Damage test results for AR coated CaF_2 windows, (two surfaces coated).

Coating Materials	Incident Energy Density (J/cm^2)	Damage
MgF_2/MgO	114	Threshold (entrance surface)
ThF_4/PbF_2	80	No visible damage
	114	" " "
	168	" " "
	256	" " "
	324	" " "
	338	" " "
ThF_4/PbF_2	247	3 successive shots, same location; No visible damage
	548	
	752	

In seeking reasons for the low damage threshold exhibited by the MgF_2/MgO coating relative to that of the ThF_4/PbF_2, attention should be focused on three material properties or conditions, including substrate surface finish, optical absorption in the 5 μm region, and residual internal stress in the coatings. The polish on the CaF_2 sample coated with MgF_2/MgO appears poorer (figures 24 and 25) than that obtained on the samples coated with ThF_4/PbF_2. Some of the laser damage in figures 24 and 25 seems to be associated with polishing defects or scratches. The cracking and buckling of the MgF_2 coating illustrated in figures 24 and 26 is, in turn, consistent with a high initial stress condition in the coating. Finally, the optical absorption of the MgF_2/MgO coating pair may be greater than that of ThF_4/PbF_2 in the 5 μm region.

Conversely, factors leading to the good results obtained with the latter coating pair on CaF_2 polished in-house, may include better substrate surfaces, lower optical absorption at 5 μm, and lower internal stresses.

6. Acknowledgements

The authors wish to thank Dr. Dennis K. Rice for his able assistance in carrying out the laser testing and calibration and for helpful discussions of the data. We also wish to express our appreciation to Mr. R. F. Schneidmiller for his superb photography of the damaged samples in the scanning electron microscope, and Mr. A. Klugman for his expert optical polishing and finishing of the substrates.

7. Figures

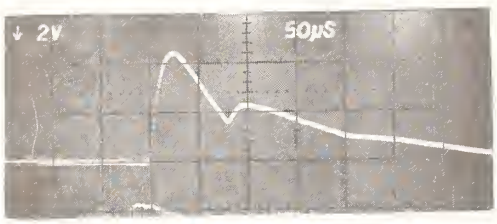

Figure 1. Typical laser output pulse shape.

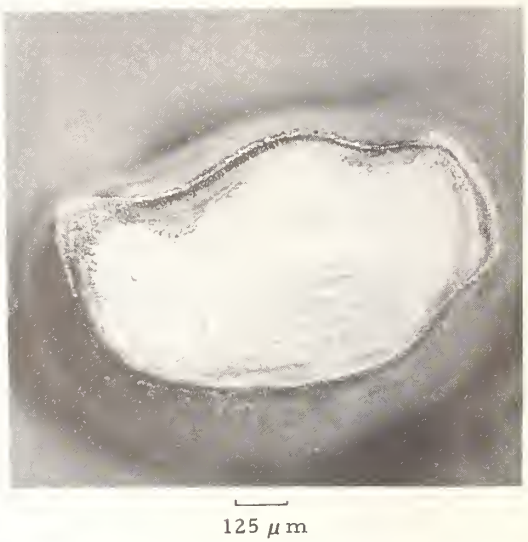

Figure 3. Vacuum evaporated ThF4/Ag coating on Berylco 25 substrate aged 4 months in ambient atmosphere. R = 0.992 (λ = 5 μm). CO laser, 278 J/cm^2 (80X).

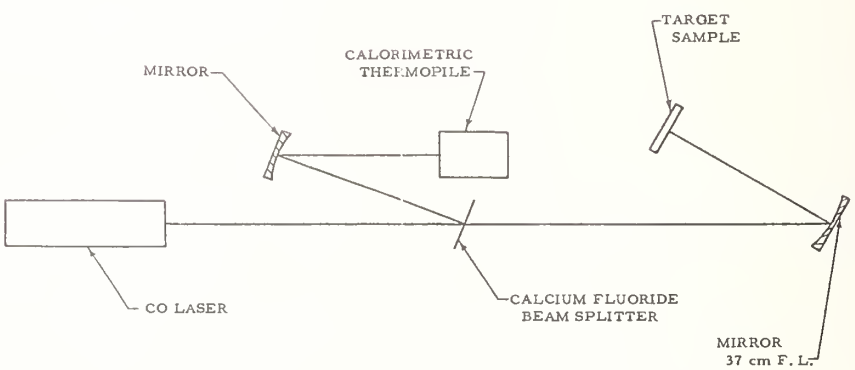

Figure 2. Schematic diagram of the CO laser damage source.

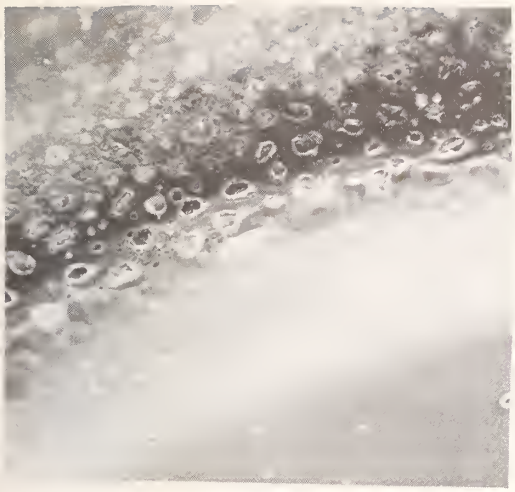

Figure 4. Detail of edge of damage area of Figure 3, 278 J/cm^2 (700X).

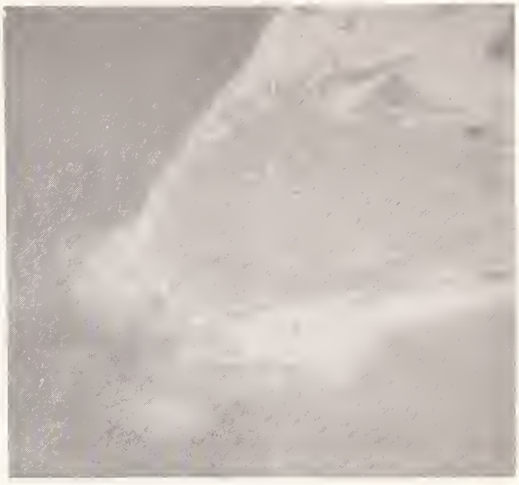

Figure 6. Damage to beryllium copper mirror coated with evaporated ThF_4/Ag, exposed to ambient air for 4 months prior to CO laser testing; R = 0.991, 416 J/cm^2 (80X).

Figure 5. Detail of ThF_4/Ag coating near main damage site (Figure 3) showing light alteration along very fine scratches in the substrate, 278 J/cm^2 (2100X).

Figure 7. Detail of part of damage area of Figure 6, showing partial removal of coating by blister formation and bursting, 233 J/cm^2 (1000X).

Figure 8. Detail of most heavily damaged part of Figure 6, showing partial removal of coating by blister formation and bursting, 233 J/cm^2 (1000X).

Figure 10. Same area as Figure 9, at higher magnification, showing damage to substrate at center, 416 J/cm^2 (230X).

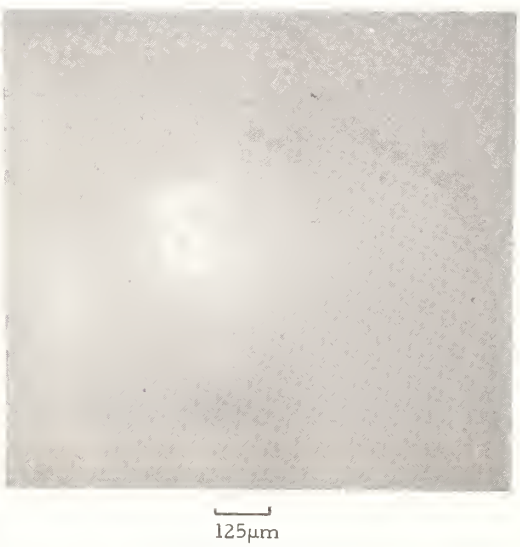

Figure 9. Damage to evaporated ThF_4/Ag coating on beryllium copper substrate; coated mirror was exposed to ambient air for 4 months prior to CO laser testing, R = 0.991, 416 J/cm^2 (80X).

Figure 11. Bias sputtered silver overcoated with vacuum evaporated ThF_4, on beryllium copper substrate. Exposed to ambient air for 4 months prior to test; R = 0.989, 227 J/cm^2 (80X).

Figure 12. Detail of damage to bias sputtered silver coating (Figure 11); 227 J/cm^2 (500X).

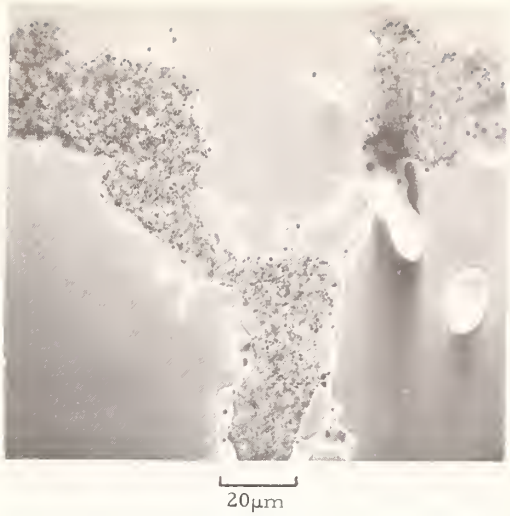

Figure 14. Detail of damage to bias sputtered silver shown in Figure 13; 395 J/cm^2 (700X).

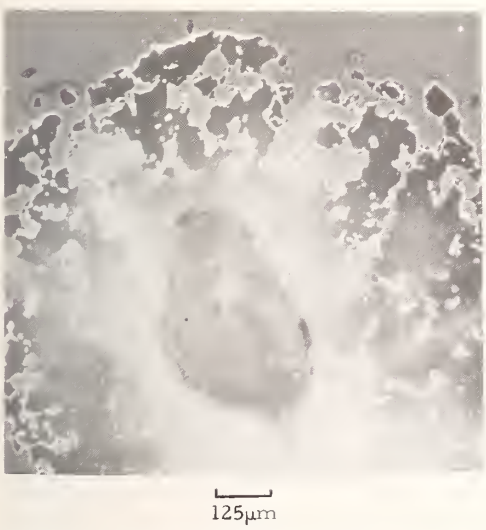

Figure 13. A portion of area damaged by CO laser; bias sputtered silver overcoated with ThF_4 on beryllium copper substrate; R = 0.989, 395 J/cm^2 (80X).

Figure 15. CO laser damaged area on vacuum evaporated silver film, beryllium copper substrate, no overcoating; exposed to ambient atmosphere for 4 months prior to testing; R = 0.993, 229 J/cm^2 (80X).

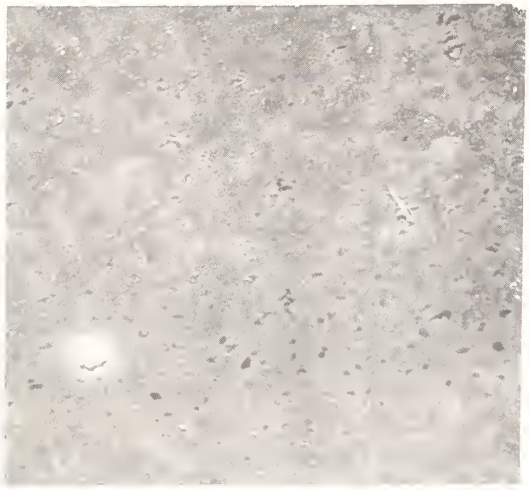

Figure 16. Detail of damaged area (larger spot) on vacuum evaporated silver film shown in Figure 15; 229 J/cm^2 (2100X).

Figure 18. Undamaged silver film approximately 10mm from the damage site shown in Figures 15-17, showing alteration due to 4 months exposure in ambient atmosphere.

Figure 17. Detail of smaller damage spot on unovercoated silver film shown in Figure 15; 229 J/cm^2 (2100X).

Figure 19. Unovercoated, evaporated gold film on beryllium copper substrate, showing CO laser damage. Exposed to ambient air for 4 months prior to testing; R = 0.990, 134 J/cm^2 (80X).

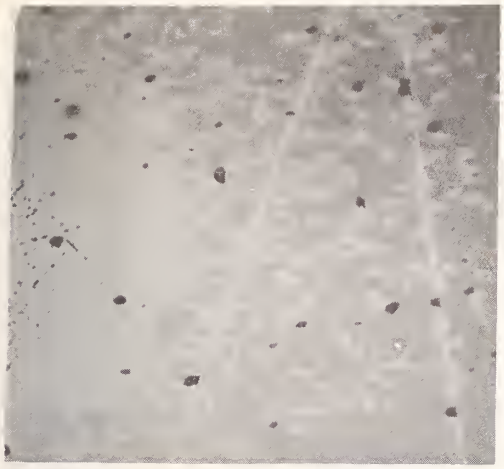

Figure 20. Detail of part of damaged area on gold film shown in Figure 19, illustrating alteration along scratches in substrate, 134 J/cm^2 (2100X).

Figure 22. Detail of edge of damaged area (Figure 21) of evaporated gold film on beryllium copper substrate. 347 J/cm^2 (2100X).

Figure 21. Damage to aged (4 months) unovercoated gold film on beryllium copper substrate; R = 0.990, 347 J/cm^2 (80X).

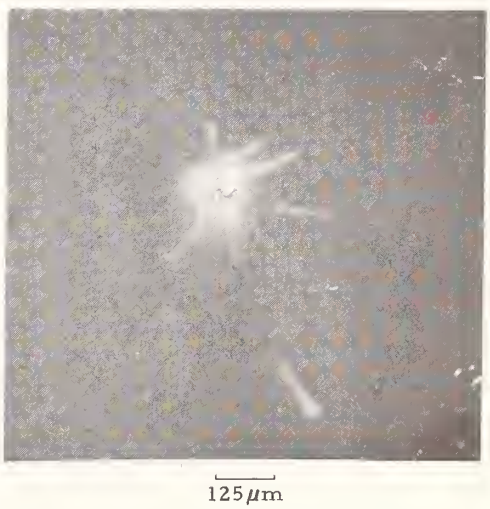

Figure 23. CO laser damage on entrant surface of CaF_2 window, AR-coated with MgF_2/MgO; 114.5 J/cm^2 (80X).

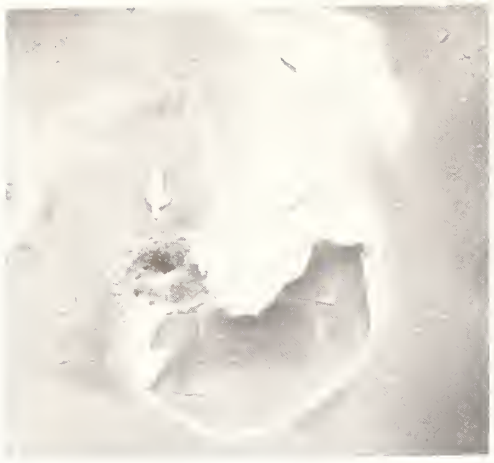

Figure 24. Detail of window damage site (Figure 23) showing melted material and thermally induced fracture of coatings; note polishing scratches, 114.5 J/cm^2 (700X).

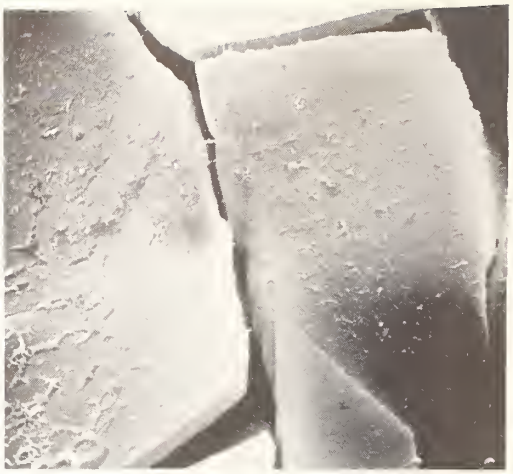

Figure 26. Detail of fractured area shown in Figure 24. $MgF_2/MgO/CaF_2$, 114.5 J/cm^2 (2100X).

Figure 25. Detail of melted area shown in Figure 24. $MgF_2/MgO/CaF_2$, 114.5 J/cm^2 (2100X).

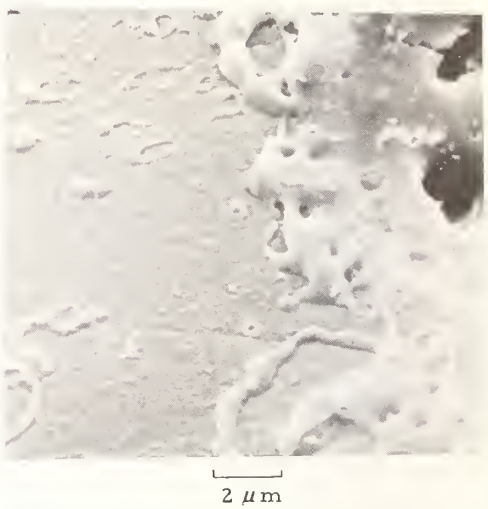

Figure 27. Detail of interface between melted area and undisturbed film shown in Figure 24. $MgF_2/MgO/CaF_2$, 114.5 J/cm^2 (5900X).

COMMENTS ON PAPER BY KRAATZ

In response to a question regarding the influence of the substrate surface quality on the damage results, the speaker responded that one would expect that if any influence was to be seen from the substrate quality it should be most evident in coatings of two layers, but probably would not be as evident in coatings of eight layers or more. However, since in these experiments no change in the damage threshold from two-layer to eight-layer coatings was observed, it was felt that the substrate surface quality and material was not playing a role in determining the surface damage threshold. This was consistant with the fact that the coatings employed were those that exhibited a rather low threshold for damage. It was felt that the only circumstances under which the influence of the substrate would be felt would be in the case of coatings of a few layers of such composition that the damage threshold in the film structure itself was high compared to the damage threshold of the substrate material. The speaker felt that the tendency to damage in an imperfect substrate would not be reduced by the filling of substrate surface imperfections by the coating material.

Pulsed CO_2 Laser Damage Studies of Windows and Window Coatings*

A.I. Braunstein, V. Wang, M. Braunstein, J.E. Rudisill, and J. Wada

Hughes Research Laboratories
3011 Malibu Canyon Road
Malibu, California

A study was made of damage thresholds and damage morphology for KCl, ZnSe, and CdTe windows subjected to a pulsed CO_2 TEA laser. Damage to KCl and CdTe was initiated at the surfaces while ZnSe windows were found to fail due to explosion of inclusions in the bulk. For As_2S_3 passivated KCl or ThF_4/As_2S_3 antireflection coated KCl, or BaF_2/ZnS antireflection coated ZnSe the damage morphology was the same as for uncoated windows — failure was not initiated by the coatings. For the two antireflection coating designs studied electric field distributions are shown, and their use in choosing between alternate designs is explained.

Key Words: CO_2 laser damage, damage thresholds, laser windows, window coatings, KCl, ZnSe, CdTe.

1. Introduction

In this paper we report preliminary data on pulsed CO_2 laser damage thresholds and damage morphology for some coated and uncoated 10.6 μm windows. The windows chosen — KCl, ZnSe, and CdTe — are those which presently appear to be the most favorable candidates for high power CO_2 laser windows. The coatings chosen are among those currently under investigation for use as low absorption passivation and antireflection coatings on these windows. For the two antireflection coating designs studied electric field distributions in the coatings are shown, and their use in choosing between alternate designs is explained.

2. Laser Damage Test Facility

The work reported here was performed using a test facility for pulsed laser damage which is described in greater detail elsewhere.[1] The laser is a uv preionized TEA laser which has a germanium etalon output coupler. The output has a single transverse TEM_{00} mode but shows evidence of longitudinal mode beating in its temporal response when measured with a photon drag detector. The pulse has a leading edge spike of approximately 200 nsec duration followed by a longer period at lower power. When expressed in terms of an equivalent rectangular pulse the width is approximately 600 nsec.

3. Determination of Damage Thresholds

For the single mode tests the sample was placed at the focus of a 130-cm mirror for damage thresholds lower than 6 J/cm^2 or a 25-cm germanium lens for thresholds between 10 and 75 J/cm^2. The output power of the laser was varied by varying the discharge voltage. (For some early multimode tests, which are also reported, the laser output was held constant while the sample was moved with respect to the focal point of the lens to vary the power on the sample.)

The damage thresholds were determined by observation of the occurrence of visual damage with a 7 to 70x stereo microscope during illumination of the samples with repetitive pulses at a rate of approximately one per second. The samples were mounted on either a rotation or translation stage so that a new area could be exposed to testing as required. The laser power level was increased until

*This investigation was partially supported by Air Force Contract No. F29601-72-C-0132 under the direction of Capt. M.J. Soileau and Capt. J. Buckmelter of the Air Force Weapons Laboratory, Kirtland Air Force Base.

[1] V. Wang, et al., this proceedings.

damage was seen to occur at a given location; adjacent areas were then tested at both higher and lower power levels. Later examination at higher magnifications was used to confirm the results.

The most appropriate means of reporting the damage thresholds is dependent on the nature of the damage mechanism in a given case. To avoid confusion caused by the complex pulse shape the thresholds are reported here in terms of the total energy density in the pulse. An average power threshold can be determined by considering the total energy density to have been uniformly distributed over the duration of the 600 nsec equivalent rectangular pulse. The peak power is approximately eight times higher than the average and occurs over a period of approximately 5 nsec due to the effect of the longitudinal mode beating.

4. Experimental Results

4.1 KCl

Several samples of KCl grown at Hughes Research Laboratories (HRL) by a reactive atmosphere process, as well as several commercial samples, were tested. All samples were polished on a flannel lap with either Linde A or Linde B abrasive and methanol. Figure 1 shows scanning electron micrographs of typical polished surfaces. In each case the surface roughness is characteristic of the size of the polishing agent.

Experimental results for the coated and uncoated samples tested are shown in table 1. It can be seen that the thresholds are significantly higher for the HRL crystals. This can be either because of their better quality (note the difference in absorption) or the fact that they have better surfaces (see figure 1). In the first four cases shown in table 1 failure was by the formation of random surface pits in the central region of the incident laser beam. When a coating was present, failure occurred at the KCl-coating interface. This is illustrated by figure 2, which shows a typical damaged region on HRL sample B24-8 at 650x. The lighter colored spot around each pit is due to the separation of the As_2S_3/ThF_4 antireflection coating from the KCl surface — in most cases the films are intact.

Table 1. Pulsed CO_2 Laser Damage — KCl

Sample	Polishing Agent	Coating	Absorption		Damage Threshold, J/cm^2
			Window, cm^{-1}	Coating, %/Surface	
HRL B24-6	Linde B	None	0.00078	—	> 75
HRL B11-11	Linde B	None	0.0007	—	>75
HRL B24-8	Linde B	As_2S_3/ThF_4 a.r.	0.00096	0.19	31
Optovac 69	Linde A	As_2S_3/ThF_4 a.r.	0.0015	0.80	6 to 10
Optovac 1-14-72	Linde A	$\lambda/2$ As_2S_3	0.024	0.22	12 (uncoated) >27 (coated)

For the last sample in table 1, failure in the uncoated region occurred by an explosive removal of a portion of the surface. A broad crater approximately 100 μm deep and an extensive fracture zone were left behind. In the area protected by a $\lambda/2$ As_2S_3 passivation coating the testing was terminated at 27 J/cm^2 when a change in the appearance of the coating occurred. Later examination, under higher magnification, showed that no damage had occurred. The regions which had been illuminated by the laser at 27 J/cm^2 were found to have increased significantly in reflectance at visible wavelengths and showed less structure than surrounding regions. A similar behavior has also been found in multilayer dielectric reflectors which have As_2S_3 outer layers.[1]

4.2 ZnSe

Three polycrystalline ZnSe samples grown by chemical vapor deposition were tested. The results are shown in table 2. The inclusions referred to in the table are apparently voids which are surrounded by a shell of zinc or zinc-rich ZnSe so that they appear black (heavy means difficult to see through, light means inclusions are hard to find by visual inspection). The failure mode in all cases

was by explosion of inclusions either near the surface or internal to the window. The inclusions were observed to first grow slowly in size on succeeding laser pulses and finally to explode to produce a spherical central region surrounded by a planar fracture zone of large extent. Damage probably occurred at a lower threshold in antireflection coated Sample R-7 than in Sample 41 due to higher internal electric fields in the coated sample.

Table 2. Pulsed CO_2 Laser Damage — ZnSe

Sample	Coating	Absorption		Damage Threshold, J/cm^2	Comments
		Window, cm^{-1}	Coating, %/Surface		
Raytheon 417	——	0.02	—	5.6	Heavy inclusions — up to 125 μm diameter. Failure mainly by surface cratering; some internal explosions
Raytheon 41	——	0.009	—	41	Intermediate inclusions — up to 100 μm diameter. Failure by surface cratering and internal explosions.
Raytheon R-7	BaF_2/ZnS a.r.	0.0041	0.27	27	Light inclusions — up to 50 μm diameter. Failure by internal explosion. Coating undamaged except where shock wave from subsurface explosion reached surface.

4.3 CdTe

Four HRL CdTe windows were tested with the results shown in table 3. In the uncoated regions random craters were produced, inside which the CdTe had melted, on both surfaces of the window. Figure 3 shows two typical craters at 650x for sample 228-7.

When $\lambda/4$ CdTe films were deposited on two of these CdTe windows in order to study the damage mechanisms in the films, a new failure mechanism was observed. The film separated from the substrate and subsequently tore away completely in the regions of highest electric field. Figure 4 shows and example of this at 100x for sample 228-7. The fringe pattern is apparently due to interference effects caused by multiple reflections from the rear surface of the window. The spacing and direction of the fringes agree with calculated values based on the measured wedge angle and direction in the window. However, this interpretation is marred by the observation of a two dimensional pattern with the same periodicity which occurs near the damage threshold as shown in figure 5. The circular spots are regions of the film which have separated from the substrate but not yet torn away. The fully developed fringe pattern can be seen to be due to the merging of this spot pattern along lines, but no explanation of its cause is available.

5. Electric Field Distributions in Antireflection Coatings

Computer calculations have been made of the electric field and absorption distributions in antireflection coatings for windows both as an aid in the selection of coating designs and to aid in the interpretation of laser damage data. The electric field distributions are shown here as an example for the two antireflection coatings included in the experimental data.

For the two layer antireflection coatings of the type used here (V-coats) there are generally two equivalent solutions for the layer thicknesses which will provide a zero of reflectance at the design wavelength (provided a solution exists at all). The electric field amplitude versus distance from the air interface for the two solutions for an As_2S_3/ThF_4 antireflection coating on KCl is plotted in figure 6. The thicknesses at which the layers terminate are marked by bars on the curves. In this case the two solutions are of almost equal total thickness, but solution 2 has a region of lower field

which is also occupied by As_2S_3 rather than ThF_4, which has a higher absorption coefficient, as in solution 1. This leads to approximately 30% lower total absorption for solution 2, if both are made with films with the same absorption coefficients, and it was therefore chosen for the experimental work.

Table 3. Pulsed CO_2 Laser Damage — CdTe

Sample	Coating	Absorption		Damage Threshold, J/cm^2	Comments
		Window, cm^{-1}	Coating, cm^{-1}		
HRL CdTe 176-2A	——	Not Measured	—	2.1 (Multimode)	Random surface pitting with melting of CdTe.
HRL CdTe 225-4	——	0.04	—	2.0 (Multimode)	Same as 176-2A.
HRL CdTe 228-7	None	0.0034	—	2.6	Damage similar to 176-2A.
	$\lambda/4$ CdTe	0.0034	~2	1.2	Film separates near threshold. Tears off above threshold; no melting.
HRL CdTe 225-6	None	Not Measured	—	>2.6	Same as 228-7.
	$\lambda/4$ CdTe	Not Measured	~2	1.2	Same as 228-7.

A plot of electric field versus depth for BaF_2/ZnS antireflection coatings on ZnSe is shown in figure 7. For this case solution 2 has much higher physical thickness and absorption, and has a region in which the electric field amplitude is higher than the free space field outside the coating. Therefore, solution 1 was chosen for the experimental work.

6. Summary

Pulsed CO_2 laser damage studies have been performed for KCl, ZnSe, and CdTe 10.6 μm windows and some representative window coatings.

KCl grown by the RAP technique was shown to have a potential damage threshold greater than 75 J/cm^2. As_2S_3/ThF_4 antireflection coatings for KCl also had a relatively high threshold, and a $\lambda/2$ As_2S_3 passivation layer significantly increased the threshold of a rather poor crystal. The dominant failure mechanism was pitting of the KCl surface which was accompanied by coating separation for the coated window samples.

ZnSe failed by explosion of absorbing inclusions at thresholds which depended on the inclusion density. A BaF_2/ZnS antireflection coating on ZnSe did not fail at energy densities which produced bulk failure via the inclusion mechanism.

CdTe was found to fail at low energy densities (~2 J/cm^2) by surface melting and crater formation on both surfaces of the window.

Examples of theoretical plots of electric field distributions in antireflection coated windows were shown, and their use in selecting between alternate antireflection coating designs was pointed out.

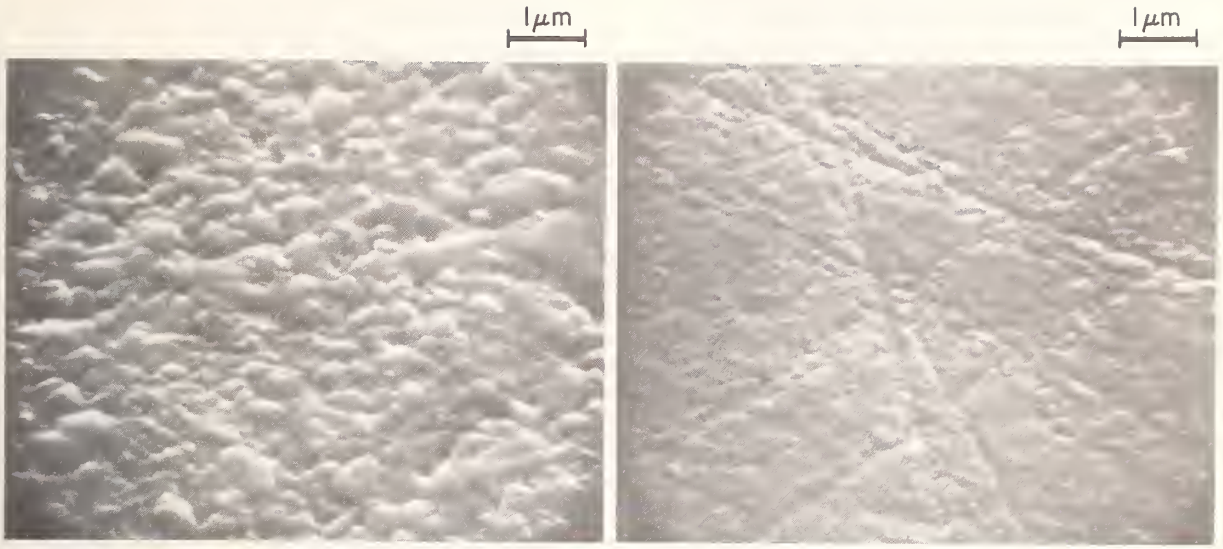

Figure 1. Scanning electron micrograph of typical polished KCℓ surfaces.

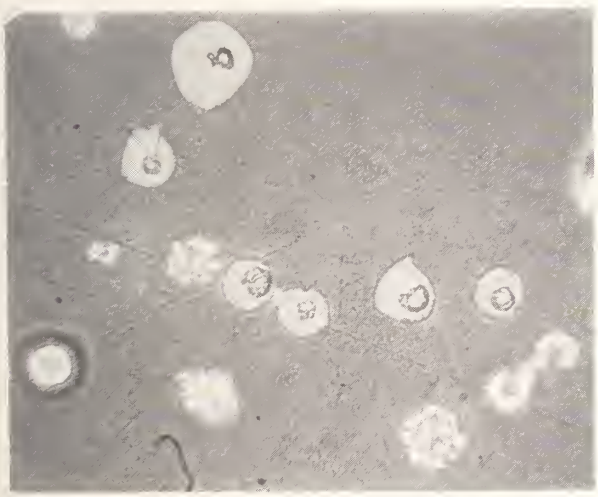

Figure 2. 650x optical micrograph of damage near threshold in sample HRL B24-8.

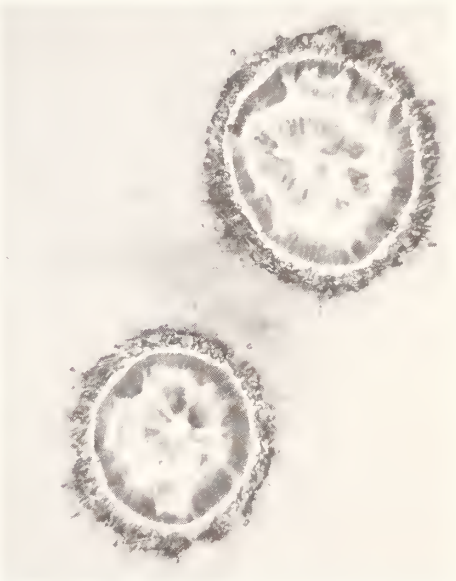

Figure 3. 650x optical micrograph of two typical craters near center of illuminated area of sample 228-7 (uncoated).

Figure 4. 100x optical micrograph of damage region on sample 228-7 coated with λ/4 CdTe film.

Figure 5. 125x optical micrograph of damage near threshold on sample 228-7 coated with λ/4 CdTe film.

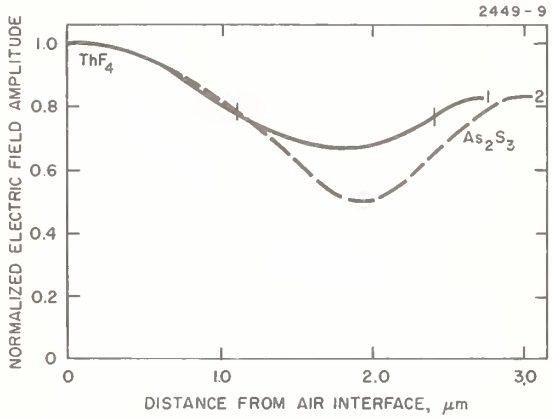

Figure 6. Electric field amplitude versus depth for As_2S_3/ThF_4 antireflection coatings on KCℓ.

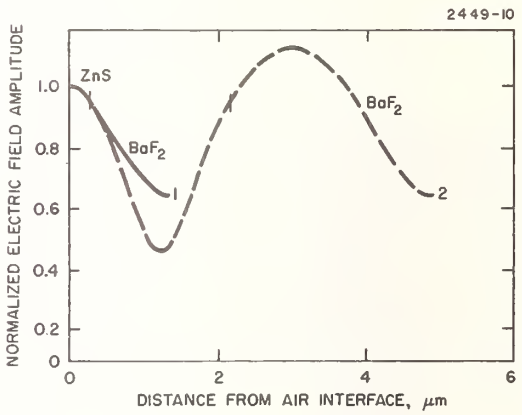

Figure 7. Electric Field amplitude versus depth for BaF_2/ZnS antireflection coatings on ZnSe.

NO COMMENTS ON PAPER BY BRAUNSTEIN.

Pulsed CO_2 Laser Damage Studies of Metal and Dielectric Coated Mirrors*

V. Wang , A. Braunstein, M. Braunstein,
J. E. Rudisill, J. Y. Wada

Hughes Research Laboratories
Malibu, California 90265

Damage thresholds measured using single transverse mode 10.6 μm radiation are reported for several metal and dielectric enhanced multilayer mirrors ($CdTe/ThF_4$, ZnTe/ZnS, As_2S_3/KCl). Typical values are in the range of several J/cm^2 for semiconductor thin films to over 30 J/cm^2 for wide bandgap dielectric thin films (pulse length 0.6 μsec). These single mode values are considerably lower than the corresponding multimode results. Scanning electron microscope, X-ray microprobe, and power dependent absorption measurements were performed in order to examine the nature of mirror surfaces before and after laser damage. Several models for potential damage mechanism (thermal, inclusion, dielectric, etc.) have been investigated. A comparison of the experimental and theoretical results has provided the basis for a possible damage model.

Key Words: As_2S_3, CdTe, dielectric reflector, inclusions in dielectrics, KCl, pulsed CO_2 laser damage, thin film damage, ZnTe.

1. Introduction

In this paper we report preliminary data on pulsed CO_2 laser damage thresholds and damage morphology for several high reflectivity multilayer dielectric enhanced reflectors and their individual films. These thresholds are compared with several analytical thermal models, and it presently appears that the damage mechanism for narrow bandgap semiconductors is most likely avalanche impact ionization. The damage tests were carried out using a single transverse mode TEA laser to obtain a more accurate estimate of the true on-axis energy density.

Using a multimode 10.6 μm TEA laser, our previous tests ranked metal mirrors, thin film coated metal mirrors and multilayer dielectric mirrors in order of decreasing damage resistance. Results presented here using a single transverse mode 10.6 μm TEA laser indicate a lower damage threshold than the multimode results, in contrast with previous results at shorter wavelengths, where damage thresholds were higher single mode.

2. Experimental Conditions

The laser induced damage studies were carried out with the aid of a UV preionized TEA laser at 1 pps or less for the most part and the threshold was determined primarily by visual observation. Tests were carried out both in air and in vacuum. TEM_{00} operation was achieved by a 240 cm optical cavity using an adjustable aperture to control transverse modes. The discharge consisted of a 50 x 5 x 2.5 cm UV preionized transverse discharge operating at 550 Torr, using a 1:1:8 mixture of CO_2:N_2:He. An apertured central region of about 0.6 cm is used with a flat Ge resonant reflector output coupler as shown in figure 1. The output was variable from 0.03 mJ to 180 mJ by controlling the discharge voltage. Due to small changes in temporal pulse shape at low energies, pulse energies below 0.03 mJ were not used.

*This investigation was supported by Air Force Contract No. F29601-72-C-0132 under the direction of Capt. M. J. Soileau, Capt. J. Buckmelter, and Capt. T. Saito of the Air Force Weapons Laboratory, Kirtland Air Force Base.

For low energy densities, up to about 6 J/cm^2, a long focal length (130 cm) off-axis spherical reflector focuses the beam to a 2-mm spot size. A short focal length system is used to achieve higher energy densities. A partially reflecting Ge flat (R = 50%) is substituted for the focusing reflector shown in figure 1 and the beam is brought to a focus by placing a 25-cm Ge lens in the sample chamber to focus the beam to a 400-μm spot size. With this system, energy densities of 10 to 75 J/cm^2 are available.

The focused output pulse was found to have a gaussian diffraction-limited spatial profile with no truncation apparent up to an order of magnitude below the peak energy density. Figure 2 is a typical semi-log plot of beam energy versus recorded diameter squared in the focal plane where the sample is located. (This procedure for spot size determination is more fully discussed in Ref. [1]).[1] The slope of the line gives the 1/e diameter of the beam and has remained linear and within a few percent of the calculated value.

A reflecting calorimeter which absorbs ~10% of the incoming beam upon an electroless nickel coated Cu mirror determines the energy in each pulse at the focal plane of the 130 cm reflector. A 40% error in energy density threshold measurements is presently considered possible due to uncertainties in calorimetric standards (any corrections would result in numerically higher thresholds). The pulse length has been determined by intercepting the beam with either a pyroelectric detector or a photon drag detector. Figure 3 shows their appearance in each detector, with the fine structure of longitudinal mode beating visible in figure 3c, using a photon drag detector and 500 MHz oscilloscope. The peak electric field due to this mode beating is about 2.8 times higher than the average electric field in figure 3a, resulting in a greater uncertainty in peak power densities (peak power estimated ~8 times average power).

Using figure 3a, an equivalent pulse length is defined by a rectangular pulse of enclosed area equal to the actual pulse area, and of height equal to the maximum pulse height.

3. Test Results

3.1 Uncoated Metal Mirrors

Two uncoated metal mirrors were tested for comparison with previous multimode tests and their damage thresholds are summarized in table 1. These mirrors represent some of the best examples of damage resistant mirrors available at the beginning of this investigation. Near the damage thresholds of these mirrors the power densities are sufficiently high to induce air breakdown simultaneously with mirror failure. To determine if mirror damage was the cause or result of this air plasma, tests were also made in a vacuum (≤1 Torr). Figure 4 illustrates the difference in damage morphology for the two cases of a test in air and a test in vacuum. It appeared that the air plasma shielded the mirror if the focal point was located in front of the mirror, but with the mirror at the focal point, air and vacuum damage thresholds remained the same.

a. CdTe

One of the lowest measured absorption coefficients is to be found in CdTe single crystals and thin films, yet CdTe exhibits a relatively low damage resistance. In these thin films, variations in starting materials, deposition techniques, measured absorption, substrate, interface, film thickness, and number of layers have not revealed any appreciable improvements in damage resistance. Table 2 summarizes some of these tests, where the power density quoted again represents the averaged power (peak power ~8 times higher). The damage occurs in localized microcraters whose appearance is identical to previous multimode tests. Figure 5 illustrates a typical microcrater in a λ/2 CdTe film.

b. ZnTe

Damage in this material is very similar to damage seen in CdTe, and damage thresholds are similarly low. Table 3 summarizes a few threshold measurements and figure 6 illustrates a typical microcrater in a multilayer mirror.

---

[1] Figures in brackets indicate the literature references at the end of this paper.

Table 1. Damage thresholds for metal mirrors

Substrate and Sample No.	Coating	Absorption	Measured Damage Threshold		Comments
			Energy Density J/cm^2	Power Density* MW/cm^2	
Mo HRL-47	None	~2%	35	58	Test in air and vacuum
Cu 11-20-72-T	None	~2%	35	58	Test in air and vacuum

*Based upon τ = 0.6 μsec

Table 2. Damage thresholds for CdTe mirrors and coatings

Substrate and Sample No.	Coating	Absorption	Measured Damage Threshold	
			Energy Density J/cm^2	Power Density* MW/cm^2
Cu 10-2-72	λ/2 CdTe	1.04% total 0.02% film	1.0	1.7
Cu 4-27-73	Sputtered λ/2 CdTe	2.16%	1.0	1.7
Cu 10-11-72-1-K	ThF_4/CdTe	0.52%	2.4	4.0
Cu 7-18-72-1	ThF_4/CdTe	0.39%	1.4	2.3
Cu 3-30-73	Ag/$(ThF_4$/CdTe$)^3$	0.28%	1.0	1.7
Cu/E-Ni 12-27-72-K	$(ThF_4/CdTe)^2$ $(BaF_2/CdTe)^2$	0.45%	1.0	1.7
Cu/E-Ni 12-28-72-K	Ag/ThF_4/CdTe/BaF_2 /CdTe/ThF_4/CdTe	0.49%	1.5	2.5

*Based upon τ = 0.6 μsec

Table 3. Damage thresholds for ZnTe mirrors and coatings

Substrate and Sample No.	Coating	Absorption	Measured Damage Threshold	
			Energy Density J/cm^2	Power Density* MW/cm^2
Cu/E-Ni 1-15-73-B	Al + λ/2 ZnTe	0.97% film 2.33% total	1.7	2.8
Cu 12-5-72B	Al/(ZnS/ ZnTe)	1.07%	1.25	2.0
Cu/E-Ni 1-8-73-B	Al/$(ZnS/ ZnTe)^2$	0.85%	2.4 to 3	4 to 5

*Based upon τ = 0.6 μsec

c. ThF_4

In this material, process control can be responsible for large variations in absorption. For high absorptions, the damage threshold can be low and the mode of failure, in a single film, is cracking and separating from the substrate. Better quality films exhibit much higher damage resistance. For example, the first entry in table 4 yielded a relatively high absorption coefficient, when compared with the films necessary to obtain the high reflectivities observed in table 1; yet the damage threshold of this film is comparable with that of the substrate. Figure 7 illustrates the type of damage which occurs in relatively low absorption ThF_4. Damage first occurs as a discoloration of the ThF_4, and in this case the presence of the interference rings are indicative of an additional interference effect due to the presence of inclusions. These rings appear to be due to the collective interference of the incident wave, a scattered wave propagating in the mode of waveguide propagation near cutoff, and the reflected wave. The fringe spacing is about 10 μm. Note also that the presence of these inclusions did not precipitate a general failure of the film.

Table 4. Damage thresholds for ThF_4 Coatings

Substrate and Sample No.	Coating	Absorption	Measured Damage Threshold		Comments
			Energy Density J/cm^2	Power Density* MW/cm^2	
Cu/E-Ni/Al 11-20-72-T	λ/2 ThF_4	2.44% total 0.88% film	32	50	
Cu 2-2-72-K	λ/4 ThF_4	2.27 total	>6	>10	Tested both in air and vacuum
Cu 1-31-73	λ/4 ThF_4	2.59% total	1.2 to 6+	1.8 to 10+	
Cu 1-17-73-1K	λ/4 ThF_4	2.70%	2.5	4.2	
Cu 1-18-73-K	λ/4 ThF_4	3.57%	2.5	7.2	
Cu 1-5-73-K	λ/4 ThF_4	8.6% total	1.0	1.7	

*Based upon τ = 0.6 μsec

d. As_2S_3/KCl

The most promising mirrors tested to date consist of two wide bandgap dielectrics. Assignment of a damage threshold for these mirrors is deceptive due to an apparent "conditioning" that is observed with gradual power increase. Sudden flux increases above 5 J/cm^2 generated a visible plasma upon the surface. However, examination of the film indicated that it was intact and suffered no apparent damage. Gradual increases of flux above ~5 J/cm^2 did not cause a visible plasma, and fluxes could be raised to as high as 65 J/cm^2 before breakdown occurred by film discoloration, separation, and cracking (Table 5). Microscopic examination of these surfaces after exposure to fluxes above 5 J/cm^2 but below the damage threshold indicated only a decrease in the number of scattering centers, which creates an effect similar to firepolishing. Figure 8a illustrates the type of damage that occurs before the final threshold in figure 8b.

3.2 Comparison of Multimode and Single Mode Output

Table 6 compares the results of two thin film samples and a typical metal mirror which were tested multimode and single mode. The appreciable devaluation of energy density in single mode tests is partly due to the shorter pulselength, but the difficulty of assigning a multimode spot size probably constitutes the primary factor. This difficulty is illustrated for a hypothetical profile in figure 9. Beam energy is measured by a calorimeter of large aperture, which measures the total energy in the beam. This would be equivalent to integrating in space as well as time all of the energy under curve A of figure 9, including the energy in the low intensity wings. The usage of a Plexiglas burn pattern to determine the spot size of the beam can result in a small spot size if the

plexiglas burn threshold is close to the test sample damage threshold. When the total beam energy is divided by this small spot size, the numerical value of energy density so obtained can far exceed the true energy density on axis. This discrepancy is a function of both the relative damage thresholds and the pulse shape. The gaussian profile of a TEM_{oo} beam makes the assignment of characteristic beam diameter a more quantitative measure of the on-axis energy density. Due to longitudinal mode beating, the temporal history of this gaussian profile can still show rapid fluctuations in amplitude and comparison with future single longitudinal mode damage tests can result in an appreciable change in damage thresholds for electric-field-dependent (power dependent) breakdown mechanisms. For such materials, the measured threshold energy density of damage with a single longitudinal mode, TEM_{oo} laser might be as much as 8 times higher.

Table 5. Damage thresholds for As_2S_3/KCl mirrors

Substrate and Sample No.	Coating	Absorption	Measured Damage Threshold		Comments
			Energy Density J/cm^2	Power Density* MW/cm^2	
Cu/E-Ni 2-2-73-T	Al/(KCl/As_2S_3)^2	1.44%	2 to 5+	3.2 to 8+	"Conditions with gradual power increase
Cu/E-Ni 3-9-73-T	Al/(KCl/As_2S_3)^3	0.23%	50	80	"Conditions with gradual power increase
Cu/E-Ni 2-23-73-T	Al/(KCl/As_2/S_3)^4	0.23%	65	110	"Conditions with gradual power increase

*Based upon τ = 0.6 μsec

Table 6. Multimode versus single mode comparison

Sample	Damage Threshold (J/cm^2)	
	Multimode $\tau \sim 2.2$ μsec	Single Mode τ = 0.6 μsec
λ/4 ThF_4 + λ/100 CdTe	7 to 14	0.87
Cu/ThF_4/CdTe Mirror	18 to 25	1.4
Cu Mirror	~200 J/cm^2	35

4. Discussion of Breakdown Models

4.1 Electromagnetic Field Distribution

Before an appraisal can be made of the damage mechanism within dielectric enhanced mirrors, the absorbed energy distribution within the mirror must be known. An approximate solution can be obtained by assuming a lossless dielectric and substrate to calculate the electric field distribution. The absorbed energy distribution can then be calculated on the basis of the measured absorptions in individual film layers. For the low absorption materials used in this program, a comparison with an exact computer aided solution proves this approximation to be quite accurate.

A typical CdTe/ThF_4 3-pair mirror design is analyzed in figure 10. The peak values of electric field decrease nearly exponentially, with a factor of 2 reduction per successive pair of CdTe/ThF_4 coatings. The peak intensity in the third dielectric pair (adjacent to the mirror substrate) is reduced to about 1/20 of the peak intensity found outside the multilayer coating. In addition to illustrating the minimal effect of absorption in the metal substrate of a high reflectivity dielectric mirror, the decrease to almost zero of the electric field at the outer surface would tend to minimize surface effects.

4.2 Thermal Responses of the Dielectric Enhanced Mirror

This electric field distribution is used to roughly calculate the thermal response of the mirror as a function of pulselength. Typical values of absorption have been assumed in figure 11 and the maximum temperature rise of the dielectrics has been calculated for the assumption of three differing thermal impedances, and an incident flux of 100 J/cm^2. The curve (A) represents a case in which the thermal barrier between the adjacent pairs is so high that thermal diffusion of energy between pairs due to conduction is assumed negligible in the range of pulsewidths indicated. The maximum temperature rise in this case occurs in the first dielectric pair and reaches about 230°C. In curve B, it is assumed that an infinite thermal barrier exists only between the third dielectric pair and the mirror substrate. The absorbed energy is partially diffused among the three dielectric pairs, with the peak temperature in the outer film increasing to an asymptotic value of 1/3 that of Case A. The third curve (C) represents a condition in which good thermal contacts exist between all interfaces including the one to a heat sinked metal substrate. The heat conduction between adjacent layers and the mirror substrate becomes an important factor for pulselengths longer than a few microseconds. For a short pulselength operation (less than 2 μsec), a reduction in the peak temperature rise is small (less than 30%). This reduction increases to a significant level (≈70%) for 10 μsec or longer pulselengths.

For CdTe mirrors, damage occurs at incident energy densities of about 1 J/cm^2, so the corresponding temperature rise is about 2°C. Thus, some other mechanism must be found to account for this relatively low damage threshold. As_2S_3/ThF_4 mirrors, with thresholds as high as 65 J/cm, and very low thermal conductivity in the film materials, might be expected to reach temperatures of several hundred degrees with a pulselength dependence closer to Curve A. Thermal stresses resulting from the large temperature gradients possible in this case might have caused the multilayer film delamination observed in AS_2S_3 in figure 8b.

4.3 Inclusion Model

The low damage thresholds/damage morphology of CdTe and ZnTe mirrors strongly suggest a model containing local absorption centers or local regions of film weakness. A rough transient analysis of the effects of localized absorption sites has been made, in a manner similar to references [2], [3], [4] and [5]. Three cases have been treated, as indicated in figure 12. Case A consists of a thin absorbing layer of material within a dielectric film of the same thermal conductivity and index as the dielectric, with a thickness much less than the thermal diffusion length. This case could model the effect of an absorbing interface between layers of high and low index, where the field in the mirror would be highest. Case B considers a spherical or disc shaped metallic absorbing inclusion, with a thermal conductivity which can be either equal ot the surrounding dielectric (Case B') or infinite (Case B). Case C models a localized spherical or disc dielectric inclusion where the absorption is assumed to take place within the bulk of the particle. It is assumed that the physical constants of the highly abosrbing dielectrics in figure 12(a) and 12(b) are identical to that of the substrate material except for the attenuation constant. As a simplifying assumption, electric field enhancement within a mirror is neglected and the absorption of the metallic particles is assumed to be a constant fraction of the incident radiation, proportional to area of the particle over the particle sizes considered.

Typical computational results obtained for a CdTe thin film substrate are summarized in figure 13. The maximum temperature rises produced on the surface of an impurity imbedded in a CdTe substrate are plotted as a function of the impurity characteristic dimensions (W and R). A typical set of laser parameters (a laser pulse length of 1 μsec and an intensity of 20 J/cm^2) in the substrate material is used.

A number of observations could be made from the first order calculations shown in figure 13. Since the average absorption of CdTe thin films is measured to be approximately 1 cm^{-1}, Case A can be excluded as a reasonable damage mechanism. For instance, if the inclusion layer is assumed to absorb 1000 cm^{-1}, then it can be no thicker than 0.01 μm, which results in a small temperature rise of about 10°.

Case B represents a more promising candidate for a damage mechanism capable of triggering self-destruction of the CdTe. Particles larger than 0.5 μm are dangerous in either Model B or B' and yet are smaller than a film thickness and just below optical resolution. An absorbing nonmetallic inclusion of 1000 cm^{-1} would also generate results similar to Case B.

Since an incident flux of around 20 J/cm^2 is required in this model to generate temperatures reasonably expected to cause some form of damage, this model also encounters difficulty in explaining the damage thresholds seen in CdTe. Inclusions large enough to cause damage would be visible to the optical microscope, larger than a typical film thickness, and of very high absorption. The predicted effects are, however, in good agreement with the damage seen in ZnSe, where the inclusions are as large as 100 μm and damage occurs near 30 J/cm^2 (Ref. 6).

4.4 Examination by SEM and X-ray Microprobe Analysis

Scanning electron micrographs and x-ray microprobe analysis of typical damage sites near threshold have been made. Figure 14 shows a typical microcrater in a two-layer $CdTe/ThF_4$ mirror by a gaussian beam much larger in diameter than the crater, viewed at an oblique angle in a SEM. Figure 14(b) shows a closeup of the characteristic crater often found within the main crater, showing the molten appearance of the underlying ThF_4, and figure 15 shows a sequence of overhead views of a typical microcrater in the x-ray microprobe machine. The central crater suggested itself as the nucleating site for the damage, so an analysis of the elements constituting the crater were made using the characteristic x-ray emission stimulated by the electron beam. Figure 15(a) shows a SEM photo for reference, and succeeding photos are the analysis for thorium, cadmium and tellurium.

These photos provide further verification that the CdTe is the first layer to damage. Further, the rim of the crater appears to be composed of a majority of tellurium. However, there is no unusual concentration of Cd or Te in the center of the crater nor any marked absence of these materials to indicate the presence of a remaining large inclusion of some other element.

In similar manner to the X-ray elemental analysis illustrated in these figures, line scans of undamaged regions of the film have been made, concentrating on visible scattering centers, but no foreign elements have been discovered. The resolution limit of this technique is about 1 μm. Thus, while the evidence presented here is far from conclusive, no evidence of metallic absorbing inclusions has been found in these CdTe films. Techniques to improve the resolution of the X-ray Microprobe scanning technique used here, and more thorough examination of undamaged films may yet reveal some small local inhomogeneity which nucleates the damage site in a process not yet understood by simple thermal considerations.

4.5 High Power Absorption Measurements

The presence of semiconductor film materials in some high reflectivity mirror designs in this program suggests an experiment to measure absorption coefficient as a function of incident power. Absorption measurements have been made in three ranges in $CdTe/ThF_4$ mirrors up to the damage threshold, and no evidence of thermal runaway or observable nonlinear absorption has been found up to the damage threshold. Absorption measurements were made in the following ranges of power density:

- 20 W/cm^2
- ~3 kW/cm^2
- 0.3-3 MW/cm^2

Measurements are routinely made at the lowest power density using a cw laser. Higher power cw measurements at ~3 kW/cm^2 using a focused beam revealed no significant changes in reflectivity nor did they indicate any significant variation with position. Pulsed absorption measurements at a pulse rate of 3 pps indicate fair agreement with lower power measurements. As summarized in figure 16, the damage threshold of the mirror is reached (as evidenced by light sparkling) before the absorption begins to rise. The observed absorption increase at values greater than the damage threshold is probably due to progressive exposure of the relatively high absorption electroless nickel substrate.

4.6 Dielectric Breakdown

Dielectric breakdown for most materials lies in the range of 10^6 V/cm, while our observed CdTe breakdown occurs at less than 10^5 V/cm. Nevertheless some form of electrical breakdown is now being considered for the low damage threshold found in CdTe and ZnTe. While the morphology of CdTe and ZnTe suggests some localized weakness in these polycrystalline films, that is not inconsistent with electrical breakdown. In addition, the damage seen in Ref. [6] strongly suggests that under certain conditions, a sharp homogeneous threshold can be obtained.

Several interesting observations in the literature can also be applied to the case of CdTe. The measured mobility of semiconductors generally implies an electron-lattice collision frequency comparable to the optical frequency. This fact should allow extrapolation of avalanche ionization measurements made at dc to optical frequencies by the Drude formula approximation. Thresholds for dc impact ionization and luminescence measured at HRL (Ref. [7]) in CdTe occurred at 12 kV/cm. Theoretical calculations as in reference [8] indicate a dc impact inionization of ~50 kV/cm. In addition, calculations and measured drift velocities in pure CdTe indicate that the onset of negative differential mobility occurs at around 12 kV/cm due to hot electron runaway. It is not presently

clear whether hot electron runaway is directly responsible for impact ionization or if some other collective form of instability is involved, but the experimental evidence clearly indicates that 12 kV/cm marks the onset of some nonlinear phoenomena.

Measured laser damage thresholds occur at an average electric field of about 20 kV/cm and a peak field of around 70 kV/cm. If a typical mobility of 200 cm^2/V-sec is assumed, and the equivalent dc field is calculated using the Drude approximation, the breakdown threshold for laser damage can be said to agree quite well with measured dc thresholds (equivalent field = 13 kV/cm). While the model for this damage mechanism is far from complete, the evidence presently available encourages further understanding of this phenomena.

5. Summary

The analytical thermal models investigated do not present a satisfying explanation of the damage seen in the semiconductor thin films. Power dependent dielectric breakdown is presently considered to be a more likely choice for the damage mechanism. The estimated electric field intensity in CdTe at the damage threshold appears to show good correlation to the measured thresholds for dc hot electron runaway effects. Further experiments to vary electron mobility and pulselength are under consideration.

The three classes of reflectors examined in this paper are summarized in table 7. The wide bandgap dielectrics such as ThF_4, As_2S_3 and KCl (as well as BaF_2, ZnS, ZnSe, and NaCl in reference [6]) demonstrate the highest damage resistance, to the extent of surpassing simple polished metal reflectors. II-VI semiconductor mirrors consistently demonstrate a low possibly "intrinsic" damage threshold in the range of 1 to 2 J/cm^2.

Table 7

Metal Reflector Cu and Mo	II-VI Semiconductor Films and Reflectors CdTe and ZnTe	Wide Bandgap Films and Reflectors As_2S_3, KCl, ThF_4
35 J/cm^2	1 to 2 J/cm^2	30 to 65 J/cm^2
τ = 0.6 μsec		

6. Acknowledgement

We wish to acknowledge the helpful discussions enjoyed with Drs. Lew Fraas and Tom McGill, and especially the able assistance of John Fitzgerald in the performance of many of these tests.

7. References

[1] Giuliano, C. R. and Tseng, D. Y., "Damage in Lithium Iodate with and without Second Harmonic Generation," this proceedings.

[2] Sparks, M. and Duthler, C. J., "Theory of Infrared Absorption and Material Failure in Crystals Containing Inclusions," this proceedings.

[3] Bennett, Herbert S., "Absorbing Centers in Laser Materials," J. Appl. Phys., 42, 2 (February 1971).

[4] Hopper, R. W. and Uhlmann, D. R., "Mechanism of Inclusion Damage in Laser Glass," J. Appl. Phys., 41, 10 (September 1970).

[5] Bliss, E. S., "Pulse Duration Dependence of Laser Damage Mechanisms," Proc. ASTM Symp. in Damage in Laser Materials, NBS, Boulder, Colorado (June 24-25, 1970).

[6] Braunstein, A. I., Wang, V., Braunstein, M., Rudisill, J. E., and Wada, J., "Pulsed CO_2 Laser Damage Studies of Windows and Window Coatings," this proceedings.

[7] Picus, G. S., DuBois, D. F., and Van Atta, L. B., "Influence of Ionized Impurity Scattering on Gunn Effect and Impact Ionization in CdTe," Appl. Phys. Lett., 12, 3 (February 1968).

[8] Picus, G. S., Van Atta, L., and DuBois, D. F., "Impact Ionization Pumped Laser in Polar Semiconductors," Final Report for Contract No. N00019-69-C-0099 (January 1970).

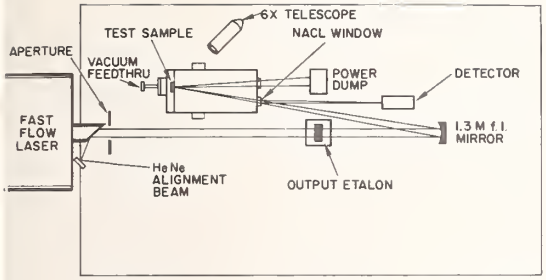

Figure 1. Test facility.

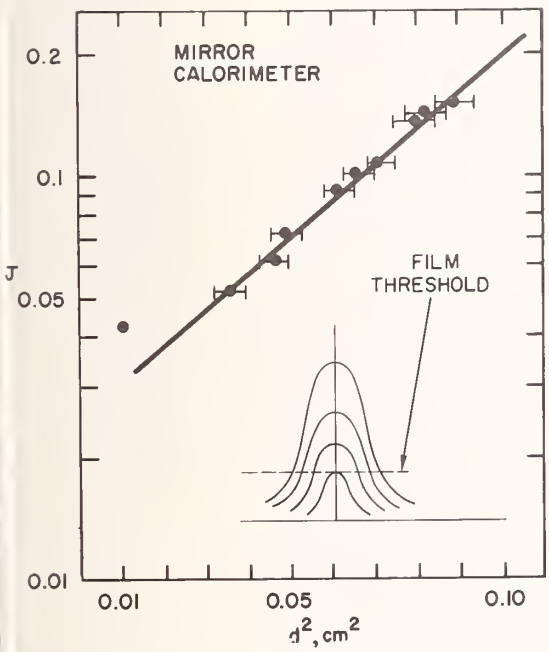

Figure 2. Beam spatial profile.

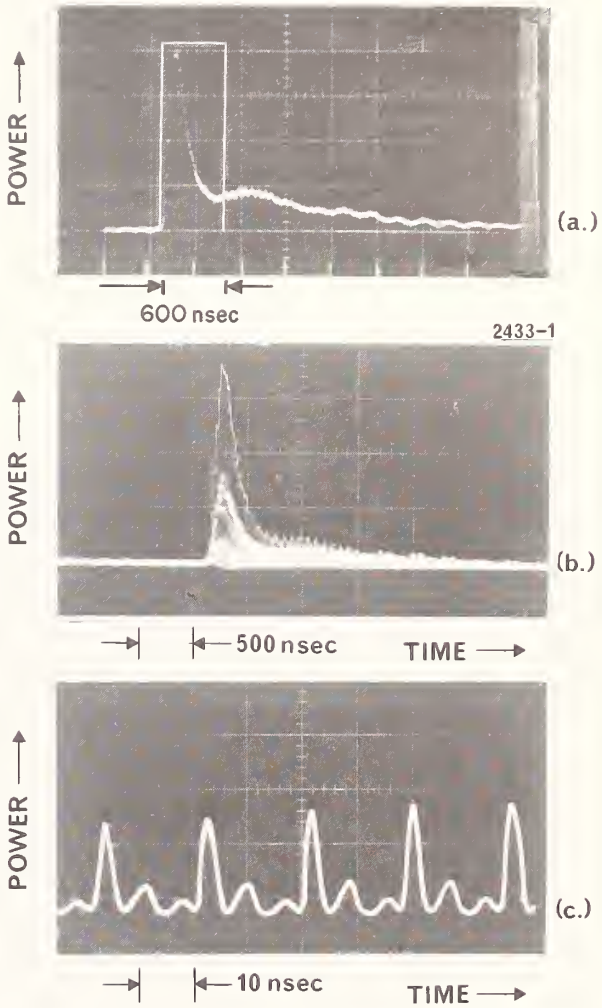

Figure 3. Temporal profile.

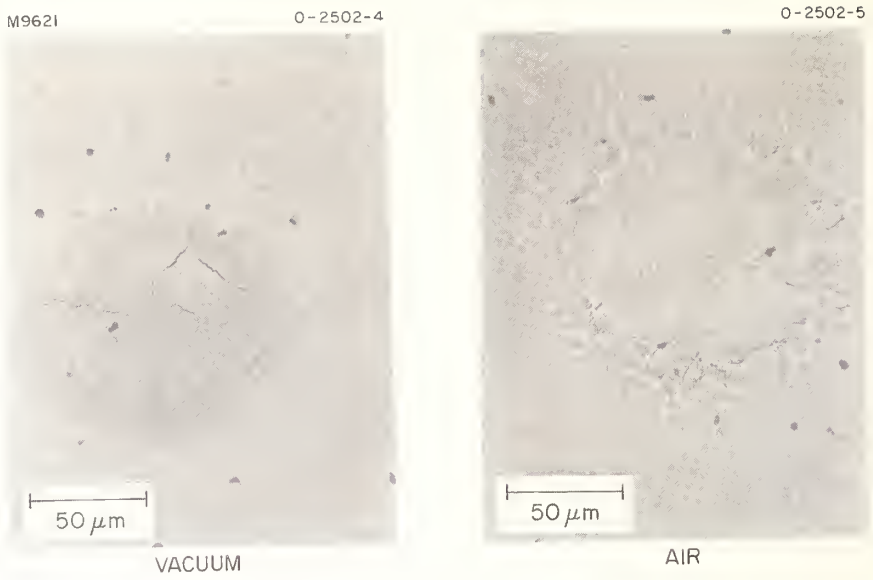

Figure 4. Damage in Mo mirror in air and vacuum.

Figure 5. λ/2 CdTe near damage threshold.

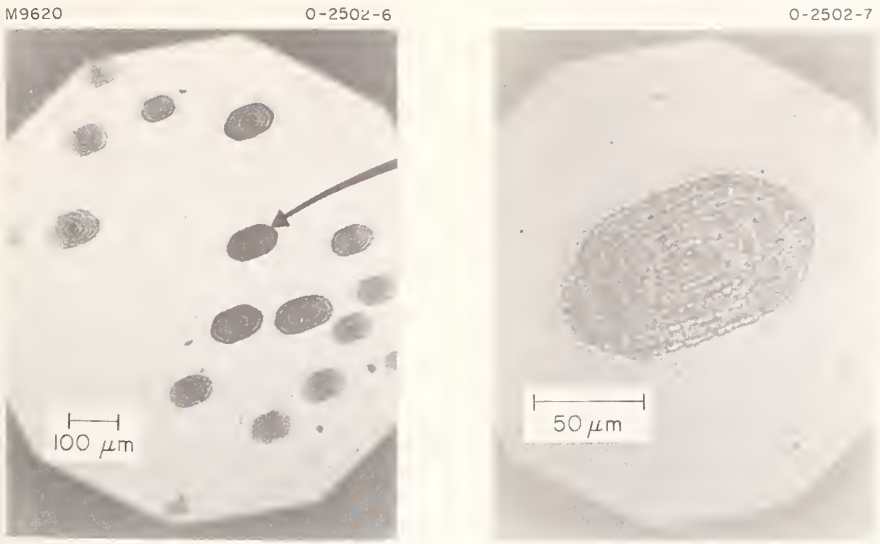

Figure 6. $(ZnTe/ZnS)^2$ reflector.

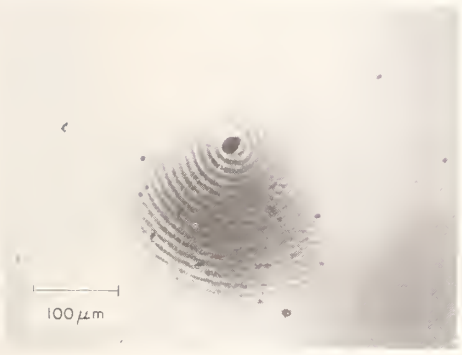

Figure 7. Scattering interference in half-wave ThF_4 film.

Figure 8a. $(As_2S_3/KCl)^4$ reflector below damage threshold.

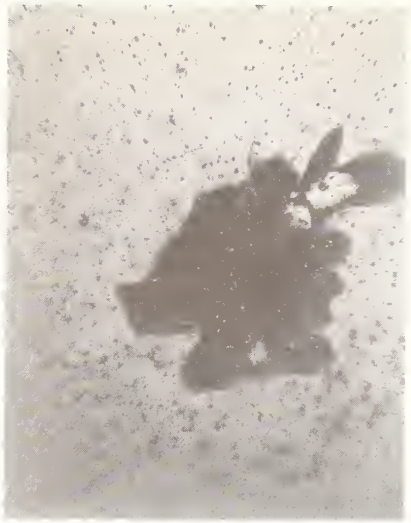

Figure 8b. $(As_2S_3/KC\ell)^4$ reflector above damage threshold.

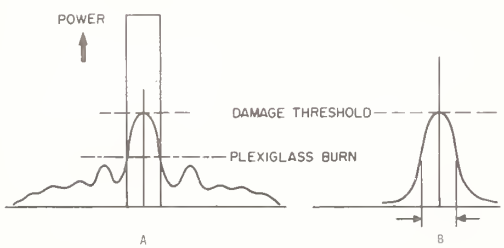

Figure 9. Comparison of single versus multimode spot size determination.

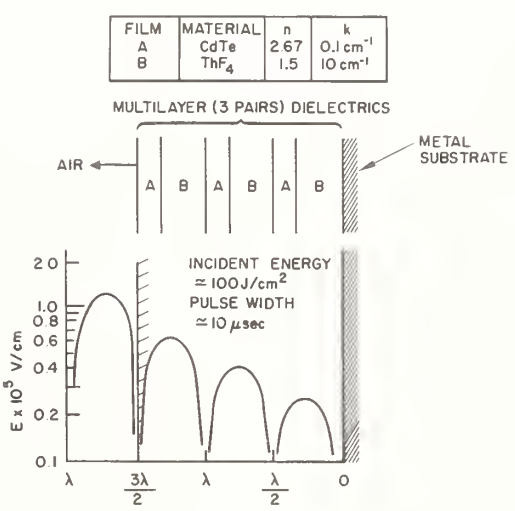

Figure 10. Electric field distribution in a $CdTe/ThF_4$ dielectric coated mirror.

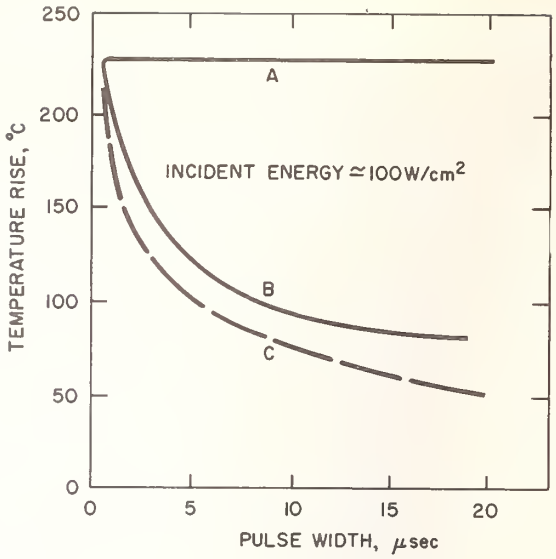

Figure 11. Transient thermal response of a $CdTe/ThF_4$ coated mirror.

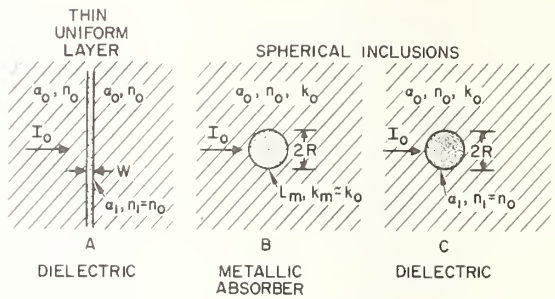

Figure 12. Simplified models for inclusions in dielectric films.

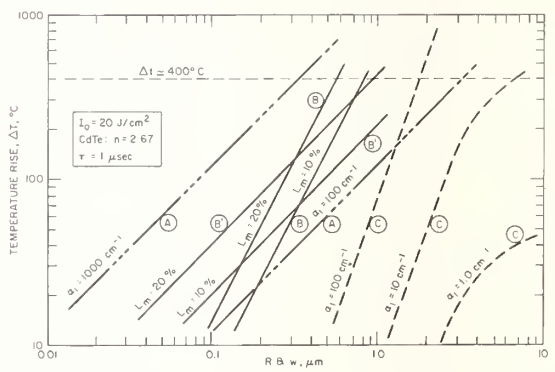

Figure 13. Calculated temperature rises of inclusions in a dielectric material (CdTe).

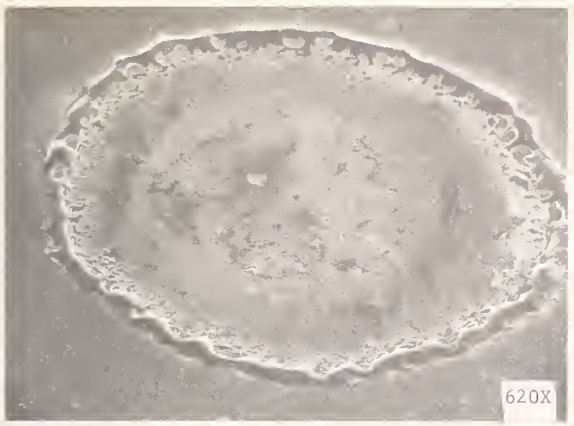

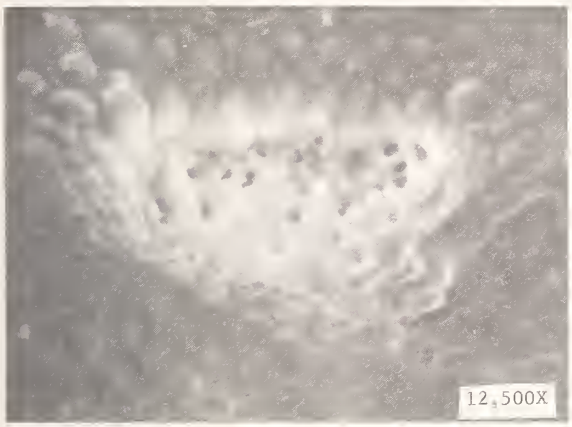

Figure 14. SEM enlargement of microcrater in $CdTe/ThF_4$ mirror.

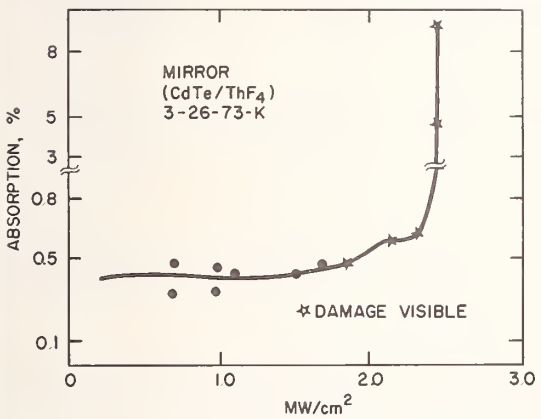

Figure 16. CdTe mirror absorption versus pulsed power.

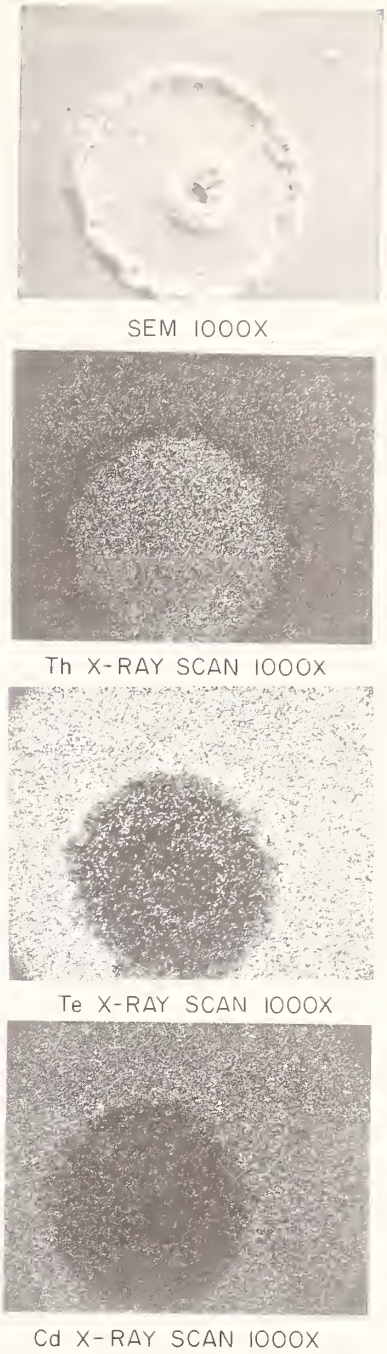

Figure 15. X-ray microprobe of microcrater in $CdTe/ThF_4$ mirror.

NO COMMENTS ON PAPER BY WANG.

Damage Threshold in 10.6 μm Laser Materials*

J. Davit

Laboratoires de Marcoussis, Division des Applications Optiques
Route de Nozay - 91 Marcoussis - France

Q-switched laser damage thresholds have been determined for three materials: Germanium (Ge), Potassium Chloride (KCl), and Sodium Chloride (NaCl). A TEM_{00} mode CO_2 laser with output at 10.6 μm wavelength and a 75 nsec pulse length was employed. For the three materials, the damage observed was surface damage. In the case of potassium chloride and sodium chloride, while the surface damage threshold was about the same as with germanium, the surface breakdown threshold was much lower. Results on anti-reflection coated materials are also reported.

Key Words: Alkali Halides, Infrared Windows, Laser Damage, TEA Laser.

1. Introduction

One problem to be solved in order to increase the energy obtained from a high power laser system is that of damage in the optical elements of the laser. In particular, because of the increasing interest in pulsed CO_2 laser systems, it is necessary to know the laser damage thresholds of different infrared materials which may be utilized in such lasers. We have determined numerical values of the damage thresholds for three materials: Ge, NaCl, and KCl, with a TEM_{00} CO_2 laser, for pulses of 75 nsec duration. The aim of this work was more to determine threshold values than to study the damage mechanisms.

2. Description of the TEA CO_2 Laser

In order to study the laser damage in materials of interest, a TEM_{00} mode laser, with a pulse length of 75 nsec, was built. The laser consisted of an oscillator with an output energy of 600 mJ and two amplifiers rotated by 90° with respect to each other. A laser output energy of 2.4 J (oscillator and amplifier) was used in the experiment. However, up to 5 J are available from this system.

2.1 Structure of the Laser

Both the oscillator and the amplifiers were transversely excited at atmospheric pressure (TEA laser) with trigger electrodes incorporated in the cathode structure. A $He\text{-}CO_2\text{-}Ne$ gas mixture in relative proportion of 4:2:2 for the amplifiers and of 3:1.5:0.5 for the oscillator was used throughout the experiments.

Excitation of the gas mixture was achieved in eight elements. Each element consists of an anode, a cathode, and two trigger electrodes, rotated about the laser axis by 45° from its predecessor. Such a configuration gives a radial gain profile which favors the excitation of the lowest order TEM_{00} mode.

2.2 Configuration of the Cavity

The geometry of the resonator was nearly semi-confocal. The optical cavity was composed of a gold coated, stainless steel concave mirror, with a radius of curvature of about 6 m, and a Ge, semi-transparent window, anti-reflection coated on one side, giving a reflectivity coefficient of 36%. The length of the cavity was 3.15 m, and an aperture of 13 mm in diameter was placed near the concave mirror.

*This work was supported by the French Commissariat a l'Energie Atomique.

2.3 Characteristics of the Beam

Measurements of the radial energy distribution in the beam have been made at different distances away from the laser by using a Ge-Au detector associated with an aperture of 0.2 mm in diameter. We have found a Gaussian profile at any distance both with the oscillator alone (600 mJ) and with the oscillator followed by two amplifiers (2.4 J).

Following Kogelnik and Li [1][1], it is known, in the case of a semi-confocal cavity, that the beam waist is located in the output mirror plane, and is given by $w = (\lambda L/\pi)^{1/2} = 3.25$ mm. However, measurements in the far field give a beam waist of 4.2 mm and indicate that its location is in the plane of the aperture near the concave mirror. The explanation of the difference between calculated and measured beam waist is well known. [2] It is the diverging lens effect caused by the transverse electric discharge better than that calculated from the geometry of the resonator. Note finally that the divergence of the beam was the same with and without the amplifiers.

Figure 1 shows the laser pulse from the oscillator alone and from the oscillator and amplifiers.

3. Experimental Results

3.1 Definition and Observation of the Damage

The laser damage was always surface damage. The damage threshold was defined in the usual way as the appearance of a visible plasma during the irradiation. However, this definition is not always sufficient because we have observed microscopic damage without plasma and also plasma without damage.

In the case of the germanium, the damage has been observed simultaneously by three means: observation of the plasma, microscopic examination of the surface, and variation of the reflectivity coefficient in the visible wavelength range (4000-6500 Å). [3] In the case of alkali halides (NaCl and KCl) only the first two means of observations were used. While in the case of germanium, the three means of observations of the damage are nearly coincident, this is not the case for the alkali halides where the visible plasma appears at any energy density much lower than energy values at which damage can be seen by microscopic examination.

3.2 Materials Studied

3.2.1 Germanium

The results are indicated in table 1. The breakdown threshold was found to be at 13 J/cm^2 in 75 nsec, with good optical cleaning of the surface. It is seen that the three means of observation of the damage, breakdown, microscopic examination, and variation in reflectance, have about the same threshold.

Many experiments have been made in order to verify that 100 irradiations at 7.5 J/cm^2 in 75 nsec give no damage because in only one case have we obtained microscopic damage without breakdown after 50 irradiations (figure 4b).

Finally, in table 1, we have also indicated the damage threshold of germanium with anti-reflection coatings on both faces. Samples with coatings obtained from different companies were tested and only the one with the highest damage threshold is indicated.

3.2.2 Alkali Halides

Two alkali halides were studied, potassium chloride and sodium chloride, each with two different orientations, <111> and <100>. No influence of the orientation on the damage threshold has been found. Experimental results are summarized in table 2. The samples were permanently kept in boxes with silica gel in order to protect them from moisture and were only taken out for damage measurements.

It is seen that the breakdown threshold is much lower than the value obtained for germanium. Also, breakdown ceases after 10 to 50 irradiations, depending on laser energy density. Up to 13 J/cm^2, no microscopic damage was observed following breakdown and the true damage threshold was obtained at 17 J/cm^2 in 75 nsec. For samples for which no special care was taken, breakdown and visible damage were observed for values of 10-15 J/cm^2. Only one sample of NaCl with anti-reflection coatings on both faces was tested, and the threshold values were found to be the same as in table 2.

[1] Figures in brackets indicate the literature references at the end of this paper.

Table 1.

A. Damage Threshold at Input Surface of Single Crystal Germanium (Resistivity 20 Ω x cm - N Type)

Number Irradiations on Spot (1 pulse/sec)	Breakdown	Microscope Examination	Reflectance of Germanium in the 4000-6500 Å Range
200 at 3.8 J/cm^2 in 75 nsec	No	No damage	No variation in reflectance
100 at 7.5 J/cm^2 in 75 nsec	No	No damage	No variation in reflectance
1 at 13 J/cm^2 in 75 nsec	Microbreakdown sometimes	No damage	No variation in reflectance
1 at 17 J/cm^2 in 75 nsec	Breakdown	Annulus damage (Fig. 2a.)	No variation in reflectance in center of the annulus
1 at 40 J/cm^2 in 75 nsec	Breakdown	Large damage (Fig. 2b.)	High decrease of reflectance in the center of the damage (Fig. 3.)
10 at 13 J/cm^2 in 75 nsec	Breakdown	Microscopic pits damage (Fig. 4a.)	Small decrease in reflectance in zone situated between the pits (Fig. 5.)

B. Damage Threshold for Germanium with Best Anti-Reflection Coatings

Number Irradiations on Spot (1 pulse/sec)	Breakdown	Microscope Examination
10,000 at 3.8 J/cm^2 in 75 nsec	No	No damage
100 at 7.5 J/cm^2 in 75 nsec	No	No damage
20 at 13 J/cm^2 in 75 nsec	Breakdown after 10 irradiations	Damage is increasing after 10 irradiations (damage after 20 irradiations-see Fig. 6a.)
1 at 17 J/cm^2 in 75 nsec	Microbreakdown	Small damage

Table 2.

Damage Threshold at Input or Output Surface of Sodium Chloride and Potassium Chloride

Number Irradiations on Spot (1 pulse/sec)	Breakdown	Microscope Examination
100 at 470 mJ/cm^2 in 75 nsec	Microbreakdown during the first 10 irradiations only	No damage
100 at 900 mJ/cm^2 in 75 nsec	Small breakdown during the first 10 irradiations only	No damage
100 at 1.9 J/cm^2 in 75 nsec	Breakdown during the first 10 irradiations only	No damage
100 at 3.8 J/cm^2 in 75 nsec	Breakdown during the first 10 irradiations only	No damage
100 at 7.5 J/cm^2 in 75 nsec	Breakdown during the first 50 irradiations only. Breakdown is decreased in dimension during first 50 irradiations.	No damage
100 at 13 J/cm^2 in 75 nsec	Same as above	No damage
1 at 17 J/cm^2 in 75 nsec	Breakdown	Damage (Fig. 6b.)

4. Conclusion

Laser damage thresholds for short laser pulses (75 nsec) at 10.6 μ are reported for three materials: Germanium, Potassium Chloride, and Sodium Chloride. It was found that the damage which limits the power density was surface damage in all cases. A numerical value to be retained as a limiting one in order to design a pulsed CO_2 laser device is 7.5 J/cm^2 in 75 nsec (100 MW/cm^2) for Ge. For alkali halides used in moisture free conditions, this value would be of the order of 13 J/cm^2. These values are not modified when the materials are coated with the best anti-reflection coating that was tried.

It must be noted that the pulse contains peaks of varying sizes due to partial mode-locking in the oscillator which may vary from pulse to pulse. However, the mode-locked structure of the pulse appeared to have no effect on the damage threshold since it is possible to define the threshold with a precision better than 5%. This means that the characteristic time constant of the damage is at least 20 nsec.

5. Acknowledgment

The author is grateful to J. Baujoin and J. Gautier for the construction of the laser, and to C. Charles for his assistance in damage testing.

6. References

[1] Kogelnik, H. and Li, T., Appl. Opt. 5, 1550 (1966).

[2] Fortin, R., et al., Can. J. Phys. 49, 1783 (1971).

[3] Donovan, T. M., et al., J. Opt. Soc. Am. 53, 1403 (1963).

7. Figures

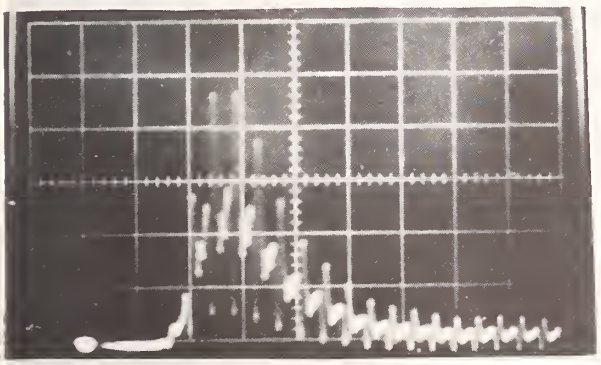

Figure 1a. Oscillogram of laser pulse (oscillator) output energy 600mJ. Vertical scale: 50 mV/div; Horizontal scale: 50 nsec/division.

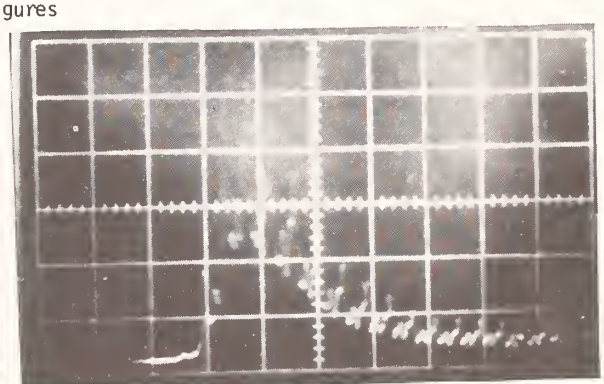

Figure 1b. Oscillogram of laser pulse (oscillator plus 2 amplifiers) output energy 2.4J. Vertical scale: 200 mV/division, Horizontal scale: 50 nsec/division.

Figure 2a. Single crystal germanium, 20 Ω x cm, n-type. One shot at 17 J/cm^2 in 75 nsec. Magnification is x 50.

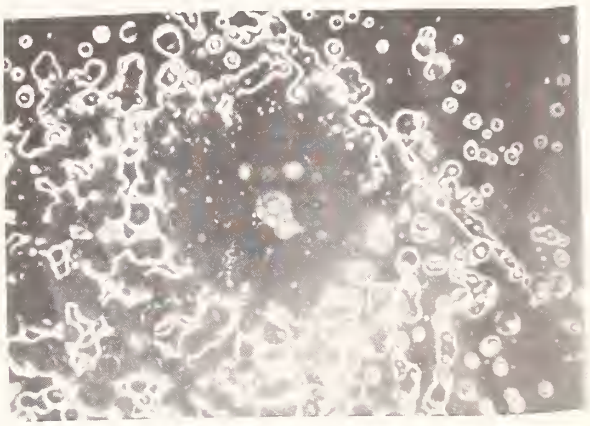

Figure 2b. Single crystal germanium, 20 Ω x cm, n-type. One shot at 40 J/cm^2 in 75 nsec. Magnification is x 50.

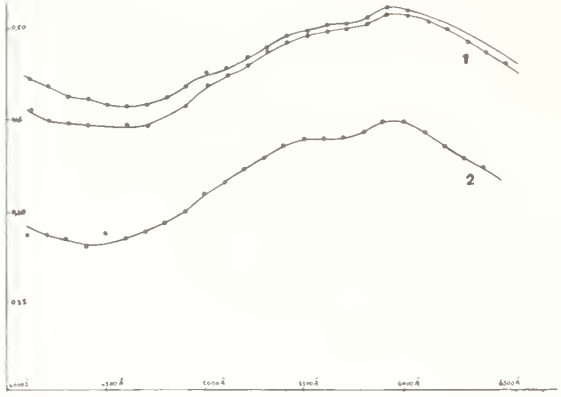

Figure 3. Variation of the reflection coefficient of single Ge crystal (20 Ω x cm, n-type) before (1) and after (2) one shot at 40 J/cm^2 in 75 nsec.

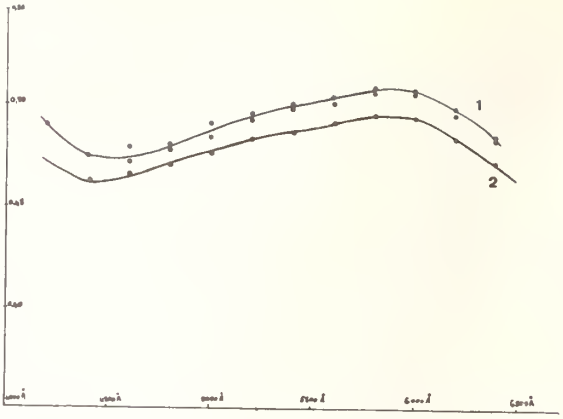

Figure 5. Same conditions as Figure 4a. (1) Spectral reflectance before illumination. (2) Spectral reflectance after illumination.

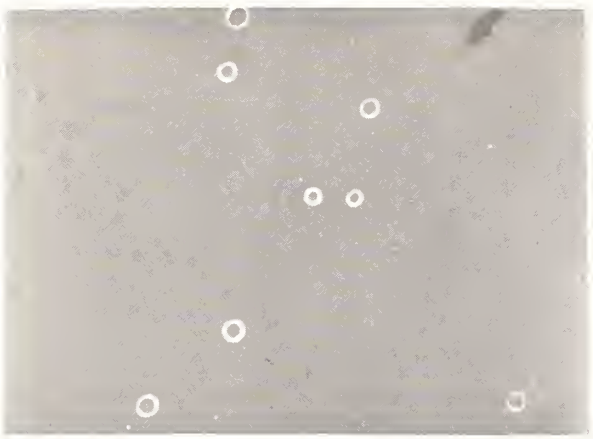

Figure 4a. Single crystal germanium, 20 Ω x cm, n-type. Ten shots at 13 J/cm^2 in 75 nsec. Magnification is x 100.

Figure 4b. Single crystal germanium, 20 Ω x cm, n-type. Fifty shots at 7.5 J/cm^2 in 75 nsec (damage obtained once only). Magnification is x 100.

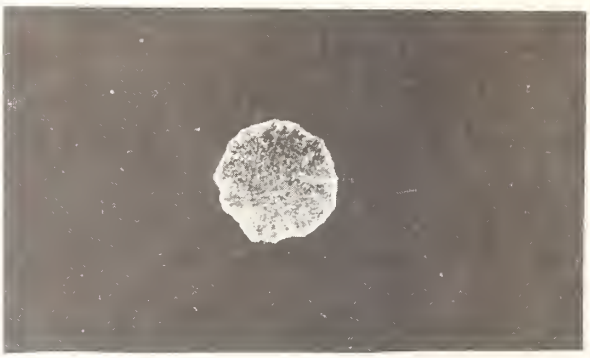

Figure 6a. Anti-reflection coated Ge. Twenty shots at 13 J/cm^2 in 75 nsec. Damage with breakdown.

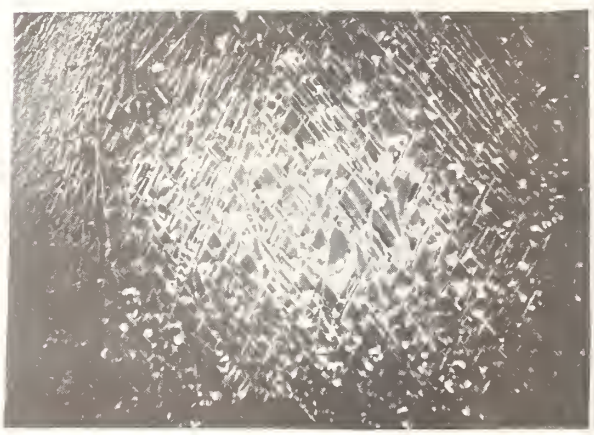

Figure 6b. KCℓ. One shot at 17 J/cm^2 in 75 nsec. Damage with breakdown.

NO COMMENTS ON PAPER BY DAVIT.

Radiation Induced Damage to NaCl by 10.6 μm Fractional Joule, Nanosecond Pulses*

Walter H. Reichelt and Eugene E. Stark, Jr.

Los Alamos Scientific Laboratory
University of California
Los Alamos, New Mexico 87544

Fractional joule nanosecond pulses from the Los Alamos pulsed CO_2 laser system have been used to obtain preliminary breakdown data for optical quality NaCl. Both surface and bulk damage have been observed. Surface damage in some samples takes the form of a rectangular craze pattern. This pattern is at the surface and similar to that observed by Bastow, et al, in TiC irradiated with light pulses from a Q-switched ruby laser. Estimated thresholds for breakdown and damage patterns are given.

Key Words: Damage threshold, exit damage, NaCl, surface damage.

1. Introduction

The development of efficient methods for pumping large volumes of CO_2 has led to the projected use of large CO_2 laser-amplifier systems in laser fusion which requires energetic pulses with time durations of the order of nanoseconds or less. In order to reduce the size of laser systems to reasonable levels, it is necessary to use as high an energy density (joules/cm^2) as possible through the system. An energy pulse of 3 joules/cm^2/nanosecond has an associated electric field of the order of 10^6 V/cm which is close to the NaCl d.c. dielectric breakdown strength. [1][1] Since NaCl is used as a window material in the laser systems, it is necessary to understand the breakdown limits of NaCl in these fields.

In this paper, we report preliminary breakdown data on optical quality NaCl irradiated by fractional joule, nanosecond pulses. The laser pulses were focused to obtain a variety of energy densities. However, the NaCl samples were not placed near the focal point; the beam was of such a diameter as to always include both extrinsic and intrinsic damage effects. Due to the experimental design, the data will be reported as a qualified damage threshold energy density. In so doing, the data sets an upper bound on the damage threshold.

The paper is divided into several sections. The first will cover the experimental setup. It will include discussions of the pulse generation, time and spatial profiles of the pulses, energy determination and damage monitoring techniques. The second section will be a presentation of the experimental results and observations.

---

*Work done under the auspices of the U. S. Atomic Energy Commission.

[1]Figures in brackets indicate the literature references at the end of this paper.

2. The Experimental Configuration

2.1 Pulse Generation

The nanosecond pulses used in this experiment were generated in three stages of the Los Alamos Scientific Laboratory CO_2 laser amplifier system. [2] This system consists of a Lamberton-Pearson type, double discharge oscillator [3] and three single pass, electron beam pumped amplifiers. Each of the three amplifier stages used in the experiment has an active optical length of 1 meter. The oscillator system generates a single P(20), millijoule, polarized, TEM_{00}, nanosecond pulse [4]; this is accomplished by electro-optically switching out a single pulse from a mode-locked train of pulses. The millijoule pulse then passes through the three amplifiers where it is amplified to the joule level. Figure 1 schematically portrays the laser amplifier system used. Amplifiers 1 and 2 are capable of yielding 1.5 - 2.0 joules/nanosecond pulses while amplifiers 1, 2 and 3 yield 20 joules/nanosecond pulses. However, in the damage threshold work, apertures were used to clean up the transverse beam; the output of amplifiers 1 and 2 was 1.0 joule/nanosecond and amplifiers 1, 2 and 3 was 4.0 joules/nanosecond.

2.2 Pulse Profiles

Time and spatial profiles of the pulses are shown in figure 2. The time profiles of typical unamplified and amplified pulses shown in figure 2(a) were taken simultaneously with the Rofin photon drag detectors and Tektronix 7904 oscilloscopes. Figure 2(a) shows the amplified pulse from amplifier 2. Time profiles from amplifier 3 retain the same general character as those from 2. Spatial profiles for the unamplified pulses were obtained with a Molectron linear array of pyroelectric detectors. The results of one such measurement are shown in figure 2(b). The large dots represent the output of individual detectors in the array. They are spaced on 0.5 cm centers. Amplified spatial profiles have not been obtained, as yet, due to the noise generated by the electron beam pumping supplies. Theoretical calculations, however, reveal that the output pulses from amplifier 2 will retain some of their Gaussian character. Burn patterns taken with Thermofax paper after apertures placed after amplifiers 2 and 3 indicated good beam quality. The Fresnel diffraction rings introduced by the apertures indicate good radial symmetry of the wave fronts incident on the apertures. Time and spatial profiles and excellent Fresnel diffraction rings are taken to mean that the beam quality in the experiments is quite good.

2.3 Samples and Sample Environment

Samples were standard optical quality NaCl flats obtained from Harshaw Chemical Co. and K. Feuer Optical Associates, Inc. The latter company polishes and markets NaCl obtained from Quartz et Silice, Paris. The samples were cleaned with reagent grade trichloroethylene. No attempt was made to improve the finish on the flats. Superpolished flats have been ordered from Harshaw and will be irradiated to find if improved factory finishes will improve damage thresholds. The samples were irradiated in a clean N_2 environment as shown in figure 1. Filtered N_2 constantly flowed through the target tube to prevent diffusion of dust to the cleaned surfaces of the NaCl sample. Energy densities of interest were far below that at which N_2 breakdown occurred. The beam entered the sample approximately normal to the surface. A slight angular offset was introduced to prevent reflections back through the system.

2.4 Energy Flux Determination

The maximum average energy density was determined in the following manner: A burn pattern was obtained for the beams on Thermofax paper. The diameter of the maximum energy density circle on the burn pattern was measured and an aperture of this diameter and location was placed in the beam path. A calibrated Scientech energy meter (Model 3604) was placed after the aperture and the average energy through the aperture measured. This energy divided by the aperture area is taken to be the average maximum energy density of the particular location. The sample was moved along the optic axis to obtain a varying incident energy density. Gaussian optics calculations according to the analysis of

Kogelnik and Li [5] confirm the geometrical approximation and indicate peak densities approximately twice the average energy for the output of amplifiers 1 and 2. For the output of amplifiers 1, 2 and 3, the geometrical approximation was used since the pulse is no longer Gaussian in nature but probably has a rather flattened front surface. The average energy density as determined above will be used in reporting the data.

Damage observations were made with the telescope shown schematically in figure 1 after every pulse. Sparking was observed visually.

3. Results and Discussion

3.1 Damage Thresholds

Due to the limited repetition rate of the present amplifier system, the data yields a threshold damage value rather than a damage probability such as that proposed by Bass, et al. [6] The latter method would have required an extremely large number of pulses. Visible plasma formation was noted with and without accompanying visible damage. The extent of visible plasma formation seems related to the surface finish since in some cases it decreases with repeated pulses. Damage generally took place at the exit side of the sample as in the case of laser induced damage in glass. This could be explained by the analysis of Boling, et al [7], wherein they calculate the electric fields at the entrance and exit sides of the samples with the result that the fields at the exit surfaces are greater than those at the entrance. Damage within the bulk of the material was also noted.

Table 1 indicates the damage threshold for three samples of conventionally polished, optical quality, single crystal NaCl. The estimated peak breakdown field strength is also indicated in the tabulation.

TABLE 1. Damage thresholds for NaCl flats for nanosecond, fractional joule 10.6 μm pulses.

Sample	Manfacturer	Thickness	Diameter of Average Energy Circle	Average Energy Density joules/cm^2	E_B V/cm (peak)
1	Harshaw	0.3 cm	0.6 cm	3.0	0.80×10^6
2	Harshaw	0.5 cm	0.25 cm	3.0	1.40×10^6
3	K. Feuer	1.9 cm	0.34 cm	2.0	1.15×10^6

The actual breakdown thresholds may be slightly less than these since the energy density was changed in steps of 0.5 joules/cm^2. At an energy density of 0.5 joules/cm^2 below those given above, damage was not observed after many pulses. The difference between the observed breakdown fields given above and the d.c. breakdown [1] ($\sim 1.5 \times 10^6$ V/cm) [5] or the intrinsic breakdown values for long pulses [8] ($\sim 2.0 \times 10^6$ V/cm) is probably due to the effects of surface finish [9] (microcracks, scratches) -- extrinsic effects -- rather than the intrinsic material effects.

3.2 Damage Observations

Figure 3 contains optical microscopy pictures of the damage sites. Figure 3(a) is the exit damage site (at 3.0 joules/cm^2) on material 2 above. This is a typical initiation of a damage site: lines looking like cleavage lines appear in two directions; at right angles presumably, along crystal axes. These lines are restricted to the surface -- they do not penetrate deeply into the bulk material. Spalling of the surface appears centered about these lines. No melting has been observed in any of the samples. Figure 3(b) shows damage at a relatively high energy density. Again, the same line structure appears as in figure 3(a). In some cases damage occurs with both line structure and spalling as in figure 3(c) where the line structure underlies the spalled area. Once damage occurs, repeated pulses quickly degrade the surface as seen in figure 3(d). Again, note that spalling occurs along the line structure. Similar damage patterns have been noted with large, gain-switched laser pulses. [10] Bulk damage was noted also; this was confined to localized sites. Figure 4(a) shows typical bulk damage in material 3. The damage sites are strung along the general beam path but are not on line as seen observed end-on in figure 4(b). The orientation of the fractures in figure 4(b) is

the same as that of the lines appearing in the surface damage. Figure 4(c) shows a similar damage site in material 1 and 2. It is not obvious whether or not these damage sites originate on inclusions, voids, or some other center.

3.3 Damage Origin

One possible explanation of the origin of the damage structure may be found in the work of Bastow, et al. [11] These investigators studied the effect of Q-switched ruby laser pulses on TiC and other materials. They observed cracking and spalling of the surfaces very similar to that reported here for NaCl. Such a damage pattern was attributed to local heating and a consequent tensile stress applied to the surface area under irradiation. The result of this stress is surface cracking and spalling.

Once surface microcracking is initiated, subsequent pulses result in extremely large fields (> breakdown fields) at the crack bases as indicated by Bloembergen. [9] The high fields result in high stresses which cause spalling, as observed, along the length of the microcracks.

4. Acknowledgements

The authors wish to acknowledge the valuable assistance of R. Johnston, E. Swickard, and C. Landahl in the operation of the amplifier system. In addition, the optical microscopy of C. G. Hoffman provided an insight into the possible mechanism of damage.

5. References

[1] Von Hippel, A., J. Appl. Phys. 8, 815 (1937).

[2] Stratton, T., Erickson, G., Fenstermacher, C., and Swickard, E., IEEE J. of Quant. Elec. 1, 157 (1973).

[3] Lamberton, H., and Pearson, P., Electronic Letters 7, No. 516 (Jan., 1971).

[4] Figueria, J., Reichelt, W., Singer, S., and Fenstermacher, C., to be published.

[5] Kogelnik, H., and Li, T., Proceed. of the IEEE 54, 1312 (1966).

[6] Bass, M., and Barrett, H., NBS Special Publication 356 (1971) p.76.

[7] Boling, N., Crisp, M., and Dubé, G., Appl. Optics 12, 650 (1973).

[8] Yablonovitch, E., Appl. Phys. Letters 19, 495 (1971).

[9] Bloembergen, N., Appl. Optics 12, 661 (1973).

[10] Wetzel, Capt. M., private communication.

[11] Bastow, T., Packer, M., and Gane, N., Nature 222, 27 (1969).

6. Figures

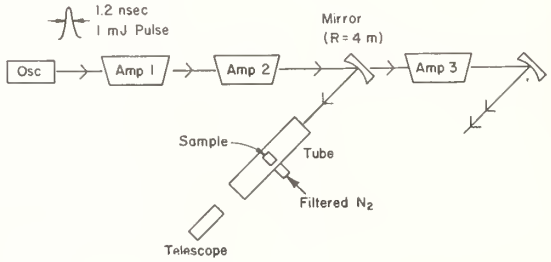

Figure 1. Experimental configuration for NaCl damage study.

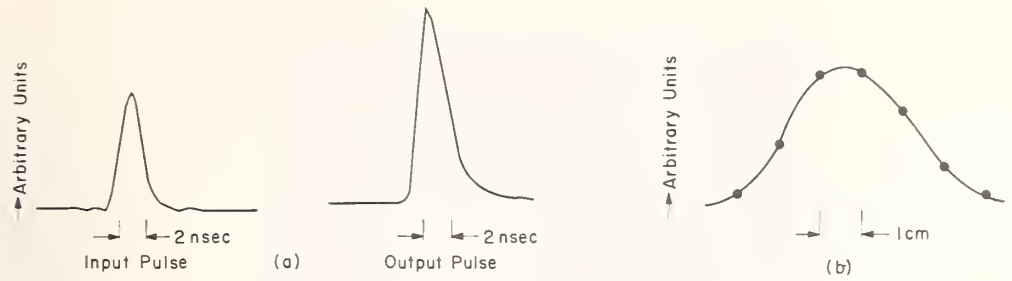

Figure 2. Time and space profiles of nanosecond pulses. (a) Time profile of unamplified and amplified pulses. (b) Spatial profile of unamplified pulse after amplifier #2.

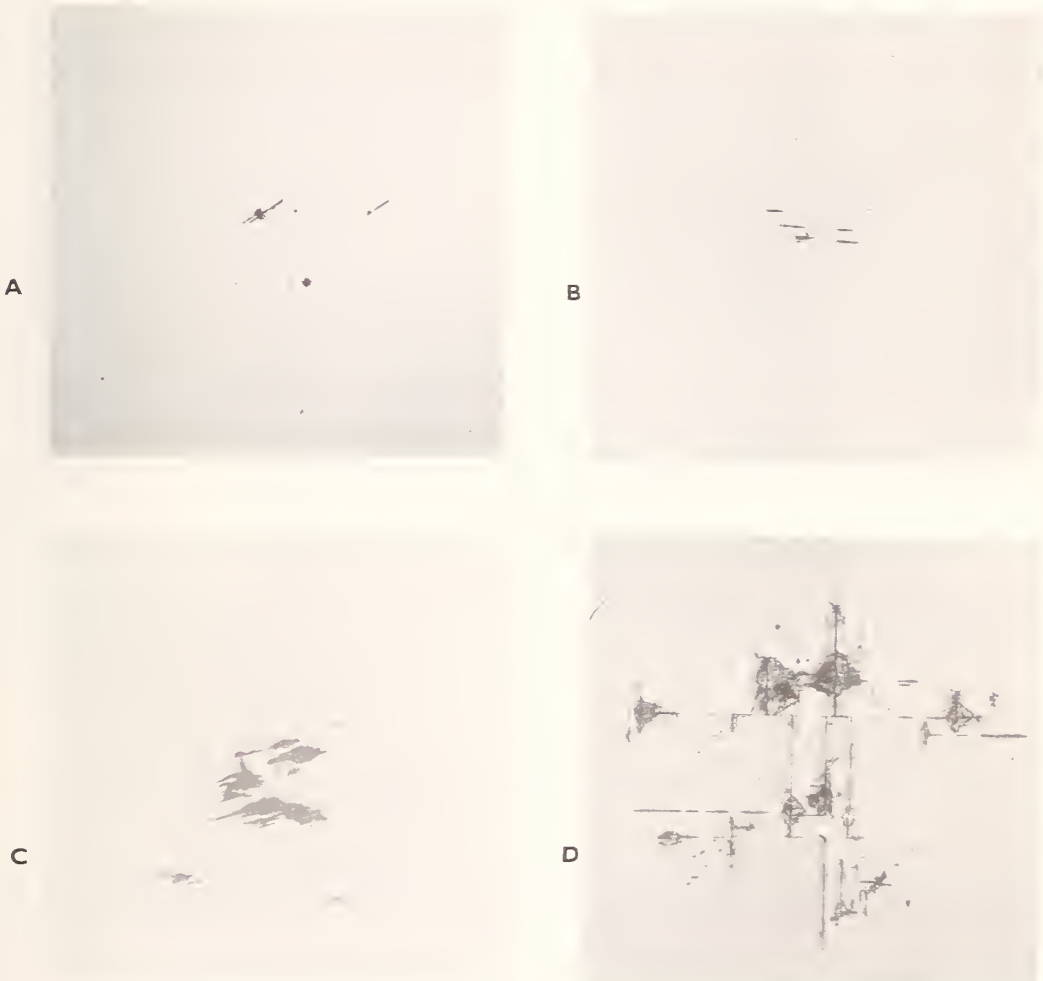

Figure 3. Typical exit damage sites. (a) at 3.0 joules/cm^2, Harshaw, 50x (b) at 3.8 joules/cm^2, Harshaw, 50x (c) at 3.8 joules/cm^2, Harshaw, 50x (d) at 2.5 joules/cm^2, Harshaw, 50x.

Figure 4. Typical bulk damage sites. (a) at 2.5 joules/cm^2, Feuer, beam from left to right, 6x (b) at 2.5 joules/cm^2, Feuer, 25x (c) at 3.0 joules/cm^2, Harshaw, 50x.

COMMENTS ON PAPER BY REICHELT

It was pointed out that the random location of the damage site in the bulk material was suggestive of inclusion damage. The speaker responded that this question had not been investigated at the time of the presentation of the paper. A question from the audience was raised regarding the meaning of the word "super-polishing" as applied to NaCl crystals. The speaker replied that this was a term used by the manufacturer representing a polishing procedure resulting in a surface that was significantly better than surfaces that had previously been available from that manufacturer. The exact nature and detail of the process were proprietary.

A Study of 10.6 μm Laser Induced Damage in Alkali Halide Crystals

H. Posen, J. Bruce, J. Comer, A. Armington

Air Force Cambridge Research Laboratories
L. G. Hanscom Field
Bedford, Massachusetts 01730

Laser induced damage at 10.6 micrometers is observed in alloy alkali halide single crystals of the ALQLOY composition ($KCl_{0.33}$ - $KBr_{0.67}$) and pure KCl, as a function of crystalline orientation. The effect of the step-wise increase in laser irradiation power is monitored by x-ray topographic techniques, Nomarski microscopy and electron microscopy of the replicated damage surface.

The relationship of the damage threshold to the crystalline orientation is explained by invoking the critical resolved shear stress law for the rock salt crystal structure of the alkali halides.

Key Words: Alkali halides, ALQLOY, damage threshold, IR coatings, IR materials, laser damage.

1. Introduction

Although laser damage thresholds have been reported for a variety of materials and a variety of laser wavelengths [1][1], the thrust of the investigations has been directed towards damage occurring under pulsed laser operation and little effort has been expended on the examination of failure mode in materials at 10.6 μm and at CW operation. Young [2] has reported some work on As_2S_3 coatings on KCl under CO_2 irradiation, but was concerned with coating failure rather than substrate failure. Posen et al [3] have examined a NaCl disk, coated with a glass, whose nominal composition was that of the Texas Instrument #1173 glass [4] that had failed under CW 10.6 μm laser irradiation. Although x-ray topographic evidence in this instance showed ⟨110⟩ dislocations associated with the damaged area, indicating plastic deformation of the substrate, an unambiguous assignment of failure initiation to the coating or to the substrate could not be made.

This research is directed toward the examination of damage thresholds in a related series of IR transmitting materials, namely the alkali halide family KCl, KBr, and the alloy ALQLOY [5] whose composition is KCl (0.33) KBr (0.67). The familial relationship of these halides is illustrated by the pseudo-binary phase diagram (figure 1).

Although there is some evidence that damage thresholds in materials are controlled by defects in the surface or near-surface of the material for pulsed laser damage, we here present evidence that for coated materials, under CW high power CO_2 laser exposure, the controlling parameter for damage threshold is the yield strength of the individual materials.

2. Theoretical Considerations

It is suggested that plastic deformation, slip or dislocation movement (the terms are somewhat synonymous) is associated with the laser damage phenomena.

Because of the discrete nature of the atomic lattice, "slip" can only occur in certain crystalline planes. This combination of slip plane and slip direction is designated a slip system, and is unique for a particular crystal structure. Thus for deformation to occur and for dislocations to be generated, an applied stress must be resolved into the slip plane along the slip direction, (figure 2).

This geometric resolution factor is embodied in the critical resolved shear stress law

$$\sigma_R = \sigma_{app} \cos\varphi \cos\psi$$

[1] Figures in brackets indicate the literature references at the end of this paper.

where φ and ψ are the angles between the applied stress σ_{app} and the slip plane normal, and the slip direction respectively. For the KCl - KBr alkali halide family, slip occurs on the (110) plane in the $\langle 110 \rangle$ direction. When the geometric factor is considered for this crystal structure, crystals oriented with the (111) and (110) faces normal to the incident stress should be stronger in terms of the stress required to move dislocations through the lattice than a crystal oriented with the (100) face normal to the incident stress.

Thus in those systems, where the failure is controlled by the plastic deformation of the material, the failure threshold will show an orientation dependence.

3. Experimental

Samples of KCl were cut from single crystal boule LQ#272 grown by the Czochralski technique. Similarly, samples of ALQLOY, KCl (0.33) - KBr (0.67) were cut from AFCRL single crystal boule LQ#282. Specimen surfaces, oriented along the three principal crystallographic directions, the (100), (110), and (111), were rough polished with alumina, and finish polished with MgO in ethanol. Samples were nominally 1.0 X 1.0 X 0.5cm in size.

The coated samples were prepared by electron beam evaporation of 99.999% pure Ge. Typical coating thickness of 12000 A° were obtained in films whose crystallinity bordered on the amorphous form. Details of the coating conditions and electron diffraction data of the films are given in reference [5].

All specimens were subjected to 10.6 μm laser irradiation, using the AFCRL 300 watt TEM_{oo} mode stabilized CO_2 laser. The distance of focussing lens to the sample was maintained at 56cm, providing a circular beam at the specimen surface of 1mm in diameter. Figure 3 illustrates the experimental configuration.

Typically the experiment starts at a low power level, well below any suspected damage threshold. Exposures to a beam, focussed at the face of the specimen, are for one minute periods. The power of the beam is gradually increased by 500 watt/cm^2 increments, and the sample is examined after each exposure for evidence of damage.

Surface quality, before and after irradiation is monitored by Nomarski phase interference microscopy, using a Zeiss Ultraphot II metallograph. Near-surface quality is examined, non-destructivity by x-ray reflection topography before and after irradiation. The x-ray topograph shown schematically in figure 4 permits selective sampling of the near-surface volume, by selecting the appropriate combination of Bragg reflection and x-ray characteristic radiation for the particular crystal composition and orientation. Once these parameters are fixed, the sample and recording plate are translated back and forth relative to the beam, thus recording a large area. The angular settings of the specimens and recording film were calculated for all possible reflections by program TOPOG [6]. Program TOPOG also yields an effective penetration depth of the x-ray radiation for a given crystal and orientation. This penetration depth can be considered as the depth of that volume of subsurface whose diffracted energy is recorded on the topographs. Topographs were recorded on Ilford G5 nuclear plates using CuK X-rays.

The setting parameters and related data are listed in table 1 for both KCl and ALQLOY. Note that because of the higher x-ray absorption of the Br ion in the ALQLOY we are only sampling 18 microns of subsurface for the (100) orientation as compared to 22 microns for the (100) orientation of KCl when using a (400) Bragg reflection.

Irradiated samples were also examined by electron microscopy.

Table 1. X-Ray Topography Parameters - Alkali Halides

Crystal	Crystal Orientation	Reflection	Penetration Depth μm	2θ(CuKα) (degrees)
KCl	(100)	[400]	22	58.6
	(110)	[220]	16	40.5
		[420]	17	66.4
	(111)	[222]	19	50.2
ALQLOY	(100)	[400]	18	56.6
		[420]	7	64.0
	(110)	[220]	13	39.1
		[420]	14	64.0
	(111)	[222]	16	48.5

4. Results and Discussion

4.1 Uncoated Samples

The uncoated KCl samples regardless of their crystallographic orientation did not fail at power levels up to 38,000 watts/cm^2 - the available limit of the 300 watt CO_2 laser.

Damage was observed in the ⟨100⟩ oriented ALQLOY sample at 28,000 watts/cm^2. Topographs were taken before irradiation and after irradiation of this sample. Figure 5 illustrates topographs of the mechanically polished sample prior to irradiation. A second sample failed at the same power density. A third (100) sample from the same boule, mechanically polished as before was then etched with concentrated HCl. Figure 6 shows topographs of this sample prior to irradiation. Note that the scratches have disappeared. However, immediately upon irradiation this sample failed at 6500 watts/cm^2. Figure 7 are "before and after" topographs of the failed (100) ALQLOY sample. We see no dislocation generation, but failure has occurred by cleavage along the (100) direction.

For completeness, a (100) mechanically polished sample of KBr was also irradiated and did not fail within the available power limits of the CO_2 laser.

Table 2 summarizes our observation on the uncoated samples.

Table 2. 10.6 μm CW Laser Damage Thresholds in Uncoated Alkali Halides

Crystal	Orientation	Damage Threshold (W/cm^2)
KCl	(100)	Greater than 38,000★
	(110)	
	(111)	
ALQLOY	(100)	28,500
	(110)	Greater than 38,000★
	(111)	
KBr	(100)	Greater than 38,000★

★ 38,000 watts/cm^2 is the maximum available power for 1mm spot size.

The surface morphology of the damage of the ALQLOY sample was examined by Nomarski phase interference microscopy. Figure 8 shows the characteristic crater, observed previously by Posen et al [3] in coated samples.

A more detailed study of the surface morphology of the damaged area was made by electron microscopy using two-stage replication techniques. The five micrographs graphically illustrate the damage morphology. As we move out from the intensely damaged center, there is a relatively clear area with small protuberances followed by a sharp transition to larger hillocks which gradually meld into the substructure of the crystal. [figure 9]

4.2 Coated Samples

For the coated samples, topographs were taken after polishing, after Ge deposition and after damage had occurred.

Figure 10 shows a full sequence of topographs for the Ge coated (110) KCl sample. The bands of alternate contrast in the ⟨100⟩ directions arise from the large mosaicity of the sample. Although the level of mosaicity and the extent of damage due to polishing make it difficult to discern the contrast attributable to dislocations, dislocation contrast can be seen in at least one instance. Figure 10 (d) and (e) showing topographs of the sub-surface using a [220] and [420] reflection after laser damage, show a [110] type dislocation (indicated by the arrow). Diffraction contrast arising from this dislocation is present on the [220] plate but not on the [420] plate. This contrast is not present on [220] topograph of the sample prior to laser damage.

The development of such dislocations is evidence of plastic deformation that has occurred in the coated KCl after laser irradiation. Table 3 summarizes our observations of damage thresholds in Ge coated KCl as a function of orientation.

Table 3. 10.6 μm CW Laser Damage Thresholds in Ge Coated KCl

KCl - orientation	Damage threshold (W/cm^2)
(100)	5,100
(110)	14,600
(111)	14,600

The damage threshold for the (111) and (110) oriented samples is almost a factor three greater than the damage threshold for failure in a (100) oriented sample. Thus the failure threshold in the coated samples is orientation dependent, in accordance with the strength hierarchy derived from the application of the critical resolved shear stress law to the KCl system.

5. Summary

Available CW CO_2 laser power (38,000 W/cm^2) did not permit failure observations in KCl and KBr samples, regardless of their orientation. Samples of (100) oriented ALQLOY, did fail at thresholds of 28,500 w/cm^2 , below the lower limit for the unalloyed samples, yet the observed yield strengths for these materials is 2300 psi vs. 700 psi for KCl or KBr. However, the observed failure is by cleavage propagation, rather than by lattice yielding. Although rupture moduli are not available for the ALQLOY material, rupture moduli for KCl is 4.4×10^7 dynes/cm^2 , as compared to an elastic limit of 2.3×10^7 dynes/cm^2. Thus failure in KCl will be by slip rather than by rupture or cleavage. For the alloy the reverse is true. In a coated window the controlling failure mechanism is the initiation of plastic deformation of the weaker member of the system (coating and window) by stresses arising from the laser irradiation of the samples. In particular, for the system KCl coated with Ge, the normal thermal stresses developed in laser heating are compressive and arise from the difference in expansion coefficient between the Ge coating and the substrate, and they are sufficient to cause yielding and subsequent failure of the system.

Significant improvements in damage thresholds for coated systems can be achieved if crystallographic substrate orientation is chosen such that the operating slip systems are considered.

6. Acknowledgment

The authors thank C. A. Bergeron and O. M. Clark for their technical assistance.

7. References

[1] Damages in Laser Materials, edited by Glass, A. J. and Guenther, A. H., NBS Special Publication 356, (1971).

[2] Young, P. A., Thin Solid Films, 6, 423 (1970)

[3] High Power Infrared Laser Window Materials, LQ-10 Quarterly Progress Report #5, Air Force Cambridge Research Laboratories AFCRL-72-0339.

[4] Compendium on High Power Infrared Laser Window Materials, edited by C. S. Sahagian, AFCRL-72-0170, TI #1173 Glass.

[5] Bruce, J., Posen, H., Armington, A., Yang, A. C., Bloom, J. H., The Inter-Relationship of Substrate Crystal Orientations and Coating in Germanium Coated Alkali Halides, Conference on High Power Infrared Laser Window Materials - Proceedings

[6] Posen, H., TOPOG-A Computer Program to Compute Penetration Depth and Setting Angles for Reflection X-ray Topography, To be Pub.

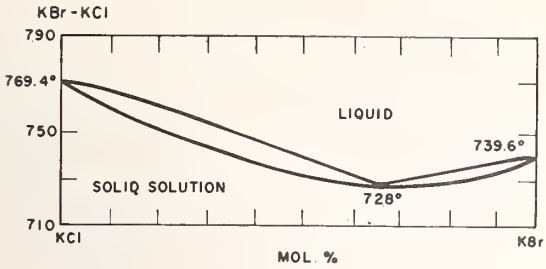

Figure 1. Pseudo Binary Phase Diagram of KCℓ - KBr System.

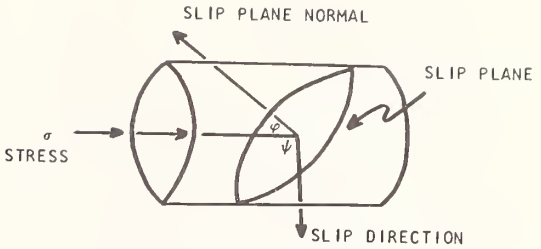

Figure 2. Diagram illustrating the Resolved Shear Stress Law.

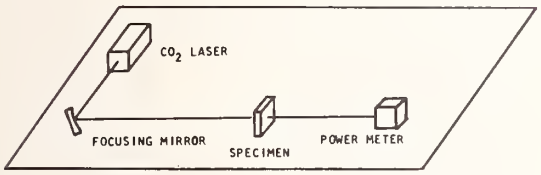

Figure 3. Experimental configuration for 10.6 μm laser damage studies.

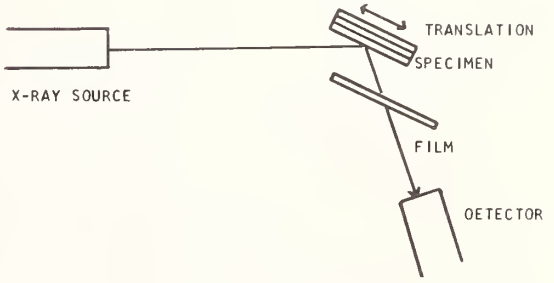

Figure 4. Experimental arrangement for symmetrical reflection topography.

Figure 5. X-ray topographs of a mechanically polished (100) ALQLOY surface.

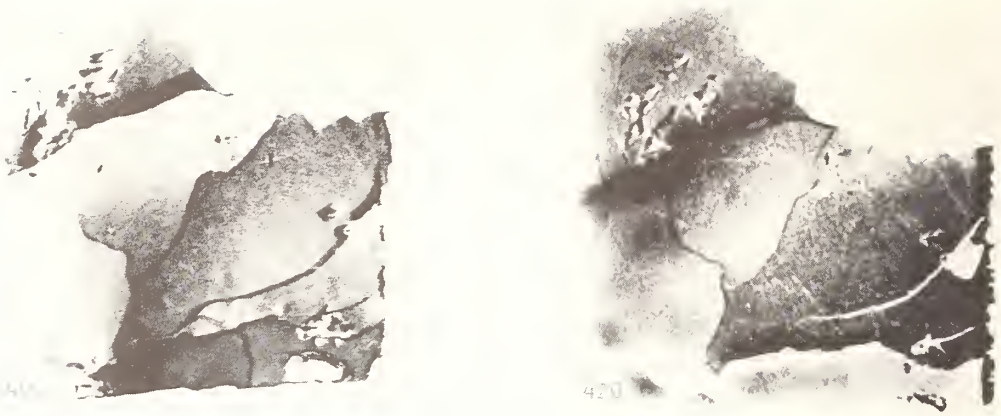

Figure 6. X-ray topographs of a (100) ALQLOY surface after HCℓ etch. Same sample as that of Figure 5.

Figure 7. [400] X-ray topographs of a (100) ALQLOY crystal before and after 10.6 μm irradiation. Same sample as that of Figure 6.

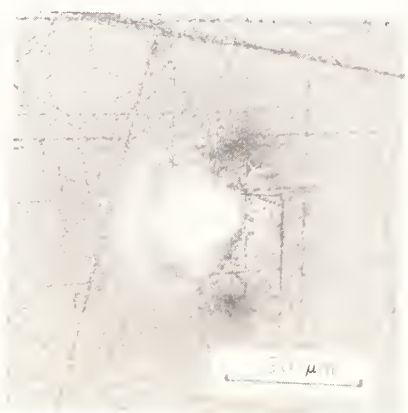

Figure 8. Photomicrograph of laser damaged (100) ALQLOY surface.

Figure 9. Electron micrographs illustrating the damage morphology of ALQLOY from the center outward edge of damaged area.

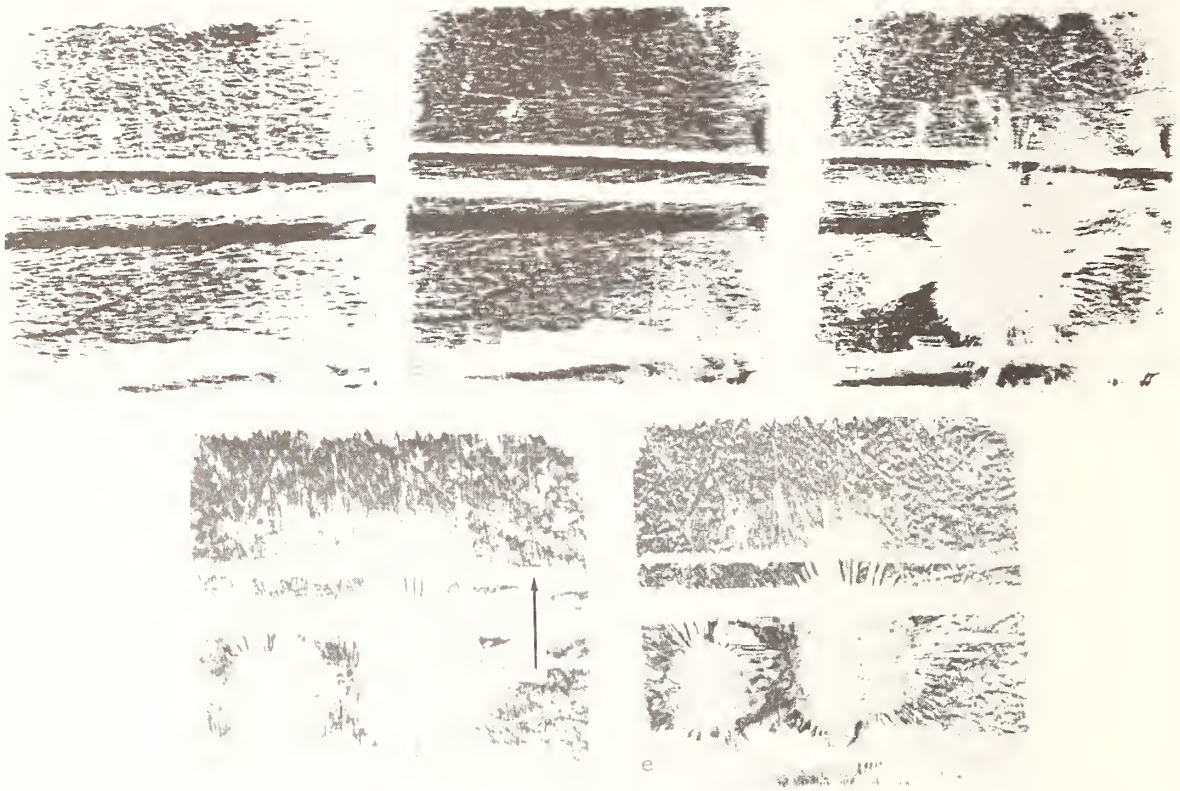

Figure 10. X-ray reflection topographs of Ge-coated (110) KCℓ; (a) [220] reflection after polishing, (b) [220] reflection after Ge deposition, (c) [220] reflection after laser damage, (d) [220] reflection after second laser irradiation (arrow indicates dislocation), (e) [420] reflection after second laser irradiation.

COMMENTS ON PAPER BY POSEN

It was noted in the paper that failure in potassium chloride was by slip rather than by rupture or cleavage. While for the ALQLOY material the reverse was true. It was brought out in the discussion that this difference might be a result of the much lower thermal conductivity exhibited by ALQLOY than by KCl. It was felt that with the low thermal conductivity the heat deposited in the sample under irradiation caused local stresses sufficient to rupture the material. This was also consistent with the fact that when metal coatings were put on the ALQLOY material failure occured by slip rather than by rupture. This was attributed to the higher thermal conductivity of the metal coating.

Surface and Coating Absorption Measurement With An Alphaphone

E. L. Kerr

The Perkin-Elmer Corporation
50 Danbury Road
Wilton, Connecticut 06877

Optical elements and coatings for high power laser applications require low surface absorption. The Alphaphone provides an instrument for rapidly measuring surface absorption at laser wavelengths. Sensitivity is 10^{-5} absorption with 10 W input and a noise bandwidth of 15 Hz. The total measuring time is a few minutes. Sensitivity down to 1.5×10^{-7} is achievable by decreasing the chopping frequency. In addition, sensitivity may be improved by signal averaging or by increasing the input power. Two surfaces of a window may be measured independently. Scattering has no significant effect.

The sample to be tested forms one wall of a thin cell filled with air. The air is heated by a small fraction of the energy absorbed at the sample surface when it is illuminated by the laser beam. The resulting pressure rise is measured by a capacitance microphone. In a demonstration we have recorded the absorption signals from two KRS-5 windows coated with anti-reflection coatings for 10.6 μm. The absorption was 1%, measured with a signal-to-noise ratio of 1000.

Key Words: Absorption, coatings, high-power laser, measurements, surface, testing.

1. Introduction

Optical elements and coatings require low surface absorption to transmit high-power laser beams without damage [1,2][1]. For example, if the surface absorption is only 0.01%, a window transmitting a 50 kW laser beam must dissipate 5 W at its surface. In developing the technology to produce such low absorption surfaces and coatings, a rapid method for measuring surface absorption is desirable.

The conventional method measures absorption indirectly as the difference between one and the sum of reflection, transmission and scattering. If an absorption of 10^{-5} is to be measured, the transmission must be measured to a precision of one part in 10^5, which is difficult.

Calorimetric methods measure absorption directly by measuring the rate of heat removal from the beam. In one calorimetric method [3] this is done by measuring the sample temperature rise in vacuum as the laser beam passes through it. The transmission and reflection need not be known very precisely. Scattering can affect the measurement if the scattered radiation directly impinges on the thermistor. The time to perform the measurement includes the time to pump down the calorimeter and the waiting time as the sample rises to a sufficient temperature for measurement. Bulk absorption and surface absorption contribute to the signal. Bulk and surface absorption may be separated only by measuring several samples with identical composition and surface preparation but different thicknesses, just as in the conventional method.

---

[1] Figures in brackets indicate the literature references at the end of this paper.

The Alphaphone is a surface absorption calorimeter. It measures surface absorption directly and provides some discrimination against bulk absorption. In the Alphaphone the signal is derived from heat absorbed by the coating and/or surface on one side of a window. The heat warms the air next to the surface, causing a measurable pressure rise. Any heat absorbed in the bulk of the window or at the other surface causes less pressure rise because it must diffuse through the window to reach the inner surface. The pressure rise in the air is measured with a capacitance microphone. The measurement is therefore completely insensitive to scattering.

2. The Alphaphone

The Alphaphone concept is a new use of an earlier instrument, the Thin Cell Spectrophone, invented [4] at Perkin-Elmer for measuring the absorption of trace gases in the atmosphere. A description of the Alphaphone, discussion of its sensitivity, and the results of a demonstration experiment follow.

2.1 Instrument Description

Refer to figure 1 for a diagram of the Alphaphone. The laser is (for example) a 10 W CO_2 laser operating in cw mode. The chopper has a 50% duty cycle and operates at a low frequency, typically 0.33 Hz. The lamp and detector associated with the chopper provide a positive signal when the beam is unblocked, and zero signal when it is blocked. The laser power is checked before and after the measurement with a power meter.

The window is clamped in the Alphaphone body, with the surface or coating to be measured inside. In the example shown in the figure, it is desired to determine the absorption of a coating alone, independent of the surface absorption of the window. Accordingly, the coating has been deposited on one half the surface of the window. Two measurements are then taken. When the mirror is in position A, the absorption due to the coating and the window is measured. In position B, the absorption due to the window alone is measured. This latter measurement may be subtracted from the first measurement to obtain the absorption attributable to the coating alone.[2] The back wall of the chamber in the Alphaphone body is gold-plated to provide a highly-reflective metal surface. The body is made of copper and sufficiently massive to provide a good sink for heat absorbed by the gold plating. The Alphaphone body is tilted slightly so the return beam does not enter the laser. The return beam can be directed into the power meter to provide continuous monitoring of the laser power during the measurement if desired.

A duct leads from the chamber in the Alphaphone body to one side of a capacitance microphone. The microphone consists of two chambers separated by a flexible steel diaphragm. Any increase in pressure in the Alphaphone chamber will deflect the diaphragm. The other chamber is maintained at a preference pressure of nominally one atmosphere. An adjustable leak allows the pressure in the two chambers to equilibrate over many chopping cycles. This reduces the sensitivity to thermal drift.

Deflection of the diaphragm is sensed by changes in the electrical capacity between it and two closely spaced electrodes. These electrodes also serve as mechanical protection for the diaphragm. Excessive overpressure on one side of the diaphragm will cause it to deflect until it rests on the opposite electrode. It can then sustain more than one atmosphere of overpressure without losing calibration.

Changes in capacity are sensed with a AC bridge circuit, then amplified and demodulated. The resulting pressure signal may be displayed on a two-pen recorder. As shown, the pressure signal rises as the irradiation portion of the cycle begins, and falls as irradiation is blocked. The amplitude of the rise and fall is proportional to the absorption.

---

[2] If the window signal is nearly equal to the signal from window and coating, the absorption in the coating is insignificant. One must first choose a window having sufficiently low absorption, and then develop a coating with low absorption.

For a high sensitivity measurement it is necessary to flush and fill the Alphaphone system with dry nitrogen to eliminate false signals from absorption by atmospheric carbon dioxide and water vapor. Also, the pressure signal and chopper reference signal may be connected to a lock-on amplifier. If the chopping frequency is 0.33 Hz, twenty cycles may be averaged in one minute.

2.2 Sensitivity

The high sensitivity of the Alphaphone for surface absorption calorimetry arises from its ability to measure a temperature rise as small as 6×10^{-6}°C or less. The ratio of this temperature rise ΔT to the ambient temperature $T = 300$°K is 2×10^{-8}. The associated fractional pressure rise $\Delta P/P$ for a gas in a fixed volume is equal to $\Delta T/T$, as may be seen by differentiating the ideal gas law, $PV = nRT$. In acoustics the reference pressure rise for 0 db is $P_o = 2 \times 10^{-10}$ atmosphere. The sound level in decibels is equal to $20 \log_{10} (\Delta P/\Delta P_o)$. A temperature rise of 6×10^{-6}°C therefore corresponds to a pressure rise ΔP of 2×10^{-8} atmosphere and a sound level of 40 db. This sound level, the level of noise in a quiet office, is easily detected with a microphone. The capacitance microphone we used is a commercial vacuum pressure guage, a Datametrics Barocel capable of measuring a maximum pressure rise of 10 mm Hg. When the upper frequency response is limited by a 66 ms RC low-pass filter, a pressure rise of 10^{-8} atmosphere is detectable.

A detailed thermal analysis of the Alphaphone has been given elsewhere [5]. When the surface coating begins to absorb energy from the beam, initially about 0.3% of the heat flows into the gas in the Alphaphone body chamber. The remaining heat flows into the window. As the window becomes saturated with heat and its temperature rises, a larger and larger fraction of the absorbed heat flows through the gas. Thus the temperature rise of the gas increases rapidly as the irradiation portion of the chopping cycle continues. If the chopping period were so long that it allowed about 20 minutes for heating and 20 minutes for cooling,, the limiting sensitivity would be about 1.5×10^{-7} measureable absorption. As this far exceeds present measurement requirements, it is possible to exchange sensitivity for shorter measuring time. The minimum period for the chopping cycle is set by the time required for heat to diffuse through the gas in the Alphaphone body chamber. For a chamber thickness of one millimeter this time constant is about 0.5 seconds. Allowing three of these time constants for heating and three for cooling, the total chopping period is three seconds. At this rate the sensitivity is 10^{-5} absorption with a noise bandwidth of 15 Hz. At present this sensitivity is adequate for most applications. However, if it is desired to measure smaller absorptions, one may use a lock-on amplifier to reduce the bandwidth, or increase the chopping period to obtain a higher temperature rise.

2.3 Demonstration Experiment

An experimental model of the Alphaphone has demonstrated its feasibility. We measured the absorption of some quarter-wave anti-reflection coatings on KRS-5 windows. The coatings were calcium fluoride, and zinc sulfide over a binder layer of thorium fluoride. The absorption of the combination of window and coating was 1% and the absorption of the windows alone was 0.1%. Typical signals are shown in figure 2. Trace (a) gives the signal for the calcium fluoride quarter-wave layer (λ = 10.6 μm) plus the contribution due to window absorption, while trace (b) gives the absorption signal due to the window alone. Trace (c) is trace (b) at 3.33 times the gain, to display its shape more clearly. All these signals may be related to trace (d), which shows the heating and cooling cycles. Trace (a) was measured with a signal-to-noise ratio of 1000. These were obtained with a CO_2 laser power of 10 W, at a chopping frequency of 1/3 Hz. The chamber thickness was 1 mm.

Direct calibration is possible by fabricating a thin-film resistor on a window and applying a known voltage and current. The total heat input is then known, and the heat flow splits between window and gas exactly as it does when the laser supplies the power. Furthermore, this calibration is independent of the calibration of the power monitor.

3. Conclusions

The Alphaphone provides a demonstrably feasible, sensitive method for calorimetric surface absorption measurement. The total cost of all components is only a fraction of the cost of the CO_2 laser. The method is convenient because there is no vacuum pump-down or cryogenic cooling. The time to make a measurement, including time to insert and remove the window, is only a few minutes. Sensitivity is great enough for absorption measurements of present high power laser components, and can be improved as materials improve. The method permits measurement of the absorption of a single surface. The measurement is insensitive to scattering. Absolute calibration is possible.

4. References

[1] D.W. Fradlin, E. Yablonovitch, and M. Bass, "Comparison of Laser Induced Bulk Damage in Alkali-Halides at 10.6, 1.06, and 0.69 Microns," in Laser Induced Damage in Optical Materials: 1972, edited by A.J. Glass and A.H. Guenther, National Bureau of Standards Special Publication No. 372 (U.S. GPO, Washington, D.C., 1972), p. 27,

[2] R.W. Hellwarth, "Fundamental Absorption Mechanisms in High-Power Laser Window Materials", ibid., p. 165.

[3] T.F. Deutsch and R.I. Rudko, Research in Optical Materials and Structures for High Power Lasers: Final Technical Report, U.S. Army Contract No. DAAH01-72-C0194, (Research Division, Raetheon Corporation, Waltham, Mass., 1973).

[4] E.L. Kerr, Gas Analyzer, U.S. Patent No. 3,727,050, April 10, 1973 assigned to the Perkin-Elmer Corporation.

[5] E.L. Kerr, "The Alphaphone--A Method for Measuring Thin Film Absorption at Laser Wavelengths," to be published in Applied Optics.

5. Figures

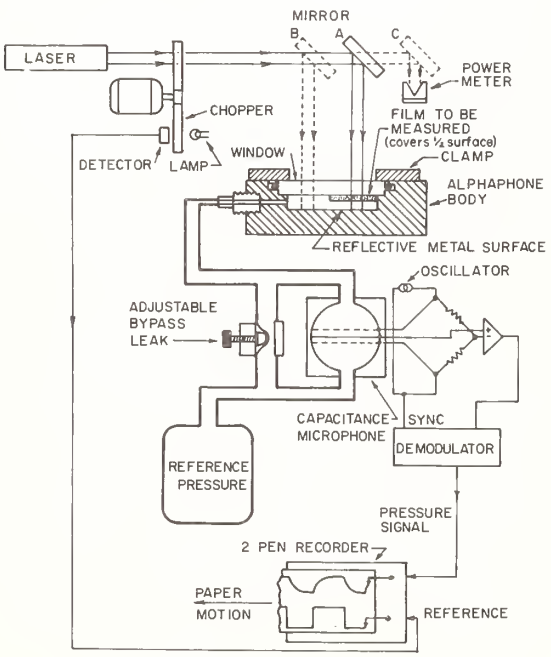

Figure 1. The Alphaphone System for measuring thin film absorption.

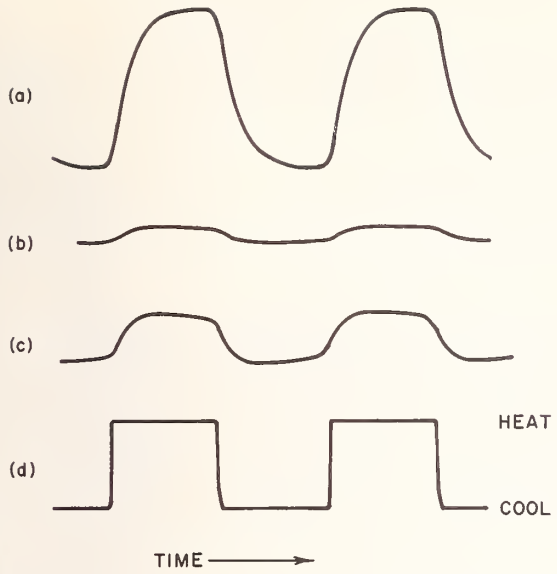

Figure 2. Typical pressure and reference signals. (a) Signal representing approximately 1% absorption by a calcium fluoride coating on a KRS-5 window. (b) Signal representing absorption by the KRS-5 window alone, at the same scale factor as (a). (c) The signal of (b) with 3.33 times more gain, for clarity. (d) Reference signal showing heating and cooling cycle of irradiation.

NO COMMENTS ON PAPER BY KERR.

Photoelastic Constants of Infrared Transmitting Materials

Bernard Bendow and Peter D. Gianino

Solid State Sciences Laboratory
Air Force Cambridge Research Laboratories
Bedford, Massachusetts 01730

Stress-induced birefringence may severely degrade or limit the optical performance of IR transmitting materials, especially in high power laser applications. The birefringence in a given material is predictable once the photoelastic tensor has been determined. In this work we carry out a first-principles calculation of the photoelastic constants p_{ij}, employing a recent theory of Humphreys and Maradudin. For ionic crystals, a Born-Mayer interatomic potential is employed, while for semiconductors a Morse potential is employed. The p_{ij} are calculated for a wide variety of rocksalt- and zinc blende-type crystals, including alkali-halides, II-VI's and III-V's. The electronic contribution to the p_{ij}'s is found to dominate in most semiconducting crystals, so that dispersion in the transparent frequency regime is generally negligible. For ionic materials, however, dispersion can be important; values at 10.6 μm, for example, may differ from those in the visible by as much as 25% to 50%, even for the better potential laser window materials.

Key Words: IR transmitting materials, photoelasticity, stress-optics.

1. Introduction

Stress-induced birefringence is a well-known and widely-investigated phenomenon in the optics of solids [1].[1] When a stress field acts on a crystal, changes in structure and symmetry are induced which lead to corresponding changes in the refractive index. The latter changes depend both on the nature of the applied stress, as well as the direction of propagation of the light. This phenomenon, known also as photoelasticity, may be characterized (within the elastic limit) by a photoelastic tensor $\vec{\vec{p}}$ defined by the relation [1]

$$\Delta(n^{-2})_{ij} = p_{ijk\ell}\tau_{k\ell} \quad , \tag{1}$$

where $n_{ij}^{-2} \equiv \epsilon_{ij}^{-1}$ and $\tau_{k\ell}$ are the elements of the inverse dielectric and strain tensors, respectively; n is the refractive index. One may analogously define stress-optic coefficients by expressing the $\tau_{k\ell}$ in terms of the stress components $\sigma_{k\ell}$. We note that for optically isotropic materials the above relations simplify considerably, and just a few independent p_{ij}'s remain.

Photoelasticity is relevant to the optics of infrared transmitting materials because it can lead to unacceptable distortion effects on the transmission of laser beams. The interference and "double refraction" associated with birefringent media are, of course, well-known [1]. In high-power applications, thermally-induced stresses contribute to the thermal lensing of spatially nonuniform laser beams and the concomitant degradation of the transmitted beam [2]. Whether the stresses inducing the birefringence are external or internal, in all cases the optical performance of laser windows may be severely compromised by the resultant distortion effects. A knowledge of the p's enables prediction of the effective temperature derivative of n, dn/dT, of IR transmitting materials; dn/dT itself being a measure of the potential for optical distortion in such materials.

The aim of the present work is to obtain theoretical predictions of the photoelastic constants of IR transmitting materials as functions of frequency. Frequency dependence is especially important because very little data is available in the IR, where such measurements are especially difficult, yet the effects of dispersion may be sizeable. We will here focus attention on two types of crystals, ionic crystals of the rocksalt (RS) type, and semiconductors of the zinc blende (ZB) type. The principal source of photoelasticity in the infrared for these materials is the change of crystalline vibrational frequencies and polarizabilities induced by stress fields. We will here employ the theory of Humphreys and Maradudin [3] (HM) to determine the latter effects. Once the p_{ij}'s have been computed, we will apply the results to obtain the frequency dependence of thermal lensing parameters governing induced distortion in laser windows.

For the cubic diatomic crystals that are investigated here, one can obtain an estimate of the p's by utilizing the relation [4]

[1] Figures in brackets indicate the literature references at the end of this paper.

$$p_{11} + 2p_{12} = \frac{1}{K}\frac{6}{n^3}\frac{dn}{dP} \quad , \tag{2}$$

where P is the pressure and K the isothermal compressibility, and a contracted index notation has been employed for the p's. With typical values of $K \sim 10^{-6}$/bar and $n^{-1}dn/dP \sim \frac{1}{2}10^{-6}$/bar, one obtains

$$p_{11} + 2p_{12} \sim \frac{3}{n^2} \quad , \qquad p_{ij} \sim \frac{1}{n^2} \quad . \tag{3}$$

Thus, the magnitude of the p_{ij}'s is roughly on the order of the inverse dielectric constant, typically about 0.1 to 0.3.

2. Theoretical Considerations

We first give a qualitative description of the frequency dependence of the p's, which will elucidate the viewpoint upon which the approach to be taken here is based. Let us assume for n the form [5, 6]

$$\begin{aligned} n^2 &= \epsilon_\infty + \frac{g^2}{\omega_T^2 - \omega^2} \\ g^2 &\equiv 4\pi e_T^{*2}/\mu v_a = (\epsilon_0 - \epsilon_\infty)\,\omega_T^2 \quad , \end{aligned} \tag{4}$$

where ϵ_0 and ϵ_∞ are the zero-frequency and electronic dielectric constants, respectively, e_T^* is the transverse effective charge, v_a is the volume per atom, μ the reduced mass, and ω_T the k = 0 transverse optic phonon frequency. The change in n induced by a strain $\Delta\tau$ is then

$$\Delta n = \frac{1}{2n}\left[\frac{\alpha\omega_T^2}{\omega_T^2 - \omega^2} + \frac{\beta\omega_T^4}{\left(\omega_T^2 - \omega^2\right)^2} + \gamma\right]\Delta\tau$$

where (5)

$$\alpha \equiv \frac{1}{\omega_T^2}\frac{\Delta g^2}{\Delta\tau} \quad , \qquad \beta \equiv \frac{-g^2}{\omega_T^4}\frac{\Delta\omega_T^2}{\Delta\tau} \quad , \qquad \gamma \equiv \frac{\Delta\epsilon_\infty}{\Delta\tau} \quad .$$

Combining Eqs. (1) and (5), the corresponding photoelastic constant p is then

$$p(\omega) = -\frac{1}{n^4(\omega)}\left[\frac{\alpha\omega_T^2}{\omega_T^2 - \omega^2} + \frac{\beta\omega_T^4}{\left(\omega_T^2 - \omega^2\right)^2} + \gamma\right] \quad . \tag{6}$$

The frequency dependence of p induced by the lattice, as contained in the first two terms on the right, is seen to be a result of the stress dependence of e* and ω_T. HM's theory essentially provides a simplified prescription for calculating α and β, once the interionic potential v(r) and dipole moment m(r) of the crystal [6] have been specified. Evaluation of the electronic parameter γ would require analogous prescriptions for stress-induced effects on the electronic frequencies and polarizabilities. As frequencies close to the electronic gap are approached, dispersion effects analogous to the lattice induced ones will arise [7]. Unfortunately, a useful first principles theory of these effects does not appear to be presently available. However, since we are not here concerned with electronic dispersion (which is, in fact, negligible for IR laser window materials), just a single measurement of p at frequencies below the electronic dispersion regime is all that is required to fix the value of γ. Such information is, in fact, available for many crystals of interest [8]. In other instances, one may still estimate γ from relationships between the p's and other measured quantities, such as in eq (3).

To make the qualitative discussion given above precise, one must properly associate the various specific p_{ij}'s with strains τ_i. As suggested by their definitions, α is principally determined by the microscopic dipole moment m(r), while β is determined by the interionic potential v(r). Using a nearest neighbor (n.n.) approximation, HM obtains for RS-type crystals the results

$$\begin{aligned} \alpha_{11} &= -g^2\left(1 - 4r_0 m''(r_0)/e_s^*\right) \\ \alpha_{12} &= -g^2\left(1 - 4m'(r_0)/e_s^* + 4m(r_0)/r_0 e_s^*\right) \\ \alpha_{44} &= -4g^2\left(m'(r_0) - m(r_0)/r_0\right)/e_s^* \end{aligned} \tag{7}$$

$$\beta_{11} = -2g^2\mu^{-1}r_0 v'''(r_0)$$

$$\beta_{12} = \beta_{44} = -2g^2\mu^{-1}(v''(r_0) - v'(r_0)/r_0) \quad ,$$

where α_{ij} and β_{ij} are the parameters corresponding to the three independent p_{ij}'s in the present case; the primes indicate derivatives, r_0 is the n.n. equilibrium distance, and e_s^* is the Szigeti charge, related to e_T^* by $e_s^* = 3e_T^*/(\epsilon_\infty + 2)$. Somewhat similar results obtain for the ZB structure as well, but these will be omitted for the sake of brevity. Thus, to compute the p_{ij}'s one requires the functions v(r) and m(r), as well the various material parameters entering the above formulae.

We choose the Born-Mayer potential, $v(r) = \pm e^2/r + Ae^{-Br}$, for ionic materials, with the parameters A and B determined by the thermodynamic prescriptions detailed in Born and Huang [6]. The correct form for m(r) is in doubt, but it is not unreasonable to assume a dependence similar to the short-range portion of v, namely $\bar{A}e^{-Br}$, with $\bar{A}$ determined from a relation between m and the Szigeti charge. In contrast to the case of ionic crystals of the RS type, the form of the interionic potential for the ZB-type crystals is not well known. HM employ a power-law potential of the form $ar^{-m} - br^{-n}$; we prefer a Morse potential, $v(r) = H(e^{-2D(r-r_0)} - 2e^{-D(r-r_0)})$, because it involves less free parameters, and is more typical in its functional dependence of true overlap potentials. Again, m(r) is modelled according to the short-range portion of v(r). The various limitations of such models, especially for tetrahedrally-bonded semiconductors, are quite apparent, as discussed at some length by HM, for example [9]. Nevertheless, the present choices do provide a reasonable starting point towards meaningful first principles calculations of photoelastic constants.

3. Computed Results

We have obtained the photoelastic constants p_{ij} for a variety of RS- and ZB-type crystals as functions of frequency in the infrared, employing the methods outlined above. The input parameters were either taken directly or computed on the basis of information available in a number of standard references [10]. The values of the principal parameters [11] are listed in table 1. Computed results for α_{ij} and β_{ij}, along with values of γ_{ij} determined from available experimental data (mostly in the visible) are given in table 2. We have calculated p_{ij}'s as a function of wavelength for all the materials listed in table 2, and these results will be made available in their entirety in a future report [12]. In figures 1–3 we display plots for just sodium and potassium salts, and several semiconductors. Values of the p_{ij} at 10.6 μm, 3.9 μm and electronic regime wavelengths are listed for comparison in table 3.

Table 1a. Material parameters (Rocksalt structure)

Material	ϵ_0	ϵ_∞	e_s^*	e_T^*	ω_T (cm^{-1})	A × 10^8 (ergs)	r_0 (A°)	B^{-1} (A°)
LiF	8.81	1.9	0.87	1.13	306	0.105	2.01	0.244
LiCl	12.0	2.7	0.73	1.14	191	0.078	2.57	0.332
LiBr	13.2	3.2	0.68	1.18	159	0.082	2.75	0.348
NaF	5.1	1.7	0.93	1.15	244	0.111	2.31	0.288
NaCl	5.9	2.25	0.74	1.05	164	0.147	2.81	0.328
NaBr	6.4	2.6	0.70	1.07	134	0.194	2.98	0.333
NaI	6.6	2.91	0.71	1.16	117	0.171	3.23	0.363
KF	5.5	1.5	0.88	1.03	190	0.194	2.67	0.302
KCl	4.85	2.13	0.81	1.11	142	0.363	3.14	0.324
KBr	4.9	2.3	0.76	1.09	113	0.393	3.29	0.334
KI	5.1	2.7	0.71	1.11	101	0.460	3.53	0.349
RbF	6.5	1.9	0.95	1.23	156	0.188	2.82	0.318
RbCl	4.90	2.2	0.84	1.18	116	0.346	3.27	0.338
RbBr	4.90	2.3	0.84	1.20	88	0.351	3.43	0.350
RbI	5.50	2.6	0.75	1.15	75	0.580	3.66	0.352
MgO	9.64	3.0	0.88	1.47	400	97.5	2.10	0.137
CaO	11.1	3.33	1.18	2.10	295	367.8	2.41	0.142
AgCl	12.3	4.0	0.71	1.42	103	16.0	2.78	0.202
AgBr	13.1	4.6	0.70	1.54	80	35.2	2.89	0.198

Table 1b. Material parameters (Zinc blende structure)

Material	ϵ_0	ϵ_∞	e_s^*	e_T^*	ω_T (cm^{-1})	H x 10^{12} (ergs)	r_0 (A°)	D $(A°)^{-1}$
GaP	10.18	8.46	0.58	2.02	367	7.11	2.36	2.02
GaAs	12.9	10.9	0.51	2.20	273	6.76	2.45	1.95
ZnS	8.3	5.0	0.96	2.24	274	6.59	2.35	2.03
ZnSe	9.2	6.1	0.72	1.94	215	3.66	2.46	1.94
CdTe	10.2	7.1	0.74	2.24	141	5.72	2.81	1.70

Table 2a. Photoelastic parameters α, β, γ (Rocksalt structure)

Material	α_{11}	β_{11}	p_{11}^e	α_{12}	β_{12}	p_{12}^e	α_{44}	β_{44}	p_{44}^e
LiF	15.56	187.93	0.019	- 9.97	-25.58	0.129	3.06	-25.58	-0.064
LiCl	62.54	351.35	-	-19.77	-51.21	-	10.47	-51.21	-
LiBr	89.46	418.74	-	-24.21	-59.82	-	14.21	-59.82	-
NaF	2.07	65.22	-	- 4.17	- 9.15	-	0.77	- 9.15	-
NaCl	25.04	72.22	0.110	- 7.38	- 9.40	0.153	3.73	- 9.40	-0.010
NaBr	33.75	80.98	-	- 8.46	-10.06	-	4.66	-10.06	-
NaI	30.92	73.44	-	- 8.02	- 9.18	-	4.33	- 9.18	-
KF	8.45	80.60	-	- 5.57	-10.17	-	1.57	-10.17	-
KCl	12.86	50.76	0.182	- 4.49	- 5.78	0.134	1.77	- 5.78	-0.026
KBr	17.71	47.42	0.241	- 4.87	- 5.30	0.191	2.27	- 5.30	-0.023
KI	22.30	41.43	0.210	- 5.09	- 4.51	0.169	2.69	- 4.51	-0.013
RbF	0.94	96.45	-	- 5.30	-12.13	-	0.70	-12.13	-
RbCl	9.84	49.68	0.288	- 4.13	- 5.67	0.172	1.43	- 5.67	-0.042
RbBr	9.59	42.97	0.293	- 3.97	- 4.84	0.185	1.37	- 4.84	-0.034
RbI	22.01	50.09	0.262	- 5.52	- 5.28	0.167	2.62	- 5.28	-0.024
MgO	25.28	254.07	-0.312	- 8.86	-17.66	-0.070	2.22	-17.66	-0.107
CaO	- 53.26	363.12	-	- 4.92	-22.73	-	- 2.85	-22.73	-
AgCl	100.72	575.07	-	-16.81	-44.91	-	8.51	-44.91	-
AgBr	114.62	593.54	-	-17.52	-43.50	-	9.02	-43.50	-

Table 2b. Photoelastic parameters α, β, γ (Zinc blende structure)

Material	α_{11}	β_{11}	p_{11}^e	α_{12}	β_{12}	p_{12}^e	α_{44}	β_{44}	p_{44}^e
GaP	- 5.92	5.36	-0.151	-15.55	9.24	-0.082	7.19	- 3.36	-0.074
GaAs	- 6.89	5.91	-0.165	-18.08	10.18	-0.140	7.08	- 2.98	-0.072
ZnS	- 11.37	17.22	0.091	-29.83	29.69	-0.010	41.01	-38.16	0.075
ZnSe	- 10.68	8.01	-	-28.02	13.82	-	6.51	- 1.82	-
CdTe	- 10.68	13.34	-	-28.02	22.99	-	27.39	-20.33	-

Table 3a. Photoelastic constants at various wavelengths (Rocksalt structure)

Material	Electronic values			3.9 μm			10.6 μm		
	p_{11}^e	p_{12}^e	p_{44}^e	p_{11}	p_{12}	p_{44}	p_{11}	p_{12}	p_{44}
LiF	.019	.129	-.064	.076	.086	-.049	-.632	-.563	.539
LiCl *	-	-	-	.047	-.015	.009	.384	-.142	.103
LiBr *	-	-	-	.033	-.009	.006	.266	-.077	.055
NaF *	-	-	-	.005	-.013	.003	-.088	-.119	.048
NaCl	.110	.153	-.010	.130	.147	-.007	.265	.104	.017
NaBr *	-	-	-	.013	-.003	.002	.105	-.027	.016
NaI *	-	-	-	.008	-.002	.001	.057	-.016	.009
KF *	-	-	-	.020	-.014	.004	.120	-.123	.048
KCl	.182	.134	-.026	.191	.131	-.025	.245	.110	-.016
KBr	.241	.191	-.023	.247	.189	-.022	.289	.178	-.017

(Continued)

Table 3a. Photoelastic constants at various wavelengths (Rocksalt structure) (Cont.)

Material	Electronic values			3.9 μm			10.6 μm		
	p_{11}^e	p_{12}^e	p_{44}^e	p_{11}	p_{12}	p_{44}	p_{11}	p_{12}	p_{44}
KI	.210	.169	-.013	.215	.168	-.012	.245	.161	-.009
RbF *	-	-	-	.001	-.006	.001	-.016	-.044	.009
RbCl	.288	.172	-.042	.292	.170	-.041	.318	.159	-.037
RbBr	.293	.185	-.034	.295	.184	-.034	.309	.179	-.032
RbI	.262	.167	-.024	.265	.166	-.024	.283	.162	-.022
MgO	-.312	-.070	-.107	-.253	-.096	-.099	-3.104	-.528	.452
CaO *	-	-	-	-.073	-.006	-.003	-1.620	-.043	-.007
AgCl *	-	-	-	.010	-.002	.001	.074	-.013	.007
AgBr *	-	-	-	.005	-.001	.000	.039	-.006	.003

* Electronic values not available; p's are computed with $p^e \equiv \gamma = 0$.

Table 3b. Photoelastic constants at various wavelengths (Zinc blende structure)

	Electronic values			3.9 μm			10.6 μm		
	p_{11}^e	p_{12}^e	p_{44}^e	p_{11}	p_{12}	p_{44}	p_{11}	p_{12}	p_{44}
GaP	-.151	-.082	-.074	-.153	-.087	-.072	-.170	-.129	-.053
GaAs	-.165	-.140	-.072	-.166	-.142	-.071	-.171	-.155	-.066
ZnS	.091	-.010	.075	.086	-.024	.094	.037	-.146	.261
ZnSe *	-	-	-	-.002	-.005	.001	-.018	-.045	.010
CdTe *	-	-	-	-.001	-.002	.002	-.005	-.014	.014

* Electronic values not available; p's computed with $p^e \equiv \gamma = 0$.

It should be pointed out that within the present approximations there are no lattice contributions to the photoelasticity of diamond-type semiconductors, since these are not infrared active ($e_T^* = 0$). Higher order lattice processes [13] do provide a small dispersion which for our purposes is negligible. Thus, for these crystals, the p_{ij}'s are determined entirely by their electronic contributions.

As mentioned previously, the p_{ij}'s are involved in the determination of thermally-induced stresses in high-power laser applications [2]. The effect of the induced birefringence on thermal lensing of spatially non-uniform beams is contained in the thermal lensing parameters S_1^α describing the induced phase shifts accompanying lensing (see Ref. 14). We now consider a circular window of a cubic diatomic crystal whose face is a {111} plane, employing results for this case due to Horrigan [15]. Also, we consider an isotropic model commonly employed in the literature [2] which ignores crystallinity. Then, explicitly,

(a) {111} Plane:

$$S_1^\rho = \partial n/\partial T + \frac{1}{12}\bar{\alpha} n^3[(1 - 4\nu)\, p_{11} + (5 - 8\nu)\, p_{12} - 2(1 + 2\nu)\, p_{44}] + \bar{\alpha}(1 + \nu)(n - 1)$$

$$S_1^\theta = \partial n/\partial T + \frac{1}{12}\bar{\alpha} n^3[(3 - 2\nu)\, p_{11} + (3 - 10\nu)\, p_{12} + 2(3 + 2\nu)\, p_{44}] + \bar{\alpha}(1 + \nu)(n - 1) \qquad (8a)$$

$$S_2^\rho = \frac{1}{24}\bar{\alpha} n^3 (1 + \nu)(p_{11} - p_{12} + 4p_{44}) \ .$$

(b) Isotropic Model:

$$S_1^\rho = \partial n/\partial T + \frac{1}{2}\bar{\alpha} n^3[(1 - \nu)\, p_{12} - \nu\, p_{11}] + \bar{\alpha}(1 + \nu)(n - 1)$$

$$S_1^\theta = \partial n/\partial T + \frac{1}{2}\bar{\alpha} n^3[p_{11} - 2\nu\, p_{12}] + \bar{\alpha}(1 + \nu)(n - 1) \qquad (8b)$$

$$S_2^\rho = \frac{1}{8}\bar{\alpha} n^3 (1 + \nu)(p_{11} - p_{12}) \ ,$$

where $\partial n/\partial T$ is the temperature derivative of the refractive index at zero stress, $\bar{\alpha}$ the linear thermal expansion coefficient, and ν Poisson's ratio. We note that $\nu = -\frac{2}{3}(s_{11} + 2s_{12} - \frac{1}{2}s_{44})/(s_{11} + s_{12} + \frac{1}{2}s_{44})$ for case (a), and, $\nu = -s_{12}/s_{11}$ for case (b), where the s_{ij}'s are elastic constants. The dispersions of the S_i^{α} are illustrated for NaCl and KCl in figure 4. The influence of stress-induced birefringence is conveniently described in terms of departures of S_1^{θ}/S_1^{ρ} from unity and S_2^{ρ}/S_1^{ρ} from zero. Values for these ratios at two different wavelengths, for the two cases mentioned above, are listed in table 4.

Table 4. Thermal lensing parameters at 1.0 and 10.6 μm

	Isotropic				{1 1 1} Plane			
	10.6 μm		1.0 μm		10.6 μm		1.0 μm	
Material	S_1^{θ}/S_1^{ρ}	S_2^{ρ}/S_1^{ρ}	S_1^{θ}/S_1^{ρ}	S_2^{ρ}/S_1^{ρ}	S_1^{θ}/S_1^{ρ}	S_2^{ρ}/S_1^{ρ}	S_1^{θ}/S_1^{ρ}	S_2^{ρ}/S_1^{ρ}
KCl	-0.327	-0.332	0.742	-0.065	0.585	-0.104	1.135	0.034
KBr	-10.000	-2.753	0.115	-0.221	-0.626	-0.404	1.267	0.068
NaCl	2.201	0.300	2.484	0.373	1.537	0.134	1.970	0.244
GaAs	0.989	-0.003	0.983	-0.004	0.943	-0.014	0.935	-0.016
Si	1.025	0.006	1.025	0.006	1.040	0.010	1.040	0.010
Ge	1.025	0.006	1.025	0.006	1.115	0.029	1.115	0.029

4. Conclusions and Discussion

We have calculated the effects of lattice dispersion on the photo-elastic constants. This dispersion is important for the case of RS-type ionic crystals, of less importance for ZB semiconductors, and of negligible importance for diamond-type semiconductors. The suppression of dispersion in semiconductors is evidenced by the relative smallness of the ratios α/γ and β/γ, and is the manifestation of a general property of such crystals: Lattice dispersion effects, as measured by the size of e_T^*, are small in comparison with electronic effects, which are, in general, enhanced by the relative smallness of the electronic gap. The change in p_{11} in going from electronic regime wavelengths to 10.6 μm is about 140% for NaCl, 35% for KCl, and 20% for KBr; on the other hand, this change is about 15% for GaP and about 5% for GaAs. A similar situation prevails with respect to thermal lensing parameters: Not only are birefringence effects weak for the semiconductors (see table 4), but they reveal negligible dispersion, as opposed to the ionic crystals, where the induced birefringence is relatively large and dispersive. Incidentally, table 4 strongly suggests that neglecting crystallinity is inappropriate, especially in the infrared dispersion regime. It turns out by a fortuitous quirk that the electronic regime values in the isotropic model, which have been the ones employed in the literature, are generally off by just a factor of two or so from {1 1 1} parameters at 10.6 μm.

Interference and double refraction effects [1] are determined by the absolute sizes of the p's and their linear combinations. Inspection of table 3 and use of dn/dP to estimate the p's suggests that the p's are of the order of ϵ^{-1}, which implies that they are, in general, somewhat smaller for the semiconductors than the ionic crystals.

Unfortunately, experimental measurements of the p's are virtually unavailable in the IR [8]. It is believed that the present theory should yield a reasonable approximation to both the absolute sizes of the p's and their frequency dependence. Corroborative experiments, providing a comparison of the latter with the theory, are badly needed and eagerly awaited.

5. References

[1] See, for example, M. Born and E. Wolf, "Principles of Optics," 2nd rev. ed. (Macmillan, New York, 1964); J.F. Nye, "Physical Properties of Crystals" (Oxford Press, London, 1964); D.A. Pinnow in "Handbook of Lasers," R.J. Pressley, ed. (Chemical Rubber Co., Cleveland, Ohio, 1971).

[2] M. Sparks, J. Appl. Phys. 42, 5029 (1971); J.R. Jasperse and P.D. Gianino, J. Appl. Phys. 43, 1686 (1972); B. Bendow and P.D. Gianino, J. Elect. Matrs. 2, 87 (1973) and Appl. Optics 12, 710 (1973).

[3] L.B. Humphreys and A.A. Maradudin, Phys. Rev. B 6, 3868 (1972).

[4] J.F. Nye, op. cit., p. 254.

[5] See, for example, J.M. Ziman, "Principles of the Theory of Solids" (Cambridge U. Press, 1967).

[6] M. Born and K. Huang, "Dynamical Theory of Crystal Lattices" (Oxford Press, London, 1954)

[7] S.H. Wemple and M. Di Domenico, Phys. Rev. B 1, 193 (1970).

[8] See, for example, D.A. Pinnow, op. cit., and, C.S. Sahagian and C.A. Pitha, "Compendium on High Power IR Laser Window Materials," AFCRL-72-0170 (1972).

[9] See, also, L.B. Humphreys and A.A. Maradudin, Phys. Rev. B (to be published).

[10] M. Born and K. Huang, op. cit.; E. Burstein in "Phonons and Phonon Interactions," T.A. Bak, ed. (W.A. Benjamin, Inc., New York, 1964); F.A. Kröger, "The Chemistry of Imperfect Crystals," Wiley, Inc. (1964); Landolt-Börnstein Tables, Vols. III/1 and 2 (Springer-Verlag, Berlin, 1966); S.S. Mitra in "Optical Properties of Solids," S. Nudelman and S.S. Mitra, eds. (Plenum, New York, 1969); J. Plendl and P.J. Gielisse, Appl. Optics 4, 854 (1965); and J. Plendl, Appl. Optics 10, 91 (1971).

[11] One of the parameters in the potential for the case of semiconductors is arbitrary; we choose D to conform to the choice of exponents in the power law chosen by HM. Reasonable variations in D about this value did not have a substantial effect on the computed results.

[12] B. Bendow and P.D. Gianino, AFCRL report (to be published).

[13] See, for example, J.M. Ziman, op. cit., and M. Born and K. Huang, op. cit.

[14] B. Bendow and P.D. Gianino, op. cit., ref. [2].

[15] F. Horrigan, private communication (and, to be published).

6. Figures

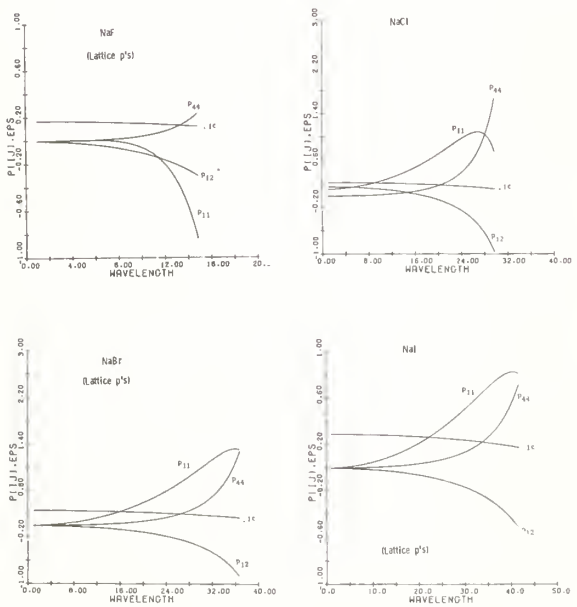

Figure 1. Photoelastic constants p_{ij} and dielectric constant ϵ as functions of wavelength in microns, for various sodium salts. "Lattice p's" indicates that due to a lack of availability the electronic contributions were set to zero in computing the p's for these materials.

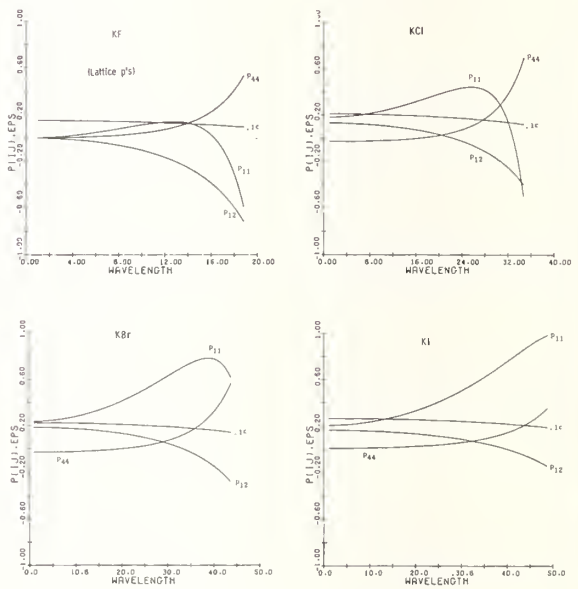

Figure 2. Same as in Figure 1, but for potassium salts. The p_{44} curve for KI, however, should be shifted uniformly downward by .026 units.

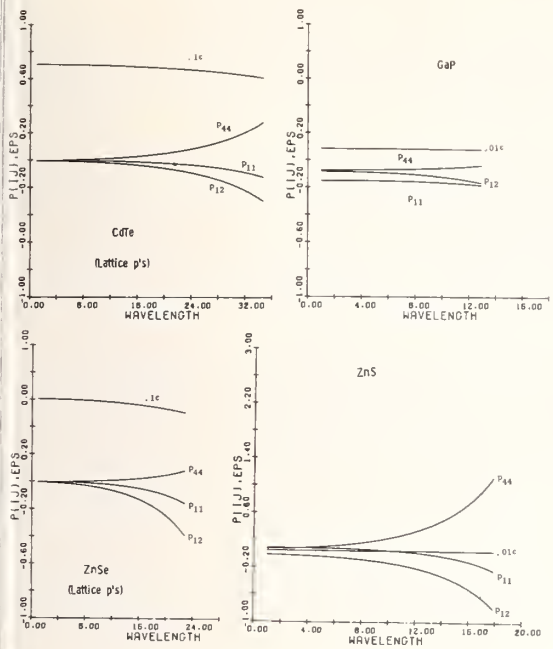

Figure 3. Same as in Figure 1, but for representative semiconductors.

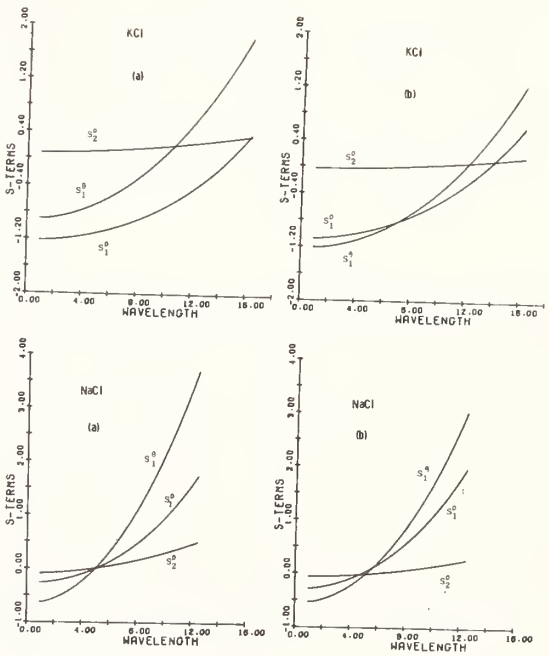

Figure 4. Thermal lensing parameters S_i^{α} as functions of wavelength in microns, for KCl and NaCl. Graphs (a) are the results for the isotropic model, while graphs (b) are for the {111} surface plane, as discussed in the text.

NO COMMENTS ON PAPER BY BENDOW

Checks of Multi-Phonon Absorption Theory*

Robert Hellwarth

Departments of Electrical Engineering and Physics
University of Southern California
University Park
Los Angeles, California 90007

There is considerable uncertainty as to the accuracy of calculations to date of multi-phonon absorption in infrared window materials. Here we show that such uncertainties can be checked by calculating various weighted integrals over frequency ("frequency moments") of the imaginary part $\chi''(\omega)$ of the electrical susceptibility, to which the absorption coefficient $\beta(\omega)$ cm^{-1} is related. We obtain expressions for six moments, evaluating a moment of the 2-phonon contribution explicitly for an anharmonic pair-interaction model. This exact result reveals inaccuracies in the dependence of absorption on ion masses and temperature predicted by approximate theories.

Key Words: Crystal absorption theory, frequency moments, infrared absorption, infrared susceptibility, infrared window materials, multi-phonon absorption.

1. Introduction

There has been a number of theoretical efforts to estimate the intrinsic infrared (IR) absorption coefficient $\beta(\omega)$cm^{-1} of IR window materials in the high-frequency "tail" of the fundamental lattice absorption. [1-7][1] This absorption is presumably "multi-phonon"; that is, an absorbed photon is converted to m-phonons so as to conserve energy and crystal momentum, and obey certain selection rules. [8, 9] Numerical predictions from the m-phonon theories for β have had to rely on rather drastic approximations that leave uncertain the magnitude of the theoretical errors. [1-7] Here we point out that various weighted integrals over frequency of the imaginary part $\chi''(\omega)$ the lattice electric susceptibility can be evaluated exactly, or at least to known accuracy. Since χ'' is related to β, the predicted values of these "moments" can be used to check the accuracy of the theories of β. We perform such a check of 2-phonon absorption in a diatomic cubic crystal, and point out errors in existing theoretical results for the mass and temperature dependence of this absorption. For example, we find that a) this absorption should be small when the ionic masses are very different, and b) when the masses are equal, the variation of the 2-phonon absorption, in going from low to high temperatures, is really about twice that predicted by previous approximate theories.

In Section 2, we review the quantum expressions for β and χ (the electric susceptibility). In Section 3, we define the moments of $\chi(\omega)$ and obtain the quantum formulae for six of them, in terms of averages over various derivatives of the interionic potential, assuming a linear relation to exist between the dipole moment operator and the ionic displacements (i.e., a "linear dipole moment"). We derive as an example in Section 4 the fifth frequency moment of the 2-phonon absorption for an anharmonic pair potential. Then in 5, we compare our predicted mass and temperature dependence with that from the approximate theories of β.

---

*This research was sponsored by Defense Advanced Research Projects Agency Contract No. F19628-72-C-0275 monitored by Air Force Cambridge Research Labs.

[1] Figures in brackets indicate the literature references at the end of this paper.

2. Quantum Theory of Absorption and Susceptibility

At optical frequencies well below the bandgap, we may picture a window material as composed of ions (labelled by greek indices $\alpha, \beta, \ldots$) having masses m_α, and interacting via a potential V that is a function of their position vectors $\vec{r}_\alpha$. The electronic interactions are absorbed in the ion dynamics via the Born-Oppenheimer approximation. This gives an effective Hamiltonian H for a subvolume L^3 of the material (where L is much less than an optical wavelength but much greater than the interionic spacing) of the form

$$H = \tfrac{1}{2}\Sigma_{i,\alpha} p_{i\alpha}^2/m_\alpha + V \tag{1}$$

where the $p_{i,\alpha}$ are the components (i=x, y, z) of the momentum operator for the ion α. The potential V does not include long range interactions between ions in L^3 and in neighboring regions. These interactions are assumed to be mediated by the long wavelength components of the electric field $\vec{E}$, that is, by the macroscopic electric field, the transverse part of which is the propagating field whose absorption coefficient we seek. The field interacts with the subvolume L^3 via a perturbation $-ME-\frac{1}{2}\chi_e E^2$ where χ_e is the electronic susceptibility with ions fixed, and M, the component of the electric dipole moment in L^3 along $\vec{E}$, is taken to be

$$M = \Sigma_\alpha e_\alpha x_\alpha \tag{2}$$

where e_α is effective charge of the ion α, and x_α is the component of the displacement from equilibrium of ion α along the direction of $\vec{E}$. We neglect here the terms in M that are not linear in the x_α as this is thought to be accurate for most polar insulating materials and has been assumed in most theories of multi-phonon absorption.

The complex ionic electric susceptibility χ_i at frequency ω of an optically isotropic crystal is defined as

$$\chi_i(\omega) = L^{-3}\langle M(\omega)\rangle / E(\omega) \tag{3}$$

Where $\langle M(\omega)\rangle$ is the expected amplitude of the electric moment in L^3 oscillating in response to the macroscopic field of amplitude $E(\omega)$. The absorption coefficient is related to $\chi=\chi_e+\chi_i$ by

$$\beta(\omega) = \frac{2\omega}{c}\,\mathrm{Im}\,[1+4\pi\chi(\omega)]^{\frac{1}{2}} \tag{4a}$$

$$\rightarrow \frac{4\pi\chi''(\omega)\omega}{nc}, \quad \chi'' << 1. \tag{4b}$$

Here χ'' is the imaginary part of χ_i, c is the velocity of light in a vacuum and n the refractive index. We now write the well-known quantum mechanical formula for χ'' in terms of the ion-ion response functions $S_{\alpha\beta}(\omega)$ for which we will derive simple moment formulae:

$$\chi''(\omega) = \pi L^{-3}\Sigma_{\alpha,\beta} S_{\alpha\beta}(\omega) e_\alpha e_\beta \tag{5}$$

where

$$S_{\alpha\beta}(\omega) \equiv \Sigma_{m,n}(P_m - P_n)\langle m|x_\alpha|n\rangle\langle n|x_\beta|m\rangle \cdot \delta(\omega-\omega_{nm})/(2\hbar) + (\alpha \rightleftarrows \beta). \tag{6}$$

Here $|m\rangle$ is an eigenstate of the Hamiltonian H for the subvolume L^3 having energy E_m and probability P_m of occupation. $\hbar\omega_{nm} \equiv E_n - E_m$. It is from this exact formulation (5) and (6) for χ'' that previous theories of $\beta(\omega)$ have started. We proceed instead to derive from (6) formulae for moments of $S_{\alpha\beta}$ and thereby for χ''.

3. Moments of Ion-Ion Response Functions

The ℓ^{th} moment $S_{\alpha\beta}^{(\ell)}$ of the ion-ion response function $S_{\alpha\beta}(\omega)$, as defined by

$$S_{\alpha\beta}(\ell) = \begin{cases} \int_{-\infty}^{\infty} d\omega\omega^\ell S_{\alpha\beta}(\omega), & \ell \text{ odd} \quad (7a) \\ \int_{-\infty}^{\infty} d\omega\omega^\ell \coth\left(\frac{\hbar\omega}{2kT}\right) S_{\alpha\beta}(\omega), & \ell \text{ even}, \quad (7b) \end{cases}$$

is seen from (6) to equal

$$\hbar^{-\ell-1}\Sigma_{m,n} P_m (E_n - E_m)^\ell \langle m|x_\alpha|n\rangle\langle n|x_\beta|m\rangle + (\alpha \rightleftarrows \beta) \tag{8}$$

for thermal equilibrium when $P_n/P_m = \exp(E_m - E_n)/kT$. From (8) it follows directly that

$$S_{\alpha\beta}^{(0)} = 2\langle x_\alpha x_\beta\rangle/\hbar \tag{9}$$

$$S_{\alpha\beta}^{(1)} = \delta_{\alpha\beta}/m_\alpha \text{ (Thomas-Kuhn-Reich sum rule)} \tag{10}$$

$$S_{\alpha\beta}^{(2)} = \langle x_\alpha (\partial V/\partial x_\beta)\rangle/(m_\beta \hbar) + \alpha \leftrightarrow \beta \tag{11}$$

$$S_{\alpha\beta}^{(3)} = \langle \partial^2 V/\partial x_\alpha \partial x_\beta \rangle / m_\alpha m_\beta \tag{12}$$

$$S_{\alpha\beta}^{(4)} = 2\langle (\partial V/\partial x_\alpha)(\partial V/\partial x_\beta)\rangle/m_\alpha m_\beta \hbar \tag{13}$$

$$S_{\alpha\beta}^{(5)} = \Sigma_{\gamma,i} \langle (\partial^2 V/\partial x_\alpha \partial r_{i\gamma})(\partial^2 V/\partial x_\beta \partial r_{i\gamma})\rangle/m_\alpha m_\beta m_\gamma \tag{14}$$

by repeated use of the identity

$$(E_m - E_n)\langle m|A|n\rangle = \langle m|[H, A]|n\rangle \tag{15}$$

where A is any operator and H is the Hamiltonian operator of (1). In (14), $r_{i\alpha}$ is the displacement of ion α in a direction i=x, y, z. In (9) - (14) the x_α are displacements parallel to the applied electric field.

4. Application to Pair Interactions With Hard Cores

The interaction potential V of ionic crystals is known to be fairly well represented by a superposition of pair potentials

$$V \to \tfrac{1}{2}\Sigma_{\alpha,\beta} v(\vec{x}_\alpha - \vec{x}_\beta + \vec{R}_\alpha - \vec{R}_\beta) \tag{16}$$

where $\vec{x}_\alpha$ is the displacement from equilibrium position $\vec{R}_\alpha$ of ion α. In multi-phonon absorption calculations, the potential V has been assumed to be made up of a harmonic part V_h, quadratic in the ion coordinates, and an anharmonic part V_{an}, which arises from the hard-core repulsion between nearest neighbors, and which has been assumed to be a power series

$$V_{an} = \Sigma_{\alpha,\beta} \Sigma_{n=3}^{\infty} c_n r_{\alpha\beta}^n/n! \tag{17}$$

in the relative ionic displacement $r_{\alpha\beta}$ along the equilibrium separation vector $\vec{R}_\alpha - \vec{R}_\beta$. ($\alpha$ and β are summed over all nearest neighbor pairs.) Since the repulsive part of v(r) is thought to be roughly of the form exp-r/ρ, the coefficients c_n are thought to be all of the same order of magnitude, and of the order of a dimensionless anharmonicity parameter λ [10]:

$$c_n \sim \lambda \tag{18}$$

where

$$\lambda \equiv \left(\frac{\hbar}{2\omega_o \mu \rho^2}\right)^{\frac{1}{2}}, \tag{19}$$

μ is the reduced mass of an ion pair, and ω_o is the transverse optical (or reststrahl) frequency. The values of ρ for alkali halide crystals have been determined from bulk modulus data and yield values of λ around 0.3.

Given some natural assumption about the exact values of c_n (e.g., $c_n = \lambda \times$ constant), the present theories for the absorption β are not able to proceed with known accuracy even to calculate two-phonon absorption; the k-space integrals are too complicated. However, we can proceed to find the moments (9)-(14) to some desired order in the anharmonicity parameter. We illustrate this here by finding the part of the fifth moment that is of order λ^2 and represents multi-phonon absorption.

An examination of $S^{(5)}$ in (14) shows that the only λ^2 terms are those proportional to $c_2 c_4$ or c_3^2. (Here we have used c_2 to symbolize the harmonic force coefficients in analogy with the anharmonic coefficients c_n for n>2 in (17).) An examination of the structure of perturbation theory shows that to order λ^2, the $c_2 c_4$ term describes a shift and broadening of the one-phonon absorption while the corresponding c_3^2 term gives rise only to multi-phonon absorption. In fact it describes the rate of all combinations of two-phonon absorption and emission among all phonon branches. This is evident because c_3 is the coefficient of all products of three phonon creation and annihilation operators in the perturbing potential, and therefore in the c_3^2 term in χ''. These terms contribute a factor to the absorption matrix element that describes the annihilation of the k=0, TO phonon (created by a photon) along with the annihilation or creation (in any combination) of two other phonons from any branches. We now calculate this "2-phonon" contribution $S_{2ph}^{(5)}$ to the fifth moment $S^{(5)}$ of χ''.

Inserting the n=3 term of (17) into (14), performing the indicated differentation, and summing over ions as indicated in (5) gives for a rocksalt structure crystal

$$S_{2ph}^{(5)} \equiv \int_0^\infty d\omega\, \omega^5 \chi''(\omega)_{2\text{-phon}} = \pi c_3^2 e^2 \mu^{-3} L^{-3} \sum_\alpha [\tfrac{1}{2} < (x_\alpha - x_{\alpha-1})^2 > - < (x_{\alpha-1} - x_\alpha)(x_{\alpha+1} - x_\alpha) > \mu / m_\alpha \,]. \tag{20}$$

Here, $x_{\alpha\pm1}$ are the relative x-displacements of the nearest neighbors to ion α in opposite directions along the crystal x-axis; e is the magnitude of the effective charges e_α and e_β, and μ is the reduced ion pair mass. The thermal averages indicated by $< >$ are needed here only in the harmonic approximation ($\lambda = 0$). For a diatomic crystal, harmonic-crystal quantum theory gives [10]

$$< x_\alpha x_\beta >_{\text{harm}} = \sum_Q \frac{\hbar U^{-1}(x, \alpha; Q) U(x, \beta; Q)}{2\omega_Q \sqrt{m_\alpha m_\beta}} \coth \frac{\hbar\omega_Q}{2kT} \tag{21}$$

where the Q labels all the normal modes of the crystal in volume L^3, and ω_Q are their frequencies. The unitary U-matrices are those which diagonalize the matrix $V_{xy,\alpha\beta}(m_\alpha m_\beta)^{-\frac{1}{2}}$ deriving from the expression

$$V_h = \tfrac{1}{2} \sum_{xy,\alpha\beta} x_\alpha y_\beta V_{xy,\alpha\beta} \tag{22}$$

for the harmonic part of the potential.

5. Comparison With Absorption Theory

There exists no explicit calculation of all 2-phonon processes for a real lattice with an explicit V_h with which we might compare the results (20) and (21) directly. However, we can obtain some interesting checks of absorption theory by examining two extreme rocksalt structure models in which there are either 1) very unequal ion masses, or 2) equal masses and nearest neighbor interactions.

5.1 $m_{\alpha+1} >> m_\alpha$

When the masses of the ions in a rocksalt cubic crystal are very different, then the light ions (α) move in a nearly rigid cage of the surrounding heavy ions, making $x_{\alpha+1} - x_\alpha \approx x_\alpha - x_{\alpha-1}$. This with the limit $m_\alpha \to \mu$ causes the two averages in (18) to cancel exactly, indicating that 2-phonon absorption vanishes when $m_{\alpha+1} >> m_\alpha$. This is reasonable, because the light ion is moving effectively in a potential having inversion symmetry, and its states have even or odd parity. Since dipole transitions are not allowed between states of the same parity, no even number phonon absorption processes will exist in this limit. No hint of this depression of the even-phonon number absorption is found in present approximate theories, although the effect can be seen in the relative experimental heights of the 2-phonon resonance peaks in different alkali halides.[11] This failure probably signals factors-of-two errors in the high-frequency tail absorption of crystals like LiF whose ionic masses are quite different.

5.2 $m_\alpha = m_{\alpha+1} = 2\mu$ and Nearest Neighbor Forces Only

When both ion masses are equal and the harmonic forces are between nearest neighbors in a cubic diatomic crystal, the normal lattice modes consist of three degenerate branches whose ion motions are polarized along x, y and z. Since we need only correlations between x-displacements in (20), the sum in (21) is over one branch only. The normal mode coordinates for this branch, as embodied in the unitary U-matrices, are the familiar plane waves

$$U(x, \alpha; Q) = (\frac{a}{L})^{\frac{3}{2}} \exp i \frac{2\pi a}{L} (Q_x \alpha_x + Q_y \alpha_y + Q_z \alpha_z) \tag{23}$$

where the modes are labelled by the integers $Q_x, Q_y, Q_z = 0, \pm 1, .. \pm \frac{L}{2a}$ and the ions by the integer coordinates $\alpha_x, \alpha_y, \alpha_z = 1, 2, \ldots L/a$. The length of the cube edge of the crystal subvolume is L and the interionic spacing is a. Diagonalizing the harmonic potential with (23) gives the eigenvalues of the potential matrix and the dispersion relation for the x-branch:

$$\omega_Q = \omega_o \sin(\pi Q_x a / L), \tag{24}$$

where

$$\omega_o \equiv (2C/\mu)^{\frac{1}{2}} \tag{25}$$

is the "TO" or fundamental (k=0) optical phonon absorption frequency for the rocksalt structure lattice with equal masses ($m = 2\mu$) and nearest-neighbor force constant C.

Substituting (23) and (24) in (21) gives for the 2-phonon absorption moment of (20)

$$S_{2ph}^{(5)} = \frac{2c_3^2 e^2 \hbar}{\mu^4 a^3 \omega_o} I(\gamma) \tag{26}$$

where

$$I(\gamma) \equiv \int_o^1 du\, u(1-u^2)^{\frac{1}{2}} \coth \gamma u . \tag{27}$$

The temperature parameter γ is

$$\gamma \equiv \frac{\hbar\omega_o}{2kT} . \tag{28}$$

At high temperatures

$$I(\gamma) \to \frac{\pi}{4\gamma} , \quad \gamma \to 0 \tag{29}$$

and at low temperatures

$$I(\gamma) \to \frac{1}{3} , \quad \gamma \to \infty . \tag{30}$$

For fixed ω_o, c_3, e, and a, the independent-anharmonic-molecule models [1-4] predicted for this, or any other type of lattice, a 2-phonon temperature factor $2\bar{n} + 1$, where $\bar{n}$ is the Planck function $[e^{2\gamma}-1]^{-1}$. Therefore these very approximate theories predict

$$\frac{S_{2ph}^{(5)}(T=0)}{S_{2ph}^{(5)}(T\to\infty)} = \gamma \tag{31}$$

rather than the exact result for this lattice model of $4\gamma/3\pi$ from (29) and (30). A plot of $I(\gamma)$ between its asymptotes is shown in figure 1 together with the $2\bar{n}+1$ function normalized to approach $I(\gamma)$ at high temperatures.

It is well-known that this model having only nearest neighbor forces does not accurately describe any real rocksalt-structure ionic crystals. However, we feel that checking a theory by applying it to this model does give a reasonable estimate of its accuracy for a more realistic model of a crystal. That is, the fact that the ratio (31) from approximate theories of absorption is 2.4 times the exact result for this (albeit poor) model is an indication of the kinds of errors for the moments of β that the independent-molecule models may yield in the 2-phonon region. It is also likely that the errors are even larger at higher frequencies (higher phonon numbers).

In summary, we have shown how calculations of frequency moments of the imaginary part $\chi''(\omega)$ of the electric susceptibility can be performed with much greater accuracy than can calculations of $\chi''(\omega)$ itself, and how the moment calculations can be used to check the more detailed calculations of multi-phonon absorption $\beta(\omega)$ as a function of frequency. Many other checks and relations may be derived from the moment expressions (9) to (14) than we have mentioned here.

6. References

[1] M. Sparks and L. J. Sham, Sol. State Comm. 11, 1451 (1972) estimated multi-step absorption in a slightly anharmonic oscillator by considering a subset of perturbation theory terms (or "diagrams"). A linear dependence of electric moment on oscillator displacement (a "linear moment") was assumed.

[2] B. Bendow, Phys. Letters 42A, 359 (1972) calculated the multi-step absorption in a harmonic oscillator arising from non-linear dependence of the electric moment on the oscillator coordinate (a "non-linear moment")

[3] T. C. McGill, R. W. Hellwarth, M. Mangir and H. Winston, J. Phys. Chem. Solids (to be published) calculated exactly multi-step absorption in slightly anharmonic oscillators with both linear and quadratic electric moments.

[4] B. Bendow, S. C. Ying, and S. Yukon (to be published) have constructed a Green's function formulation of the anharmonic lattice having a nonlinear electric moment, and estimated Debye-Waller factors.

[5] M. Sparks and L. J. Sham, Phys. Rev. (to be published) have estimated multi-phonon absorption from a real lattice, having a linear moment, by neglecting crystal-momentum conservation.

[6] A. A. Maradudin and D. L. Mills (to be published) have found the classical limit of the high frequency absorption of a charged particle moving in a variety of potentials.

[7] H. B. Rosenstock, Bull. Am. Phys. Soc. 18, 674 (1973), has summed the thermal phonon population factors over the modes of KCl to obtain better estimates of the temperature dependence of its multi-phonon absorption than come from single-frequency models.

[8] J. L. Birman (to be published) has examined selection rules for the combinations of phonons that can be created by absorbing a photon.

[9] R. A. Cowley, in "Phonons in Perfect Lattices and in Lattices with Point Imperfections" pp. 170-207 (ed. R. W. H. Stevenson, Plenum Press, N. Y. 1966) reviews multi-phonon perturbation theory and some calculations of specific diagrams and spectral features.

[10] L. van Hove, N. M. Hugenholtz, and L. P. Howland "Quantum Theory of Many Particle Systems" (W. A. Benjamin, N. Y. 1961)

[11] L. Genzel, in "Festkörper Probleme" Vol. VI, p. 32 (ed. O. Madelung, Pergamon Press, Oxford 1967).

7. Figures

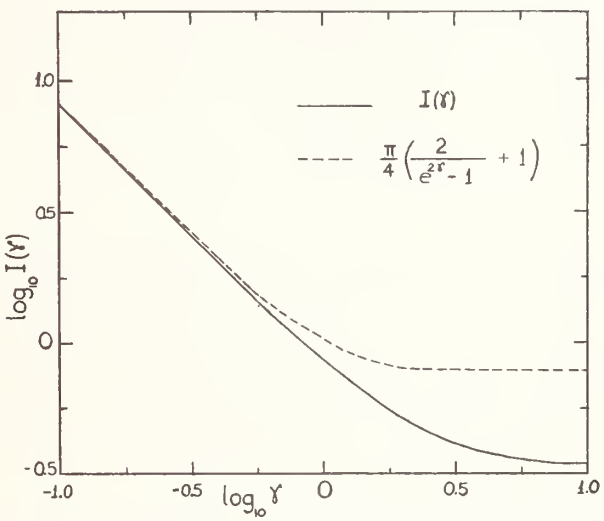

Figure 1. Plot of the temperature factor $I(\gamma)$ calculated for the fifth frequency moment of all 2-phonon contributions to the imaginary part χ'' of the susceptibility of a rocksalt-structure crystal with nearest neighbor interactions. The factor $2n+1$ predicted from the independent-molecule approximation for the same moment is shown for comparison, normalized arbitrarily to approach the exact result at high temperatures. ($\gamma \equiv \hbar\omega_o/2kT$)

COMMENTS ON PAPER BY HELLWARTH

It was shown in the paper presented by Stierwalt in this Symposium that samples of potassium chloride, for example, showed an increase in absorption with decreasing temperature. Hellwarth commented that this observation could not be attributed to intrinsic mechanisms in the material, but must be due to extrinsic factors, known commonly as "dirt". He commented that all theories indicate a decrease in absorption with decreasing temperature, except for very weak effects, like phonon-assisted electronic transitions, which enter at much lower values. He was reluctant to speculate on the exact nature of the extrinsic factors present. There was also considerable discussion of the fact that the far wings of the absorption lines in multiphonon absorption are indicated to be exponential in form, and that this result is implicit in the existence of the successive moments of the ion-ion response function. Although the existence of the moments does not necessarily indicate a true exponential form, it does indicate that the wing is not described by a finite power. It was suggested in the discussion that the quasi-exponential form of the wing of the absorption line may be due to very general properties of the interaction potential.

Theory of Material Failure in Crystals Containing Infrared Absorbing Inclusions*

C. J. Duthler and M. Sparks

Xonics, Incorporated, Van Nuys, California 91406

Small amounts of macroscopic inclusions in or on the surface of infrared-transmitting materials (in some cases a fractional volume of 10^{-7} to 10^{-8}) increase the average value of the optical absorption coefficient β and cause localized heating that could lead to material failure at high-power levels. The frequency dependence of β ranges from increasing as ω^2, to independent of ω, to exponentially decreasing with ω. Temperature dependence ranges from independent of T, to increasing as T^p in the high-temperature limit, where $p \cong 1 - 4$ typically. Simple expressions for the absorption cross section are used to derive expressions for β for large inclusions of strong and weak absorbers and small inclusions of dielectric and metallic particles. Material failure resulting from local heating of inclusions is a far greater problem in high-intensity short-pulse systems than in low-intensity long-pulse or cw systems having the same average intensity. Microsecond pulses with energy densities as low as a few joules per square centimeter can cause material failure.

Key Words: Dielectric particles, inclusions, laser damage, thermal damage.

1. Introduction

Extrinsic absorption by macroscopic inclusions either in the bulk or on the surface of nonabsorbing host crystals is investigated in relation to the current interest in lowering the value of the optical absorption coefficient β and studying high-power limitations in infrared-transmitting materials. Optical absorption by inclusions increases the spatial average of β, thus increasing overall heating of the material. This could cause either irreversible system failure (thermally induced fracture) or reversible failure (thermal defocusing). [1-3][1] In addition, local heating in the region of the inclusion can cause discrete material failure or optical distortion of the beam by the heated host material in the neighborhood of the inclusion.

Heating of both dielectric and metallic spherical inclusions in transparent hosts is considered as a function of inclusion radius and laser pulse length, using simple, realistic models for the absorption cross section and for heat transfer from the inclusion to the host. A detailed analysis of the results presented here will be published elsewhere.[4]

2. Analysis of Absorption Cross Sections

The absorption cross section of an individual spherical inclusion of radius a is not generally equal to the geometrical cross section πa^2. For $ka \ll 1$, where $k = 2\pi/\lambda_H$, with λ_H the wavelength of the radiation in the host material, the value of σ_{abs} typically is small ($\sigma_{abs} \ll \pi a^2$). In the case of $ka \gg 1$ and $|\epsilon| \gg 1$, where $\epsilon = \epsilon_I/\epsilon_H$, with ϵ_I and ϵ_H the dielectric constants of the inclusion and host, respectively, the reflection at the surface of the sphere is great, which again makes $\sigma_{abs} \ll \pi a^2$. Exact absorption cross sections for spheres of

*This research was supported by the Advanced Research Projects Agency of the Department of Defense and was monitored by the Defense Supply Service - Washington, D. C. under Contract DAHC15-73-C-0127.

[1]Figures in brackets indicate the literature references at the end of this paper.

arbitrary size can be obtained from the classic result of Mie.[5,6] The Mie solutions are complicated in general, but reduce to simple results in the limits ka >> 1 and ka << 1 which are presented in this section and used to calculate material failure at discrete sites in the crystal in the following section. The overall absorption coefficient β of a sample containing N_I inclusions per unit volume also can be obtained from σ_{abs} using

$$\beta = \sigma_{abs} N_I$$

and is discussed in Ref. 4.

For small spheres (ka << 1), the Mie series is well approximated by the first term, which yields

$$\sigma_{abs} \cong \frac{12\,\epsilon_{\mathcal{J}}\,ka}{(\epsilon_{\mathcal{R}}+2)^2+\epsilon_{\mathcal{J}}^2}\,\pi a^2 \quad , \qquad \text{for } ka \ll 1 \, , \tag{2.1}$$

where $\epsilon = \epsilon_{\mathcal{R}} + i\,\epsilon_{\mathcal{J}}$. Two limiting cases of (2.1) are of interest. For $\epsilon_{\mathcal{J}} \ll \epsilon_{\mathcal{R}}$, which is satisfied for nonmetals at frequencies not too near the fundamental resonance frequency or the high-frequency absorption edge, β_I and $\epsilon_{\mathcal{J}}$ are related by the expression

$$\beta_I = 2 n_{\mathcal{J}}\, k \cong \frac{\epsilon_{\mathcal{J}}\, k}{n_{\mathcal{R}}} \quad , \tag{2.2}$$

where $n = n_{\mathcal{R}} + i n_{\mathcal{J}}$. Using this result to eliminate $\epsilon_{\mathcal{J}} k$ in (2.1) gives

$$\sigma_{abs} = \frac{12\, n_{\mathcal{R}}}{(\epsilon_{\mathcal{R}}+2)^2}\,(\beta_I a)\,\pi a^2 \quad , \qquad \epsilon_{\mathcal{J}} \ll \epsilon_{\mathcal{R}} \tag{2.3}$$

The second limiting case is that of small metallic inclusions. The Drude expression for the dielectric constant is [7]

$$\epsilon = \epsilon_\infty - \frac{\omega_p^2}{\epsilon_H(\omega^2 + i\omega\Gamma)} \quad , \tag{2.4}$$

where Γ is the electron relaxation frequency (often written as $1/\tau$), ϵ_∞ is the contribution to ϵ from the core electrons, and $\omega_p = (4\pi N e^2/m)^{1/2}$ is the plasma frequency, which has a typical value of $\omega_p = 5 \times 10^{15}\ \text{sec}^{-1}$. At 10.6 μm, $\omega \cong 1.9 \times 10^{14}\ \text{sec}^{-1}$. There are two contributions to the relaxation frequency Γ: $\Gamma = \Gamma_{Bu} + \Gamma_{Su}$, where the bulk contribution $\Gamma_{Bu} \cong 5 \times 10^{13}\ \text{sec}^{-1}$, typically. The value of the surface scattering contribution [8] Γ_{Su} is $\approx v_F/a$, where the Fermi velocity $v_F \cong 10^8$ cm/sec for many metals. With $\Gamma_{Bu} \cong 5 \times 10^{13}\ \text{sec}^{-1}$ and $v_F \cong 10^8$ cm/sec, $\Gamma_{Su} > \Gamma_{Bu}$ for $a < a_\Gamma \cong 200$ Å.

For typical metals at 10.6 μm, $\omega_p^2 \gg |\,\omega^2 + i\omega\Gamma\,|$, and (2.4) gives

$$\epsilon\,\epsilon_H \cong -\frac{\omega_p^2}{\omega^2 + i\omega\Gamma} = -\frac{\omega_p^2}{\omega^2+\Gamma^2}\left(1 - i\,\frac{\Gamma}{\omega}\right) \quad , \qquad \epsilon_{\mathcal{R}} + 2 \cong \epsilon_{\mathcal{R}} \, . \tag{2.5}$$

Both the real and imaginary parts of the dielectric constant are large in magnitude for small particles of typical metals at 10.6 μm. Substituting (2.5) into (2.1) gives

$$\sigma_{abs} = 12\,\epsilon_H^{3/2}\,\frac{\omega^2}{\omega_p^2}\,\frac{\Gamma a}{c}\,\pi a^2 \;; \qquad \omega_p^2 >> |\,\omega^2 + i\omega\Gamma\,| \;, \tag{2.6}$$

for metals with $ka \ll 1$.

Next consider the case of large spheres ($ka >> 1$). Using geometrical optics and the identity $1+x+x^2+\cdots = (1-x)^{-1}$, where $x \equiv R_i \exp(-\beta_I d)$, with R_i the internal reflection coefficient and d the distance the ray travels in traversing the sphere once, gives

$$\sigma_{abs} = \pi a^2 \int_0^1 d(\cos^2\theta)\,(1-R)\left(1-e^{-\beta_I d}\right)\left(1-R_i e^{-\beta_I d}\right)^{-1} \tag{2.7}$$

where $R = (|\,r_p\,|^2 + |\,r_n\,|^2)/2$, with r_p and r_n the Fresnel reflection coefficients for the two polarizations, d the distance that the refracted ray travels through the sphere, and θ the angle of incidence.

Two limiting cases of (2.7) are of interest. First, for $\beta_I a >> 1$, which is typically satisfied for metals and strongly absorbing dielectrics, (2.7) yields

$$\sigma_{abs} \cong \pi a^2 (1 - \langle R \rangle) \tag{2.8}$$

where the average reflection coefficient $\langle R \rangle$ is defined as

$$\langle R \rangle = \int_0^1 R\, d(\cos^2\theta) \;.$$

For $\beta_I a << 1$, in the limit of small index of refraction, using $|\,n_R - 1\,| << 1$, $R \cong R_i \cong 0$, and $d \cong a\cos\theta$ in (2.7) yields

$$\sigma_{abs} \cong \frac{4}{3}\,\beta_I \pi a^3 \;. \tag{2.9}$$

For metallic inclusions, figure 1 illustrates the absorption efficiency $\sigma_{abs}/\pi a^2$, obtained by sketching the results (2.6) and (2.8). The dashed line represents the asymptotic values obtained from (2.6) with $\Gamma \sim a^{-1}$ (for $a << a_\Gamma$), from (2.6) with $\Gamma \sim a^0$ (for $a_\Gamma << a << k^{-1}$), and from (2.8) (for $a >> k^{-1}$). The extrapolated dashed curve from (2.6) with $a >> a_\Gamma$ intersects the dashed curve from (2.8) at

$$a_k = \frac{\omega_p^2\, c\,(1-\langle R \rangle)}{12\,\epsilon_H^{3/2}\,\omega^2\,\Gamma_{Bu}} \tag{2.10}$$

which occurs near k^{-1} for many metals in the infrared. The solid curve schematically illustrates the results in the intermediate regions $a \sim a_\Gamma$ and $a \sim a_k$.

In dielectric inclusions, $\beta_I a << 1$ typically is satisfied except for very strong absorbers with rather large radii. (For example, $\beta_I a = 1$ for $\beta_I = 10^4\,cm^{-1}$ and $a = 1\,\mu m$.) For $\beta_I a << 1$, the absorption cross section is given by (2.3) for $ka << 1$ and by (2.9) for $ka >> 1$. Since these two limiting results both are of the form $\sigma_{abs} \sim \beta_I a^3$, with only slightly different coefficients, the approximation $\sigma_{abs} = A\beta_I a^3$, with A the average of the two coefficients, will be used for all values of ka.

The absorption efficiency for dielectric inclusion is qualitatively similar to that sketched in figure 1 for metallic inclusions, with two exceptions. First, for $ka \ll 1$, (2.3) indicates that $\sigma_{abs}/\pi a^2 \propto a$, and the constant region at small a does not occur for dielectrics. Second, the extrapolated linear region crosses the large a asymptotic region near β_I^{-1}, rather than k^{-1}.

For large-bandgap semiconductors, such as AlP, SiC, and ZnS, the dielectric-inclusion results above can be applied. The absorption by small-bandgap semiconductors is more complicated than that by dielectrics and metals in general, and will not be considered explicitly. Problems can occur involving temperature dependence of the electrical conductivity, increased absorption caused by free carriers that are created in the absorption process, and the resulting thermal runaway. [9]

3. Material Failure from Local Heating

The heating of macroscopic inclusions can give rise to localized regions of high temperature that can cause material failure when the intensity is great. This is usually important only at relatively high intensities. For times short with respect to a characteristic time for heat to diffuse a distance a, very roughly speaking, most of the energy absorbed by the inclusion remains in the inclusion. Thus, the temperature in the inclusion increases linearly with time. For times large with respect to the characteristic time, part of the absorbed energy has diffused into the host crystal, and the temperature rise in the inclusion is considerably less than the value obtained by neglecting diffusion.

The criterion for failure of the window material depends on the details of the laser system and the type of material and inclusions. Since there is no universal criterion, it will be assumed that a temperature rise of 1000 K, which is approximately the correct value for melting temperatures and fracture-inducing temperatures, constitutes failure.

Two important features of high-power laser-window failure are that failure of the weakest part of the window, i.e., a single inclusion, can constitute system failure, and that fatigue and other multiple-pulse effects must be considered when repeated pulses must be withstood. Bloembergen [10] has suggested that local field enhancement, such as that occurring at the edge of a crack in a material, may give rise to local intensities up to 100 times greater than the nominal external intensity. Thus, an inclusion in the high-intensity region could lower the failure intensities calculated below by a factor of the order of 100. Local field enhancement can also occur when one inclusion is at the focal point of another. Since focusing is limited by diffraction when $ka \lesssim 1$, the focusing by large, weakly absorbing inclusions is most severe. Focusing by surface imperfections also could occur.

Simple solutions to the heat-flow equation

$$-K \nabla^2 T + C \frac{\partial T}{\partial t} = S \tag{3.1}$$

will be derived for a series of limiting times for the cases of uniform heat generation within the volume of the inclusion and of uniform heat generation over the surface of the inclusion. In (3.1), S is the rate at which heat is generated per unit volume.

First consider the case of spatially uniform heat generation within the inclusion at the rate

$$S = 3 \sigma_{abs} I / 4 \pi a^3 \tag{3.2}$$

per unit volume, where I is the incident intensity. This applies for dielectric inclusions with $\beta_I a \ll 1$ or for metallic inclusions with skin depth $\delta > a$. Roughly speaking, the thermal time constant

$$\tau = Ca^2/4K \tag{3.3}$$

is the time required for heat to diffuse a distance a in either the inclusion or the host when the appropriate values of C and K are used. Subscripts I and H will denote the values of τ in the inclusion and in the host crystal, respectively. For short times $t \ll \tau_H$, the diffusion of heat out of the inclusion is negligible. The term $K_I \nabla^2 T$ in (3.1) is then negligible. The temperature at the center of the inclusion is, from (3.1) and (3.2),

$$T_C = 3\sigma_{abs} It/4\pi a^3 C_I , \qquad \text{for } t \ll \tau_H \tag{3.4}$$

for T defined as zero at the time the laser is turned on ($t = 0$).

For long times $t \gg \tau_I, \tau_H$, equilibrium is reached with the host material conducting heat away from the inclusion at the same rate that it is generated within the inclusion. In this case the temperature is obtained by solving (3.1) with $\partial T/\partial t = 0$ in both the inclusion and the host. Using $\nabla^2 r^2 = 6$, $\nabla^2 (1/r) = 0$ for $r > a$, and the boundary conditions that the temperature and the heat flow be continuous at the inclusion surface, yields the steady-state value at the inclusion center,

$$T_{C\infty} = \frac{3\sigma_{abs} I}{8\pi a K_{eff}} , \qquad \frac{1}{K_{eff}} \equiv \frac{1}{3}\left(\frac{2}{K_H} + \frac{1}{K_I}\right) \tag{3.5}$$

For short and long times, the temperatures are approximated by (3.4) and (3.5), respectively. These are shown as dashed lines in figure 2, while the actual temperature is sketched as the solid line. The extrapolated short-time curve intersects the steady-state value at the time $\tau_{eff} = (2K_I/K_{eff})\tau_I$, which is found by equating (3.4) and (3.5).

Next consider the case of heat generated near the surface of the inclusion, as is the case for metallic inclusions in dielectric hosts, where a typical value for the skin depth δ is 40 Å. For spherical inclusions with radius $a \gg \delta$, it is assumed that heat is generated uniformly within a layer of thickness δ over the entire surface of the inclusion.

Three characteristic times are of interest. First,

$$\tau_\delta = 4C_I \delta^2/\pi K_I \tag{3.6}$$

is roughly the time in which heat diffuses out of the skin depth. Second,

$$\tau_a = 4C_I a^2/9\pi K_I \tag{3.7}$$

is roughly the time in which heat diffuses from the inclusion surface to the center. Third,

$$\tau_H = C_H a^2/3K_H \tag{3.8}$$

is roughly the time in which heat diffuses into the host, a distance equal to the radius of the inclusion.

For $t \ll \tau_\delta$ and $\delta \ll a$, the spherical shape of the inclusion surface is not important, and the solution to the simpler problem of heat generation in a thin plane slab can be used. In this case, the temperature, obtained from the Laplace-transform solution of (3.1), [11] is

$$T_S = \frac{1}{C_I}\,\frac{\sqrt{C_I K_I}}{(\sqrt{C_I K_I} + \sqrt{C_H K_H})}\,\frac{I\sigma_{abs}}{4\pi a^2 \delta}\,t \cong \frac{I\sigma_{abs}}{4\pi a^2 \delta C_I}\,t , \qquad t \ll \tau_\delta . \tag{3.9}$$

In (3.9) and in the equations below, the approximate equalities are valid for $C_I K_I >> C_H K_H$. For $\tau_\delta << \tau << \tau_a$, the heat generation in a plane-slab problem can be approximated by a delta-function source at x = 0. Again using the method of Laplace transforms and keeping the dominant term for small t yields

$$T_S = \frac{2}{\sqrt{\pi}\,(\sqrt{C_H K_H} + \sqrt{C_I K_I})} \frac{I\sigma_{abs}}{4\pi a^2} t^{1/2} , \qquad \tau_\delta << t << \tau_a . \tag{3.10}$$

When $t >> \tau_a$, the temperature inside the spherical inclusion reaches a spatially uniform value. The present problem then is equivalent to uniform heat generation within an inclusion of infinite conductivity and the previous result (3.4) can be used to obtain

$$T_S = \frac{3 I \sigma_{abs} t}{4\pi a^3 C_I} , \qquad \tau_a << t << \tau_H . \tag{3.11}$$

For $t >> \tau_H$, the temperature inside the spherical inclusion reaches an equilibrium value that is spatially uniform. This case is again equivalent to uniform volume heating within an inclusion of infinite conductivity, and (3.5) yields

$$T_{S\infty} = \frac{I\sigma_{abs}}{4\pi a K_H} \qquad t >> \tau_H . \tag{3.12}$$

The temperature at the surface of the spherical inclusion is sketched in figure 3 for the various time regimes in (3.9)-(3.12).

Next consider the effect of inclusion size on the failure intensity I_f. The various time regimes in figure 3 depend on inclusion size in such a way that if the pulse length is fixed, long times in the figure are associated with small inclusions. In the case of metallic inclusions, t_δ is independent of radius and is typically of the order of 10^{-13} sec, which is much less than most laser pulse durations of interest. To determine the temperature in a pulsed system as a function of the inclusion radius, the dependence of σ_{abs} on a in (3.9)-(3.12) also must be included. The dashed curve of figure 1 is used as an approximation for σ_{abs}. For a given type of inclusion in a particular host, the radii a_Γ and a_k at which the functional dependence of the cross section changes are independent of the pulse duration, while the radii a_t and a_{eq} are both proportional to $t^{1/2}$ and decrease with decreasing pulse length.

There are six combinations of the sequence of a_Γ, a_k, a_t, a_{eq} which can occur for different pulse lengths. The temperature as a function of inclusion size is sketched for each of these cases in figure 4, with the pulse duration decreasing in going from A to F. For a given type of inclusion, the curves C and D cannot both occur. The applicable case will depend on the relative size of ratios a_t/a_{eq} and a_k/a_Γ.

For typical metallic inclusions in dielectric host materials with the laser wavelength equal to 10.6 μm, curve A applies to millisecond pulses, curve B to microsecond pulses, curve C or D to nanosecond pulses, curve E to picosecond pulses, and curve F to subpicosecond pulses.

Maximum temperature for a microsecond pulse occurs for $a_{eq} < a < a_k$ in figure 4B, where $a_{eq} \cong 1\,\mu$m. Using typical values for the parameters in (3.11), the failure temperature of 1000 K occurs for a pulse energy of 3 J/cm^2.

With a nanosecond duration pulse, the maximum temperature again occurs near $a = a_k \cong 1\,\mu$m in figure 4D and is determined from (3.10). In this case, the failure temperature occurs at a pulse energy of 2 J/cm^2.

At laser wavelengths other than $10.6\,\mu m$, the various curves of figure 4 correspond to pulse durations different from those listed above. Consider the case of platinum inclusions in a glass host with $\lambda = 1\,\mu m$. In this case curve A applies for pulses longer than a nanosecond duration, and the maximum temperature T_{max} occurs at $a = a_{eq}$. For a 30 nsec pulse duration, T_{max} occurs at $a_{eq} \cong 0.2\,\mu m$, where the failure temperature of 1000 K occurs at a pulse energy of $0.5\,J/cm^2$.

In the case of dielectric inclusions, volume heating is used for $\beta_1 a < 1$, and surface heating for $\beta_1 a > 1$. The time τ_{eff} separating the two regions of figure 2 corresponds to a radius $a_{eff} = (2K_{eff}t/C_1)^{1/2}$ for a pulse of duration t. In the volume heating range with $\beta_1 a < 1$, the absorption cross section is proportional to a^3 with slightly different coefficients for $ka \ll 1$ in (2.3) and for $ka >> $ in (2.9). Using $\sigma_{abs} \propto a^3$ with the average of the two coefficients for the entire volume heating region, (3.4) gives $T_c \propto a^0$ for $a_{eff} < a < \beta_1^{-1}$ and (3.5) gives $T_c \propto a^2$ for $a < a_{eff}$ where it is assumed that $\beta_1 < k$ (see left side of Fig. 5).

For surface heating of strongly absorbing dielectric inclusions, τ_δ is of the order of 10^4 sec. This value is much greater than pulse lengths of interest, and the first linear region of Fig. 3 given by (3.9), which was only of academic interest for metals, is now the only surface heating region that applies. Because $\beta_1 a > 1$ for surface heating and generally $ka >> 1$, the absorption cross section is $\sigma_{abs} = (1 - \langle R \rangle)\pi a^2$, according to (2.8). Substituting (2.8) for σ_{abs} into (3.9), the surface temperature is independent of a (see right side of figure 5).

In figure 5 the maximum temperature occurs for $a_{eff} < a < 1/\beta_1$. Using $\sigma_{abs} = 0.8\beta_1\pi a^3$, $C_I = 2\,J/cm^3K$, and β_1 ranging from 10 to $10^4\,cm^{-1}$, the failure temperature of 1000 K occurs for pulse energies ranging from $0.3\,J/cm^2$ to $300\,J/cm^2$. For microsecond duration pulses a_{eff} is of the order of 10^{-4} cm, and for nanosecond pulses is of the order of 300 Å, where $K_{eff} = 10^{-2}\,W/cm\,K$ is used.

Many other examples could be derived using the simple results developed above. Using the dashed rather than solid curves in the intermediate regions, as in figure 1, tends to overestimate the temperature, or underestimate the pulse energy at the damage threshold in the transition regions near the crossings of the limiting curves, but only by factors typically of order 2.

4. Conclusions

Simple limiting expressions for the absorption cross sections of inclusions derived in Sec. 2 are used in Ref. 4 to obtain expressions for the optical absorption coefficient β for the cases of large ($ka > 1$) and small ($ka < 1$) dielectric and metallic inclusions. For various types of inclusions, the frequency dependence of β ranges from increasing as ω^2, to independent of ω, to exponentially decreasing with ω. The temperature dependence ranges from independent of T to increasing as T^p in the high-temperature limit, where $p \cong 1-4$ typically. For strongly absorbing dielectric or metallic inclusions, impurity volume fractions as small as $f = 10^{-8}$ can result in infrared absorption coefficients of the order of $10^{-4}\,cm^{-1}$, which are currently observed.[4] The impurities are not necessarily limited to the bulk of the crystal, but may be on the surface as would occur for a surface contaminated by polishing compounds, which generally have large absorption coefficients.

In Sec. 3 failure due to local heating of dielectric and metallic inclusions in pulsed and cw systems is examined, and schematic results are given for many limiting cases. Local heating is a far greater problem in short-pulse systems than in long-pulse or cw systems having the same average intensity as the short-pulse system. In the case of micron-size metallic or dielectric-inclusions, pulse energies of a few joules per square centimeter are sufficient to cause local damage. In special cases where the inclusion is adjacent to a crack or other imperfection or near the focal point of another inclusion or other imperfections, the damage thresholds could be lower than our calculated values by as much as two orders of magnitude.

5. References

[1] M. Sparks, J. Appl. Phys. 42, 5029 (1971).

[2] M. Sparks, "Optical Distortion by Heated Windows in High-Power Laser Systems," Rand Corporation Report No. R-545-PR, September 1971.

[3] M. Sparks, "Physical Principles, Materials Guidelines, and Materials List for High-Power 10.6μ Windows, Rand Corporation Report No. R-863-PR, August 1971.

[4] M. Sparks and C. J. Duthler, "Theory of Infrared Absorption and Material Failure in Crystals Containing Inclusions," (to be published J. Appl. Phys. July 1973).

[5] G. Mie, Ann. Physik 25, 377 (1908).

[6] H. C. Van de Hulst, Light Scattering by Small Particles (Wiley, New York, 1957).

[7] C. Kittel, Introduction to Solid State Physics, 4th ed. (Wiley, New York, 1971).

[8] A. Kawabata and R. Kubo, J. Phys. Soc. Jap. 21, 1765 (1966).

[9] F. Horrigan and T. Deutsch, Raytheon Research Division Quarterly Technical Reports Nos. 1 and 2, Contract DA-AH01-72-C-0194, 1972 (unpublished).

[10] N. Bloembergen (to be published Appl. Opt.)

[11] H. S. Carslaw and J. C. Jaeger, Conduction of Heat in Solids, 2nd ed. (Oxford Clarendon, London, 1959).

6. Figures

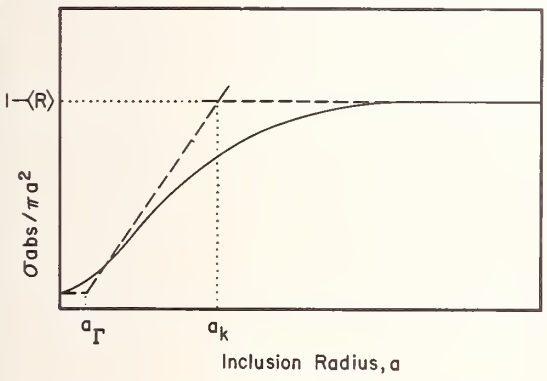

Figure 1. Absorption efficiency of a spherical metallic inclusion as a function of radius.

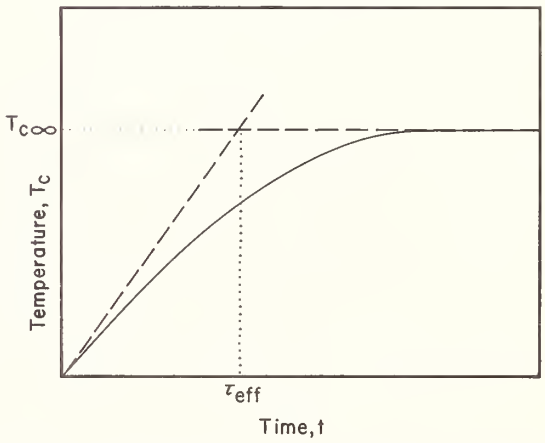

Figure 2. Temperature at the center of a spherical inclusion as a function of time in the case of surface heating.

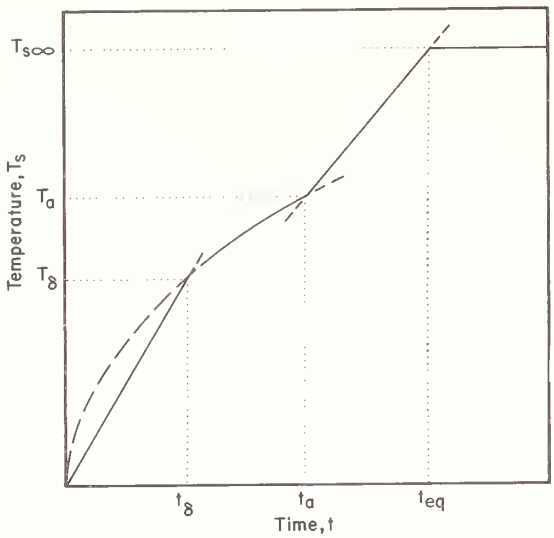

Figure 3. Temperature at the surface of a spherical inclusion as a function of time in the case of surface heating.

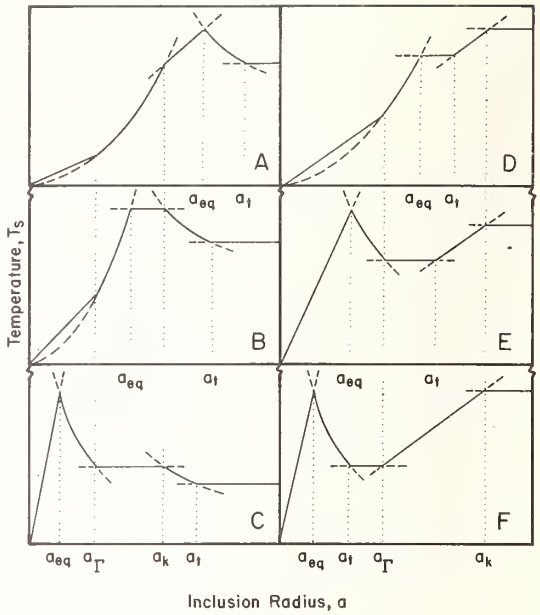

Figure 4. Temperature at the surface of a metallic inclusion as a function of radius for various pulse durations.

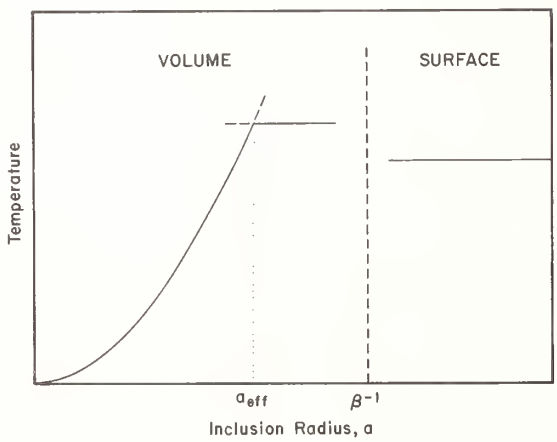

Figure 5. Temperature of a dielectric inclusion as a function of radius.

NO COMMENTS ON PAPER BY SPARKS.

Surface Damage by Laser Induced Collective Electron Oscillations

R. A. Shatas, L. M. Narducci*, J. Lynn Smith, H. C. Meyer, and S. S. Mitra†

Quantum Physics, Physical Sciences Directorate
U. S. Army Missile Command
Redstone Arsenal, Alabama 35809

Recent experiments with high pressure infrared molecular lasers demonstrate that the surface damage of ancillary optical components is the performance limiting factor. Intensities of a few tens of MW cm^{-2} in the pulse regime of fractional μsec are sufficient to damage the optical components; this performance is considerably less than what one would expect from the analysis of the intrinsic dielectric strength. It is proposed that the principal damage mechanism is associated with the damping of collective electron oscillations which have been driven beyond the linear regime by resonant photon-plasmon interaction. If the mobility of the carriers in a typical optical component is sufficiently high (such as for example in GaAs), one can adequately model the collective behavior of the carriers by a collisionless plasma. Thus the threshold for instabilities can be calculated on the basis of the Vlasov equation. In particular, the threshold for parametric instabilities in GaAs illuminated by 10.6 μm radiation is shown to be of the order of 10^5 V cm^{-1} which is in close agreement with recent experimental results. The mechanism responsible for producing the critical electron density is proposed to be field-assisted electron tunneling. The required tunneling probability for electric fields of the order of the instability threshold is attained if the energy separation of bound to free state is less than the crystalline bandgap. Adsorbed impurities and bending of the crystal bands at the surface account for the lowered value of the effective pseudo gap; hence the damage is seen first at the surface of the material.

Key Words: Electron avalanche, electron tunneling in alternating fields, laser damage of GaAs, laser damage processes, laser-induced surface damage, parametric plasma instability, resonant plasmon-photon interaction, solid state plasma.

1. Introduction

We are primarily concerned here with CO_2 laser damage to optical components observed under typical operational conditions. These differ substantially from laboratory prepared surfaces in their damage thresholds. Thus for TEA or cold-cathode e-beam preionized, electrical-discharge pumped molecular lasers operated in the gain-switched mode at 3-5 atm pressure, the performance-limiting factor is window damage which takes place at flux levels slightly above 10^7 W cm^{-2} [1-3][1]. Similar flux levels induce surface damage in GaAs [4]. In section 2, we discuss some of the shortcomings of the electron avalanche hypothesis with respect to the situation analyzed in this paper. Section 3 deals with the rate equations governing the growth of the free carrier density to its critical value (where the laser frequency is just above the electron plasma frequency) at or near the surface of the laser illuminated material. The quantum mechanical tunneling induced by alternating electric fields is proposed in section 4 as the mechanism responsible for creation of free or nearly free electronic states.

More specifically, we propose a tunneling mechanism of the Zener-Houston type in which the effective pseudo-gap at the surface of the material is substantially below the bandgap associated with the crystal eigenstates. Alternate model calculations based on the consideration of the field-induced

---

*Permanent address: Department of Physics, Worcester Polytechnic Institute, Worcester, Mass.

†Permanent address: Department of Electrical Engineering, University of Rhode Island, Kingston, RI.

[1]Figures in brackets indicate the literature references at the end of this paper.

transition probability between semilocalized states have led to comparable results for values of the effective pseudo-gap which are closer to the crystal bandgap than those needed in the Zener-Houston model. Subsequently, in section 5, we discuss thresholds for surface plasmon instabilities; at fluxes exceeding the parametric instability threshold, surface plasmons extract readily the energy from the electromagnetic wave, and, consequently, an exponential growth of the parametric oscillations is experienced. The subsequent damping of these oscillations by lattice ions accounts for the localized destructive damage at and near the surface.

2. Electron Avalanche Ionization

We want to discuss briefly why the electron avalanche process suggested by Bloembergen [5] and Fradin [6] for the bulk damage is not likely to be applicable to the surface damage. Let us designate with indices i, r, t the incident, reflected and transmitted components of the real part of Poynting's vector $\vec{S} = (c/8\pi)\, \vec{E} \times \vec{H}^*$. We assume that the low intensity absorption in the window is negligible, such that the relation $S_i - S_r = S_t$ holds, that the material parameters are $\varepsilon > 1$, $\mu = 1$, that we are dealing with plane monochromatic waves specified by $\vec{B}(z,t) = \vec{H}(z,t) = \hat{e}_y B_o e^{i(kz-\omega t)}$ $\vec{E}(z,t) = \hat{e}_x E_o e^{i(kz-\omega t)}$. Because of the relation $B_o = \sqrt{\mu\varepsilon}\, E_o$, the electric field inside the material associated with the normally incident flux S_i is given by

$$E_o = \sqrt{\frac{8\pi S_i}{c}}\ \frac{2}{1+\sqrt{\varepsilon}}\ . \qquad (1)$$

In writing eq (1), we neglected interference effects on the magnitude of the electric field. For window materials with a high dielectric constant, they may cause spatial and temporal variations of E_o which ought to be included for a fully quantitative discussion. The values of E_o associated with fluxes at which the surface damage has been reported at the 10.6 μm wavelength [1-4] are shown in table 1.

Table 1. Electric field inside material created by the incident flux expressed in MW cm^{-2}. At quoted incident fluxes, surface damage is seen after a single pulse of 50...100 nsec duration. $\mathcal{E}_g$ refers to the band gap, and $\hbar\omega_\lambda$ is the photon energy of 0.117 eV.

	$\mathcal{E}_g$	$\mathcal{E}_g/\hbar\omega_\lambda$	Incident flux	Field
GaAs	1.47 eV	12	(30 ± 10) MW cm^{-2}	70 kV cm^{-1}
NaCl	~ 5	43	30 MW cm^{-2}	120 kV cm^{-1}

The crystalline lattice values of $\varepsilon_\infty = 10.9$ and $\varepsilon_\infty = 2.25$ have been used for GaAs and NaCl, respectively. Because there are no free electrons prior to the illumination, their contribution to the complex ε is neglected; hence the electric field refers to the beginning of the laser pulse.

The argument for the avalanche breakdown is essentially built on the extention of Shockley's mechanism [7] originally conceived for a DC field to an alternating field. A few "lucky electrons" experience momentum-reversing collisions just in time of the reversal of the alternating field such that the acceleration of the electron continues throughout the several optical cycles needed to impart to the electron the kinetic energy above the ionization potential. This argument predicts that the rms value of the alternating field must be higher than that of the DC field to obtain an avalanche breakdown. A slight increase in the breakdown field in alkali halides indeed has been demonstrated [6] by Fradin and Bass for the bulk damage; however, the electric field associated with the laser flux at which surface damage is seen decreases with increasing frequency as shown in table 2 for GaAs.

We have included the ruby laser data for GaAs in table 2 just for comparison since the corresponding photon energy is above the crystal bandgap, and, consequently, no avalanche is needed since free carriers are created by single-photon across-the-gap ionization. For the Nd^{3+}-glass laser, however, the photon ionization multiplicity is two. The distance traversed by a free electron in GaAs during the half-cycle of breakdown field at CO_2 wavelength is given by $E_o\, \mu\, \tau' \approx 10^3$ Å. For these distances, one must consider carrier scattering processes associated with normal crystal modes even if the carrier becomes free at the surface. However, because of the relatively high mobility of free carriers in GaAs, the probability that the electron will undergo any collision during the half-period of the oscillatory electric field is small. A hard, momentum-reversing collision is of course much less probable. In table 3, we show half-cycle to average scattering time ratios for GaAs and NaCl. Inspection of table 3 indicates that perhaps one can extend Shockley's arguments to laser avalanche in NaCl; however, the free electron considered individually is essentially collision-free in GaAs with respect to any laser frequency. Thus the electron avalanche approach is not applicable as already inferred by the data shown in table 2.

Table 2. Electric field-frequency dependence for surface damage in GaAs and bulk damage in NaCl as given by Fradin and Bass [6]. The DC field refers to the dielectric breakdown field of pure materials.

Laser		Electric field (V cm^{-1})	
Wavelength (μm)	Frequency (sec^{-1})	GaAs [Ref 4]	NaCl [Ref 6]
dc	dc	$\sim 10^6$ (bulk)	1.5×10^6
10.6	2.83×10^{13}	$(7.0 \begin{smallmatrix}+1.0\\-1.3\end{smallmatrix}) \times 10^4$	$(1.95 \pm 0.20) \times 10^6$
1.06	2.83×10^{14}	$(4.6 \begin{smallmatrix}+0.8\\-1.0\end{smallmatrix}) \times 10^4$	$(2.3 \pm 0.46) \times 10^6$
0.694	4.32×10^{14}	$(3.6 \begin{smallmatrix}+0.4\\-0.5\end{smallmatrix}) \times 10^4$	$(2.2 \pm 0.44) \times 10^6$

Table 3. Half-cycle to average carrier scattering time ratio for different laser frequencies. The average scattering time τ^* is calculated from room temperature mobility data for pure GaAs and NaCl.

Laser		τ/τ^* Ratio	
		GaAs	NaCl
Wavelength (μm)	Half period τ' (sec)	$\tau^* = 1.6 \times 10^{-13}$ sec	$\tau^* = 5.7 \times 10^{-15}$ sec
10.6	1.76×10^{-14}	1.1×10^{-1}	3.1
1.06	1.76×10^{-15}	1.1×10^{-2}	3.1×10^{-1}
0.694	1.65×10^{-15}	7×10^{-3}	2.05×10^{-1}

3. The Free Electron Rate Equations

When the electron plasma frequency $\omega_p^2 = 4\pi ne^2/(m^*\epsilon)$ approaches that of the laser frequency from below, the nearly resonant collective electron oscillations are driven unstable above a certain threshold value of the alternating electric field. The approximate densities of free electrons needed to attain the resonance condition for CO_2, Nd^{3+}-glass and ruby laser wavelengths are given in table 4.

Table 4. Critical free electron density for a resonant laser light-collective electron interaction.

Laser wavelength μm	Critical electron density cm^{-3}
10.6	$\leqslant 10^{19}$
1.06	$\leqslant 10^{21}$
0.694	$\leqslant 2.3 \times 10^{21}$

Let N,n [cm^{-3}] be, respectively, the density of valence and free electrons with lifetime τ. The rate equation for free electrons can be written as follows:

$$dn/dt = Nw - n/\tau \quad , \tag{2}$$

where w designates the transition rate [sec^{-1}] from the bound to the free state. The solution of eq (2) is given by

$$n = \frac{wN_o}{\tau^{-1} + w}\left[1 - e^{-t(w+1/\tau)}\right] \quad , \tag{3}$$

where N_o is the initial density of bound electrons. The typical lifetime of free carriers in GaAs is of the order of several nsec. Because of the eventual saturation of various electron traps, the lifetime τ will also involve direct band-to-band transitions which are concentration-dependent; therefore, for a complete analysis, terms dependent upon $n(N_o - n)$ ought to be added to eq (2). However, a reasonable estimate for w can be obtained by assuming that the steady-state condition $dn/dt = 0$ is approximately satisfied in a fraction of the duration of a laser pulse. Thus we obtain $w = n/(N\tau) = 10^4 \ldots 10^5$ [sec^{-1}] as the typical transition rate required to attain a critical free electron density at the CO_2 laser wavelength for pulse durations typical to gain-switched high-pressure devices. In the next section, we will analyze conditions under which we can obtain the required transition rates by electric field assisted tunnel effect.

4. Alternating Field Assisted Tunneling

In this section, we discuss an elementary tunneling mechanism by which a sufficient number of electrons can be elevated into an essentially free state. It is well known that, as early as 1933, Zener discussed the theory of dielectric breakdown in terms of electric field-induced tunneling and evaluated the barrier penetration probability for a given applied field and energy separation between the initial and final electronic states.

Various adaptations of the original calculations have been performed by several authors [8] under the assumption of a steady applied electric field.

The physical situation discussed in this paper is one in which the field is, in fact, time varying. In order however to arrive at an estimate of the tunneling rate, we still use Zener's results as though the illuminating field on the target was steady or slowly varying. The justification for this assumption is based on the fact that the tunneling time through the forbidden gap is very much smaller than the optical period of oscillation.

Hence, in fact, the electron is expected to react to the instantaneous value of the electric field. To attain the free electron creation rate w discussed in the previous section with an applied field of the order of 10^5 V cm^{-1}, we parametrize the effective energy separation between the ground and the free state.

Assume that the tunneling process may be described by the Zener expression

$$w = \frac{e E_o d}{h} \exp \left\{ - \frac{\pi^2 m d (\Delta E)^2}{h^2 e E_o} \right\} \quad [sec^{-1}] \quad , \tag{4}$$

where m is the electron mass, E_o is the applied electric field amplitude, ΔE is the appropriate band gap and d is the lattice constant ($d = 5.65 \times 10^{-10}$ m for GaAs).

In table 5, we list a few typical values of the tunneling rate.

Table 5. Zener tunneling rate for different values of the effective pseudo-gap for GaAs.

Gap (eV)	Tunneling rate (sec^{-1})
0.33	2.36×10^3
0.32	7.87×10^3
0.31	2.53×10^4
0.30	7.83×10^4

While the Zener result is quite sensitive to small variations of the numerical value of the exponent, it is nonetheless apparent that an estimate of the tunneling rate in the range 10^4-10^5 (sec^{-1}) is consistent with the reasonable value of the effective pseudo-gap $\Delta E \simeq 0.30$-0.33 eV. There is, in fact, evidence that due to impurities and surface bending, the effective pseudo-gap on the surface of the optical component should be considerably smaller than the bulk band gap.

Corresponding to the estimated tunneling rate, the ejection probability per electron over the duration of the 10 nsec fraction of the laser pulse is of the order of 10^{-4}-10^{-3}. Since the density of

carriers in the upper valence band at room temperatue is of the order of Avogadro's number, we estimate that 10^{18}-10^{19} electrons/cm^3 should be ejected by the CO_2 laser pulse of $\sim 10^7$ W cm^{-2} intensity into a free or quasi-free state.

Due to the relatively high mobility of GaAs carriers, it is expected that the free electrons will behave quite similarly to a hot collision-free plasma. The calculation presented in the next section indeed supports the idea that a density of free electrons of the order of 10^{18}-10^{19} cm^{-3} should be sufficient to generate plasma instabilities, which give rise to surface wave damping and subsequent damage.

To approach the present argument on a more quantitative basis, we also propose the following model calculation. Since we expect the tunneling probability per electron to be quite small due to the large frequency mismatch between the gap frequency and that of the incoming laser pulse, we imagine an electron in the valence band to be under the action of a perturbation which causes small displacements away from the equilibrium condition characterized by a given unperturbed surface state. In view of the smallness of the perturbation (relative to the local fields), we argue that the charged particle will be acted upon by small restoring forces which in a crude sense should force it into a harmonic motion. The advantage of this model is that it can be treated exactly from an analytical point of view even for arbitrary time variations of the applied electric field.

The Schrödinger equation for a quantum oscillator driven by an external time dependent force is

$$i\hbar \frac{\partial \psi}{\partial t} = - \frac{\hbar^2}{2m} \frac{\partial^2 \psi}{\partial x^2} + \frac{m\omega^2}{2} x^2 \psi - f(t)\, x\psi \quad , \tag{5}$$

where in our case the external force is given by

$$f(t) = e\, E(t) = e\, E_o \cos\, \omega t \quad , \tag{6}$$

E(t) being the applied laser field. Assuming an initial condition of the form

$$\psi(x,o) = \left(\frac{m\omega}{\pi\hbar}\right)^{\frac{1}{4}} \exp\, (- \frac{1}{2} \frac{m\omega}{\hbar} x^2) \quad , \tag{7}$$

corresponding to the lowest energy configuration, it is easy to verify that the exact solution at any time t is given by

$$\psi(x,t) = \exp\left(i \frac{m}{\hbar} \dot{\xi}(x - \xi)\right) \exp\left(\frac{i}{\hbar} \int_o^t L(t')\, dt'\right)\left(\frac{m\omega}{\pi\hbar}\right)^{\frac{1}{4}} \exp\left(- \frac{1}{2} \frac{m\omega}{\hbar} (x - \xi)^2 - i\omega t\right) \quad , \tag{8}$$

where the function L(t) is given by

$$L(t) = \frac{1}{2} m\dot{\xi}^2 - \frac{1}{2} m\omega^2 \xi^2 + f(t)\, \xi \quad , \tag{9}$$

and $\xi(t)$ is the "classical" displacement due to the applied perturbation.

Explicitly we have

$$\xi(t) = \frac{e}{m} E_o \frac{\cos\, (\omega_o t) - \cos\, (\omega t)}{\omega^2 - \omega_o^2} \quad , \tag{10}$$

ω_o being the angular frequency of the laser field and ω the frequency associated with the effective surface pseudo gap.

The transition probability from the ground state to the first excited state is given by

$$P_{0\to 1}(t) = \left| \int_{-\infty}^{+\infty} dx\, \psi_1^*(x)\, \psi(x,t) \right|^2 \quad , \tag{11}$$

and is explicitly time dependent. We have calculated its time average over the duration of the pulse. The result is

$$\overline{P_{0\to 1}(t)} = \frac{m\omega}{2\hbar} \left(\frac{e}{m} E_o\right)^2 \frac{1}{(\omega^2 - \omega_o^2)^2} \left[2 - \frac{1}{2}\left\{1 - \left(\frac{\omega}{\omega_o}\right)^2\right\}\right] \quad . \tag{12}$$

In table 6, we summarize our numerical estimates based on the above calculations. We see that, unlike Zener's result, our tunneling probability is relatively insensitive to small variations of the parameters.

Table 6. Tunneling probability per electron evaluated from the harmonic oscillator model.

Gap (eV)	Tunneling probability per electron
0.36	6.33×10^{-4}
0.34	7.10×10^{-4}
0.32	8.07×10^{-4}
0.30	9.35×10^{-4}

Again, the results of our estimate support the hypothesis that a sufficient electron density can be obtained in a free state by the field induced tunneling.

In estimating the tunneling probability, we have used the value of the free electron mass in all calculations of this section. Whether the effective mass of the one-electron effective-mass approximation should be used instead, is an open question under current consideration. The use of the effective electron mass for GaAs ($m^* = 0.07$ m) would increase the effective pseudo-gap at the surface to a value of the order of 1 eV.

5. Instability Threshold for Laser Driven Collective Electron Excitations

The one-electron effective-mass model is usually employed in solid state theory to describe the dynamics of a free electron. The parametrized values of the effective mass and effective charge are used in the single-particle Hamiltonian, and this parametrization to a surprising degree of accuracy accounts for the many-body effects which a free electron experiences in the lattice. However, when the applied electric field is large, the kinetic energy of the electron increases to the point where the ratio of potential to kinetic energy becomes small and the collective behaviour of the electrons dominates the picture [9]. Qualitatively speaking in terms of the Silin criterion for instability [10], when the energy fed to the electron by an external driving source is large with respect to the initial energy in random motion, the electron system becomes unstable with respect to large fluctuations from the zero-field distribution function. In general, these large fluctuations in distribution are lumped together under the term of plasma instabilities. Because of a large variety of multibody effects admissible in a many-electron system, the enumeration of all conceivable instabilities is an onerous task [11]. In fact, one looks for a lowest threshold for the onset of instabilities known from the classical laser-plasma interaction work. For a hydrogen-isotopic plasma and CO_2 laser wavelength, the thresholds for the parametric and the two-stream instabilities have been calculated [12].

To make a comparison with our case, the three important processes of the classical plasma, namely, the electron-electron, electron-ion and ion-ion collisions, must be replaced by their solid-state counterparts. Since the electron-electron interaction is already taken up inexplicitly in the one-electron effective mass approximation and the ions are immobile, the most important criterion involves the free carrier mobility μ and its corresponding electron-phonon scattering time τ^* related to the parameters of the effective mass approximation by the expression $\mu = e\tau^*/m^*$. The scattering times of interest are given in table 3. On the other hand, the electron-ion collision time in classical plasmas is given [13] by $\tau_{ei} = 5 \times 10^4 \, T_e^{2/3}/(nZ^2)$. For comparison, we set $\tau^* = \tau_{ei}$ and employ a hydrogenic model for singly-ionized GaAs. The equivalent classical plasma would have to be heated to keV temperatures to possess collisional damping properties equivalent to the free carriers in GaAs. Since ion energies of the order of 0.1 eV are sufficient to destroy the lattice structure of GaAs by thermal action and the collisional electron-ion equilibration in GaAs is attained in a fraction of the duration of the laser pulse under consideration, electron temperatures above 0.1 eV imply the destruction of GaAs lattice. Thus an intuitive threshold value for a kind of parametric instability can be guessed by multiplying the value derived from eq (5) of ref. 12 by a factor of 10^{-4} or 10^8 W cm^{-2}. Since this value is close to the threshold of experimentally observed surface damage, we proceed now in describing a parametric surface plasmon-photon interaction process. Because of the essentially collisionless character of the electron plasma in GaAs, the linearized Vlasov equation can adequately describe the hydrodynamic equations of motion. The electron distribution function $f(q,p,t)$ is taken to consist of the sum of a zero-order part in a homogeneous field and a spatially dependent part accounting for the plasma-wave interaction. Finally, the velocity of the electron is obtained from the classical equations of motion of Kane's [14] effective mass Hamiltonian which demonstrates the nonparabolic character of the energy-momentum relation of free carriers. Thus the energy-momentum relation is

formally similar to the case of the Dirac relativistic electron Hamiltonian. In fact, this approach has been employed by Gersten and Tzoar [15] to arrive at the threshold condition

$$E_o = [4/3\ \mathcal{E}_g\ \omega_\lambda/\mu \cdot e]^{\frac{1}{2}} \qquad (13)$$

for an instability associated with the direct conversion of two identical photons into two plasmons. In this instability, the plasma excitation occurs within a distance of the order of one wavelength from surface; hence the crystalline band gap value for $\mathcal{E}_g$ is appropriate in evaluating eq (13). This yields a threshold value of 10^5 V cm^{-1} for the electric field near the surface of GaAs at room temperature, in good agreement with experimental data shown in table 1 [16]. However, the experimental threshold for NaCl for this instability is lower than predicted by eq (13). Because of the much shorter average scattering time of free carriers in NaCl as shown in table 3, this discrepancy is not surprising.

6. Discussion

In this work, we have attempted to combine the quantum mechanical approach of a single particle problem with the hydrodynamic approach for the many-body problem. In cases where approximations were used, we usually did not go beyond the zero or first order in perturbation. Also, the radiation field was considered in the classical formalism of the Maxwell equations. The amount of physical information which can be extracted from such an approach, of course, is limited by the physical restrictions inherent in the approximations. For example, the damping of the two photon-two plasmon parametric instability which would be useful in considering the damage for fields beyond the threshold (e.g., in considering pulse duration-damage threshold relation) requires the inclusion of higher order terms in section 5. Also, the demonstration of the magnitude of the effective pseudo-gap at the surface used in section 4 requires theoretical tools beyond the Tamm's tight binding method usually considered in surface physics [17]. Here, new theoretical approaches such as suggested by Alldredge and Kleinman may be useful [18]. Finally, to put the matter and the radiation field on equal footing, one would like to reformulate the problem in terms of the nonrelativistic quantum field theory. The system would be described by the Hamiltonian $H = H_e + H_\ell + H_r + H_{ee} + H_{\ell\text{-}r} + H_{ee\text{-}r} + H_{ee\text{-}\ell}$ where the subscripts e, ℓ, r stand for the electron, lattice, and radiation fields, respectively. Unfortunately, this Hamiltonian cannot be solved by the available quantum theoretical methods, and a great deal of fundamental theoretical work is required in incorporating a strong interacting radiation field into this treatment. Nevertheless, we think that we illustrated in this paper the need for a quantum mechanical treatment of the laser damage processes if our understanding of the problems involved should reach beyond the Edisonian approach.

7. Acknowledgment

The authors would like to thank Drs. John D. Stettler of this laboratory and C. Alton Coulter of the University of Alabama for valuable discussions concerning the photon assisted tunneling probability.

8. References

[1] Cason, C., Dezenberg, G. J., and Huff, R. J., Appl. Phys. Letters, to be published (1973).

[2] Hunter, R. O., Sullivan, G., Beggs, W., Benze, J., and Canavan, G. H., IEEE J. Quantum Electron. 9, 680 (1973).

[3] Kembry, J. and MacPherson, R. W., Technical Note DREV TN-2013/72, July 1972, Defence Research Establishment, Valcartier, Quebec, Canada.

[4] Smith, J. Lynn, elsewhere in these proceedings (1973).

[5] Yablonovich, E. and Bloembergen, N., Phys. Rev. Letters 29, 907 (1972).

[6] Fradin, D. W. and Bass, M., Appl. Phys. Letters 22, 206 (1973).

[7] Bass, M. and Barrett, H. H., IEEE J. Quantum Electron. 8, 338 (1972).

[8] Duke, C. B., "Tunneling in Solids," Solid State Physics-Advances in Research and Applications (Academic Press, 1969), Vol. 10, p. 39.

[9] See, e.g., Platzman, P. M. and Wolff, P. A., "Waves and Interactions in Solid State Plasmas," Solid State Physics-Advances in Research and Applications (Academic Press, 1973), Vol. 13.

[10] Fedorov, M. V., SP-Tech. Phys. 16, 671 (1971).

[11] Rukhadze, A. A. and Silin, V. P., S.P.-Uspekhi 11, 659 (1969).

[12] Meyer, H. C. and Shatas, R. A., Phys. Fluids 15, 1542 (1972).

[13] See, e.g., Artsimovich, L. A., Controlled Thermonuclear Reactions (Gordon and Breach, 1964), p. 41.

[14] See, e.g., Madelung, O., Physics of 3-5 Compounds (Wiley, 1964), p. 30.

[15] Gersten, J. I. and Tzoar, N., Phys. Rev. Letters 27, 1650 (1971).

[16] Meyer, H. C., Smith, J. L., and Shatas, R. A., EB4, Bull. Southeastern Section Am. Phys. Soc., November 1972.

[17] See, e.g., Davison, S. G. "Surface States," Advances in Solid State Physics, eds. Ehrenreich, Seitz, and Turnbull (Academic Press, 1970), Vol. 25.

[18] Alldredge, G. P. and Kleinman, L., Phys. Rev. Letters 28, 1264 (1972).

NO COMMENTS ON PAPER BY SHATAS.

Studies of Intrinsic Optical Breakdown

David W. Fradin*

Harvard University
Cambridge, Massachusetts 02138

and

Michael Bass‡

Raytheon Research Division
Waltham, Massachusetts 02154

Previous work demonstrated that intrinsic optical damage is caused by electron avalanche breakdown. We have conducted a number of recent studies of intrinsic damage which have reinforced the original identification of the damage process and which have probed various characteristics of avalanche breakdown.

By using a ruby laser to induce damage in the alkali halides, we have observed frequency dispersion in the relative breakdown fields. This dispersion, which was not apparent at 1.06 μm, provides insight into the development of the avalanche. A mode-locked Nd:YAG laser with output pulses of 300 to 15 ps duration was used to induce damage in NaCl, and the results were compared to Q-switched studies. It was found that the rms breakdown field increased by almost an order of magnitude to over 10^7 volts/cm as the pulse duration was reduced from 10 ns to 15 ps. This result agrees at least qualitatively with published dc breakdown measurements. A statistical character to bluk optical damage was observed in a number of materials including sapphire and fused quartz and found to be indistinguishable from statistics observed in surface damage. This observation and measurements of the ratio of surface to bulk breakdown fields show that the intrinsic mechanisms for surface and bulk breakdown are identical. Finally, the effect of crystalline disorder on the breakdown strength of solids was studied by measuring the intrinsic damage fields for a polycrystal, an alloy, and an amorphous insulator and comparing the results to the damage fields for the respective single crystals.

Key Words: Alkali halides, avalanche breakdown, intrinsic breakdown.

1. Introduction

It was determined in previous work [1,2][1] that intrinsic optical damage in transparent solids occurs as the result of an electron avalanche. During the past year we have extended the original studies of intrinsic breakdown in solids in order to ascertain the dependences of intrinsic damage fields on laser and material characteristics.

---

*Supported by the Joint Services Electronics Program at Harvard University under Contract No. N00014-67-A-0298-0006.

‡Supported by the Advanced Research Projects Agency of the Department of Defense and was monitored by the Air Force Cambridge Research Laboratories under Contracts No. F19628-70-0223 and No. F19628-73-C-0127.

[1]Figures in brackets indicate the literature references at the end of this paper.

Our recent work was conducted for two reasons. The first was to gather experimental information which could provide a basis for a realistic theory of avalanche breakdown. Although avalanche breakdown has been studied for over 40 years [3] , very little progress has been made in understanding the details of an avalanche process. Not only is the proper modeling of this highly complex process beyond the present level of solid state theory, [4] but experiments on dc breakdown are difficult to conduct and often hard to interpret. [3] For example, no estimates of effective electron collision rates can be obtained from dc experiments, and the time dependence of the avalanche can only be studied indirectly.[5] Avalanche breakdown at optical frequencies, on the other hand, is experimentally simpler to study and the great versatility of the laser can be exploited to probe aspects of the process that are inaccessible to dc investigators.

The second reason for conducting this work was to answer the following important practical questions: (1) What are the magnitudes of intrinsic damage fields in various materials ? (2) How do these fields change with increasing laser frequency and decreasing pulse duration? (3) What is the relationship between surface and bulk optical damage? This information is important to the development of more damage resistant surfaces and coatings and to establish measured upper limits for material damage resistance.

In Sects. 2 and 3 new and previously published results are presented which extend the damage measurements in the alkali halides to higher frequencies and shorter pulse durations. It will be shown, in particular, that frequency dispersion begins to develop at 0.69 μ m and that the damage field in NaCl increases with decreasing pulse width. These two observations provide an experimental estimate of the high-field electron-phonon collision frequency and an experimental measure of the avalanche ionization rate. An apparent anomaly in the frequency dispersion suggests the possibility that deep lying exciton levels may affect the breakdown strength of NaF. A comparison of the optical frequency ionization rate to estimates based on dc data [5] show at least qualitative agreement. A short experiment described in Sect. 4 investigates the effects of lattice disorder on the intrinsic breakdown strengths of materials.

In Sect. 5 data will be summarized which show that the bulk damage process in a number of materials, including NaF, has a statistical character. Measurements of the distribution of breakdown starting times are compared to the surface damage experiments of Bass and Barrett [6] and found to be consistent with those experiments. Sect. 6 summarizes a study which confirms Bloembergen' s model of electric field enhancement at polishing defects in optical surfaces. This enhancement makes conventionally finished surfaces damage more easily than the bulk while imperfection free surfaces break down at the same field which is required to produce internal breakdown. Finally, some of the implications of our experimental results for avalanche theory are discussed in Sect. 7 .

2. Avalanche Breakdown Induced by Ruby Laser Light

We have completed measurements of intrinsic bulk breakdown in nine single crystal alkali halides using a TEM_{00}, single-longitudinal mode ruby laser. Since this work has already been published, only the result will be given here.[8] Self-focusing was absent in these studies, and damage from inclusion absorption was distinguished from intrinsic damage. It was found that at 0.69 μm the relative breakdown strengths of the alkali halides have begun to differ from values obtained at 1.06[2] and 10.6 μm [1] and at dc [9]. The onset of this frequency dispersion in the avalanche breakdown process enables one to estimate the high-field electron-phonon collision frequency.

The laser system and techniques for avoiding and confirming the absence of self-focusing are described in detail in Refs. 2 and 10. Damage from inclusions was distinguished from intrinsic damage by examining both the morphology of the damage sites [1] and the temporal shape of light pulses transmitted through the sample. The latter technique employed the fact that a damaging light pulse is attenuated in a manner which is characteristic of the cause of damage. Only data obtained from intrinsic damage events were considered in the present work.

Figure 1 and table 1 summarize the results of this study, the 1.06μm data from Ref. 2, and accepted dc results. [9] In figure 1 the damage fields of the various alkali halides are normalized to that of NaCl at the appropriate frequency. This makes the variation in trends between the 1.06 μm and the 0.69 μm measurements more easily seen. The relative breakdown strengths at 1.06 μm are virtually identical to those measured at dc. Although the corresponding data at 10.6 μm [1] are not displayed, they too follow the same trend. This is not the case at 0.69 μm, however, even when the 10 to 15 percent measurement errors are considered.

Table 1 lists the rms damage fields of NaCl for these experiments. The agreement found in the four experiments is heartening because there are particular difficulties in determining the absolute damage fields in dc measurements. [3] Root-mean-square values of the electric field strength are given because for laser pulses of this intensity, the buildup time of an electron avalanche to damaging levels is on the order of 10^3 to 10^4 cycles of the optical field. Heating of the electron population is thus effectively averaged over many cycles.

A complete theoretical description of avalanche breakdown has not been developed. The onset of frequency dispersion can be qualitatively understood, however, by using the results of models based on relaxation time approximations. [3, 11] These models predict that the damage field will scale with frequency as

$$E_{rms}(\omega) = (1 + \omega^2\tau^2)^{1/2} E_{dc} \quad (1)$$

where $\omega = 2\pi\nu$ is the laser radian frequency and τ is an effective, high-field, electron-phonon collision time. Since each material has a different value of τ, the relative breakdown fields for the alkali halides should begin to change at high frequencies. Data such as shown in Figure 1 can be used to infer approximate relative values of τ for a variety of theoretical models.

Perturbation calculations of τ have been performed which are applicable for electron energies greater than the longitudinal optical photon energies. [3] If $\omega\tau \approx 0.5$ for NaCl, then the results of these calculations can explain qualitatively the change in relative breakdown strengths observed at ruby frequencies for most of the alkali halides. The collision time for NaCl under this assumption is about 2×10^{-16} sec. For NaF these calculations predict that the relative breakdown field (E_{NaF}/E_{NaCl} in figure 1) will decrease at ruby frequencies, contrary to the change which is experimentally observed. This discrepancy may be the result of the inadequacy of the modeling of the electron-phonon interaction or it may indicate that the frequency dependence of the electron avalanche is not determined by the electron-phonon collision frequency alone.

Seitz [12] has suggested that the presence of deep-lying exciton bands may influence the dielectric strength of alkali halide crystals. If this is the case, then as the field frequency ω is increased, direct excitation out of these bands becomes possible and the damage field will decrease. NaF, which has the deepest lying bands (1.5-2.0 eV) of the materials studied, [13] will experience this effect at a higher frequency than the other alkali halides. Such considerations of the relative importance of the exciton bands may explain the observed large increase in the relative NaF damage field at 0.69 μm.

Multiphoton absorption directly across the bandgap cannot explain the changes in relative breakdown strength which have been observed. In addition, theoretical calculations of the fields at 0.69 μm necessary to induce damage from multiphoton ionization or from its low-frequency limit, tunnel ionization, give damage fields which are about an order of magnitude larger than those measured.

In this part of our work, we have measured the intrinsic optical breakdown fields of nine alkali halides using a ruby laser. Although the absolute and relative damage fields are comparable to the damage fields observed at 1.06 μm and at dc, differences are observed which suggest that at $\nu = 4.3 \times 10^{14}$ sec^{-1}, avalanche breakdown is no longer identical to dc avalanche breakdown. Current theories of avalanche breakdown do not appear to explain the details of this observed difference.

Table 1. Absolute Breakdown Strength of NaCl

E_{peak}(dc)*	1.50×10^6 V/cm
E_{rms} (10.6 μm)*	$(1.95 \pm 0.20) \times 10^6$ V/cm
E_{rms} (1.06 μm)*	$(2.3 \pm 0.46) \times 10^6$ V/cm
E_{rms} (0.69 μm)	$(2.2 \pm 0.44) \times 10^6$ V/cm)

*These values are taken from Refs. 9, 1, and 2 respectively.

3. The Pulse-Duration Dependence of Optical Avalanche Breakdown

Measurements are reported here of optical damage induced by subnanosecond laser pulses. [4] These measurements were performed by focusing mode-locked YAG:Nd laser pulses having durations of 15 and 300 picoseconds inside single crystal NaCl. Because the experimental procedures used in the present work were identical to those used in the studies of Ref. 2 with a Q-switched YAG:Nd laser, the subnanosecond measurements can be directly compared to the results of those studies. It was found that the intrinsic breakdown field increased by almost an order of magnitude to over 10^7 volts/cm as the laser pulsewidth was decreased from 10 ns to 15 ps. The dependence of the damage field on laser pulse duration was used to calculate a field-dependent ionization rate. This rate was compared to that derived by Yablonovitch and Bloembergen from published values of the dc dielectric strength of NaCl [5] and good qualitative agreement found.

The laser used for the present work was a passively mode-locked Nd:YAG laser operating in a TEM_{00} mode at 1.06 μm. Without intercavity etalons, this oscillator produced bandwidth-limited light pulses of 15 picosecond duration. When the cavity output mirror was replaced with a sapphire etalon, the pulsewidth was lengthened to about 300 picoseconds. Two-photon-fluorescence measurements failed to detect substructure with pulses of either duration. A laser-triggered spark gap was used to select a single light pulse which, after attenuation, was focused through a 14 mm focal length lens about 2 mm into the sample. As in Ref. 2 care was taken to insure that spherical aberrations from both the lens and the plane entrance surface of the sample being tested were unimportant. An energy monitor recorded the energy in each laser pulse.

Although the intrinsic damage process in transparent materials is an inherently statistical process [6] (see Sect. 4) it is virtually threshold-like in NaCl. Consistent with Ref. 2, the damage field was defined as that value of root-mean-square electric field inside the sample which produced damage on a single shot with a probability of 0.5. Damage was identified by the occurrence of a faint spark and was accompanied by a small melted region ($\leq 2 \times 10^{-9}$ cm^3) inside the crystal. At least 20 data points were taken for each pulse duration at the 0.5 probability point.

Beam distortion from self-focusing was avoided by confining the laser input powers to well below the calculated critical powers for catastrophic self-focusing. (See table 2.) Tests discussed in Ref. 2 were used to confirm the absence of self-focusing. The absence of inclusion damage was confirmed in the manner discussed in Refs. 2 and 10.

Table 2 summarizes the results of the present measurements and relevant data from Ref. 2. An increase in breakdown strength was observed as the duration of the laser pulse was decreased. As the pulse duration was changed from 10.3 ns to 15 ps, there was a total change by a factor of 5.8 in damage field strengths or a factor of 33 in damage intensity. The experimental points are plotted in figure 2 along with the semi-empirical predicted curves from Ref. 5.

The existence of a pulsewidth dependence to intrinsic damage can be explained qualitatively by classical theories of electron avalanche ionization. [3, 11] These theories, which are summarized in Ref. 15, predict that the density of conduction-band electrons, N(t), increases with time as

$$N(t) = N_0 \exp\left[\int \alpha(e)\, dt\right] = M_c(t). \qquad (2)$$

Table 2. Experimental Breakdown Fields and Calculated Self-Focusing Parameters in NaCl

Pulsewidth (10^{-12} sec)	P_{input} (10^6 watts)	P_c (10^6 watts)* electrostriction	P_c (10^6 watts)* electronic	E_{rms} (10^6 volts/cm) relative	E_{rms} (10^6 volts/cm) absolute
15	1.5	2.9×10^4	18	E(15ps)/E(300ps)	12.4 ± 3.7
300	0.22	82	18	$= 2.6 \pm 0.7$	4.7
4.7×10^3	0.030	1.8	18	E(4.7ns)/E(10.3ns)	2.3 ± 0.4
10.3×10^3	0.033	1.8	18	$= 1.1 \pm 0.05$	2.1

*P_c is the calculated critical power for catastrophic self-focusing

Eq (2) is valid when, as is the case with laser breakdown, [5] electron diffusion and trapping can be ignored. N_o is the low density of conduction electrons before the application of the electric field and α is the ionization rate which increases monotonically with increasing electric field. Breakdown occurs when the density of electrons becomes high enough to cause a material irreversibility such as a phase change. As the time available for the avalanche to develop to damaging proportions decreases, the rate of ionization and hence the electric field must be increased in order to produce damage.

It is desirable to compare the laser data to dc results. Such a comparison cannot be made directly, because impulse dc measurements with subnanosecond impulse durations have not been made. As Yablonovitch and Bloembergen [5] have suggested, however, dc measurements on samples with varying thickness provide an indirect comparison because the maximum duration of the dc avalanche is limited to the electron drift time from cathode to anode. [3] By considering limits on the electron drift velocity, Yablonovitch and Bloembergen have calculated α (E) for dc fields using eq (2) and previously published measurements of dc damage fields in thin samples of NaCl. [16] Breakdown was assumed to occur when M_c in eq (2) reached a value of 10^8. The ionization rates for the laser data can be found by replacing the integral in eq (2) by $\alpha(E_{rms})t_p$ where E_{rms} is the root-mean-square field on axis at the peak of the laser pulse and t_p is the laser pulsewidth. Then $\alpha(E_{rms})$ is given by

$$\alpha(E_{rms}) = \frac{1}{t_p} \ell n\, M_c \approx 18/t_p \qquad (3)$$

This relation has been used to convert the quantity α (E) used along the vertical axis in the figure of Ref. 5 to our figure which used t_p^{-1}. We have shifted the curves along the horizontal axis to obtain agreement with the experimental values for the breakdown field E_{rms} for the long pulses.

In figure 2 the four laser measurements are plotted with the computed curve from Ref. 5. The two branches to the computed curve correspond to two limits on the high-field electron drift velocity. Within experimental error, the laser data overlap the upper curve of Ref. 5 which was derived on the assumption that the mobility in the hot electron gas is independent of E_{rms}. Quantitative agreement should not be emphasized, however, because the present analysis is based on at least two important assumptions which may not be valid over the range of damage fields considered.[15] The first assumption is that factors in the dc experiments such as space charges and electrode effects do not change as the sample thickness is reduced to approximately a micron. And the second assumption is that the same intrinsic mechanism dominates over the range of laser pulse widths in table 2. Another intrinsic mechanism -- multiphonon ionization [18] -- may cause damage at lower fields than required for avalanche breakdown when the laser pulsewidth is extremely short. Estimates for 1.06 μm radiation in NaCl indicate that when the laser pulsewidth is less than about a picosecond, multiphoton ionization is responsible for intrinsic damage.[5] Since the shortest pulsewidth considered in the present work is 15 ps, the neglect of multiphoton ionization appears to be justified. If the estimates of Yablonovitch and Bloembergen are inaccurate, however, and damage from multiphoton ionization is occurring, the ionization rate determined from the 15 ps pulse is an upper bound for the actual value of α at E_{rms} = 12.4 MV/cm.

Intrinsic laser-induced damage has been shown to be a pulse duration dependent process. As the laser pulse duration was decreased to 15 ps, the damage field in NaCl increased to over 10^7 v/cm. From the pulse duration dependence of the optical damage field, a field-dependent ionization rate was determined and found to agree at least qualitatively with experiments using dc fields. The agreement underscores the basic similarity between intrinsic laser-induced damage at 1.06 μm and dc electron avalanche breakdown.

4. Effects of Disorder on the Intrinsic Damage Field

Measurements are reported here of optical bulk damage in three disordered systems -- polycrystal KCl, a single-crystal KBr-KCl alloy, and fused quartz. In each case the damage field for the disordered system is compared to the optical strength of the corresponding crystal. These measurements were made in order to determine if the optical breakdown field increases with severe lattice disorder as had been observed in dc breakdown experiments [1, 19] and as predicted by simple theories of avalanche breakdown. [3]

The laser system and the experimental techniques used here were identical to those of Ref. 2 except that manner of attenuation of the transmitted laser light, rather than inspection of the damage was used to distinguish inclusion damage.[10]

It was found that the damage field of the large-grain (20 μm) polycrystal was the same as that measured in the single crystal and that the damage fields for the alloys were intermediate between the damage fields of the constituents. In quartz, on the other hand, the disordered (amorphous) form was noticeably stronger than the crystal, the ratio of damage intensities being 5 ± 1. This ratio is identical to the corresponding ratio of surface damage fields measured by Bass and Barrett.[6]

It is to be expected that the large-grain polycrystal should have the same damage field as the single crystal. The average grain diameter (20 μm) and the laser focal diameter are comparable so that in the high intensity region near the beam axis where breakdown is observed to initiate, the sample looks like a single crystal.

By a simplified argument we can predict the approximate crystallite size necessary to affect the breakdown strength. Classical theories of avalanche breakdown (see Ref. 15) predict that the dynamics of electrons with energies greater than the longitudinal optical (LO) energy determine the characteristics of the avalanche. The LO energy in the alkali halides corresponds to electron momenta of about 0.1 times the reciprocal lattice vector, G. Thus the important electrons have $k \geq 0.1\,G$. Phonons with values of $q \geq 0.1G$ will interact most strongly with these electrons. Because such lattice vibrations have wavelengths equal to 10 lattice constants or less, we expect that unless crystal disorder appears on the scale of about 10 lattice constants (~50A) or less, the damage field should be unaffected by disorder.

Amorphous systems may be disordered on such a scale. Our observation that fused quartz is more resistant to damage than crystalline quartz is, therefore, consistent with the argument just presented. This result can be explained in somewhat more quantitative terms. As is shown below, the rate of energy input into the electron population decreases with decreasing electron mobility, μ. In low electric fields the electron mobility in disordered media is less than in crystalline forms.[20] If the mobility in disordered media is also lower in the enormous fields characteristic of avalanche breakdown, then it should be more difficult to heat the electron distribution in fused quartz and, as observed it should be more damage resistant than the crystalline form.

Equation (1-1) of Ref. 15 gives for the volume rate of energy deposition:

$$\frac{dW}{dt} = Ne\mu \frac{E^2}{(1 + \omega^2\tau^2)}$$

The breakdown fields for various single crystal alloys of KBr and KCl are summarized in figure 3. It is seen that the damage strengths of the alloys are intermediate between those of the constituents. There is no evidence that alloying caused disorder sufficient to increase the breakdown strength of these materials. The variation of damage strength with composition can be qualitatively understood by noting that many material parameters such as bandgap, lattice constant, dielectric constant, and phonon frequencies have values intermediate between those of the constituents. According to simple models of avalanche breakdown, [3, 11] the breakdown field depends on these various material parameters so that it is reasonable to expect the breakdown strengths of the alloys to also be intermediate between those of the constituents.

It thus appears that only extreme lattice disorder such as present in highly disordered amorphous systems has a measurable effect on intrinsic damage fields. Further work is needed, however, to ascertain any general correlations between lattice disorder and breakdown fields. Such work is important not only to an understanding of avalanche breakdown but it is also important from a practical viewpoint to the design of more damage-resistant optics.

5. Laser Damage Statistics

In a recent study by Bass and Barrett [6] it was found that the resistance of surfaces to optical damage has a statistical character. This observation, which could apparently not be explained either by laser fluctuations or by fixed material inhomogeneities, was interpreted in terms of an electron avalanche model. Previously a number of investigators had measured a statistical character to dc breakdown in both gases [21] and solids. [22,23] Statistics in dc experiments were assumed to arise either from the details of an electron avalanche or from the dynamics of space charge formation.

The laser damage techniques of the present work can be applied to the study of breakdown statistics. There are, in fact, several advantages to using these techniques. First, the intrinsic damage process has been identified, at least in the alkali halides. Secondly, because damage from absorbing inclusions can be distinguished and space charges will presumably not develop in optical fields, major experimental uncertainties in the surface studies and dc measurements are avoided. And finally, the bulk of crystals is far better characterized than surfaces in terms of structure and composition.

We present new experimental evidence to support the conclusion that there exists a statistical nature to laser-induced damage both in the bulk and on the surfaces of transparent materials. [10] It will be shown that the new experimental data is compatible with the results of Ref. 6.

It was observed in Ref. 6 that a precisely defined threshold for laser induced surface damage does not exist in the ten different solids which were studied. Instead, there is a range of power levels within which damage can develop on each shot with some finite probability, p_1, such that $0 < p_1 \leq 1$. The damage probability, p_1, at some power level was defined as the ratio of the total number of damage sites to the total number of laser shots. It was found that p_1 as a function of the electric field, E, appears to satisfy the relationship

$$p_1 \propto \exp(-K/E). \tag{3}$$

Additional evidence for the probabilistic nature of laser damage was obtained in experiments in which an image converter streak camera was used to measure the distribution of breakdown starting times for surface damage to two different materials. [24]

During the Q-switched damage experiments on the alkali halides, evidence was recorded which supports the statistical viewpoint. By monitoring the transmitted laser light with a fast photodiode-oscilloscope combination (risetime $\equiv$ 0.5 ns), we observed that the laser light is attenuated when damage develops. The first instant of measurable attenuation can occur before, at, or after the peak of the laser pulse, so that no well-defined relationship exists between the laser intensity and the first instant of attenuation. Figure 4 shows examples of such observations made with a ruby laser beam focused to produce damage inside NaCl. The laser pulses are fully time-resolved as verified by Fabry-Perot studies. In figure 5 another ruby laser pulse was focused into NaCl but did not cause damage whereas a second pulse, apparently identical to the first, did induce damage when focused into the same volume of the crystal. Nothing was moved between the two laser shots, and the laser was firing automatically at a repetition rate of about 1 pulse/5 sec. Similar observations were recorded at 1.06 μm where the automatic firing rate was just over 1 pps.

The relationship between laser light attenuation and the size of the electron avalanche is difficult to establish. A reasonable estimate indicates that the transmitted light is unaffected by the avalanche until the density of conduction-band electrons reaches a level of about 10^{18} cm^{-3}. It is not strictly correct, therefore, to associate the first instant of attenuation with the breakdown or avalanche starting time. We will assume, however, as a simplification that the two instants of time are identical within experimental error. It should be noted, incidentally, that the time interval over which the transmission drops from effectively unity to nearly zero may have no simple relationship to the ionization rate, $\alpha(E)$, defined in Sect. C. Because the density of electrons is quite high by the time measurable attenuation occurs, electron-electron collisions may alter the avalanche development and reflection from the plasma may become important, particularly at longer laser wavelengths.

Encouraged by our experimental observations, we decided to conduct careful measurement of the statistical time lag in a number of materials. Figures 6 and 7 summarize measurements made in fused quartz at 1.06 μm, in NaF at 0.69 μm. Similar results were obtained for sapphire at 1.06 μm. As usual, self-focusing was found to be absent under the conditions of our measurements. Techniques discussed in Refs. [2] and [10] were used to verify that the statistics were not occurring because of the presence of point-to-point material inhomogeneities such as inclusions.

The distributions of breakdown starting times for surface and bulk damage to fused quartz are shown in figure 6 to be virtually identical for the same value of p_1. These distributions have the same characteristics as those reported by Bass and Barrett for entrance surface damage. [24] The breakdown can begin at any time over a relatively long interval which includes times after the peak intensity in contrast to the very sharply defined breakdown starting time expected for a threshold-like process. The most probable time for damage is, in all cases, before or at the instant of maximum intensity or optical field, and as the applied field is reduced (p_1 is lowered), the time of maximum damage probability shifts to the peak of the pulse. (Compare Figures 6c and d.) These qualitative properties were shown in Refs. 10 and 24 to be explained by the probabilistic point of view.

In Ref. 10 a detailed comparison is made between the results of Ref. 6 and the present data. Figure 8 summarizes the important results of that comparison. A computed distribution of bulk breakdown starting times in fused quartz, obtained from eq (3) and appropriate measured parameters is compared to the observed distribution for bulk damage in fused quartz. [10] Good qualitative agreement is obtained. For times after the peak of the laser pulse, there is some quantitative discrepancy between the computed curve and the experimental results. As discussed in Ref. 10, this discrepancy appears to be the result of the finite formation time for the avalanche.

The present work confirms the existence of a statistical character to the laser induced intrinsic damage process and supports the notion that the intrinsic damage mechanism both on the surface and in the bulk is an electron avalanche with statistical starting times.

6. Optical Surface Damage

In the experiments of Bass and Barrett, [6] the laser beams were focused to about 25 μm in diameter ($1/e^2$ in intensity) in order to induce damage on the surface. For such focal diameters the laser beam was effectively collimated over a distance of about 50 μm near the focus, and yet damage was consistently observed to develop within the first 0.25 μm of material. Because surface contaminants were apparently not responsible for damage in this study, this surprising result indicated that the surfaces of conventionally polished solids have a lower intrinsic threshold than the bulk. The same conclusion follows from a later work by Giuliano [25] in which it was observed that the surface damage field for sapphire was increased when the surface was ion-beam polished, a procedure that removed most but not all of the polishing scratches on his samples.

A quantitative relationship between surface damage fields and those of the bulk was not established experimentally in these or in any earlier study, because until the work of Yablonovitch, [1] no accurate measurements of intrinsic optical bulk damage had ever been made. Using the bulk damage techniques of Ref. 2 and the surface focusing scheme of Ref. 6, we have completed a study of surface damage at 1.06 μm in which surface damage fields were measured for a variety of surface preparations and compared to bulk damage fields. Because this work has already appeared in the literature, [26] , only a brief summary of the results will be given.

The surface breakdown fields, E_s, were determined for various materials whose surfaces had been prepared by three techniques: conventional abrasive polishing, a bowl-feed technique developed by Itek Corp., and Ar-ion beam polishing. For each sample, a measurement of the bulk intrinsic damage field, E_B, provided a direct comparison and reference.

Table 3 summarizes the measured ratios E_B/E_S and table 4 lists the measured values of E_B in the three materials studied. These data show that the clean but conventionally polished surface of a transparent medium is generally more easily damaged than the bulk. On the other hand, when care is taken to achieve imperfection-free surface finishes by the use of bowl-feed or ion polishing, the bulk and damage fields are equal.

Bloembergen has shown that the discontinuities in the dielectric constant occurring at structural defects can enhance the electric field over its average value. [7] The following expressions for the ratios E_B/E_S when small surface defects are present were given in Ref. 7:

spherical void	$3\epsilon/(2\epsilon + 1)$
cylindrical groove	$2\epsilon/\epsilon + 1)$
"Vee" groove	ϵ

where ϵ is the optical dielectric constant. These were used to obtain the predicted ratios in table 3.

The mechanical defects that result from standard abrasive polishing [27] are responsible for the agreement between the predicted and experimentally measured ratios for conventionally finished surfaces. The bowl-feed and ion-beam polished samples appear to have only gentle variations in surface topography [8] which should lead to little if any measurable field enhancement. In agreement with this idea we found no difference between surface and bulk breakdown fields for these samples.

It should be noted, incidentally, that good quality conventional polishes appear spatially uniform to a 20 μm-diameter laser beam and so the distribution of defects does not cause damage statistics. Intrinsic damage on such a surface will produce damage statistics of the form of figures 6 and 7 in Sect. 5.

This work has shown that the incident laser fields for intrinsic entrance surface and bulk damage to transparent solids are the same as for imperfection-free surfaces. When structural imperfections are present, they enhance the optical field locally so that the surface damages more easily than the bulk. The present results and those of Sect. 5 demonstrate that the intrinsic mechanisms for optical damage to surfaces and to the bulk of transparent solids are the same, namely electron avalanche breakdown.

Table 3. Comparison of Bulk and Surface Damage Fields for Different Samples and Surface Finishes

Material	Finishing Procedure Finish Quality[a]	Predicted Ratio E_B/E_S Spherical Void	Cylindrical Groove	"Vee" Groove	Measured E_B/E_S	Surface Damage Morphology
Fused Quartz	Conventional #1 Standard 0-0 (see Fig. 1a)	1.21	1.35	2.1	1.3±0.1	b
	Conventional #2 Standard 0-0	"	"	"	1.5±0.1	b
	"Bowl" feed finish See Fig. 1b	"	"	"	1.0±0.1	c
	Ion beam polish Standard 0-0 with final 1.25 1.25 μm removed by Ar ion beam	"	"	"	1.0±0.1	c
Sapphire	Conventional Many scratches and digs with 50X mag and dark field	1.29	1.50	3.00	2.0±0.2	b
BSC-2 Glass	Conventional Standard 0-0	1.23	1.39	2.25	1.3±0.1	b
	"Bowl" feed finish (see Fig. 1c)	"	"	"	1.0±0.1	b,c

a. All surfaces were cleaned with collodion

b. Very faint pit ~ 20 μm in dia. and ~ 0.25 μm deep

c. Extensive cracking out to ~ 150 μm with central hole ~ 20 μm dia. and ~3-10 μm deep

Table 4. Measured Intrinsic Bulk Damage Fields at 1.06 μm

	Material	E_B(MV/cm)[a]
Fused Quartz	Conventional #1 Conventional #2 Bowl feed finish Ion beam polishes	5.2 ± 1.3
	Sapphire	6.3 ± 1.6
	BSC-2 Glass	4.7 ± 1.2

(a) RMS field values are listed
Measurements were made relative to E_B in NaCl
Pulse duration ~ 10 nsec (FWHM)

7. Implications of Experimental Results to Theory

A complete theory of avalanche breakdown has not been developed. The basis of the difficulty in modeling the avalanche is the fact that the relevant interactions cannot be treated separately. It is not strictly correct, for example, to consider electron excitations as distinct from those of the lattice. The electron-phonon interactions in the alkali halides are so strong that effective collision times appear to be about 2×10^{-16} sec. Such short times imply an electron energy uncertainty of the order of the ionization energy. In addition, lattice distortions from electric fields having rms values of 10^6 V/cm or more cannot properly be treated as a perturbation on the energy spectrum of the electron-lattice spectrum.

Our present experimental results provide valuable data for understanding aspects of the avalanche process. In addition to measuring accurate breakdown fields, we were able to infer an approximate ultra-high-field electron-phonon collision time in NaCl, a parameter which cannot be obtained by other experiments. We have, in addition, confirmed that the avalanche breakdown mechanism is pulse duration dependent. This latter conclusion refutes a number of avalanche models which view breakdown as the result of a discontinuous jump in electron density as the external field is raised. [3]

The data on the pulse-duration dependence of breakdown fields has been used to infer an ionization rate α (E) which in turn can be compared to the predictions of simple models of breakdown. One such model is that of Shockley [26] who found that the ionization rate α (E) should have the functional form A exp (-B/E) where A and B are appropriate constants. A comparison to Shockley's model is made in figure 9 where it is seen that Shockley's result is not an unreasonable approximation to the experimental data.

The high value of effective electron-phonon collision frequency $1/\tau$ can be shown [15] to imply that the electron-phonon interaction appropriate to a description of breakdown in insulators is not described by the Frohlich Hamiltonian as widely assumed. [3, 11] A deformation or nonpolar interaction discussed many years ago by Seitz [12] may be more useful in describing the effective electron-lattice interaction in avalanche breakdown than is the Frohlich interaction.

Our measured values of breakdown fields can be shown to imply that the average electron energy is much less than the ionization energy when the avalanche occurs. [15] This observation lends support to the conclusions of Baraff [29] and Holway [11] who have found, using simplified classical models, that the diffusion of electrons towards the high energy tail of the energy distribution appears to be more important than the average electron energy in determining the avalanche characteristics.

Finally, we have seen that severe crystal disorder can increase the damage fields for solids and that the avalanche process has a statistical character. Both observations can be shown to support the identification of the damage process as being an electron avalanche [6, 15]. The measured characteristics of the damage statistics may, in addition, provide valuable insight into the physical development of the avalanche.

In conclusion, although a complete theory of avalanche breakdown may be many years distant, we can understand many features of our experimental results in terms of relatively simple models. Experiment must lead theory in this area, and data gathered in work such as we have reported here may provide both a basic foundation for and a test of future theories of avalanche breakdown.

8. Summary

The intrinsic optical damage process in transparent solids has been shown to be electron avalanche breakdown. This process has been a frequency and pulse-duration dependence. Severe crystal disorder can increase the breakdown strength of materials, and the damage process itself has been shown to have a measurable statistical aspect.

Such results are important for the theoretical understanding of avalanche breakdown. They also provide measured upper limits for the propagation of high intensity light in solids and indicate how these limits change with laser pulse and material characteristics. By using techniques appropriate to the study of intrinsic damage, we have been able to clarify the relationship between optical surface and bulk damage and to gather information which may be useful in the development of more highly damage resistant materials and coatings.

9. Acknowledgments

We have benefited greatly from discussions with Prof. N. Bloembergen and J. P. Lettelier. These experiments could not have been conducted without the skillful assistance of D. Bua.

The Q-switch laser damage studies were conducted on lasers developed by D. Bua and one of the authors (M.B.) at Raytheon Research Division, and the subnanosecond damage studies were conducted at the Naval Research Laboratories by one of us (D.F.) in collaboration with N. Bloembergen and J. P. Letellier.

10. References

[1] Yablonovitch, E., Appl. Phys. Lett. 19, 495 (1971).

[2] Fradin, D. W., Yablonovitch, E., and Bass, M., Appl. Optics 12, 700 (1973).

[3] O'Dwyer, J. J., The Theory of Dielectric Breakdown of Solids (Oxford University Press, London), (1964).

[4] Conwell, E. M., High Field Transport in Semiconductors, Solid State Physics Supplement 9 (Academic Press, New York and London), (1964).

[5] Yablonovitch, E. and Bloembergen, N., Phys. Rev. Lett. 29, 907 (1972).

[6] Bass, M., and Barrett, H. H., IEEE J. Quant. Elect. QE-8, 338 (1971).

[7] Bloembergen, N., Appl. Optics 12, 661 (1973).

[8] Fradin, D. W. and Bass, M., Appl. Phys. Lett. 22, 206 (1973).

[9] von Hippel, A., J. Appl. Phys. 8, 815 (1937).

[10] Bass, M. and Fradin, D. W., IEEE J. Quantum Elect., to be published (Sept. 1973).

[11] Holway, L. Jr., Phys. Rev. Lett. 28, 280 (1972).

[12] Seitz, F., Phys. Rev. 76, 1376 (1949).

[13] Teegarden, K., and Baldini, G., Phys. Rev. 155, 896 (1967).

[14] Fradin, D. W., Bloembergen, N., and Letellier, J. P., Appl. Phys. Lett., to be published (15 June 1973).

[15] Fradin, D. W., Final Report for Joint Services Electronics Program at Harvard University under Contract No. N00014-67-A-0298-0006 (May 1973).

[16] Watson, D. W., Heyes, W., Kao, K.C., and Calderwood, J. H., IEEE Trans. Elec. Insul. EI-1, 30 (1965).

[17] Prof. Y. R. Shen has suggested (private communication, 1972) that local field effects may be important in an electron avalanche and may explain the difference in absolute field strengths between dc and optical frequencies. The damage fields reported in the literature, however, are not corrected for local fields because it is normally assumed that any local field effects are averaged out by the electrons' rapid movement across the unit cell. The validity of this latter assumption has not been established.

[18] Slusher, R.E., Giriat, W., and Brueck, S.R.J., Phys. Rev. 183, 758 (1969).

[19] von Hippel, A., and Mauer, R. J., Phys. Rev. 59, 820 (1941).

[20] Kittel, C., Introduction to Solid State Physics, Third Edition (John Wiley and Sons, New York), (1967).

[21] Wijsman, R. A., Phys. Rev. 75, 833 (1949).

[22] Kawamura, H., Ohkura, H., Kikuchi, T., J. Phys. Soc. Japan 19, 541 (1954).

[23] Watson, D.W., Heyes, W., Kao, K.C. and Calderwood, J. H., IEEE Trans. Elect. Insul. EI-5, 58 (1970).

[24] Bass, M., and Barrett, H.H., Applied Optics 12, 690 (1973).

[25] Giuliano, C.R., Appl. Phys. Lett. 21, 39 (1972).

[26] Fradin, D.W. and Bass, M., Appl. Phys. Lett. 22, 157 (1973).

[27] Khan, J. M., private communication (1972).

[28] Shockley, W., Czech. J. Phys. B11, 81 (1961) and Sol. St. Elect. 2, 35 (1961).

[29] Baraff, G.A., Phys. Rev. 128, 2507 (1962).

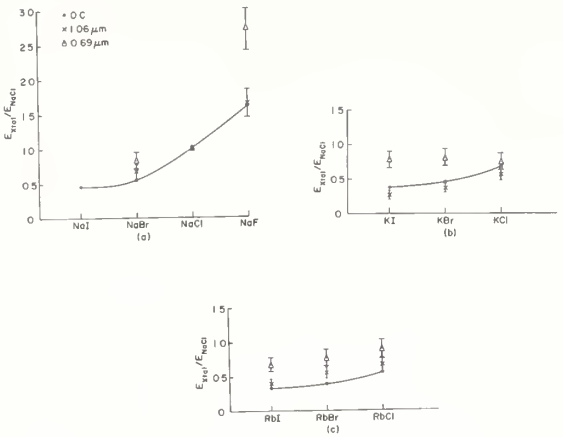

Figure 1. RMS Electric Fields Necessary to Induce Damage in Nine Alkali Halides Normalized to the Damaging Field for NaCl. The dc data is taken from Ref. 10 and 1.06 μm is taken from Ref. 7.

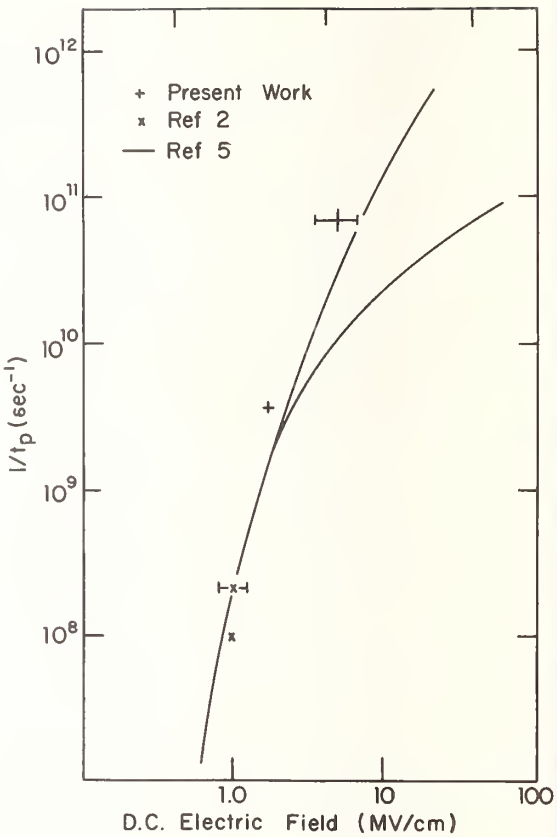

Figure 2. The Rate of Ionization in NaCl as a Function of Electric Field. The two branches of the solid curve correspond to two limits on the highfield electron drift velocity which were used in Ref. 5 to calculate the dc ionization rate. Corresponding laser data at 1.06 μm is plotted. It should be note that the changes in the damage field as the pulse duration is lowered from 300 to 15 ps and from 10.3 to 4.7 ns are known to higher precision than the absolute field strengths. The error bars reflect the experimental uncertanties in the absolute field strengths.

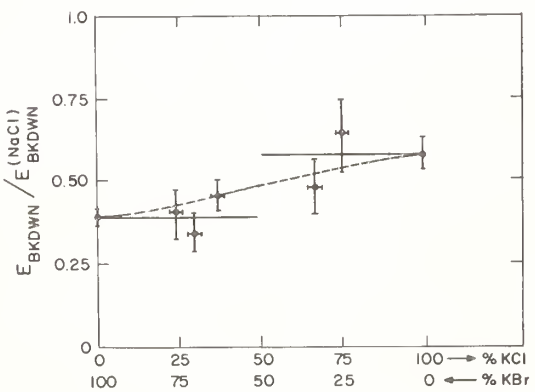

Figure 3. Measured Relative 1.06 μm Breakdown Field for KCl-KBr Alloys.

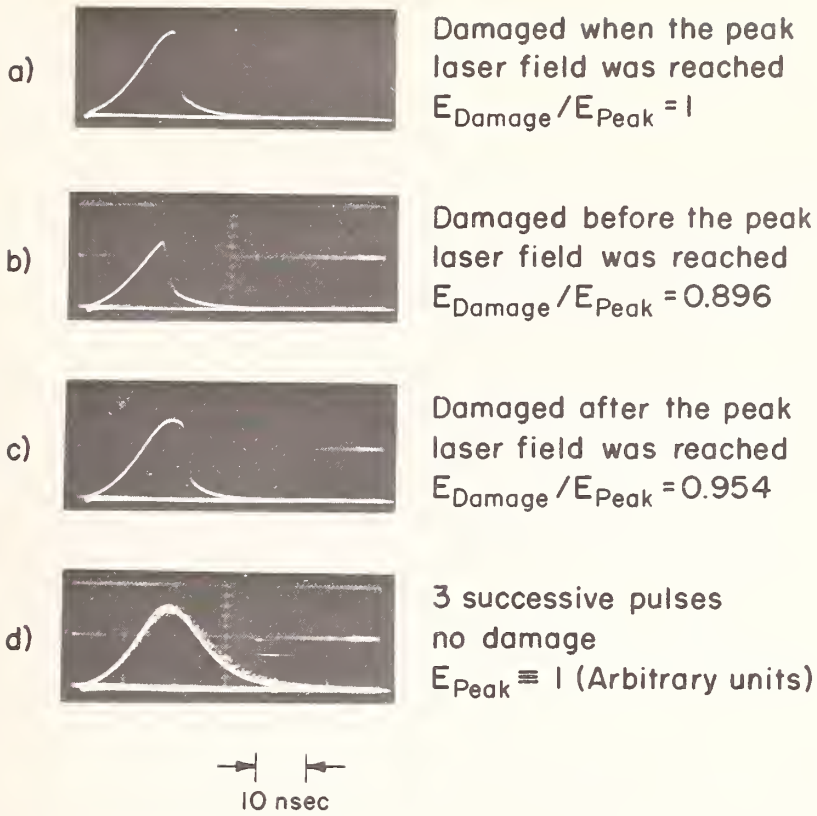

Figure 4. The Occurrence of Internal Damage in NaCl Due to Ruby Laser Irradiation. The laser intensity transmitted through the sample is shown in these photos.

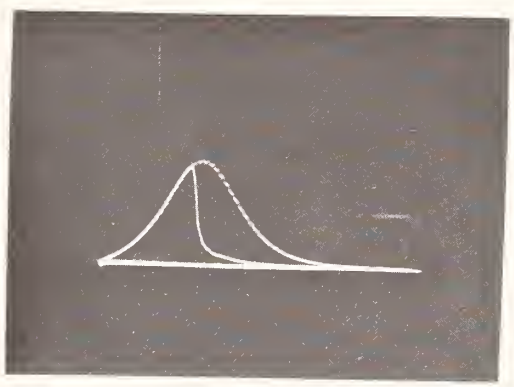

Figure 5. Intrinsic Bulk Damage Occurring in NaCl on the Second of Two Ruby Pulses. Five seconds passed between pulses.

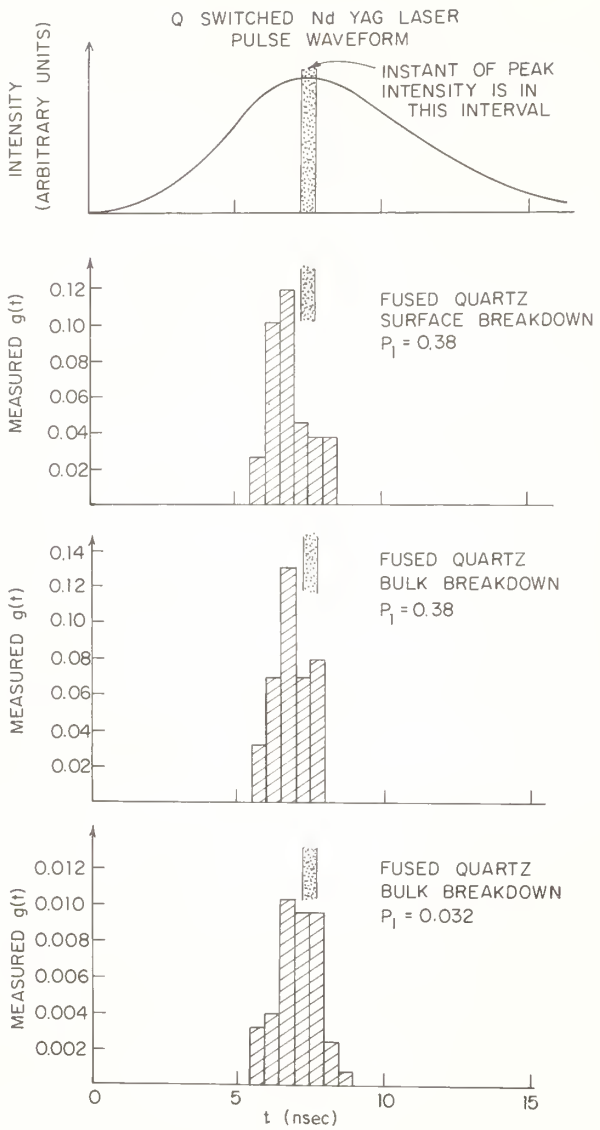

Figure 6. Measured Distributions of Breakdown Starting Times for Fused Quartz Using Nd:YAG Laser Irradiation.

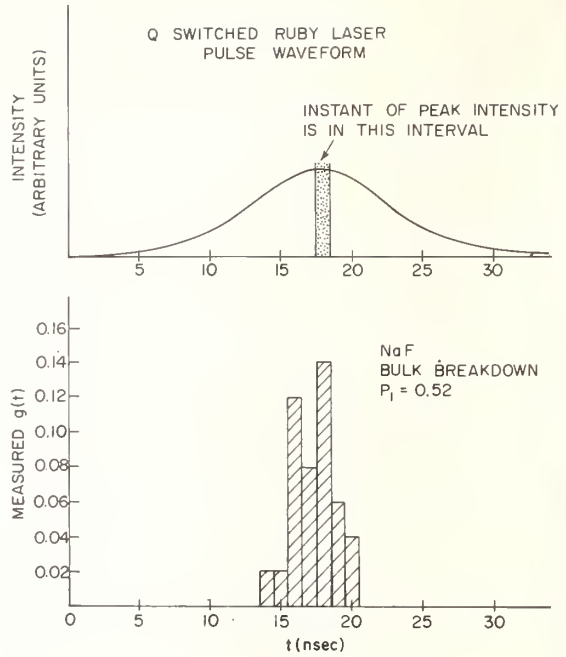

Figure 7. Measured Distribution of Breakdown Starting Times for NaF Using Ruby Laser Irradiation.

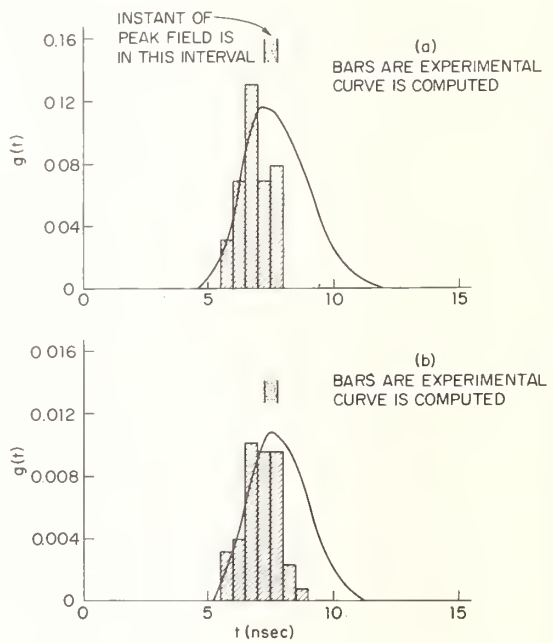

Figure 8. Measured and Calculated Distributions of Breakdown Starting Times for Bulk Damage in Fused Quartz using a Nd:YAG Laser.

NO COMMENTS ON PAPER BY FRADIN.

Laser-Induced Surface Damage in Proustite (Ag_3AsS_3) at 1.06 μm and 0.694 μm*

C. R. Giuliano and D. Y. Tseng

Hughes Research Laboratories
3011 Malibu Canyon Road
Malibu, California 90265

The results of a number of experiments on laser-induced entrance surface damage in proustite (Ag_3AsS_3) are presented. Morphology for pulsed and cw surface damage is discussed and illustrated. Damage at 1.06 μm where most of the work was done was studied with single pulse, repetitively pulsed, and continuous radiation; damage at 0.694 μm was studied with single pulses. It was found that the surface damage threshold at 1.06 μm is independent of pulse repetition rate from single pulse to 500 pps. Results of measurements taken for pulses of different duration are interpreted in terms of a thermal mechanism.

Key Words: Ag_3AsS_3, proustite, pulse duration dependence, repetition rate dependence, surface damage, 1.06 μm, 0.694 μm.

1. Introduction

Because of its nonlinear optical properties, proustite (Ag_3AsS_3) is an especially attractive material for parametric oscillators [1-3][1] and infrared up-converters [4-6]. However its propensity for being rather easily damaged has generated some doubts as to its value for high power applications. We have undertaken a series of damage investigations in order to obtain some clues as to the nature of its laser damage mechanisms in order to better evaluate it as a candidate for nonlinear optical applications.

2. Experimental

2.1 Lasers Used on Proustite Damage Experiments

A few damage experiments have been carried out at 0.694 μm using a single mode Q-switched ruby laser. This laser is described elsewhere [7] and will not be further described here.

Two different Nd:YAG lasers were used for damage studies at 1.06 μm. The laser referred to as the high power Nd:YAG laser is described in detail in another paper in these proceedings [8].

The low power Nd:YAG laser (as schematically shown in figure 1 is continuously pumped by a Kr-arc lamp and acousto-optically Q-switched. It has the capability of being operated continuously, single pulsed, or repetitively Q-switched at rates up to 50 kHz. The pump cavity utilizes an elliptical 2-in. long cylinder with walls coated with evaporated gold. The Nd:YAG rod is 0.25-in. diameter by 2-in. long, while the Kr-arc lamp discharge is 2-in. long with a 4-mm bore diameter.

The resonator cavity is formed by two 1-m radius-of-curvature mirrors separated by a distance of 65 cm. For the experiments, a 4.2% transmission output mirror was used. An internal aperture of variable diameter provided the transverse mode control.

*This work was supported in part by Air Force Avionics Laboratories and the Advanced Research Projects Agency through Air Force Cambridge Research Laboratories.

[1]Figures in brackets indicate the literature references at the end of this paper.

By decreasing the aperture size, the TEM_{00} output mode of the laser can be obtained by progressively eliminating the higher order transverse modes. The TEM_{00} is then selected with the collapse of the degenerate TEM_{10} mode. A UV-excited IR phosphor screen is utilized for visual selection of the TEM_{00} mode.

At full power, multimode output of 54 W is obtainable using a single 2.5-kW Kr-arc lamp. However, due to the well-known thermally induced birefringence of the Nd:YAG rod, the TEM_{00} output was drastically reduced to approximately 1.5 W maximum. (No attempt was made to compensate the induced birefrincence.) This resulted in peak powers of about 1 kW at low repetition rates (<500 pps). The peak power decreased monotically for high repetition rates. Pulsewidths of between 180 to 300 nsec resulted, depending on the repetition rate used. Amplitude stability was ~±3% when the laser was properly adjusted.

The laser characteristics are presented in table 1.

Table 1. Characteristics of Lasers Used for Proustite Damage Studies

Properties	High Power Nd:YAG	Low Power Nd:YAG	High Power Ruby Laser
Wavelength	1.06 μm	1.06 μm	0.694 μm
Operating Characteristics	Single shot to 10 pps	Single shot to 50,000 pps or cw	Single shot
Mode Properties	TEM_{00}	TEM_{00}	TEM_{00}
Peak Power (Pulsed Mode)	300 kW	1 kW	1MW
Energy per Pulse	~6 mJ	~0.25 mJ	~15mJ
Pulse Width (FWHM)	18.5 nsec	260-300nsec	~20 nsec
Av Single Mode CW Power	- -	1.5 W	- -
Measured Beam Radius[a] at Lens Focus for Damage Experiments	86 μm	37 μm	56 μm
Focal Length of Lenses Used in Damage Experiments	11 cm	11 cm	19 cm

[a]The beam radius is defined here as the 1/e radius for the electric field, which corresponds to the $1/e^2$ radius for the intensity.

2.2 Experimental Procedure for Damage Measurements in Proustite

In all the damage threshold measurements carried out on this program, a specific procedure was followed to obtain the desired data. The sample was prepared in a prescribed way (see below) and inspected with the aid of a microscope for cleanliness and quality of surface finish. Then it was mounted so that it could be accurately positioned relative to the focusing lens with respect to both lens-to-sample distance and to transverse position of the beam relative to any point on the surface. (A He-Ne alignment laser was not used as an aid for locating the desired point on the surface of proustite because it was discovered that proustite is damaged by microwatt levels of illumination at 6328Å.) For single pulse experiments, the laser was fired at a given level initially chosen to be below damage threshold and the sample was examined between shots using a low power (20x) microscope that could be moved in and out without disturbing the sample. If no damage was observed after several shots at a particular level, the power was increased by 5 to 10% and the sample again irradiated until damage was observed. In the repetitively pulsed experiments, a similar method was employed but instead the sample would be exposed for a predetermined time (usually 10 sec) at a given power and subsequently examined for damage. Again, if no damage was seen, the power was increased by 5 to 10% and another exposure made. This procedure was repeated until damage was observed.

The visual detection of damage near inception requires experience and practice in viewing through the microscope and also in choosing the proper illumination of the surface. It was found that many of the more subtle damage areas escaped detection in the earlier stages of this work because of these critical illumination requirements. The quality of the surface finish is important, not only for determining how easily the damage can be seen, but also in determining the threshold at which damage occurs. Because proustite is so soft, it is virtually impossible to obtain an optical finish that is free of scratches by conventional abrasive polishing. In addition, a freshly polished surface that stands in air for a few hours begins to take on a cloudy appearance. This cloudiness increases slowly and is accompanied by a gradual decrease in the measured damage threshold by as much as a factor of 2 to 3 over that of the freshly polished surface.

Therefore, to obtain more meaningful and reproducible data for the detailed damage experiments, all data was taken as soon as possible after a final polish was given to a proustite sample - usually on the same day. In addition, the sample surface was lightly repolished periodically, whenever damage thresholds were seen to begin to drift downward. After polishing and before any damage experiments were undertaken, proustite samples were rinsed thoroughly with 1,1,2 trichloroethane, followed by alcohol and finally deionized water, and then dried with a fine jet of Freon from a pressurized container. This procedure maximized the reproducibility of the experimentally obtained threshold quantities and resulted in much less experimental scatter than was obtained in earlier experiments.

All proustite samples studied were obtained from crystals either grown at HRL or obtained from the Royal Radar Establishment. All experiments performed were done on entrance surfaces of samples that varied in thickness from 2 to 10 mm.

3. Damage Morphology in Proustite

Three distinctly different types of damage are seen on proustite entrance surfaces. The occurrence of a particular type depends on the character of the irradiation (i.e., whether pulsed or continuous) and also to some extent on the quality of the surface finish. The three types are described in the following paragraphs.

3.1 Molten Craters

These have been seen to occur only during cw illumination at relatively high cw powers or when a previously created pulse damage site is illuminated with a relatively low cw power. The formation of these craters is accompanied by a plume of yellow smoke (presumably sulfur), which sometimes settles on the undamaged surface in the vicinity of the crater, depending on the direction of air currents in the laboratory. The craters have slightly raised rims and relatively flat shiny bottoms that appear black in color and are apparently the result of molten puddles of decomposed material. Crater depth is typically 25 μm. This type of damage is the most catastrophic of the three types observed. Examples of this type of damage are seen in figures 2 and 3 where we present optical and scanning electron micrographs.

By being especially vigilant while irradiating the sample with continuous illumination at 1.06 μm, it is possible to cut off the light incident on the sample before the catastrophic crater formation takes place. An example of the damage formed at inception is shown in the scanning electron micrographs in figure 3 where we see evidence of some local melting in a region about 20 μm across.

Chemical changes are evident in the molten crater damage as illustrated in figure 4. Here we show x-ray micrographs produced by an electron microprobe, indicating the relative concentrations of Ag, As, and S in the region of a damage crater compared with the surrounding undamaged area. The brightness of the individual spots is proportional to the local x-ray intensity characteristic of the particular element of interest. From these micrographs we see for example, that there is a buildup of arsenic at the crater rim and a deficiency at the center while silver is lacking at the rim relative to the center of the crater. The sulfur concentration is asymmetric as suggested by the plume distribution as noted above. The molten crater damage is the only type of damage for which any detectable chemical changes have been observed using the electron-induced x-ray micrograph technique.

3.2 Micromelting

This type of damage occurs with either single-pulsed or repetitively pulsed illumination. It is characterized by a series of somewhat randomly spaced tiny molten regions. The number and density of these regions depends on both the local surface finish and the incident power. When the power is appreciably above threshold, the molten regions merge to form a large variegated damage spot. At lower powers, there is tendency for these small globular sites to cluster along lines of surface scratches. When observed through the low-power microscope in the laboratory damage threshold setup, they appear to have a metallic luster, and the region in which they are clustered has a darker color than the surrounding undamaged surface. Figure 5 shows optical micrographs of proustite damage formed close to threshold. Figure 6 shows scanning electron micrographs of proustite damage for both single and multiple pulses.

3.3 Ghost Sites

This type of damage occurs with continuous illumination at 1.06 μm and was a source of much confusion when first observed. Under low magnification in the laboratory setup, it is similar in appearance to the damage described in the preceding paragraph; that is, it appears as a speckled area with a metallic luster. This kind of damage is easily visible with the unaided eye as a small scattering region on the surface. Depending on the incident laser power and exposure time, however, the damage fades within 30 sec to 30 min after the laser is turned off and sometimes disappears completely. This type of damage happens at very low cw power, and as the power is increased, it takes longer to fade away until finally a power level is reached at which some of the damage appears to be permanent. Ghosting has been seen also at high repetition rate illumination, but only if the surface finish has the cloudy appearance referred to in the beginning of this section.

4. Results of Damage Threshold Experiments

4.1 Damage in Proustite for Continuous Illumination at 1.06 μm

As mentioned earlier, two kinds of damage occur with cw illumination: the molten craters and the speckled ghost sites. The first type occurs at relatively high cw powers and requires long exposure times (sometimes several minutes) before suddenly occurring. The conditions under which it occurs (power and exposure time) vary so drastically that we were unable to obtain meaningful quantitative data. A threshold for the latter type of damage also was difficult to define, but it is possible to quote some limiting conditions under which it occurs. The power density for which this speckling persists after five minutes was taken as one limit. This value is approximately 2.3 kW/cm^2. The power density at which no speckling was observable at all for several minutes of exposure is about 300 W/cm^2. Between these two values, the speckled ghost sites appear to varying degrees; after the laser is turned off, they fade and gradually disappear.

4.2 Damage Threshold in Proustite as a Function of Pulse Repetition Rate

A series of threshold measurements were carried out on proustite at different pulse repetition rates. All the measurements were taken on the same sample. The results of these measurements are presented in table 2. The damage threshold intensities listed are those levels for which damage was observed according to the procedure described earlier.

It should be pointed out here that most of the sites where damage was observed at a particular power level were subjected to a large number of shots at predamage powers, which were a few percent below the level at which damage was finally seen to occur. A typical example is a damage site which at 60 pps was subjected to over 4,000 shots whose powers ranged in steps from 78 to 93% of the power at which damage finally occurred. We cite another example at 500 pps in which the site of interest was subjected to 30,000 nondamaging shots, whose powers ranged from 55 to 90% of the power at which damage occurred. Hence we interpret the range of threshold data obtained for proustite as reflecting a variation in surface damage resistance from point to point.

Table 2.

Damage Thresholds for Proustites as a Function of Pulse Repetition Rate

Pulse Repetition Rate	Relative Damage Threshold	Range	No. of Thresholds Measured
Single shot	1.0	0.83 to 1.2	11
60 pps	1.02	0.87 to 1.2	11
300 pps	0.94	0.84 to 1.1	16
500 pps	0.96	0.83 to 1.2	10

4.3 Optical Damage in Proustite at 1.06 μm for Pulses of Different Duration

One of the main interests for this study has been to measure the damage threshold for proustite at 1.06 μm for pulses of different duration in an attempt to obtain some insight into the nature of the damage mechanism. This was done on the same sample (sample A) using two different Nd:YAG lasers having pulse durations (FWHM) of about 20 nsec and 260 to 300 nsec. The results are presented in table 3 along with data for other samples for comparison.

Table 3.

Entrance Surface Damage Thresholds in Proustite for Different Pulse Durations

Sample	λ, μm	Damage Threshold[a] Power Density, MW/cm^2 Av Value	Range[c]	Damage Threshold[a] Energy Density, J/cm^2	τ, Pulse Duration (FWHM), nsec	Beam Radius,[b] μm
A	1.06	11.1	6.9-16.0	2.88	260-300	37.3
A	1.06	40.8	31-55	0.715	17.5	86.0
B	1.06	42.1	38-51	0.737	17.5	86.0
C[d]	1.06	1.61	1.4-1.9	0.40	300	74.0
(Ref. 9)	1.06	~29	-	0.50	17.5	650
D	0.694	60	54-69	1.08	20	56.0

[a] These values are given as total power (or energy) divided by the beam area defined as $\pi\alpha^2$, where α is the 1/e radius for the electric field. The on-axis intensities (energy densities) are twice as large as the values quoted in the table.

[b] Defined at the 1/e points for the electric field.

[c] These are the maximum and minimum values observed for a series of 25 to 30 measurements on a given sample.

[d] This is the sample for which data are given in Table 2.

The values for sample A in table 3 show that the energy density for damage increases for longer pulses qualitatively suggesting a thermal mechanism. The ratio of damage threshold energy densities for sample A is proportional to $\tau^{1/2}$ which is indicative of either absorption in a thin surface layer [10] or absorption of short pulses by inclusions [11] or other types of absorbing centers. The surface damage morphology close to threshold as illustrated in figures 3 and 5 suggest that the latter mechanism is more likely.

The above conclusion is based on data taken at only two pulse durations and should be further investigated by obtaining points for pulse durations between 20 and 300 nsec. Recent unpublished results by other workers [12] indicate that the single shot damage threshold for proustite occurs at a constant energy density for pulses from 20 to 80 nsec, a result that would suggest that the half-power dependence is not operative in this time regime. This apparent disagreement can only be resolved by further detailed experiments over these pulse duration regimes.

The threshold data for sample C in table 3 are substantially lower than those of the same pulse duration for sample A. Because past experience with different proustite samples has indicated a wide variation in properties both optical and otherwise from one sample to another, it is not surprising to see such a difference. In fact, it is more surprising to note the reasonably close agreement of threshold values obtained at 17.5 nsec pulse duration between our results and those of Hanna, et al. [9]. The fact that the threshold data in Table 2 are independent of laser spot size at the entrance surface coupled with the damage morphology observed further supports the mechanism of local absorption in regions (e.g. inclusions) that are small compared with the beam size.

4.4 Surface Damage on Al_2O_3-Coated Proustite

Recently the idea arose that it might be advantageous to provide a protective coating for proustite that would result in better damage properties. The combined facts that sapphire (Al_2O_3) has a high damage threshold and a refractive index (1.76) that is close to the geometric mean between that of proustite (~3) and air made it a good potential candidate as a low-reflectivity, damage resistant coating for proustite.

A wafer of proustite about 15-mm diameter and 2-mm thick was coated in three different regions with sputtered Al_2O_3 coatings of different thicknesses: 1450Å, 1700Å, and 1970Å which correspond to 0.24λ, 0.28λ, and 0.33λ at 1.06 μm. A fourth region of the sample remained uncoated.

Damage threshold measurements were made on all four regions of the sample using the high-power Nd:YAG laser (pulse duration 17.5 nsec) focused on the entrance surface. The results of these measurements are presented in table 4.

Table 4. Damage Thresholds for Al_2O_3-Coated Proustite

Region	Al_2O_3 Coating Thickness, Å	Damage Threshold[a] Energy Density, J/cm^2	Damage Threshold[a] Power Density, MW/cm^2	Measured Transmission, T	Intensity Reflection Coefficient at Entrance Surface, R	Corrected Threshold[a] Energy Density, J/cm^2
A	Uncoated	0.737 ± 6.5%[b]	42.1	0.324 ± 0.010[b]	0.204	0.587
B	1450	0.858 ± 8.9%	49.0	0.398 ± 0.018	0.0238	0.838
C	1700	0.729 ± 8.3%	41.5	0.413 ± 0.023	(-0.0151) ~0	0.729
D	1970	0.615 ±10.6%	40.2	0.402 ± 0.013	0.0134	0.607

[a]These values are given as total power (or energy) divided by the beam area defined as $\pi\alpha^2$, where α is the 1/e radius for the electric field. The on-axis intensities (energy densities) are twice as large as the values quoted in the table.

[b]The values listed are the average deviations taken from 25 to 30 measurements for each region.

The damage threshold energy and power densities listed in the second and third columns of Table 4 are the measured values incident upon the sample surface. However, because a fraction of the light is reflected from the sample, the actual energy available at the surface for creating damage should be multiplied by the quantity 1-R, where R is the intensity reflection coefficient. Therefore, a more valid comparison of the entrance surface damage thresholds for the coated regions compared with the uncoated region accounts for the difference in entrance surface reflectivities.

The reflectivities of the coated surfaces were not measured directly, but they can be obtained by a comparision of the measured transmissions as listed in table 4. The energy transmission T of a slab of absorbing material having reflection coefficients at the entrance and exit surfaces of R_1 and R_2, respectively, is given by

$$T = \frac{(1-R_1)(1-R_2)e^{-\alpha d}}{1-R_1R_2e^{-2\alpha d}} \qquad (1)$$

where d is the sample thickness and α is the absorption coefficient.

Using the above equation and the computed value for the reflectivity of the uncoated surface of R= 0.204 (from a value of the refractive index taken to be 2.65) it is possible to obtain the absorption loss and the reflectivities of the coated regions of the sample. The small negative reflectivity listed for region C is not real, of course, but a result of the experimental error in measurement of the transmissions and the assumption that the absorption and reflectivity are uniform throughout the sample.

The corrected threshold energy densities listed in table 4 are obtained by multiplying the appropriate measured value by $(1-R_1)$. Here we see that all three coated regions have thresholds higher than the uncoated region, although the values for regions A and D lie within experimental error of each other.

In all cases, the damage of Al_2O_3-coated proustite occurs at the interface between the coating and the surface and the damage morphology is essentially the same as that for the uncoated surface suggesting that the same factors are governing the damage limit for the coated as for the uncoated sample.

The moderate increase in threshold observed in some instances for sapphire-coated proustite offers some promise as a protective coating, but it is evident that the quality of the proustite itself must be improved with regard to both freedom from impurities and inclusions and quality of surface finish. The nature of the observed damage morphology suggests very strongly that the damage threshold values obtained so far are not a measure of the intrinsic damage resistance of proustite, but indicate a limitation governed by impurities and/or inclusions as well as surface fabrication.

5. Conclusions

The surface damage in the best proustite that is presently available appears to be limited by absorption due to inclusions, impurities or other local surface entities and not by an intrinsic property of the material. This conclusion is based on the fact that the damage threshold energy density depends on the half power of the pulse duration for measurements made at 20 and 300 nsec. It is further supported by the damage morphology close to threshold which shows small globules on the surface suggestive of local melting. The possibility of improving the damage resistance of proustite is suggested by providing better quality material, improved surface fabrication and protective coatings of more damage resistant materials such as sapphire.

6. Acknowledgment

The authors wish to express their appreciation for many helpful suggestions and discussions by V. Evtuhov and V. Wang, for the technical assistance of G. R. Rickel and R. Morrison and to A. L. Gentile who provided the HRL-grown proustite and H. L. Garvin who provided the sputtered sapphire coatings.

7. References

[1] Ammann, E. O., and Yarborough, J.M., Appl. Phys. Lett. 17, 233 (1970).

[2] Hanna, D. C., Luther-Davies, B., Rutt, H. N., and Smith, R. C., Appl. Phys. Lett. 20, 34 (1972).

[3] Hanna, D. C., Luther-Davies, B., and Smith, R. C., Appl. Phys. Lett. 22, 440 (1973).

[4] Warner, J., Appl. Phys. Lett. 12, 222 (1968).

[5] Klinger, Y. and Arams, F., Proc. IEEE 57, 1797 (1969).

[6] Tseng, D. Y., Appl. Phys. Lett. 21, 382 (1972).

[7] Giuliano, C. R., and Hess, L. D., in Damage in Laser Materials, edited by Glass, A. J. and Guenther, A. H., U. S. National Bureau of Standards Special Publication No. 341 (U. S. GPO, Washington, D. C. 1970), p. 76.

[8] Giuliano, C. R., and Tseng, D. Y., these proceedings.

[9] Hanna, D. C., Luther-Davies, B., Rutt, H. N., Smith, R. C., and Stanley, C. R., IEEE-JQE 8, 317 (1972).

[10] Ready, J. F., Effects of High-Power Laser Radiation, Academic Press, N.Y. (1971), Ch. 3.

[11] Bliss, E. S. in Damage in Laser Materials, edited by Glass, A. J., and Guenther, A. H., U. S. National Bureau of Standards Special Publication No. 341. (U.S. GPO, Washington, D. C. 1970), p. 105.

[12] Smith, R. C., University of Southampton, private communication.

8. Figures

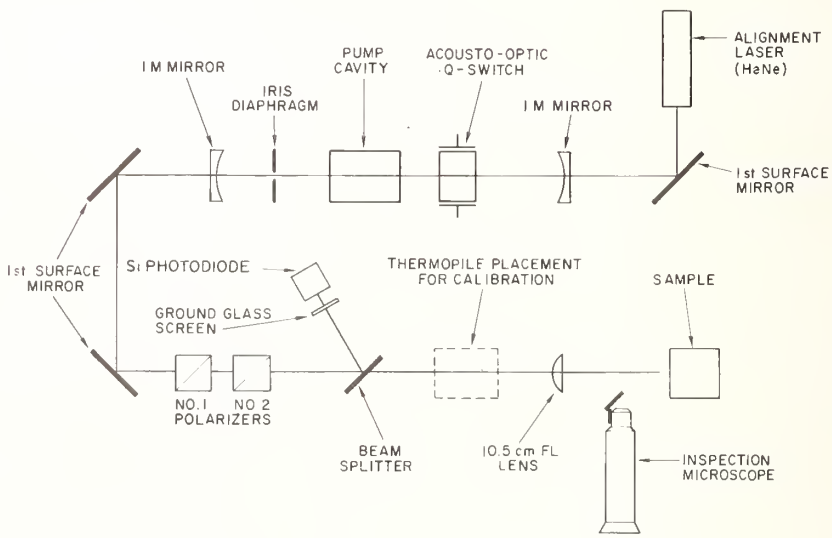

Figure 1. Experimental setup for damage experiments using the loe-power Nd:YAG laser.

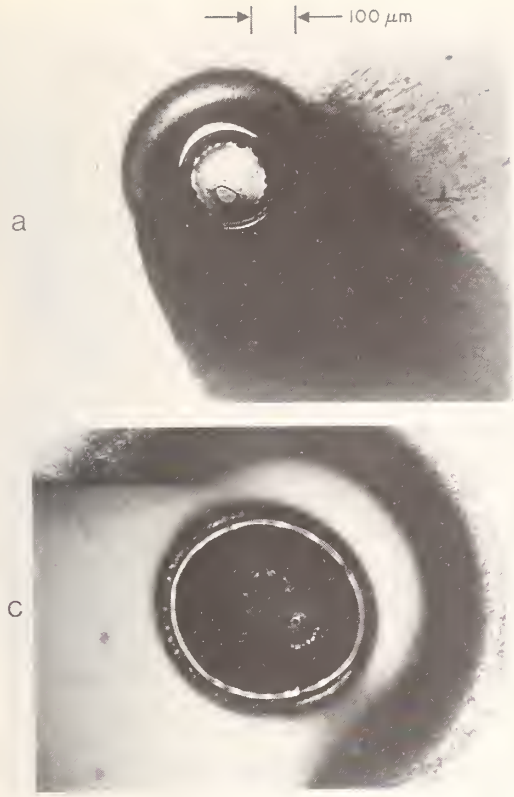

Figure 2. Optical micrographs of molten crater surface damage on proustite formed by cw illumination at 1.06 μm.

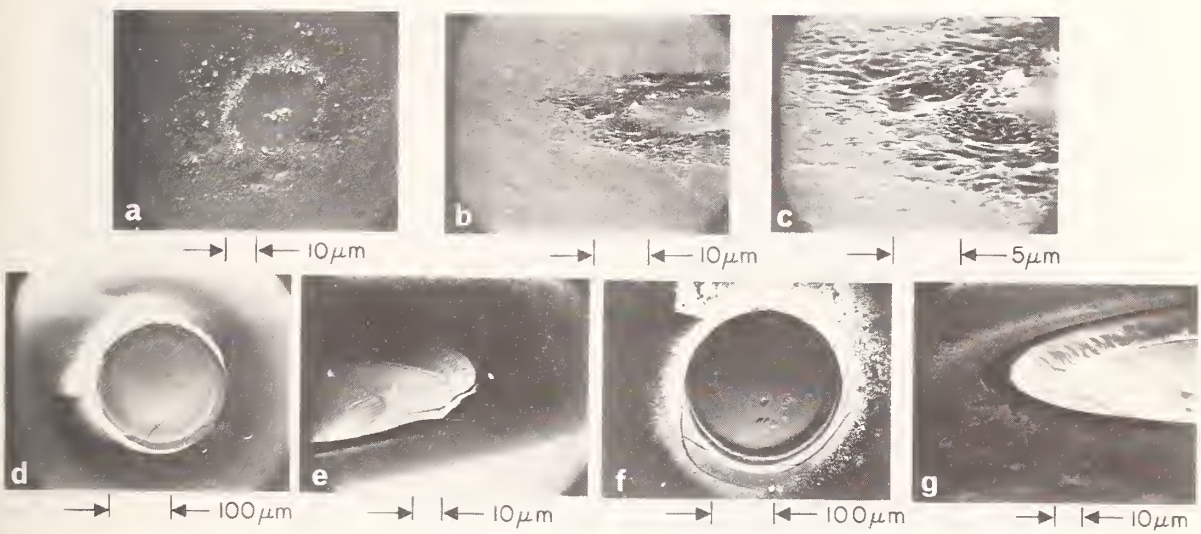

Figure 3. Scanning electron micrographs of molten crater damage on proustite at 1.06 μm. (a) - (c) Different views of the same site formed close to threshold. (d) - (g) Views of molten craters taken at normal incidence and 70° from normal.

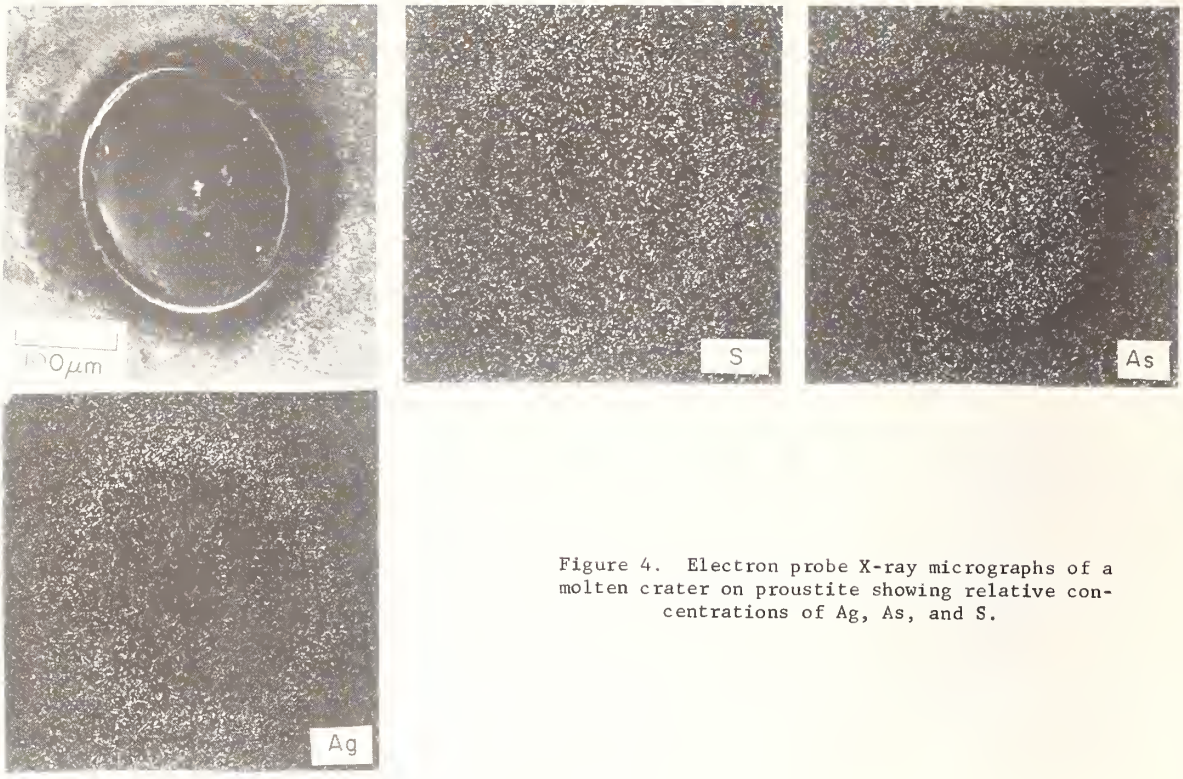

Figure 4. Electron probe X-ray micrographs of a molten crater on proustite showing relative concentrations of Ag, As, and S.

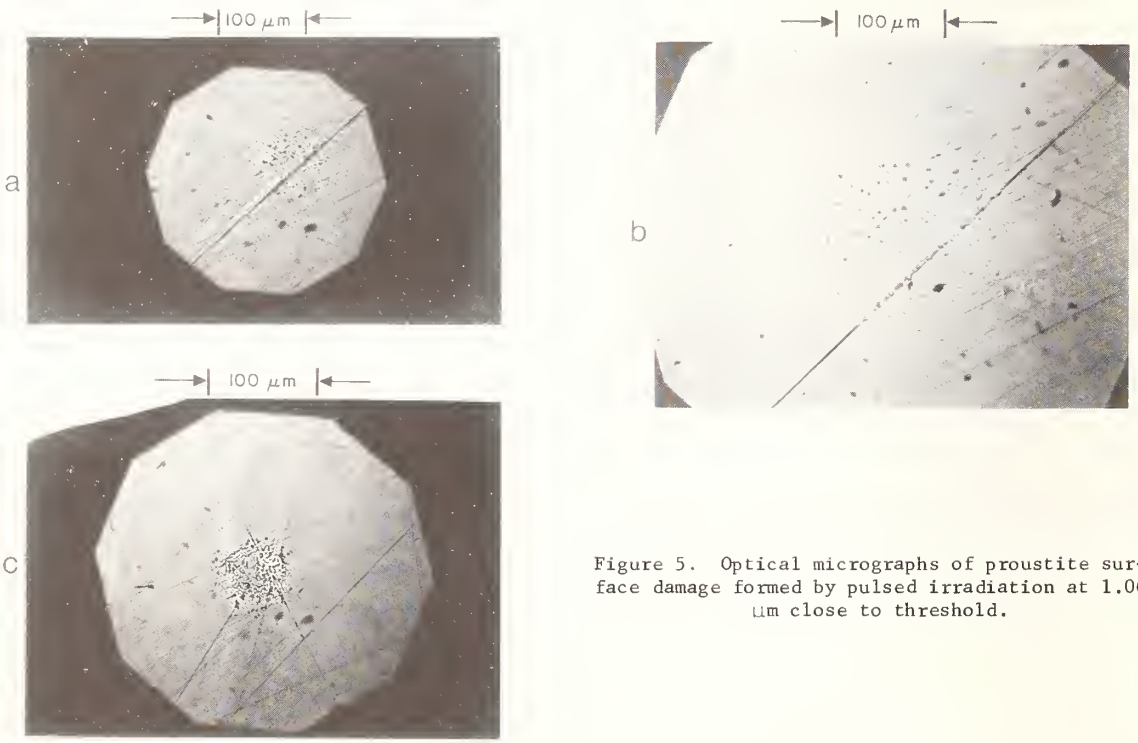

Figure 5. Optical micrographs of proustite surface damage formed by pulsed irradiation at 1.06 μm close to threshold.

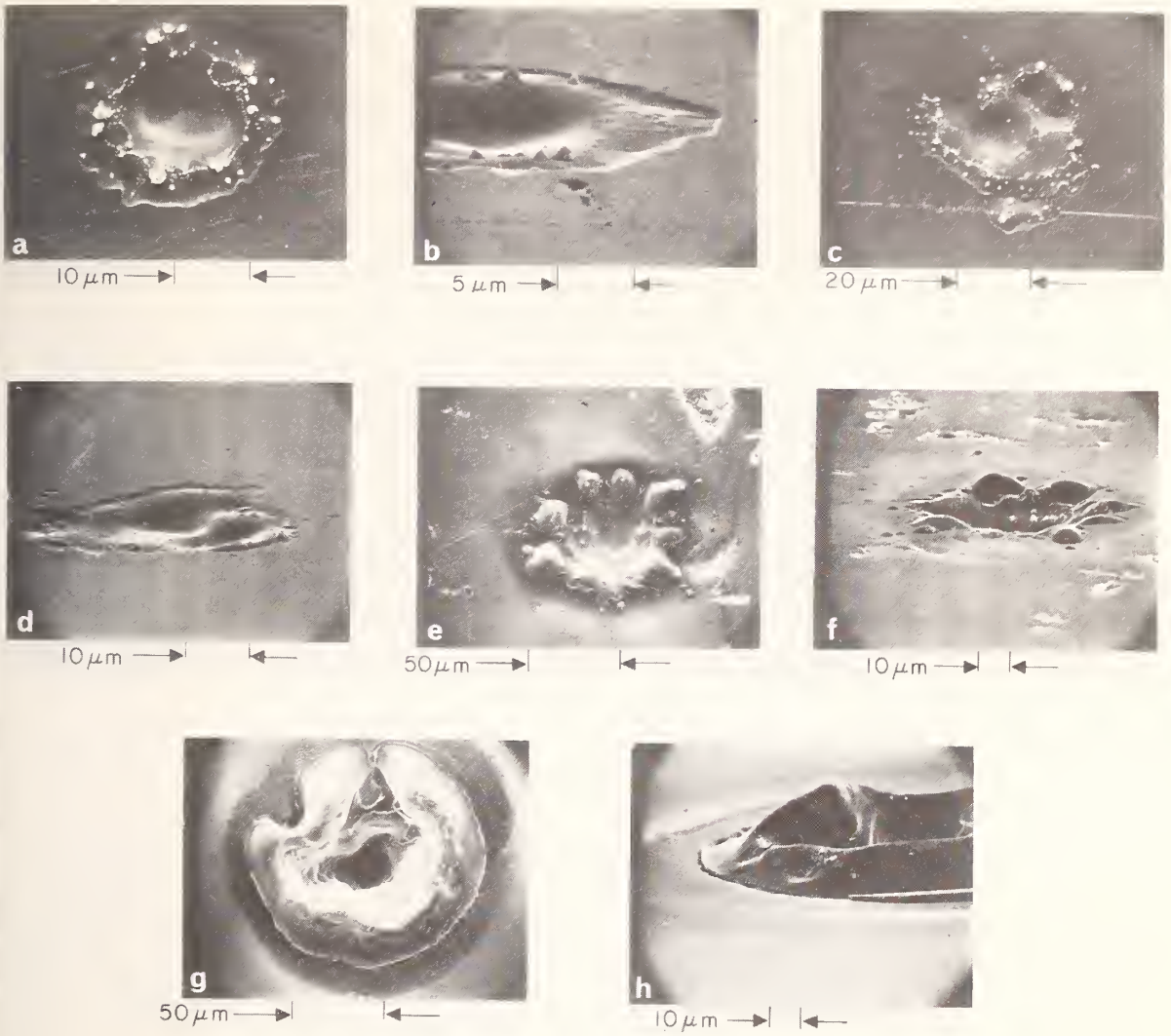

Figure 6. Scanning electron micrographs of proustite surface damage formed by pulse irradiation at 1.06 μm. Pictures occur in pairs showing a particular site viewed at normal incidence and 70° from normal. (a) - (d) Formed by single shot, (e) and (f) Formed by 10 shots, (g) and (h) Formed at 500 pps for 1 sec.

COMMENTS ON PAPER BY GIULIANO

Discussion centered on the difference between Giuliano's results and work previously reported in which a difinite distinction was observed between the damage threshold with second harmonic generation and without. The speaker pointed out that in the earlier work results were obtained using the non-linear crystal in a intracavity frequency doubler operating in a cw mode, whereas the results presented here were in a pulsed mode, outside the cavity. It was further commented from the audience that there was some evidence of the reduction of threshold in cesium dihydrogen arsinate. The damage that was observed took the form of bulk damage. It was noted that there was a significant increase in the power absorbed by the crystal when the second harmonic was present. This was ascertained by measuring the total power through the crystal with and without frequency doubling. When a significant amount of the fundamental was converted to the harmonic, a lower percentage of the total power was transmitted through the crystal.

Spectral Emittance Measurements on Several Crystalline Samples

D. L. Stierwalt

Naval Electronics Laboratory Center
San Diego, California 92152

Emittance spectra were obtained at 273°K and 373°K from 3 to 15 microns on several samples supplied by AFCRL. The specimens included KBr, CdTe, $ZnSe_xTe_{1-x}$, ZnSe, and four samples of Pb-doped KCℓ. Values of absorption coefficient were derived from the emittance data. Curves of absorption coefficient versus wavelength will be presented.

Key Words: Absorption coefficient, emittance spectra, KBr, CdTe, ZnSe, $ZnSe_xTe_{1-x}$.

Emittance spectra were taken from 3 to 15 microns at 373°K and from 5 to 15 microns at 273°K for a series of crystalline samples provided by Air Force Cambridge Research Laboratory. These included four samples of KCℓ, one of CdTe, two of $ZnSe_xTe_{1-x}$, and one of ZnSe. The measurements were made by the method reported at the Conference on High Power Infrared Laser Window Materials.[1]

Absorption coefficient values were calculated from the emittance data and sample thickness. These results are presented in figures 1 through 9. The first four figures show the spectra for the KCℓ samples. Absorption bands at about 6, 9.5 and 12.5 microns are observed in all four speciments, but with varying intensities. Absorption coefficients at 10.6 microns for these four samples ranged from .004 to .017 cm^{-1}. Thicknesses were 6 to 10 millimeters. Solid lines are 373°K data and dashed lines are 273°K data.

Figure 5 shows similar data for a 6.64 millimeter thick sample of KBr. The bands are quite similar to those observed in the KCℓ samples, suggesting that they are caused by bulk impurities or surface contamination rather than multiphonons.

Data for a 6.4 millimeter CdTe sample is given in figure 6. Notice the increase in absorption coefficient at the lower temperature. A thin (1.74 millimeter) specimen of ZnSe is shown in figure 7. This sample exhibits no appreciable temperature dependence.

Figures 8 and 9 present data for two thicknesses of $ZnSe_xTe_{1-x}$ from the same boule. These samples have a high absorption coefficient. The bands are much stronger in the thinner sample, indicating that they are due to surface rather than bulk absorption.

A second group of KCℓ samples were recently submitted by AFCRL and some of the results are included here. Figure 10 shows the absorption coefficient of a specimen approximately 15 millimeters thick at 373°K. The bands are much lower than in the earlier KCℓ samples. Figure 11 shows data from another KCℓ sample at 373°K, this one 10 millimeters thick. In order to separate the surface and bulk absorptions, a sample 5 millimeters thick from the same boule and with the same surface treatment was measured. From these measurements the bulk absorption coefficient shown in figure 12 was calculated. The bands are still present, indicating that they are due at least in part to a bulk absorption process.

1. Reference

[1] Spectral Emittance Techniques and Measurements, D. L. Stierwalt, Conf. on High Power Infrared Laser Window Materials, Hyannis, Mass., 1972.

2. Figures

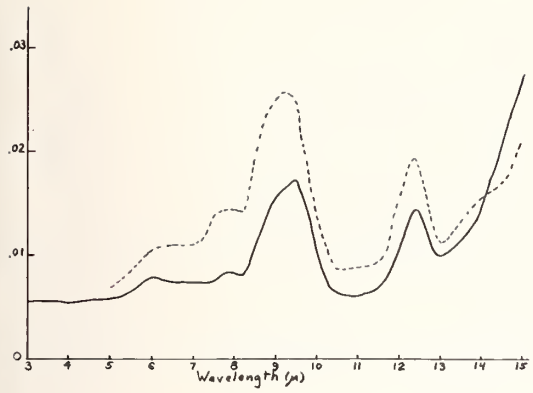

Figure 1. Absorption Coefficient of KCℓ, LQ-121 at 273°K and 373°K.

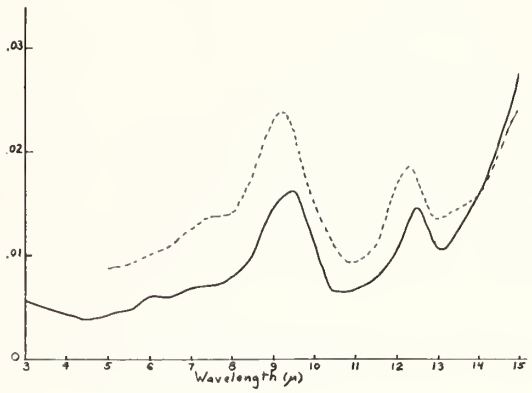

Figure 2. Absorption Coefficient of KCℓ, LQ-122 at 273°K and 373°K.

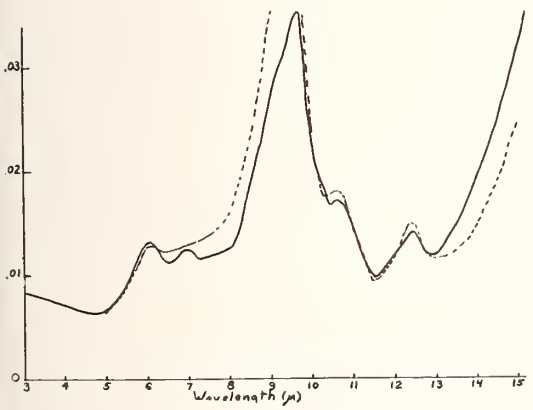

Figure 3. Absorption Coefficient of KCℓ, LQ-120 at 273°K and 373°K.

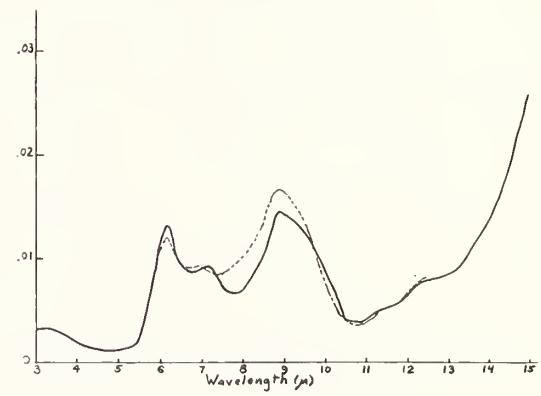

Figure 4. Absorption Coefficient of KCℓ, LQ-90 at 273°K and 373°K.

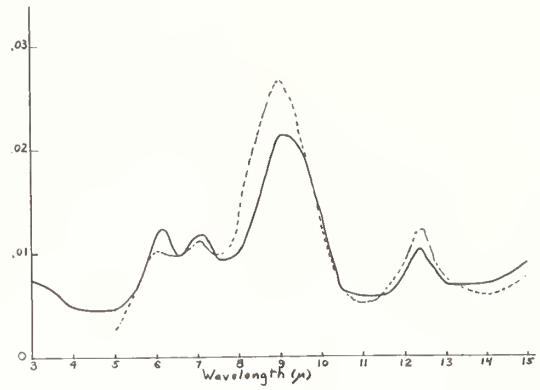

Figure 5. Absorption Coefficient of KBr at 373°K and 273°K.

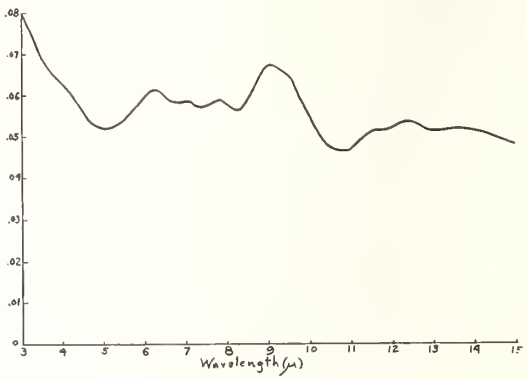

Figure 6. Absorption Coefficient of CdTe

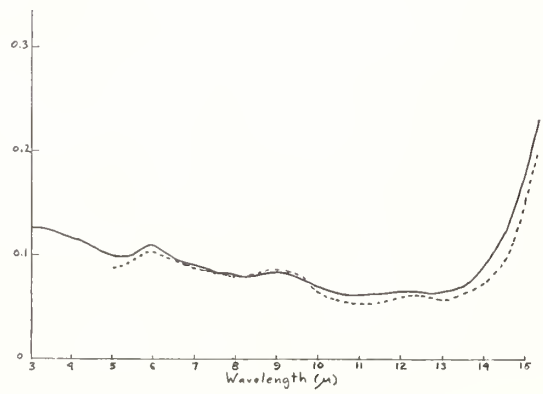

Figure 7. Absorption Coefficient of ZnSe at 373°K and 273°K.

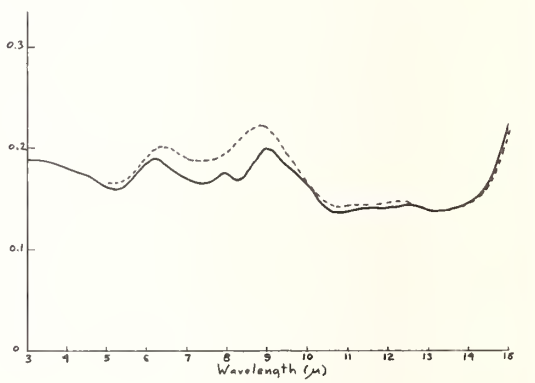

Figure 8. Absorption Coefficient of $ZnSe_xTe_{1-x}$ at 273°K and 373°K where d = 0.79mm.

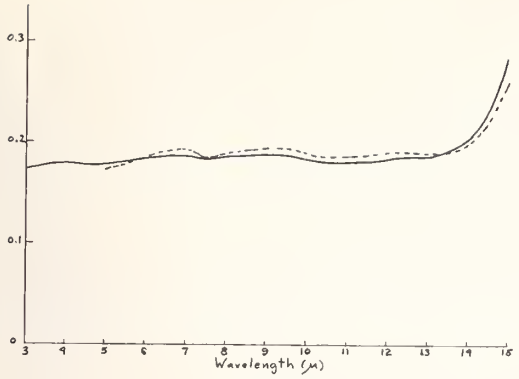

Figure 9. Absorption Coefficient of $ZnSe_xTe_{1-x}$ at 273°K and 373°K where d = 5.90mm.

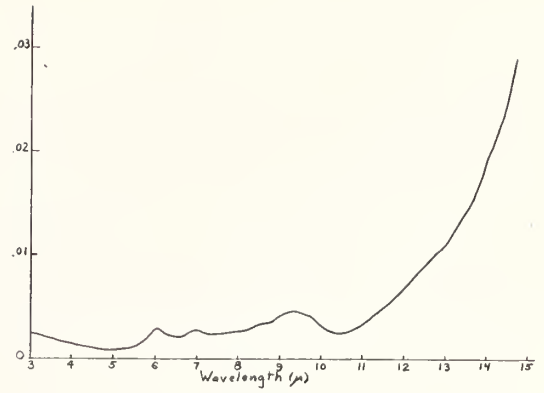

Figure 10. Absorption Coefficient of KCℓ, LQ-279.

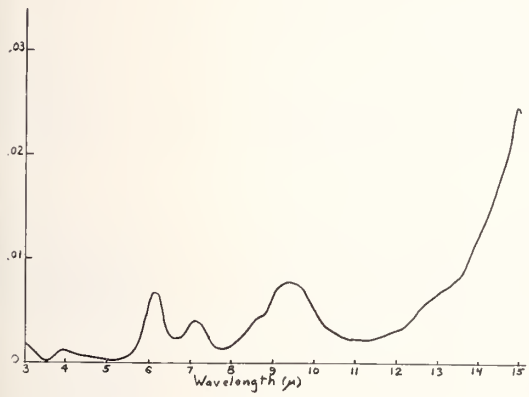

Figure 11. Absorption Coefficient of KCℓ, LQ-280.

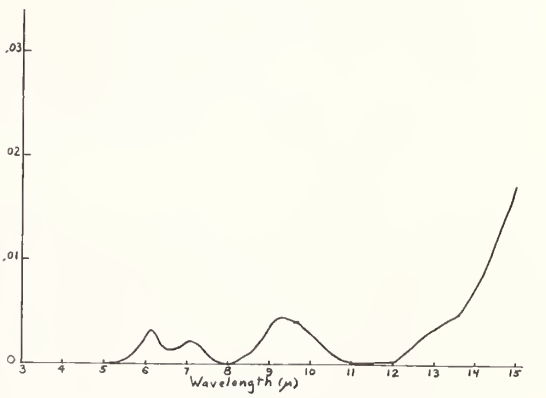

Figure 12. Bulk absorption coefficient of KCℓ derived from emittance measurements of two thicknesses of LQ-280.

COMMENTS ON PAPER BY STIERWALT

The speaker was asked if he would propose any theoretical reason why the absorption in potassium chloride would seem to increase with decreasing temperature. He was not inclined to speculate on the source of this variation. He further commented that some of the data obtained on semiconductor material also showed significant temperature dependence. In response to a question concerning the precision, accuracy, and resolution of the instrument, the speaker indicated that the precision in determining the absorption constant (in reciprocal centimeters) was approximately 2×10^{-4}. The accuracy was somewhat less well defined, with an uncertainty of about 5×10^{-4}, due to base line variation. The resolution of the instrument was quoted to be 0.25 micrometers at 10.6 micrometers, 0.3 micrometers at 5 micrometers, and 0.5 micrometers at 3 micrometers. The question was raised concerning the surface polishing of the samples that were used in this study. The samples had been provided by the Air Force Cambridge Research Laboratory. Representatives of that laboratory indicated that they had observed a significant variation in the absorption in samples with varying degrees of care exercised in surface finishing. They indicated that the samples supplied to the speaker late in the study were finished with considerable care. It was also commented that calorimetric checks are presently underway at the Air Force Cambridge Research Laboratories to confirm the results presented by the speaker.

A Sensitive Interferometric Null Method for Measuring Stress-Induced Birefringence

George Birnbaum and Earl Cory

Rockwell International Science Center
Thousand Oaks, California 91360

A sensitive apparatus for measuring induced birefringence utilizing a scanning Fabry-Perot interferometer excited by circularly polarized laser radiation has been developed. Because of birefringence in the sample located within the interferometer, its resonance wavelengths for radiation polarized parallel and perpendicular to the direction of applied stress are different. The voltage on a Kerr cell properly oriented within the interferometer is adjusted to cancel the sample birefringence. The wavelength difference is observed by using the scanning interferometer as a spectrum analyzer and comparing the resonance curves associated with each polarization. The stress-induced birefringence in YAG, sapphire and fused silica at 0.633μ in the temperature range 26 to 75°C has been measured.

Key Words: Birefringence, fused silica, optical spectrum analyzer, photoelastic effect, sapphire, scanning Fabry-Perot interferometer, and YAG.

1. Introduction

Stress-induced birefringence in solids has been studied for many years and a variety of methods have been developed to investigate this effect. [1,2][1] We present here a brief description of a new method for measuring birefringence employing a scanning Fabry-Perot interferometer in which a Kerr cell is placed to cancel the sample birefringence. Because of the long optical paths through the sample and Kerr cell by virtue of the multiply reflected radiation within the interferometer, and the use of a null measurement technique, a sensitive instrument was achieved. The results of measurements on YAG, sapphire and fused silica at 0.633 μm in the temperature range 26 to 75° C are discussed.

2. Description of the Apparatus

The arrangement of the various components of the apparatus is shown schematically in figure 1. Collimated radiation from a stabilized He-Ne laser passes through a polarizer and quarter-wave plate which acts as an isolator to reduce the coupling between the laser and a scanning Fabry-Perot interferometer. The radiation leaving the isolator is circularly polarized and consists of components differing in phase by $\pi/4$ and polarized in the $\parallel$ and $\perp$ directions, the former being along the direction of the applied stress. This radiation excites two modes with $\parallel$ and $\perp$ polarizations when the resonance frequency of each mode is equal to the laser frequency. This is accomplished by periodically moving an interferometer mirror at constant velocity with a piezoelectric element, thereby amplitude modulating the radiation by the resonance characteristic of the interferometer. [3] The $\parallel$- and $\perp$-polarized radiation leaving the interferometer is separated into two beams by a polarizing beam splitter. When each of these beams is detected by a photodiode, amplified and applied to an oscilloscope whose sweep is synchronized with the mirror drive, the resonance curves of the two interferometer modes are displayed. In practice the resonance pulses are sharpened, differentiated, amplified to saturation, and their difference is observed on the oscilloscope. A Kerr cell within the interferometer is oriented to produce a birefringence cancelling that produced by the stressed specimen. The voltage on the Kerr cell is adjusted to bring the two resonance pulses into coincidence and thereby obtain a null signal on the oscilloscope.

By measuring the width of the resonance curve with and without the sample in the interferometer, the loss in the sample may be determined. [4] The instrument was not used this way, although it was valuable to monitor the width of the resonance pulses (figure 2) in aligning the interferometer and sample since minimum width or lowest loss was indicative of proper alignment.

[1] Figures in brackets indicate the literture references at the end of this paper.

The load on the sample was supplied by an Ohaus 20 kg balance modified to exert pressure on a vertical shaft attached to the sample as illustrated in figure 3. The balance was securely mounted to a milling machine cross and vertical feed which was useful for positioning the sample in the interferometer with respect to the laser beam. In the present investigation the laser beam was approximately centered on the face of the sample. A block was attached to the balance platform with a hole to accomodate an $A\ell_2O_3$ post. Upright posts were attached to the balance base and a backing bar. By sandwiching the sample between the $A\ell_2O_3$ posts, stress could be applied to the sample by loading the balance with weights. The backing block could be rotated by a lever to align the sample so that the light beam was incident normally on it.

The sample was pressed into copper blocks at each end, and to improve the fit, tin foil was placed in the depression provided for the sample. A steel ball bearing was seated between the copper block attached to the sample and a copper block attached to the end of the $A\ell_2O_3$ post to ensure that the axis of the posts and specimens coincided. The oven for heating the sample (figure 3) also enclosed the copper blocks and ball bearings.

3. Theory of Measuring Birefringence

The resonance wavelength for the $\parallel$- and $\perp$-polarized modes will be equal and coincide in time as the interferometer is scanned if the relative path retardations in the sample and Kerr cell cancel, namely,

$$\ell(\Delta n_o + \Delta n) + \ell'\Delta n' = 0 \quad , \tag{1}$$

where ℓ is the sample length, Δn_o and Δn are its residual and induced birefringence, respectively, ℓ' is the length of the Kerr cell and $\Delta n'$ its birefringence. The birefringence induced in the Kerr cell by an applied voltage V is given by

$$\Delta n' = KV^2 \quad , \tag{2}$$

where K is a constant for a given wavelength, cell geometry and fluid. Because of the latter, however, K is not only a function of temperature, but may vary in an unpredictable way because of impurities which remain even after purification and appear after repeated use of the cell. [5] To circumvent these problems K is determined by adjusting the Kerr cell voltage, V_o, so that the $\parallel$ and $\perp$ resonances are displaced by exactly one order. This is obtained when

$$\ell'\Delta n' = \lambda_o/2 \quad , \tag{3}$$

where λ_o is the wavelength of the radiation in vacuum. Equations (2) and (3) determine K and with this result (1) becomes

$$\ell(\Delta n_o + \Delta n) = -(\lambda_o/2\ell)(V/V_o)^2 \quad . \tag{4}$$

If Δn is due to the application of a stress $\sigma(dyn/cm^2)$ then

$$\Delta n = n_\parallel - n_\perp = C\sigma_\parallel \quad , \tag{5}$$

where C is the relative stress-optic coefficient in cm^2/dyn.

4. Experimental Results

Commercial sources supplied samples of YAG, sapphire and fused silica very accurately fabricated in the form of parallelepipeds approximately 0.5 cm in width and breadth and 1.5 cm in length, the direction of the applied stress. The sapphire sample was oriented with the C-axis perpendicular to the faces transmitting the laser beam. For this geometry the natural birefringence of sapphire, a trigonal crystal, does not appear. The sample of YAG, which is cubic, was oriented with the (100) plane parallel to one of the faces. The surfaces perpendicular to the direction of stress and light have multilayer dielectric coatings and reflect less than 0.25 percent radiation of this wavelength at $0.633\mu m$

Typical plots of V^2, where V is the voltage on the Kerr cell, versus the sample load in kg are shown in figure 4. By substituting the intercept and slope obtained from such plots in (4) with $V_o^2 = 1.4147\times10^8$, we obtain the values of Δn_o and C given in table 1. The errors are rms values and represent the precision of the measurement. Since the method of rotating the sample about an axis parallel to the long face did not allow sufficiently precise control, it was not possible to obtain reproducible values for the residual birefringence in sapphire. The value in table 1 was the lowest obtained. This lack of precision in aligning the sample was not important with the isotropic materials.

Since the residual birefringence may vary appreciably in different regions of the sample, the values given in table 1 should not be taken as typical for the sample, but as indicative of the precision of the measurement. The ratios of Δn_o for YAG and sapphire to fused silica are comparable with similar ratios for C. The strain birefringence for T22 Suprasil-W1 is reported to be 0.5×10^{-6} whereas our value for a particular region of a given sample is 2×10^{-6}.

The accuracy of the results depends on the accuracy of measuring the birefringence and on the accuracy of applying and measuring a uniform stress. The former depends primarily on the assumption that the electric field in the Kerr cell averaged along the light path is directly proportional to the applied voltage. Fringing of this field should cause no error because the measurement depends on the ratio of voltages. However, the electrostatic field between high-voltage electrodes immersed in a dielectric fluid may become distorted by the presence of free charges in the liquid. [6] This matter was not investigated although the good agreement between the present results and other workers would indicate that it is not serious.

The balance system for applying stress was carefully aligned and it is believed that the stress applied to the sample was uniform and axial. However, by varying the loading in small steps above and below a given loading, hysteresis loops were obtained. Using such hysteresis data for fused silica we find that $\Delta n_o = (1.64 \pm 0.02)10^{-6}$ and $C = (3.535 \pm 0.003)10^{-13}\text{cm}^2/\text{dyn}$, which differ from the values in table 3 by amounts greater than the indicated precisions.

Table 1. Optical constants of YAG, sapphire and fused silica. The errors of the present results are rms values and are measures of the precision. Δn_o is the residual birefringence, and C is the stress-optic coefficient.

Material	Δn_o (10^{-6})	$C(10^{-13}\text{cm}^2/\text{dyn})$ Present	$C(10^{-13}\text{cm}^2\text{dyn})$ Other
YAG	0.252 ± 0.009	-0.523 ± 0.002[a]	-0.52[c]
Sapphire	0.74 ± 0.02	-1.546 ± 0.006[b]	-1.58[d]
Fused silica	1.92 ± 0.02	-3.554 ± 0.009[a]	-3.52[e]

[a] The values are an average of the results obtained at four temperatures between 26°C and 75°C.
[b] Measured at 35°C.
[c] Computed from the photoelastic constants p_{11} and p_{12} measured at room temperature with 0.63μ radiation by Dixon, R. W., J. Appl. Phys. 38, 5149 (1967).
[d] Waxler, R. M. and Farabaugh, E. N., J. Res. Nat. Bur. Stand. A 74, 215 (1970).
[e] Extrapolated to 0.6328 μm from measurements at 0.6440 μm and 0.5892 μm by Primak, W. and Post, D. J. Appl. Phys. 30, 779 (1959).

5. Summarizing Remarks

A new method for measuring birefringence and measurements of stress-induced birefringence in YAG, sapphire and fused silica have been presented. Despite the sensitivity of the method it proved to be convenient to use and reliable in its operation. The method used to stress the sample allows easy positioning of the sample with respect to the laser beam and should be useful in applications where measurements at different sample locations are required.

6. Acknowledgments

The authors thank Mr. K. Gow for discussions and suggestions on many aspects of the experimental design, Professor S. Geller for discussions on material properties, and Mr. P. Crandall for designing and assembling the system for applying stress.

7. References

[1] Coker, E. G. and Filon, L.N.G., Treatise on Photo-Elasticity, Cambridge University Press, London (1931).

[2] Krishnan, R. S., Progress in Crystal Physics, S. Viswanathan (1958).

[3] Hercher, M., Appl. Optics 7, 951 (1968).

[4] Rack, A. J. and Biazzo, M. R., B.S.T.J. 43, 1563 (1964).

[5] Cassidy, E. C. and Cones, H. N., J. Res. Nat. Bur. Stand. C 73, 5 (1969).

[6] Croitoru, Z., in Progress in Dielectrics 6, Birks, J. B. and Hart, J., editors, Academic Press, Inc., N.Y. pp. 103-146 (1965).

8. Figures

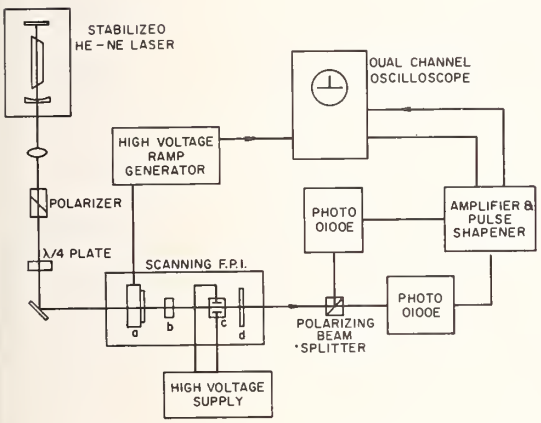

Figure 1. Schematic diagram of the optical and electronic arrangement of the apparatus. (a) piezoelectric ceramic element for translating attached mirror; (b) sample; (c) Kerr cell; and (d) interferometer mirror.

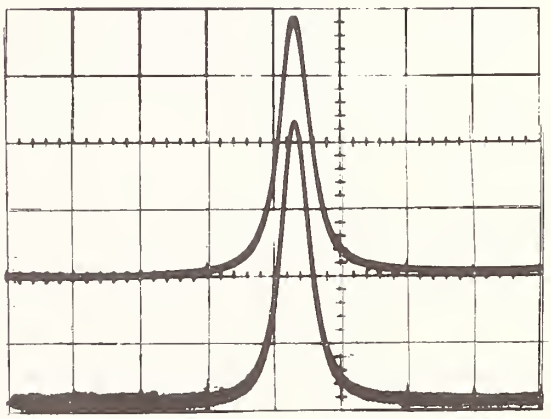

Figure 2. Interferometer resonance pulses of the parallel and perpendicularly polarized modes photographed on the oscilloscope. The resonance frequencies are nearly equal.

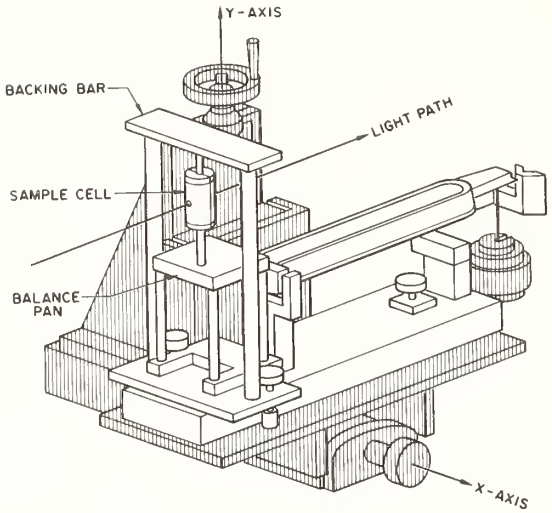

Figure 3. Schematic drawing illustrating the use of a balance to apply a load to a sample. The balance is mounted on milling machine feeds for positioning in two orthogonal directions. The sample is enclosed by an oven.

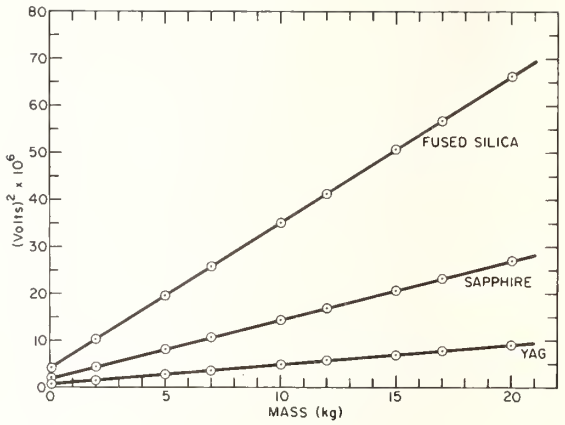

Figure 4. Plots of voltage squared versus the loading in kg for fused silica, sapphire, and YAG at 35°C. The intercepts at zero loading represent the residual birefringence.

COMMENTS ON PAPER BY BIRNBAUM

The speaker remarked that the technique is also applicable to the measurement of weak absorption. In particular, that it should be possible to measure absorptions of the order of a part per thousand by this method. The most sensitive method is to measure the amplitude of the transmitted peak of the Fabry-Perot spectrum. In the discussion, the question came up as to how one would distinguish losses due to scatter from losses due to true absorption. The only possible distinction seems to be the fact that absorption energy is removed in an absolute fashion from the light wave, whereas in scattering it is possibly coupled into other modes of the Fabry-Perot resonator. This would appear to be a difficult distinction to make experimentally, and therefore the technique would seem to be more applicable to the measurement of extinction rather than absorption.

Appendix

Participants

A

W. B. Alexander	Schott Optical Glass, Inc., 400 York Ave., Duryea PA 18642
N. Alyassini	Dept. of Physics, University of Southern California, Los Angeles CA 90007
L. J. Aplet	MS L-119, Hughes Aircraft Co., Culver City CA 90230
R. R. Austin	MS 405, Perkin-Elmer, Main Ave., Norwalk CT 06851

B

W. P. Barnes, Jr.	Optical Systems Div., Iteck Corp., 10 Maguire Rd., Lexington MA 02173
M. Bass	Research Div., Raytheon Co., 28 Seyon St., Waltham MA 02154
E. G. Bernal	Honeywell Research Center, 10701 Lyndale Ave., So. Bloomington MN 55420
B. Bendow	Air Force Cambridge Research Lab./LQS, Hanscom Field, Bedford MA 01730
H. E. Bennett	Michelson Lab., Code 6018, Naval Weapons Center, China Lake CA 93555
G. Birnbaum	Science Center, Rockwell International, 1049 Camino dos Rios, Thousand Oaks CA 91360
E. S. Bliss	Lawrence Livermore Lab./L-217, P. O. Box 808, Livermore CA 94550
N. L. Boling	Owens-Illinois, Inc., 1700 N. Westwood Ave., Toledo OH 43666
H. S. Boyne	Quantum Electronics Division, National Bureau of Standards, Boulder CO 80302
R. A. Bradbury	Air Force Cambridge Research Lab., Hanscom Field, Bedford MA 01730
P. F. Braunlich	Bendix Research Labs., Bendix Center, Southfield MI 48075
A. Braunstein	Hughes Research Labs., 3011 Malibu Canyon Rd., Malibu CA 90265
M. Braunstein	Hughes Research Labs., 3011 Malibu Canyon Rd., Malibu CA 90265
N. J. Brown	Lawrence Livermore Lab./L-140, P. O. Box 808, Livermore CA 94550
J. A. Bruce	Air Force Cambridge Research Lab./LQO, Hanscom Field, Cambridge MA 01730
P. Bryce	Dept. of Electrical Engineering, University of Alberta, Edmonton 7, Alberta, Canada

C

R. J. Carbone	Los Alamos Scientific Lab./TA-35, P. O. Box 1663, Los Alamos NM 87544
E. L. Church	SMUFA L4100-150-2, U.S. Army - Frankford Arsenal, Philadelphia PA 19137
D. R. Cohn	MIT National Magnetic Lab., 170 Albany St., Cambridge MA 02138
R. S. Cooper	Los Alamos Scientific Lab., P. O. Box 1663, Los Alamos NM 87544
H. S. Corey	Stop 2, Union Carbide, P. O. Box Y, Oak Ridge TN 37830
V. R. Costich	Coherent Radiation, 3210 Porter Dr., Palo Alto CA 94304
M. D. Crisp	Owens-Illinois, Inc., 1020 N. Westwood Ave., Toledo OH 43601
S. J. Cytron	U.S. Army - Frankford Arsenal, L-3200 Pitman-Dunn Lab., Philadelphia PA 19137

D

B. L. Danielson	Quantum Electronics Division, National Bureau of Standards, Boulder CO 80302
J. Davit	(Contributed paper - did not attend)
D. J. Dentz	Airtron, Div. of Litton Ind., 200 E. Hanover Ave., Morris Plains NJ 07950
L. G. DeShazor	Dept. of Physics, University of Southern California, Los Angeles CA 90007
J. Detrio	(Address unknown)
T. M. Donovan	Code 6018, Naval Weapons Center, China Lake CA 93555
R. Doussain	Laboratoire National d'Essais, 1, Rue Gaston Boisseir, Paris 15°, France
C. J. Duthler	Xonics, Inc., 6837 Hayvenhurst Ave., Van Nuys CA 91406

E

D. F. Edwards	Dept. of Electrical Engineering, Colorado State University, Fort Collins CO 80521

F

M. D. Feit	Lawrence Livermore Lab./L-71, P. O. Box 808, Livermore CA 94550
A. Feldman	Materials A-259, National Bureau of Standards, Washington DC 20234
J. R. Fenter	Air Force Materials Lab./LPL, Wright-Patterson AFB OH 45433
J. A. Fleck	Lawrence Livermore Lab./L-17, P. O. Box 808, Livermore CA 94550
R. C. Folweiler	Sanders Associates, Inc., MER 12-1220, 95 Canal St., Nashua NH 03060
H. Foster	Ministry of Defence, P. E., Services Electronics Res. Lab., Baldock, Herts., England
D. W. Fradin	Gordon McKay Lab., Harvard University, 9 Oxford St., Cambridge MA 02138
D. L. Franzen	Quantum Electronics Division, National Bureau of Standards, Boulder CO 80302
A. D. French	HMES - ADE, General Electric Co., Court Street Plant, Syracuse NY 13102

G

J. Giuliani	Code 6552, Naval Research Lab., 4555 Overlook Ave., Washington DC 20390
C. R. Giuliano	Hughes Research Labs., 3011 Malibu Canyon Rd., Malibu CA 90265
A. J. Glass	Lawrence Livermore Lab./L-215, P. O. Box 808, Livermore CA 94550
A. T. Glassman	Lawrence Livermore Lab./L-140, P. O. Box 808, Livermore CA 94550
L. M. Goldman	Laboratory for Laser Energetics, University of Rochester, Rochester NY 14527
J. W. Greene	Lawrence Livermore Lab./L-71, P. O. Box 808, Livermore CA 94550
A. H. Guenther	Air Force Weapons Lab./DYD, Kirtland AFB NM 87117
J. C. Guyot	Laboratoires de Marcoussis, Route de Nozay 91, Marcoussis, France

H

Y. H. Hahn	CVI Laser Corp., 200 Dorado Pl., Albuquerque NM 87123
F. T. Harris	Raytheon, 4 Standish Circle, Andover MA 01810
W. B. Harrison	Honeywell, Inc., 1885 N. Douglas Dr., Golden Valley MN 55422
R. W. Hellwarth	Dept. of Physics, University of Southern California, Los Angeles CA 90007
G. L. Hennessey	Optical Coating Div., Valpey Corp., Holliston MA 01746
L. M. Hobrock	Optics Dept., Hughes Aircraft Co., Culver City CA 90230
S. J. Holmes	Northrop, 3401 W. Broadway, Hawthorne CA 90250
D. T. Hon	Hughes Aircraft Co., Culver City CA 90230
D. Horowitz	Materials A-259, National Bureau of Standards, Washington DC 20234
F. A. Horrigan	Research Div., Raytheon, 28 Seyon St., Waltham MA 02154
R. H. Hoskins	Apollo Lasers, 6357 Arizona Cr., Los Angeles CA 90045
R. A. House II	Air Force Weapons Lab./DYX, Kirtland AFB NM 87117
J. E. Howard	KMS Fusion, Inc., P. O. Box 1567, 3941 Research Park Dr., Ann Arbor MI 48106

I

J

L. E. Jenkins	Code 6041, Naval Weapons Center, China Lake CA 93555
G. Johnston	(Address unknown)
E. D. Jones	Div 5214, Sandia Labs., P. O. Box 5800, Albuquerque NM 87115

K

E. L. Kerr	MS 283, Perkin-Elmer, Main Ave., Norwalk CT 06852
J. M. Khan	Lawrence Livermore Lab./L-503, P. O. Box 808, Livermore CA 94550
P. Kraatz	Northrop, 3401 W. Broadway, Hawthorne CA 90250
J. R. Kurdock	MS 420, Perkin-Elmer Corp., 77 Danbury Rd., Wilton CT 06897

L

J. A. Lancelot	C. E. A. Limeil, BP 27, Villeneuve 1'Georges 94, France
G. D. Lassahn	Dow Chemical Co., P. O. Box 888, Golden CO 80401
H. A. Lee	Owens-Illinois, Inc., Laser Products, P. O. Box 1035, Toledo OH 43666
K. M. Leung	Center for Laser Studies, University of Southern California, Los Angeles CA 90007
J. P. Letellier	Code 6540, Naval Research Lab., Washington DC 20375
H. G. Lipson	Air Force Cambridge Lab./LQS, Hanscom Field, Bedford MA 01730
G. M. Loiacono	Isomet Corp., 103 Bauer Dr., Oakland NJ 07436
J. S. Loomis	Air Force Weapons Lab./LRE, Kirtland AFB NM 87117
J. E. Lowder	Optics Div., MIT Lincoln Lab./L-109, 244 Wood St., Lexington MA 02173

M

P. Mace — Los Alamos Scientific Lab., P. O. Box 1663, Los Alamos NM 87544
R. W. MacPherson — CRDV/DREV, Electronics Div., P. O. Box 880, Courcelette, Quebec, Canada
R. P. Madden — A-247 Physics Bldg., National Bureau of Standards, Washington DC 20234
I. H. Maltison — A-251, National Bureau of Standards, Washington DC 20234
J. H. Marburger — Dept. of Physics, University of Southern California, Los Angeles CA 90007
P. S. McLeod — Optical Coatings R/E 991, Dow Chemical Co., P. O. Box 888, Golden CO 80401
D. Milam — Laser Physics Branch, Air Force Cambridge Res. Lab., Hanscom Field, Bedford MA 01730
D. W. Morelli — Optical Coatings Lab., Inc., 2789 Giffen Ave.,. Santa Rosa CA 95403
L. P. Mott — Optical Coatings Lab., Inc., 2789 Giffen Ave., Santa Rosa CA 95403

N

B. E. Newnam — Los Alamos Scientific Lab./L-2, P. O. Box 1663, Los Alamos NM 87544

O

A. Owyoung - Div. 5214, Sandia Labs., Albuquerque NM 87115

P

H. Posen — Air Force Cambridge Res. Lab./LQO, Hanscom Field, Bedford MA 01730

Q -

R

S. Refermat — Laser Energy, Inc., 320 N. Washington St., Rochester NY 14625
V. Rehn — Code 6013, Naval Weapons Center, China Lake CA 93555
W. H. Reichelt — Los Alamos Scientific Lab./L-1, P. O. Box 1663, Los Alamos NM 87544
C. W. Reimann — A-537, National Bureau of Standards, Washington DC 20234
P. M. Rushworth — MP 276, Martin-Marietta Corp., P. O. Box 5837, Orlando FL 32805

S

T. T. Saito — Air Force Weapons Lab./LRE, Kirtland AFB NM 87117
G. T. Schappert — Los Alamos Scientific Lab./L-1, P. O. Box 1663, Los Alamos NM 87544
R. A. Shatas — (Contributed paper - did not attend)
C. Y. She — Dept. of Physics, Colorado State University, Fort Collins CO 80521
R. E. Sladky — Union Carbide Nuclear, Y-12 Plant, Bldg. 9203, Oak Ridge TN 37830
A. F. Slomba — Perkins-Elmer Corp., MS 416, 77 Danbury Rd., Wilton CT 06897
J. L. Smith — U.S. Army - Redstone Arsenal, AMSMI-RRD, Redstone Arsenal AL 35809
R. L. Smith — Quantum Electronics Division, National Bureau of Standards, Boulder CO 80302
M. J. Soileau — Code 6018, Naval Weapons Center, China Lake CA 93555
M. Sparks — (Contributed paper - did not attend)
W. J. Spawr — Spawr Optical Research, 130 N. Sherman Ave., Corona CA 91720
K. B. Steinbruegge — Research Labs., Westinghouse Electric Corp., Pittsburgh PA 15235
C. M. Stickley — Materials Sciences Office, Advanced Research Projects Agency, 1400 Wilson Blvd., Arlington VA 22209
D. L. Stierwalt — Code 2600, Naval Electronics Lab. Center, 271 Catalina Blvd., San Diego CA 92152
J. C. Stover — Mech R&D, Bldg. 881, Dow Chemical Co., P. O. Box 888, Golden CO 80401
D. L. Sullivan — MS B-156, Hughes Aircraft Co., Culver City CA 90230
B. R. Suydam — Los Alamos Scientific Lab./T-6, P. O. Box 1663, Los Alamos NM 87544
H. F. Swift — Research Institute, University of Dayton, 300 College Park Ave., Dayton OH 45469

T

J. H. Tillotson — KMS Fusion, Inc., P. O. Box 1567, 3941 Research Park Dr., Ann Arbor MI 48106

U -

V

T. V. Vorburger — A-251 Physics, National Bureau of Standards, Washington DC 20234

W

J. J. Walls Jr.	U.S. Army - Frankford Arsenal, N5300 - Bldg. 201-2, Philadelphia PA 19137
V. Wang	Hughes Research Lab., 3011 Malibu Canyon Rd., Malibu CA 90265
R. Webb	Materials Research Center, Allied Chemical Corp., P. O. Box 1021-R, Morristown NJ 07960
E. D. West	Quantum Electronics Division, National Bureau of Standards, Boulder CO 80302
R. V. Wick	Air Force Weapons Lab./ABQ, Kirtland AFB NM 87117
C. B. Willingham	Research Division, Raytheon, Waltham MA 02154

X -

Y -

Z -

☆ U. S. GOVERNMENT PRINTING OFFICE :1973--542-652/101

FORM NBS-114A (1-71)

U.S. DEPT. OF COMM. BIBLIOGRAPHIC DATA SHEET	1. PUBLICATION OR REPORT NO. NBS-SP-387	2. Gov't Accession No.	3. Recipient's Accession No.

4. TITLE AND SUBTITLE

Laser Induced Damage in Optical Materials: 1973

5. Publication Date: November 1973

6. Performing Organization Code

7. AUTHOR(S) Various: Edited by Alexander J. Glass, Lawrence Livermore Labs., and Arthur H. Guenther, Kirtland AFB NM

8. Performing Organization

9. PERFORMING ORGANIZATION NAME AND ADDRESS

NATIONAL BUREAU OF STANDARDS, Boulder Labs.
DEPARTMENT OF COMMERCE
Boulder, Colorado 80302

10. Project/Task/Work Unit No. 2710900/2710569/2712585

11. Contract/Grant No.

12. Sponsoring Organization Name and Address

Naval Research Laboratory,
American Society for Testing and Materials, and
National Bureau of Standards (Div 271, Boulder CO)

13. Type of Report & Period Covered: Final

14. Sponsoring Agency Code

15. SUPPLEMENTARY NOTES

16. ABSTRACT (A 200-word or less factual summary of most significant information. If document includes a significant bibliography or literature survey, mention it here.)

The Fifth ASTM-ONR-NBS Symposium on Laser Induced Damage in Optical Materials was held at the National Bureau of Standards in Boulder, Colorado on May 15 and 16 of this year. These Symposia are held as part of the activities of Subcommittee II on Lasers and Laser Materials, of the ASTM. Subcommittee II is charged with the responsibilities of formulating standards and test procedures for laser materials, components, and devices. The chairman of Subcommittee II is Haynes Lee, of Owens-Illinois, Inc. Co-chairmen for the Damage Symposia are Dr. Arthur H. Guenther, Scientific Director, Technology Division of the Air Force Weapons Laboratory, and Dr. Alexander J. Glass, Head, Basic Studies, Y Division, Lawrence Livermore Laboratory.

Approximately 135 attendees at the Symposium heard 25 papers on topics relating to laser induced damage in crystalline and non-linear optical materials, at dielectric surfaces, and in thin film coatings as well as discussions on damage problems in the infrared region due both to cw and pulsed irradiation. In addition, several reports on the theoretical analysis of laser-materials interaction, relative to the damage process were given, along with tabulations of fundamental materials properties of importance in evaluation of optical material response to high power laser radiation. Several papers presented by title only are included within the proceedings for completeness.

The proceedings of these Symposia represent the major sources of information in the field of laser induced damage in optical materials. The Symposia themselves, along with the periodic meetings of Subcommittee II, provide a unique forum for the exchange of information regarding laser materials specifications among the manufacturers and users of laser devices, components, and systems. The Symposia also serve as a mechanism of information gathering to enable the Subcommittee to write informed and realistic specifications.

IR windows and mirrors; laser damage; laser materials; self-focusing; thin films.

18. AVAILABILITY STATEMENT	19. SECURITY CLASS (THIS REPORT)	21. NO. OF PAGES
[X] UNLIMITED.	UNCLASSIFIED	285
[ ] FOR OFFICIAL DISTRIBUTION. DO NOT RELEASE TO NTIS.	20. SECURITY CLASS (THIS PAGE) UNCLASSIFIED	22. Price $2.65

USCOMM-DC 66244-P71

NBS TECHNICAL PUBLICATIONS

PERIODICALS

JOURNAL OF RESEARCH reports National Bureau of Standards research and development in physics, mathematics, and chemistry. Comprehensive scientific papers give complete details of the work, including laboratory data, experimental procedures, and theoretical and mathematical analyses. Illustrated with photographs, drawings, and charts. Includes listings of other NBS papers as issued.

Published in two sections, available separately:

- **Physics and Chemistry (Section A)**

Papers of interest primarily to scientists working in these fields. This section covers a broad range of physical and chemical research, with major emphasis on standards of physical measurement, fundamental constants, and properties of matter. Issued six times a year. Annual subscription: Domestic, $17.00; Foreign, $21.25.

- **Mathematical Sciences (Section B)**

Studies and compilations designed mainly for the mathematician and theoretical physicist. Topics in mathematical statistics, theory of experiment design, numerical analysis, theoretical physics and chemistry, logical design and programming of computers and computer systems. Short numerical tables. Issued quarterly. Annual subscription: Domestic, $9.00; Foreign, $11.25.

DIMENSIONS, NBS

The best single source of information concerning the Bureau's measurement, research, developmental, cooperative, and publication activities, this monthly publication is designed for the layman and also for the industry-oriented individual whose daily work involves intimate contact with science and technology —*for engineers, chemists, physicists, research managers, product-development managers, and company executives.* Annual subscription: Domestic, $6.50; Foreign, $8.25.

NONPERIODICALS

Applied Mathematics Series. Mathematical tables, manuals, and studies.

Building Science Series. Research results, test methods, and performance criteria of building materials, components, systems, and structures.

Handbooks. Recommended codes of engineering and industrial practice (including safety codes) developed in cooperation with interested industries, professional organizations, and regulatory bodies.

Special Publications. Proceedings of NBS conferences, bibliographies, annual reports, wall charts, pamphlets, etc.

Monographs. Major contributions to the technical literature on various subjects related to the Bureau's scientific and technical activities.

National Standard Reference Data Series. NSRDS provides quantitative data on the physical and chemical properties of materials, compiled from the world's literature and critically evaluated.

Product Standards. Provide requirements for sizes, types, quality, and methods for testing various industrial products. These standards are developed cooperatively with interested Government and industry groups and provide the basis for common understanding of product characteristics for both buyers and sellers. Their use is voluntary.

Technical Notes. This series consists of communications and reports (covering both other-agency and NBS-sponsored work) of limited or transitory interest.

Federal Information Processing Standards Publications. This series is the official publication within the Federal Government for information on standards adopted and promulgated under the Public Law 89–306, and Bureau of the Budget Circular A–86 entitled, Standardization of Data Elements and Codes in Data Systems.

Consumer Information Series. Practical information, based on NBS research and experience, covering areas of interest to the consumer. Easily understandable language and illustrations provide useful background knowledge for shopping in today's technological marketplace.

BIBLIOGRAPHIC SUBSCRIPTION SERVICES

The following current-awareness and literature-survey bibliographies are issued periodically by the Bureau:

Cryogenic Data Center Current Awareness Service (Publications and Reports of Interest in Cryogenics). A literature survey issued weekly. Annual subscription: Domestic, $20.00; foreign, $25.00.

Liquefied Natural Gas. A literature survey issued quarterly. Annual subscription: $20.00.

Superconducting Devices and Materials. A literature survey issued quarterly. Annual subscription: $20.00. Send subscription orders and remittances for the preceding bibliographic services to the U.S. Department of Commerce, National Technical Information Service, Springfield, Va. 22151.

Electromagnetic Metrology Current Awareness Service (Abstracts of Selected Articles on Measurement Techniques and Standards of Electromagnetic Quantities from D-C to Millimeter-Wave Frequencies). Issued monthly. Annual subscription: $100.00 (Special rates for multi-subscriptions). Send subscription order and remittance to the Electromagnetic Metrology Information Center, Electromagnetics Division, National Bureau of Standards, Boulder, Colo. 80302.

Order NBS publications (except Bibliographic Subscription Services) from: Superintendent of Documents, Government Printing Office, Washington, D.C. 20402.

U.S. DEPARTMENT OF COMMERCE
National Bureau of Standards
Washington, D.C. 20234